AGEING AND AXIAL CYCLIC LOADING STUDIES OF DISPLACEMENT PILES IN SANDS

By

Siya Paul Rimoy

A thesis submitted to Imperial College London
in partial fulfilment for the degree of Doctor of Philosophy
and Diploma of Imperial College London

Department of Civil and Environmental Engineering

May 2013

Abstract

An investigation is presented into the mechanisms governing both the ageing and axial cyclic loading characteristics of displacement piles in silica sands.

The thesis considers first the state–of–knowledge regarding the axial capacity of displacement piles in silica sands. Three main areas of uncertainty are identified; the stress regime setup by installation, the mechanisms of ageing that lead to capacity increases with time (set-up), and the effects of axial cyclic loading.

New laboratory experiments are then described that involved tests with extensively instrumented 36mm diameter Mini-Imperial College Piles (Mini-ICP) with roughened (R_{cla} ~3.5μm) stainless steel shafts and 60^0 conical tip bases, that could measure axial loads, and interface radial and shear stresses at multiple positions along their shafts. Less extensively instrumented piles with varying diameters were also tested. Ten installations were made in the 1.2m diameter, 1.5m deep Grenoble–INP calibration chamber. Fresh pluviated sand masses were formed for each installation, which were typically instrumented with multiple commercially sourced (Kyowa and TML) miniature sensors to measure radial, vertical and circumferential stresses in the sand mass during pile installation, ageing, and axial static and cyclic loading tests. Key parameters that might affect pile behaviour were then isolated and considered in turn.

The interpretation links the model tests to instrumented field studies and the ageing trends established from a field database. The model piles' axial cyclic loading responses are analysed by developing cyclic interaction diagrams which are linked to full scale tests and laboratory experiments to identify the key mechanisms governing field cyclic behaviour. The interaction diagrams provide a straight-forward screening tool for addressing axial cyclic loading in practice. Reference is made to more elaborate procedures and to the experiments' scope for validating numerical models.

Declaration

The work presented in this thesis was carried out in the Geotechnics section of the Department of Civil and Environmental Engineering at Imperial College London, and in the 3S-R Laboratory at Grenoble-INP from September 2009.

This thesis is the result of my own work, and any quotation from, or description of the work of others is acknowledged herein by reference to the sources, whether published or unpublished.

This thesis is not the same as any that I have submitted for any degree, diploma or other qualification at any other university.

London. May, 2013.

Table of contents

Abstract 2
Declaration 3
Table of contents 4
Acknowledgements 10
Notations & Abbreviations 11
Chapter 1 17
1 Introduction 17
1.1 Introduction 17
1.2 Background to the study 17
1.2.1 The axial capacity of displacement piles in sands 17
1.2.2 Pile ageing and axial cyclic behaviour 19
1.3 Motivation of the study 21
1.4 Study objectives and research methodology 22
1.5 Organisation of thesis 23
Chapter 2 27
2 Axial static capacity of single displacement piles in silica sands 27
2.1 Introduction 27
2.2 Pile load testing in practice 27
2.3 Pile end-bearing resistance 28
2.4 Factors affecting base resistance interpretations 34
2.5 Pile shaft resistance 38
2.6 Installation cyclic loading effects on shaft resistance 48
2.7 Variants of the CPT–based ICP-05 method 54
2.8 Predictive reliability of the modern CPT-based design methods 57
2.9 Summary and conclusions 64
Chapter 3 65
3 Ageing behaviour of axial capacity of displacement piles in sands 65
3.1 Introduction 65
3.2 Hypothesized mechanisms 65
3.3 Load test case studies involving aged piles 69
3.4 Assessment of the database 78
3.5 Concluding remarks on load testing of aged piles 81
Chapter 4 88
4 Axial cyclic loading behaviour of single displacement piles in sands 88

4.1 Introduction 88
4.2 Current practice 88
4.3 Axial cyclic loading field studies 91
4.4 Laboratory model pile studies 93
4.5 Characterisation of pile interface behaviour 102
4.6 Summary conclusions 104
Chapter 5 106
5 Apparatus and its principles 106
5.1 Introduction 106
5.2 The Grenoble–INP 3S-R Laboratory Calibration Chamber 106
5.2.1 Background 106
5.2.2 Calibration chamber features and application to the study 108
5.2.2.1 Background 108
5.2.2.2 Calibration chamber boundary conditions 110
5.2.2.3 Calibration chamber temperature control 112
5.2.2.4 Miniature sand stress sensors 112
5.2.2.5 Pile installation and loading apparatus 113
5.3 Sand Stress Sensors features and calibration 113
5.3.1 SSS features and application to the study 113
5.3.2 SSS calibrations 117
5.4 Other instrumentation installed in the CC 121
5.5 Mini Imperial College Pile (Mini–ICP) 122
5.5.1 Background 122
5.5.2 Mini–ICP features and application to this study 123
5.5.2.1 Axial Load Cells 123
5.5.2.2 Surface Stress Transducers (SST) 124
5.5.2.3 Printed Circuit Board (PCB) 125
5.5.3 Mini–ICP calibration 128
5.5.3.1 Transducers compliance 128
5.5.3.2 Calibration Procedure 129
5.5.4 Assembling of the Mini–ICP 133
5.6 Micro and driven piles 134
5.7 Ancillary apparatus 135
5.8 Tests control and data acquisition 136
5.9 Concluding remarks 136

Chapter 6 138
6 Test sands, preparation methods and experimental plan 138
6.1 Introduction 138
6.2 Description of test sands 138
6.2.1 Sourcing, index and physical properties 138
6.2.2 Rationale for test sand selection 140
6.3 Calibration chamber preparations 145
6.3.1 Introduction 145
6.3.2 Achieving in-situ states 145
6.3.3 3S-R calibration sand chambers pluviation procedures 146
6.4 Pile installation techniques 151
6.5 Interface sampling techniques 151
6.6 Test programme 152
6.7 Final remark – the pile modelling parameters 153
Chapter 7 158
7 Observations during laboratory model pile installation 158
7.1 Introduction 158
7.2 End bearing resistance 158
7.3 Pile shaft resistances 165
7.3.1 Shear stresses 165
7.3.2 Radial stresses 172
7.4 Stresses developed in the sand mass during pile installation 177
7.4.1 Stress measurements 177
7.4.2 Sand mass stress profiles along the Mini-ICP pile axis 179
7.4.3 Contouring the sand mass stresses around the Mini–ICP piles 185
7.4.4 Radial variation of radial stresses at fixed depths above Mini-ICP pile tip 192
7.5 Summary conclusions and remarks 195
Chapter 8 197
8 Mini-ICP tests stress measurements compared to other studies 197
8.1 Introduction 197
8.2 Comparison with closed–ended field displacement piles 197
8.3 Comparison with CC tests with closed-ended displacement piles 198
8.4 Comparison with CC experiments with open-ended model piles 199
8.5 Comparison with centrifuge closed-ended driven model piles 202
8.6 Comparison with Finite Element (FE) analyses 204

8.7 Comparison with Coupled Eulerian-Lagrangian (CEL) FE analyses 205
8.8 Comparison with FE analysis incorporating grain crushing 207
8.9 Summary remarks and conclusions 208
Chapter 9 209
9 Short term static axial load tests on laboratory model piles 209
9.1 Test programme 209
9.2 Pile axial load – displacement behaviour 209
9.2.1 EOD tests on Mini-ICP piles in NE34 sand 211
9.2.2 EOD tests on all other piles 214
9.3 Effective stress paths followed at pile–sand interface 220
9.4 ICP-05 predictions of the model piles short term static axial capacities 224
9.5 Potential rate effects on pile resistance behaviour in sand 227
9.6 Summary conclusion 230
Chapter 10 231
10 Ageing behaviour of laboratory model displacement piles in sands 231
10.1 Introduction 231
10.2 Pile ageing 231
10.2.1 Tests programme 231
10.2.2 Stress and load behaviour of ageing model piles 234
10.2.2.1 'Standard' ageing test with the Mini-ICP in dry NE34 sand 234
10.2.2.2 Scale effects 238
10.2.2.3 Moisture effects 240
10.2.2.4 Calibration chamber boundary conditions 243
10.2.2.5 Effect of cyclically changing the boundary stresses 244
10.2.2.6 Ageing piles interface effective stress paths 251
10.3 Pile behaviour on static testing after ageing 253
10.4 Model piles aged capacity log-time trends 268
10.5 Implications from the ageing study 270
Chapter 11 272
11 Laboratory model piles behaviour under axial cyclic loading 272
11.1 Testing Programme 272
11.2 Styles of axial cyclic loading responses 273
11.3 Assessment of pile behaviours during the axial cyclic loading tests 277
11.4 Stability interaction diagram 290
11.5 Axial cyclic pile stiffness 293

11.6 Local stress mechanisms governing pile axial cyclic loading stability behaviour 297
11.7 Influence of boundary conditions on model piles cyclic loading behaviour 301
11.8 Proposed implications to design practice 306
11.9 Summary remarks and conclusions 307
Chapter 12 310
12 Re-analysis of axial cyclic loading response of full scale piles driven at Dunkirk . 310
12.1 Introduction 310
12.2 Scope of study 310
12.3 Scaling of tests 313
12.4 Test programme 313
12.5 Results and interpretation 315
12.5.1 Cyclic failure criteria 315
12.5.2 Pile axial cyclic stiffness 316
12.5.3 Accumulated cyclic displacements 323
12.5.4 Cyclic displacements 329
12.6 Summary and conclusions 330
Chapter 13 332
13 Conclusions, implications and recommendations 332
13.1 Introduction 332
13.2 Review of earlier studies 332
13.3 Laboratory model pile studies 334
13.4 Conclusions and implications from the laboratory and full scale studies 335
13.4.1 Stress and load observations during laboratory model piles installations 335
13.4.2 Laboratory model piles ageing and post-ageing static load tests 337
13.4.3 Laboratory model piles and full scale piles responses under axial cyclic loading .. 338
13.5 Recommendations for further studies 340
13.5.1 Towards establishing the mechanisms for pile ageing trends 340
13.5.2 Towards modelling installation and in-service cyclic loading effects 340
13.5.3 Further optimisation of calibrations chamber boundary conditions 341
13.5.4 Further characterisation of finer sands particle size scale effects 341
References 342
List of figures 356
List of tables 368
Appendices 370
I Appendix I – Tests sands data sheets 371

II Appendix II – Miniature sand stress sensors layout plans 373
III Appendix III – Sand mass stress measurements..... 378
IV Appendix IV – Pile–sand interface observations..... 395

Acknowledgements

The Author is grateful to the Commonwealth Scholarship through the University of Dar es Salaam, for funding the PhD study fees and subsistence, and to Engineering and Physical Science Research Council (EPSRC) UK, Health and Safety Executive (HSE), Shell (UK), Total (France), Imperial College and Grenoble–INP for their joint sponsorship of the experimental works, travels and stays at Grenoble.

The Author is most sincerely grateful to his supervisor, Professor Richard Jardine, for his keen interest in the study, and significant guidance during the experimental work and thesis writing. Individual thanks to Professor Pierre Foray, Matias Silva and Jean-Benoit Toni at Grenoble-INP working with whom has been invaluable to the Author's study. High appreciation is given to Steve Ackerley, Alan Bolsher and Graham Keefe for their extensive technical assistance to the study, and to John Baxter, Sue Feller and Fionualla Ni Dhonnabhain for their necessary administrative assistance. The guidance of Prof. Zhongxuan Yang, Dr. Christina Tsuha and Dr. Fatin Altuhafi at various stages of the project is also fully appreciated.

Special thanks to Clive Dalton, Robert Whittle, and all at Cambridge In-situ Ltd, for their extensive work on the Mini-ICP and assistance related to calibration works.

The Author is thankful for the encouragement received from fellow PhD researchers he worked parallel to at their research office; Dr. Reinhard Schütz, Dr. David Taborda, Dr. Aikaterini Tsiampousi, Dr. Konstantinos Giannopoulos, Antonio Pedro, Bo Han and Wenjie Cui.

Special thanks from the Author to colleagues at the Department of Transportation and Geotechnical Engineering of University of Dar es Salaam for their continuous well wishes.

Finally, the Author expresses heartfelt acknowledgements to his wife, Dorina; son and daughter, Aichi and Aika; dad and mum, Strato and Aggripina Mosha; brother, Baraka; his in-laws' family; relatives and friends; for their love, support and encouragement over the period of the study.

Notations & Abbreviations

English

a	Accumulated cyclic displacement
A	Pile cross-section area
A_b	Complete pile base area
A_p	Area of the pile circumscribed by the outside diameter
A_r	Pile base effective area ratio
$A_{rb,eff}$	Pile base final effective area ratio
AAU	Aalborg University
ALC	Axial Load Cell
ANSI	American National Standards Institute
API	American Petroleum Institute
B	Width of square piles
BC	Boundary Condition
BOR	Beginning of Re-strike
BRE	Building Research Establishment
CAPWAP	Case Pile Wave Analysis Program
CC	Calibration Chamber
CEM	Cavity Expansion Method
CNL	Constant Normal Load
CNS	Constant Normal Stiffness
CoV	Coefficient of Variation
CPT	Cone Penetrometer Test
C_u	Coefficient of uniformity
d	Sensor diaphragm diameter
d_c	Sensor diameter
d_{cyclic}	Cyclic displacement
$d_{chamber}$	Calibration chamber inner diameter
$d_{50\%}$	Sand particle effective size
D	Pile outer diameter
D_{CPT}	Standard CPT cone tip diameter (35.7mm)
D_i	Pile internal diameter
D_R	Relative density (Density index)
DNV	Det Norske Veritas
e_0	Initial voids ratio

E_{cell}	stress sensor diaphragm Young's modulus
E_p	Young's modulus
E_{soil}	Sand Young's modulus
EIOD	End of Initial Drive
EOD	End of Drive
EPSRC	Engineering and Physical Sciences Research Council UK
EURIPIDES	European Initiative on Piles in Dense Sands
f_s	CPT sleeve friction
FFR	Final Filling Ratio
G	Non-linear shear modulus
G_0	Small strain shear modulus
G_s	Specific gravity
GeoPIV	Geotechnical Particle Image Velocimetry
GOPAL	Grouted Offshore Piles for Alternating Loading
GWT	Ground Water Table
h	Axial (vertical) distance measured from the pile base
HSE	Health and Safety Executive UK
I_D	Density index
I_r	Rigidity index
IAC	Intact Ageing Capacity
ICM	Imperial College Method
ICP	Imperial College Pile
ID	Inner Diameter
IFR	Incremental Filling Ratio
ISO	International Organization for Standardization
JIP	Joint Industry Project
k_l	Pile axial cyclic load-displacement secant stiffness during loading
$k_{N=1}$	Pile axial cyclic load-displacement secant stiffness at 1st cycle
k_{Ref}	Pile initial reference load-displacement secant stiffness
k_u	Pile axial cyclic load-displacement secant stiffness during unloading
K_0	Coefficient of earth pressure at rest
K_f	Coefficient of earth pressure on the pile during axial static loading to failure
L	Pile embedded length
LVDT	Linear Variable Differential Transformer
MCC	Modified Cam Clay

MEMS	Micro Electro Mechanical Systems
Mini-ICP	Mini – Imperial College Pile
MiP	Micro Pile
MBA	Multiple Blow Analysis
MS	Meta–stable axial cyclic loading condition
MTD	Marine Technology Directorate
N	Load cycles
N_f	Number of cycles to failure in pile axial cyclic loading
N_q	Dimensionless bearing capacity factor
NGI	Norwegian Geotechnical Institute
OD	Outer Diameter
PCB	Printed Circuit Board
PPP	Pore Pressure Probe
PTP	Phase Transformation Point
p'	Mean effective stress
p'_0	In-situ mean effective stress
p_a	Absolute atmospheric pressure
p_{lim}	Cavity expansion limit pressure
q_{ann}	Pile annulus unit resistance
q_b	Pile end-bearing unit resistance
$q_{b,0.1D}$	Base unit resistance at a settlement of 10% the pile diameter
$q_{b,\,lim}$	Limit base unit resistance
q_c	CPT tip unit resistance
q_{ca}	Arithmetic average of q_c in a specified zone depending on the design method
$q_{c,average}$	Average CPT tip resistance ±1.5D around pile base
q_{eg}	Geometric average of q_c in a specified zone
q_{plug}	Pile plug resistance
q_{res}	Residual base stress
Q_B (Q_b)	Pile base axial load resistance (capacity)
Q_{Br}	Base residual load
$Q_{b,0.1D}$	Base capacity at a settlement of 10% the pile diameter
$Q_{b,lim}$	Limit base capacity
Q_c	Calculated axial load capacity
Q_C	Total compression axial load resistance (capacity)
Q_{cyclic}	Axial cyclic load amplitude

Q_m	Measured axial load capacity
Q_{max}	Maximum axial cyclic load
Q_{min}	Minimum axial cyclic load
Q_{mean}	Mean axial cyclic load
Q_{Ref}	First axial load step applied
Q_S	Pile shaft axial load resistance (capacity)
Q_T	Tension axial load resistance (capacity)
r	Radial distance measured from the pile axis
R	Pile outer radius
R_i	Pile inner radius
R_{max}	Maximum surface roughness
R_N	Normalised surface roughness (= $R_{cla}/d_{50\%}$ after Kishida & Uesugi 1987)
RO	Rated Output
R*	Pile equivalent radius
R_{cla}	Mean centre-line surface roughness
RP2A	Recommended Practice for Planning Designing and Constructing Fixed Offshore Platforms
RSA	Residual Stress Analysis
S	Stable axial cyclic loading condition
SPT	Standard Penetrometer Test
SSS	Sand Stress Sensors
SST	Surface Stress Transducer
t	Sand stress sensor diaphragm thickness
t_c	Sand stress sensors thickness
t_w	Pipe pile wall thickness
T	Static tension capacity test
u_0	Initial (equalisation) pore pressure
u_2	Pore pressure measured behind CPT cone tip
ULS	Ultimate Limit State
US	Unstable axial cyclic loading condition
UWA	University of Western Australia
V_0	Excitation Voltage
V	Output voltage
WSD	Working Stress Design
y_m	Midpoint deflection of the sensing diaphragm

z	Depth

French

CEN	Centre d'Etudes de la Neige
CERMES	Centre d'Enseignement et de Recherche en Mecanique des Sols
CLAROM	Club pour les actions de recherches sur les ouvrages en mer
INPG	Institut Polytechnique de Grenoble (Grenoble–INP)
Lab 3S-R	Laboratoire Sols, Solides, Structures – Risques
SOLCYP	Projet National Comportement des pieux soumis à des sollicitations cycliques
UJF	Université Joseph Fourier

Greek

α_c	CPT α–type driven pile design methods base factor
α_s	CPT α–type driven pile design methods shaft factor
β $(=\tau_f/\sigma_{v0})$	Shaft friction factor
γ'	Effective unit weight
γ_w	Unit weight of water
δ	Angle of interface shear resistance
δ_{cv}	Angle of constant volume interface shear resistance
δ_f	Failure angle of interface shearing resistance
$\delta_{mobilised}$	Mobilised angle of interface shearing resistance
Δ	A change in a parameter
ε_{vol}	Volumetric strain
μ	Arithmetic mean
μ_{gR}	Geometric mean
σ	Standard deviation
σ_a	Triaxial test axial compression stress
σ_n	Normal stress
σ_r	Radial stress[1,2]
σ_θ	Circumferential (hoop) stress[1]
σ_z	Vertical stress[1]
σ_{v0}	Free field in-situ vertical stress
σ_{lnR}	Standard deviation of the natural log
ρ_{dry}	Dry density
φ	Angle of shearing resistance
φ_{cv}	Angle of constant volume shearing resistance

φ_p	Angle of peak shearing resistance
ψ	Angle of soil dilation
τ_{rz}	Local shear stress[1]
τ_f	Local shear stress at failure
$\tau_{f,lim}$	Limit local shear stress at failure
ν	Poisson's ratio

Notes:

(')	Refers to the effective stress behaviour/ component where applied

Can be used with the following further subscripts:

1:	m – moving; max – maximum; min – minimum; s – stationary
2:	d – dilation; f – failure, c – end of primary consolidation

Chapter 1

1 Introduction

1.1 Introduction

This PhD study examines the mechanisms that govern three aspects of the behaviour of displacement piles in silica sand; the stress regime setup by installation, the effects of ageing on pile axial capacity increase (set-up) and the pile axial response to cyclic loading. In this thesis *displacement piles* refers to pre-fabricated pile foundations installed by driving or jacking, causing full or partial in-situ sand displacement depending on the piles end conditions. Similarly, the load resistance of a single pile refers to that of the pile–sand system and not the structural member of the pile. Each pile's total axial resistance in compression (Q_C) comprises a summation of its base (Q_B) and shaft (Q_S) sand resistance less the pile self-weight, and its shaft resistance alone plus the pile self-weight and any suction or reverse resistance (typically negligible in sands) when loaded in tension (Q_T).

This chapter describes the background and motivation of the study, sets out the premises of the research and outlines the organization of the thesis.

1.2 Background to the study

1.2.1 The axial capacity of displacement piles in sands

Mandolini et al. (2005) reported roughly equal usage of displacement and non-displacement (replacement) piles in mainstream civil engineering piling. However, offshore piling is traditionally dominated by high capacity large-scale driven steel displacement piles (e.g. McClelland 1974, Thomas 1990). The American Petroleum Institute Recommended Practice for Planning Designing and Constructing Fixed Offshore Platform (API RP2A) has been the dominant design method and its guidance is recognised internationally as a preferred method for estimating capacities of piles driven for offshore oil and gas platforms, wind turbines, high capacity bridge and harbour foundations. The API issued its RP2A Main Text Method first edition in 1969 which based the design of axial base and shaft capacity of displacement piles in sands on conventional shallow capacity ultimate bearing capacity theory and lateral earth pressure theory respectively. The fundamental mechanics of the API's Main Text Method for sand have essentially remained unchanged since then including the latest edition ANSI/API Recommended Practice 2GEO for Geotechnical and Foundations Design Considerations (2011) which is offered jointly with the American National Standards Institute (ANSI) and co-ordinated with parallel International

Organization for Standardization (ISO) recommendations. More 'modern' Cone Penetrometer Test (CPT) based methods are, however, included in the 'commentary' annexe section.

Research over the last two decades (e.g. Lehane et al. 1993, Randolph et al. 1994, Chow 1997 and White 2005) has challenged the basic API premises and extensively improved the understanding of axial capacity development for displacement piles in sands. It was found experimentally that the mechanisms governing base and shaft resistance under axial loading are very different to and more complex than assumed by API (1969). The mainstream industry practice has been to collate pile load test databases which are then used to evaluate capacity estimation methods and calibrate the parameters specified by the capacity model assumed in each proposed design method. However, the historical databases were surprisingly sparse. To the Author's knowledge the first high quality database that included an adequate number of axial pile load tests on piles driven in sands was compiled by Chow (1997) at Imperial College during the development of the Marine Technology Directorate (MTD) pile design method described by Jardine & Chow (1996), which led to the updated Imperial College Pile (ICP-05) method set out by Jardine et al. (2005a). Other databases assembled since have included the Norwegian Geotechnical Institute (NGI) 2001 database used to develop the NGI-05 method Clausen et al. (2005), the FUGRO (2004) database which led to the FUGRO-05 method (Kolk et al. 2005), and University of Western Australia (UWA) database complied by Lehane et al. (2005b) during the development of the UWA-05 approach (Lehane et al. 2005a).

These recent databases are perhaps just large enough to allow the variations between the piles calculated and measured capacities, Q_c/Q_m to be evaluated statistically, leading to reportable coefficients of variation (CoV = standard deviation of (Q_c/Q_m)/ mean (Q_c/Q_m)) that can give significant measures of the predictive reliability of the potential design methods. For example, in Table 1-1 Lehane et al. (2005b) used the UWA database to assess the predictive reliability of the ICP-05, NGI-05, FUGRO-05 and UWA-05 methods commonly referred to as offshore or modern CPT based methods as well as the API RP2A Main Text Method (2000). They reported CPT-based methods that offered marked improvements and led to changes in the API RP2GEO (2011) recommendations. The four CPT-based methods are now included in the commentary/ annex of API RP2GEO (2011) as alternative design procedures to the Main Text Method. Although the main text cites the new methods' improved reliability, it also notes the methods' relatively short track record of application to offshore environments. The longest experience has been accumulated with the MTD/ ICP-05 approach which has been in effective use since 1995 (Overy 2007).

Table 1-1 shows that each design method has an associated spread of shaft, base and total axial capacities resulting from its implicit pile–soil model and treatment of factors such as pile slenderness (embedded length, L/ outer diameter, D), pile-end conditions or direction of loading

(tension or compression capacity), as well as the inherent qualities of the background research and calibrating databases; see also Gavin et al. (2011). Additional uncertainties to the design method development exist regarding; (i) the practical effects of variable pile installation processes, (ii) ageing of the piles in–situ, and (iii) nature of the imposed sustained axial static or cyclic loading on the capacities of displacement piles. The following section introduces the selection of issues which will be examined in this thesis.

1.2.2 Pile ageing and axial cyclic behaviour

There are several factors that complicate the interpretation of axial static pile capacity databases when making reliability assessments of capacity estimation procedures (e.g. Lehane et al. 2005b, Augustesen 2006, Jardine & Chow 2007, Gavin et al. 2011).

The first factor is to separately assess the pile base loads from the shaft stress distributions developed along pile shafts. This is hard to achieve with tests piles that are not instrumented with strain gauges or other devices, as is usually the case. Tension tests on un–instrumented piles can show tensile shaft resistance as their base capacities are negligible.

A second factor is that static pile load tests tend to be undertaken relatively shortly after installation because of the logistics of setting-up equipment on active sites. It has been interpreted in pile load test database studies that ageing after driving may influence the capacities seen in delayed static tests (e.g., Schmertmann 1991, Chow et al. 1998 or Jardine et al. 2006) and this may contribute to the scatter in the predictive reliability of practical procedures that do not explicitly incorporate time effects. 'Well designed' static pile load tests have indicated a systematic increase in the capacities of piles driven in sands at times far beyond those required for full pore pressures equalisation. For example, Figure 1-1 shows static tension capacities more than doubling within a year of installation for 457mm diameter by 19m long open–ended full-scale steel driven piles in dense silica marine sand at Dunkirk in France, Jardine et al. (2006). Similar beneficial capacity trend observations have been reported by Tavenas & Audy (1972), Skov & Denver (1988), Chow et al. (1998) and Axelsson (2000); although some studies have also reported non-beneficial time effects where capacities relaxed over time (for example York et al. 1994).

The third factor affecting the design of displacement piles for many applications (especially offshore foundation) is the piles' behaviour under axial cyclic loading, which occurs during both driving and at various stages in–service. It is usual in driven pile design to estimate the profiles of number of blows required to achieve a penetration with given hammers. However predictions depend on many factors and may vary considerably from field performance. Although the background research suggests a sensitivity of axial capacity to the numbers of blows applied, three of the four modern CPT-based design methods referred to earlier prefer to use net shear displacement of the shaft interface h at any given level (or the relative pile base depth) normalised

by the pile radius R or the equivalent solid pile radius R* for open-ended piles (Jardine et al. 2005); h/R or h/R*, to account for the installation cyclic loading effects (and pile geometry factors) on the stress distribution developed along the shaft of the displacement piles. The axial static shaft capacity formulations do not explicitly account for the number of blows or cycles applied with blow counts used instead primarily to monitor driving success or difficulties. Each driving blow applies 'pulses' of axial cyclic loading to the pile shaft as the pile head is taken to failure in compression and back to zero load in between blows. The pile shaft experiences two-way cyclic loading, alternating between a residual load condition established from a previous blow, (which typically develops as a downward shear force that counteracts accumulated upward residual base loads), to full compression failure as the pile advances under the next blow.

Jardine & Standing (2000, 2012) demonstrated that axial cyclic loading affects the behaviour of full scale piles driven in sands. Low–level tension axial cycling (with load cyclic amplitude Q_{cyclic} < ~20% the operational static shaft capacity Q_T) led to minimal cyclic displacements that accumulated at stabilising rates with almost no impact on pile stiffness and potentially enhancement of the pile's static tension capacity. However, high–level two-way load cycling led to rapid degradation of the operational static shaft capacities and rapidly accruing displacements that led to cyclic failure. Jardine & Standing (2012) developed a normalised cyclic interaction diagram approach (Figure 1-2) which categorised the observed load–displacement responses into three classes; Stable (S), Meta–stable (MS) and Unstable (US) behaviours.

Experiments with highly instrumented Mini-Imperial College Pile (Mini-ICP) laboratory test piles in which the Author participated allowed Tsuha et al. (2012) to develop a similar model–pile cyclic interaction diagram at a laboratory scale. The study related the global pile responses to local pile–sand interface behaviour while Yang et al. (2010) examined the particle crushing and interface shearing observed during the Mini-ICPs' installation and loading stages. Particle crushing was induced by the high installation stresses developed beneath the pile tip followed by further shearing abrasion and crushing along the shaft with each axial load cycling imposed by installation. The crushing processes increased the density of the sand at the interface which resulted in net contraction of radial stresses measured on the pile shaft. The modification of the sand near to the interface led to improved static shaft resistances for piles cycled within stable conditions while radial stress contractions dominated the meta-stable and unstable responses leading to potentially markedly lower operational shaft resistances.

This PhD study adopted, developed and elaborated the laboratory arrangements utilised by Yang et al. (2010) and Tsuha et al. (2012). The intensive instrumentation of the pile–sand system, allowed the effects of scale, sand density and moisture states, boundary conditions and mode of

installation to be considered one–by–one in an extended new study of the ageing and axial load cycling behaviour of displacement piles in sands.

1.3 Motivation of the study

The literature on piling engineering generally acknowledges that the mechanisms governing the interpreted axial capacity ageing set-up of displacement piles in sands are not yet fully understood. Different studies have suggested alternative mechanisms focusing on the pile shaft, as base resistance is not thought to be affected in the same way (Schmertmann 1991, Chow et al. 1998). The postulated mechanisms can be considered in three categories;

i) Those where ageing affects the mechanical properties around the pile improving the sand's strength, dilation or stiffness properties (e.g. Schmertmann 1991, Chow et al. 1998, Axelsson 2000, Bowman and Soga 2005).

ii) Mechanisms where re-equalisation of radially varying post–installation circumferential and radial stresses leads to higher on–pile radial effective stresses (e.g. Åstedt et al. 1992, Chow et al. 1998, White et al. 2005).

iii) Those involving physiochemical interactions between the pile surfaces and the sand, or within the sand alone, giving potentially interface volume and pile roughness increases due to corrosion and sand-pile 'welding' (e.g. Chow et al. 1998, Bea et al. 1999 and White & Zhao 2005).

All of above remain hypotheses with neither their potential circumstances of occurrence nor repeatability being fully determined to date. However, significant benefits have been made in recognising beneficial pile ageing on capacity. The piles driven for Jamuna Bridge in micaceous sand in Bangladesh provide one example. Allowing large-scale driven piles to age for several months led to considerable capacity gains and economic benefits that were verified by field testing (Tomlinson 1996). In general though, pile designers remain cautious and this is likely to continue until the influencing factors are identified and quantified.

It was clear from the Dunkirk field tests reported by Jardine and Standing (2000, 2012) that pile capacities can either be augmented or damaged in service under axial cyclic loading. However, the field testing programme was limited by the absence of pile-sand instrumentation as well as the durations (generally < 1 day and < 1000 cycles) of the loading sequences applied. A key aim in the Author's research was to study potentially negative cyclic effects in parallel with the possibly beneficial ageing trends to pile capacity behaviour.

1.4 Study objectives and research methodology

The first study objective was to establish a well-supported explanation for the mechanisms leading to time-related (ageing) increase in axial capacities of displacement piles in sand. The second was to better understand the axial cyclic effects during installation and how further load cycling after installation affects the pile axial response, aiming to identify the key governing mechanisms. Incorporation of ageing and load cycling effects into axial capacity estimation procedures would improve both foundation cost effectiveness and design reliability. The study focus was entirely on silica sand; the Author's testing concentrated on closed-ended pile base conditions.

To achieve the above aims, the study needed to isolate the ageing and axial cyclic loading related effects through systematic testing of alternative hypotheses. This required representatively scaled model displacement piles and silica sand masses incorporating instrumentation appropriate for long-duration axial static and cyclic load testing in which, loads and stresses measurements could be made in a closely controlled environment. Although no particular physical modelling method has received universal acceptance for investigating penetration mechanisms (Jiang et al. 2006), laboratory calibration chamber arrangements offer the opportunity to measure and control testing aspects that are otherwise uncontrollable in the field especially over extended durations.

This PhD study involved a sophisticated calibration chamber and model pile set-up that was established for collaborative research between Imperial College and Grenoble–INP, France. Imperial College brought its experience with the instrumented field test pile ICP to produce a reduced scale Mini-ICP version (Jardine et al. 2009) while the Grenoble–INP 3S-R laboratory has a 20 year history of innovative testing with 1.2m diameter by 1.5m deep steel pressurised calibration chamber, which was modified extensively for the Author's research.

The early stages of the full research project involved post doctoral input by Drs. Emerson, Zhu, Yang and Tsuha leading to a spread of publications (Jardine et al. 2009, Zhu et al. 2009, Yang et al. 2010, Tsuha et al. 2012 and Jardine et al. 2013a,b). The Author's PhD study is the first of two doctoral studies that are carrying the work forward. The second, by Matias Silva, is scheduled to complete in 2014.

The study specific testing objectives entailed close examination of the stress regime induced by installing displacement piles in the calibration chambers filled with sand and interpreting the measurements from the highly instrumented pile and sand chamber sensors. Short-term axial static pile load tests of the installed model piles were correlated with static capacities computed by the field–validated ICP-05 method. Each freshly installed displacement pile was monitored over extended ageing periods with a particular focus on the possible effects on the piles' static axial

capacity. For each installed pile, one or two parameters or features were varied in isolation to examine its potential influence. The variables considered were;

1) Calibration chamber – to – pile diameter ratio
2) Sand particle – to – pile diameter ratio
3) Calibration chamber boundary conditions
4) Sand density effects
5) The influence of sand water saturation, and
6) Mode of pile installation.

After ageing, axial static and cyclic loading programmes were applied to examine the effects of cyclic loading conditions as well as number of cycles on the evolution of the pile static operational shaft capacities, axial stiffness, pile interface and sand mass stresses and cyclic displacements. The observations from the laboratory tests were corroborated by a new analysis of the stiffness and cyclic displacement responses from the field axial cyclic loading experiments of driven open-ended pipe piles (Jardine & Standing 2000, 2012).

Ancillary studies were conducted into pile surface roughness sensing and particle scale index characterisation in parallel with the main pile tests. Synthesis of the numerous measurements has led to a framework for data presentation that is to aid understanding, critical evaluation and practical application.

1.5 Organisation of thesis

The thesis is organised in thirteen chapters; the current **Chapter 1** provides the introduction and sets out the background to the research.

Chapter 2 considers the background developments regarding static axial capacity of displacement piles in sands, reviewing the most important scientific findings that have informed advances in understanding and designing displacement piles. Particular emphasis is given to the modern CPT-based design methods which comprise the current state-of-the-art.

Chapter 3 reviews reported field pile load test studies that interpreted capacity ageing set-up trends. This led to the collation of a new ageing database. The hypotheses available on pile ageing mechanisms were then tested against the new database as a tentative assessment for any patterns of influence.

Chapter 4 first introduces the current practice of designing displacement piles in sands for axial cyclic loading highlighting the use of cyclic interaction diagrams. It then moves to review field cyclic loading tests noting the dearth of studies. The level of understanding of the mechanisms involved in pile axial cyclic loading behaviour is revealed in combination with the relatively greater

number of laboratory model piles cyclic loading studies and need for further assessment of cyclic effects identified.

Chapter 5 describes and illustrates the apparatus and equipment adopted for the study. These comprised the Mini Imperial College Pile (Mini-ICP); CPT cone tipped displacement pile; Micro pile (MiP); driven pile and the driving system; 3S-R Calibration Chamber (3S-R CC); and the Sand Stress Sensors (SSS). A brief description is also given of other enabling calibration equipments, including the Talysurf-Hobson roughness sensing device and microscopy–based sand index property equipment.

Chapter 6 describes the test sands, sample preparation procedures, pile installation and ageing, and axial static and cyclic loading procedures. The detailed testing programme is presented.

Chapters 7 to **9** report and review the data recorded during pile installation. The stress and load measurements made on the pile and in the sand chamber are considered and their sensitivity to the alternative chamber boundary conditions is reviewed. Their potential matches with field studies, other laboratory model scale studies, numerical and analytical studies are also explored.

Chapter 10 critically examines time-related pile ageing stress and load trends observed during the long-duration ageing studies and interprets the pile axial capacities obtained post-ageing. This is followed by analysis of the post-ageing axial cyclic loading tests presented in **Chapter 11**.

Chapter 12 corroborates the model piles cyclic loading responses with an analysis of the cyclic displacements and stiffness responses of the Dunkirk full scale open-ended driven pipe piles axial cyclic loading experiments by Jardine & Standing (2012).

Chapter 13 brings the thesis to its end by drawing conclusions, considering implications for practice and recommending areas for future studies.

Appendices offered at the end provide extended details of the respective main text discussions as has been referred to.

Database	Method	Average Q_c/Q_m	CoV
32 Driven Closed End Piles Compression	API-00	0.78	0.56
	FUGRO-05	1.24	0.39
	ICP-05	0.99	0.33
	NGI-05	1.16	0.40
	UWA-05	0.98	0.33
10 Driven Closed End Piles Tension	API-00	1.12	0.84
	FUGRO-05	0.97	0.41
	ICP-05	1.02	0.30
	NGI-05	1.27	0.50
	UWA-05	1.00	0.29
17 Driven Open End Piles Compression	API-00	0.75	0.68
	FUGRO-05	1.14	0.30
	ICP-05	0.89	0.28
	NGI-05	1.01	0.25
	UWA-05*	0.98	0.19
15 Driven Open End Piles Tension	API-00	0.72	0.76
	FUGRO-05	0.90	0.32
	ICP-05	0.90	0.27
	NGI-05	1.01	0.35
	UWA-05*	0.91	0.23
74 piles Full database	API-00	0.81	0.67
	FUGRO-05	1.11	0.38
	ICP-05	0.95	0.30
	NGI-05	1.11	0.37
	UWA-05*	0.97	0.27

*The UWA open-ended pile assessments involved use of Incremental Filling Ratio (IFR) measurements made during installation that are generally not available at the design stage.

Table 1-1: Predictive reliability of four modern CPT-based axial static capacity design methods of driven piles in silica sands based on a UWA database (Lehane et al. 2005b).

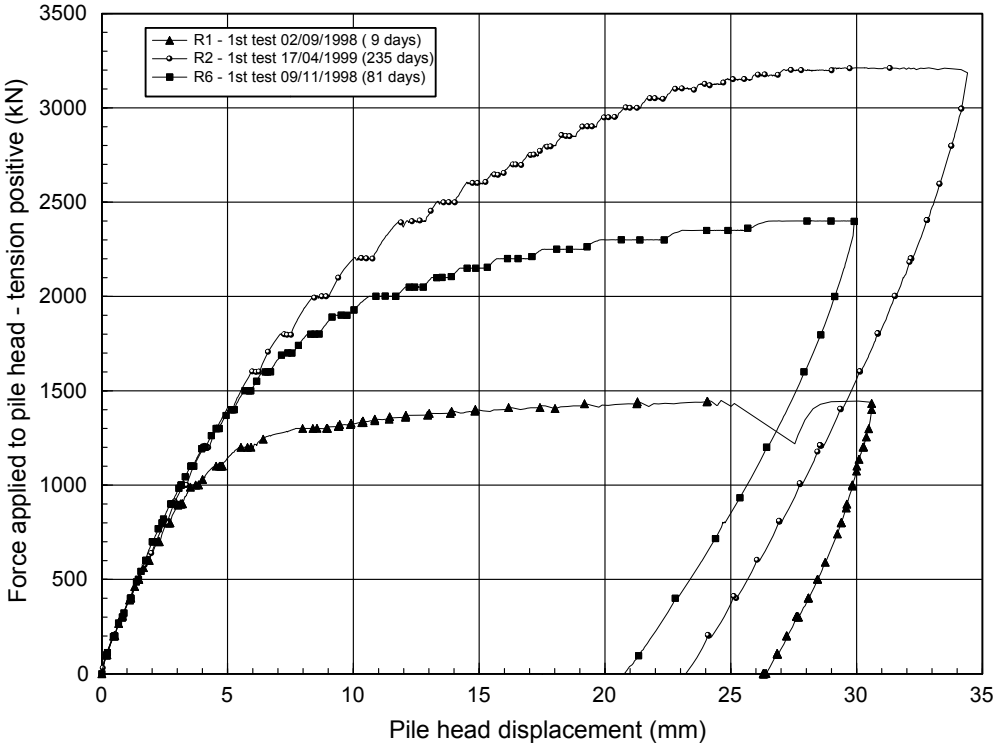


Figure 1-1: First-time tension tests to failure on three field tests of 457mm diameter by 19m long open-ended driven pipe piles in dense silica Dunkirk marine sands (Jardine et al. 2006).

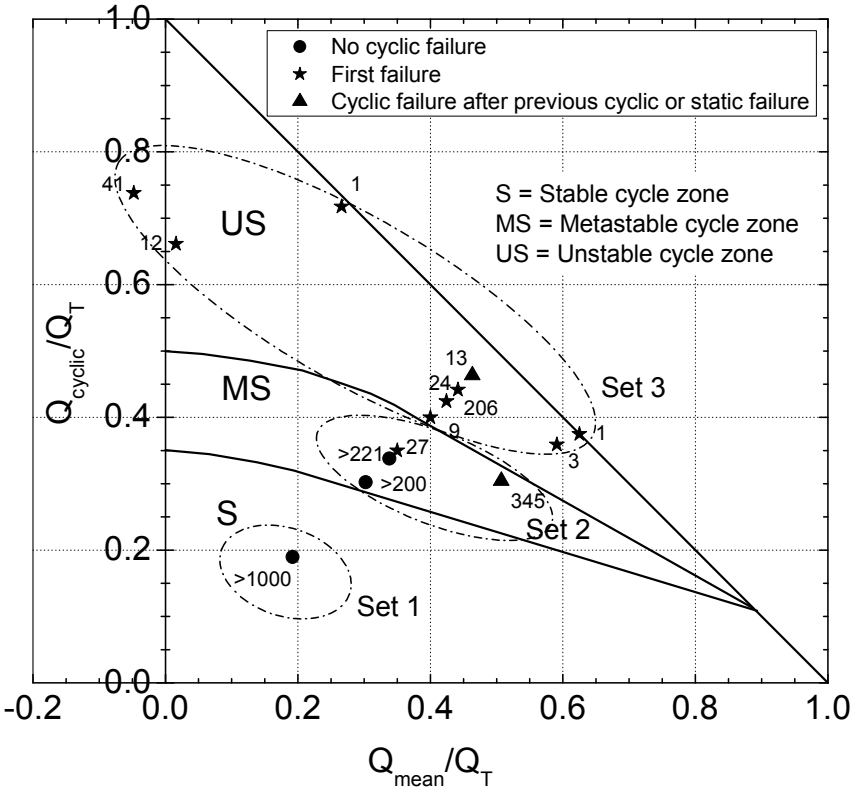


Figure 1-2: Interaction diagram on axial cyclic response of displacement piles in Dunkirk marine silica sands of normalised loading parameters Q_{cyclic}/Q_T against Q_{mean}/Q_T with the number of cycles to failure and tentative stable, meta-stable and unstable zones (Jardine & Standing 2012).

Chapter 2

2 Axial static capacity of single displacement piles in silica sands

2.1 Introduction

This chapter reviews recent advances in understanding of the axial static behaviour of single displacement piles in silica sand, considering the processes experienced during their installation. The review focuses on the effective stress state generated around displacement piles which controls the piles' axial static capacities. The estimation of shaft and base resistances is reviewed, referring to reliability studies. Implicitly, this chapter considers the capacities and stiffnesses available within a few days of pile installation by jacking or driving. The impacts of time and ageing on the measured axial static capacities and the responses to axial cyclic loading are discussed in the following Chapters 3 and 4.

2.2 Pile load testing in practice

High quality pile load tests are fundamental to understanding the base and shaft resistance behaviours and predicting of axial capacity for displacement piles in sands. England & Fleming (1994) emphasised that pile tests should replicate the intended long-term field load paths as closely as possible. However, cost and time constraints lead to a range of practical procedures that can develop different capacities for the same pile at any given time after installation.

Two key attributes of a well designed pile load test are 1) it should mobilise the base and shaft resistance fully during the test and, 2) separately assess the base resistance and the shaft resistance distribution. Traditionally pile capacity has been defined at a (pile head or base) displacement of 10% the diameter of the pile (Vijayvergiya 1977, API 2000), although this is often insufficient to fully mobilise the pile base capacity in sands. To separately assess the base and shaft resistances a test pile needs on-pile strain gauging or load cell instrumentation. Relatively few studies report full–scale instrumented displacement piles (e.g. Brucy et al. 1991, Bullock et al. 2005), and in practice most displacement piles are installed un-instrumented. Also instruments usually face very low survival rates during driving (NGI 2012). Where such instruments survive beyond installation, they usually have to be re-zeroed before load testing to overcome shifts that developed during installation. Residual loads develop at the base and then on the shaft during installation that are often then ignored in the pile load test interpretation. Various methods have been proposed to help account for residual loads during the pile load tests analysis; Hunter & Davisson (1969), Briaud & Tucker (1984), Fellenius (1989), Altaee et al. (1991), Rausche et al. (1996), Alawneh & Malkawi (2000), Costa (2001). However, most can only be applied if the

appropriate steps (such as a tension test to failure) have been taken in the field. Even the best collated test databases in sands (e.g. Chow 1997) contain some cases where it may be argued that residual loads effects have not been addressed adequately; White & Bolton (2005). Shaft behaviour cannot be explicitly analysed unless the loads developed at the pile base are fully understood.

2.3 Pile end-bearing resistance

Historically the ultimate end–bearing resistance of piles driven in sands has been derived by analogy with shallow foundation bearing capacity theory; Terzaghi (1943). For example Berezantzev et al. (1961) presents an analysis considering slip planes that extend from the pile base to the surface and are linked to the sand friction angle. Empirical design methods such as the API RP2A (1969) for offshore piles specify base resistance relationships that depend on sand type and relative density, by the shallow foundation formulae;

$$Q_{b,0.1D} = A_b.q_b \le Q_{b,\lim} \quad where \quad q_b = N_q.\sigma'_{v0} \qquad 2\text{-}1$$

Where $Q_{b,0.1D}$ is the base capacity at a settlement of 10% the pile diameter, A_b the area of the pile base and N_q is a dimensionless bearing capacity factor that depends classically on the internal angle of shearing resistance of the sand deposit. Lambe and Whitman (1979), Coyle and Castello (1981) have noted the wide range of theoretical and empirical expressions for N_q, see Figure 2-1. Equation 2-1 predicts that piles driven in uniform sands will show Q_b values that increase linearly with effective overburden stress, σ'_{v0}. However, this is unsupported by field observations made with penetrometers (White & Bolton 2004) which tend to have non-linear nearly parabolic relationships with depth in uniform sands. Failure around displacing pile bases involves kinematically constrained mechanisms without slip planes that extend to the ground surface. Base resistance is therefore controlled by the pressure dependent, non-linear stiffness of the sand around the base as well as the sand's strength; Vesic (1967), Randolph et al. (1994). In this regard, N_q varies with the rigidity index $\left(I_r = G/p_0'\right)$ (Kulhawy 1984 or Gupta 2002) and G increases by a power less than unity with depth, p'_0 increases with depth while φ' decreases with increase of p' (Bolton 1986). These features lead N_q to decrease with depth, z, and for a pile of fixed area of base in a uniform sand, dQ_b/dz reduces and may even tend to zero with depth e.g. Kerisel (1964), Vesic (1970). Such studies suggested that q_b trends to a constant value in uniform sands below a 'critical depth'.

The API RP2A (1969) 1st edition recommended N_q values for loose to very dense sands and prescribes upper limit base resistances to cope with the above discussed limitations. The RP2A base capacity guidelines were significantly updated in 1984 after a review by Olson & Dennis (1982)

and have in principle remained the same up to the latest edition RP2 GEO (2011) on Table 2-1. Kulhawy (1984) demonstrated that the proposed limiting end-bearing resistances proposed by API could easily be exceeded as did Chow (1997). Klotz & Coop (2001) similarly discuss the discrepancies in prescribing limiting end–bearing resistance in relation to their centrifuge tests with model piles in carbonitic Dogs Bay sand and silica Leighton Buzzard sand. In the latest edition the designer is referred to the offshore (modern) CPT-based methods in the commentary/ annex of the guide for the areas which the main text method is inapplicable and relatively un-conservative. These methods do not set limits to q_b.

Theoretical attempts have been made to improve the prediction of end–bearing resistance studies by applying spherical Cavity Expansion Methods (CEM) around the pile tip (Figure 2-2), Randolph et al. (1994). The end-bearing resistance can be shown to be $q_b = p_{\lim}\left(1 + \tan\phi' \tan\alpha\right)$, Gibson (1950), and on assumption of a conical shearing mechanism developing immediately beneath the pile base, if the friction angle φ' is taken as φ'_{cv} then $\alpha = 45 + \varphi'_{cv}/2$. The limit pressure for cavity expansion in sand may be evaluated after Yu & Houlsby (1991) based on elastic-perfectly plastic soil with a Mohr–Coulomb failure criterion and a fixed rate of dilation; this is of course incompatible with critical state soil behaviour and the soil stiffness behaviour being non–linear and pressure dependent. Randolph et al. (1994) list the required input parameters as the in-situ mean effect stress p_0', friction angle for the soil φ', dilation angle for the soil ψ, equivalent value for non-linear shear modulus G and Poisson's ratio *v*. The CEM captures the diminishing increase of the end-bearing with depth therefore does not need to prescribe limits to the q_b resistances, however it requires a number of input parameters and is based on an idealised soil model leading to limited practicality.

Alternative treatments have been proposed that rely on the geometrical similarity of the failures around CPT probes to displacement piles and the CPT's advantage of continuous profiling in variable deposits (Yu 2000). Direct CPT based procedures have been employed for some decades and these related the pile base resistance, q_b to the CPT tip resistance q_c and the pile shaft resistance to either CPT q_c or sleeve friction f_s. Other indirect CPT–based procedures use CPT results to estimate sand strength parameters which are used to estimate pile capacity after theoretical or semi-empirical methods. Focusing on the direct procedures, these can be categorised as simplified CPT (α–type methods) and the 'modern' CPT–based design methods. The α–type methods relate the pile base resistance to the CPT q_c as $q_b = \alpha_c q_c$.

The various formulations for some ten methods summarised by Cai et al. (2008) take the forms shown on Table 2-2. A broad range of α_c factors (0.1 – 0.6) are proposed on the basis of

different calibration databases giving a range of predictions of the end–bearing capacity under similar conditions.

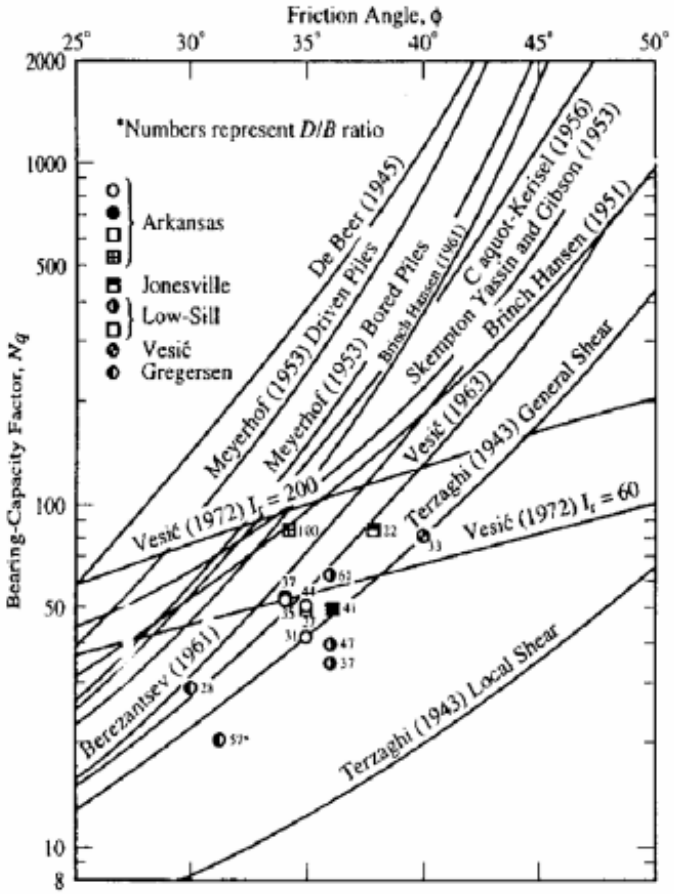
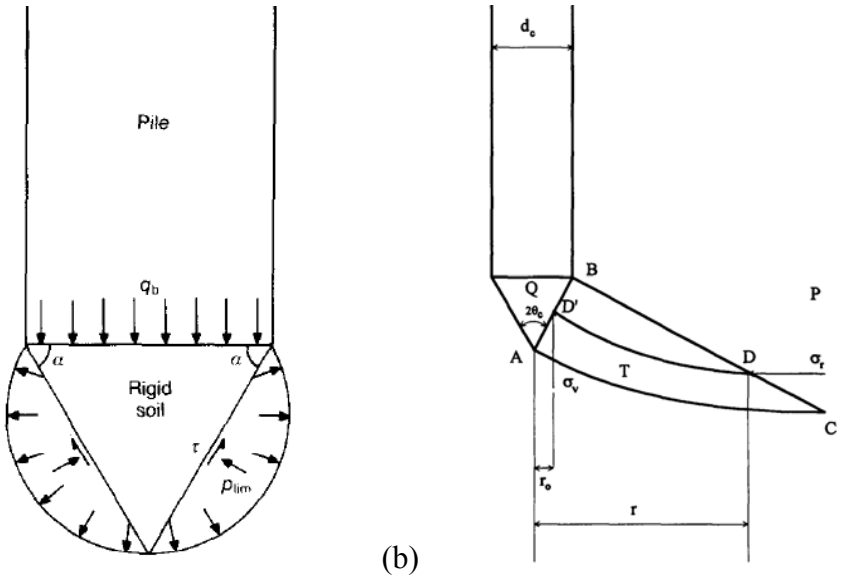


Figure 2-1: Bearing capacity factor N_q from Lambe & Whitman (1979) with the plotted field data points from Coyle & Castello (1981).

Density index, I_D (%)	**Soil description**	**N_q**	**$q_{b,\,lim}$ (MPa)**
Very loose (0 – 15)	Sand	N/A	N/A
Loose (15 – 35)	Sand		
Loose (15 – 35)	Sand-Silt		
Medium (35 – 65)	Silt		
Dense (65 – 85)	Silt		
Dense (65 – 85)	Gravel		
Medium (35 – 65)	Sand-silt	12	3
Medium (35 – 65)	Sand	20	5
Dense (65 – 85)	Sand-silt		
Dense (65 – 85)	Sand	40	10
Very dense (85 – 100)	Sand-silt		
Very dense (85 – 100)	Sand	50	12

Table 2-1: API RP2 GEO (2011) recommend practice for geotechnical engineering pile base capacity design parameters for cohesionless soils.



(a) (b)

Figure 2-2:(a) Relation of cavity expansion limit pressure and end-bearing capacity (Randolph et al. 1994) (b) Slip pattern under pile tip or cone penetrometer (Salgado 1993).

SN	Reference	Unit end–bearing capacity (q_b)
1	Schmertmann (1978)	$q_b = (q_{c1} + q_{c2})/2 \leq 15MPa$ q_{c1}: minimum of the average of q_c values of zones ranging from 0.7 to 4D below tip. q_{c2}: average of minimum q_c values 8D above the cone tip (Dutch Method)
2	De Ruiter and Beringen (1979)	Similar to Schmertmann (1978)
3	LCPC – Bustamante & Gianeselli (1982)	$q_b = \alpha_b q_{c,average}$ α_b: 0.15 – 0.6 depending on soil type and installation procedure $q_{c,average}$: equivalent average of q_c values of zone ranging from 1.5D below pile tip to 1.5D above pile base
4	Tumay and Fakhroo (1982)	Similar to Schmertmann (1978)
5	Aoki and De Alencar (1975)	$q_b = \alpha_b q_{ca} \leq 15MPa$ α_b reducing factor that depends on pile type (e.g. = 0.57 for concrete piles)
6	Price and Wardle (1982)	$q_b = \alpha_b q_{ca}$ α_b depends on pile type = 0.35 for driven piles
7	Philipponnat (1980)	$q_b = \alpha_b q_{ca}$ α_b depends on soil type = 0.4 for sand
8	Penpile – Clisby et al. (1978)	$q_b = 0.125 q_{ca}$
9	Eslami and Fellenius (1997)	$q_b = q_{eg}$ q_{eg} is the geometric average of q_c values over the influence zone after correction for pore pressure on shoulder and adjustment to effective stress.
10	Takesue et al. (1998)	$q_b = 0.1 q_c$

q_{ca} - is the arithmetic average of q_c in a specified zone that depends on the method

Table 2-2: Simplified base capacity CPT and CPTu – based α–type design methods (after Cai et al. 2008).

Major advances in understanding the stress state developing around closed–ended displacement piles were achieved by the Imperial College field studies made with instrumented Imperial College Pile (ICP) first in loose silica dune sand by Lehane (1992), Lehane et al. (1993) and then in dense silica marine sand by Chow (1997). The ICP was equipped with 'leading', 'following', 'trailing' and 'lagging' instrument clusters each with radial and shear surface stresses transducers (SST) and associated Axial Load Cells (ALC) designed by Bond et al. (1991) (see Chapter 5). These studies examined the radial and shear interface stresses around the 101.6mm diameter by up to 7.54m length (L/D = 74) pile which were installed by multiple jack–stroke cycles involving full unloading between each stroke. These studies helped to clarify the pile base capacity behaviour. The ALC measurements showed very clearly the direct links between q_b and q_c, Figures 2–3 and 2–4. Base resistance profiles from the API RP2 GEO (2011) are plotted on the same plots showing the potential under-prediction of the pile base capacity. Lehane (1992) observed stratum boundaries appeared to be less sharply defined by the tip resistance q_b of the relatively larger diameter (101.6mm) ICP to the q_c traces by the smaller diameter (35.7mm) CPT suggesting the zone of influence of the two penetrometers are in proportion to their diameters. This observation is in keeping with the proposals of the design methods in Table 2-2 that q_b may be derived by averaging the q_c variation in the vicinity of the pile tip over distances proportional to the pile diameter.

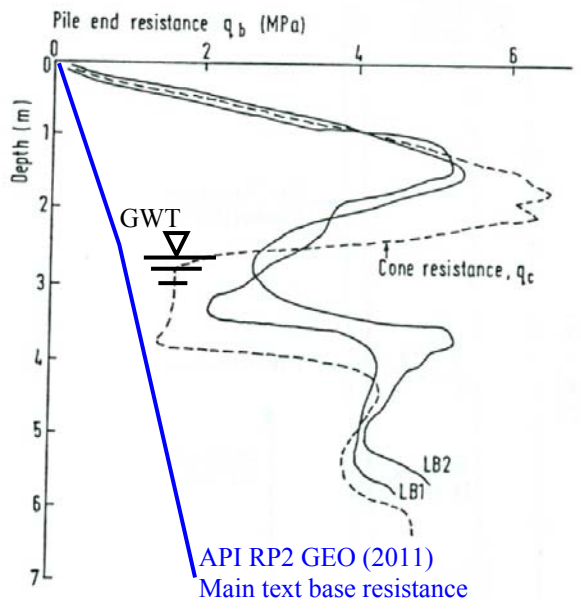


Figure 2-3: Pile end resistances of jack installed ICPs LB1 and LB2 compared with the in-situ sand CPT q_c profile at Labenne loose dune silica sand (Lehane 1992) and with the RP2 GEO (2011) main text design.

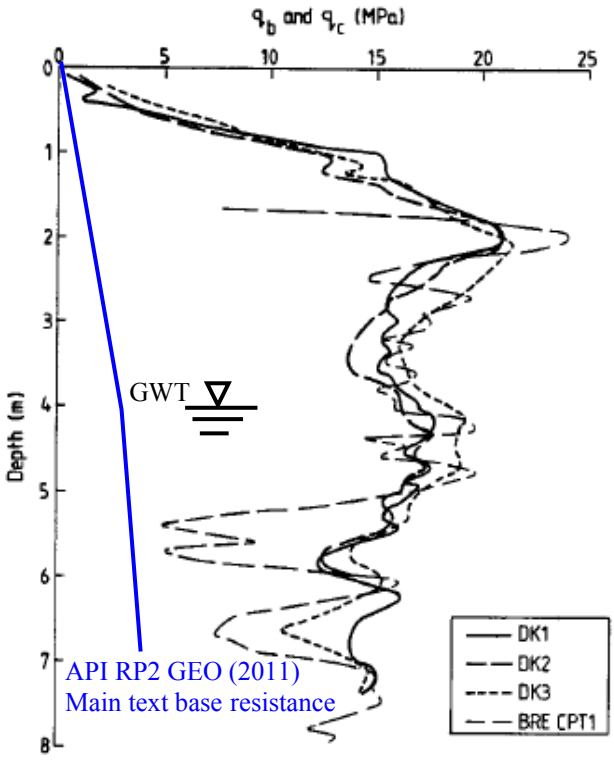


Figure 2-4: Pile end resistances of jack installed ICPs DK1 to DK3 compared with the in-situ sand CPT q_c profile BRE CPT1 at Dunkirk medium dense marine silica sand (Chow 1997) and with the RP2 GEO (2011) main text design.

The MTD/ ICP-05 design method by Jardine & Chow (1996) and Jardine et al. (2005a) recognised that the ICP tests could not show whether the ratio q_b/q_c varied with pile scale or in-situ stress level. The ICP tests also didn't offer insights into how open-ended piles might differ from close–ended piles. Additional field database studies by Chow (1997) suggested that a scale effect applied, even to closed-ended piles, as shown in Figure 2-5. The MTD/ ICP-05 recommended the ratio q_b/q_c would be less that unity in sands and fall with pile diameter. Such scale effects on ultimate resistance of a penetrometer are not predicted by continuum approaches. Jardine et al. (2005a) suggest possible causes include; 1) Particle scale processes such as localised crushing zones or shear banding within the zone of contained failure beneath the pile base, 2) Partial mobilisation of pile capacity at the pile head displacement of 0.1D, i.e. lack of plunging failure and 3) Effects of sand state variations over short intervals of depth. The ICP-05 suggested for closed-ended piles the base resistance is;

$$q_{b,0.1D} = q_{c,average}\left(\max\left[1-0.5\log\left(D/D_{CPT}\right),0.3\right]\right) \qquad 2\text{-}2$$

The tip resistance averaging, $q_{c,average}$ is recommended following Bustamante and Gianeselli (1982) taking an arithmetic average of q_c in a range ±1.5D around the pile base. The presence of

any significantly weaker than average layer in the vicinity of the base should be allowed for by selecting a design q_c below this average.

For open–ended pipe piles the base capacity was considered to be contributed by a relatively small contribution from the pile internal skin-friction acting through the core soil column and the resistance beneath the annular area of the pipe. Inferences from pile plugging studies by Chow (1997) and database studies with open–ended test pipe piles (including the CLAROM tests at Dunkirk, Brucy et al. 1991), led to the suggestion that piles would core during load testing if $D_i \geq 0.02\left(I_D - 30\right)$ and $D_i \geq 0.083\left(q_{c,average}/p_a\right)D_{CPT}$, D_i is the internal diameter of the pile in metres, I_D in %, and p_a the absolute atmospheric pressure = 100kPa. In these conditions the base capacity is given as;

$$q_{b,0.1D} = A_r q_{c,average} \qquad 2\text{-}3$$

where $A_r = 1 - \left(D_i/D\right)^2$ is the effective area ratio.

Otherwise, when the open-ended pile plugs during static loading the base capacity is given as;

$$q_{b,0.1D} = q_{c,average}\left(\max\left[0.5 - 0.25\log\left(D/D_{CPT}\right), 0.15, A_r\right]\right) \qquad 2\text{-}4$$

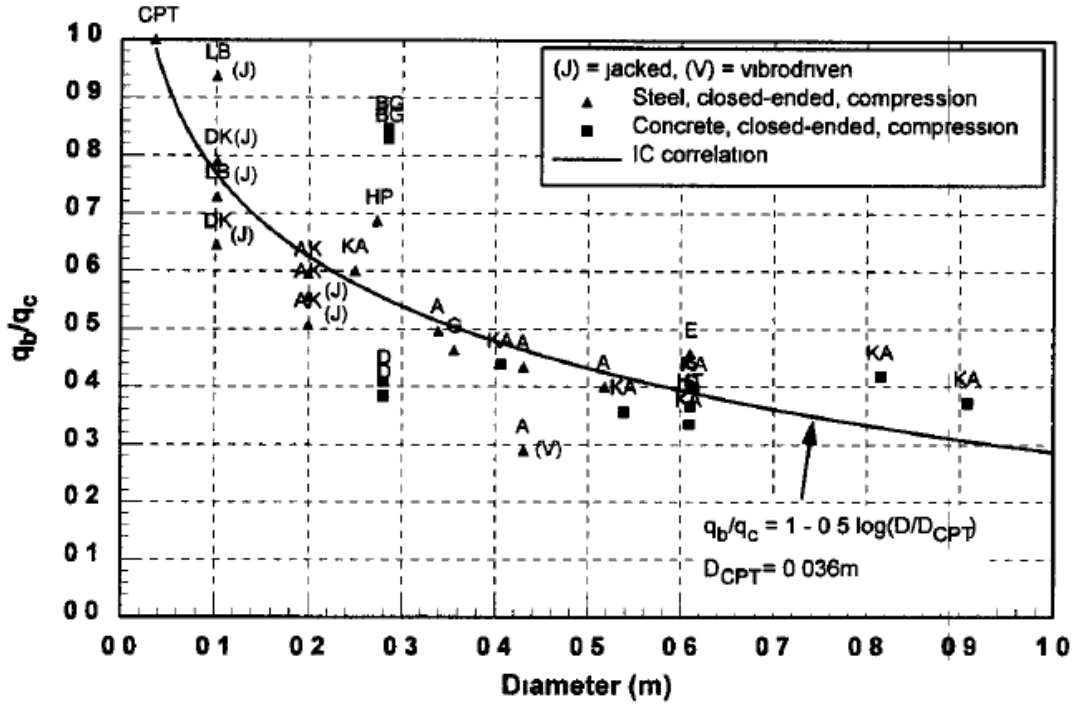


Figure 2-5: Normalised pile base resistance, $q_{b,0.1D}/q_c$ plotted against diameters of closed-ended displacement piles in silica sands (Chow 1997).

2.4 Factors affecting base resistance interpretations

As noted at the outset pile load tests that continue to plunging failures would provide the least ambiguous measurements of ultimate capacity although practical limitations in rig capacities

and jack displacement travels often limit tests in practice. Changes in stratification within the volume of influence of the pile base also requires appropriate weighting of q_c values when averaging between the respective soil layers to select suitable single values for capacity assessment. Both these aspects lend subjectivity to q_b determination.

White and Bolton (2005) re–analysed Chow's (1997) closed-ended piles database re-examining the ratio q_b/q_c. They argue, after accounting for partial embedment of pile bases into harder layers underlying a weak layer as well as partial mobilisation of the base resistance rather than full plunging criterion, the ultimate q_b/q_c ratio of closed ended piles has a mean of 0.9 showing no trend with pile diameter, Figure 2-6. They attribute the difference from unity in q_b/q_c to underestimation of plunging loads in pile tests for which steady penetration had not been reached. Reduction due to progressive failure was not considered. It is argued that the contained failure around the base does not cause shear bands to propagate along planes of slip-up to the ground surface as in shallow foundations. Further possibilities of progressive failure from peak to critical state strengths were not considered to be related to scale and were therefore discounted. However, Yang et al. (2010) reports development of shear bands around the Mini-ICP piles in the earlier calibration chamber tests.

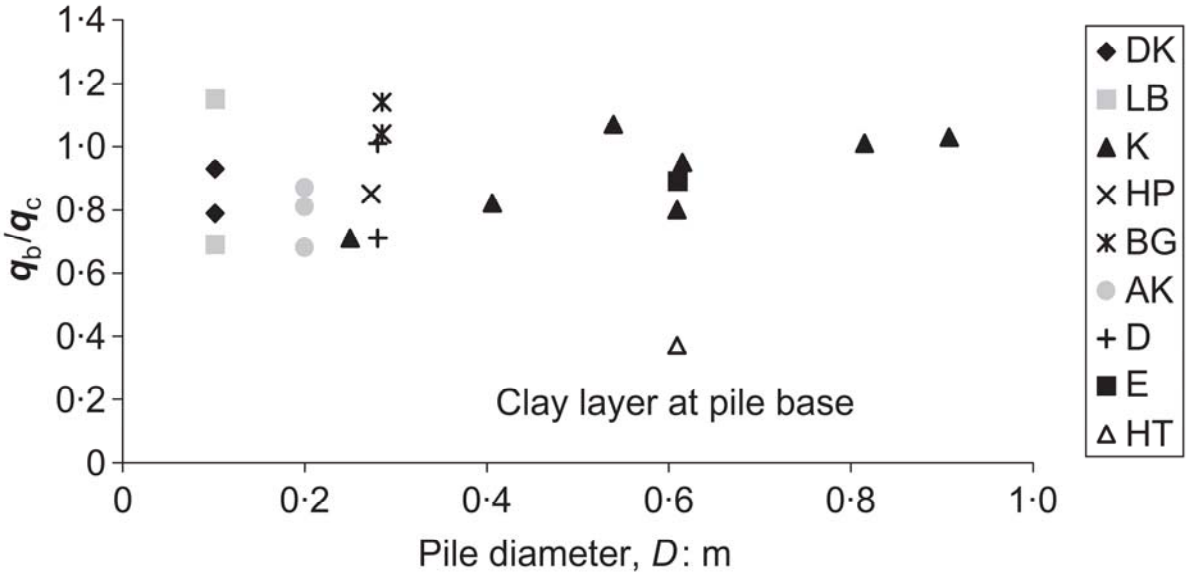


Figure 2-6: White & Bolton (2005) q_c-normalised closed-ended displacement piles in sands base plunging resistance q_b/q_c plotted against pile diameter for the sites Dunkirk (DK), Labenne (LB), Kalo (K), Hunter's Point (HP), Baghdad (BG), Akasaka (AK), Drammen (D), Hsia Ta (HT) and Lower Arrow Lake (E) from Chow (1997) database.

The other factors affecting the quality of pile base ultimate resistance measurements is the residual loads that accumulate during pile driving as locked-in base axial compression loads which are counter-balanced by partially mobilised shaft shear loads at the end of installation, Figure 2-7. Such residual loads develop most markedly in driven piles and are unseen unless piles are

continuously instrumented to separately determine the base and capacities. The effects of residual loads include over-estimation of the shaft capacity and under-estimation of the base capacity from capacities calculated from typically zeroed strain gauges before testing, Fellenius (2002). Neglect of residual locked–in loads also had contributed to the interpretation of the 'critical depth', Fellenius & Altaee (1994), for unit shaft friction as a result of the typical "squeezed S" shaped axial load distribution that is often interpreted from pile tests when residual loads are ignored; see Figure 2-8.

Hunter & Davisson (1969) proposed a rational graphical procedure for estimating and correcting for residual stresses in interpretation of static pile load tests. Rausche et al. (1996) described CAPWAP analyses with Residual Stress Analysis (RSA) and Multiple Blow Analysis (MBA) to estimate the residual stresses from dynamic monitoring of pile driving. In this a sequence of blows is implemented with the stress state (on the pile and in the soil) at the end of the first blow is used to set the initial conditions for the subsequent blow. This MBA signal matching technique requires the selection of a series of 'typical' records and parameter adjustments to yield a satisfactory match on all blows in the series, so emphasizing the importance of capturing the residual stresses generated between blows. The signal match for the last blow is considered the final loading condition that defines the post installation residual loads. Costa et al. (2001) recommended DINEXP analysis for residual loads estimation which they consider more rigorous and reliable with piles with high base resistances, as for example in sands, (cf. WEAP by Goble et al. 1998). However Fellenius (2002) argued that such procedures do not fully account for the residual loads developed during driving.

This study focuses on the characteristics of closed–ended displacement piles in uniform silica sand deposits but other factors that potentially affect the estimation of the pile base resistance are (i) the scaling procedure applied to the CPT q_c values to account for differences between pile–and–penetrometer diameters and (ii) the allowance made for open–ended pile conditions. The ICP-05 procedure uses simple arithmetic averaging of the CPT q_c over 1.5 pile diameters above–and–below the pile base, and the designer is encouraged to select lower values if notably weaker layer are anticipated in the vicinity of the base. Other recommendations include the Dutch technique after Schmertmann (1978) and de Ruiter & Beringen (1979) as used, for example, in the UWA-05 method (Lehane et al. 2005a). Another is to simply adopt the local tip resistance at the pile base level e.g. NGI-05 method (Clausen et al. 2005). No consensus has been reached regarding the best practice.

The ICP-05 qualified open-ended piles as either (i) having plugs that remain stationary during static pile load tests or (ii) tending to core during the pile load tests, offering empirical rules for each case. Essentially for an open–ended pile that is plugged during static load testing the base resistance available at a displacement of 0.1D becomes half that for closed-ended piles while the

average q_c is considered on the annular area of a coring open–ended pile. It is argued such approach doesn't explicitly account for the sand displacement induced during pipe-pile driving, Xu et al. (2008). Xu et al. proposed using an effective area ratio in the form $A_{rb,eff} = 1 - FFR\ (D_i^2/D^2)$ where FFR is the Final Filling Ratio of the pile base defined as the Incremental Filling Ratio (IFR) = $\Delta l/\Delta z$ (incremental change of plug length/ incremental change of pile embedment during driving) measured over the final stages of the pile installation. The formulations of the base capacity of the UWA-05 method (Lehane et al. 2005b) and two other 'modern' CPT–based methods are summarised in Section 2.7 while the predictive performance of these methods is compared in Section 2.8. While using FFR offers one route to explicitly accounting for partial filling, it is only measured during pile driving and when designing (inevitably before driving) FFR has to be estimated. The ratio depends on several factors, sand density, pile diameter and modes of driving that are simply not easy to predict. Hind casts that employ site FFR measurements can therefore be expected to give better predictions than designs that have to incorporate FFR forecasts, as noted earlier in relation to Table 1-1.

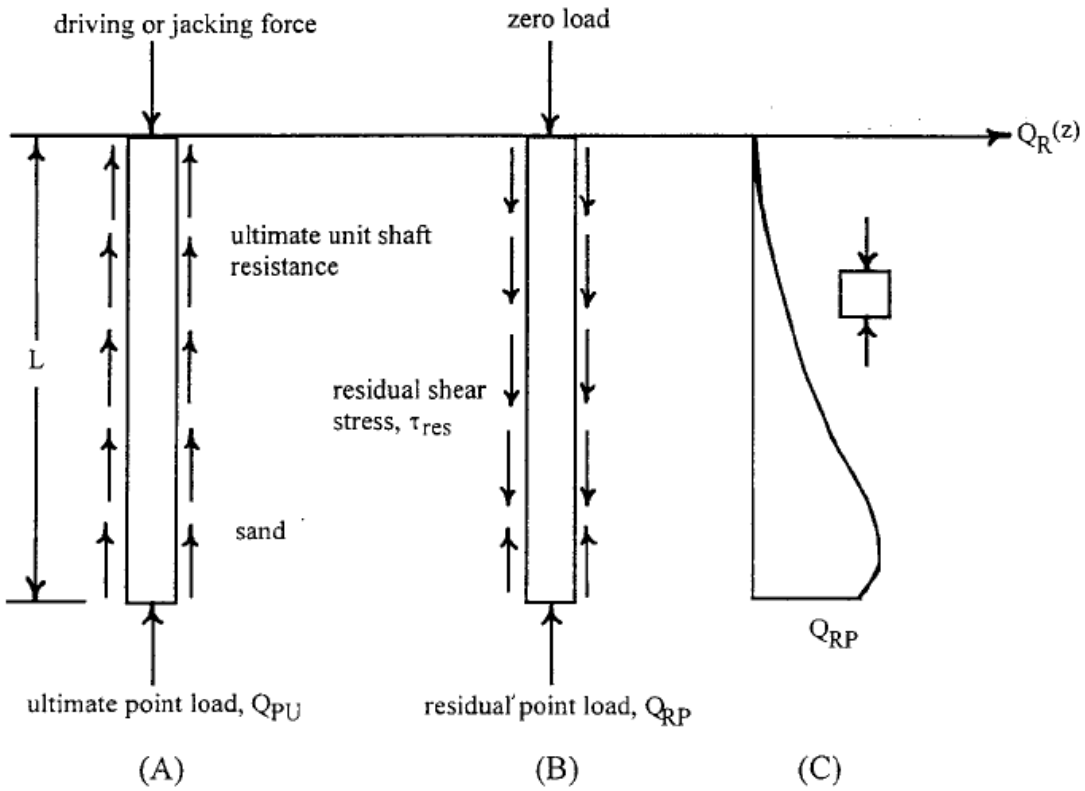


Figure 2-7: (A) A pile in sand under compression load during installation process (B) Residual stresses at the end of the installation or compression test. (C) Variation of residual load with depth (Alawneh & Malkawi 2000).

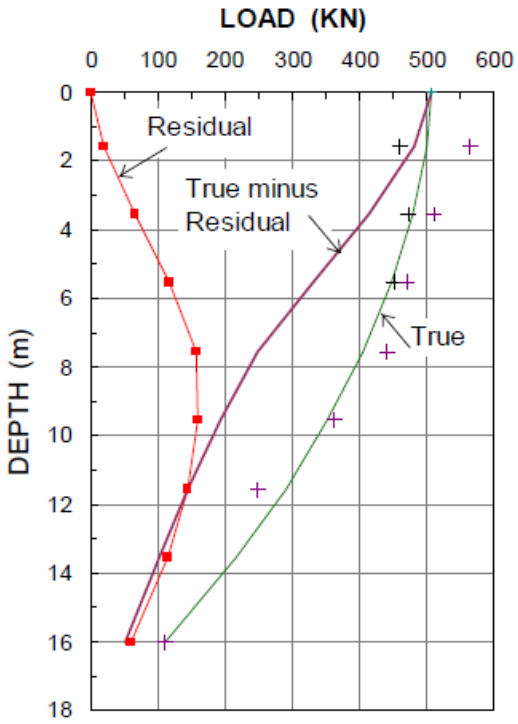


Figure 2-8: Load distributions along a displacement pile with residual axial loads showing the true load and the apparent loads (true minus residual) on neglect of residual load (Fellenius 2002).

2.5 Pile shaft resistance

The shaft resistance of displacement piles in sands has been estimated by assuming the radial stresses acting on the pile shaft at failure can be treated by an earth pressure approach with $\sigma'_{rf} = K_f \sigma'_{v0}$, then relating the shaft shear stresses to σ'_{rf} through a friction angle δ_f by a Coulomb failure criterion.

$$\tau_f = K_f \sigma'_{v0} \tan \delta_f \leq \tau_{f,\lim} \qquad 2\text{-}5$$

$$Q_s = A_s \int_{h=0}^{h} \tau_f dh \qquad 2\text{-}6$$

where σ'_{v0} is the in-situ effective vertical stress before pile installation, K_f is a coefficient of earth pressure on the pile during axial static loading to failure, and δ_f the interface angle of shear resistance. The earth pressure based approach proposed by Meyerhof (1951) was adopted as the main text method of the API RP2A recommendations in its first edition. The first edition's recommended design values for cohesionless soils did not explicitly incorporate sand density states. Instead δ_f were estimated by reducing estimates for 'typical' medium–dense shearing resistances φ' by 5^0 with the values increasing with grain size. No database was provided to justify the values

selected. Empirically chosen K_f values of 0.7 and 0.5 were recommended for shaft compression and shaft tension capacity respectively as shaft resistance was considered lower in tension.

In the 1984 15th edition the API RP2A parameters were significantly revised following a review by Olson and Dennis (1982). Although the approach to determine shaft shear resistance remained essentially the same, Olson and Dennis (1982) recommended addressing the density state as a variable in addition to grain size distribution in the parameters selection process. In 1993 Pelletier et al. offered an extensive review of the API design method but it has essentially remained unchanged until its current guidance, API RP2 GEO (2011), which maintains a modified version of the earth pressure approach as the main text method and incorporates in its commentary ICP-05, FUGRO-05, NGI-05 and UWA-05 'modern' CPT-based approaches. In the API RP2 GEO (2011), Table 2-1, the term '$K_f\tan\delta$' has been replaced by β to reduce confusion with measured δ values and the risk of errors, Jeanjean et al. (2010). To remove un-conservatism, the original main text method is no longer recommended for very loose and loose sands, loose sand silts and medium dense silts, and dense silts.

Density index, I_D (%)	**Soil description**	**Shaft friction factor $\beta = \tau_f/\sigma'_{v0}$**		**$\tau_{f,lim}$ (kPa)**
		Closed-end	**Open-end**	
Very loose (0 – 15)	Sand	N/A	N/A	N/A
Loose (15 – 35)	Sand			
Loose (15 – 35)	Sand-Silt			
Medium (35 – 65)	Silt			
Dense (65 – 85)	Silt			
Dense (65 – 85)	Gravel			
Medium (35 – 65)	Sand-silt	0.36	0.29	67
Medium (35 – 65)	Sand	0.46	0.37	81
Dense (65 – 85)	Sand-silt			
Dense (65 – 85)	Sand	0.57	0.46	96
Very dense (85 – 100)	Sand-silt			
Very dense (85 – 100)	Sand	0.70	0.56	115

Table 2-3: API RP2 GEO (2011) recommend practice for geotechnical engineering pile shaft capacity design parameters for cohesionless soils.

The API combined the earth pressure approach with imposing limiting shaft shear stress $\tau_{f,lim}$ values that act as cut-offs to the otherwise continuously increasing τ_f trends with depth. It had been suggested that critical depths existed, which were functions of initial density and pile diameter, below which the average shaft and base resistance effectively remained constant; Vesic (1970) or Meyerhof (1976). However instead of limiting shaft resistances with depth, Toolan et al. (1990)

postulated before Altaee et al. (1993) or Lehane et al. (1993) measured that displacement piles showed a tendency for the unit shaft resistance developed at any fixed depth below ground level to decrease as the pile tip advances. The shaft shear stresses exhibit maxima when the pile base reaches the fixed depth in question and attenuates as a result of geometrical 'friction fatigue' or other effects, as elaborated further later in this Chapter. Altaee et al. (1993) argued that Vesic's critical depth interpretation was hampered by measurement errors with displacement piles resulting from residual loads.

Alternative shaft capacity treatments to the earth pressure approach have been proposed. Some widely used design methods relate shaft shear resistance of displacement piles directly to pressuremeter limit pressures (e.g. Baguelin et al. 1986) or SPT blow counts (e.g. Canadian Geotechnical Society (1985)). CPT–based pile capacity estimation procedures are the preferred in several studies. Indirect CPT–based procedures use CPT results to estimate sand strength parameters which are used to estimate pile capacity after theoretical or semi-empirical methods. For the direct procedures, they can categorise into simplified CPT (α–type methods) and the modern CPT–based design methods. The α–type methods relate the shaft resistance to the CPT q_c as;

$$\tau_f = {q_c}/{\alpha_s} \le \tau_{f,\lim} \qquad 2\text{-}7$$

Although CPT sleeve friction measurements f_s were designed to help estimate shear resistance of piles their measurements are far more sensitive to testing variables and have lower reliability than q_c data making the latter a better parameter correlation with resistance. Abu–Farsakh and Titi (2004), Cai et al. (2008) and Schneider et al. (2008) have assessed the predictive reliability of the popular α–type methods. In such predictive reliability exercises the assessment of design methods typically revolves around comparing calculated pile axial capacities Q_c to the measured pile ultimate loads Q_m. Statistical analysis of the ratio Q_c/Q_m for each of the methods leads to mean ratios and Coefficients of Variation (CoV) (= standard deviation/ mean) that enable objective comparisons between the design methods. An ideal method applied to a perfect database would give $Q_c/Q_m = 1$ and CoV = 0; neither can be achieved in practice.

Abu-Farsakh and Titi (2004) used a very limited database of square prestressed precast concrete piles only in clay (26 piles) and clayey sands (9 piles) with embedded lengths between 9 – 38m and widths of 356 to 762mm to assess the methods 1 – 8 on Tables 2-2 and 2-4 reporting Bustamante and Gianeselli's (LCPC) (1982) method as giving mean Q_c/Q_m of 1.07 (i.e slightly un-conservative) and CoV of 0.24 and De Ruiter and Beringen (1979) with a mean Q_c/Q_m of 0.98 and CoV of 0.25 as the methods with the best performance. Cai et al. (2008) extended the exercise using similarly limited database of 32 piles in clay (21) and sand (11) with lengths between 12.5 and 24m

and diameters of 400 – 600mm to evaluate the same set of methods with two further methods referred to as CPTu methods (again on Tables 2-2 and 2-4) proposed by Eslami and Fellenius (1997) giving Q_c/Q_m of 1.04 and CoV of 0.21 and Takesue et al. (1998) giving Q_c/Q_m of 0.95 and CoV of 0.26 suggesting improved predictability over Bustamante and Gianeselli LCPC's Q_c/Q_m of 1.07 and CoV of 0.25 and De Ruiter and Beringen's Q_c/Q_m of 0.94 and CoV of 0.28. However, far worse results have been reported by reliability studies which use much bigger databases on the α–type methods. Schneider et al. (2008) assessment of the Bustamante and Gianeselli LCPC (1982) and Eslami and Fellenius (1997) along with the four modern CPT-based methods and the API RP2A standard API-00 (essentially API 1993) is reported in Section 2.8.

The α–type methods are mostly calibrated to specific databases. For example, Bustamate & Gianeselli (1982) concentrated mainly on closed–ended piles used in road and bridge works. The α-type formulations are not related to the physical mechanisms and processes applying around the displacement piles but use lump-sum approaches. They may be reliable when predicting capacities for piles with similar characteristics to their parent databases but any translation to other pile conditions (larger, smaller, different soils, tip conditions or L/D ratios) cannot be made without recalibrating the methods.

SN	Reference	Shaft friction (f)
1	Schmertmann (1978)	$Q_s = k\left[\sum_{d=0}^{8D}(d/8D)f_s A_s + \sum_{d=8D}^{L} f_s A_s\right]$ d – Depth to the f_s value being considered, D – pile width or diameter, A_s – Pile soil contact area per f_s depth interval, k values depend on d/D ratio
2	De Ruiter and Beringen (1979)	f = min [f_s; q_{ca}/300 (compression); q_{ca}/400 (tension); 120kPa]
3	Bustamante & Gianeselli (1982) LCPC	f = $q_{c,average}/k_{s1}$ k_{s1} = 30 – 150 depending on soil type, pile type and installation procedure $q_{c,average}$: equivalent average of q_c values of zone ranging from 1.5D below and above the pile shaft point being considered
4	Tumay and Fakhroo (1982)	$f = mf_{ca} \le 72kPa$, $m = 0.5 + 9.5\,e^{-0.09 f_{ca}}$ f_{ca} – average sleeve friction (kPa)
5	Aoki and De Alencar (1975)	$f = q_{ca}\alpha_1 / F_{s2} \le 120kPa$ α_1 = 1.4 – 6 depending on soil type F_{s2} depends on pile type (e.g. = 3.5 for concrete driven piles)
6	Price and Wardle (1982)	$f = \alpha_2 f_s$ α_2 depends on pile type = 0.53 for driven piles
7	Philipponnat (1980)	$f = q_{ca}\alpha_3 / F_{s2}$ α_3 depends on pile type (= 1.25 for concrete driven piles) F_{s2} = 50–200 depends on soil type
8	Clisby et al. (1978) - Penpile	$f = f_s / (1.5 + 14.47 f_s)$ f and f_s in MPa.
9	Eslami and Fellenius (1997)	$f = C_s q_c$ C_s - shaft correlation coefficient determined from the soil profiling chart. q_c - cone point resistance after correction for pore pressure on the cone shoulder and adjustment to effective stress.
10	Takesue et al. (1998)	For Δu < 300: $f = \left(\frac{\Delta u + 950}{1250}\right) f_s$ For 300 < Δu < 1250: $f = \left(\frac{\Delta u - 100}{200}\right) f_s$ Where $\Delta u = u_2 - u_0$, u_2 = Pore pressure measured behind the CPT cone tip, u_0 initial pore pressures in kPa.

Note: q_{ca} is the arithmetic average of q_c in a specified zone that depends on the method.

Table 2-4: Simplified CPT and CPTu – based α–type design methods (after Cai et al. 2008).

The ICP tests conducted in loose silica dune sand by Lehane (1992) then in dense silica marine sand by Chow (1997) allowed considerable advancements in the understanding of the shaft resistance behaviour. Figure 2-9 presents the ground profile and CPT profile for the loose sand site at Labenne, South France and Figure 2-10 shows the medium dense sand ground profile and CPT profile at Dunkirk, North France. The shaft shear stresses measured locally and inferred as averages from inter-cluster axial load cell data during installation at Labenne are shown in Figure 2-11. Figure 2-12 presents the corresponding local shear stresses during the moving and stationary phases of each stroke of installation at the Dunkirk site and Figure 2-13 plots the stationary radial stresses during the pause stages of jack installation. It is clear the interface stresses developed at both sites are not related to the σ'_{v0} trends but correlate instead with the fluctuating in-situ CPT profiles. The shear stresses in the loose sand are, as expected, globally less than in the dense sand, reflecting the lower CPT profiles in the loose sand. There is a clear attenuation of radial and shear stresses at any position above the advancing pile tip of the cyclically jack–stroke installing pile, Figure 2-13. Bond (1989), Lehane (1992), Chow (1997) and Jardine and Chow (1996) referred to this stress attenuation as the 'h/R effect'; h being the relative depth of the pile base below any given layer and R the pile radius. They argued that several factors acted to produce the attenuation including geometry and load cycling. However, others including Randolph et al. (1994) and White (2005) have preferred to use the term 'friction fatigue' coined first for pile driving in clays by Heerema (1979).

Along with the plots of the reported field measurements, unit shaft resistance profiles estimated using API RP2 GEO (2011) main text recommendations are plotted. In Figure 2-11 where the loose to medium dense sand local unit shaft resistance shows a strong h/R effect, the API tends to under-estimate the shaft stresses for short piles (low h/R) then potentially over-estimate shaft resistance as increasing penetration makes the pile more slender (higher h/R) while in the dense sand Figure 2-12 the API profile is seen to under-estimate the unit shaft resistance even for the most slender case.

Lehane (1992), Lehane et al. (1993) found that the shaft resistance in compression (Figure 2-14) is controlled by the Coulomb failure criterion;

$$\tau_f = \left(\sigma'_{rs} + \Delta\sigma'_{rd}\right)\tan\delta_f \qquad 2\text{-}8$$

where τ_f is the shaft shear resistance, σ'_{rs} is the stationary radial stress on the pile shaft, $\Delta\sigma'_{rd}$ is a shaft radial stress increment caused by local dilation on loading and δ_f is the constant volume/ critical state angle of interface shear resistance which maybe determined from interface ring or

direct shear tests and is not dependent on sand density state. The radial stress dilation on loading was estimated from simple elastic cylindrical cavity expansion as;

$$\Delta\sigma'_{rd} = 2G\Delta r / R \qquad 2\text{-}9$$

G is the operational shear modulus along the shaft and Δr is the dilation at the pile interface. Chow (1997) confirmed the same features in her ICP tests in denser Dunkirk sand.

Jardine and Chow (1996), Jardine et al. (2005a) extended the observations from closed–ended (full displacement) piles studies to large capacity open–ended (partial displacement) driven piles by considering alternative hypotheses for σ'_{rs} on instrumented CLAROM open–ended steel pipe pile driven at Dunkirk (Brucy et al. 1991), then checked their preferred hypothesis against a high quality static load tests database of 81 piles. The pile shaft resistance is similarly defined by the Coulomb failure criterion after Lehane (1992) by;

$$\tau_f = a\left(b.\sigma'_{rs} + \Delta\sigma'_{rd}\right)\tan\delta_f \qquad 2\text{-}10$$

where *a* is prescribed as 0.9 for open-ended piles failed in tension reducing the shaft shear resistances by 10%, otherwise it is set as 1.0 for all other cases; *b* reduces the final stationary stresses on the pile in account of the axial loading direction and is taken as 0.8 for piles in tension and 1.0 for piles in compression. Lehane (1992) found that a power law can be used to estimate the stationary radial stresses acting on the shaft after installation. Chow (1997) found that equation 2-11 offered the best fit to the combined Labenne and Dunkirk databases. The first part $q_c/34$ represents the maximum stationary radial stress developed at the shoulder of the pile base at end of installation, the $(h/R)^{-0.38}$ term accounts for the rapid attenuation of the stress for points above the pile base while $(\sigma'_{v0}/p_a)^{0.13}$ refers to a weak relationship with the existing in–situ overburden pressure.

Chow (1997) also incorporated for open–ended partial displacement piles the term R* which is the equivalent radius $(R^2 - R_i^2)^{0.5}$ of an equivalent solid pile, basing this on her interpretation of open ended instrumented pile tests at Dunkirk and theoretical consideration to account. The shaft shear modulus G used to estimate dilation stresses is obtained from CPT q_c correlation by Baldi et al. (1986), h/R* is limited to ≥ 8. The critical state angle of interface shear resistance should be determined from interface ring shear tests. This angle does not vary with density and guidance charts are also given that captures the potential reduction of δ_{cv} with increasing $d_{50\%}$ by Jardine et al. (2005a).

$$\sigma'_{rs} = 0.029 q_c \left(\sigma'_{v0} / p_a\right)^{0.13} \left(h / R*\right)^{-0.38} \qquad 2\text{-}11$$

Slightly different approaches have been adopted for estimating the shaft shear resistance in the FUGRO-05 and UWA-05 variants on the ICP as summarised in section 2.7.

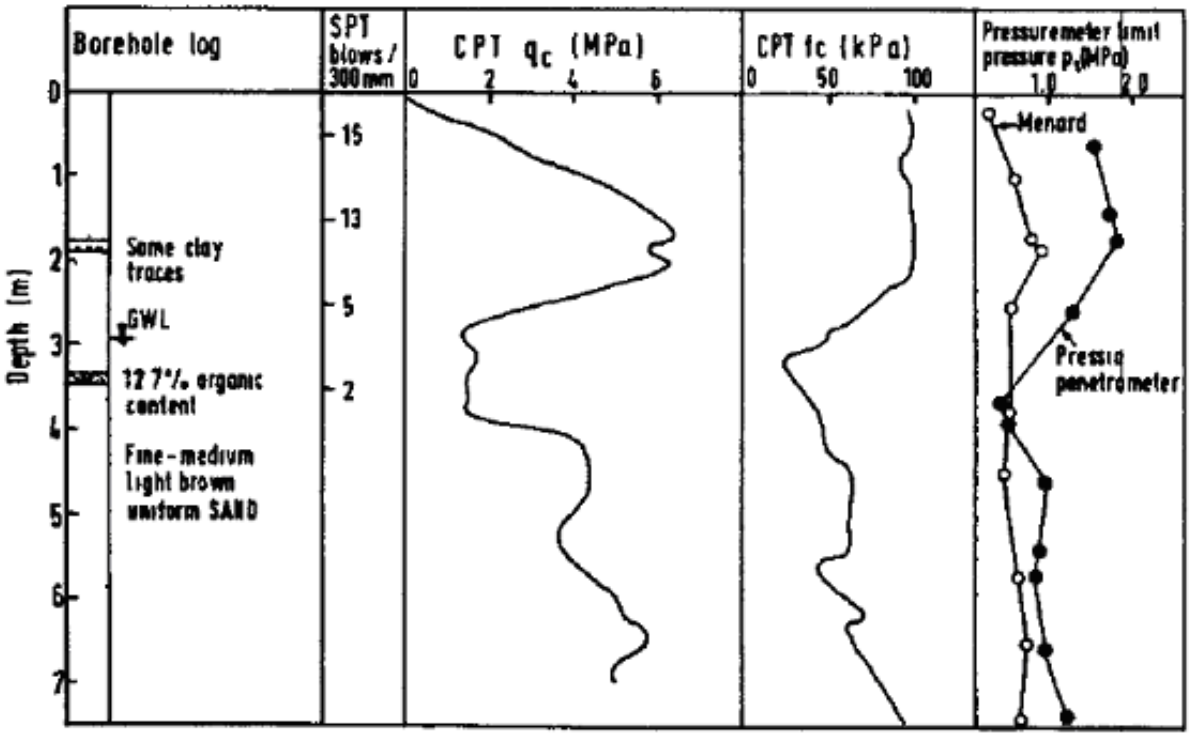


Figure 2-9: Borehole log and in-situ test results for loose dense dune sand at Labenne, France (Lehane, 1992).

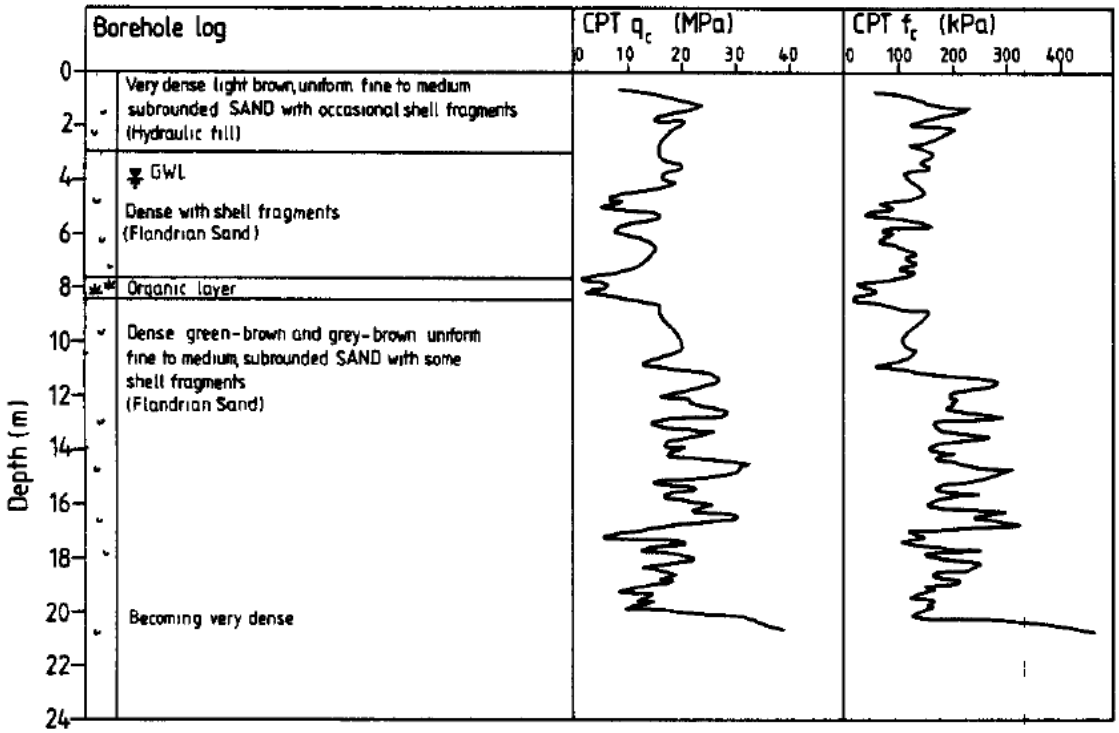


Figure 2-10: Dunkirk dense silica marine sand borehole log and CPT profile (Chow, 1997).

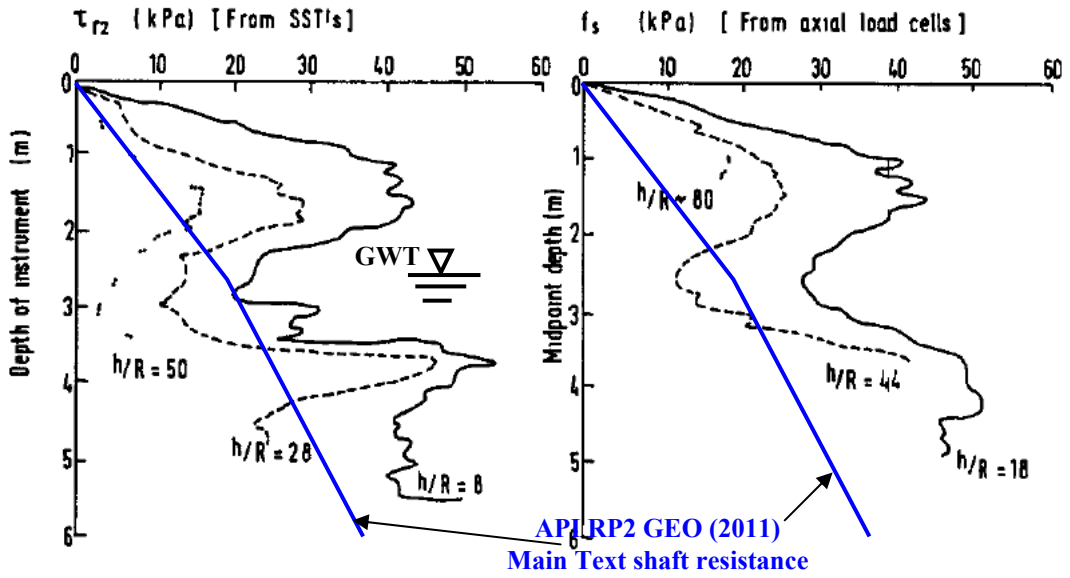


Figure 2-11: Displacement piles τ_{rz} and f_s measurements during installation in Labenne dune sand by Lehane (1992) and the corresponding API RP2 GEO (2011) main text design shaft resistances.

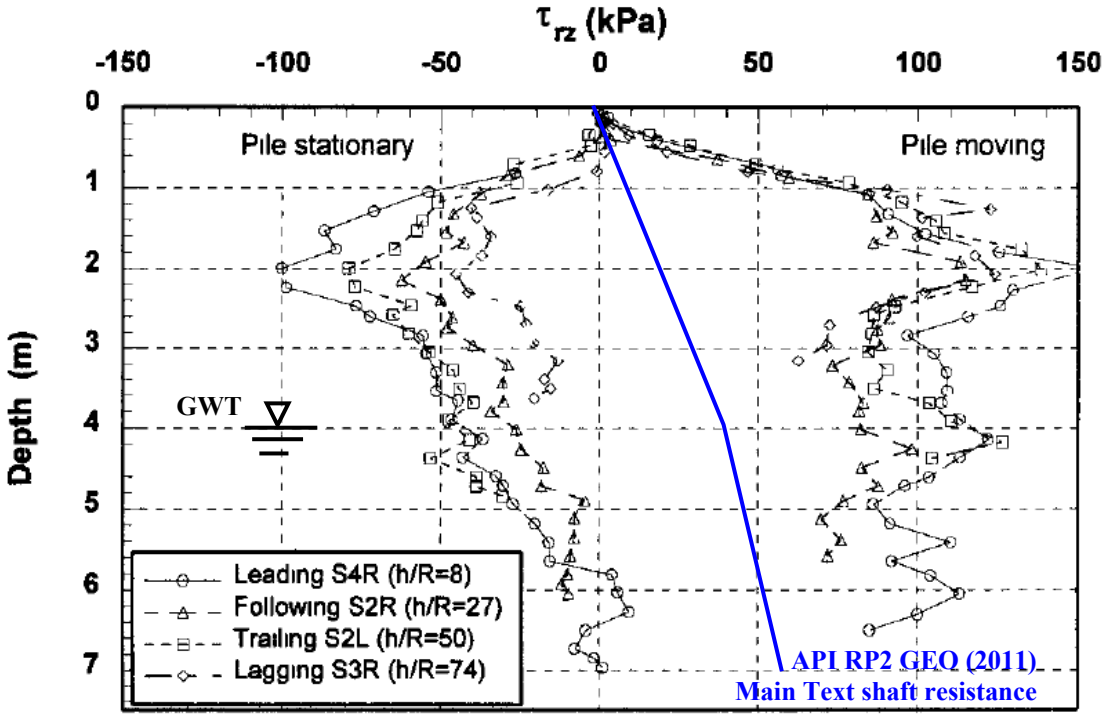


Figure 2-12: Local shear stress measurements from the Surface Stress Transducers during installation of displacement pile DK2 in medium dense Dunkirk marine silica sand (Chow, 1997).

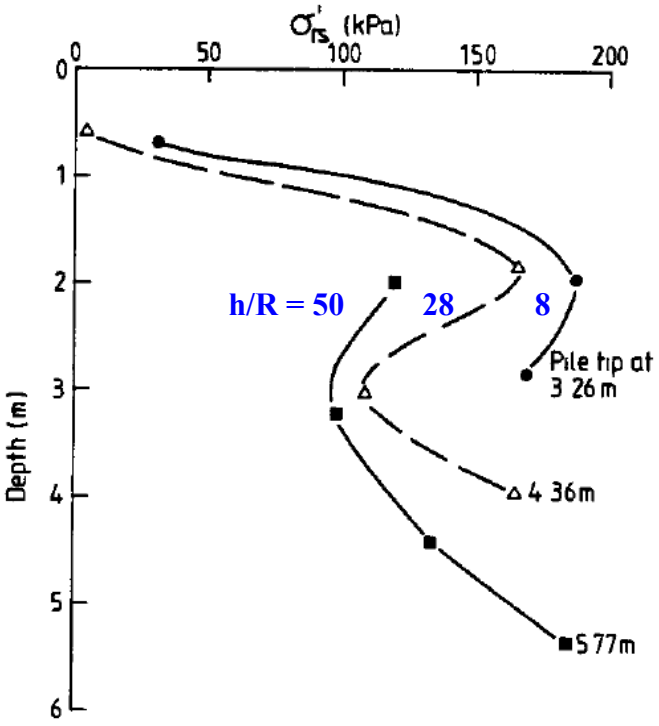


Figure 2-13: Stationary radial effective stresses during displacement pile DK2 installation in medium dense Dunkirk marine silica sand (Chow, 1997).

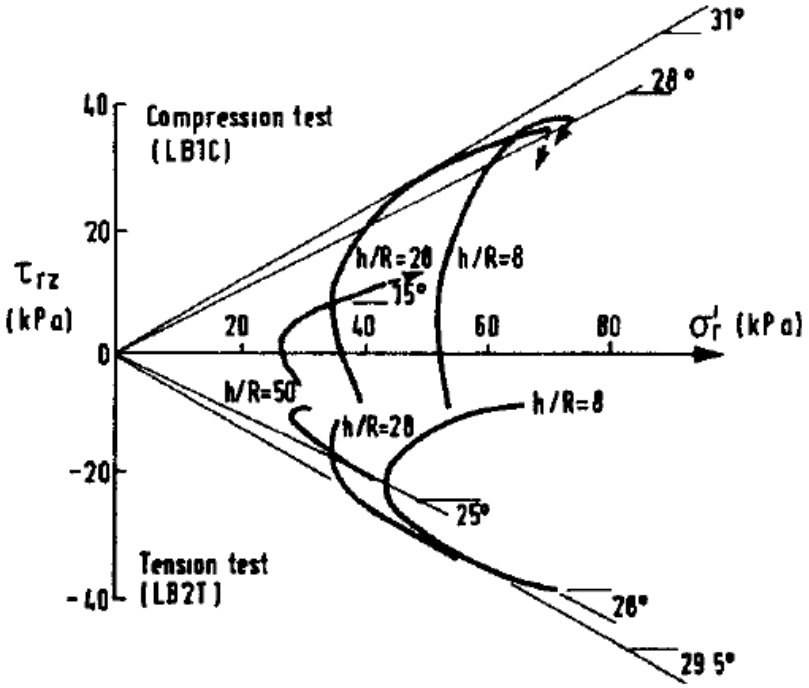


Figure 2-14: Labenne loose dune sand displacement piles static loading interface effective stress paths, (Lehane 1992).

2.6 Installation cyclic loading effects on shaft resistance

It is rational to consider how the mode of installation of displacement piles, jacked or driven, impacts on the static axial capacities realised. Lehane et al. (1993) considered the attenuation of stationary radial stresses σ'_{rs} along the shaft with reference to relative pile base depth or normalised net shear displacement at the interface (h/R). This σ'_{rs} formulation does not explicitly account for the number of blows or cycles applied to the displacement piles. It is usual to estimate the blows required for pile driving and the blow-counts are used to help monitor driving. The number of blows depends on many factors which generally can not be pre-determined accurately before installation. The possible effects of the absolute number of cycles involved in installation remains a point of debate.

Some field and model piles test studies indicate that installation effects on the on-pile radial stresses are dominated by the number of shearing cycles. The CPT (D_{CPT} = 43.7mm) sounding shown in Figure 2-15(a) presents data gathered by DeJong (2001) in medium dense sand using an instrument equipped with four friction sleeves located at h/R = 8 to 70. The CPT was installed effectively monotonically by 1m long strokes and sleeve friction was reported as practically constant over the h/R range considered implying τ_{rz} was not varying with h from h/R > 8, although an alternative trend of τ_{rz} attenuating with h/R can be proposed, Figure 2-15(b), on considering the S4 measurements are an outlier.

White and Lehane (2004) performed drum centrifuge (1.2m outer diameter, 0.8m inner diameter ring and 0.3m deep) tests with instrumented 9mm square stainless steel (R_{cla} = 0.55μm) model displacement piles (centrifuge channel: pile width (B) ratio = 22.2) in uniform rounded fine silica sand ($d_{50\%}$ = 0.18mm, I_D varied with depth from 20% - 90%) to investigate the relationship between σ'_{rs} on the piles to the height behind the tip or number of cycles during installation, as shown in Figure 2-16. They argued a clearer correlation of the shaft σ'_{rs} to the number of cycles of installation than to the net shear displacements, the greatest degradation being in the range 0 – 50 cycles with q_c–normalised σ'_{rs} (= their σ'_{hc}) stresses remaining about constant thereafter. However, the pile surface stress measurements were made by Kyowa PS-5KA miniature stress sensor devices which were found by Zhu et al. (2009) to need close cyclic calibrations as they suffer from marked cell-action effects in sands. No details of the sensors calibration were reported and these features may have affected the centrifuge results.

White and Lehane (2004) showed the implications of the effect of the number of cycles on the construction of a 350mm square precast concrete pile that was initially installed in a uniform medium dense sand deposit with $q_c \approx$ 22MPa by applying 1.5m long jack–strokes to a depth of 6.3m then the installation process was changed to 22 strokes each 0.075m long, Figure 2-17. The pile

showed at this point a change to a practically flat pile head force-depth trend indicating in this case a clear sensitivity to the absolute number of cycles applied.

White (2005) cites similar behaviour in jacked model pile tests conducted in uncemented weak marine calcareous sands at North Rankin site, offshore Western Australia, Figure 2-18. Tension tests were conducted on model piles of 60mm diameter and 2500mm length (L/D = 42) monotonically jacked below a borehole base. Friction on the model jacked piles was comparable to the site's CPT sleeve friction (~55kPa) which led to the North Rankin piles being designed at τ_{sf} = 40kPa (Renfrey et al. 1988). The latter estimate over-predicted the full-scale driven pile capacity as proven by pile runs in the field and resistance of 4 to 19kPa pull-out tests on 762mm diameter hammer-driven conductors. Dolwin et al. (1988), Randolph (1988) reported the progressive reduction in shaft resistance shown in Figure 2-18 during continuous driving deduced by CAPWAP analyses of main piles driving data.

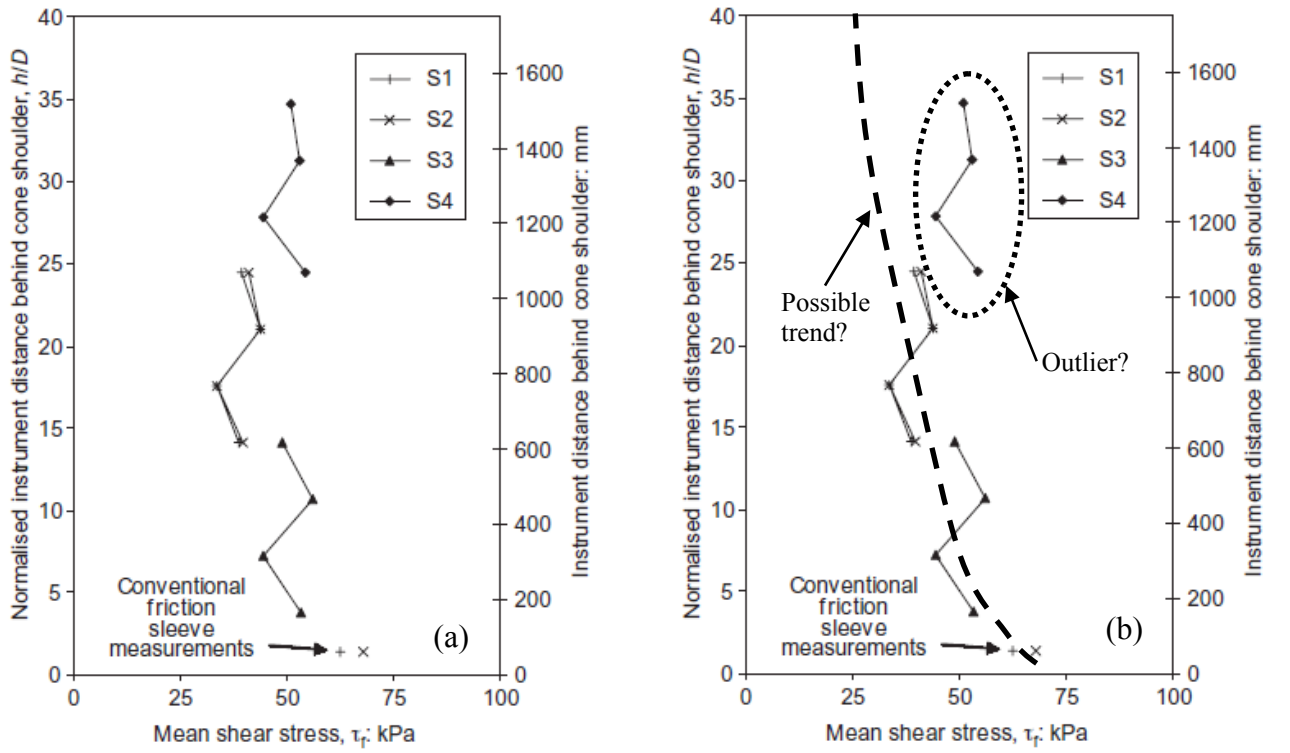


Figure 2-15: (a) Distribution of shaft friction on a multi–friction sleeve CPT instrument with 43.7mm diameter (DeJong, 2001), (b) Author's suggested alternative trend.

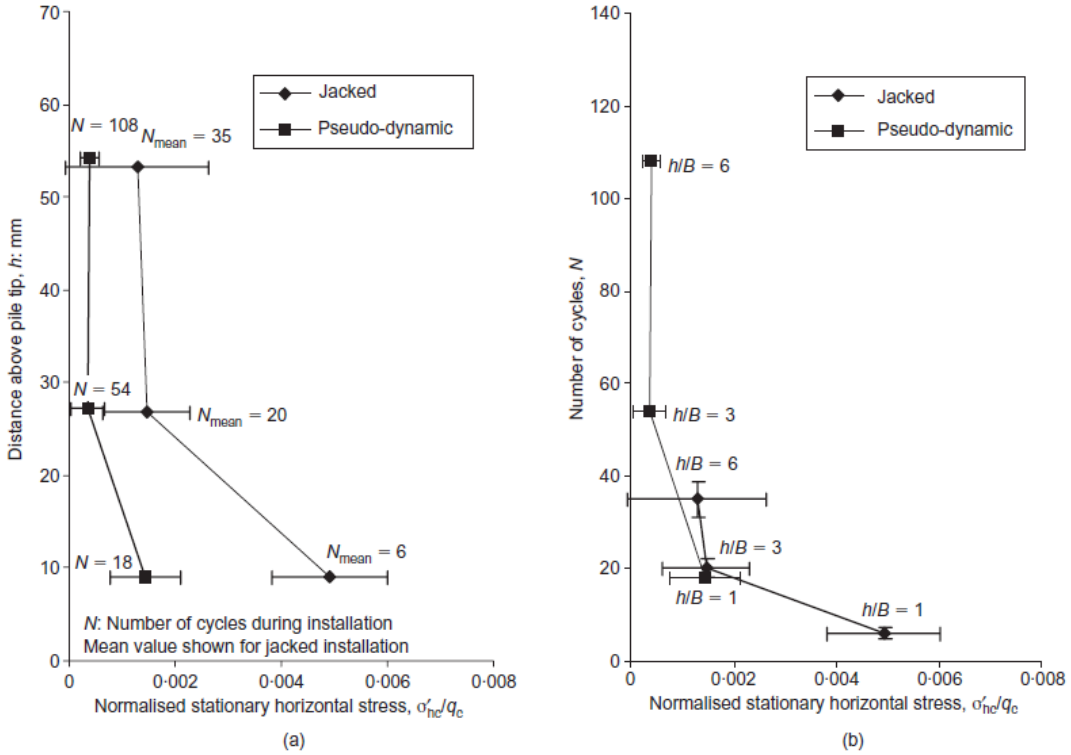


Figure 2-16: Influence of loading cycles during installation on stationary horizontal stress (a) normalised horizontal stress against distance above pile tip; (b) normalised horizontal stress against number of cycles (White and Lehane, 2004).

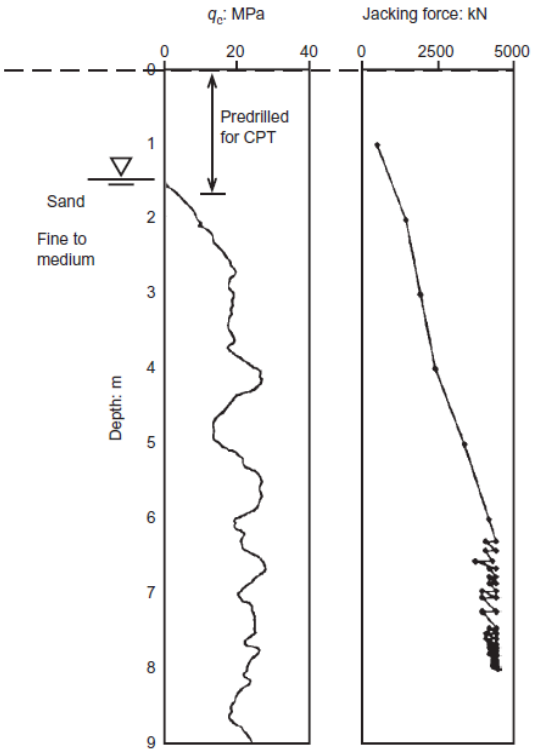


Figure 2-17: Jacking record for a precast concrete pile in sand installed by 1.5m long jack–strokes to a depth of 6.3m followed by 0.075m long strokes to a depth of 7.95m (White & Lehane, 2004).

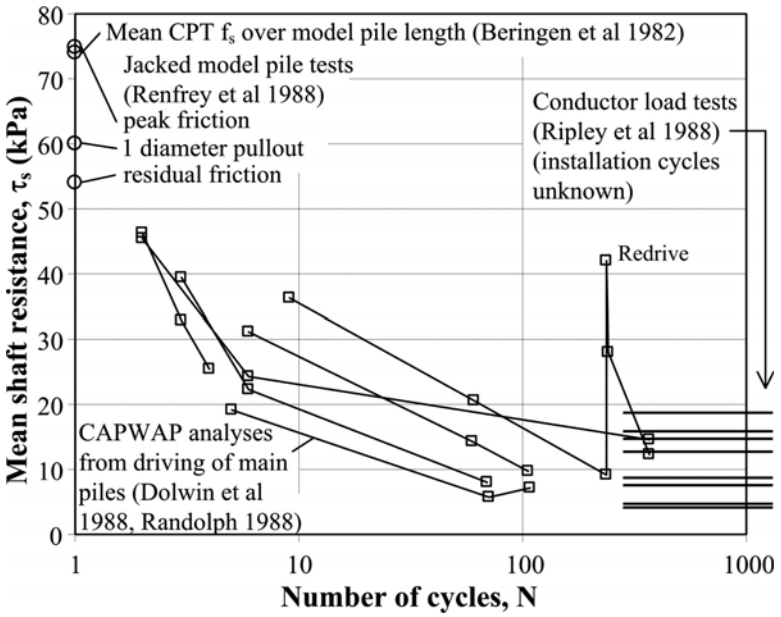


Figure 2-18: Influence of number of loading cycles (i.e. hammer blows) on shaft resistance in uncemented weak marine calcareous sands at North Rankin, (White, 2005).

Gavin & O'Kelly (2007) reported field tests with an instrumented stainless steel tubular closed-ended 73mm outer diameter displacement piles installed to various lengths with L/D up to ~40 aiming to study the different behaviours of jacked and driven piles. The piles were installed in heavily over-consolidated, glacially derived, very dense fine Blessington sand with average CPT tip $q_c \approx 15 - 18$MPa with sleeve friction, f_s increasing from 100kPa to 280kPa with depth. The piles were either jacked-in monotonically at rates of 20mm/s or subjected to total unloading after each stroke to simulate pile driving installations. They observed higher side friction on the monotonically installed piles to the cyclically installed comparator. The stationary effective radial stresses controlling the shaft friction resistance were also greater for the monotonic installation (although details on the calibration of their Entran total earth–pressure cells are not provided) and reportedly dependent on the CPT q_c profile, the h/D ratio and the number of load cycles. The stationary effective radial stresses were also observed to reduce during initial load cycling applied after installation especially at higher cyclic loading levels. Although the radial stress levels acting on the monotonically installed piles were initially much higher than those recorded for the cyclically installed piles, the values were indistinguishable after application of relatively small number (~ 50) of load cycles.

Jardine et al. (2013a) reported stresses measured on and around the shaft of closed–ended 36mm OD stainless steel (R_{cla} 3-4μm) Mini-Imperial College Pile (Mini–ICP) as well as standard CPT cone tip–ended piles singly installed in a calibration chamber (1.2m diameter by 1.5 deep, $d_{chamber}/D = 33.3$) of medium dense NE34 Fontainebleau sand ($d_{50\%} = 0.21$mm, $e_0 = 0.62$ and $I_D = 72\%$) investigating the effects of jack-stroke installation modes as well as number of cycles on

installation. Figure 2-19 shows the moving and stationary radial stresses generated in the sand mass at a distance 5R from the installing pile CPT1 where the jack load was maintained in between installation strokes and CPT2 where the jack load was fully removed in between strokes. Sand stress measurements were made by miniature Kyowa and TML type total stress sensors that had been closely calibrated to account for cell-action effects, following Zhu et al. (2009). Marginal effects of changing the number of strokes on the normalised radial stresses are reported for the 'pause period' stresses and a slightly lower maximum stress developed in CPT2. But generally the decay of the jacking stresses in the sand mass was found to be less heavily influenced by the number of jacking cycles than the interface stress measurements discussed above.

The stresses developed in the sand mass during installation by jack strokes of two displacement piles Mini-ICP1 and Mini-ICP2 pushed in by 92 10mm (to 920mm) and 198 5mm (to 990mm) length strokes respectively are presented in Figure 2-20. The radial moving stresses at two positions 2R and 3R away from the pile are plotted against both the number of cycles of installation N and the normalised pile tip distance from the sensor level h/R. The stress decay curves in the sand mass are more compatible when plotted against the h/R rather than N. Jardine et al. (2013a) accept that the number of cycles may be more influential when considering stress degradation at the pile interface although no consistent difference in the stress degradation was reported at the interface for the Mini-ICP1 and Mini-ICP2 tests. Doubling the number of cycles did not lead to any significant interface stress changes.

Other studies that have reported stress measurements in the sand mass around displacement piles in sands including the field study with closed-ended pile in Dunkirk marine silica sand by Chow (1997), Gavin & Lehane's (2003) open-ended model pile in a laboratory calibration chamber filled with Blessington sand and Allard's (1990) centrifuge testing of driven closed-ended model piles in Nevada silica sand. These are reviewed and compared with the Author's measurements in Chapter 8.

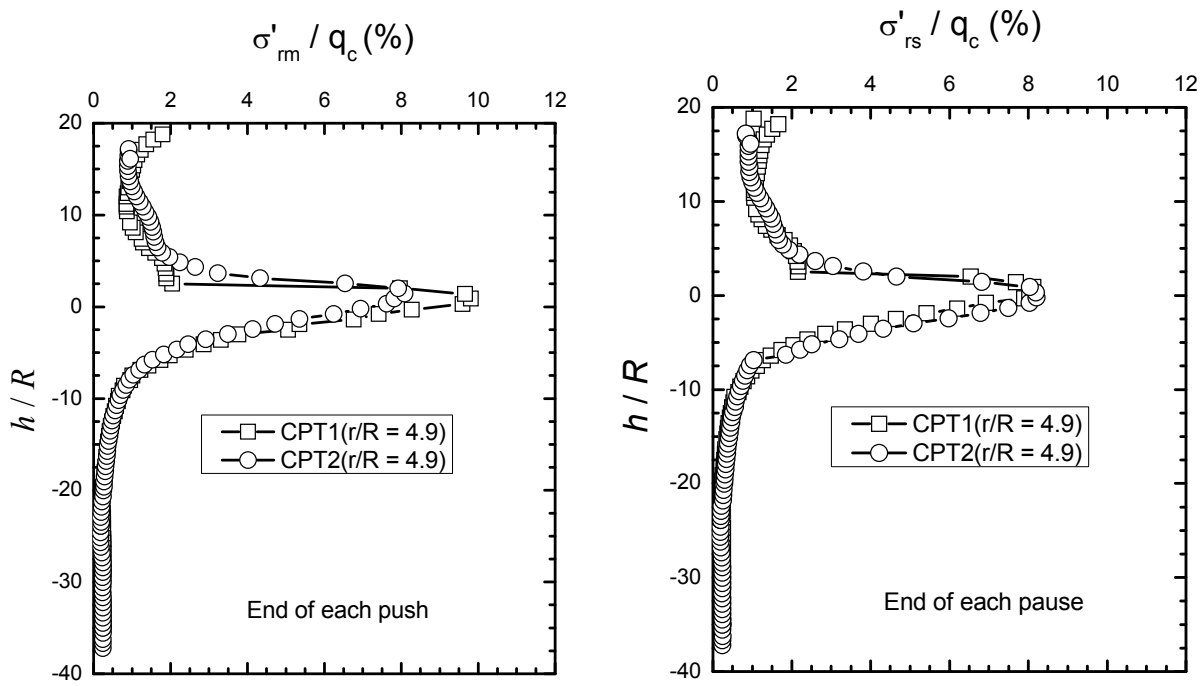


Figure 2-19: Effect of installation method on radial stresses (a) at the end of each push, and (b) at the end of each pause for CPT1 and CPT2 (Jardine et al. 2013a).

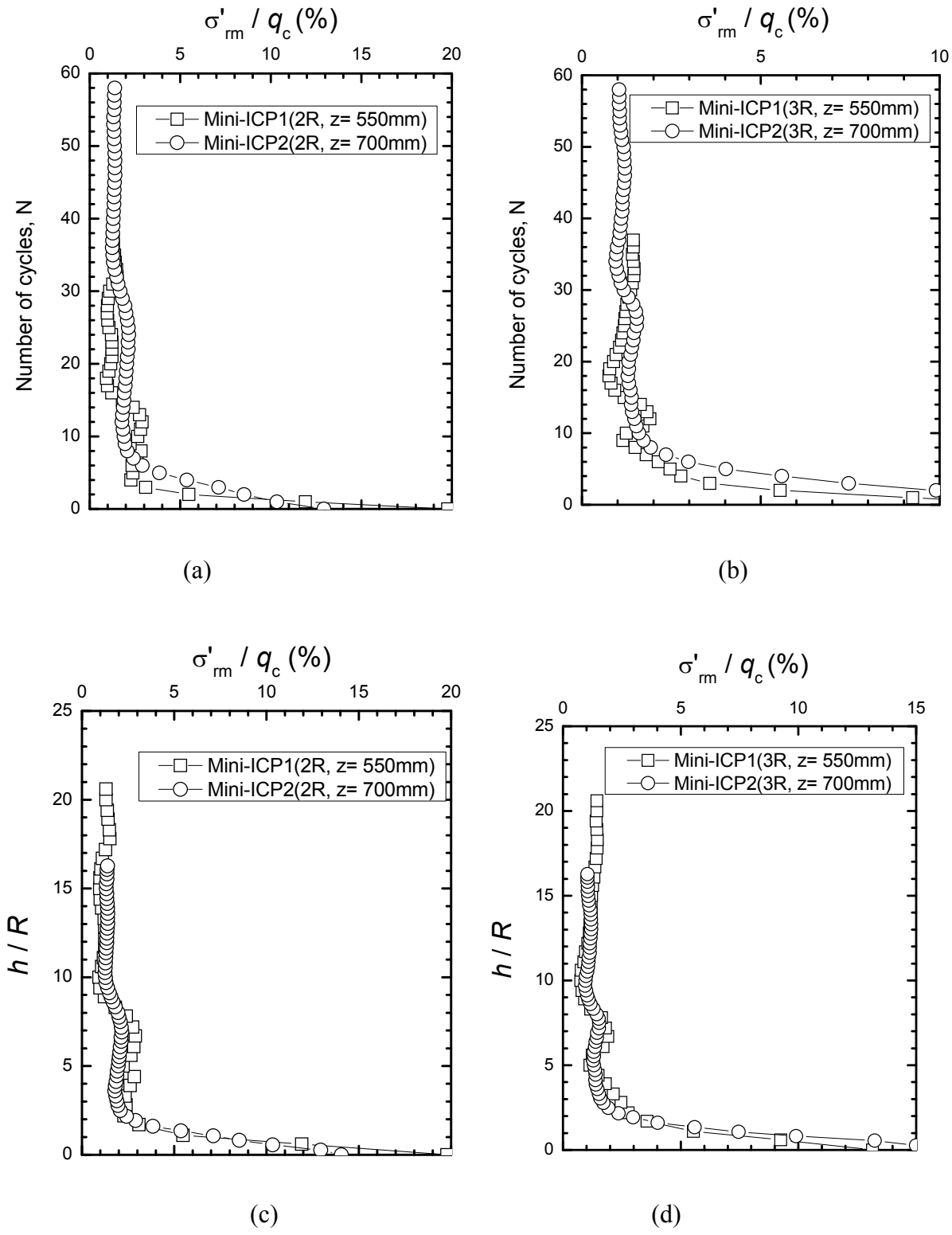


Figure 2-20: Comparative influences of number of cycles N (a & b) and relative pile tip depth h/R (c & d) on moving radial stresses (Jardine et al. 2013a).

2.7 Variants of the CPT–based ICP-05 method

Three modern CPT-based design methods FUGRO-05 (Kolk et al. 2005a), NGI-05 (Clausen et al. 2005) and UWA-05 Lehane et al. (2005a,b), have been included together with ICP-05, into the API RP2 GEO commentary as alternative design procedures. Schneider et al. (2008) summarised

the base and shaft resistance design formulations of these four methods for siliceous sands as shown on Table 2-5 for base resistance and Table 2-6 for shaft resistance.

FUGRO-05 aimed to improve the ICP-05 design criteria by calibrating the formulation more precisely for axially loaded driven pipe piles in sands. For this, the ICP-05 was re-fitted to a restricted database of 45 (24 tension and 21 compression) pile load tests. The database included large-scale instrumented load tests reported by (Kolk et al. 2005b, c) and Fugro (1995) with other well known open and closed-ended steel pipe piles load tests. However, the database featured some tests in non-siliceous cemented sands, silts and clay from the Ras Tanajib test site and micaceous sands from Jamuna Bridge. FUGRO-05 adopted the Coulomb failure criterion for shaft capacity, as with the ICP-05. The interface angle of shearing, although was taken as constant $\delta = 29^0$ for all cases. Interface dilation during loading was ignored and the shaft resistance formulations were calibrated by regression to give the forms in Table 2-6.

The FUGRO-05 predicts higher stresses at h/R* = 4 than ICP-05 and assumes more rapid attenuation of stresses beyond that. FUGRO-05 defined the base resistance for both large displacement and small to non-displacement piles as being independent of diameter. As far as time effects on capacity are concerned Kolk et al. (2005) reported increase in frictional capacity with time from their dataset indicating that FUGRO-05 will overpredict capacities of piles loaded within 50 days but underpredict the tensile capacities of piles tested after longer set-up periods.

The NGI-05 'CPT–based' sand method (Clausen et al. 2005) requires only three sand parameters; unit weight, pore water pressures and relative density. CPT cone resistances (or SPT, PMT or pile driving resistance values) are only used to obtain the sand relative density. Installation 'friction fatigue' effects along the pile are incorporated using a sliding triangle approach similar to that of Toolan et al. (1990) and the shaft resistance mobilised by open-ended piles in sand is assumed to be about one-third lower than closed-ended piles. Based on 85 pile load tests from 35 locations, most with CPT test data (56) the shaft and base resistances were formulated as in tables that follow. Neither the shaft nor the base resistance of the NGI-05 method are considered pile diameter dependent. Clausen et al. (2005) recognised potential time effects on capacity but did not offer any treatment because the time between driving and load testing was not known for most of their piles.

UWA-05, was developed by the University of Western Australia by Lehane et al. (2005a) after API commissioned a review of the ICP, FUGRO and NGI CPT-based methods to assess their predictive reliabilities and inform the revision of the RP2A design guidelines. The UWA-05 was calibrated against a database of 77 pile load tests with diameters greater than 0.2m (and primarily less than 0.8m) with lengths greater than 5m (mainly between 10 and 20m) and typical maximum static capacities (at base displacements of 0.1D) less than 5MN. Their elaboration of the ICP-05

incorporated alternative q_b approach by Xu et al. (2008) as covered in section 2.3, for open ended piles using the effective area ratio which incorporates the Incremental Filling Ratio (IFR) after White et al. (2005) as summarised in Table 2-6 below. The attenuation of stresses along the pile shafts was treated by an h/R term that did not explicitly incorporate dependency on number of jacking cycles or driving blows N.

The next section summarises selected published assessments of the relative improvements the modern CPT-based methods offer in predictive reliability compared to the API main text method recommendations.

Methods	End condition	Design equations
Fugro-05	Closed and open ended	$q_{b0.1}/q_{c,avg}=8.5(p_{ref}/q_{c,avg})^{0.5}A_r^{0.25}$
ICP-05	Closed ended	$q_{b0.1}/q_{c,avg}=$maximum $[1-0.5\log(D/D_{CPT}),0.3]$
	Open ended	if $D_i \geq 2.0(D_r-0.3)$ or $D_i \geq 0.083 q_{c,avg}/p_{ref} D_{CPT}$, D_i in meters, then the pile is "unplugged," and $q_{b0.1}/q_{c,avg}=A_r$ if not, the pile is "plugged," and $q_{b0.1}/q_{c,avg}=$maximum $[0.5-0.25\log(D/D_{CPT}),0.15,A_r]$
NGI-05	Closed ended	$q_{b0.1}/q_{c,tip}=F_{D_r}=0.8/(1+D_r^2)$
	Open ended	$q_{b0.1}=$minimum [plugged $q_{b0.1}$, unplugged $q_{b0.1}$] the plugged $q_{b0.1}$ value is calculated as: $q_{b0.1}/q_{c,tip}=F_{D_r}=0.7/(1+3D_r^2)$ the unplugged $q_{b0.1}$ is calculated as: $q_{b0.1}=q_{b,ann}A_r+q_{b,plug}(1-A_r)$; $q_{b,ann}=q_{c,tip}$, and $q_{b,plug}=12\tau_{f,avg}L/(\pi D_i)$ $\tau_{f,avg}$: averaged external skin friction (Clausen et al. 2005); L: pile embedment depth
UWA-05	Closed and open ended	$q_{b0.1}/q_{c,avg}=0.15+0.45A_{rb,eff}$

Notes: D: pile outer diameter; D_i: pile inner diameter; $p_{ref}=100$ kPa; $D_{CPT}=0.036$ m; A_r (area ratio) $=1-(D_i/D)^2$; $A_{rb,eff}$ (effective area ratio) $=1-FFR(D_i/D)^2$; FFR: IFR $(=\Delta L_p/\Delta z)$ averaged over last $3D$ of the pile penetration; $q_{c,avg}=q_c$ averaged $\pm 1.5D$ over pile tip level for Fugro-05 and ICP-05 methods; $q_{c,avg}=q_c$ averaged using Dutch averaging technique for UWA-05 method; $D_r=0.4\ln(q_{c1N}/22)$; as decimal, nominal relative density which may be greater than 1.0 for NGI method.

Table 2-5: Modern (offshore) CPT-based design methods for base resistance of driven piles in siliceous sands after Schneider et al. (2008).

Methods	Design equations	
Fugro-05[a]	$\tau_f = 0.08 q_c \left(\frac{\sigma'_{v0}}{p_{ref}}\right)^{0.05} \left(\frac{h}{R^*}\right)^{-0.90}$	(compression loading for $h/R^* \geq 4$)
	$\tau_f = 0.08 q_c \left(\frac{\sigma'_{v0}}{p_{ref}}\right)^{0.05} (4)^{-0.90} \left(\frac{h}{4R^*}\right)$	(compression loading for $h/R^* \leq 4$)
	$\tau_f = 0.045 q_c \left(\frac{\sigma'_{v0}}{p_{ref}}\right)^{0.15} \left[\max\left(\frac{h}{R^*}, 4\right)\right]^{-0.85}$	(tension loading)
ICP-05	$\tau_f = a\left[0.029 b q_c \left(\frac{\sigma'_{v0}}{p_{ref}}\right)^{0.13} \left[\max\left(\frac{h}{R^*}, 8\right)\right]^{-0.38} + \Delta\sigma'_{rd}\right]\tan\delta_f$	
	a=0.9 for open-ended piles in tension and 1.0 for all other cases	
	b=0.8 for piles in tension and 1.0 for piles in compression	
NGI-05	$\tau_f = z/L p_{ref} F_{D_r} F_{sig} F_{tip} F_{load} F_{mat} \geq \tau_{min}$	
	$F_{D_r} = 2.1(D_r - 0.1)^{1.7}$	
	$D_r = 0.4 \ln(q_{c1N}/22)$	[nominal relative density (which may be greater than 1.0)]
	$F_{sig} = (\sigma'_{v0}/p_{p_a})^{0.25}$	
	F_{tip}=1.0 for driven open ended and 1.6 for driven closed ended	
	F_{load}=1.0 for tension and 1.3 for compression	
	F_{mat}=1.0 for steel and 1.2 for concrete	
	$\tau_{min} = 0.1\sigma'_{v0}$	
UWA-05	$\tau_f = \frac{f_t}{f_c}\left[0.03 q_c A_{rs,eff}^{0.3}\left[\max\left(\frac{h}{D}, 2\right)^{-0.5}\right] + \Delta\sigma'_{rd}\right]\tan\delta_f$	
	$A_{rs,eff}$(effective area ratio)$= 1 - \text{IFR}(D_i/D)^2$	
	A_r(area ratio)$= 1 - (D_i/D)^2$	
	IFR($=\Delta L_p/\Delta z$). When IFR is not measured, average IFR $=\min[1, (D_i(\text{m})/1.5)^{0.2}]$	
	f_t/f_c=ratio of tension to compression capacity (equal to 1 for compression and 0.75 in tension)	

Note: τ_f=local ultimate shaft friction; δ_f=interface friction angle; p_{ref}=100 kPa=reference stress; L=pile length; z=element depth; h=height above pile tip; R^*=equivalent pile radius$=(R^2 - R_i^2)^{0.5}$ where R_i=internal pile radius$=D_i/2$. For noncircular piles, an equivalent circular area is used to assess R^* and D. $\Delta\sigma'_{rd} \approx 4G\Delta y/D$=change in radial stress during pile loading; $G \approx 185 q_c q_{c1N}^{-0.7}$=operational level of shear modulus; see Eq. (8*b*) for calculation of q_{c1N}; $\Delta y \approx 2R_a \approx 0.02$ mm=radial displacement during pile loading; and R_a=average roughness of the pile.

[a]The format of the equation for compression shaft friction within $4R^*$ of the pile tip differs slightly from Kolk et al. (2005a) due to a typing error in that paper.

Table 2-6: Modern (offshore) CPT-based design methods for local shaft friction of driven piles in siliceous sand after Schneider et al. (2008).

2.8 Predictive reliability of the modern CPT-based design methods

Studies of the predictive reliability of driven piles axial capacity design methods have been undertaken to; 1) Evaluate the reliability of each individual design approach, 2) Offer guidance on the selection of design approaches, and 3) To indicate how the approaches can be improved.

As defined earlier, predictive reliability is typically evaluated by the ratio Q_c/Q_m for each of the methods leading their mean ratios and CoV for comparisons across methods. Assessments of design methods for a particular soil can be on a full (mixed/ comprehensive) database or on selective databases exploring particular characteristics such as load test directions; (compression or tension); shaft or base resistance, pile materials; (concrete, steel, timber) or pile geometry (open/closed, square/cylindrical). Statistical bias and skew have similarly been investigated to reveal particular characteristics of procedures in relation to parameters such as pile slenderness L/D or sand density state.

Several predictive reliability studies have been performed focusing on the CPT–based approaches' improved predictive reliability relative to the API-RP2A main text method. The API poor predictive performance, clear skew and biases (with sand density states and slenderness ratios) have been reported by various studies as summarise by Jeanjean et al. (2010) in Figures 2-21 to 2-24. Here, three independent predictive reliability studies were sampled and summarised as representative.

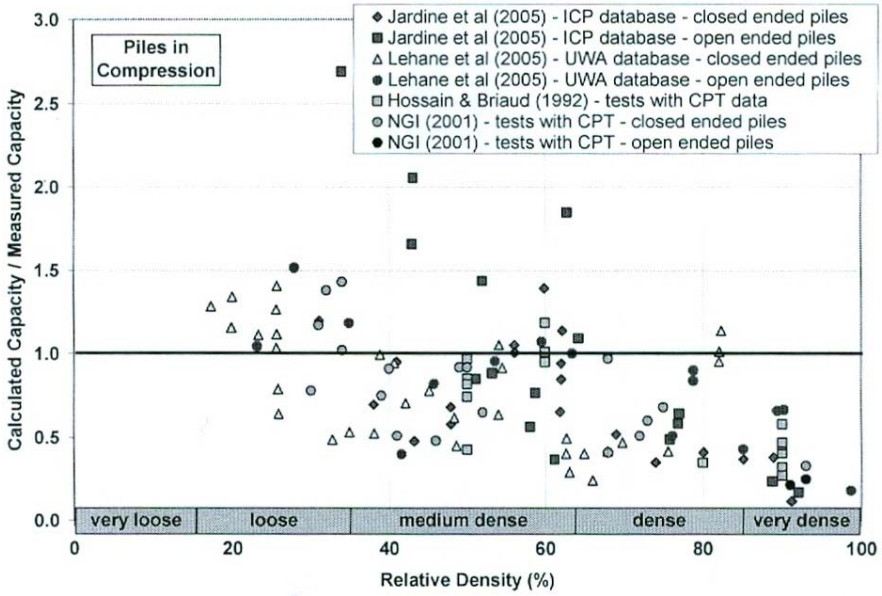


Figure 2-21: Q_c/Q_m pile compression capacity using API Main text method as a function of sand density index (Jeanjean et al. 2010).

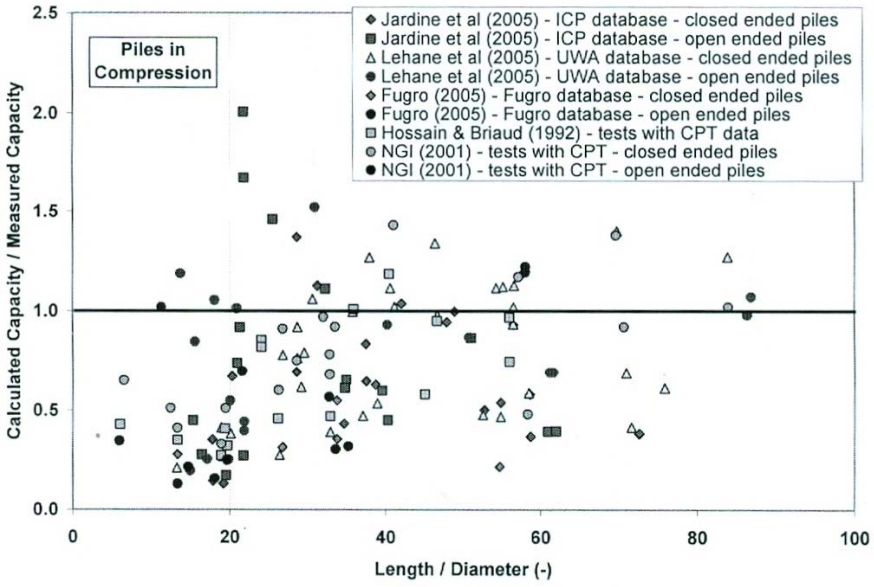


Figure 2-22: Q_c/Q_m pile compression capacity using API Main text method as a function of pile slenderness ratio (Jeanjean et al. 2010).

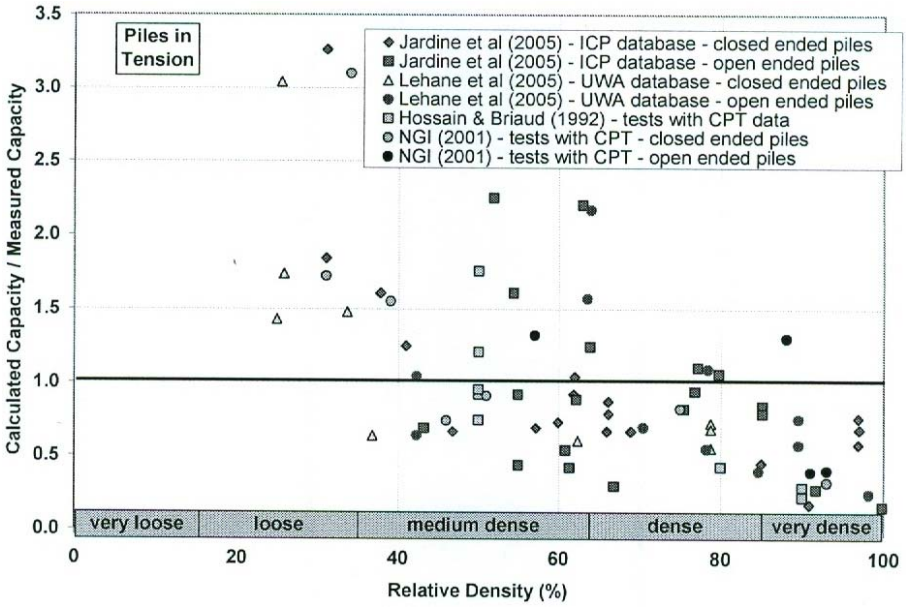


Figure 2-23: Q_c/Q_m pile tension capacity using API Main text method as a function of sand density index (Jeanjean et al. 2010).

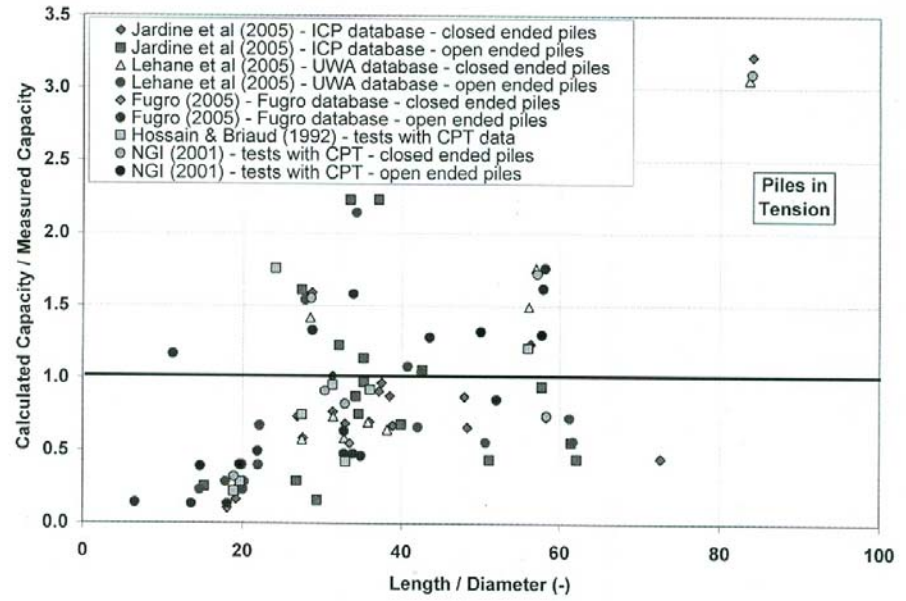


Figure 2-24: Q_c/Q_m pile tension capacity using API Main text method as a function of pile slenderness ratio (Jeanjean et al. 2010).

Lehane et al. (2005b) then Schneider et al. (2008) reported a predictive reliability study of seven displacement piles in siliceous sand design procedures; simplified (α–type) CPT methods LCPC (Bustamante and Gianeselli, 1982) and EF-97 (Eslami and Fellenius 1997), API main text method (2000) and the four modern CPT-based methods using the UWA database that calibrated the UWA-05 method Lehane et al. (2005a). The database was analysed as a whole (Table 2-7) and in subsets of closed–ended concrete piles in compression (17 pile load tests), closed–ended steel piles in compression (15), closed–ended piles in tension (12), open–ended steel pipe piles in

compression (17) and open–ended steel pipe piles in tension (16). Observations from the assessment included;

1) The design procedures considered tended to overpredict pile capacity in calcareous or micaceous sands and underpredict pile capacity in residual soils while capacities measured at a given site tended to increase with time.
2) The API main text method showed the highest variation for each of the subset databases which was, for example, upto four times the ICP-05 in the open ended piles tension capacity subset.
3) Bias in length and density implied that the API method overall remained conservative towards the database but with the largest scatter as cited.
4) The simplified (α-type) CPT-based methods overpredicted the capacity of open-ended piles in tension and compression. It is noted that these methods were not intended for use with open-ended piles. Predictions in compression were observed to be worse than tension indicating poorer reliability in end-bearing formulations.
5) Fugro-05 tends to overpredict the capacity of piles in compression and slightly underpredict the capacity of piles in tension. This tendency was attributed to be partly related to an end-bearing formulation which allowed q_b/q_c to be greater than unity and comparatively higher h/R* exponent resulting into steeper stresses attenuation on the shaft.
6) The NGI-05 procedure tends to provide the closest Q_c/Q_m mean value over the entire database being slightly less conservative while ICP05 and UWA05 appear marginally conservative in the full as well as all sub categories.
7) UWA-05 treatment of the influence of pile plugging during driving using measured IFR data where available appeared to reduce predictive scatter for the open ended piles compression.

	Entire database		
Method	μ_{gR}	Median	$\sigma_{\ln R}$
API-00	0.76	0.78	0.60
LCPC-82	1.23	1.27	0.40
EF-97	1.40	1.36	0.42
Fugro-05	1.04	1.11	0.35
ICP-05	0.91	0.92	0.27
NGI-05	1.01	0.96	0.31
UWA-05	0.92	0.90	0.25

Table 2-7: Performance of design methods against the entire UWA database where μ_{gR} is the geometric mean and σ_{lnR} standard deviation of the natural log of Q_c/Q_m (after Schneider et al. 2008).

Augustesen et al. (2005) evaluated three methods API-RP2A (1987 – 1993), NGI–99 (recently recast as NGI-05) and ICM–96 (recast as ICP-05) on a Danish Aalborg University database (AAU) (32 pile tests from 9 sites), an NGI database (122 pile tests from 52 sites) and the combined AAU and NGI database, Table 2-8. The NGI database featured 34 'super' pile tests which were used to develop and calibrate the NGI-99 design method (NGI 2001). Other piles are drawn from the databases Olson (1988), Randolph et al. (1994) and Chow (1997). The total database included 152 relevant pile tests from 59 sites (2 pile tests and sites from the AAU were excluded in the total) with pile diameter between 0.10m and 2.0m with the longest penetrating to 94m in deposits with q_c between 2.5 and 29MPa. The following are summary conclusions of Augustesen et al. (2005) regarding the combined and subset databases;

1) No time correction was employed as the time duration between installation and testing was unknown in most of the database case studies. However, generally Q_c/Q_m was observed to decrease with time from end of driving to load testing; that is the prediction methods were relevant in the short–term however in the medium to long term capacities tended to improve rendering the prediction methods conservative.
2) API-RP2A provided better estimate of the full database in terms of average Q_c/Q_m though with a higher variation than ICM-96.
3) Capacities of piles loaded in compression or tension are better predicted by the API main text in terms of the average Q_c/Q_m, though similarly with augmented scatter to the ICM-96.
4) ICM-96 showed more reliable predictions of the concrete piles subset database whereas API-RP2A and NGI-99 were more reliable for piles made of steel.
5) From subset databases with shorter or longer than 15m piles, it was recommended to use NGI-99 for piles longer than 15m and ICM-96 for piles with penetration depths less than 15m independent on whether the piles are driven open-ended or closed-ended.
6) ICM-96 provided more reliable estimates for piles with equivalent diameters less than 0.4m while API-RP2A was considered more reliable for piles with diameters exceeding 0.4m.
7) Generally, the calculation methods are very sensitive towards the way the soil profile and pile tests are interpreted.

	No. of piles / No. of sites	NGI-99 μ_{CM} / σ_{CM} [a]	API-2 μ_{CM} / σ_{CM} [a]	ICM-96 μ_{CM} / σ_{CM} [a]
All piles [b]:				
All piles in category	154 / 61	1.14 / 0.50	1.00 / 0.46	0.91 / 0.34
All piles:				
All piles in category	152 / 59	1.11 / 0.41	0.98 / 0.43	0.89 / 0.30
Piles loaded in compression	98	1.11 / 0.38	0.98 / 0.40	0.85 / 0.28
Piles loaded in tension	54	1.12 / 0.48	1.01 / 0.48	0.95 / 0.32
Piles driven open-ended	54	1.06 / 0.44	0.97 / 0.45	0.82 / 0.36
Piles driven closed-ended	98	1.14 / 0.40	0.98 / 0.42	0.92 / 0.25
Steel:				
All piles in category	115 / 46	1.10 / 0.43	0.94 / 0.41	0.87 / 0.30
Piles loaded in compression	68	1.08 / 0.39	0.92 / 0.43	0.81 / 0.28
Piles loaded in tension	47	1.14 / 0.49	0.95 / 0.38	0.95 / 0.32
Piles driven open-ended	50	1.09 / 0.44	0.99 / 0.46	0.84 / 0.36
Piles driven closed-ended	65	1.11 / 0.43	0.89 / 0.36	0.89 / 0.25
Concrete:				
All piles in category	37 / 13	1.15 / 0.36	1.11 / 0.46	0.95 / 0.28
Piles loaded in compression	30	1.18 / 0.34	1.03 / 0.30	0.95 / 0.26
Piles loaded in tension	7	1.00 / 0.43	1.41 / 0.84	0.96 / 0.37
Piles driven open-ended	4	0.71 / 0.16	0.75 / 0.16	0.57 / 0.26
Piles driven closed-ended	33	1.20 / 0.34	1.15 / 0.47	1.00 / 0.25
Group 4 [c]:				
All piles in category	61 / 15	1.09 / 0.30	1.01 / 0.50	0.94 / 0.28
Piles loaded in compression	43	1.08 / 0.25	0.98 / 0.43	0.88 / 0.23
Piles loaded in tension	18	1.10 / 0.40	1.07 / 0.66	1.09 / 0.34
Piles driven open-ended	23	1.15 / 0.40	0.88 / 0.39	0.97 / 0.36
Piles driven closed-ended	38	1.05 / 0.22	1.08 / 0.55	0.92 / 0.22

a) μ and σ are the mean value and the standard deviation of the *C/M*-ratios.
b) Cases with IDs 8 and 9, Kolding forrenseanlæg, are only included in these investigations.
c) This category includes all cases, where soil and pile data belong to Group 4 ($Q_{r,soil} = Q_{r,pile} = 4$), i.e. cases, where soil and pile data are especially well-described.

Table 2-8: Assessment of NGI-99, API-2 and ICM-96 predictive reliability against the combined AAU and NGI database (Augustesen et al. 2005).

Finally, Gavin et al. (2011) have provided a reliability assessment of existing design methods related to the estimation of tension capacity of open ended piles in sands as critical to multi-pile foundations such as for offshore wind turbines. The limited database was cumulated from Chow (1997), Jardine et al. (2006), Kolk et al. (2005b) and others and consisted 17 piles from 11 sites all with diameters greater than 300mm and lengths more than 5m. Six design methods were tested against the database; API-07, Design of offshore wind turbine structures (DNV-07), plus the four modern CPT-based methods. Table 2-9 summarises the results of the methods evaluation. The following can be observed and summarised from the predictability assessment;

1) ICP05 and UWA-05 offered the best predictability with the least scatter while the API-07 and DNV-07, which are similar in their formulation, had the poorest predictability and the greatest scatter.
2) Apparent skew was reported on DNV-07 and API-07 from the methods bias to underestimate the pile capacities in short piles (L/D < 30) and in dense sands (I_D > 75%).

3) FUGRO-05 showed tendencies to provide better predictions for shorter piles and in dense sands.

The design methods formulations skews and biases are made apparent with a tension shaft capacity design example for pile foundations in dense sands of a 5MW offshore wind turbine shown on Figure 2-25 in which for any fixed pile diameter selected the procedures predict a range of lengths in cases more than double each other.

	API-07	DNV-07	NGI-05	Fugro-05	ICP-05	UWA-05
Mean	0·75	0·80	1·18	0·86	0·95	1·01
COV	0·49	0·49	0·41	0·32	0·26	0·27

Table 2-9: Arithmetic mean and CoV reliability of displacement piles in sands design approaches on a database of tension tests on open–ended piles in sand (Gavin et al. 2011).

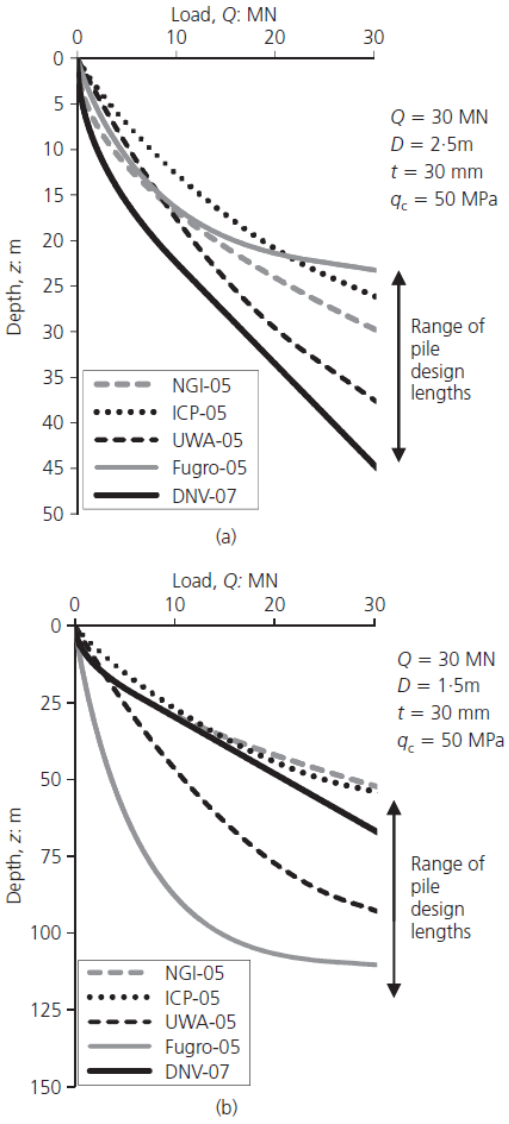


Figure 2-25: Estimate of pile length required to support a 5MW offshore wind turbine (a) Pile diameter, D = 2.5m (b) D = 1.5m (Gavin et al. 2011).

2.9 Summary and conclusions

This chapter reviewed the state–of–knowledge on axial static behaviour of single displacement piles in silica sand, considering the processes experienced during their installation. The review focused on the effective stress state generated around displacement piles as this controls the piles axial static capacities. Understanding regarding the estimation of shaft and base resistances has been reviewed as related to reliability studies and the best available approaches were summarised. Implicitly, this chapter considered the capacities and stiffnesses available within a few days of pile installation by jacking or driving. The following overall observations are drawn;

1) Considerable progress has been made regarding the understanding of i) Stresses developed around the base of piles, ii) The attenuation of the stresses along the shafts, and iii) The mechanisms developing at the interfaces during static loading of the piles.

2) The modern (offshore) CPT–based axial capacity design methods that address base conditions and shaft stresses attenuation above the tip offer up to 52% improvement in the predictive reliability of measured pile capacities compared to the conventional earth pressures approaches (the current main text method in API RP2 GEO) or the simplified α–type CPT design methods.

3) Although full adoption of one or all of the CPT-based methods hasn't been made yet for the API recommended practice, the Imperial College approach ICP-05 has been in use effectively since 1996; see Overy (2007).

4) The pile load test databases used for design methods calibration affect the outcomes of predictive reliability checks due to; (i) the low numbers of tests, (ii) potentially partially mobilised load capacities, (iii) possible inclusion of non-silica sand cases, and (iv) un-accounted residual loads.

5) Perspectives have emerged regarding possible improvement of the modern CPT-based approaches by explicit incorporation of cyclic installation effects. However all four methods currently cited in the API RP2GEO (2011) adopt implicitly lumped 'h/R effect' or 'friction fatigue' factors.

6) Persisting uncertainty regarding time effects limit the ability of any single design method to predict the potentially "moving target" of axial capacity without addressing time and ageing explicitly.

Chapter 3

3 Ageing behaviour of axial capacity of displacement piles in sands

3.1 Introduction

Age (time) related changes appear to apply to the axial capacity of displacement piles in sands. Beneficial ageing which results in capacity increase is frequently referred to as pile 'set-up' or 'freeze' while non-beneficial ageing is called pile 'relaxation'. Chow (1997), Yang & Liang (2009) found that set-up is more common than relaxation. While the mechanisms governing pile ageing have yet to be fully demonstrated, hypotheses have been posed by among others, Schmertmann (1991), Åstedt et al. (1992), Chow et al. (1998), Bea et al. (1999), Axelsson (2000), White et al. (2005), Bowman & Soga (2005) and White & Zhao (2006).

Authors including Skov & Denver (1988), Svinkin et al. (1994), Tan et al. (2004), Bullock et al. (2005), Alawneh et al. (2009) or Yang & Liang (2009) have suggested empirical procedures for estimating potential ageing benefits from collated load tests on aged piles.

If proven to be sufficiently reliable, routine design procedures could be modified, and, design and construction re-optimised to take benefits of ageing. Re-assessments could be made of how much additional loading could be applied to structures founded on aged piles. Further, foundations for which installation monitoring or potential under-design concerns are raised could be re-evaluated to assess whether any short–falls could be covered by long term set-up. However, incorporation of ageing processes into pile capacity estimation procedures is not yet routinely addressed because of uncertainties over: 1) Which are the influential factors, and 2) The reliability and repeatability of the potential ageing processes. Schneider (2007), for example, considered that studies involving long–term measurements of stresses around displacement piles would be required to provide reliable information on ageing processes that might feed into improved axial capacity pile design approaches.

3.2 Hypothesized mechanisms

Komurka et al. (2003) suggested the three potential pile set-up patterns illustrated in Figure 3-1 which involved;

(i) A logarithmically non-linear steeply varying period of capacity gain associated with initial excess pore water pressure dissipation in low permeability soils, typically $k < 10^{-6}$ m/s (after Casagrande & Fadum 1940)

(ii) A logarithmically linear rate of capacity change associated with any longer term than excess pore water pressure dissipation.

(iii) An extended logarithmically linear ageing period that is not associated with pore pressure change.

When considering piles driven in sand, processes (i) and (ii) are typically referred to as short–term and those related to (iii) as medium to long term, although mixed processes can be expected around a pile in a real soil of finite permeability over the short term; Axelsson (2000). For displacement piles in clean sands pile set-up is dominated by the medium to long term ageing processes.

Case histories have suggested that beneficial ageing of total axial capacity of piles results principally from gains in shaft resistance and either no change or relaxation of the pile base capacity with time, Schmertmann (1991). Chow et al. (1998) proposed three possible mechanisms governing the increase in shaft capacity with time through ageing alone.

a) Radial stress increases linked to relaxation of circumferential (hoop) stresses in a sand arch formed around the displacement pile during installation. They postulated that initially elevated hoop stresses shield the pile shaft from higher radial stresses that act further away from the shaft and sketched the pattern as shown in, Figure 3-2. A similar mechanism was suggested independently by Åstedt et al. (1992).

b) Sand ageing leading to increases in interface dilation due to better interface interlocking and stiffness increases in the soil around the pile leading to additional radial effective stresses ($\Delta\sigma'_{rd} = 2G\Delta r/R$) acting against the shaft during static axial loading to failure. Chow et al. noted from their laboratory tests that the pile–sand interface angles δ_{cv} did not change with time in interface shear tests involving sands and inert stainless steel.

c) Physiochemical action/ corrosion between an active (corrodible) pile and the surrounding sand leading to increased interface roughness, increased circumference of shearing and either migration of the shearing surface into the surrounding soil or additional radial stresses developing as the volume of the interface increases.

Field and laboratory studies by Axelsson (2000) led to his interpretation of increased dilation (mechanism b) as the main pile set-up mechanism. Chow et al. (1998) and White & Zhao (2006) report that set-up can develop through physiochemical processes (mechanism c) on corrodible piles, while Bea et al. (1999) suggested sand ‘welding’ on steel piles increases roughness, diameter and dilation at the interface. Bowman and Soga (2005) suggested an elaboration of mechanism (b), reporting that laboratory triaxial creep tests show strong dilation after certain elapsed times which could be accelerated by small cyclic perturbations (see Rimoy & Jardine 2011). They argued that under the kinematically constrained conditions imposed around pile shafts, dilation increases the radial stresses and pile capacities. White & Bolton (2004) and White et

al. (2005) followed Chow et al. (1998) in considering that long–term re-distribution of the radial stresses set-up by displacement piles installation in sands (mechanism a) would raise the shaft radial stresses and give the observed increases in axial capacities.

The radial and circumferential effective stresses re-equalisation mechanism (a) has since been relatively widely accepted and attempts have been made to model the process by numerical or cavity expansion analysis.

FEM analyses by König and Grabe (2006) simulated 200 to 400mm diameter and 4m long displacement piles undergoing monotonic and non-monotonic installation. An axisymmetric continuum sand body of 10m radius and 20m depth was simulated with a 'zipper' technique applied at the sand-pile interface and a kinematic contact formulation with a low Coulomb interface shearing criterion of $\delta_{cv} = 10°$. Adaptive re-meshing was used to regenerate the mesh after certain increments so as to avoid large distortions of the elements during pile penetration; see Mahutka, König and Grabe (2006) for further information on the model. While the simulated monotonic installation showed high effective radial stresses remaining at the pile shaft at the end of penetration (compared to the imposed K_0 stresses in the far field) without any markedly raised circumferential stresses developing, 'pulsed' installation produced cyclic shearing at the pile shaft and densification at the interface that allowed the effective radial stresses immediately around the pile to relax while being compensated for by increased circumferential stresses.

White et al. (2005) presented a simple elastic perfectly plastic ($\varphi = 32.5°$) cylindrical cavity–expansion–contraction scheme to model the stress reduction behind a pile tip of a cyclically driven pile, Figure 3-3. In the near field, $r/R < 4.5$, the circumferential stresses predicted around the pile exceeded the effective radial stresses. White et al. argued that creep induced stress re-equalisation could increase the radial stresses on the pile and give shaft capacity growth with time. Chow et al. (1998) and White & Zhao (2006) noted that ageing is not widely reported for replacement (bored or CFA) piles in sands, suggesting that the installation-induced stress regime on displacement piles appears to be a necessary condition for ageing benefits. The fact that ageing benefits are seen with concrete, steel, and timber piles also imply that physiochemistry of the interface material is not a dominant variable, Chow et al. (1998).

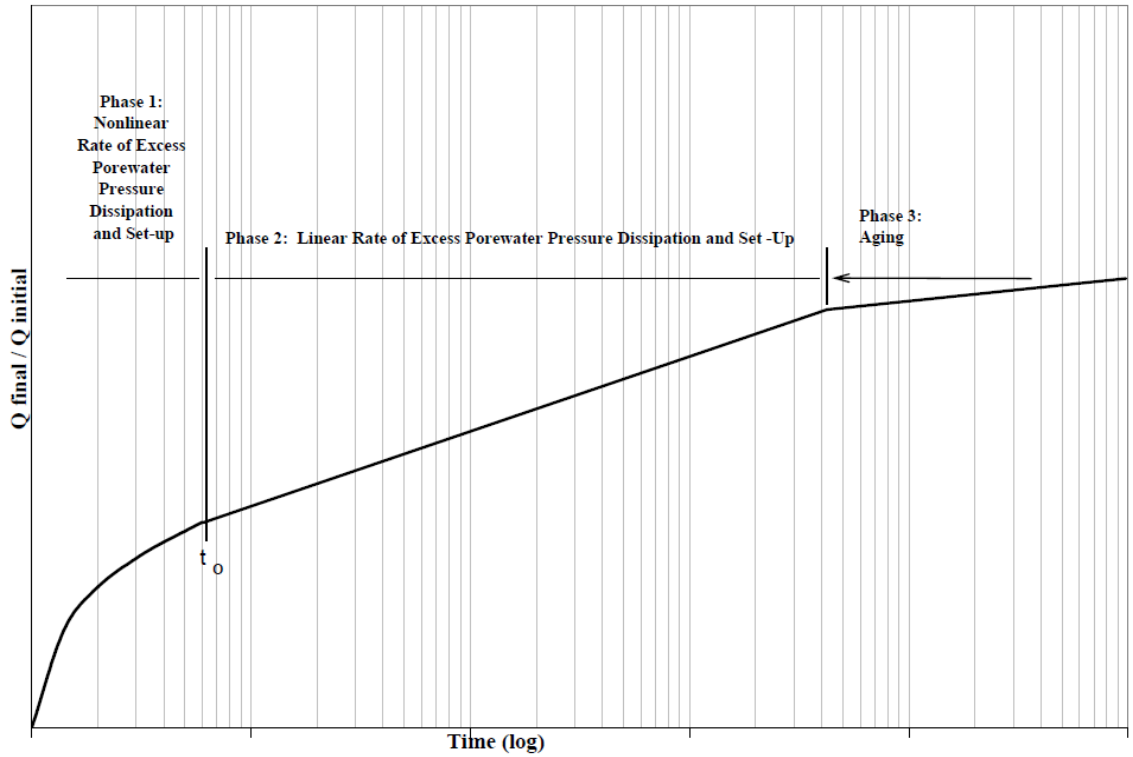


Figure 3-1: Idealised schematic of pile set-up phases showing change in the ratio of final pile capacity Q_{final} to initial capacity $Q_{initial}$ with log time (Komurka et al. 2003).

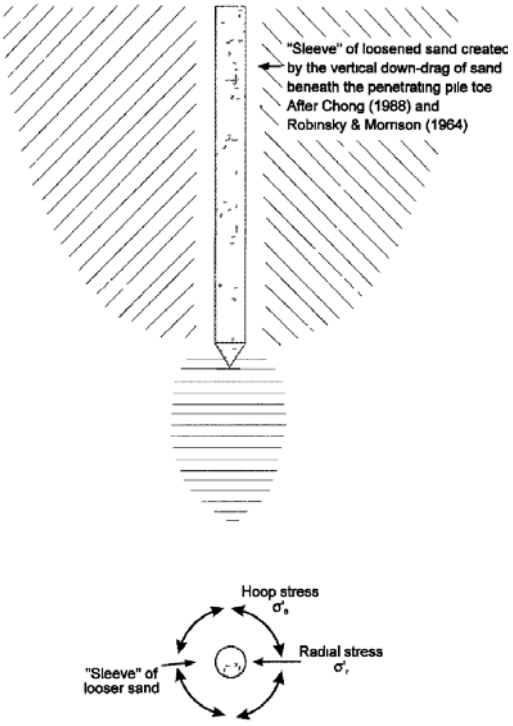


Figure 3-2: Arching mechanism around the pile shaft of a displacement pile in sands (Chow 1997).

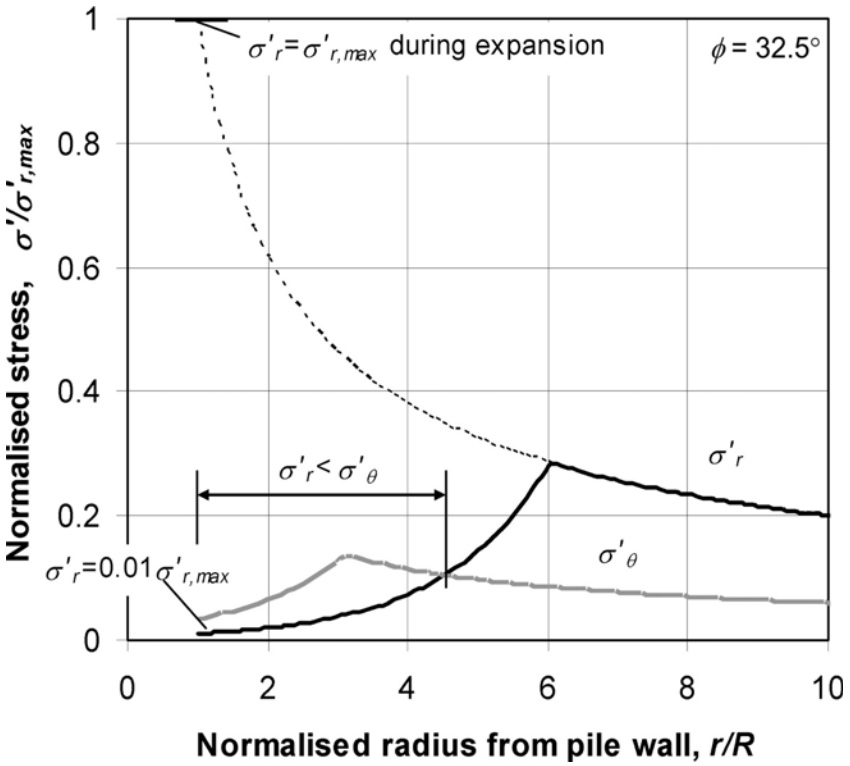


Figure 3-3: Simple analysis of radial variation in stress near pile after unloading behind pile base (White et al. 2005).

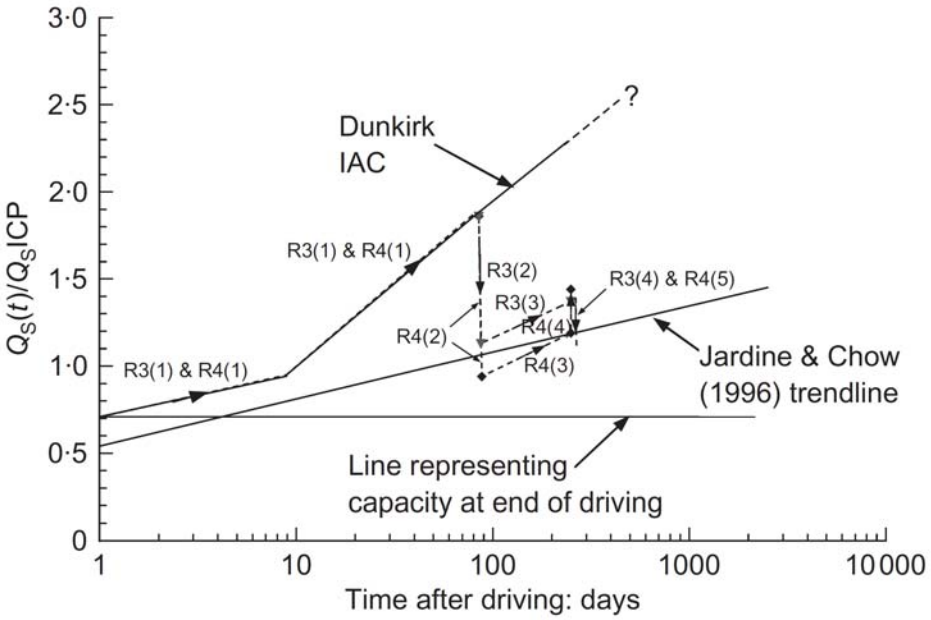
3.3 Load test case studies involving aged piles

Tavenas (1969) provides one of the earliest reports of pile ageing phenomena in sand. Chow et al. (1998), Long et al. (1999), Axelsson (2000), Jardine et al. (2006), Yang & Liang (2009) and Alawneh et al. (2009) have since collated or reported case histories where beneficial ageing effects led to axial capacity increases on time staged pile load tests. Various correlations have been proposed between pile axial capacity and the time of testing from installation, and a log-linear capacity relationship is the most widely adopted. Significant scatter is observed with all the reported trends. Chow et al. (1998) attributed the scatter to:

1) Variation in the time at which initial pile capacity is defined in the case histories where reference capacity is either taken at End of Initial Drive (EIOD) or a short period of time (hours) after. Although sand is free draining short-term stress equalisation may play different roles depending on scale and fines contents.
2) Dynamic and static load tests are not always distinguished, and
3) Different static pile load capacity criteria are used in the various cases collated.

Further, Jardine et al. (2006) argued that very different ageing trends applied to intact piles (those tested to their capacity only once after various extended post–driving periods) and multiply tested single piles. As shown on Figure 3-4, the set-up trends of shaft capacities of the pile load test reaction piles R3 and R4 used in the GOPAL project at Dunkirk (Parker et al. 1999) progressively

shift by decreasing from the Dunkirk Intact Ageing Capacity (IAC) when tested from intact state, to the trendline applying for multiply re-tested piles after Jardine & Chow (1996). A further difficulty lies in unambiguously isolating the shaft from base capacity components. Isolation is often only possible in static tension tests.



R3(1): virgin path for pile R3 (end point estimated to be similar to that for R6)
R3(2): decrease in capacity from two phases of cycling testing
(end point proven by second test)
R3(3): increase in capacity (end point proven by third test)
R3(4): decrease in capacity indicted by brittle response of third test to failure

R4(1): virgin path for pile R4 (end point estimated to be similar to that for R6)
R4(2): decrease in capacity from two phases of high-level cycling
(end point proven by second test)
R4(3): increase in capacity (end point estimated by drawing line parallel to that proven for R3(3))
R4(4): increase in capacity from low-level cycling
(end point proven by third test)
R4(5): decrease in capacity indicated by brittle response of third test to failure

Figure 3-4: Shaft capacities normalised by ICP-05 method predictions against time for first-time and pre-failed tension tests as described in the legend for reaction piles R3 and R4 used in the GOPAL project (after Jardine et al. 2006).

The accessible source references reported in the previous databases and other recent case histories have been compiled by the Author into a new database summarised on Table 3-3 which comprises.

i) 22 references reported between 1972 and 2013, citing 23 sites, across 9 countries.

ii) 147 test piles made of concrete (75), steel (71) and timber (1).

iii) 328 load tests, of which 59% are dynamic compression tests, 19% static compression tests and 22% static tension tests.

iv) Piles of lengths ranging from 2.5m to 58.5m, with diameters between 0.034m and 1.219m, and a minimum slenderness (L/D) of 17.

v) 44 (30%) of the 147 piles were reportedly tested only once from their 'intact state' and the remaining 70% were multiply tested.

vi) The load tests were staged up to 1.8 years after installation in compression and 4.7 years in tension, although 86% of the tests were conducted within 100 days of driving.

Here, as in most previous ageing studies, the capacities of the aged piles are normalised by the short-term pile capacity determined between 0 and 1 day after installation as noted and analysed against the logarithm of time at load testing.

First, the normalised static axial tension shaft capacities of the intact piles in the database are plotted against the time of testing on Figure 3-5. Pile load tests from only two sites/cases meet this criterion giving a relatively sparse data-set. However a clear shaft capacity ageing trend can be seen that is greater than or equal to 100% per log time cycle.

The axial tension shaft capacities of both intact and re-tested aged piles are plotted similarly on Figure 3-6. The scatter is greater and a larger proportion show negligible capacity growth. However, the piles tested by Schneider (2007) involving multiple re-tests exhibited interestingly higher shaft capacity resistance growth than the intact piles.

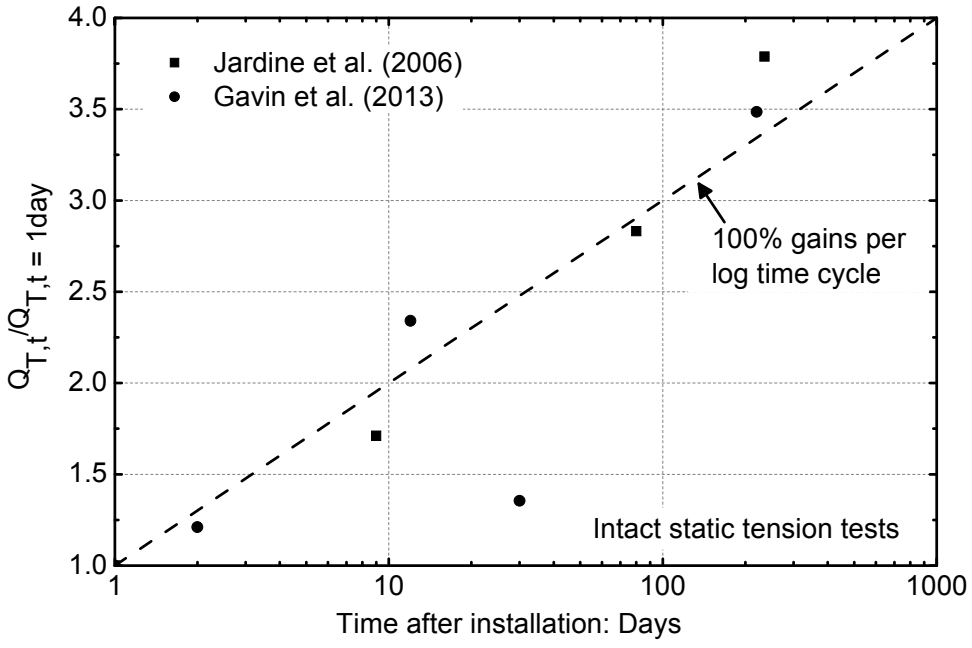


Figure 3-5: Normalised static axial tension capacities of intact aged piles plotted against the time of testing after installation.

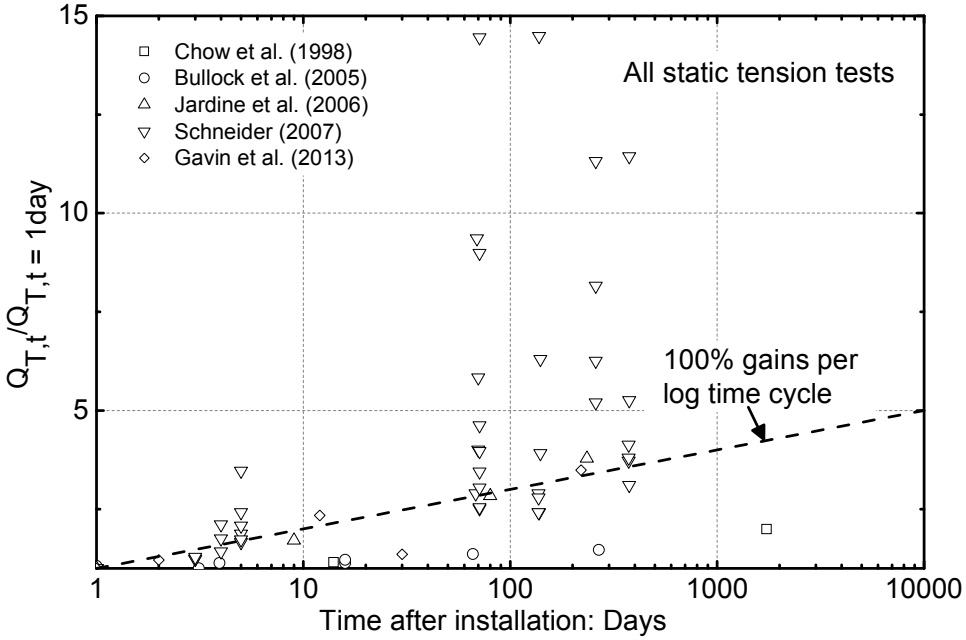


Figure 3-6: Normalised static axial tension capacities of intact and re-tested aged piles plotted against the time of testing after installation.

Tavenas & Audy (1972) offer the only case in the database that reports static compression tests on aged intact piles. Their results for total (base + shaft) capacities are plotted on Figure 3-7. Clearly there is a range of response from constant capacities with time ($Q_{C,t}/Q_{C,t = 1day} = 1$) to nearly 100% gains per log time cycle. The ~44% increase per log time cycle average trend observed from the Tavenas & Audy (1972) and the 100% increase per log time cycle trend from static tension tests (Figure 3-5) are both plotted on Figure 3-7 for comparison. The lower rates of intact total compression capacity gain compared to the tension shaft capacity set-up suggests that the gains are less significant for the bases than on the shafts. This is further shown in Figure 3-8 by the base capacity database comprising of multiply tested piles using dynamic or static procedures. The data scatter between gains and losses; on average base capacities increased marginally (~5%) per log time cycle.

Static compression capacity trends have also been interpreted from analyses of dynamic tests conducted at the end of initial drive (EOID), as plotted on Figure 3-9, normalising again by the reference short-term capacity from the dynamic tests. Similar to the static tests on intact aged piles, the compression capacity trends cover a range and average around 38% gains per log time cycle. Figure 3-10 plots the pile capacities from single re-strike dynamic tests normalised by the reference dynamic capacity at installation against the time of testing the data scatters again around an average trend of 38% gain per log time cycle.

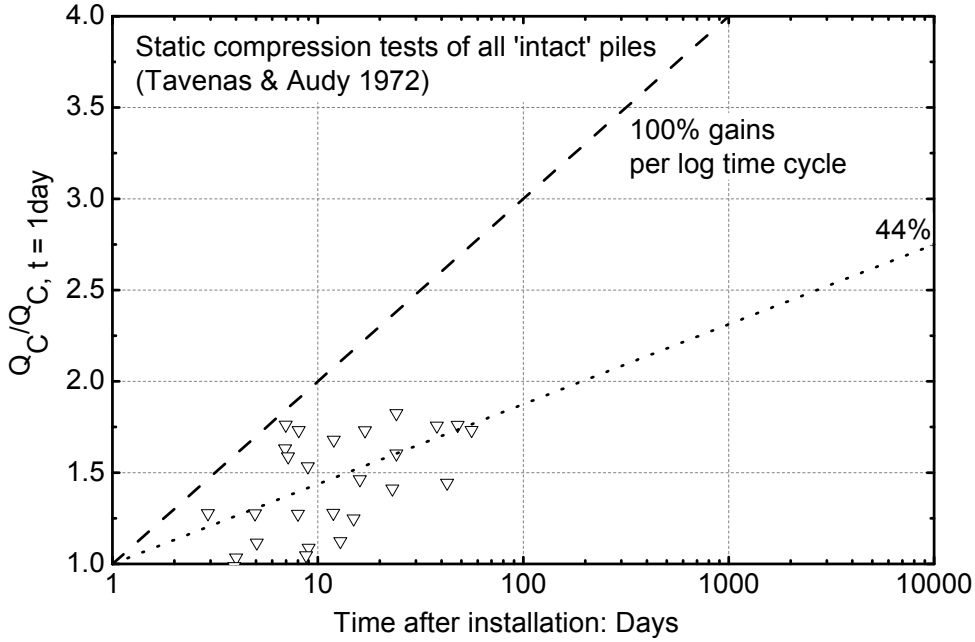


Figure 3-7: Normalised static axial compression total capacities of intact aged piles plotted against the time of testing after installation.

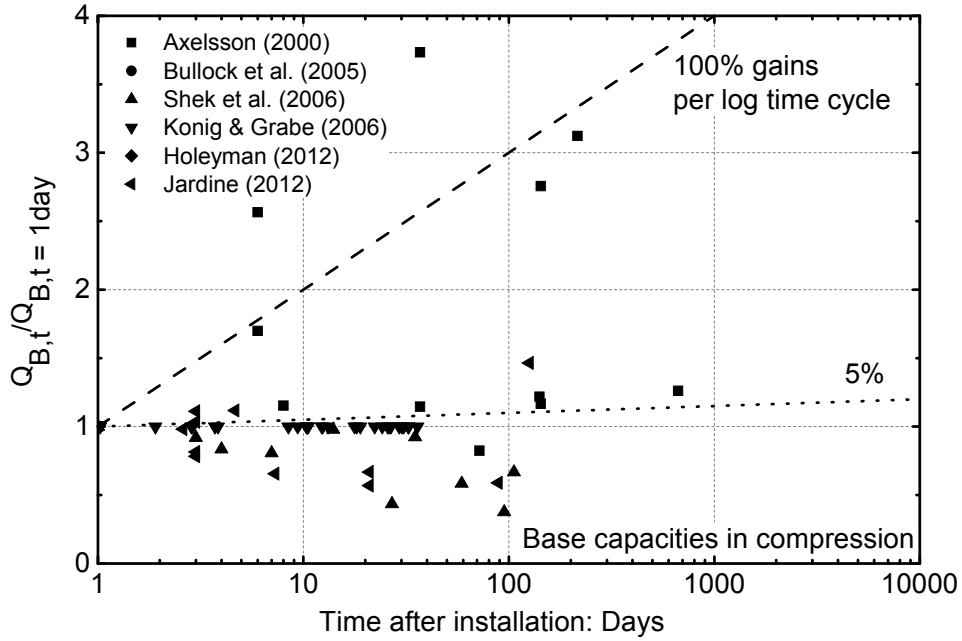


Figure 3-8: Normalised static axial compression base capacities of re-tested aged piles plotted against the time of testing after installation.

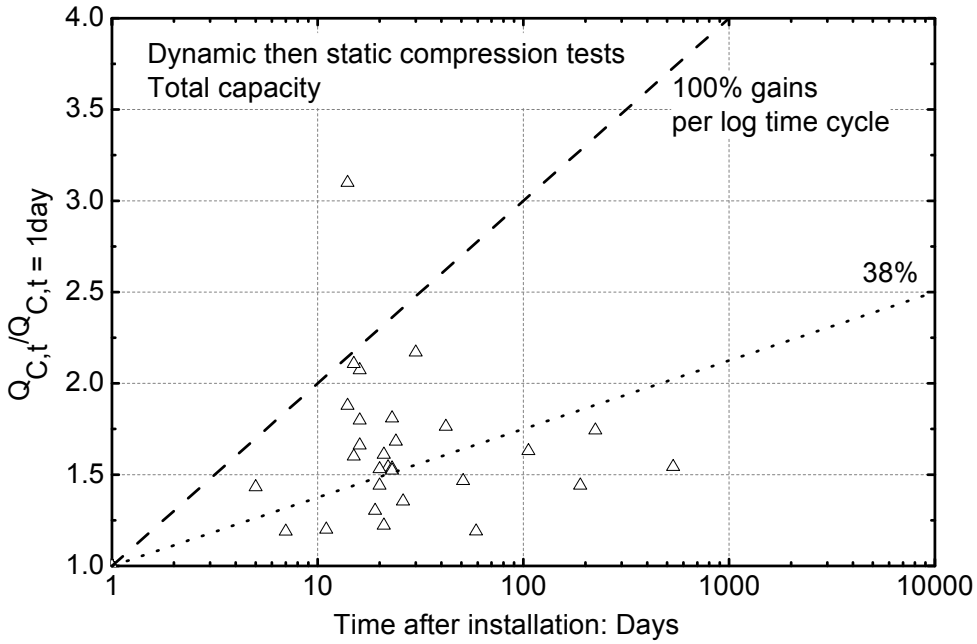


Figure 3-9: Static axial compression total capacities normalised by reference dynamic capacities plotted against the time of testing after installation.

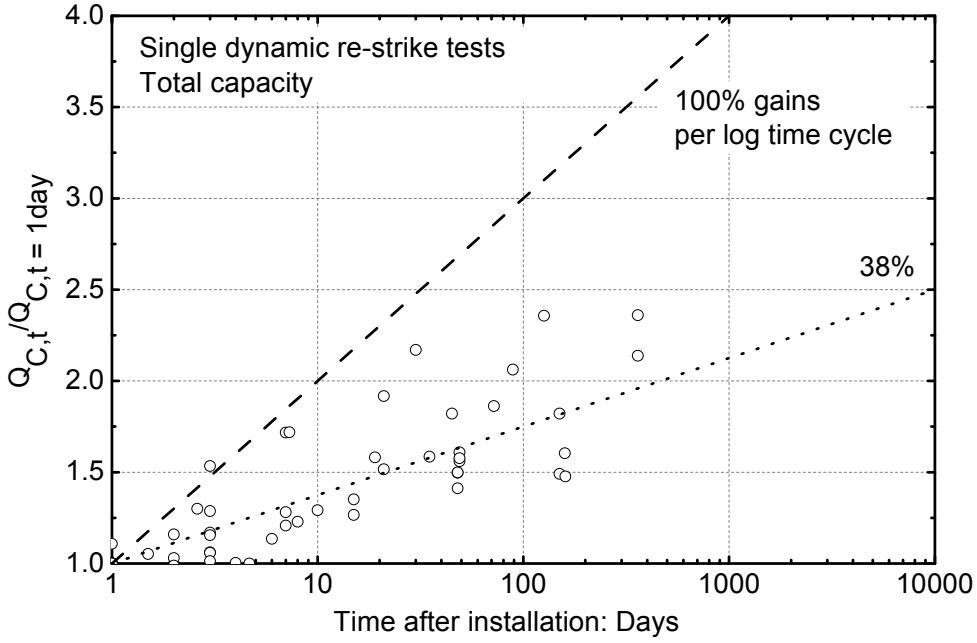


Figure 3-10: Single re-strikes dynamic axial compression total capacities normalised by the reference dynamic capacities plotted against the time of testing after installation.

Figure 3-11 shows single and multiple dynamic re-strike tests' axial compression total capacity trends while Figure 3-12 presents all the static and dynamic tests' axial compression total capacities from the entire database. The capacities scatter between constant capacity with time and an upper bound of 100% capacity gain per log cycle. The global regression average runs at 38%

gains per log time cycle, similar to Figure 3-9. This average falls below the 44% per log time cycle prescribed by Tavenas & Audy (1972) for axial compression total capacities on intact piles possibly reinforcing the different trends of re-tested piles emphasized by Jardine et al. (2006).

Multiple re-tests increase scatter and can show no to very low capacity growth with time depending on their staging sequence. To explore this further, Figure 3-13 plots normalised compression total capacities of re-tested piles against the number of pile re-tests conducted, showing the average times after installation for each particular set of re-tests. Also shown are the total capacities expected for intact aged piles from the average 50% gain per log cycle trend. The potential loss of ageing benefits sustained through multiple pile re-tests (defined as the difference between the capacity of aged intact and re-tested pile at the same time after installation normalised by the short term reference capacity) are plotted on Figure 3-14.

The final ageing trend to be evaluated is the shaft capacity during compression loading and this has been examined from the dataset where both base and shaft capacities measurements were made either during static (6%) or dynamic (94%) compression load tests. The base capacities were shown on Figure 3-8 while the shaft capacities are presented on Figure 3-15. Similar to the tension shaft capacities on aged piles, the compression shaft capacities ageing trends cover a range up to (and above) 100% gain per log time cycle, with a mean trend of ~50%.

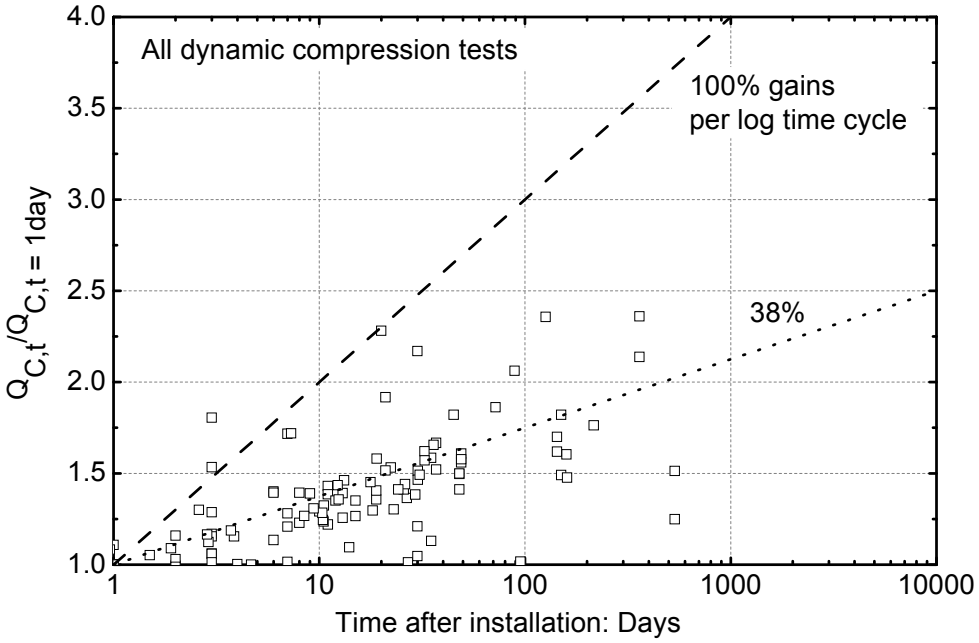


Figure 3-11: Normalised dynamic axial compression total capacities plotted against the time of testing after installation.

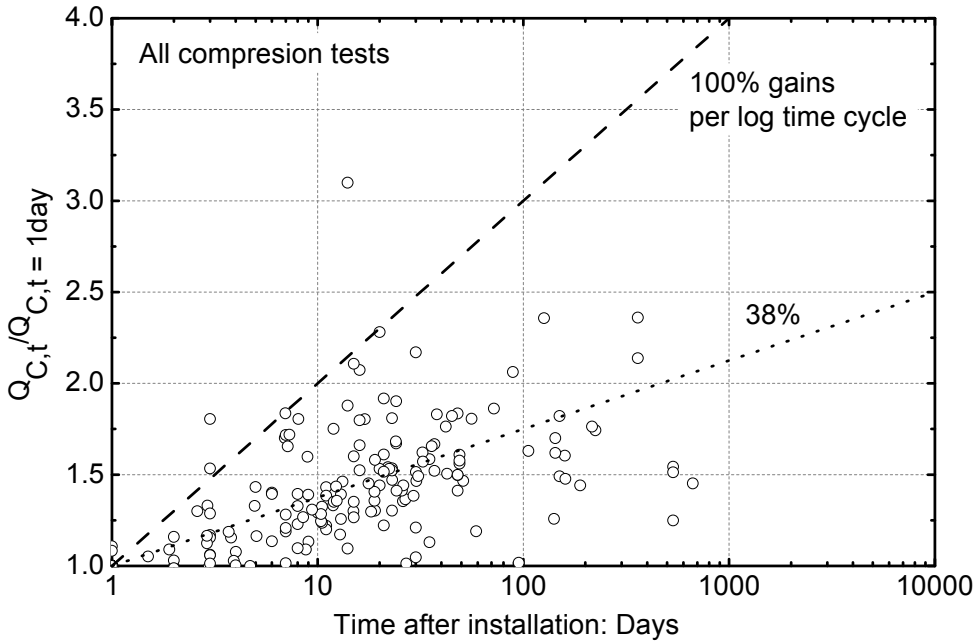


Figure 3-12: Normalised static and dynamic axial compression total capacities plotted against the time at testing after installation.

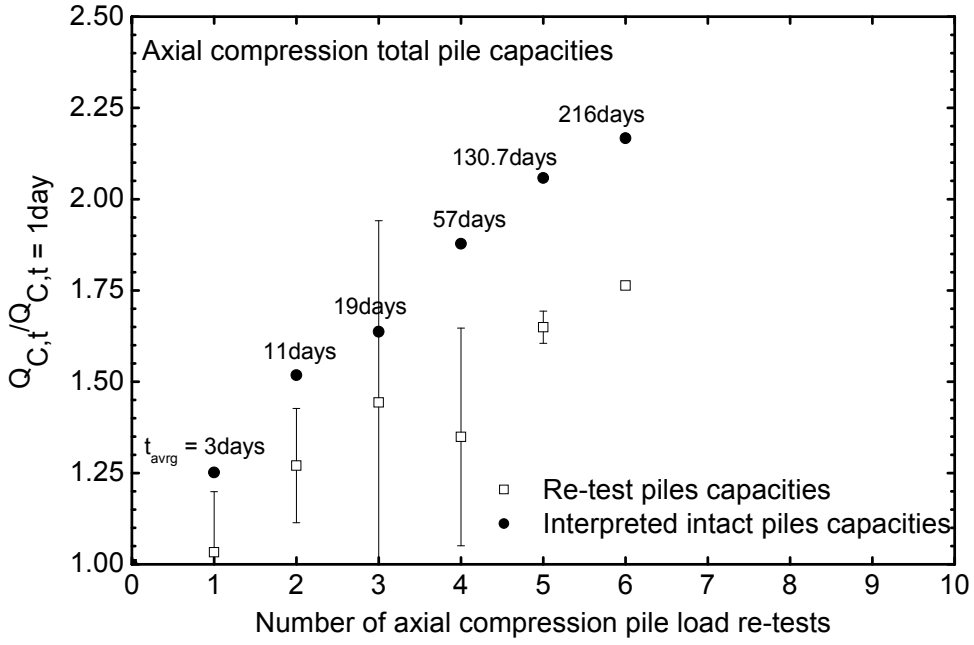


Figure 3-13: Normalised axial compression total capacities of re-tested piles plotted against the number of load re-test.

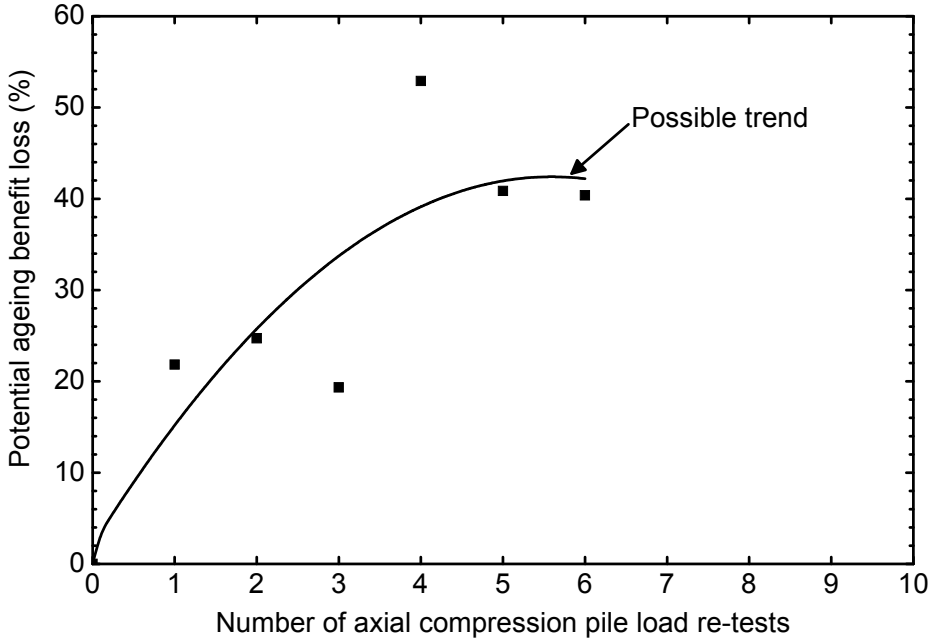


Figure 3-14: Potential ageing benefit loss of axial compression capacities of re-tested piles.

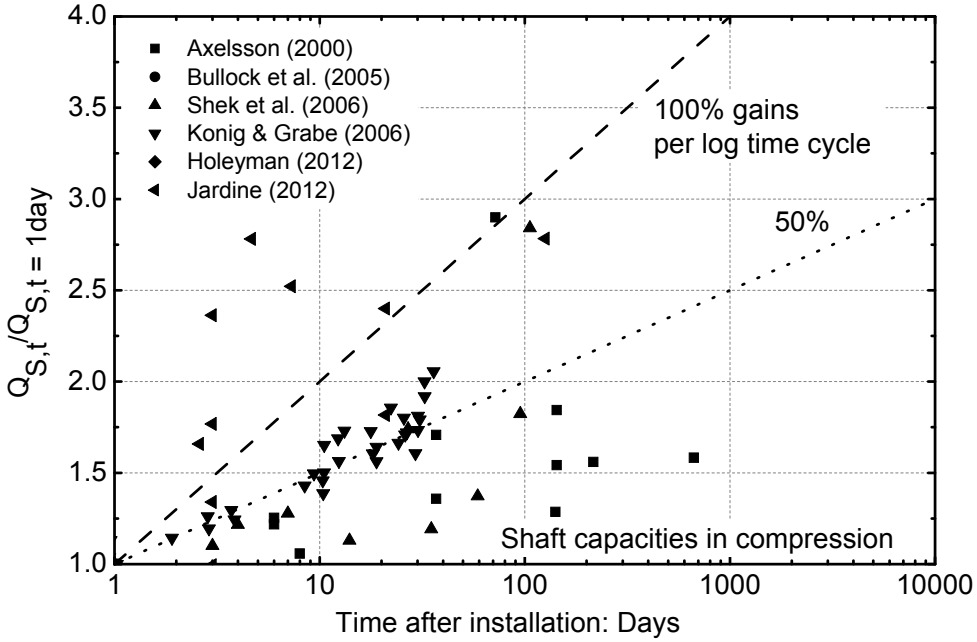


Figure 3-15: Normalised static and dynamic axial compression shaft capacities plotted against the time at testing after installation.

3.4 Assessment of the database

One way to assess the potential influence of interface radial stress dilation on the capacity ageing is to investigate the relationship between aged piles capacities and their diameters. As interface stress dilation is given by $\Delta\sigma'_{rd} = 4G\Delta r/D$, any decrease in pile ageing effect with pile diameter is compatible with dilation being a positive governing mechanism for observed shaft capacity gains. Figure 3-16 (a) plots the compression total capacities of 10 days' aged piles normalised by end–of–installation reference capacities against their pile diameters; the broadly flat trend of the data scatter suggests the aged piles' ageing trends are not sensitive to pile diameter over the range considered. Figure 3-16 (b) presents normalised tension capacities after 10 days' ageing plotted against the inverse of pile diameter shows a weak trend of shaft capacity set-up decreasing with diameter although the dataset is limited by the available pile size range and sites and dominated by small diameter piles/ rods of 34mm to 114mm. Regression on the dataset suggests only marginal ageing trends shifts within the range of diameters for industrial scale driven piles (> 0.5m).

As a preliminary assessment of the possible pile capacity ageing effects from physiochemical actions in the sand and on the pile interface, Table 3-1 lists those sites in the database where the ground water may be influenced by tides or have high salinity. This is assessed by the sites' proximity to and elevation above the ocean or other high salinity water bodies. Such sites constitute 60% of the database entries. Figure 3-17 plots the aged piles compression total capacities from these 'coastal' sites and the 'non-coastal' sites in the database separately to assess the potential effects of physiochemical actions on the ageing trends. Similar average trends are observed on both cases indicating that salinity was not an essential or preferential driving feature in the studied sites.

Next section summarises the key conclusions from the database study and concerns related to the pile load testing approaches used in ageing assessment.

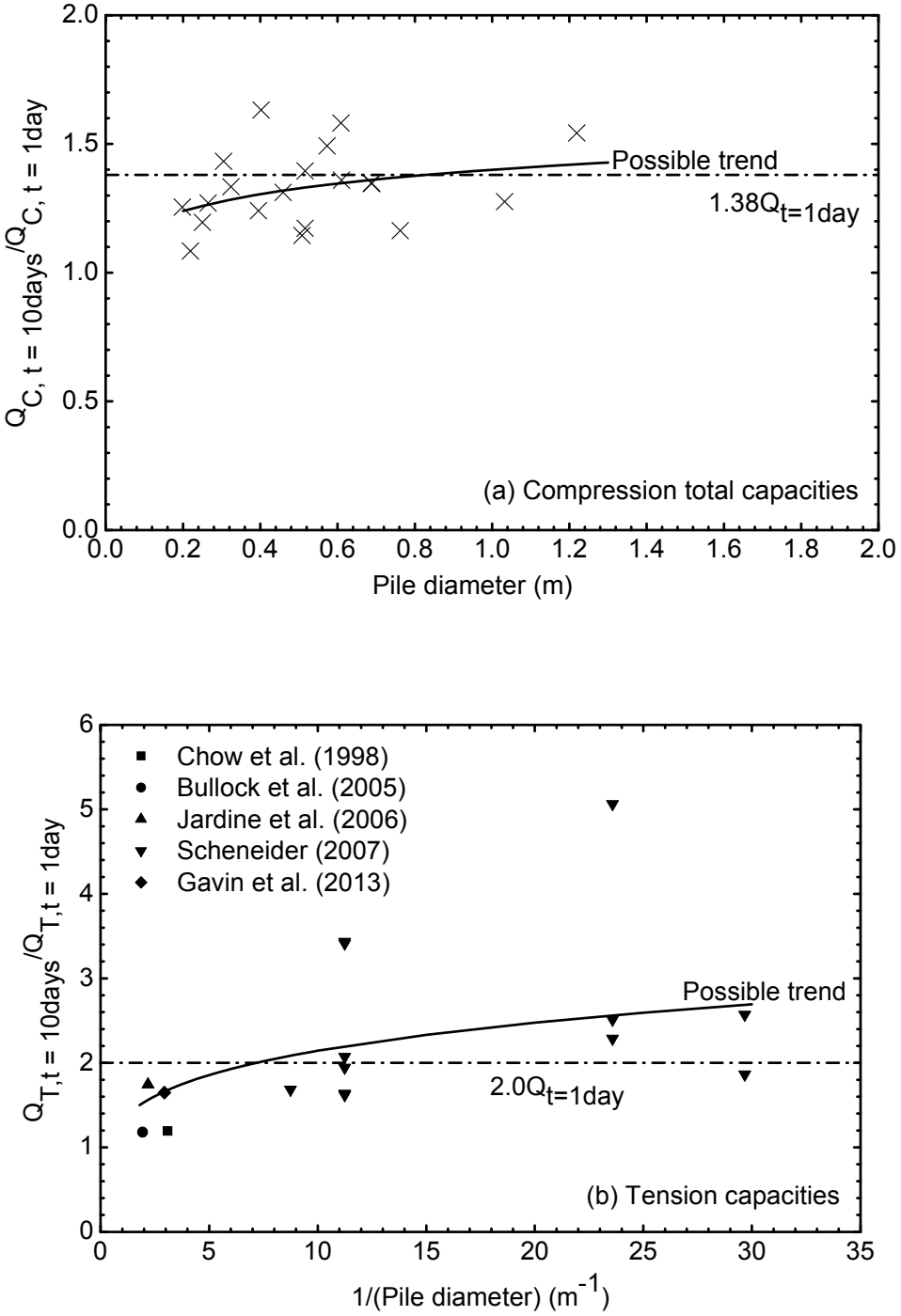


Figure 3-16: 10 days' aged piles normalised capacities (a) from compression load tests plotted against pile diameter (b) from tension load tests plotted against 1/ pile diameter.

No.	Reference	Site	Pile material
1	Tavenas & Audy (1972)	St Charles River, Quebec City, Canada	Concrete
2	Skov & Denver (1988)	Südkai, Hamburg Harbour, Germany	Steel
3	Seidel et al. (1988)	Barwon River, City of Geelong, Victoria, Australia	Concrete
4	Zai (1988)	Shanghai, China	Steel
5	York et al. (1994)	JFK International Terminal, Jamaica, New York, USA	Steel
6	Chow et al. (1998)	Port Autonome de Dunkerque, France	Steel
7	Attwooll et al. (1999)	Salt Lake City, Utah, USA	Steel
8	Fellenius & Altaee (2002)	JFK International Terminal, Jamaica, New York, USA	Steel
9	Bullock et al. (2005)	Vilano Bridge East, Florida, USA	Concrete
10	Shek et al. (2006)	Kowloon, Hong Kong	Steel
11	König & Grabe (2006)	Hamburg, Germany	Concrete
12	Jardine et al. (2006)	Port Autonome de Dunkerque, Dunkirk, France	Steel
13	Holeyman (2012)	Loon Plage, Dunkirk, France	Steel
14	Jardine (2012)	Red Sea port development	Steel

Table 3-1: Sites in the pile ageing database with ground water table influenced by tides or high salinity

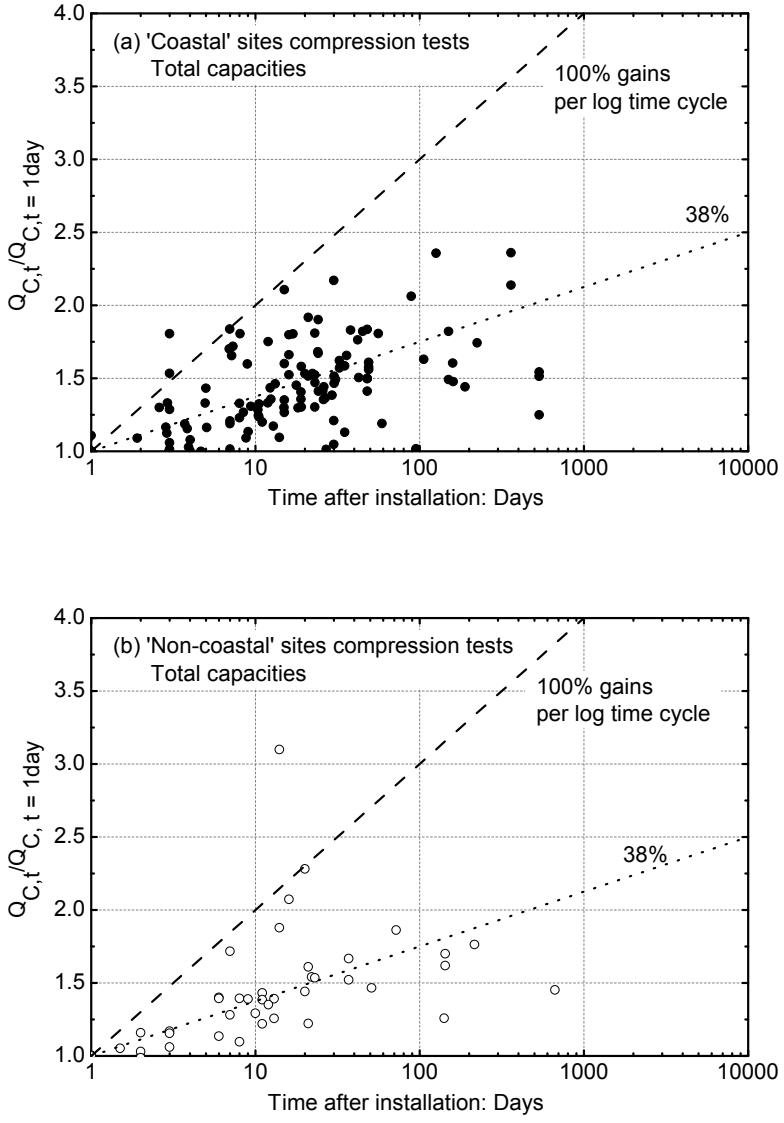


Figure 3-17: Normalised axial compression total capacities versus time at testing after installation for (a) 'Coastal' (b) 'Non-coastal' sites, assessing potential effects of physiochemical actions on ageing trends.

3.5 Concluding remarks on load testing of aged piles

The collated database of case studies on aged piles load tests considered separately the following sub-sets of load tests to examine potential pile capacity ageing trends;

a) Short–term static compression or tension load tests followed by static load tests on the same or a similar aged pile
b) Dynamic compression tests at or shortly after End of Initial Drive (EOID) followed by dynamic compression tests at the Beginning of Re-strike (BOR) or static compression load tests on the same or a similar aged pile.

Table 3-2 draws out a summary of the key evaluated outcomes from the datasets presented. The following points emerge:

1) The limited Tavenas & Audy (1972) dataset of static axial compression load tests on intact driven piles in sands shows an average total capacity ageing trend of 44% per log time cycle. As most industrial piles are intended to work in compression it would be useful to assess the generality of their conclusions, but this is not feasible at present due to a lack of test data.

2) Static axial compression capacity trends defined from re-tested aged piles are not reliable as they are affected by pre-loading effects leading to both potential damage to shaft friction and progressively enhanced mobilisation of particularly base capacity which may be erroneously interpreted as an ageing effect; see Fellenius' (2002) re-interpretation of Axelsson (2000) aged field pile static load tests study, and laboratory studies by Joshi et al. (1995) and White & Zhao (2006).

3) Two of the database references, Tucker & Briaud (1988) and Skov and Denver (1988), reported pile shaft capacities being maintained with time (no capacity gains) in coarse sands. It is possible that more 'neutral' pile load test cases are encountered and that their 'un-interesting' time trends go unreported.

4) The majority (76%) of the time–staged compression pile load tests were performed by dynamic testing. The literature contains several articles arguing that dynamic testing is unsuitable for determining the ultimate capacity of piles because;
    a. Substantial differences might exist between dynamic and static resistance due to inertia and velocity dependant soil resistances. Successfully dynamic testing interpretation relies on assuming appropriate relationships between dynamic and

static soil resistance including an assessment of how dilatant soil behaviour may enhance dynamic static resistance in saturated sands; Eiksund (1994).

b. Displacement piles develop residual loads during installation that can be difficult to consider in dynamic capacity analysis; Fellenius (2002).
c. The dynamic capacities determined by dynamic CAPWAP analyses (Rausche et al. 1985) are often correlated with static pile capacities estimated by the Davisson (1972) criterion, which generally delivers capacities lower than the ultimate (plunging) static pile capacity.
d. Likins & Rausche (2008) report even when dynamic and static tests are performed at essentially the same time (or at Time Ratio = 1 in their jargon) there is a scatter between the CAPWAP and static capacities averaging at 0.954 (±0.145). Re-strikes conducted up to 9 days after installation imply trends ranging from set-up to relaxation.
e. Despite the cost advantages of dynamic testing, static load testing remains the preferred method for determining design pile capacity. Other procedures are only recommended when a close calibration to the static axial capacity is available (Eurocode 7 Geotechnical Design General Rules EN 1997 – 1:2004 section 7.5.3).

5) The steepest capacity set-up trends (up to 100% per log cycle and greater) are those observed in static axial tension tests on intact and re–tested driven aged piles. The key concerns on concluding that such behaviour is typical of driven piles in sands are;

a. The static tension load tests on intact and re-tested piles comprise a minor subset, of only 5 of the 23 cases in the full database.
b. If shaft capacity set-up depends on shaft interface stress dilation (Figure 3-16 (b)) the potential ageing benefits decrease with pile diameter, suggests that ageing effects may be less significant with larger diameter driven piles. However, the review presented in this Chapter suggests that interface dilation and pile material type are not powerful factors driving ageing gains; although they may provide contributing factors.

Factor	Critical data available	Evaluated outcome
Shaft capacity in tension	Interpreted from a limited dataset of tension static tests on 7 'intact' piles, ~5% of the 147 piles in the total database.	Strong positive shaft capacity set-up of 100% per log time
Shaft capacity in compression	Evaluated from axial compression load re-tests dataset of piles with separate assessments of base and shaft capacities from 6 (6%) static and 91 (94%) dynamic load tests	Positive shaft capacity set-up averaging at 50% per log time
Base capacity	--"--	Wide scatter with both positive and negative effects with a mean trend of 0% to 5% gains per log time
Total capacity in compression	Interpreted from a limited dataset of axial compression static tests on 'intact' piles from Tavenas & Audy (1972) making ~19% of the total database (147 piles).	Positive shaft capacity set-up with an average trend of 44% per log time
Effects of re-testing in tension	Interpreted from a dataset with static tension load re-tests	General trend of growth with much greater scatter and lower average rate as re-testing inhibits ageing. However, smaller diameter piles showed steeper trends similar to and even greater than 'intact' large diameter piles.
Effects of re-testing in compression	Evaluated by multiple datasets of either dynamic testing only or dynamic followed by static testing	General trend for growth with high scatter and marginally lower average rate of set-up at 38% per log time cycle as re-testing inhibits ageing.
Dynamic compared to static testing	Two datasets determine the capacity ageing trends from dynamic followed by static tests to those in dynamic then dynamic tests.	Similar ageing trends which suggested equivalent interpretations of dynamically assessed static pile capacities to the statically determined.
Proximity to salt water bodies and tides	Sites with the potential influence of physiochemical effects on pile capacity ageing trends identified as 60% of the database and their axial compression load tests were compared to the remaining 40%.	No preferential ageing trend is established in the 'coastal' sites which suggest physiochemistry is not a dominant ageing driving mechanism of the dataset.

Table 3-2: Summary table of the evaluated outcomes based on the critical data available from the ageing database study.

No.	Reference	Site location	Ground description	G.W.T	Pile description						Load test description		
				b.g.l	Numbers	Material	Section	Average length	Diameter**	L/D	Type	Direction	Re-test
				(m)				(m)	(m)		D/S*	C/T*	Y/N*
1	Tavenas & Audy (1972)	St Charles River, Quebec City, Canada	Medium uniform sand SPT average N = 23 k = 10^{-4} m/s	5	28	Concrete	Hexagonal	11	0.305	36	S	C	N
2	Samson & Authier (1986)	Jasper, Alberta, Canada	Gravelly medium to fine sand SPT average N = 16	5	1	Steel	H-Pile 310 X 79	14	0.198	70	D/S	C	Y
3	Skov & Denver (1988)	Hamburg, Germany	Sand and silt	N/M	6	Concrete	Square	21	0.395	53	D/S	C	Y
		Südkai, Hamburg Harbour, Germany	Coarse medium to medium fine sand and fine gravel	-10.2	1	Steel	Pipe	33.7	0.762	44	D/S	C	Y
4	Seidel et al. (1988)	Australia	Loose to dense sand	N/M	1	Concrete	Square	11	0.508	21	D/S	C	Y
5	Tucker & Briaud (1988)	Mississippi River , Alton, Illinois, USA	Clayey gravelly medium to coarse sand	River	4	Steel	H-Pile 360 X 108	14	0.235	60	S	T	N
6	Zai (1988)	China	Fine sand	N/M	5	Steel	Pipe	41.4	0.609	68	D	C	Y
7	DiMaggio (1991)	Mobile County, Alabama, USA	Saturated silty sand	0.6	5	Concrete	Square	21.5	0.688	31	D/S	C	Y

No.	Reference	Site location	Ground description	G.W.T	Pile description						Load test description		
				b.g.l	Numbers	Material	Section	Average length	Diameter**	L/D	Type	Direction	Re-test
				(m)				(m)	(m)		D/S*	C/T*	Y/N*
8	Svinkin et al. (1994)	Various sites, USA	Silty clayey fine sand	N/M	3	Concrete	Square with void	38	0.573	66	D/S	C	Y
						Concrete	Square	27.4	0.402	68			
						Steel	Closed ended pipe	25.3	0.324	78			
9	York et al. (1994)	JFK International Terminal, Jamaica, New York, USA	Organic silty clays and peats underlain by fine to medium glacial sand	1.2 – 2.4	13	Steel	Open ended tapered monotube	19.9	0.355 tapered to 0.2 over 7.6m		D/S	C	Y
					1	Timber	N/M	15.8	N/M				
					1	Steel	Pipe	20.7	N/M				
10	Chow et al. (1998)	Port Autonome de Dunkerque, Dunkerque, France	Medium to dense marine silica sand q_c average 21MPa	4	2	Steel	Open ended pipe	16.5	0.324	51	D/S	C/T	Y
11	Attwooll et al. (1999)	Salt Lake City, Utah USA	Unsaturated dense sand	15	1	Steel	Closed ended pipe	10.1	0.324	31.2	D/S	C	Y
12	Axelsson (2000)	Fittja Strait, Vårby, Stockholm, Sweden	Loose to medium dense glacial sand. q_c 2 - 8MPa, < 50% silica	2	4	Concrete	Square	17.4	0.265	65.8	D/S	C	Y

No.	Reference	Site location	Ground description	G.W.T	Pile description						Load test description		
				b.g.l	Numbers	Material	Section	Average length	Diameter**	L/D	Type	Direction	Re-test
				(m)				(m)	(m)		D/S*	C/T*	Y/N*
13	Fellenius & Altaee (2002)	JFK International Terminal, Jamaica, New York, USA	Fine to coarse medium dense to dense glacial sand	N/M	1	Steel	Monotube open	18	0.45	40	D	C	Y
					1		Tapertube open	18	0.45 – 0.2 over 7.6m	90	D	C	Y
14	Tan et al. (2004)	Terminal 18 & First Avenue South Bridge, USA	Loose to medium dense sand	N/M	3	Steel	H-pile 356	37			D	C	Y
					2		Closed ended pipe	34	0.61	55.7			
15	Bullock et al. (2005)	Buckman Bridge, Florida, USA	Dense fine sand	N/M	1	Concrete	Square	9.2	0.516	17.8	D/S O-cell	C/T	Y
		Vilano Bridge East, Florida, USA			1			10.7		20.7			
16	Shek et al. (2006)	Kowloon, Hong Kong	Fine to coarse sand, medium dense to dense sand (CDG)	3	2	Steel	55C H piles 338 X 326	57.2	0.219	261.2	D/S	C	Y
17	Jardine et al. (2006)	Port Autonome de Dunkerque, Dunkerque, France	Medium to dense marine silica sand q_c 20MPa	4	3	Steel	Open ended pipe piles	19.02	0.457	41.6	S	T	N

No.	Reference	Site location	Ground description	G.W.T	Pile description						Load test description		
				b.g.l	Numbers	Material	Section	Average length	Diameter**	L/D	Type	Direction	Re-test
				(m)				(m)	(m)		D/S*	C/T*	Y/N*
18	König & Grabe (2006)	Hamburg, Germany	Sand hydraulic fill to medium sand q_c 20MPa	5 – 7 Tidal	27	Concrete	Square - various	25.5	0.460	55.4	D	C	Y
19	Schneider (2007)	Shenton Park, Western Australia	Unsaturated siliceous sand q_c = 2.5 - 6.2MPa	N/M	12	Steel	Open and closed ended pipe piles	3.33	0.042 – 0.114	47.4	S	T	Y
20	Holeyman (2012)	Loon Plage, Dunkerque, France	Medium to dense marine silica sand q_c 0 - 50MPa	N/M	1	Steel	Open ended pipe piles	13	0.406	32	D	C	Y
21	Jardine personal comm. (2012)	Red Sea port development	Dense coral granitic gravels & sands with cementation	On the shore - Tidal	13	Steel	Open ended pipe piles	31.8	1.219	26.1	D/S	C	Y
22	Gavin et al. (2013)	Blessington, Ireland	Dense fine glacial sand; q_c 10 - 20MPa	13	4	Steel	Open ended pipe piles	7	0.34	20.6	S	T	N

*C: Compression, T: Tension, D: Dynamic testing with PDA and analysed by CAPWAP (Rausche et al. 1985), S: Static testing, N/M: Not Mentioned, Y: Yes, N: No.

Further comments on the case studies:

1) **For piles with non-circular cross-sections the diameter of an equivalent circular cross-section base area is used
2) Tavenas & Audy (1972) aged piles capacities obtained from Fig. 15 of the reference
3) König & Grabe (2006) aged piles capacities obtained from Fig. 3 of the reference
4) Schneider (2007) presented peak average shaft friction, $\tau_{f, avg}$, citing strain softening response of many of his piles

Table 3-3: Database of case studies on short to medium term pile ageing in silica sands.

Chapter 4

4 Axial cyclic loading behaviour of single displacement piles in sands

4.1 Introduction

Interest in the response of a displacement pile to axial cyclic loading starts as early as during its installation as displacement piles are typically installed driven by hammer blows applying extreme axial cycles. The load–displacement history of the pile shaft is considered as one factor that defines the end of installation pile capacities through the cyclic or 'friction fatigue' aspect of the h/R effect. It may as well play an important role in the processes that govern medium to long term pile capacity changes in sands and the post-installation performance of piles subjected to axial cyclic loading in service. This chapter reviews the current design practice and understanding of the mechanisms governing the behaviour single displacement piles during axial cyclic loading and identifies the investigative aspects that the Author's study is going to advance. In the discussion cyclic loading refer entirely to repeating (alternating) non-dynamic loading.

4.2 Current practice

Axial cyclic response of displacement pile foundations has conventionally been considered important in the design of offshore oil and gas platforms and onshore facilities such as towers and pylons (Poulos 1988, Jardine 1991). It is even more critical in offshore wind turbines that rely on tripods or jacket structures, (see Seidel 2007 or Gavin et al. 2011). The lateral and moment loads imposed by wind or wave action can be large in comparison to self-weights, leading to multiple modes of axial and lateral cyclic loading acting on the foundation piles.

Jardine et al. (2012) reviewed the potential effects of cyclic loading on offshore piles and considered how these may be addressed in practical design. They outlined the indicative ranges for cyclic loading components that might apply to a range of multiple piled structures listed in Table 4-1, where Q_{cyclic} is the amplitude and Q_{mean} is the mean or average of the axial cyclic loading applied. They note that the loads vary with platform weight, water depth, metocean environment and structural form and in these examples the worst storm events (100 year return period for oil/gas and 50 year return period for wind energy) set the design-critical conditions. The average ratio of Q_{cyclic}/Q_{mean} on the windward side is ~7.8 while that on the leeward is just above 1.0 the limiting value for the pile loads to become tensile. The maximum compressive loads, $Q_{max} = Q_{mean} + Q_{cyclic}$, developed on the leeward side usually comprises the critical conventional design case. Cyclic effects are more marked for the tensile load cases, but there are broad spreads of ratios between both wind turbines and conventional oil and gas jackets.

Merritt et al. (2012) argued that the cyclic response under the most severe hundred or so cycles developed in design storms represent the most critical condition. Jardine et al. (2012) summarized data from field investigations involving pile response to axial cyclic loading where they noted 14 case histories in clay and only one in silica sands – that at Dunkirk, France reported by Jardine & Standing (2000, 2012) where multiple suites of axial cyclic loading on full scale steel pipe piles were applied up to 1000 cycles.

Jacket code, Location and type	Water depth m	Leeward Q_{cyclic}/Q_{mean}	Windward Q_{cyclic}/Q_{mean}
A West of Shetland, oil/gas	140	0.36	6.69
B China sea, oil/gas	36	0.60	3.0
C China sea, oil/gas	49	3.18	4.68
D North sea, oil/gas	70	0.72	2.47
E North sea, Wind-turbine jacket	35	0.72	1.25
F North sea, Wind-turbine jacket	50	1.13	35.0
G North sea, Wind-turbine tripods	26 to 33	0.88	1.66

Table 4-1: Indicative ranges for cyclic loading components; sites A to F predominantly clay, site G mainly sand (after Jardine et al. 2012).

A range of approaches have been adopted in practical applications to explicitly address axial cyclic loading of pile including Aldridge et al. (2010), Evans et al. (2010) or Merritt et al. (2012). These put central emphasis on the use of interactive cyclic stability diagrams in guiding the assessment of global axial cyclic load capacity degradation for driven piles as advocated previously by amongst others Karlsrud et al. (1986), Poulos (1988) and Jardine & Standing (2000). Cyclic stability diagrams consider interaction effects of cyclic amplitude (Q_{cyclic}) and mean (Q_{mean}) loads (normalised by static capacity before cycling, Q_T or Q_C) and the number of cycles applied. Such interaction diagrams may be zoned to identify cyclically Stable (S) region where there is no reduction of load capacity after N cycles, a Meta-stable (MS) area where some reduction of load capacity occurs after N cycles and Unstable (US) zone where cyclic failure develops within a small specified number of cycles. Analogous definitions based on the shakedown theory (see Martin 1975) have been used in piles lateral cyclic loading interaction diagrams (see Levy et al. 2009). The pile lateral cyclic loading behaviour is categorised as Purely elastic behaviour if there is no soil yielding along the entire pile length and cyclic deflections do not accumulate beyond the first cycle, Shakedown behaviour if plastic deflections occur after a few cycles followed by the pile-soil system 'shakedown' to steady deflections with progressive cycling, and Incremental collapse or Ratchetting behaviour when the pile deflections do not stabilise and continue at constant rates to eventual failure of the global system.

Figure 4-1 describes a first stage screening process for pile axial cyclic loading design demonstrated by Jardine et al. (2012). The most critically loaded piles from the range of storm conditions on the platforms listed in Table 4-1 are plotted on the Dunkirk Jardine and Standing (2012) cyclic interaction diagram (after Figure 1-2). This illustration assumes for simplicity that all the piles were designed to give Working Stress Design (WSD) factors of safety of 1.5 with respect to their most critical single Ultimate Limit State (ULS) storm load, i.e. $Q_T/(Q_{cyclic} + Q_{mean}) = 1.5$. The illustrative cases shown have ULS events that plot above the stable contour, suggesting some damage could be expected for each installation if founded in deposits comparable to the Dunkirk medium dense marine sand. Cases B, D, E, F and G show a progression of reducing proximity to the $N_f = 1000$, upper bound contour for stable zone, and hence increasing potential of cycling loading degradation. Case C plots above the $N_f = 100$ contour, indicating a considerable potential impact on this structure's foundation performance. It becomes apparent cyclic loading can reduce very significantly the safety factor below the 1.5 based on static shear strength, but by degrees that differ in each of the cases considered.

The following sections examine the understanding of mechanisms governing piles' axial cyclic loading behaviour in sands through a selection of field and laboratory studies.

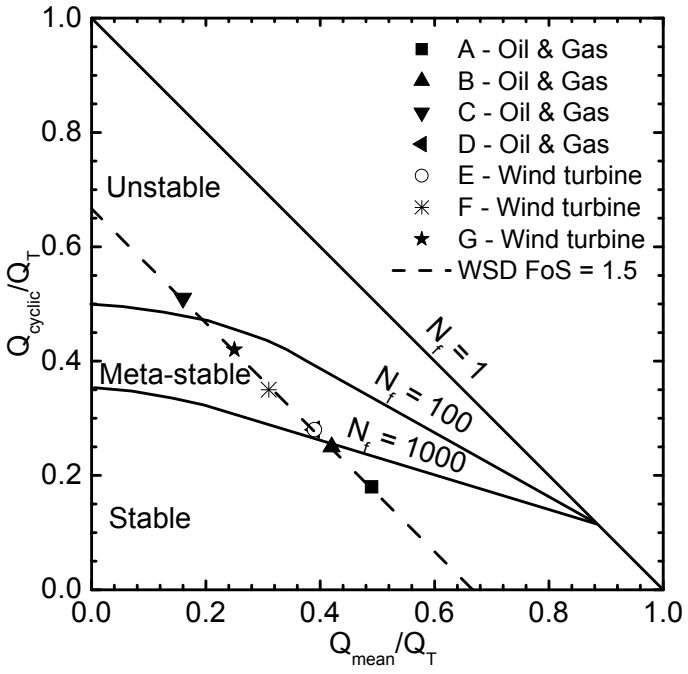


Figure 4-1: Illustration of potential cyclic effects for WSD FoS = 1.5 design conditions compared to Dunkerque contours of Stable, Meta-stable and Unstable condition in a normalised cyclic interaction diagram.

4.3 Axial cyclic loading field studies

To the Author's knowledge exceptionally few field studies have been conducted on piles installed in sands. Lehane (1992) reported limited tension axial cyclic loading of an ICP pile installed in loose to medium dense Labenne (France) dune sand applying just 40 cycles with $Q_{cyclic} = 0.15Q_T$ about a $Q_{mean} = 0.55Q_T$, noting shaft capacity was essentially maintained (modest ~3% reduction). Chow (1997) studied the cyclic response of the ICP pile installed 7.5m into Dunkirk marine silica sand applying 61 tension cycles (1cycle/minute) with $Q_{cyclic} = 0.31Q_T$ about a $Q_{mean} = 0.5Q_T$ reporting a modest increase (~8%) in static tension capacity after cycling. The effective radial stress measurements made on the ICP attributed the capacity increase to a 12% radial stress increase during equalisation before the subsequent static load test and a more dilative behaviour of the interface after the cyclic loading. Figure 4-2 shows how the shear stresses developed at four levels of the ICP evolved during cycling experiments by Chow (1997) at Dunkirk. The peak–to–trough variations in shear stresses confirm a top-down (unzipping) progressive failure process, as postulated by Poulos (1988) and Jardine (1991).

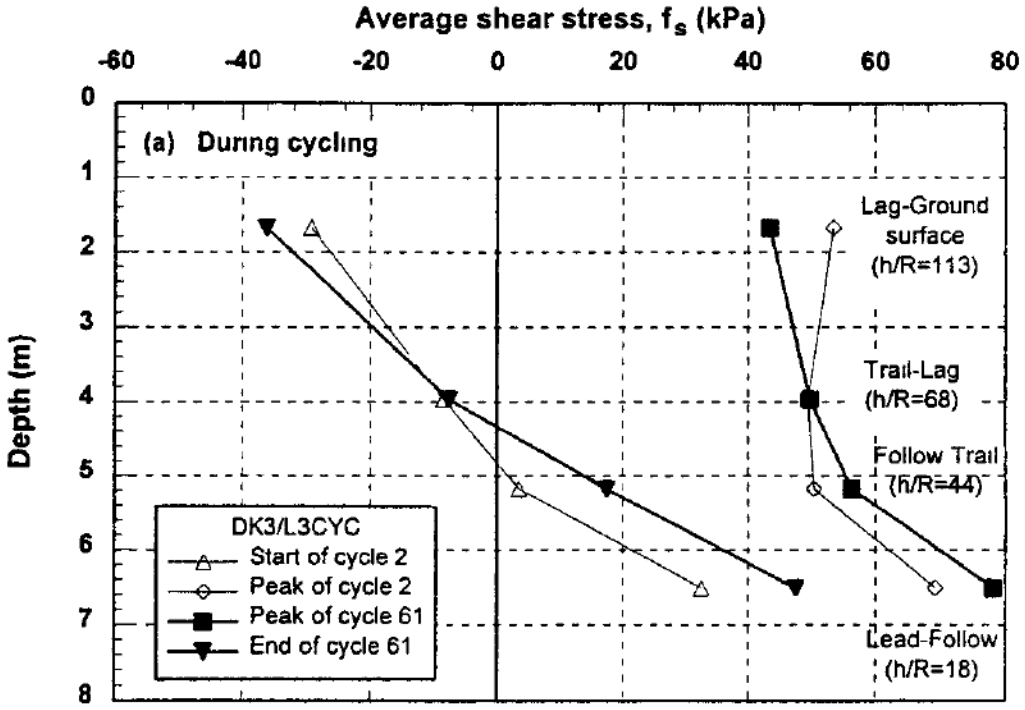


Figure 4-2: Peak and trough shear stresses developed on the instrumented sections of the ICP after 61 cycles of axial load ($Q_{cyclic}/Q_T = 0.31$, $Q_{mean}/Q_T = 0.5$) in Dunkirk marine silica sand (Chow 1997).

Xie (1999) reported results of field cyclic loading tests on 350mm square precast reinforced concrete piles strain gauged on their shafts. A total of 4 piles were driven 7.8m and other 4 piles 12.8m into predominantly silty clay to medium coarse sand and fine to coarse saturated gravels. Half the piles were loaded cyclically under one-way compression only (referred to by Xie as

repeated loading) and the other half in two-way compression to tension (referred to by Xie as reciprocated loading) at relatively very slow rates of loading of between 1cycle in 30 to 355 minutes. Up to 30 cycles were applied with one–way loading and 23 under two–way loading. One-way loading involved applying four cyclic loading batches in sequence with $Q_{mean}/Q_C = Q_{cyclic}/Q_C$ equal to 0.083, 0.167, 0.25 and 0.33. In the two-way tests two batches of (Q_{mean}/Q_C, Q_{cyclic}/Q_C) equal to (0, 0.167) and (0, 0.33) were applied. Pile movements increased with the applied number of cycles, expectedly downwards for the one way compression loaded and upwards for the two-way cyclic loaded. Both compression and tension static load test applied after cycling registered severe (up to ~70%) capacity and stiffness degradation. Cyclic effects became more pronounced for $Q_{cyclic} > 0.4Q_T$. Xie reports that capacities did not show signs of set-up even when the static load tests were delayed by up to 13 days after completion of load cycling.

Jardine and Standing (2000, 2012) reported cyclic tests on six 457mm diameter open-ended steel pipe piles driven in medium-to-dense marine sands at Dunkirk, France. One cyclic test pile had been driven to about 10m (L/D = 21.9) and five others to about 19m (L/D = 41.6). A comprehensive load controlled cyclic loading testing programme was undertaken at about ~1cycle/minute depending on pile response. Both one–way tension only and two–way tension and compression cycling were undertaken with both high and low amplitudes being imposed relative to the pile static ultimate shaft capacity. Quick reference tension tests were performed after most of the cyclic loading suites to determine the effects of the prior cyclic loading. Figure 1-2 summarised the cyclic parameters investigated in a normalised (non-dimensional) axial cyclic interaction diagram where the three zones of response, Stable (S), Meta-stable (MS) and Unstable (US), were identified that defined the piles capacity performance. Jardine and Standing (2000, 2012) discussed the pile capacities changes associated with the cyclic stability modes while the stiffness and displacement responses re-analysed by the Author as part of the current study are presented in Chapter 12 and published by Rimoy et al. (2013).

More recently a full-scale axial cyclic loading test programme (Benzaria 2013) has been undertaken under a French National Programme investigating the cyclic loading of piles (SOLCYP). The latter involves full-scale tests, calibration chamber and centrifuge cyclic loading experiments on model piles and other laboratory or theoretical studies; Puech et al. (2012). Various modes have been considered following procedures similar to those adopted by Jardine & Standing (2000). While there is a dearth of cyclic testing on full-scale displacement piles in sands rather more laboratory axial cyclic loading studies have been undertaken with model piles which are reviewed in the following section.

4.4 Laboratory model pile studies

Chan and Hanna (1980) published an early study with strain gauged instrumented model piles in which they postulated factors they considered likely to affect the behaviour of piles subjected to axial cycling as; 1) the number of load cycles, 2) magnitude of the mean repeated load as a percentage of the maximum (ultimate load) static capacity, 3) amplitude of the load, 4) frequency of the cyclic load application, 5) characteristics of the soil, 6) load history of the pile and 7) embedded depth of the pile. They investigated the first three of these factors with 19mm diameter high strength aluminium alloy tubes conical tip–ended with embedded shaft length of 570mm into a dry uniform sand ($d_{50\%}$ = 0.24mm and C_u = 1.8) chamber (380mm diameter by 965mm height) with smooth and rigid lateral boundaries, rigid bottom boundary and a 100kPa surcharge vertical stress controlled through a steel plate top boundary. Their arrangement gave a ratio $d_{chamber}/D$ = 20 and pile slenderness (L/D) of 30. Their medium dense dry sand (I_D = 62%, e_0 = 0.67) was placed by pluviation and the model piles were installed by a hydraulic jack. Trapezoidal waveform cyclic loading was applied at 1cycle/minute by means of a double hanger and lever system acting in conjunction with a reciprocating machine. Up to 200,000 load cycles were applied with accumulated displacements allowed to progress to limits of 1 to 3 pile diameter.

Chan and Hanna (1980) identified two states of pile relative stability in terms of rates of movement under cyclic loads as shown in Figure 4-3. Cyclic loading with small amplitude cycles ($Q_{cyclic}/Q_C = Q_{mean}/Q_C$ up to 0.1) led to a stable response over some thousands of load cycles. However, even such stable tests could end with abrupt failures if cycling continued for ten times longer as shown in Figure 4-4 (see also Gudehus & Hettler 1981). Increasing the cyclic loading amplitude ($Q_{cyclic}/Q_C > 0.1$) meant the piles went to cyclic failure (accumulated displacements > 10% D) in progressively reducing number of cycles. Similar sets of pile response were observed with tension and tension to compression cyclic loading. While one–way low–level tensile cyclic loading improved the performance of the piles showing reducing rates of pile head movement per cycle, piles subjected to high level compression or tension cycling failed after relatively fewer cycles. Reductions in shaft stresses were implied from measurements of axial loads and recorded changes in the base to shaft load split under compression. Their instrumented piles shaft axial load distribution during cycling suggested the top-down shear stress degradation observed in field studies.

Van Weele (1979) reported 36mm diameter model pile tests pushed between 0.66 to 0.7m (L/D ≈ 20) into a rigid steel tank of 1.1m diameter ($d_{chamber}/D$ = 30.5) containing 1.2m depth of saturated well compacted medium dense fine silica sand ($d_{50\%}$ = 0.17mm, ρ_{dry} = 16.4kN/m^3, e_0 = 0.38). CPT q_c resistances in the tank are reported as showing a concave parabolic from the surface to ~27MPa at 0.65m then constant to 0.9m deep. The study investigated the influence of frequency

of loading, number of cycles and cyclic loading amplitudes on the axial cyclic loading behaviour of the piles. Sine waveform cyclic loads were applied at frequencies between 0.1 and 5Hz in compression up to 200,000 cycles. Van Weele reports tests where $Q_{cyclic} = Q_{mean} = 0.25Q_C$ led to cyclic failure (accumulated displacement > 0.1D) within 3000 cycles. Cycling at as low amplitudes as $Q_{cyclic} = Q_{mean} = 0.125Q_C$ led to cyclic failure with accumulated settlements equivalent to the pile diameter after 10,000 cycles. For all tests conducted, displacements continued to increase with increasing numbers of loading cycles even with Q_{cyclic} as low as 5% the ultimate static capacity though did not exceed the cyclic failure criteria within the number of cycles tested. Accumulated displacements at the same number of cycles increased with loading frequency signifying rate effects in this saturated medium dense fine sand potentially as a result of progressive partial drainage.

Le Kouby et al. (2004) noted significant gains in shaft capacity after repeated low amplitude cycling using the Paris-Tech calibration chamber (UMR Navier – CERMES). The same chamber has been used as part of the studies by Weinstein (2008) and Tali (2011). Weinstein (2008) studied monotonically jacked (1mm/sec) friction sleeve and tip instrumented micropiles of 20mm diameter by 0.5m height (L/D = 25) and R_{max} = 0.21mm in a calibration chamber filled with loose dry Fontainebleau sand ($d_{50\%}$ = 0.21mm, I_D = 38.9%, ρ_{dry} = 13.4kN/m^3). The chamber has 524mm diameter ($d_{chamber}/D$ = 26.2) with lateral (100 kPa) and bottom (250kPa) stress controlled boundaries (K_0 = 0.4). Axial cycling was applied load controlled or displacement controlled with constant amplitudes between 0.0004mm and 1mm per cycle and at frequencies between 2500 cycles and 1 cycle per minute. The initial stiffness and peak load resistance developed by the micropile under monotonic loading tests was considered rate independent. Load-controlled cyclic tests naturally showed increasing cyclic displacement with cyclic amplitudes. Test conducted at a relatively low cyclic load (Q_{cyclic}/Q_C = 0.2), showed low and decreasing rates of accumulated displacements from 300 cycles then stabilising at 1000 cycles up to the 5,000 cycles applied.

Tali (2011) extended the Navier - CERMES axial cyclic loading studies using friction sleeve and tip instrumented 20mm (R_{cla} = 9.26 – 27.12) and 36mm (R_{cla} = 11.19 – 11.67) diameter displacement piles in the same chamber ($d_{chamber}/D$ = 26.2 and 14.6) testing Fontainebleau sand at relative densities between 37% and 92%. He applied vertical stresses between 125 and 375 kPa, maintaining a lateral boundary K_0 of 0.4 in all tests. Pile installation was by monotonic jacking at 1mm/sec to a depth of 0.5m (L/D = 13.9 and 25). Displacement controlled sinusoidal axial cyclic loading tests were undertaken ±0.25mm or ±0.5mm for between 1000 and 100,000 cycles at frequencies between 0.01 and 2Hz.

Interesting results were observed on the displacement controlled (±0.25mm) cyclic tests in a dense sand chamber (I_D = 90%) as shown Figures 4-5 and 4-6. Average shaft shear and tip stresses increased over the first few cycles (indicating stiffness gains) followed by decreases in both until

minima were reached after 1000 to 3000 cycles. Following from this, unexpected improvements were seen in both up to 100,000 cycles. Figures 4-7 and 4-8 shows how a brittle improvement in average shaft shear stress resulted, and an overall improvement in tip resistance was obtained. These led to the total capacity improvement shown in Figure 4-9 apparently due to the cyclic after the cyclic loading. Testing in the more elaborate 3S-R calibration chamber and Mini-ICP pile arrangements by the Author presented in Chapter 11 examines the impact of the chamber boundary conditions on such observed behaviour, confirming that the features observed by Tali (2011) may be artefacts of the chamber arrangements.

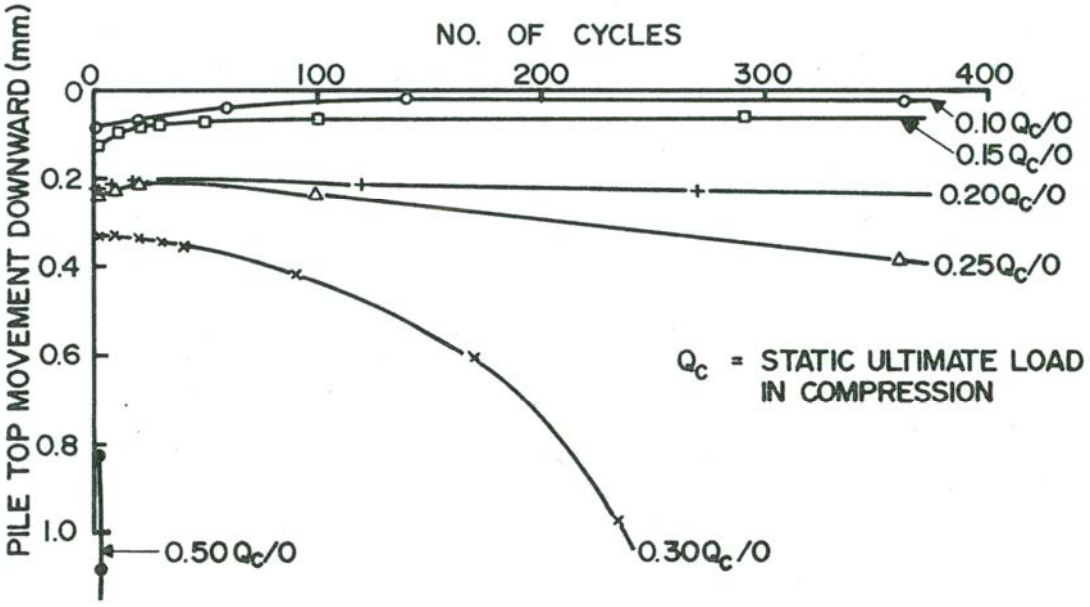


Figure 4-3: Pile top movement versus initial number of load (Q_{max}/Q_{min}) cycles applied (Chan & Hanna 1980).

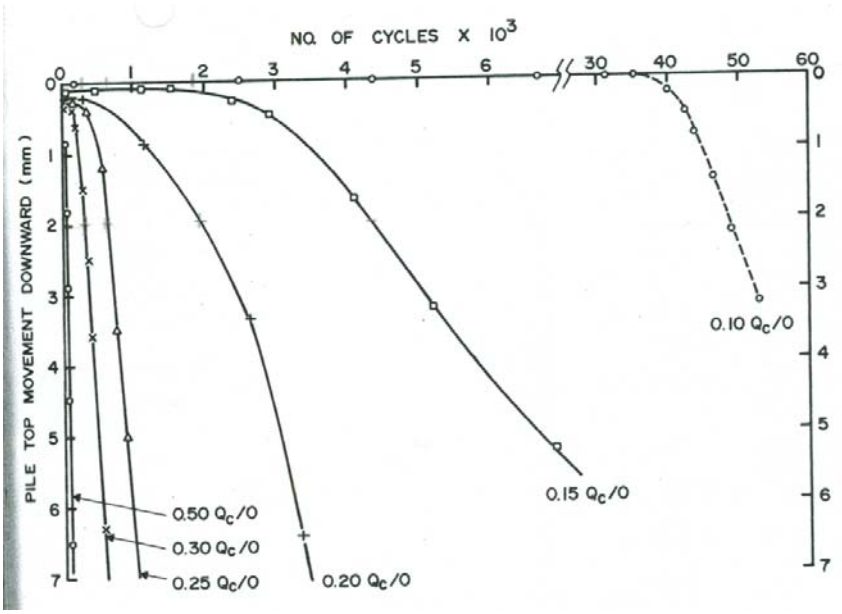


Figure 4-4: Pile top movement versus overall number of load (Q_{max}/Q_{min}) cycles applied (Chan & Hanna 1980).

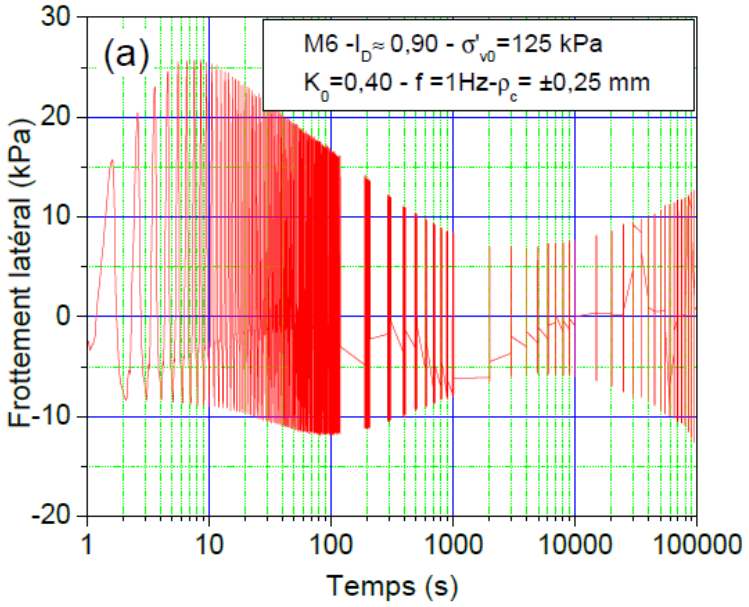


Figure 4-5: Shaft shear stresses evolution with time (s) during displacement controlled axial cyclic loading of displacement pile M6 in stress controlled calibration chamber (Tali, 2011).

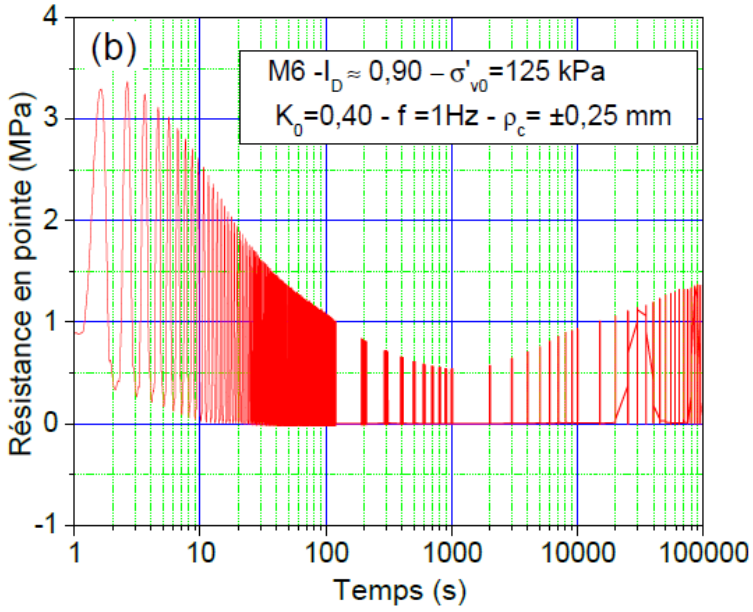


Figure 4-6: Base stress q_b evolution with time (s) during displacement controlled axial cyclic loading of displacement pile M6 in stress controlled calibration chamber (Tali, 2011).

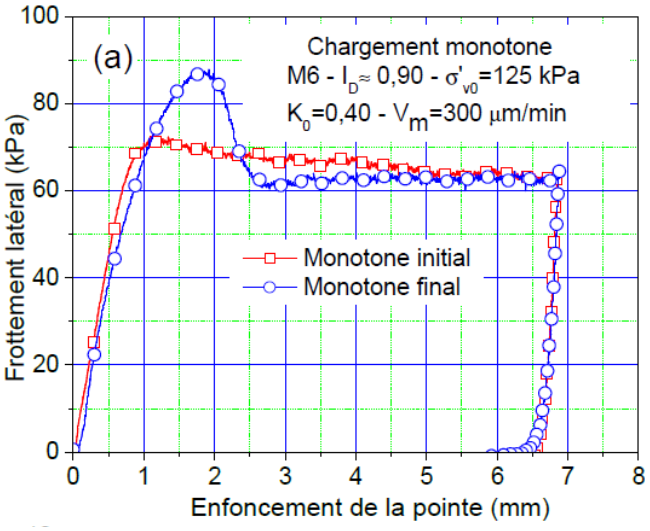


Figure 4-7: Static Shaft friction before and after the cyclic loading test M6 plotted against pile head settlement from compressive monotonic tests (Tali 2011).

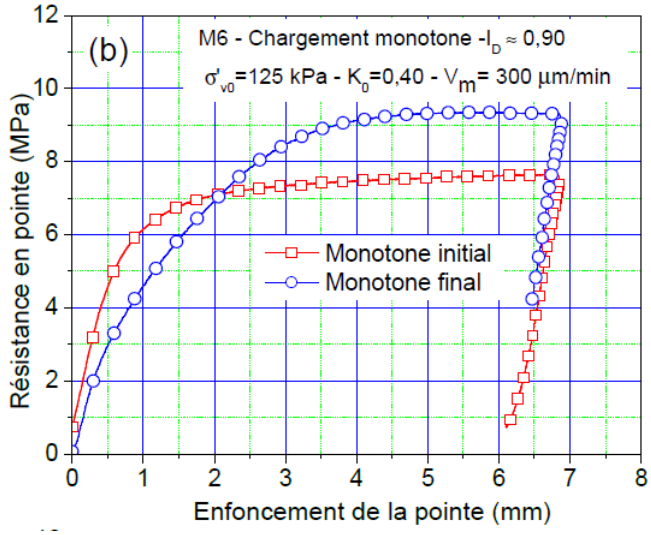


Figure 4-8: Static base resistance before and after the cyclic loading test M6 plotted against pile head settlement from compressive monotonic tests (Tali 2011).

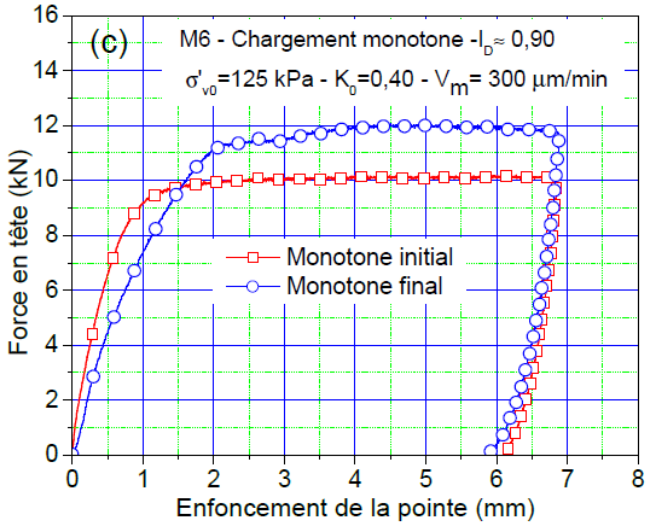


Figure 4-9: Total load before and after the cyclic loading test M6 plotted against pile head settlement from compressive monotonic tests (Tali 2011).

Tsuha et al. (2012) reported model scale tests conducted with the highly instrumented model equipment used later (see Chapter 5) by the Author (with some modification) to investigate the axial cyclic behaviour of displacement piles in sand. The test series ICP01 to ICP04 (with the Author participating in the series ICP04 and being a co-author of Tsuha et al. 2012), involved the 36mm by 0.99m length (L/D = 27.5) 60° conical-tip ended Mini-ICP installed into miniature stress sensors instrumented medium dense NE34 Fontainebleau sand in a calibration chamber that gave a $d_{chamber}/D$ ratio = 33.

Tests involving both low and high level one–way and two–way cyclic loading conditions were performed. Cyclic stability definitions similar to those of Jardine & Standing (2000, 2012) but scaled to the model piles were adopted leading to the stability diagram described in Figure 4-10. The Author's subsequent study extended the testing programme reported by Tsuha et al. (2012) by focusing on;

1) Further testing to define more closely the boundaries and the transitions between the stable, meta-stable and unstable zones.
2) Longer–term cyclic testing to investigate the effects of sustained cycling on the displacement and stiffness characteristics of the piles.
3) Cyclic testing with various chamber boundary conditions, moisture state and particle scale and density state to establish possible effects on the observed pile responses.

The highly instrumented Mini–ICP and sand calibration chamber helped to link the pile global load-settlement response to the fundamental behaviour of the pile-sand system. Figures 4-11 and 4-12 show the effective stress paths (τ_{rz}, σ'_r) developed at three levels at the pile surface as revealed by the Mini-ICP's Surface Stresses Transducers (SST) and in the sand mass by sand stress sensors. Tsuha et al. show trends that were typical of stable, meta–stable and unstable cyclic tests and set out an interpretation linked to the kinematic multi-yielding surfaces (Y_1, Y_2 and Y_3) as proposed by Jardine (1992) and Kuwano and Jardine (2007). While all cycling modes exhibit radial stress contractions with their cycling stress paths consistently migrating to the left, the stable stress path loops remained far from the interface failure envelopes with tight loops that kept well within the proposed expanding and relocating Y_2 surface. Unstable tests mobilise the interface failure envelope during their first few cycles and engage their Y_3 surfaces leading to rapid degradation. The intermediate meta-stable condition invoked effective stress paths that developed continuously, opening up more energy dissipative cyclic loops as they migrated to the left showing radial effective stress contractions. The interpretation was that these paths drag the kinematic Y_2 surfaces with them during the cycling until they engage the interface failure envelopes. Static axial tension tests performed after cycling indicated a range of responses with capacity increasing after stable

cycling, partial capacity decreases after meta–stable testing and large capacity degradations after unstable cycling. The capacity increases from the stable tests were associated with enhanced dilative tendencies at the pile interface resulting from earlier interface compaction during cycling, Yang et al. (2010), which led to re-orientation of the effective stress path directions under later static loading.

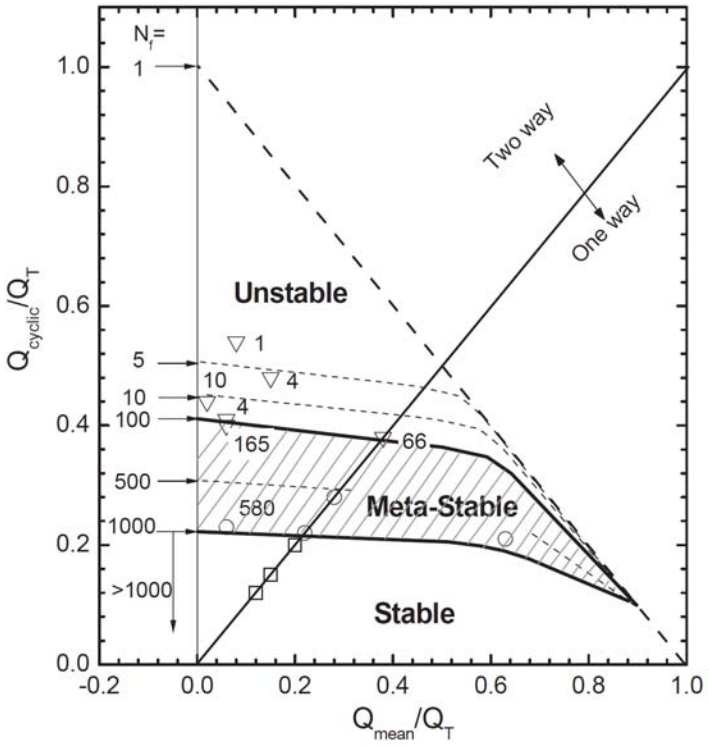
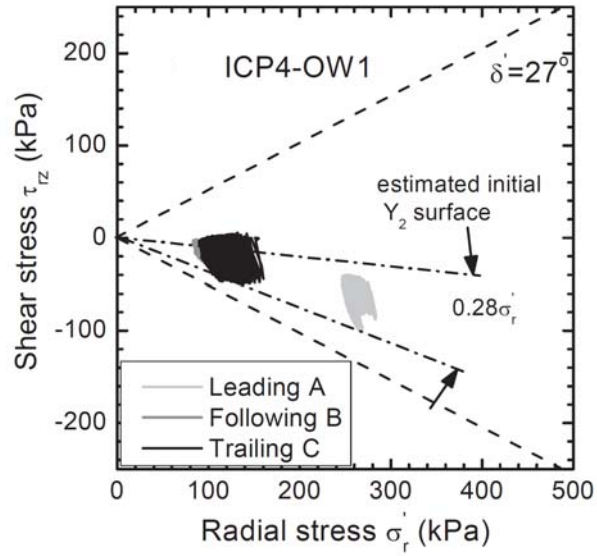
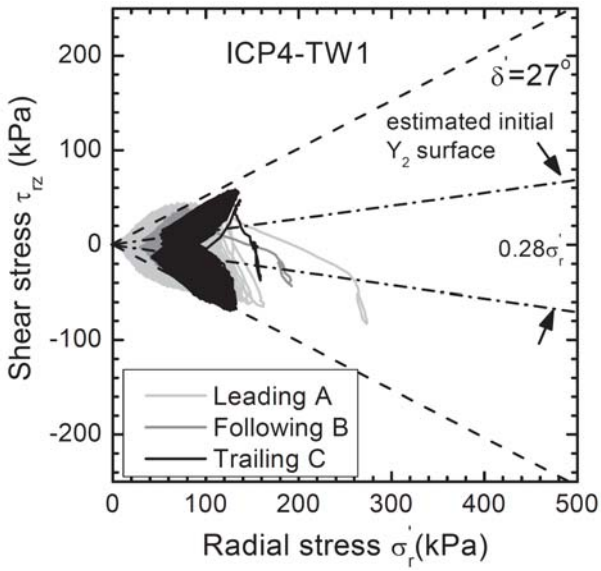


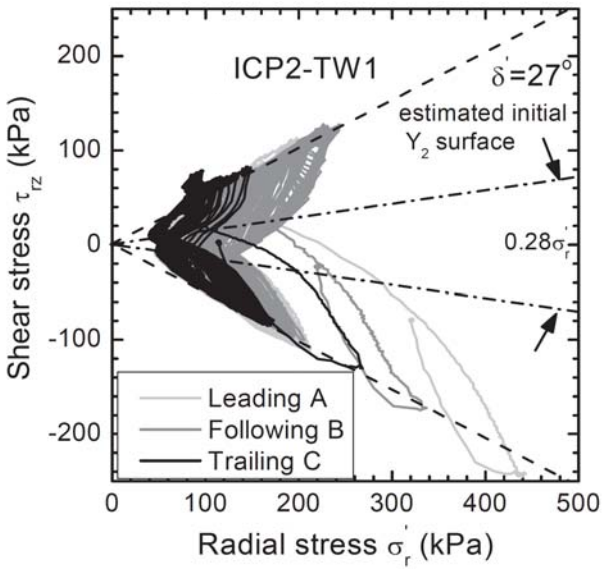
Figure 4-10: Mini-ICP displacement piles in silica NE34 sand axial cyclic behaviour stability interaction diagram after Tsuha et al. (2012). N_f number of cycles to failure; where no number is shown there was no cyclic failure.



(a)

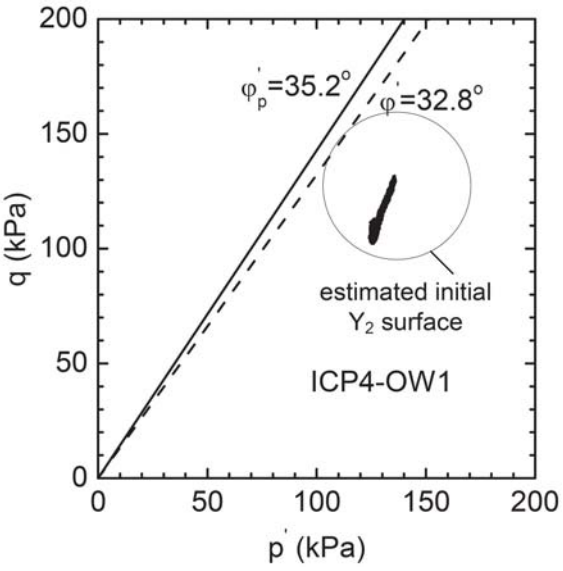


(b)

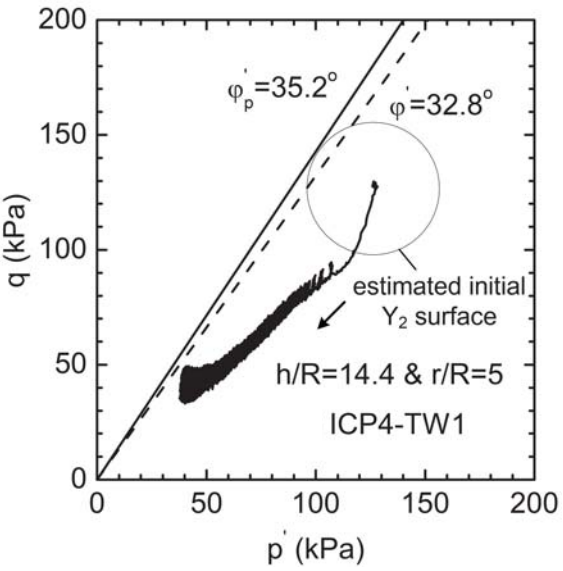


(c)

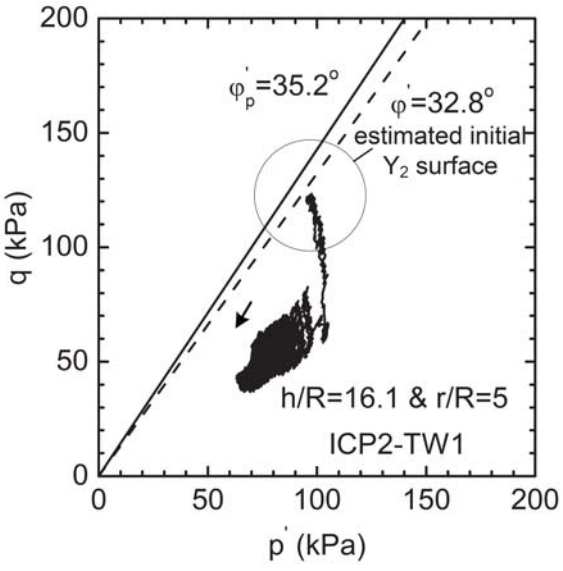
Figure 4-11: Interface effective stress paths from the axial cyclic loading with Mini–ICP tests typifying (a) Stable, (b) Meta- Stable and (c) Unstable tests (Tsuha et al. 2012).



(a)



(b)



(c)

Figure 4-12: Sand mass effective stress paths for the axial cyclic loading behaviour of Mini–ICP after Tsuha et al. (2012) (a) Stable (b) Meta–stable (c) Unstable (Tsuha et al. 2012).

4.5 Characterisation of pile interface behaviour

Shearing conditions adjacent to displacement piles in sands have been compared to those applying in Constant Normal Stiffness (CNS) interface shear tests, interface direct shear tests and interface ring shear tests. CNS interface shear tests have been considered as appropriate models for the constrained dilation that takes place at the sand–pile interface, by representing the resistance offered by the interface surrounding sand mass with a constant stiffness boundary condition during shearing. A pile with radius R would develop in an elastic soil a radial stress change $\Delta\sigma'_{rd} = 2G\Delta r/R$ if a radial displacement of Δr was induced by dilation at the soil-pile interface, giving a CNS, $K = \Delta\sigma'_{rd}/\Delta r = 4G/D = 2G/R$ (Johnston et al. 1987, Lehane et al. 1993, White 2005, Jardine et al. 2005a). Boulon & Foray (1986) suggested large shear displacements during pile loading are localised within a thin zone around the shaft so that the surrounding soil could be considered to have a fixed 'elastic' radial shear modulus.

Classical direct shear procedures usually apply Constant Normal Load (CNL) conditions although constant normal height/ volume controls can also be applied. Pile-sand interface shearing conditions fall between these two limits. Airey et al. (1992) reported cyclic CNL and CNS direct shear tests on dense calcareous sand and used the latter to estimate the shear friction degradation observed along a pile subjected cyclic loading. Comparison of CNS results with model pile tests in uncemented calcareous sand by Al-Douri (1992) in Figure 4-13 revealed similar patterns of response although different rates and magnitudes of the normalised shear friction reduction with similar behaviour expected in silica sands. The key issue with CNS is that it is now appreciated that the shear stiffness G varies with density, shear strain and stress level in the field, so that stiffness is hardly constant. Secondly CNS depends inversely on pile diameter and is not purely a sand parameter.

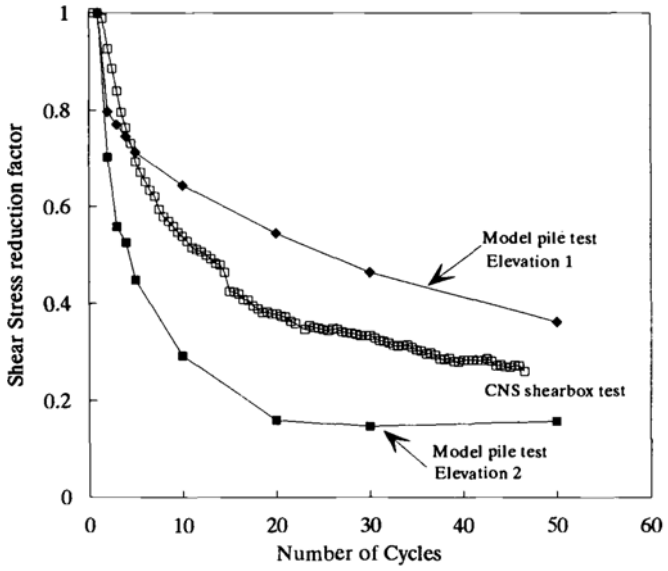


Figure 4-13: Comparison of shear stress reduction in CNS (displacement ±1mm, K = 1600kPa/mm) and model displacement pile tests in calcareous sand (Airey et al. 1992).

Lehane (1992) found that high precision direct shear testing gave good predictions for the field constant volume interface shearing resistances $\delta_{cv} \approx \tan^{-1}(\tau_{rz}/\sigma'_r)$ values measured at Labenne with Chow (1997) reporting the same at Dunkirk. However, this may not apply with different grain sizes and following work summarised by Ho et al. (2011), Jardine et al. (2005a) recommended conducting interface ring shear interface testing which allows much larger shear displacements. Their δ_{cv} measurements were controlled by the sand's granulommetry, shaft material and surface roughness, but were independent of the sand's initial density. Their recommendations are incorporated in ICP-05. Kolk et al. (2005a) assumed a constant value of 29^0 for all sands and UWA-05 (Lehane et al. 2005a) retained the same default value in the absence of ring-shear tests.

Yang et al. (2010) and Ho et al. (2011) investigated ring shear interface particle crushing and shear zone thickness growth using the Imperial College interface ring shear equipment reporting large scale particle crushing in tests involving up to 8m of shear displacement. The particle crushing and interface polishing influenced the δ_{cv} in sands that were either finer or coarser than those at Labenne or Dunkirk ($d_{50\%}$ = 0.04 – 1.46mm). Ho et al. reported that crushed materials were localized in a shear band which grew under monotonic shearing to large displacements from between 4 to 15 times the sands $d_{50\%}$ size with an upper limit of 5mm in tests involving 8m shear displacement under maximum normal effective stress of 800kPa. Yang et al. (2010) used similar particulate measurement procedures to characterise particle crushing around the Mini-ICP shaft in tests on NE34 Fontainebleau sand. They also quantified the pile and test interface surface roughness changes as functions of shearing history enabling a quantification of the evolution of δ_{cv} with normalised interface roughness reporting a good correlation between δ_{cv} along the pile shafts with the normalised roughness $R_N = R_{cla}/d_{50\%}$ (Kishida & Uesugi 1987).

Dejong et al. (2003) presented a microscale investigation of the interface load transfer degradation during cyclic loading on uncemented materials by incorporating GeoPIV measurements (White 2002) of interface shear. Their measurements of the monotonic dilative response to interface shear agreed with the proposed trough to peak interface dilation argument proposed by (Jardine and Chow 1996, Chow 1997, Jardine et al. 2005a), although their global dilation was spread through volumetric strains occurring within the shear zone, rather than being explicitly localised at the interface. The total global dilation measured appeared to be independent of specimen thickness but dependent on shear zone thickness which grew as cycling continued. The magnitude of contraction increased with number of cycles. Load-controlled two-way cycling led to more marked contraction and an increase in shear displacement amplitude. The shear band stiffness fell and a longer phase of dilation was required to recover the volume lost during the contractile phase. Displacement controlled two-way cycling led to reductions in the normal stress and therefore the horizontal shear stress.

Kelly (2001) reported a series of one and two-way cyclic interface ring shear experiments with a 1m diameter interface ring shear apparatus at University of Sydney, Australia. Figure 4-14 shows trends from four 40mm thick dense silica sand samples (I_D = 81%) that had been initially monotonically sheared for about 110mm at σ'_{v0} = 150kPa followed by ten displacement controlled two-way cycles of shearing with various levels of shear displacements. After cycling the samples were monotonically sheared again for 100mm. Initial monotonic shearing led to a dilation of ~0.4mm. Subsequent cyclic shearing resulted to interface contractions which increased with the cyclic displacement amplitude imposed. The interface contracted and showed enhanced dilation on subsequent monotonic shearing. The 'lower-level' cyclic shear displacement amplitudes (±0.28mm, ±0.56mm, ±1.11mm) show the most enhanced degree of dilation at the end of shearing while 'high level' (±2.78mm) cyclic displacements led to hysteretic 'butter-fly wings' of volumetric changes with contraction, phase transformation and dilation all developing within each cycle.

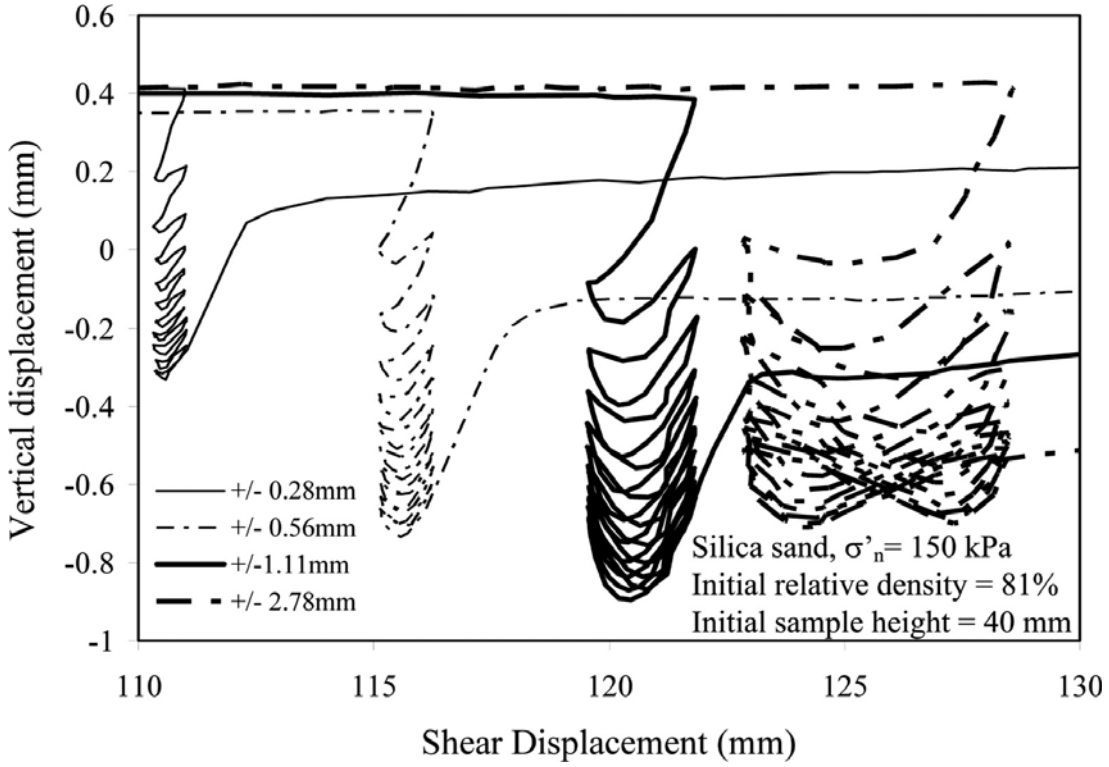


Figure 4-14: Vertical and shear displacements from two-way cyclic loading tests in a University of Sydney 1m diameter interface ring shear apparatus (Kelly, 2001).

4.6 Summary conclusions

A review of the current design practice and understanding of the mechanisms governing the behaviour single displacement piles during axial cyclic loading has been presented that identified aspects investigated further in the Author's study. The following summary points are drawn from this review:

1) Axial cyclic loading can significantly reduce the ultimate static capacity of a pile as estimated through, for example, a Working Stress Design method. More specific consideration of load cycling effects is required in design.
2) A paucity of full–scale axial cyclic loading of displacement piles in sands is noted. The only earlier comprehensive reported study (Jardine & Standing 2000), involved low and high level axial load cycling and up to 1000 cycles.
3) A greater number of model piles cyclic loading test studies have been conducted which applied up to 200,000 cycles. However, little consideration has been given to how scaling affects the model piles responses in comparison to those in the field.
4) Axial cyclic pile responses were categorised into Stable (S), Unstable (US) or Meta–stable (MS), defining zones that can be mapped on stability interaction diagrams.
5) While capacity can increase or be maintained in the stable load cycling mode, large capacity losses are observed in the unstable cycling and moderate capacity degradation is associated with the transitional meta-stable mode.
6) Laboratory cyclic interface characterisation techniques included constant normal stiffness interface shear, direct interface shear and interface ring shear techniques. It is emphasised that to be appropriate laboratory modelling has to replicate the stress, stiffness and granulometry properties adjacent to the sand–pile interface.

Chapter 5

5 Apparatus and its principles

5.1 Introduction

The essential equipment employed in this study consisted of the Grenoble–INP 3S-R Laboratory instrumented Calibration Chamber (CC), the Mini Imperial College Pile (Mini–ICP) with its array of multiple gauges and associated calibration rigs. Other utilised penetrometer equipments included a CPT cone–tipped pile, an un-instrumented micro pile and a model un-instrumented driven pile with its driving system. This study also involved numerous pile surface roughness measurements with a Taylor Hobson Pneumo Form Talysurf Series 2 as well as granular material characterisation with a QicPic laser optical measurement system, a surface Interferometer, and a Microsurf 3D Microscope. High resolution digital photography and analysis was also undertaken along with some standard soil mechanics laboratory measurements.

The first main section of this chapter details the 3S-R Laboratory calibration chamber's features and instrumentation. The following section (5.3) describes the miniature sand stress sensors deployed for the study and their calibration procedures, while section 5.4 summarises various ancillary CC equipment. Section 5.5 details the Mini-ICP's main features and the calibration of its transducers. Part 5.6 describes the micro pile, the CPT cone–tipped pile, and the model driven pile. Brief descriptions on the application of the other apparatus employed in the ancillary studies are given on section 5.7.

5.2 The Grenoble–INP 3S-R Laboratory Calibration Chamber

5.2.1 Background

The calibration chamber at Grenoble Technical University (INPG) 3S-R Laboratory illustrated in Figures 5-1 and 5-2 comprises of three metal rings, 1.2m inner diameter and 0.5m depth each, bolted together at their end flanges to form the 1.5m deep chamber. The chamber is recessed into the laboratory's floor and has a rigid circular steel base. It has a 100mm thick circular steel cover with a central 50mm diameter port to allow model pile installation. The model test piles' installation is guided by three roller assemblies mounted around the central port. The cover has three smaller through holes near the perimeter of the chamber which conduct the wires from the sensors installed in the sand mass to the data logger. The chamber walls inside were lined with either a latex membrane sheet that reduced friction between the sand and the rigid chamber walls, or with three neoprene individually pressurisable membranes. A range of top pressurisable neoprene membrane arrangements were installed to apply the main vertical surcharge loads/ stress. The specific boundary conditions used in this study are discussed in 5.2.2.



Figure 5-1: Above ground layout at the 3S-R Laboratory Calibration Chamber.

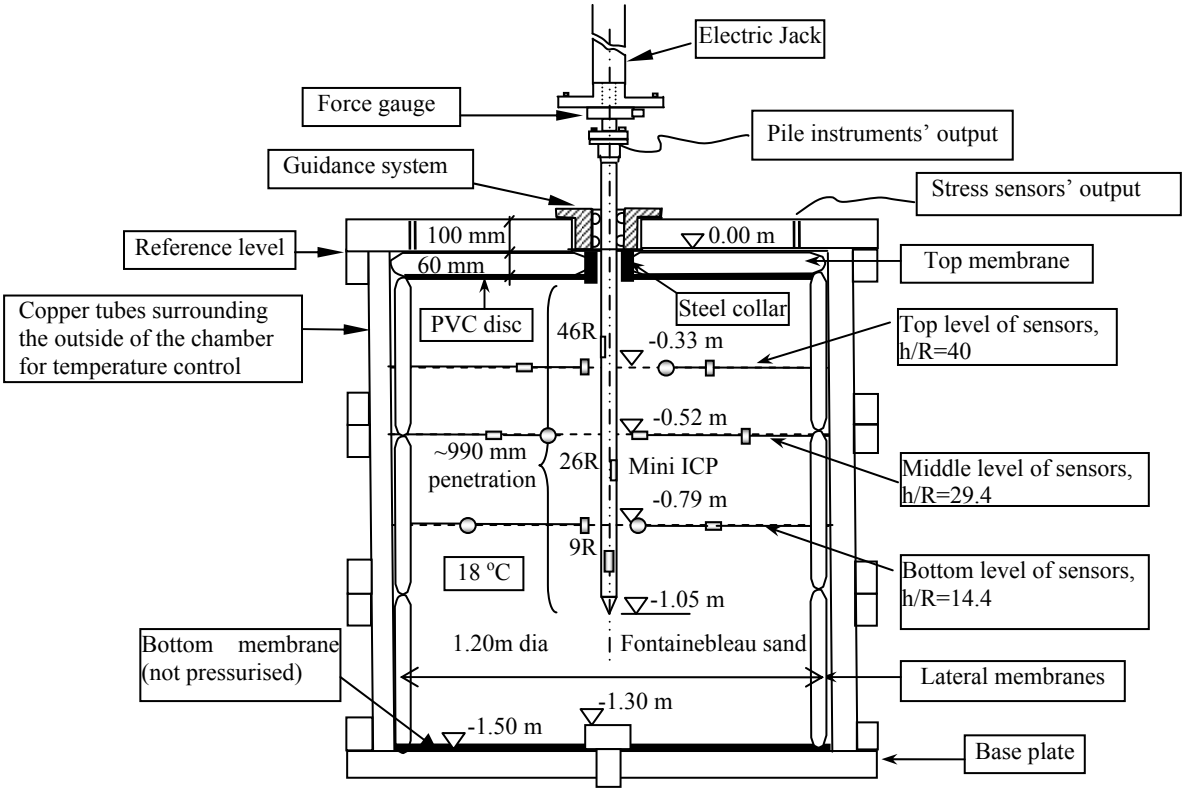


Figure 5-2: Vertical section of the instrumented 3S-R Laboratory CC with the Mini–ICP installed in the final arrangement deployed during this study for tests ICP07 and 08.

5.2.2 Calibration chamber features and application to the study

5.2.2.1 Background

Jardine et al. (2009) and (2013a) described the procedures developed for the 3S-R laboratory calibration chamber prior to this study and noted the steps required to improve the chamber's boundary conditions and model piles installation experimental procedures as follows.

1) The calibration chamber pressurisable top membrane which has an annulus shape and applies the main vertical surcharge loads/ stress as shown in Figure 5-2 was revised from having a 200mm inner diameter to a 50mm inner diameter after observations that the latter better defined the q_c profile at the shallow depths as shown in Figure 5-3.
2) The depth of penetration of the model piles during installation was restricted to just less than 1m to avoid the chamber bottom boundary affecting the observed pile base load profile.

These settings were adopted for the current study. However, radial and shear stress measurements made on the pile surface during installation of the instrumented Mini–ICP piles showed "unnatural" peaks as the measuring clusters passed through a narrow shallow depth range (< ~ 0.2m) as shown in Figure 5-4(a). The radial stress peaks measured during the ICP04 became progressively marked at the same depth as the leading Mini-ICP cluster A was followed by cluster B and trailed by cluster C. The 50mm inner diameter top boundary membrane appears to have introduced local stress concentrations at shallow depths which could be attributed to two mechanisms;

1) Radially inward shear traction developing at the sand surface during top membrane pressurisation imposing radial normal stresses near the pile axis at shallow depths in the sand mass.
2) Restricted displacements of the sand surface applying around the pile during installation.

The pile and sand mass stress sensors showed trends returning to the expected patterns at depths greater than 0.2m into the chamber, verifying that the effect is localised. Two further improvements were made to avert or reduce this undesirable feature;

1) A steel collar was introduced around the pile at the ground surface to reduce the membrane's lateral spreading on to the pile. Figure 5-4(b) shows the resulting relative reductions in stress concentrations seen in test ICP06, but the effect was not eliminated completely.
2) An additional friction reducing PVC circular placard was laid between the sand surface and the neoprene membrane (see Figure 5-2) from ICP07 onwards which further reduced the stress peaks.

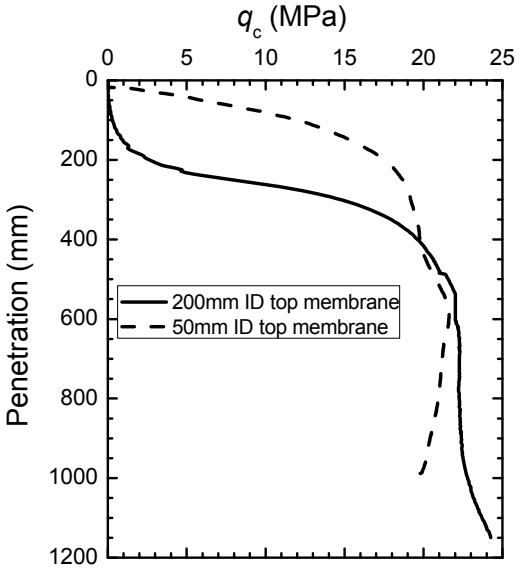


Figure 5-3: Cone resistance q_c profiles for alternative top-membrane designs (Jardine et al. 2013a).

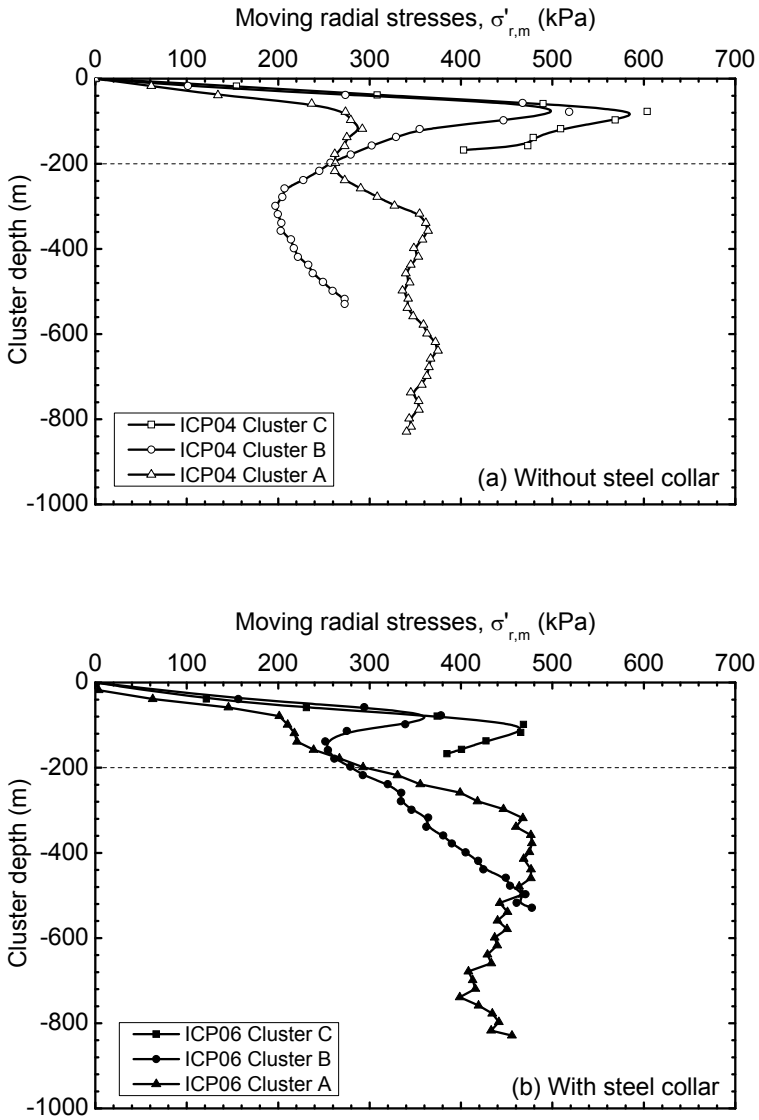


Figure 5-4: Moving radial stress profiles recorded on the Mini–ICP pile shaft clusters showing stress peaks at the shallow depth of the 3S-R calibration chamber.

5.2.2.2 Calibration chamber boundary conditions

Further steps have been implemented with the calibration chamber during this study to arrive at the boundary conditions that best match the sand state developed in field tests. The influence of the relative size of the calibration chamber on the penetrometer/ pile resistance is usually characterised in terms of the CC internal diameter ($d_{chamber}$)–to–pile outer diameter (D) ratio. Ideal scaling should ensure that the stresses developed by the pile in a calibration chamber match the stresses in a free field penetration. Cylindrical cavity expansion analysis suggests that the pile base cavity pressures developed by displacement piles can be expected to be 20–100 times the in–situ vertical effective stress, as reflected by the values of bearing capacity factor N_q (White et al. 2005).

Idealised elastic-plastic cavity expansion solutions by Yu & Houlsby (1991) indicate that the plastic radius from the penetrometer beyond which the soil is no longer at failure is in excess of 20 times the penetrometer radius for practical values of friction angle φ'. More stringent criteria result if the fully non-linear elasto–plastic sand behaviour is modelled more realistically, see Figure 5-5. Plane strain cylindrical cavity expansion studies by Salgado et al. (1998) suggested that ratios greater than 100 may be required. While the 1.2m diameter chamber and 36mm diameter Mini–ICP and CPT cone-tipped piles used in this study offer lower diameter ratio of 33.3, a ratio of 100 was achieved in test series MiP01 that employed a micro-pile of 12mm OD. It is also instructive to recall from Baldi et al. (1986), Schnaid and Houlsby (1991) and Salgado et al. (1997) that penetrometer resistance in calibration chambers is more influenced by the imposed lateral than vertical stress conditions.

The first calibration chamber boundary used in this study, as adopted from the prior arrangements prescribed by Jardine et al. (2013a), involved a constant top vertical surcharge stress of 150 – 152kPa imposed throughout a test and rigid lateral boundaries lined with friction reducing latex membrane sheets. The boundary condition is classically referred to as BC3. This and other boundary conditions are summarised on Table 5-1 and illustrated on Figure 5-6.

It has been argued that the BC2 and BC3 arrangements augment penetration resistances compared to the free field ideal because of the higher radial stresses generated by the rigid boundary, at radii where displacements can occur in the field. In their attempts to model better the free field conditions Huang & Hsu (2005) recommended a servo-controlled lateral boundary free-field simulator which imposes intelligent conditions at the chamber boundary, depending on the radial displacements induced by the penetrometer as it is installed in the chamber. This study followed the Huang & Hsu (2005) approach and adopted arrangement BC5 as a 'free-field simulator'. The procedure was to actively re-apply at the chamber boundaries the maximum radial stress measured at the boundary through the pressurised water filled neoprene membranes whose

pressures were monitored while keeping them at constant volumes ($\varepsilon_{vol} = \Delta V/V = 0$) during the piles installation. The maximum pressures measured at the membranes at the end of pile installation were considered representative of the field stress state and were re-applied constantly during the ageing periods of the piles, reflecting the stabilising action of the strain energy stored in the sand mass around the pile shafts.

Boundary Condition	Top and Bottom Control		Lateral Control	
	Stress	Strain	Stress	Strain
BC1	Constant	N/A	Constant	N/A
BC2	N/A	Zero	N/A	Zero
BC3	Constant	N/A	N/A	Zero
BC4	N/A	Zero	Constant	N/A
BC5	Constant	N/A	Servo-controlled	

Table 5-1: Boundary conditions in calibration chamber tests (after Huang & Hsu 2005).

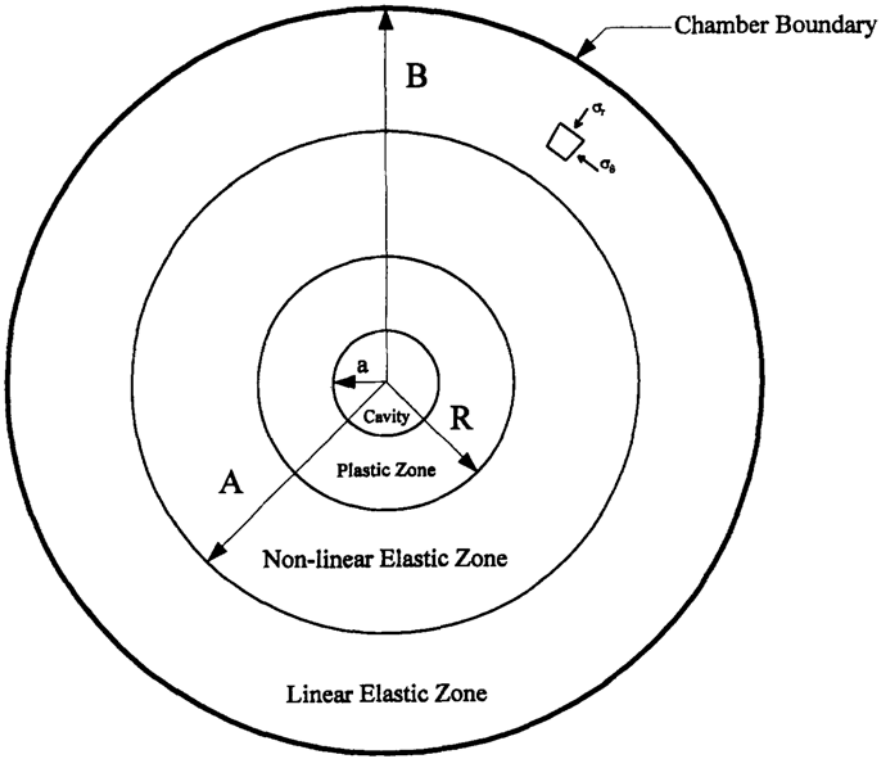


Figure 5-5: Illustration of the zones of sand deformations around a penetrometer in an ideal calibration chamber (after Salgado et al. 1998).

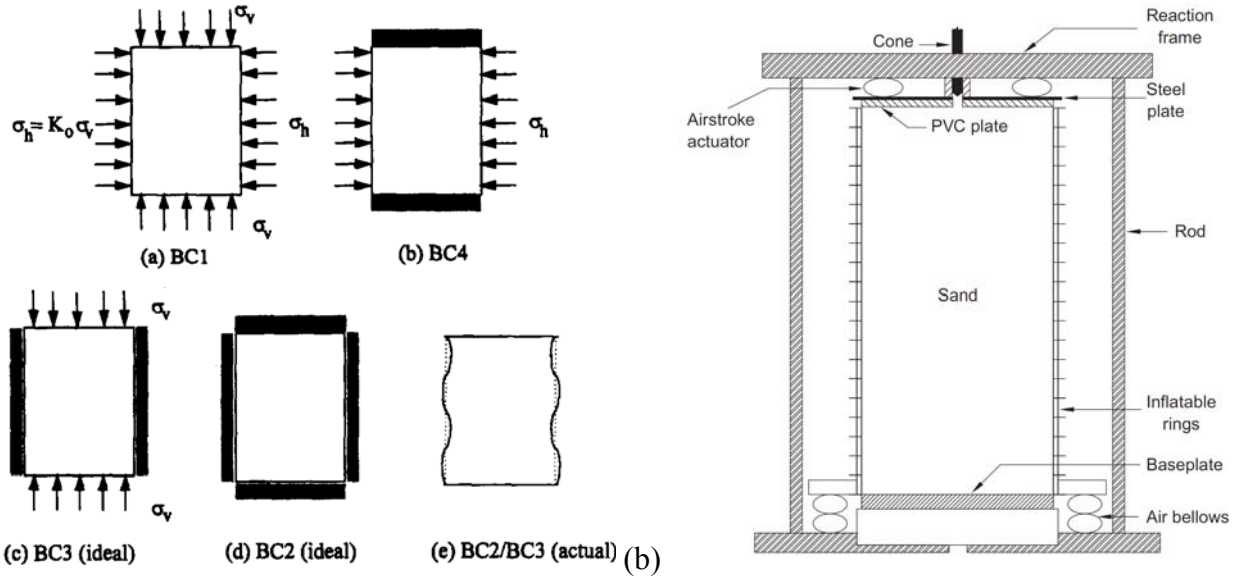


Figure 5-6: Illustrations of (a) calibration chambers classical boundary conditions (Salgado et al. 1998) (b) servo–controlled free field simulator calibration chamber (Huang & Hsu 2005).

5.2.2.3 Calibration chamber temperature control

Temperature regulation was achieved in the CC tests by circulating water at a constant temperature (typically 18.5^0C) through copper tubing surrounding the CC, which is protected by substantial exterior thermal insulation. The automated regulator system was re–filled with water every 10 or so days, countering any minor leaks developed as water circulated through a nominally closed loop. Insulation involved thick Polystyrene elements placed over the entire chamber exterior. Temperature sensors were placed at the sand mass levels where the miniature stress sensors were installed. Other temperature sensors were installed on the CC exterior; in the space within the floor recess around the tank, and on a sensor termination box housed in this space. The working space around the CC had two ventilator systems that automatically regulated the air temperature to reduce thermal variations.

At best the system kept diurnal variations to ±0.1°C, however, the system was not able to correct sharp laboratory temperature changes instantly. The soil and pile stress and temperature sensors showed clear responses to even minor sand mass temperature shifts. It was considered important for this study to maintain constant temperatures during the pile ageing. The effects of temperature variations on the ageing stresses and load measurements are detailed further in Chapter 10.

5.2.2.4 Miniature sand stress sensors

Five of the Author's calibration chamber pile experiments (Series ICP04, ICP05, ICP06, ICP07, ICP08 and DII) were instrumented with miniature Sand Stress Sensors (SSS). Between 9 and 36 of these gauges were deployed in each case set on 1 to 3 levels as the sand was pluviated into place. They were positioned at carefully prescribed levels and radial distances from the

chamber axis/ installed pile position using the precision laser guided surveying described by Jardine et al. (2009), to a specifically planned layout that minimised potential mutual interference between the sensors.

The measuring faces of the sensors were orientated such that the vertical, radial or circumferential/ hoop total stresses (σ_z, σ_r or σ_θ) could be measured at the intended radial distances from the pile axis. The wires from all sensors were guided to the outer perimeter where they were secured by tape and then conducted over the vertical surcharge membrane and out of the chamber cover through the wire access ports before being terminated at a central data logger location. Specific details on the design and calibration of the SSS are discussed in section 5.3.

5.2.2.5 Pile installation and loading apparatus

Pile installation by monotonic or cyclic jacking was achieved with an electro-mechanical Rosier Electro-Thrust 35kN capacity jack. The jack was instrumented with a 50kN load cell and global pile head movement instrumentation. An LVDT was mounted on the free standing length of the installed pile that rested on the CC cover plate prior to axial static and cyclic pile load testing. It determined the relative axial movement between the pile and the CC eliminating the errors associated with loading system compliance (which affected the globally measured displacements). The jack assembly is mounted on a rigid steel frame that spans the CC and can move on two rails either side of the CC, allowing the jack to be moved to the side during sand chamber preparation. Jack verticality is maintained by the frame, which also provides reaction for the jack during installation, or static/ cyclic axial loading. Section 5.8 briefly describes the jack's operational control through the Labview 8.2 programmable system.

5.3 Sand Stress Sensors features and calibration

5.3.1 SSS features and application to the study

Commercially sourced sensors with capacities of 7MPa (made by Kyowa Electronic Instruments Company, Kyowa), or 3MPa and 1MPa (made by Tokyo Sokki Kenkyujo Company, TML) were deployed to instrument the sand surrounding most of the pile tests. The sensors were disk shaped and had wires emerging from the side or back of their measuring faces as shown in Figure 5-7; the sensors' dimensions and rated outputs are listed on Tables 5-2 and 5-3.

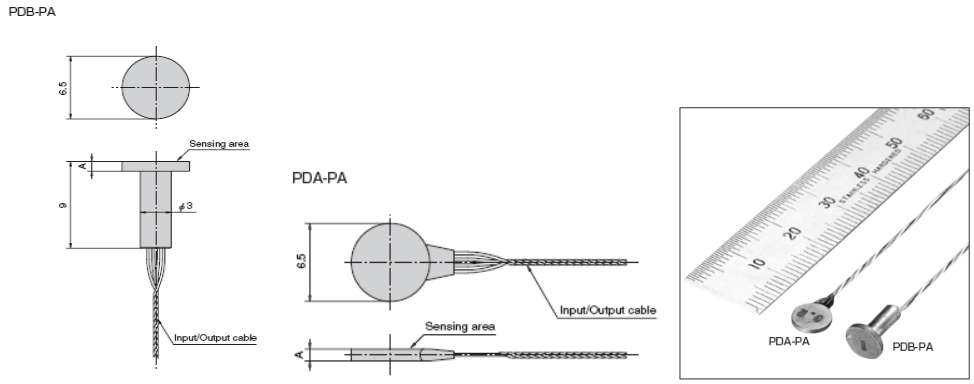
Inclusion of even miniature stress sensors into the sand affects the in–situ stress state unless the sensors' load–displacement properties exactly match the sands' non-linear elasto–plastic constitutive properties. Diaphragm-type miniature stress sensors behave linearly and elastically when hydrostatically loaded by a fluid medium producing the calibration factors supplied by manufacturers. However their response in granular media over the stress ranges encountered around the displacement piles becomes (i) non-linear to linear on first loading, but (ii) hysteretic on

unloading and re-loading paths. These phenomena are due to cell-action processes illustrated on Figure 5-8.

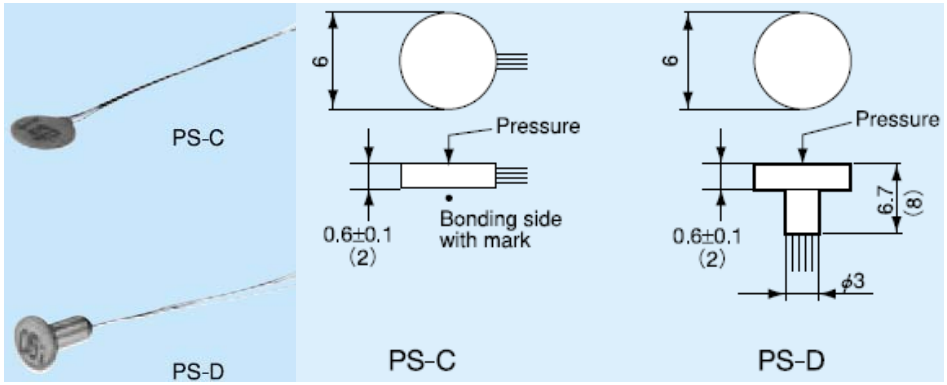
Several recommendations have been proposed to guide the choice of soil stress sensors. Weiler & Kulhawy (1982) recommended a minimum ratio of 10 between the diameter of the sensing diaphragm and the sand's mean particle size ($d/d_{50\%} > 10$) to prevent 'point load' problems with the sensors. Collins et al. (1972) and Tory & Sparrow (1967) recommended the sensors' aspect ratio defined as sensor diameter to thickness ratio (d_c/t_c) should exceed 5 with the sensors wire exiting from the sensors' side in the plane of the sensing face. Monfore (1950) then Tory & Sparrow (1967) suggested that the relative ratio of the sensing section (with diameter d) to the total sensor area effectively $(d/d_c)^2$ should be less than 0.25 to ensure uniform loading on the diaphragm while keeping the diaphragm away from the stress concentration on the sensors edge. Tory & Sparrow (1967) showed that for a sensor installed in an elastic soil, the stiffness ratio $S = E_{soil} \Big/ E_{cell} \left(d \Big/ t \right)^3$ should be less than 0.3. Solutions from Roark (1954) or Timoshenko & Woinowsky-Krieger (1959) give the midpoint deflection of the sensing diaphragm for a simply supported circular plate or a circular plate rigidly clamped at its ends as $y_m = \left(3(5+\nu)(1-\nu^2)qr^4\right) \Big/ \left(16(1+\nu)Et^3\right)$ or $y_m = 3(1-\nu^2)qr^4 \Big/ 16Et^3$ respectively where y_m is the midpoint deflection of the sensing diaphragm, ν is the Poisson's ratio, r and t are the radius and thickness of the sensing diaphragm, q is the stress applying on the sensor and E the Young's modulus. To avoid arching around the sensing diaphragm a diaphragm diameter–to–maximum deflection ratio of up to 5,000 is recommended.

Table 5-4 shows that apart from the aspect ratio and $d/d_{50\%}$ ratio, the Kyowa and TML sensors fall short of the published soil-stress sensor recommendations. Considerable cell action effects can therefore be expected in use. Alternative sensors made by the Precision Measurement Company (PMC) (with capacities 6.9MPa and 13.8MPa, Figure 5-7(c)) were sourced for the ICP06 tests involving wet NE34 sand chamber because of their reported ability to perform under water without further modification. Table 5-2 includes the sensors' dimensions and Table 5-3 the sensors specification while Table 5-4 assesses their compliance to the prescribed recommendations for minimal cell action effects. The PMC sensors also fail to meet most of the detailed recommendations and their smaller sizes implied they would be more susceptible to 'point load' effects compared to the Kyowa or TML gauges. Trial calibrations with the PMC sensors in the Imperial College calibration oedometer filled with NE34 sand showed relatively marked cell action effects and poor repeatability; they were therefore not used further.

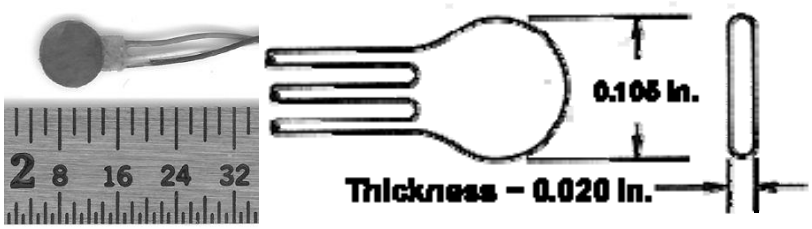
For sensors to meet the stated recommendations, they would need to have $d_c \geq 7.5$mm, $t_c \leq 1.4$mm with the sensing diaphragm as $d \geq 5$mm and $t \geq 0.54$mm for minimal cell action effects in the test sands used. As such gauges could not be sourced commercially or manufactured by our workshops; the best-available gauges had to be accepted. However, the special calibration procedures described by Zhu et al. (2009) were employed to reduce measurement errors by accounting for the applied stress–to–measured stress (sensor output) interactions of the Kyowa and TML sensors in the sands used. Broadly similar approaches have been followed independently by other researchers including Allard (1990) and DiPalma (2011).



(a) TML PDA and PDB sensors (dimensions in mm)



(b) Kyowa sensors (dimensions in mm)



(c) PMC miniature pressure transducers (dimensions in inches)

Figure 5-7: Schematics of the miniature stress sand sensors employed in this study (after supplier's data sheets).

Sensor type	Capacity (MPa)	Sensor Size		Diaphragm size	
		d_c (mm)	t_c (mm)	d (mm)	t (mm)
TML PDA/B	1	6.5	1	5.6	0.20
TML PDA/B	3	6.5	1.4	5.6	0.33
Kyowa PS/D	7	6	0.6	5.0	0.30
PMC 105S	6.8 and 13.8	2.7	0.5	N/M	N/M

Table 5-2: Dimensions of the miniature sand stress sensors in this study.

Type	TML PDA/B		Kyowa PS/D	PMC-105S	PMC-105S
Capacity (MPa)	1	3	7	6.8	13.8
Rated Output (mV/V)	1		1	1.145	2.305
Rated Output (μstrain)	2000		2000	2290	4610
Calibration factor (μV/V/kPa)	Varies		0.118	0.166	0.167
Non-linearity	1%RO		1%RO	0.15%RO	0.11%RO
Hysteresis	1%RO		1%RO	1.75%RO	1.84%RO
Temperature effect on zero	1%RO/^{0}C		0.2%RO/^{0}C	N/M	
Temperature effect on span	1%/^{0}C		0.2% /°C	N/M	
Temperature compensation	-10 ~ 60^{0}C		0 ~ 50^{0}C	Calibrated at 22^{0}C	
Temperature range	-20 ~ +70^{0}C		-20 ~ +70^{0}C	Up to 100^{0}C	
Input/ Output resistance	350Ω		350Ω	350Ω	
Recommended excitation voltage	< 2V		1 ~ 2V	1 ~ 2V	
Allowable excitation voltage	5V		< 3V	3 ~ 5V	

RO = the Rated Output

Table 5-3: Manufacturers' specifications of the miniature sand stress sensors in this study.

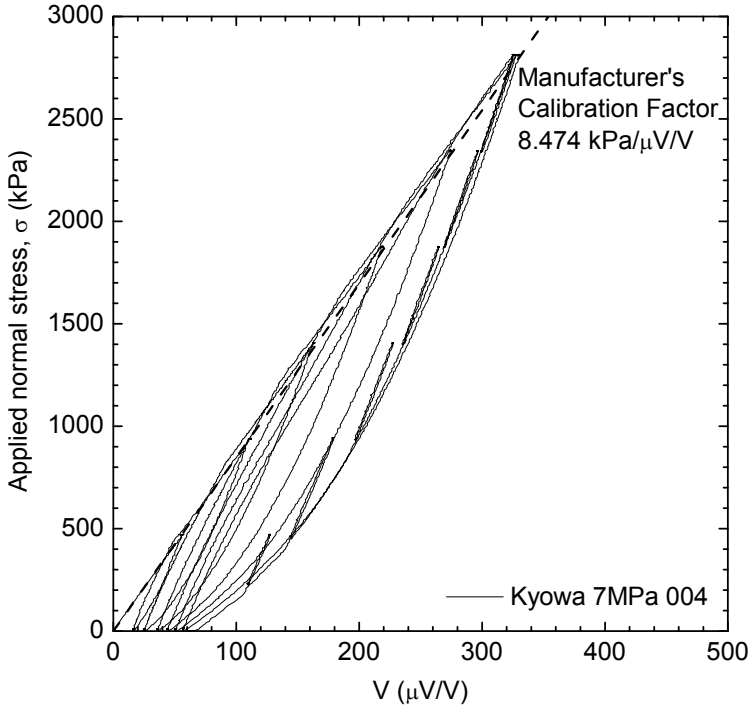


Figure 5-8: Kyowa 7MPa miniature stress sensor showing cell-action effect interaction of output and normal stress applied with dense GA39 Nemours sand in the Imperial College special calibration oedometer.

Aspect	Requirement	Kyowa	TML PDA/B		PMC
		MPa	MPa		MPa
		7	3	1	6.8 and 13.8
$d/d_{50\%}$	> 10	23.8	26.7	26.7	~10.8
Cell aspect ratio d_c/t_c	> 5	10	4.6	6.5	5.2
Sensing area ratio, d^2/d_c^2	< 0.25 – 0.45	0.69	0.74	0.74	~0.72
Diaphragm diameter/ deflection ratio	> 2000 – 5000	356	≤ 787		588
Soil-sensor stiffness ratio, S	< 0.5	2.6	≥ 2.74		1.6

Table 5-4: Comparison of characteristics of sand stress sensors in the current study to the minimum design requirements.

5.3.2 SSS calibrations

The cell-action effects of the miniature sand stress sensors calibration were accounted for in a similar way to the process designed by Zhu et al. (2009), to reflect the calibration chamber pile testing sequence. It was particularly important to characterise the stress–sensors' interactive unload–reload behaviour with the sand to follow the cyclic installation and pile load testing paths. As an example, Figure 5-9 summarises the range of σ'_r measurements interpreted from a single sensor output during the installation of a Mini-ICP test pile ICP05.

Zhu et al. (2009) developed at Imperial College the special 'oedometer' cell shown in Figure 5-10 for their stress sensor calibrations. In this study's calibrations' the 92mm diameter by 302mm height oedometer cell was filled with either NE34 or GA39 test sand, dry pluviated and tamped to the same density (or slightly denser) than in the CC; Zhu et al. (2009) show that the calibrations are practically unaffected by adopting a slightly denser state for the calibrating sand, although looser states were to be avoided. The sensor is placed flat at a depth > 100mm from the top of the cell and at the centre of the cell with its measuring face upwards. After multiple trials, Zhu et al. (2009) recommended that a sand thickness of at least $7d_c$ is required between the cell and loading platen. The cell is topped of with dense sand and subjected to the load–unload–reload–unload calibration sequence prescribed on Figure 5-11 which was automatically implemented by a computer controlled air pressurised bellofram cylinder loading a piston with a circular plate end that acted at the top of the sand oedometer. The designed calibration load sequence covers the range of the loading paths envisaged in the chamber as the pile is advanced by multiple jack–strokes leading to stress maxima developing when the pile tip is nearest to the sensor. Stresses rise and fall then fall systematically as the tip passes the sensor level. A fresh sand mass is prepared for each calibration and multiple calibrations undertaken per sensor in each sand type (with either dry or wet test conditions) to maximise the reliability of the calibration.

Zhu et al. (2009) defined for each sensor separate calibration factors for the first loading curves, the unloading path and for the reloading stages/states. These relationships are combined for use in the data reduction process. A power law function (equation 5-1) is used for the fresh loading (L) of the sensor, accounting for the non-linear to linear sand response, V/V_0 being sensor output per excitation voltage, while σ_m is the applied change in total normal stress, Figure 5-12. Zhu et al. (2009) report that cell–action effects lead to under-registration (even on first loading) that exceeds 70% for the (relatively soft) lower capacity (1MPa) cells but falls around 10% for the stiffer 7MPa cells.

Exponential fitting curves are used to reproduce Unloading (U) curves after normalising the unloading stresses by the maximum stresses σ_{max} and output voltage by the maximum output voltage V_{max} attained before unloading; see Figure 5-13. This gives six calibration factors (y_0, x_0, A_1, A_2, t_1, t_2) for each sensor in the form of equation 5-2 for each unloading occurrence; Figure 5-13. Zhu et al. (2009) report unloading check tests starting from maximum loads other than those at which the sensor has been calibrated indicated potential maximum errors between true loads and those expected from the sensor output between 0.5% and 5.7% with the higher 7MPa and 0.5MPa capacity sensors respectively.

The sensors' reload (R) paths can be normalised by the overall maximum stress and maximum output voltage attained in the calibration sequence, Figure 5-14. Zhu et al. (2009)

suggested the sensors' re-load behaviour was primarily dependent on the starting stresses (independent of maximum stress applied) and could be fitted with multiple linear fits, as defined by equation 5-3 where σ_{min} is the minimum stress for the reload branch, V_{min} the corresponding cell output and S_r is the slope of the linear fit corresponding to the σ_{min} value paths. Where reloading starts at stress levels other than the σ_{min} applied in the calibration sequence reloading branches, the slope S_r can be approximated by fitting the known values of S_r using the polynomial function defined in equation 5-4, C_1, C_2, C_3 and C_4 are fitting parameters determined for each sensor, P_a is the atmospheric pressure for stress normalisation. In general, the relative fitting errors assessed by the described procedure decreased with the capacity (and stiffness) of the sensor.

The combined loading, unloading and reloading calibration factors were used in a Microsoft Visual Basic procedure developed by Zhu & Yang (2009) to reduce into engineering units the data gathered in the sand mass during initial CC pressurisation, cyclic (jacking) pile installation, ageing, static testing and cyclic loading of the piles.

$$\sigma_m = a\left(V/V_0\right)^b \qquad 5\text{-}1$$

$$\sigma/\sigma_{max} = y_0 + A_1 e^{\left(V/V_{max} - x_0\right)/t_1} + A_2 e^{\left(V/V_{max} - x_0\right)/t_2} \qquad 5\text{-}2$$

$$\sigma = \sigma_{min} + S_r\left(V - V_{min}\right)\sigma_{max}/V_{max} \qquad 5\text{-}3$$

$$S_r = C_1\left(\sigma_{min}/P_a\right)^3 + C_2\left(\sigma_{min}/P_a\right)^2 + C_3\left(\sigma_{min}/P_a\right) + C_4 \qquad 5\text{-}4$$

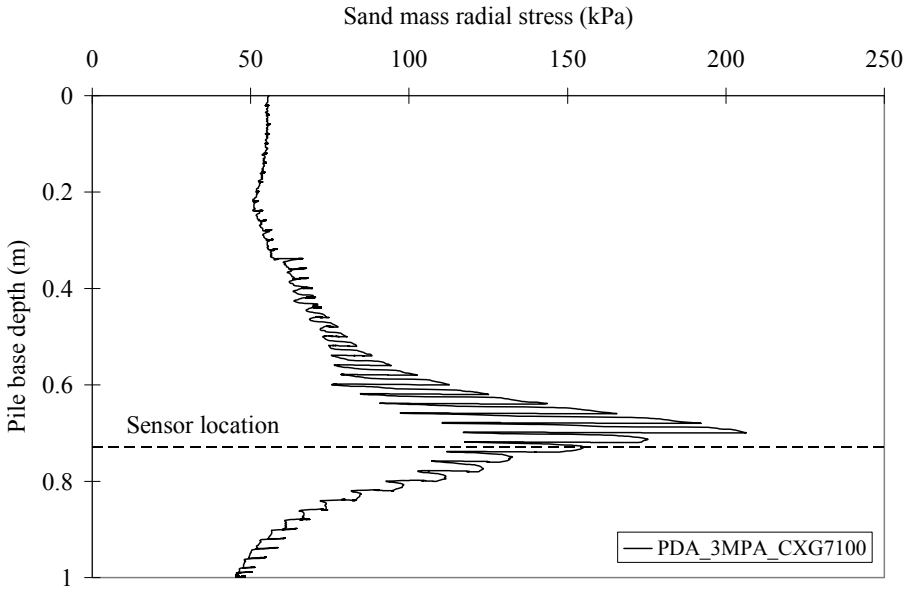


Figure 5-9: Radial stresses on a 3MPa PDA-7100 placed at 144mm (8R) from the pile axis and 0.73m (h/R = 14.4) below ground level during Mini–ICP installation in ICP05 test involving dry GA39 Nemours sand.

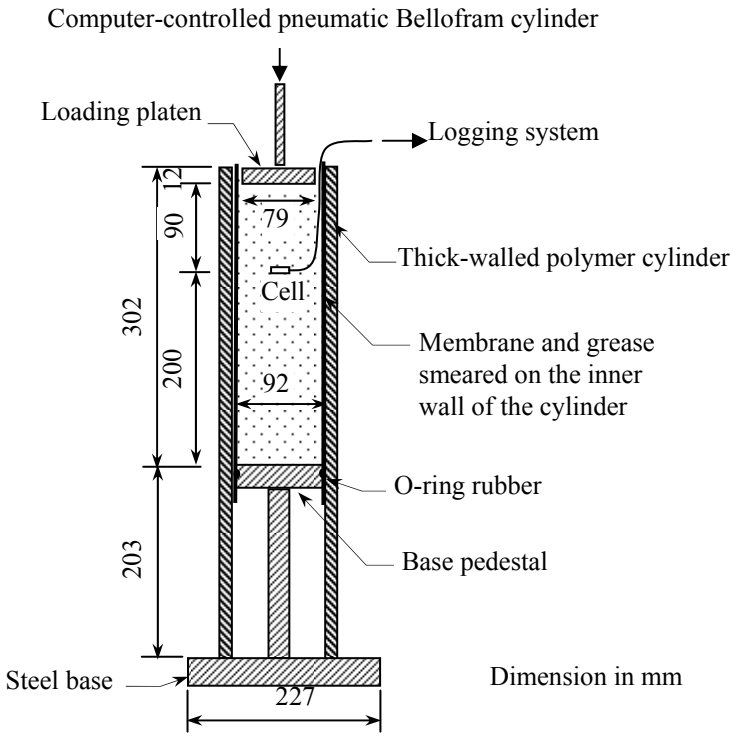


Figure 5-10: Sand stress sensor calibration rig (Zhu et al. 2009).

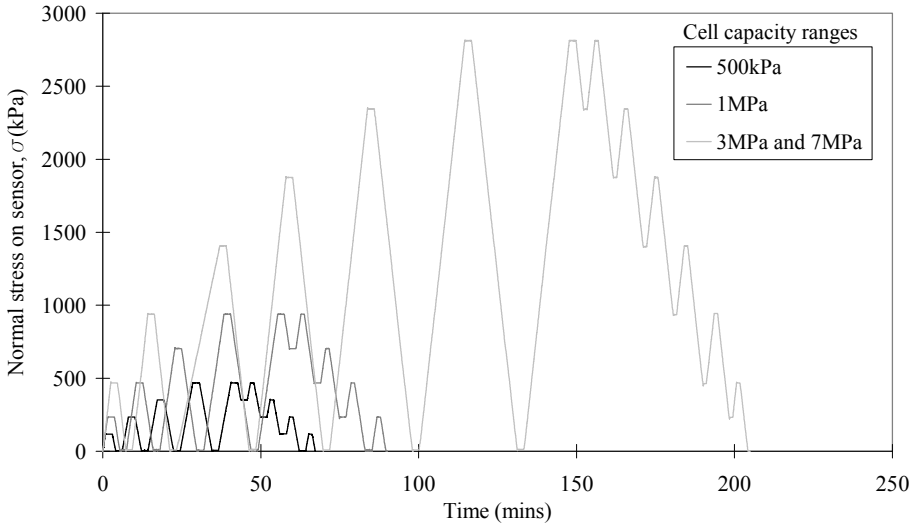


Figure 5-11: Load – Unload and reload calibration sequences adopted for the miniature sand stress sensors for the four nominal capacity ranges.

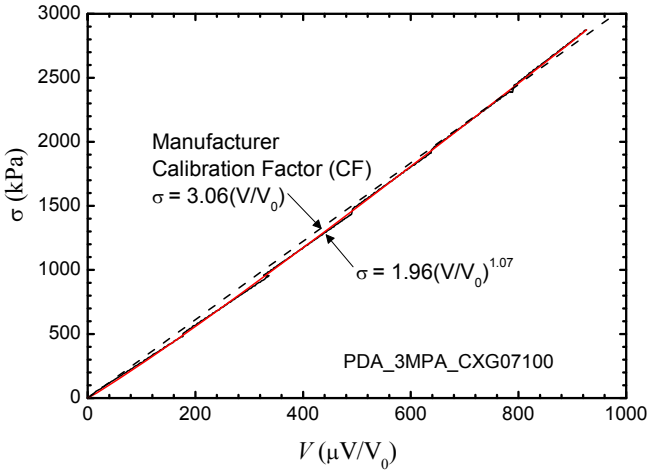


Figure 5-12: Normal load versus stress sensor's output response in fresh loading calibration.

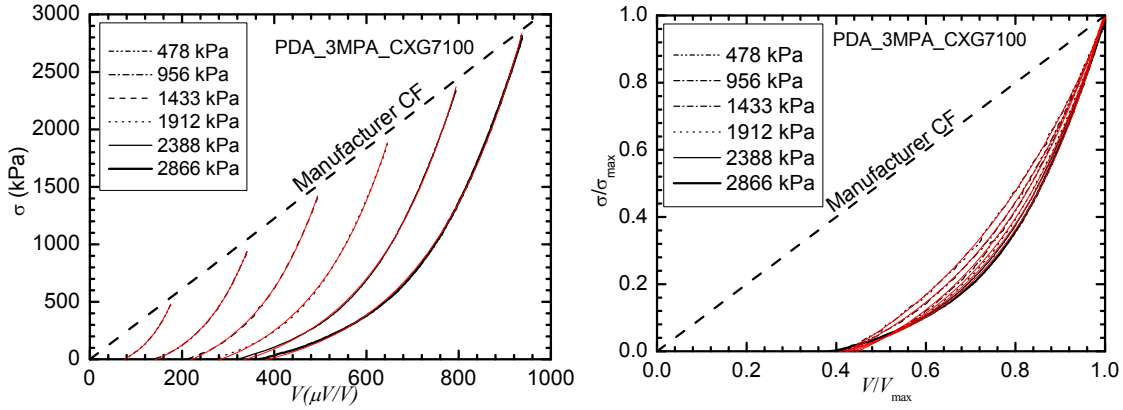


Figure 5-13: Normal load versus stress sensor's output response during unloading calibration.

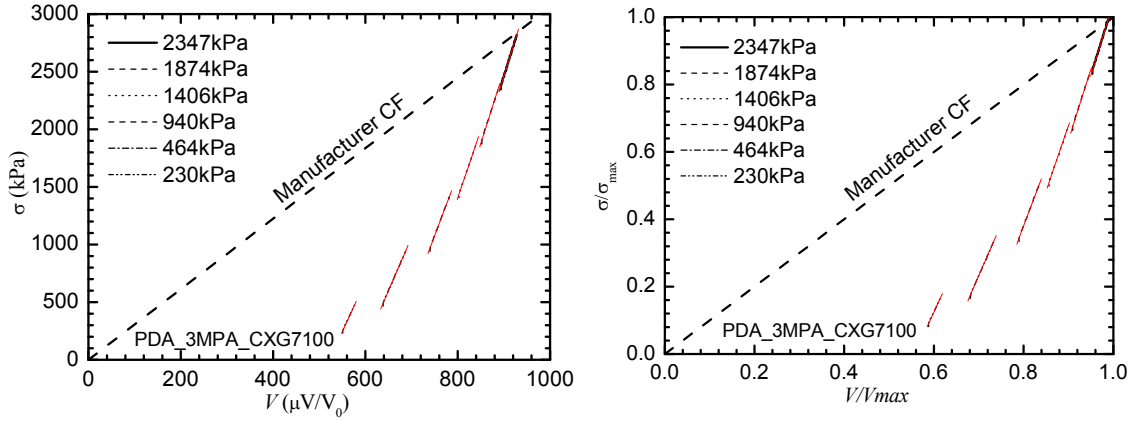


Figure 5-14: Normal load versus stress sensor's output response for re-loading calibration.

5.4 Other instrumentation installed in the CC

The axial displacements imposed on the piles installed in the CC by the electro–mechanical Rosier jack were monitored by an encoder/ converter unit within the jack that analysed its output signals. The axial load applied was measured by an axial load cell (type AEP TC4-5T) with 50kN capacity and a sensitivity of ~2mV/V (energized at 10V) whose calibrations indicated a mean error from the best straight line of 0.05% (±0.025kN). Four Keller PAA23S piezo-resistive absolute

pressure sensors were installed in the chamber, one to monitor the vertical stress membrane water pressure and three for the lateral stress membranes. Each had a 500kPa capacity and was energized at 24V and at nominal 0.1% precision. Resistance Temperature Detectors (RTDs) of Class A and type Pt 100 (made of Platinum with 100Ω at 0^0C) which had a working range of -50^0C to 250^0C and could resolve temperatures to 0.15^0C were used in the chamber and surrounding enclosed recess. An LVDT (type RDP DCTH/500A) energized at 15V with range ±12.5mm and sensitivity of around 300mV/mm was attached to the pile shaft at the end of installation during static and cyclic load testing to better define the axial displacements of the pile head.

5.5 Mini Imperial College Pile (Mini–ICP)

5.5.1 Background

Imperial College acquired its first instrumented displacement pile from Southampton University (Johnston 1972, Butterfield and Johnston 1973). Jardine (1985) overhauled the pile by adding new surface stress transducers, axial load cells and pore pressure sensors and reported useful pilot experiments in London Clay at Canon's Park, North London. However, further improvement to the measuring instruments was required and Bond et al. (1991) undertook comprehensive re-development of the instrumented pile. After several attempts Bond et al. arrived at a fully successful device that they referred to as the Imperial College Pile (ICP). The ICP was a steel, closed–ended, tubular pile of 101.6mm diameter with an adjustable length between 6m and 20m and a 60^0 conical tip. The pile was used in testing by Bond (1989), Lehane (1992), Chow (1997) and Pellew (2002) with 3 to 4 sets of stainless steel measuring instrument clusters, each complete cluster containing;

1) An Axial Load Cell (ALC) measuring axial loads on the pile
2) A Surface Stress Transducer (SST) measuring radial and shear stress acting on the pile
3) Two Pore Pressure Probes (PPP) diametrically opposite the pile sides measuring pore pressures
4) A temperature sensor

Each cluster's instrumentation provided redundancy of measurements, and good output stability over the measurements made during installation, equalisation and load testing. The ICP has been successfully used in stiff heavily over-consolidated London Clay (Bond 1989 and Pellew 2002), stiff heavily over-consolidated Cowden glacial till, soft sensitive Bothkennar Clay and loose Labenne dune sand (Lehane 1992) and normally consolidated low plasticity Pentre Clay and dense Dunkirk marine sand (Chow 1997).

This study employed a new Mini Imperial College Pile (Mini–ICP) which comprises an ICP, type device scaled down to 36mm outer diameter for laboratory calibration chamber testing (Jardine

et al. 2009). The Mini–ICP was developed by Imperial College in conjunction with Cambridge Insitu Ltd of Little Eversden, Cambridge, drawing on the experience gained in making and operating the field ICP.

5.5.2 Mini–ICP features and application to this study

The Mini–ICP summarized in Figure 5-15 is a stainless steel 1.5metres long, 36mm outer diameter pile with a 60^0 closed–ended conical base. Its shaft is air–abraded over its full length to a uniform centreline roughness (R_{cla}) of 3 – 4μm before each installation. The Mini–ICP has three transducers instrumented clusters commonly referred to as A 'leading', B 'following' and C 'trailing' from the base upwards, and an axial load cell near the base for measuring the pile base loads. Each cluster consists of;

1) An ALC for measuring the axial loads on the pile at the cluster positions.
2) Surface Stress Transducers (SSTs) measuring the radial stresses on the pile through two independent radial stress strain gauged "pillar" circuits, and two strain gauged 'shear web' circuits to measure the shear stress developed on the pile surface.
3) A digital temperature sensor.
4) An XYZ Micro Electro Mechanical Systems (MEMS) inclinometer chip.
5) An Analogue/ Digital (A/D) converter circuit board that sends data to the surface via a single cable set.

5.5.2.1 Axial Load Cells

The Mini–ICP has an ALC at its base to provide base load measurements and others integrated with the top of each main instrument cluster's SST. Under a protective sleeve that isolates the cells from external radial stresses, the ALCs comprise thinned-wall 17/4 Precipitation Hardening (PH) martensitic stainless steel 16mm long and thinned tubular sections each of 25mm outer diameter; see Figure 5-16(a). A Poisson Wheatstone bridge circuit with 4 axial and 4 circumferential 120Ω strain gauges is mounted on each ALC wall giving good resolution and minimal sensitivity to bending effects. Wiring from the ALC wall goes through a 1.5mm diameter drill hole on the ALC ridge into a central channel of the pile's cluster section to the Printed Circuit Board (PCB) at the top of the cluster.

The cell is designed to give a full-scale output of 27mV/V under a normal maximum load of 180kN which imposes an axial strain of 0.2%. The test loads imposed generally fall far below this limit and average at 35kN. The ALCs external sleeves interconnect with the main stainless steel shaft sections with Nu-lip rubber O-rings fitted at the cluster–pipe pile joint sections to keep out external material (sand or water).

5.5.2.2 Surface Stress Transducers (SST)

The SST devices employ Cambridge–type boundary earth pressure cells made out of a 2014A aluminium alloy. Figure 5-16(b) shows the Computer Numerically Controlled (CNC) machine–milled SST cell with the shear stress webs and normal/ radial stress pillars strain gauge arrangements. The cell consists of a 'dog-bone' shaped central part, 33mm in length and 18mm at its maximum width with a 8mm wide central web and uniform thickness of 5mm. The 'dog-bone' is connected to the 53mm long by 18mm wide cell platform by four vertical pillars which are strain gauged to measure primarily the normal/ radial stresses applied to the SST cells face through two independent 'top' and 'bottom' circuits. The dog-bone is also connected to a raised central platform by four horizontal shear web struts that are strain gauged to measure primarily the shear stresses/ forces applied to the SST cell's face. The strain gauged struts are all 4.5mm long, 3mm wide and 0.5mm thick which are made with radial transitions (0.5mm in diameter) to the main cell body.

The complete strain gauged SST is fastened onto a recessed part of the SST housing through 2 holes (3.3mm diameter to a depth of 7mm) on each side of the cell's platform. The wired cell is then covered by a two-part frame and pane window of outer planar size 85mm long by 33.2mm wide with a smooth convex central raised section of 11mm. The window frame and pane are joined together along the edges of the pane and inside the frame in a hot bonded rubber seal moulding process. The pane is 51mm long by 16mm wide and has the convexity of the pile radius, with two 4.5mm diameter holes, counter bored to 9mm, through which it is fastened to the cell. Protection from water ingress into the cell is achieved by an O–ring underneath the window frame bearing on to the lower housing, the hot bonded rubber around the pane, Dowty bonded washers and Hylomar gasket sealants on the screws connecting the pane to the cell. Jardine et al. (2009) report tests that showed that ≈ 45% of the radial pressure applied over the 2mm wide bonded rubber joint formed around the pane was transferred to the pane and on to the dog-bone cell. Other tests demonstrated that the rubber seal contributed about 17% of the overall radial stiffness of the cells.

Figure 5-17 shows a schematic of the strain gauging of the SSTs and Figure 5-18 a circuit diagram of the strain gauge wiring for the three stress transducers incorporated into each cell (two normal stresses and a shear stress). Twenty four 350 Ohm foil strain gauges were used per cell with each normal/radial stress pillar having two gauges, one on each side, and eight 'dummy' gauges on the bottom platform of the cell (four beneath each flange), wired into a Wheatstone half–bridge. Each half–bridge (for either the top or bottom normal stress transducer) has strain gauges on opposite sides of adjacent vertical webs wired in series and then parallel to two dummy strain gauges from the platform of the cell. Full bridge circuits were employed for the shear webs with two gauges on opposite sides of each adjacent strut. This aimed to give full shear output stability against web bending as well as temperature compensation. Eight wires from the cell, 2 for

energisation, and 2 from each SST's shear, normal (top) and normal (bottom) circuits go through a 2.5mm diameter semi-circular chamfer centred at the end of the cell platform into the central channel of the cluster to the Printed Circuit Board.

5.5.2.3 Printed Circuit Board (PCB)

Each of the three clusters has a Printed Circuit Board (PCB) that carries a regulated voltage supply unit and can take up to 16 analogue channels and deliver 24 bit digital voltage outputs. The PCB is energised at 12V DC which is regulated to 5V on the board. Data is processed from the on-board A/D converter and sent to the pile head via an RS232 communications cable. Each of the three PCBs can be set as a slave or master board which enables the boards to be tested independently. When running the complete pile setup the top board (at cluster C) is set to be a master that communicates with the lower boards (at clusters B and A) which are set to be slave units.

Each SST provides three channels of data. A further three are occupied by the Micro Electro Mechanical Systems (MEMS) 3-axis inclinometers. A single channel is used for the input from the onboard temperature sensor while the integrated ALC uses a further channel. The isolated Mini–ICP base ALC unit is read through a simplified PCB with two channels and is set as a slave to the nearest (cluster A) main PCB.

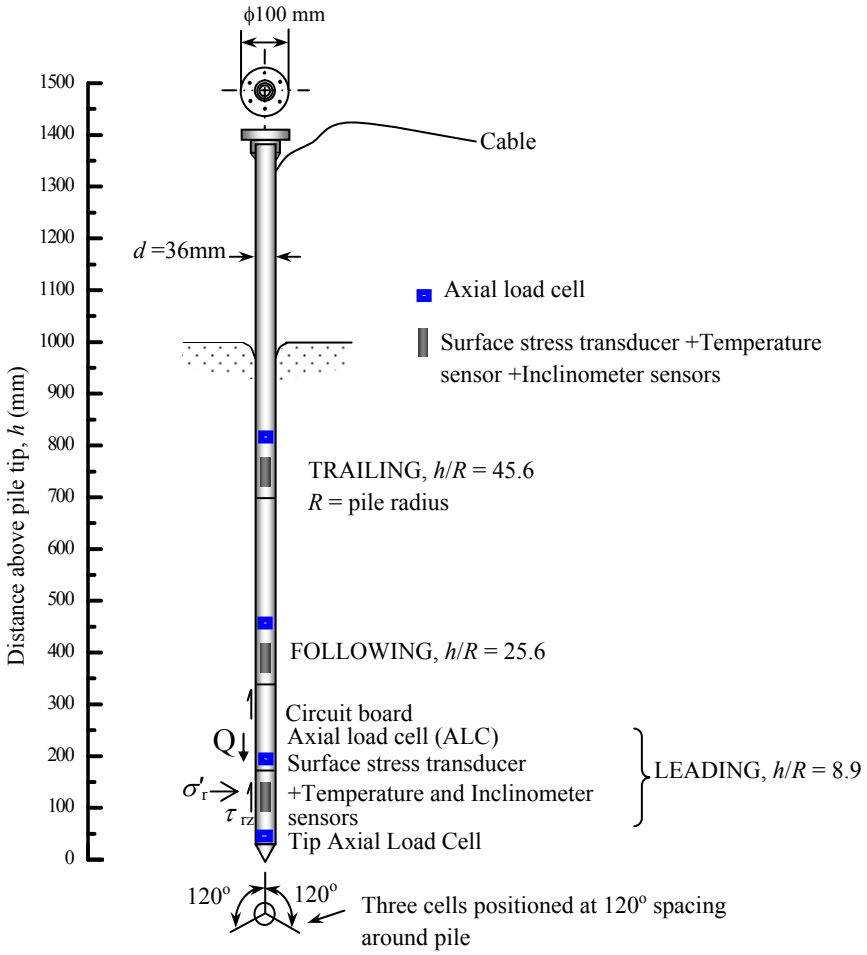
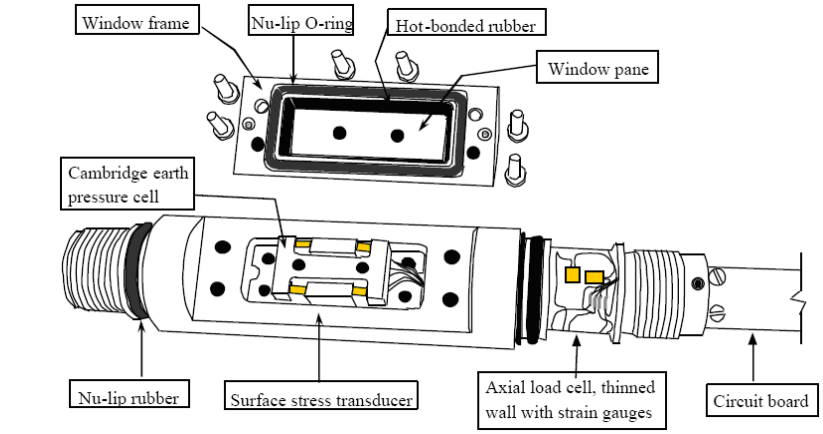
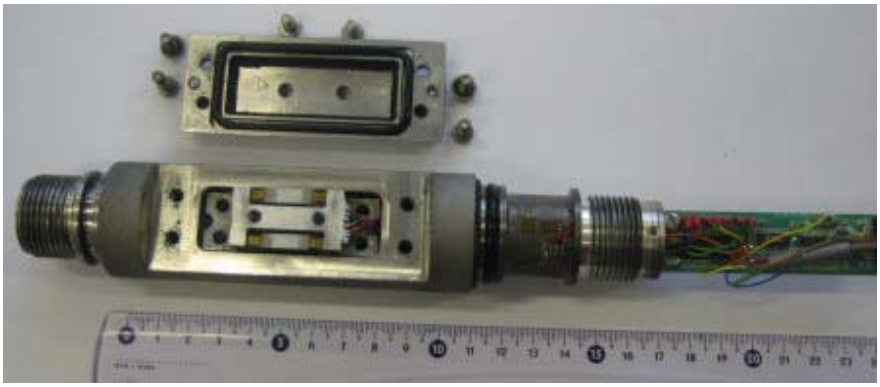
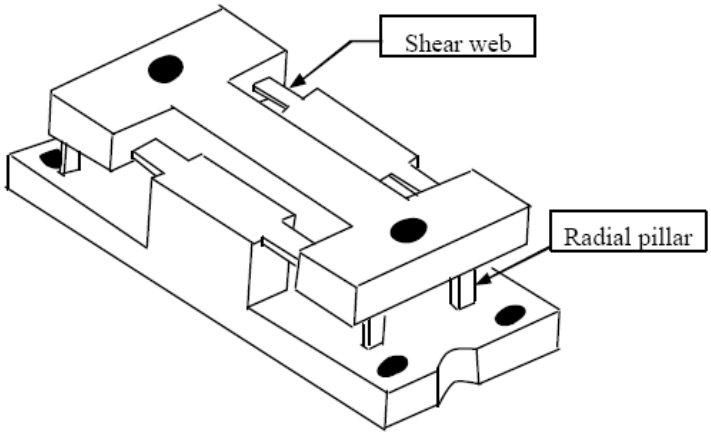


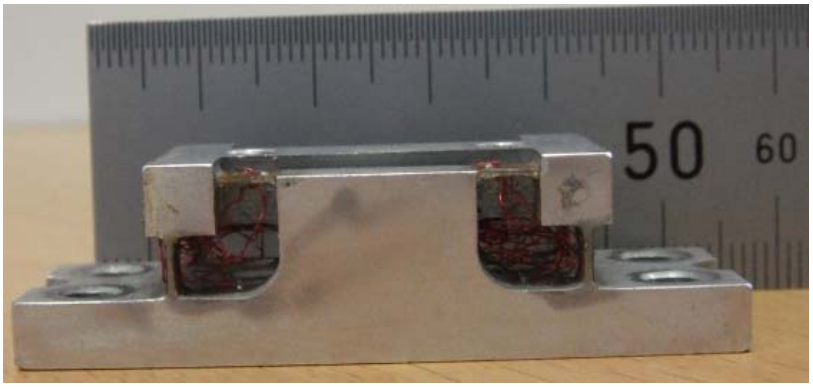
Figure 5-15: Mini–ICP illustrated (after Jardine et al. 2009).





(a)





(b)

Figure 5-16: Mini-ICP cluster schematics described (after Jardine et al. 2009).

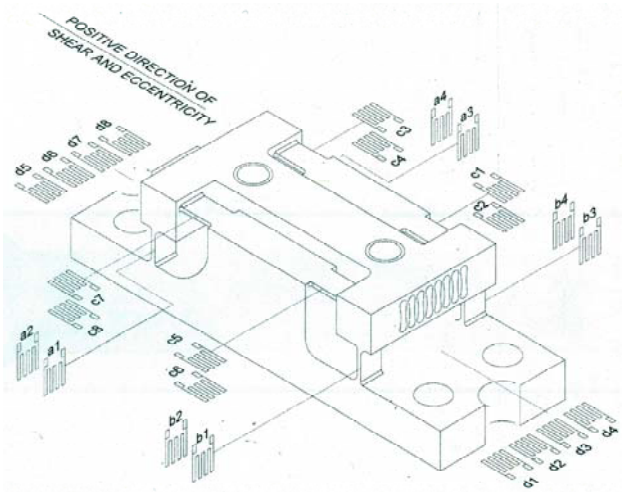


Figure 5-17: Strain gauging schematic of the Cambridge-type earth pressure cell Surface Stress Transducers on board the Mini–ICP by Cambridge In-situ (2009).

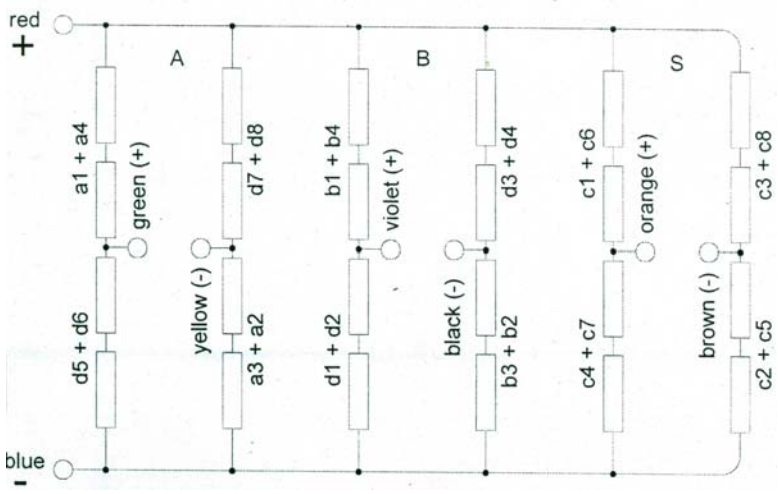


Figure 5-18: Circuit diagram for the strain gauging of the SSTs on board the Mini–ICP by Cambridge In-situ (2009).

5.5.3 Mini–ICP calibration

5.5.3.1 Transducers compliance

The radial stress pillars and shear stress webs of the Mini–ICP SSTs were made to be very stiff in order to minimize the cell action effects seen with diaphragm devices. However, the SSTs' curved surfaces make it difficult to perform direct checks for cell action effects. Jardine (1985), Bond et al. (1991) and Jardine et al. (2009) employed elastic theory to estimate the cell action errors and also counter-checked the SST stress measurements during testing with fully independent shear transfer data derived from the ALCs. Bond et al. (1991) assessed the potential errors on the measurements made in elastic soils as: $\delta_e = 1/(1+1/\psi)$ where ψ = (f/a)[G/(1-ν)]C and f = the cell's compliance, a = the equivalent radius of the loading platen, G = the soil's shear stiffness, ν = the soil's Poisson's ratio and C = a shape factor.

Jardine et al. (2009) calculated Mini–ICP's SST radial stress compliance as f = 1.02x10^{-8} m/kPa and its shear stress compliance as f = 1.07X10^{-8}m/kPa. The maximum potential error is found by inputting the small strain (G_{max}) shear modulus of the sand as estimated from its cone resistance by Baldi et al. (1989) $G = q\left[A + B\eta - C\eta^2\right]^{-1}$ and $\eta = q_c\left(p_a\sigma_{v0}'\right)^{-0.5}$ where A = 0.0203, B = 0.00125, C = 1.216X10^{-6}, q_c is the cone resistance from CPT tests, p_a the atmospheric pressure (100kPa), and σ'_{v0} the effective overburden vertical stress. Taking a nominal $\nu = 0.25$ for the silica sand, a shape factor of 0.79 and 1.2 for radial and shear stress transducers respectively, a = 18mm and a cone resistance ~21MPa (as in the dry NE34 sand instrumented CC tests) Jardine et al. (2009) estimated a maximum potential under-registration error of ~11% and ~8% for the radial and shear stresses respectively when responding to an instantaneous soil stress change applied to a stationary pile. Smaller errors were anticipated during steady penetration or during a load test to failure. Cross checking by independent ALC data from the Author's study (see Chapter 7) indicates that the typical cell action errors are indeed lower than the estimated upper bounds.

5.5.3.2 Calibration Procedure

When the ALC and SSTs are assembled together into clusters they show some cross–sensitivity between their channels. The full set of sensitivities are collated into a matrix of direct and cross sensitivities the inverse of which gives the calibration factors for the respective measured components as shown on Equations 5-5 to 5-10; where $\Delta\sigma_{rr}$ is the change of normal/ radial stress, $\Delta\tau_{rz}$ is the change of shear stress, ΔQ is the change of axial load and ΔT is the change of temperature on the cluster. ΔV_{xx} is the output of a transducer x, S_{xx} is the direct sensitivity of a transducer, S_{xy} is the cross–sensitivity of transducer x due to change in component y, and C_{xx}, C_{xy} are the calibration factors (inverse of sensitivity).

The Mini–ICP SSTs and ALCs were repeatedly calibrated before and after each test. Calibration of the SSTs' radial and shear stress transducers were made by a dead-weight bi-axial calibration jig (see Figure 5-19) assembled at Cambridge Insitu Ltd's workshop at Little Eversden, Cambridgeshire UK. The jig enabled independent calibrations of the normal and bi-directional shear stresses on the pile at maintained room temperatures. Each cluster is positioned on the cradle of the calibration jig and a specially made loading platen is placed on the window pane from which two screws of the window pane have been removed and special temporary screws are used to secure the platen to the pane. The normal load on the loading platen transfers to the window pane direct and the shear load is applied by the two screws bearing into the web of the dog-bone section of the cell.

The clusters' radial or shear transducers are first given multiple loading and unloading cycles as an 'exercising procedure' after each calibration setup designed to minimise hysteresis and

'bed-in' all connections. The clusters are then calibrated by several cycles involving small steps of loading and unloading sequentially with normal stresses alone, then with positive shear stress (applied in the direction that opposes pile installation and compression load on the pile) and finally the reverse 'negative' shear stress direction. During shear calibration the cluster carries a sustained normal load which matches the test conditions and maintains the calibration loading assemblage's stability. The SST's direct sensitivities were generally repeatable and gave similar characteristics between the clusters showing the uniformity of manufacture and consistency of the calibration procedure. Tables 5-5 and 5-6 summarise the calibration factors in the current series of testing and Figures 5-21 and 5-22 show representative calibrations plots.

The Axial Load Cells (ALCs) were calibrated individually by a dead-weight Budenberg calibration jig as well in addition checks were made in fully assembled mode in a specially arranged hydraulic loading frame, see Figure 5-20. Multiple cycles of load–unload were conducted as part of the exercising procedure before the ALCs were calibrated in small steps of loading and unloading. Table 5-7 summarises the calibration factors used in the current series of testing and Figure 5-23 are representative plots of the calibrations sequences. The clusters had normal and shear stress proof capacities of 880kPa and 840kPa respectively, and an axial load proof capacity of 180kN, with typical measuring resolutions (Figure 5-24) of 1.0kPa (0.1%), 0.5kPa (0.6%), and 0.1kN (0.05%) respectively. The temperature calibrations reported by Jardine et al. (2009) were used throughout the current study.

$$\Delta V_{rr} = S_{rr}\Delta\sigma_{rr} + S_{r\tau}\Delta\tau_{rz} + S_{rA}\Delta Q + S_{rT}\Delta T \qquad 5\text{-}5$$

$$\Delta V_{\tau\tau} = S_{\tau r}\Delta\sigma_{rr} + S_{\tau\tau}\Delta\tau_{rz} + S_{\tau A}\Delta Q + S_{\tau T}\Delta T \qquad 5\text{-}6$$

$$\Delta V_{AA} = S_{Ar}\Delta\sigma_{rr} + S_{A\tau}\Delta\tau_{rz} + S_{AA}\Delta Q + S_{AT}\Delta T \qquad 5\text{-}7$$

$$\Delta V_{T} = S_{Tr}\Delta\sigma_{rr} + S_{T\tau}\Delta\tau_{rz} + S_{TA}\Delta Q + S_{TT}\Delta T \qquad 5\text{-}8$$

$$\begin{Bmatrix} \Delta V_{rr} \\ \Delta V_{\tau\tau} \\ \Delta V_{AA} \\ \Delta V_{TT} \end{Bmatrix} = \begin{bmatrix} S_{rr}S_{r\tau}S_{rA}S_{rT} \\ S_{\tau r}S_{\tau\tau}S_{\tau A}S_{\tau T} \\ S_{Ar}S_{A\tau}S_{AA}S_{AT} \\ S_{Tr}S_{T\tau}S_{TA}S_{TT} \end{bmatrix} \begin{Bmatrix} \Delta\sigma_{rr} \\ \Delta\tau_{rz} \\ \Delta Q \\ \Delta T \end{Bmatrix} \qquad 5\text{-}9$$

$$\begin{Bmatrix} \Delta\sigma_{rr} \\ \Delta\tau_{rz} \\ \Delta Q \\ \Delta T \end{Bmatrix} = \begin{bmatrix} S_{rr}S_{r\tau}S_{rA}S_{rT} \\ S_{\tau r}S_{\tau\tau}S_{\tau A}S_{\tau T} \\ S_{Ar}S_{A\tau}S_{AA}S_{AT} \\ S_{Tr}S_{T\tau}S_{TA}S_{TT} \end{bmatrix}^{-1} \begin{Bmatrix} \Delta V_{rr} \\ \Delta V_{\tau\tau} \\ \Delta V_{AA} \\ \Delta V_{TT} \end{Bmatrix} = \begin{bmatrix} C_{rr}C_{r\tau}C_{rA}C_{rT} \\ C_{\tau r}C_{\tau\tau}C_{\tau A}C_{\tau T} \\ C_{Ar}C_{A\tau}C_{AA}C_{AT} \\ C_{Tr}C_{T\tau}C_{TA}C_{TT} \end{bmatrix} \begin{Bmatrix} \Delta V_{rr} \\ \Delta V_{\tau\tau} \\ \Delta V_{AA} \\ \Delta V_{TT} \end{Bmatrix} \qquad 5\text{-}10$$

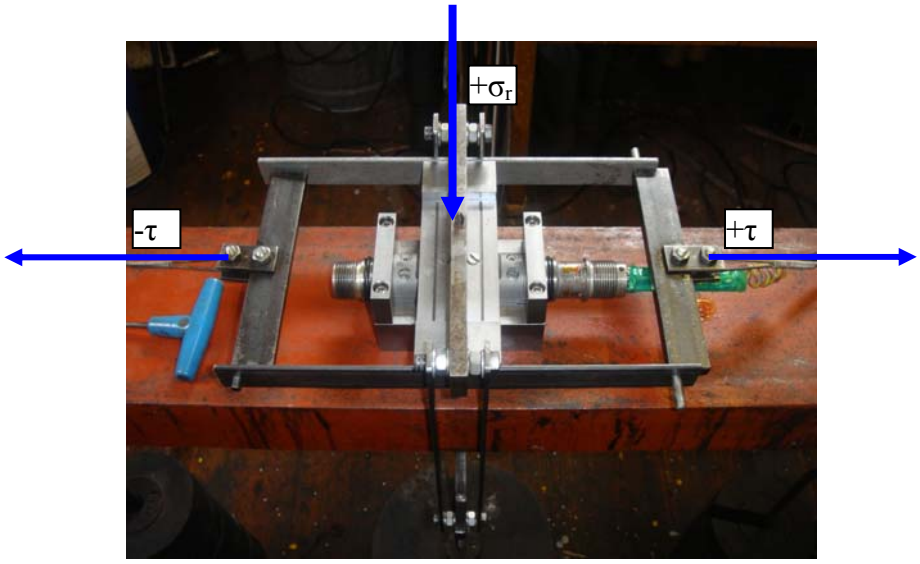
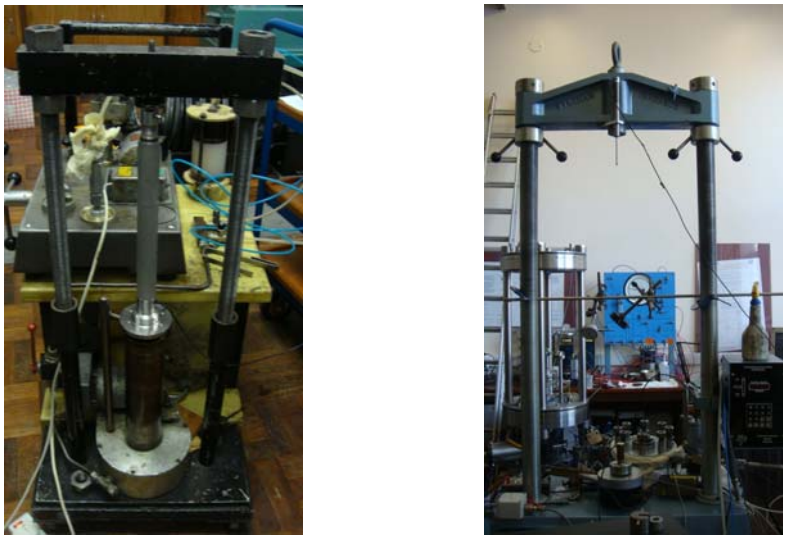


Figure 5-19: Calibration of radial and shear stress transducers (SSTs) by a dead-weight bi-axial calibration jig.



(a) (b)

Figure 5-20: (a)Budenberg deadweight calibration jig calibrating cluster C of the Mini–ICP and (b) the triaxial loading frame for full-length calibration of the Mini–ICP ALCs.

Radial stress transducer	Sensitivity	R^2
Direct, S_{rr} (μV/kPa)	10.07 ± 1.03	1.00
Cross sensitivity to shear stresses, $S_{r\tau}$ (μV/kPa)	0.16 ± 1.26	0.55
Cross sensitivity to axial loads, S_{rA} (μV/kN)	-40.49 ± 6.65	0.95

Table 5-5: Mean direct and cross sensitivity factors of the radial/ normal stress transducers of all the cluster cells' used in this study.

Shear stress transducer	Sensitivity	R^2
Direct, $S_{\tau\tau}$ (μV/kPa)	20.66 ± 3.96	1.00
Cross sensitivity to radial stresses, $S_{\tau r}$ (μV/kPa)	-0.07 ± 0.84	0.81
Cross sensitivity to axial loads, $S_{\tau A}$ (μV/kN)	0.53 ± 2.59	0.43

Table 5-6: Mean direct and cross sensitivity factors of the shear stress transducers of all the cluster cells' used in this study.

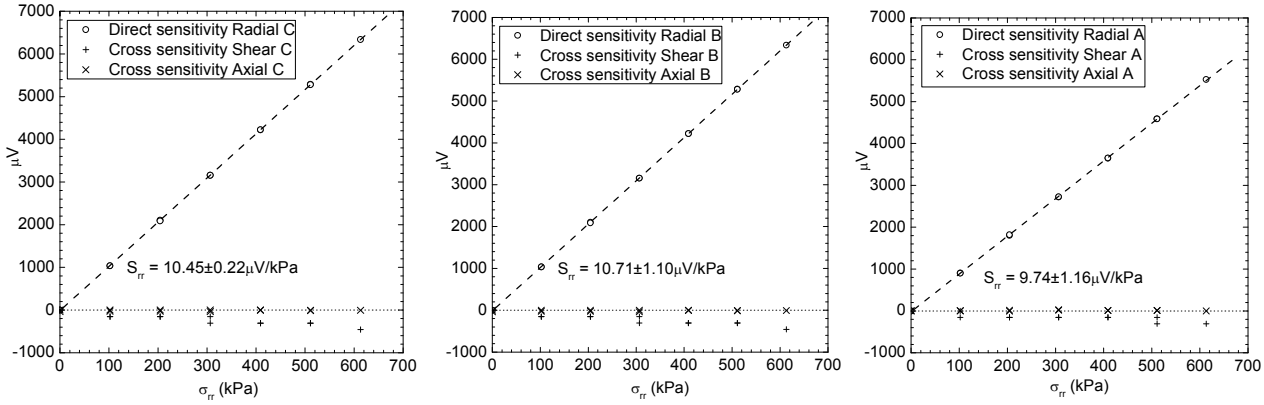


Figure 5-21: SSTs radial stress transducer output versus applied normal stress/ load on a typical Mini–ICP calibration sequence.

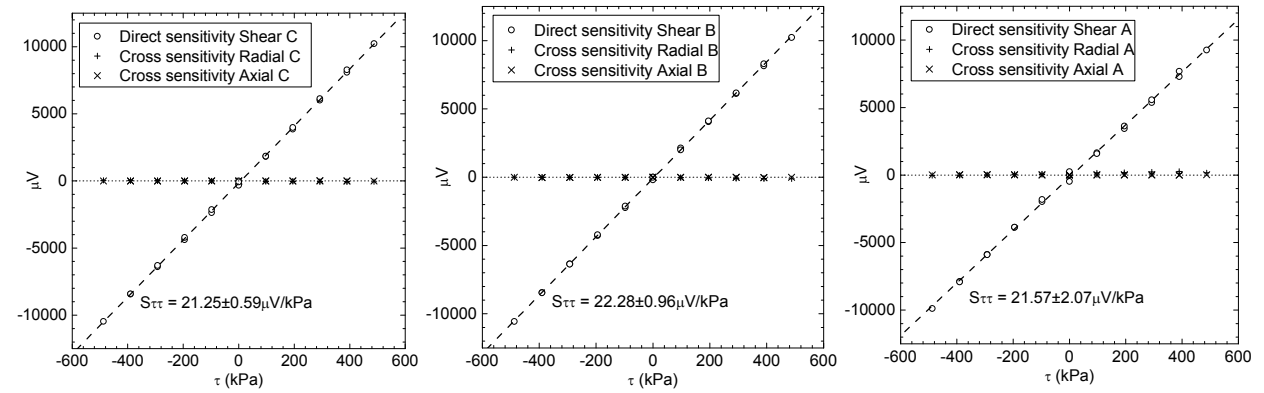


Figure 5-22: SSTs shear stress transducer output versus applied shear stress/ load on a typical Mini–ICP calibration sequence.

Axial Load Cells	Sensitivity	R^2
Clusters		
Direct, S_{AA} (μV/kN)	136.83 ± 3.26	1.00
Cross sensitivity to radial stresses, S_{Ar} (μV/kPa)	0.01 ± 0.07	0.08
Cross sensitivity to shear stresses, $S_{A\tau}$ (μV/kPa)	0.00 ± 0.03	0.06
Tip		
Direct sensitivity, S_{AA} (μV/kN)	170.92 ± 38.07	1.00

Table 5-7: Mean direct and cross sensitivity factors of all Axial Load Cells' used in this study.

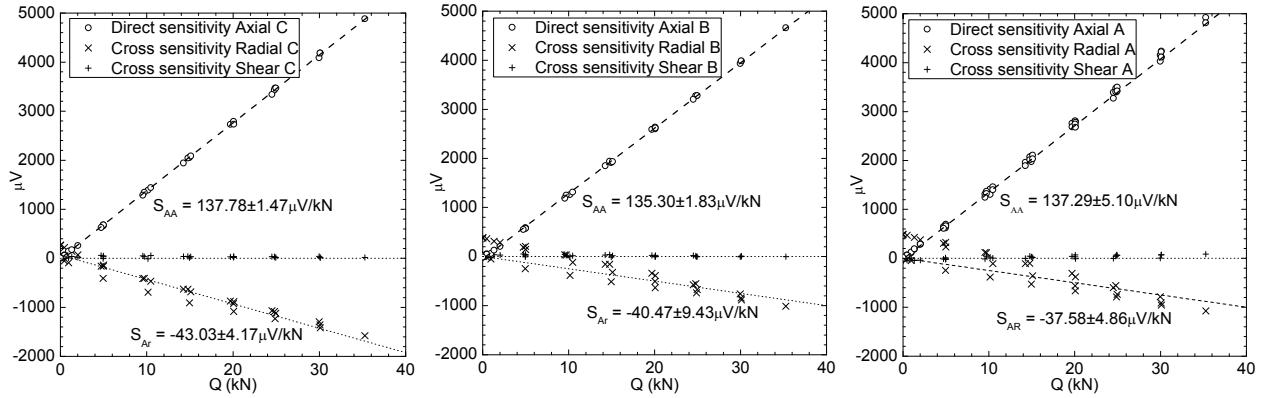


Figure 5-23: ALCs output versus load on a typical Mini–ICP calibration sequences.

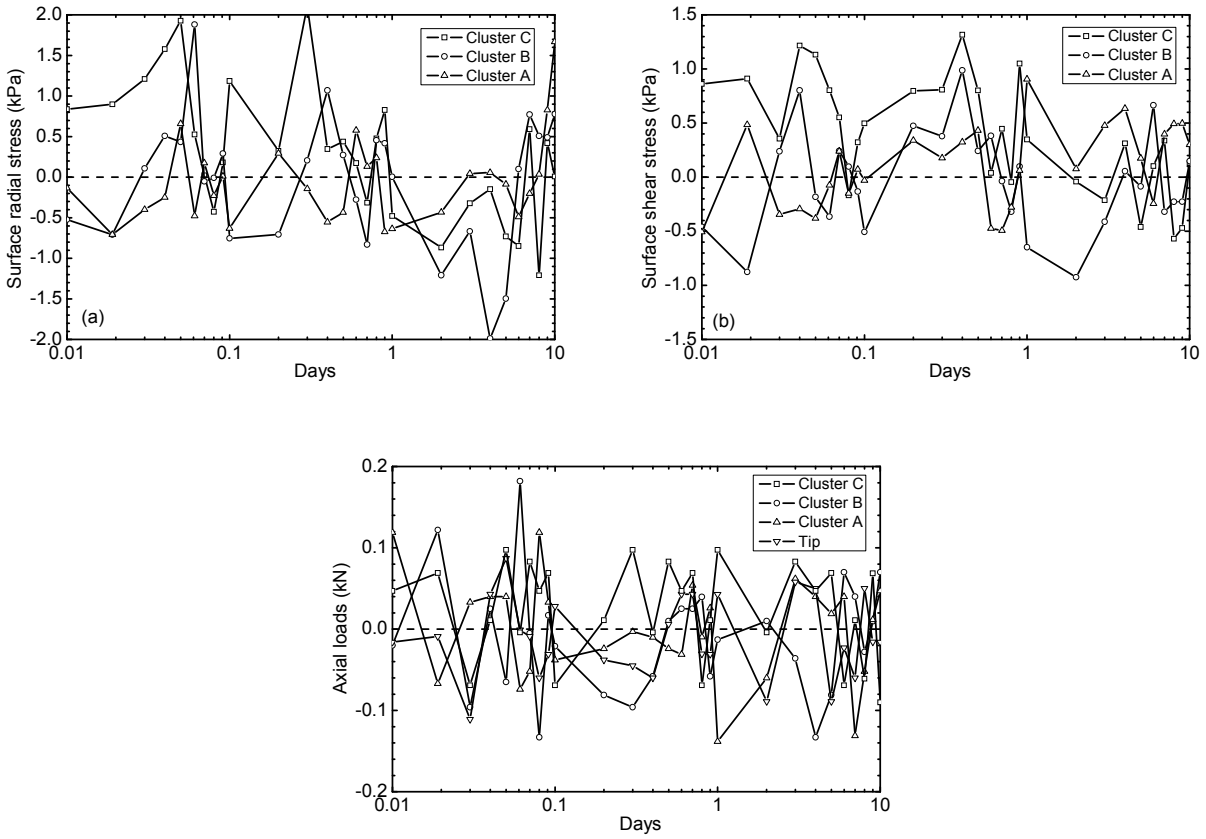


Figure 5-24: Mini–ICP transducers check for measurements resolution and drifts and over a 10 days period (a) Radial stresses (b) Shear stresses and (c) Axial loads.

5.5.4 Assembling of the Mini–ICP

The Mini–ICP was assembled in all cases starting with the base ALC followed by the 'leading' cluster A, 'following' cluster B and finally the 'trailing' cluster C. A wire running down the pile axis interconnected the base ALC to the clusters from the top of one cluster's PCB to the bottom of the following cluster through seat–in connectors. The base ALC integrates with the bottom of cluster A then two stainless steel pipe sections of different lengths and threaded at both ends interconnect clusters A to B and B to C. A longer section connects cluster C to the pile cap. Each of the steel sections was carefully fastened on to the clusters it connected while ensuring the wire running at the centre pile was not unduly twisted during the assembly. The final positions of the clusters were 120° from each other hence measuring stresses around the pile. The results analysis Chapters (7 to 11) refers to the final positions of the SSTs in terms of their distance from the pile base tip (h) normalised by the pile radius (R); cluster A with h/R = 8.94; cluster B with h/R = 25.61 and cluster C had h/R = 45.61.

5.6 Micro and driven piles

Noting that the CC (inner) diameter to model–pile (outer) diameter ratio may affect the behaviour of the model displacement piles, an un-instrumented 12mm diameter conical tip closed–ended and relatively smooth (R_{cla} = ~1 - 2μm) stainless steel model pile (MiP) was fabricated and employed for series MiP01. The pile was fitted a cap to connect to the Rosier installation jack and penetrated 0.99m into the medium dense dry NE34 sand chamber.

The effects of pile installation mode on ageing, static and cyclic loading behaviours were also examined by developing a dynamically driven pile system. Full driving is rarely employed for heavily instrumented displacement pile research (see Bullock et al. 2005) because of the difficulty of designing sensitive gauges that can survive impact loading, NGI (2012). The Mini-ICP, CPT cone–tipped pile and the micro-pile had been installed by cyclic jack stroke procedures involving full displacement pushes followed by full unloading in each stroke to model the stress regime around displacement piles (Jardine et al. 2013a) while ensuring that the instrumented piles remained undamaged by the impact loading from driving. However, concerns that this 'artificial' procedure could be influencing the results unduly led to a driven pile being commissioned and tested. This was a simple uninstrumented conical tip closed–ended stainless steel tube of 36mm outer diameter, roughened outside to a surface centreline roughness of 3 – 4μm, consistent to the Mini–ICP.

The pile driving system shown on Figure 5-25 was designed and fabricated in the 3S-R Laboratory. The driving system comprised an aluminium frame with four 3m long aluminium pipes of 30mm diameter embedded into a 300mm diameter plate fixing the system on to the CC cover at the pile installation position (CC axis). The top of the assembly carried a similar plate equipped with a pulley for a drop–weight lifting mechanism. Two other plates are mounted between the bottom and top; one connects to the pile cap as a loading plate; the other (together with a set of weights) constitutes the pile hammer. The driving mechanism applied the potential energy from the hammer self-weight (varied between 20kgs to 25kgs) falling from prescribed heights (1 – 2m) and impacting the pile head delivering required driving energy to the pile. The hammer drop-height was selected to install the pile into the chamber with ~50 blows, matching the typically 49 jack-strokes used for the Mini–ICP and Micro pile installations. A combination of a plumb bob, a spirit level and the three roller guidance system at the chamber top pile installation position were used to ensure verticality of the pile and driving system during driving. Further details of the equipment and its operations are given by Silva (2014).

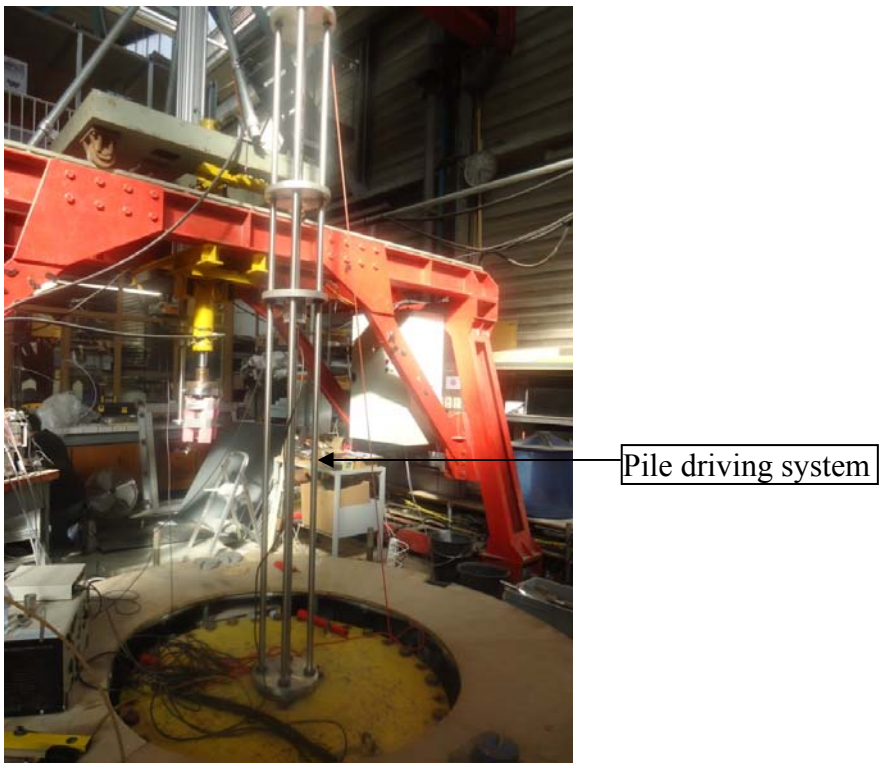


Figure 5-25: Deadweight-type model pile driving system installed at the calibration chamber pile axis.

5.7 Ancillary apparatus

Hobson Talysurf, Qicpic, 3D microscope apparatus and high resolution digital photography were all used for ancillary studies. Roughness characterisation of the Mini–ICP before and after testing was conducted with the Hobson Talysurf equipment. The mean centreline roughness of the pile surface was measured at four points set at 90^0 degrees to each other around the pile circumference and at multiple points along the shaft set about 100mm apart. Each roughness measurement was made over a 4mm length.

QicPic particle size and shape analysis (http://www.sympatec.com/) and 3D microscopy studies were made on the test sands with the main objective of comparing sands' particle index and surface properties to help select a scaled down alternative of the NE34 sand, leading to the GA39 sand (with a 50% lower $d_{50\%}$ value) being adopted to investigate grain size effects on the ageing characteristics of the displacement piles.

Multiple high resolution digital photographs were taken of interface samples recovered around the Mini-ICPs during exhumation at the end of the testing series. The thickness of the interface layer samples were then dimensioned, see Appendix IV, by employing the freeware code GIMP (http://www.gimp.org/). Further analysis of the recovered interface samples by the Qicpic optical grain sizing and shape assessment system can lead to density of the interface layers, particle size distributions and shape characteristic distribution.

5.8 Tests control and data acquisition

Data acquisition from the Mini–ICP was achieved through the "Mini-pile" program custom-made by Cambridge Insitu Ltd with back–up from the Freeware "Docklight" program (http://www.docklight.de/). Docklight directly reads and stores the hexadecimal output from the RS232 Mini-ICP systems described earlier, acquiring data with an update rate of 2 secs. Docklight proved more stable than Mini-pile and was used for long term acquisition during ageing and axial cyclic loading, providing real time acquisition while the Mini-pile program, converted the hexadecimal files acquired in Docklight to decimal (comma separated) values. Mini–pile was more convenient for shorter term logging of pile calibrations, installations and pile static load tests.

The calibration chamber's sensors and transducers were connected to a separate National Instruments (NI) Compact FieldPoint station that combined data acquisition, loading jack control and pressure regulation functions. The system was monitored through a PC with the NI Labview 8.2 program. The system had 5 modules (type cFP-SG140) for conditioning and acquisition of sand stress and force sensors with +/-4mV/V input (sensors excitation at 2.5V). It filtered–out frequencies greater than 60Hz and offered a 16 bit resolution. A separate module (cFP-RTD124) was employed for the conditioning and acquisition of temperature data, filtering again at 60Hz and resolving to 16 bits. The LVDT and pressure sensors were acquired through an additional module (cFP-AI112) with input +/-10V that filtered at 50Hz (also resolving to 16 bits). The control of the jack, temperature and membrane pressures was achieved through a final module (cFP-AIO610) with output +/-10V (filtering at 350Hz and resolving to 12 bits). The update rate of the Field Point system was set at 1 value per second. The test setup was installed with a Syrius MSII 6000 power supply with a reserve power capacity of up to 90 minutes with full power use, and longer when set to standby use.

5.9 Concluding remarks

Significant effort was expended in the design of the study testing arrangements. The adaptation of the 3S-R Laboratory calibration chamber boundary conditions to a free field simulator has been described. Further, the temperature control systems were fully optimised to ensure maintained environmental conditions of the test setup in the long duration ageing tests, and a stand–by power back-up provided for the least interruption to a running test.

The Mini–ICP pile was worked on extensively and continuously in conjunction with Cambridge Insitu Ltd over the study duration. A new base ALC (with its associated A/D converter, power supply and PCB) was added to improve the separation of the base and shaft contributions to the total pile capacity. Cluster B instrument had to be replaced after being damaged during a

calibration and the new cluster's SST cell had again to be replaced after the cell was excessively strained during calibrations prior to series ICP04. The wiring between the clusters was improved by seat-in plug and socket connections at the bottom of each cluster. A more robust deadweight bi-axial calibration rig manufactured by Cambridge Insitu ltd was used following a review of results obtained with a simpler prior set-up assembled at Imperial College. The pile had to be waterproofed to perform test series ICP06 in wet NE34 sand. Waterproofing entailed ensuring all interconnection seals worked well and exclude water from the inside of the pile as well as the screws on the clusters are water sealing. Despite thorough pre-checking, a major leakage occurred some days into ICP06 through a single Dowty sealed screw connection seal failing in the 'leading' instrument cluster A. As a result, the pile had to undergo a major overhaul before the ICP07 test. This entailed a new cell being made for cluster A and two new spare cells, as well as more robust printed circuit signal conditioning boards being made and installed for all the clusters and the base ALC.

The miniature sand stress sensors and cables were water-proofed at Imperial College soils laboratory workshop for test ICP06 with wet NE34 sand. The procedure applied to these delicate cells was not easy to perfect and a considerable number of sensors were damaged irreparably. Only 9 sensors were waterproofed, but all of these successfully survived the experiments.

Chapter 6

6 Test sands, preparation methods and experimental plan

6.1 Introduction

This chapter describes the NE34 Fontainebleau and GA39 Nemours silica test sands and how they were used in the study. The sourcing, index properties and physical characteristics of the sands are reported and the rationale for their selection explained. The techniques employed for preparing the sand calibration chamber masses are outlined. The methods adopted for installing the Mini–ICP, CPT cone–tipped piles, Micro-pile (MiP) and the driven piles are explained; and the sand-interface sampling conducted on pile exhumation is outlined. The testing programme is summarised and the model scaling principles are discussed.

6.2 Description of test sands

6.2.1 Sourcing, index and physical properties

The industrially mined and processed NE34 and GA39 test sands were supplied dry in 25kgs bags, stacked in 1200kg shrink wrapped pallets by SIBELCO-France's quarries at Fontainebleau and Nemours, South of Paris. NE34 is regularly used as French standard geotechnical test sand while GA39 sand was introduced in the course of this study.

Table 6-1 summarises the index properties measured in this study, along with the silica content from the supplier's data sheet (Appendix I). Published mechanical shear strength parameters for NE34 sand are summarised on Table 6-2. The equivalent data for GA39 sand do not appear to have been published and preliminary interface ring-shear tests were made by the Author to aid this study. As shown in Figure 6-1 GA39 shows a constant volume large displacement interface shear resistance (δ'_{cv}) around 27^0 when sheared against stainless steel with an initial surface average centreline roughness of 2.5 – 3.5μm, marginally greater than that for NE34.

Sand	Grain shape	SiO_2 (%)	G_s	$d_{10\%}$ (mm)	$d_{50\%}$ (mm)	$d_{60\%}$ (mm)	C_u	e_{max}	e_{min}
NE34	Sub-angular, sub-rounded	99.70	2.65	0.150	0.210	0.230	1.53	0.90	0.51
GA39	Sub-angular, sub-rounded	98.60	2.65	0.100	0.127	0.132	1.32	1.01	0.56

Table 6-1: Index properties for NE34 Fontainebleau and GA39 Nemours sand.

Tests	Parameter	Reference
Direct shear box test	$\varphi'_p = 35.2^0$ $\varphi'_{cs} = 32.8^0$ (I_D = 72%, 50 < σ'_n < 500kPa)	Yang et al. (2010)
Triaxial compression	$\varphi'_p = 36.5^0$ $\varphi'_{cs} = 29^0$ (I_D = 68.8%, p'_0 = 60kPa)	Gaudin et al. (2005)
	$\varphi'_{cs} = 32.6^0$ (I_D = 78%, e_0 = 0.63, p'_0 = 20kPa)	Sim et al. (2013)
	$\varphi'_{cs} = 33^0$ (I_D = 70% - 83%, e_0 = 0.59 – 0.63, p'_0 = 150 - 500kPa) Test stress paths modelled the stress history of a sand element at the pile tip by K_0 (= 0.43) consolidation from initial p' = 20kPa up to σ'_r = 6.9MPa followed by triaxial active shear compression to σ'_a = 20MPa then unloaded to the p'_0 before final shearing to failure.	Altuhafi & Jardine (2011)
Sand–stainless steel interface ring shear test (R_{cla} 3.1±0.3μm)	$\delta_{cv} = 25^0 – 27^0$ (I_D = ~72%, σ'_n = 100 – 800kPa)	Yang et al. (2010) Ho et al. (2011)
K_0	NC: 0.34 – 0.47 (I_D = 45.1% – 84.2%)	Gaudin et al. (2005)

Table 6-2: NE34 Fontainebleau sand mechanical strength characteristics.

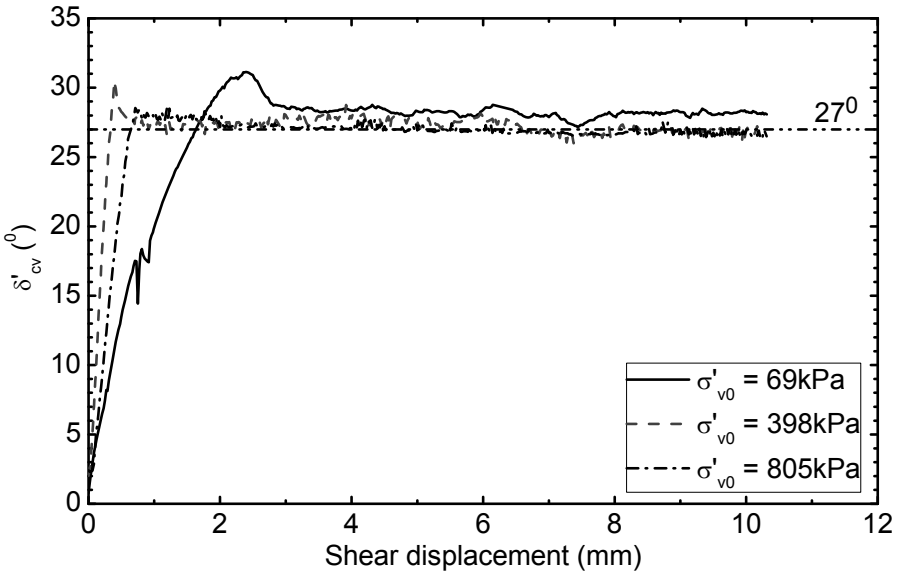


Figure 6-1: Interface ring shear tests on medium–dense to dense (I_D = 72%) GA39 Nemours sand against roughened (R_{cla} 3.1 ± 0.3μm) stainless steel.

6.2.2 Rationale for test sand selection

This study aimed to investigate under laboratory conditions the ageing, and axial static and cyclic loading behaviours that could give further insight to those observed with full–scale driven open-ended steel pipe piles in the Dunkirk marine silica sand site by Jardine et al. (2006) and Jardine & Standing (2000, 2013). The aim was to explore the detailed mechanisms with highly instrumented scaled model tests that could capture the stress conditions that could not be measured in the field. The Dunkirk site offered a relatively deep profile of dense sands similar to many southern North Sea offshore oil and gas production platforms, making the location suitable for the late 1980s driven pile study by the French CLAROM group (Brucy et al. 1991) and later the Imperial College studies by Chow (1997) and Jardine & Standing (2000, 2013) as well as the associated 1998 GOPAL Joint Industry Project (Parker et al. 1999).

NE34 sand was selected as a highly reproducible model for the Dunkirk sand, giving a generally good match to the latter's Particle Size Distribution (PSD) envelope as shown in Figures 6-2 (after Chow 1997) and 6-3 (after Yang et al. 2010). Tables 6-3 and 6-4 show the index properties and mineralogy of Dunkirk sand. Comparison with Table 6-1 shows similar specific gravity. But the purely NE34 silica sand avoids any potential physiochemical effects that might result from carbonate shell fragments, trace minerals or salt in the Dunkirk sand. The mechanical properties of Dunkirk sand and NE34 sand can also be compared from Tables 6-2 and 6-5. The sands display similar critical state, peak shearing resistances and interface shear characteristics in tests performed involving similar states and stress conditions.

In test series ICP05 the Nemours GA39 sand was substituted for NE34 sand at the dry pluviation calibration chamber filling stage. This test was intended to examine sand particle size effects on the ageing and axial cyclic mechanisms of the installed model displacement piles. Discussions with the supplier SIBELCO France focused on obtaining a more finely graded alternative to NE34 that matched NE34's mineralogy, surface roughness and grain shapes. Around half as fine as NE34 sand, GA39 sand provided the closest alternative, and this was confirmed by particle roughness and shape measurements made by the QicPic laser analysis apparatus and Microsurf 3D Microscope image analysis techniques as seen in Figures 6-4 and 6-5.

Sand	Grain shape	G_s	d_{10} mm	d_{50} mm	d_{60} Mm	C_u	γ_{sat} kN/m^3	I_D %
Dunkirk sand	Sub-rounded, rounded	2.656	0.150	0.210	0.230	1.53	19.9	75

Table 6-3: Dunkirk Flandrian sand average index properties (after Jardine & Standing 2000).

Sand	SiO_2 (%)	Feldspar (Albite and Microcline) (%)	Calcium carbonate (Shell fragments) (%)
Dunkirk sand	84	8	8

Table 6-4: Dunkirk Flandrian sand mineralogy (after Jardine & Standing 2000).

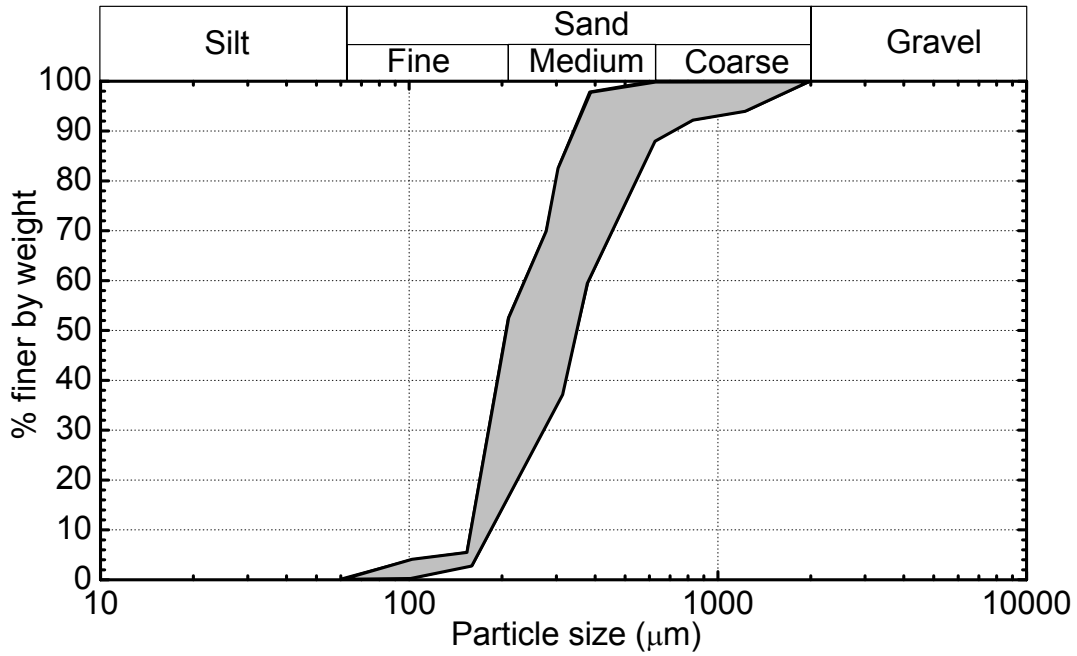


Figure 6-2: Particle Size Distribution for Dunkirk sand from CLAROM Borehole (after Chow 1997).

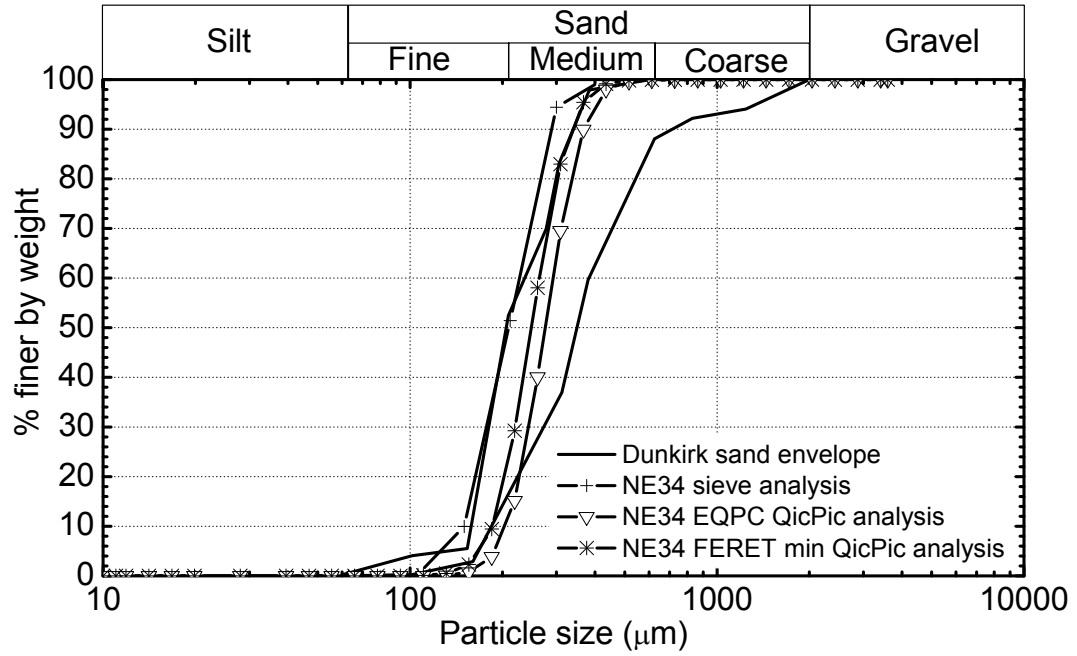
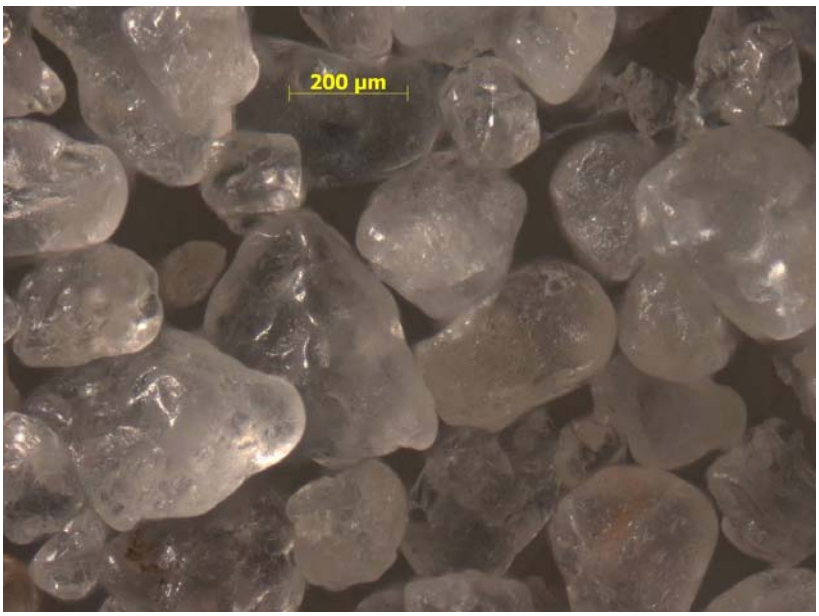


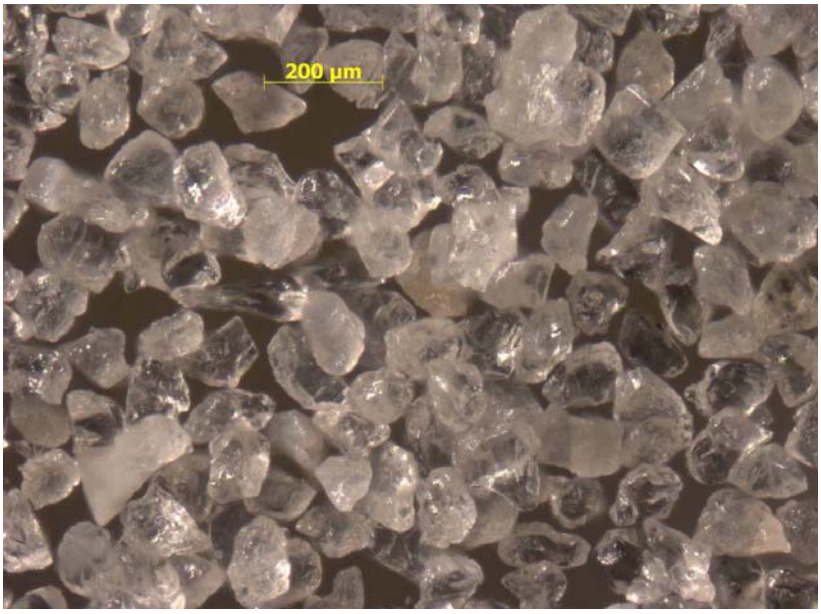
Figure 6-3: Particle size distribution for NE34 Fontainebleau sand (after Yang et al. 2010) compared to Dunkirk sand.

Tests	Parameter	Reference
K_0 (= 0.35) consolidated undrained (CK_0U) triaxial stress path tests (K_0 of 0.40 – 0.45 was assessed from strength and Yield Stress Ratio data.)	Compression $\varphi'_p = 37^0$ Extension $\varphi'_p = 35^0$ $\varphi'_{cs} = 32^0$ (I_D = 75%, p'_0 = 60 - 200kPa)	Kuwano (1999)
K_0 (= 0.35) consolidated undrained (CK_0U) triaxial stress path tests shear modulus at ε_s = 0.005%	Compression G = 111MPa Extension G = 230MPa (I_D = ~75%, p'_0 = 200kPa and Yield Stress Ratio = 1) Behaviour strongly anisotropic, highly non-linear and stress level dependent.	Kuwano (1999)
Sand direct shear tests	$\varphi'_p = 39.4^0$, $\varphi'_{cv} = 31.1^0$ (I_D = 85%, σ'_n = 150kPa)	Kuwano (1999)
Sand–mild steel interface (R_{cla} = 9.8μm) direct shear test	$\delta'_p = 30.8^0$, $\delta'_{cv} = 26.8^0$ (I_D = 85%, σ'_n = 300kPa)	
63 days' aged sand–stainless steel interface (R_{cla} = 9.8μm) direct shear test	$\delta'_p = 31^0$, $\delta'_{cv} = 27.5^0$ (I_D = 85%, σ'_n = 300kPa) No change of either δ'_{cv} or δ'_p with ageing. Creep densification, increased shear stiffness and stronger dilation with ageing supposedly from micro-structural rearrangement of the sand grains and their contacts	Chow (1997)

Table 6-5: Physical properties of Dunkirk sand.

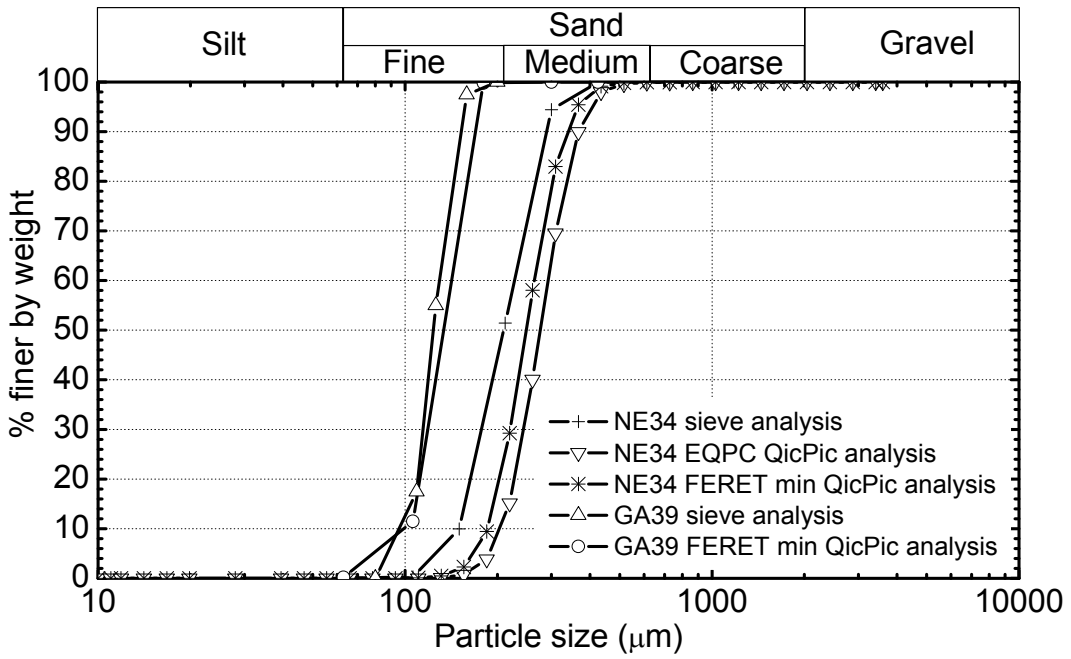


(a)

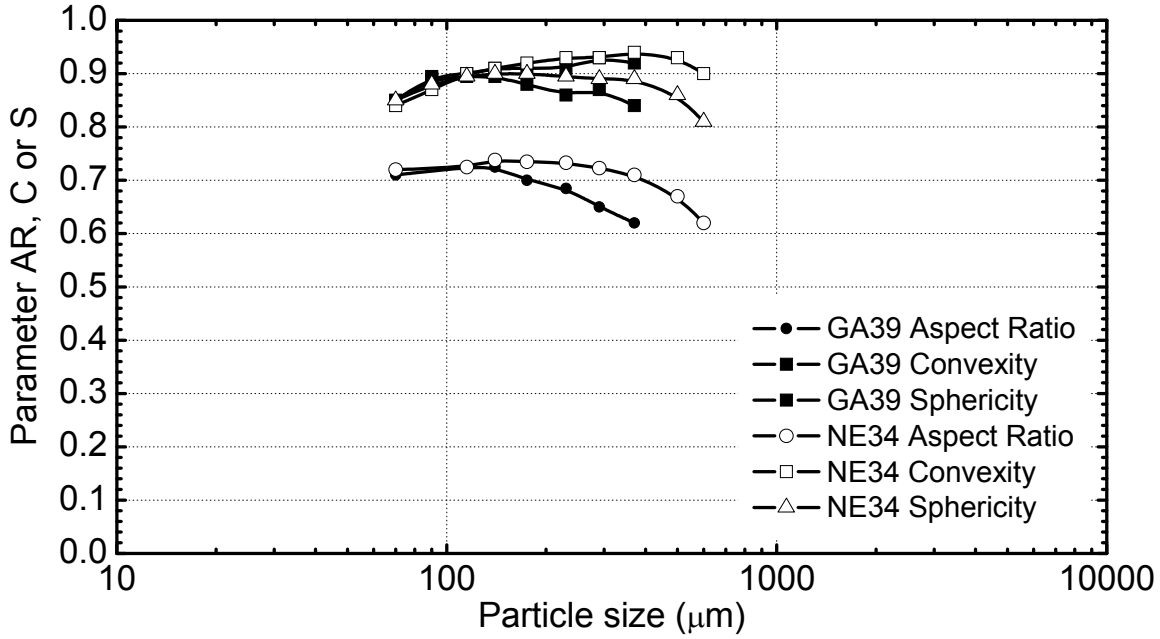


(b)

Figure 6-4: Microscope images at same scale (10x) of (a) NE34 and (b) GA39 from Microsurf 3D Optical Profiler by Nanotech.



(a)



(b)

Figure 6-5: (a) NE34 and GA39 Sand PSD comparisons (b) NE34 and GA39 sands' particle Aspect Ratio (AR), Convexity (C) and Sphericity (S) comparisons as obtained with Sympatec Gradis QicPic apparatus, employing FERET minimum particle size scale.

6.3 Calibration chamber preparations

6.3.1 Introduction

The mechanical behaviour of sands depends predominantly on their grain shapes, gradings, density state, depositional fabric particle properties and orientation, effective stress level and major principal stress axis orientation. Oda et al. (1985) suggested that the intrinsic anisotropy and fabric obtained by pluviation duplicate those developed in natural sediments. Mahmood et al. (1976) reviewed the effects of specimen preparation methods on the fabric of medium-grained sand; air pluviation produces a random orientation of grains while preferential orientation results from vibratory densification. Ishihara (1993) considered the conditions achieved in clean sand by three formation techniques; dry deposition, moist placement, and water sedimentation. He reports that the fabric-dependency (seen at a given void ratios) is most significant at moderate strains and has a considerable effect on the minimum strength available at Phase Transformation.

Control of the initial sand density can be achieved during calibration chamber preparation. Samples made by air pluviation, dropping from fixed fall heights without further compaction, the sand densities achieved in the calibration chamber are controlled by the compaction energy retained by the particles contacting the sand surface. The compaction energy is equivalent to the particles' kinetic energy less any energy losses on contact. The kinetic energy is a function of the kinetic friction (Stoke's Law) and the particles' buoyancy (upthrust) in air. For maximum compaction energy and density, the velocity at contact has to reach the terminal (maximum) settling velocity which is achieved when the drop height is equal to or exceeds the particular limiting height at which the three particles forces (particle weight, kinetic friction and upthrust) are in equilibrium; any greater drop height does not improve the density, while lesser drop heights give lower density. The coarser the sand particles, the higher the compaction energy for the same drop height. To maintain a uniform chamber density the drop height is kept constant throughout pluviation. Vaid & Negussey (1984) showed varying the drop height between 0 – 0.5m has the greatest influence on the achieved density as also reported by Krailem (1988). Vaid & Negussey (1984) suggested for small containers the density is also affected by container dimensions and wall roughness. Sand pluviation involving very high flow rates may introduce interference that inhibits compaction at the sand surface, Rad and Tumay (1987).

6.3.2 Achieving in-situ states

The Flandrian Dunkirk sand was formed by deposition under water over three local transgressions between 2100 and 900 years before present (Sommé 1969). To model the Dunkirk site conditions the current study targeted the average density index assessed by Chow (1997) of 75% (see Table 6-3) and average CPT q_c of 21MPa from Figure 2-10. To achieve this medium-

dense state with NE34 sand, the sand masses were dry air pluviated; all but one sand mass were tested dry. Sand mass preparation involved a repetitive procedure where a maximum volume 1.56m^3 (1.18m diameter by 1.43m height) of sand was placed by 'sand rain' air pluviation without further densification by compaction. Densification by compaction could have affected the final positions of the in-sand stress sensors and created radial locked-in effective stresses (inconsistently increasing K_0) that affected the q_c values at a similar density state, Lunne et al. (1997). The single wet dense NE34 sand experiment was performed to investigate possible effects of water presence on the ageing, axial static and cyclic loading pile behaviour. Testing wet previously air pluviated sand entailed considerable difficulties in waterproofing the miniature sand stress sensors and the cables deployed in the chamber as well as waterproofing the Mini–ICP as discussed in section 5.9; this discouraged extensive wet testing.

Difficulties were encountered in controlling pluviation with the finer sand and the single GA39 sand mass was inadvertently pluviated in a looser state than originally intended, see Table 7-1.

6.3.3 3S-R calibration sand chambers pluviation procedures

Air pluviation was performed with a sand hopper and double sieve arrangement shown on Figures 6-6 and 6-7. The sand (supplied in 25kgs bags) was inspected for dirt and any untypical stray particles then emptied into the sand rainer's hopper. The rainer was mounted on the calibration chamber and the perforated steel base of the hopper opened. The sand fell first through a set of double cross-sieves kept at a constant height of 0.5m above the sand chamber surface before settling on the sand surface in the chamber.

On achieving the sand level where sensors are to be installed, the sand surface was trowelled to a level plane and laser surveying performed with a special radial template system that locates the surface sensors around the axis of the intended pile installation. Sensors were installed at prescribed distances typically 2, 3, 5 and 8 pile radii (R) from the axis as shown on Table 6-6 and Appendix II.

The full sets of sensors installed at a particular level and radial distance combinations usually included vertical, radial and circumferential total stress sensors designated by the orientation of their sensing face relative to the pile and perpendicular to the stress component to be measured. Sensor installation entailed lowering a specially made platform near to the sand level at which a person could sit (curled-up) and position the sensors with aid of working lamps and lit vertical laser survey lines. Temperature sensors were installed at each stress sensors level, and all sensors wires made to follow the chamber walls upwards, secured by adhesive tape and along the top of the centred surcharge membrane once it is placed after completion of pluviation. The cables exit through three holes on the perimeter of the 100mm thick steel cover placed over the top neoprene membrane with a central hole at the pile installation location and 600mm thickness when

pressurised. The top membrane is filled with pressurised water to a constant pressure ~152kPa after the final assembly and the sand mass is left to creep and age under load until volume changes subside to less than 0.001% volumetric strain per day as measured by the water volumes input to the boundary membranes, Figure 6-8. A step by step summary of the pluviation procedure is detailed on Figure 6-9.

The sand pluviation technique was re-set for the finer GA39 sand experiment, aiming to achieve the same medium-dense states as the NE34 experiments and Dunkirk field tests. The pluviation height and sand flow intensity were revised repeatedly but the process was made difficult by the tendency of individual fine sand particles to float in air. As reported in Chapter 7 the final density states were lower than intended and test ICP05 effectively investigated the effects of both particle scale and density index on pile ageing and cyclic behaviour.

The standard NE34 pluviation procedure was employed for the wet test ICP06 which studied the possible effects of water followed by carbon dioxide (CO_2) gas injection from the bottom of the chamber fed from pressurised cylinders. The completion of the CO_2 (which is heavier than air) filling the sand mass was ascertained by candle flames placed at the top of the sand chamber being extinguished, confirming the displacement of the lighter air. De-aired water was then percolated upwards through the sand chamber from below by applying a water head set at between 1.8m to 4.0m above the bottom of the chamber. The water was intended to displace or dissolve the CO_2 gas.

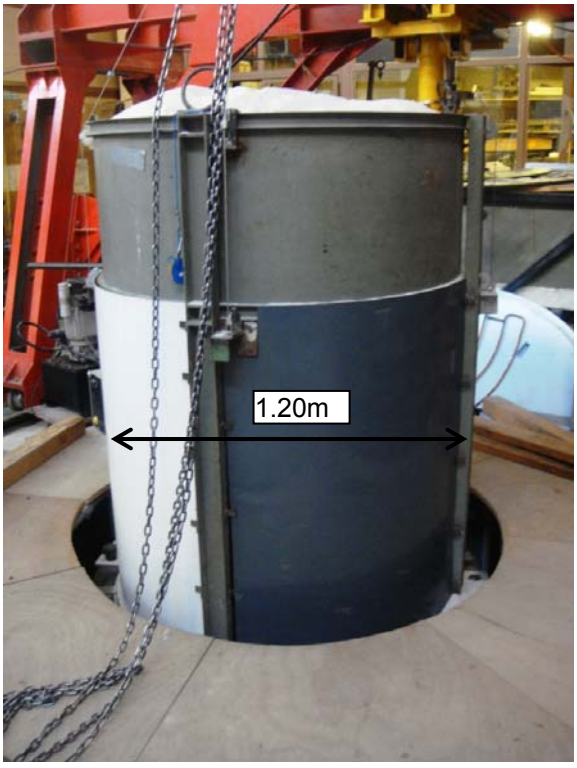


Figure 6-6: Sand rainer on the calibration chamber in preparation of the sand chamber for test ICP04.

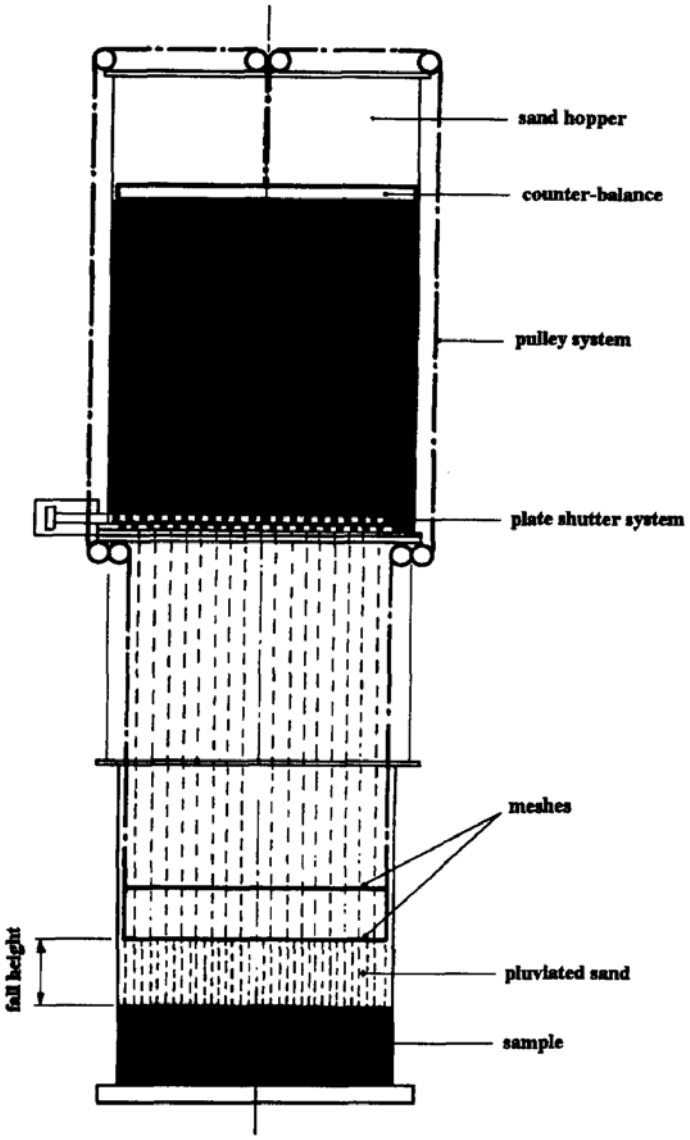


Figure 6-7: Illustration of a typical sand raining arrangement used for calibration chamber sand pluviation (Salgado et al. 1998).

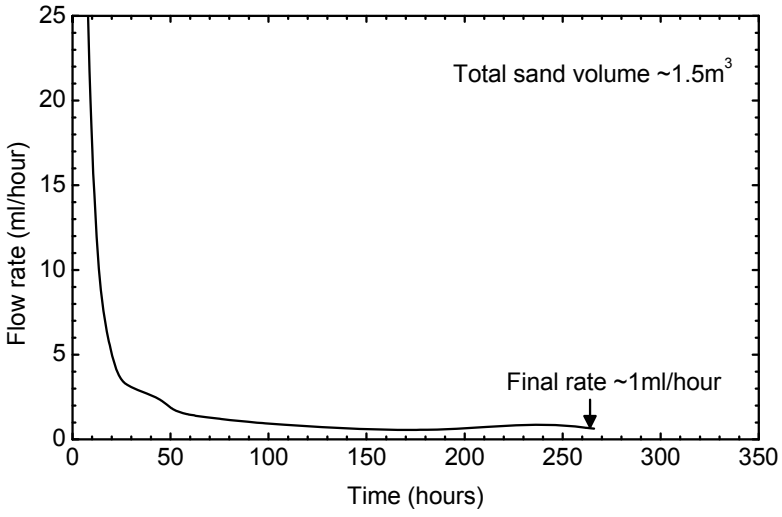


Figure 6-8: Example of volume straining during pressurisation of dry NE34 sand mass chamber for test ICP04.

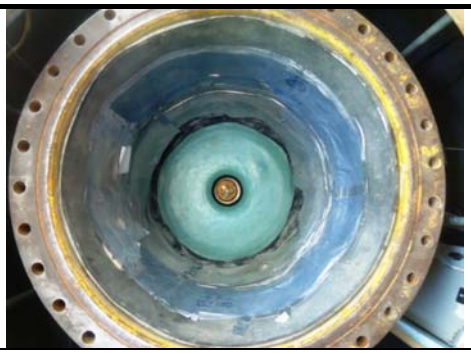
Test series	*Vertical level of sensors from the final pile tip depth (h/R)*	*Sensors radial position from the pile axis (r/R)*		
		Radial stress	*Vertical stress*	*Circumferential stress*
ICP04	40.0	2,3,5,8	2,3,5,8	2,3,5,8
	29.4	″	″	″
	15.0	″	″	″
ICP05	40.0	2,3,5,8	2,3,5,8	2,3,5,8
	29.4	″	″	″
	15.0	″	″	″
ICP06	15.0	2,3,5,8	2,3,5,8	5
ICP07	39.2	2,3,5,8	2,3,5,8	--
	29.4	″	″	2,3,5,8
	13.9	″	″	″
ICP08	40.6	2,3,5,8	2,3,5,8	8
	30.0	″	″	2,3,5,8
	15.0	″	″	″

*r/R : Relative radial distance from the pile axis (R = pile radius, r = sensor distance from pile axis)

Table 6-6: Miniature sand stress sensors layouts adopted for the ageing and axial static and cyclic behaviour studies with mini-ICP displacement piles.



(a) Empty chamber with non-inflated bottom membrane and 2mm thick lateral latex membrane for friction reduction in boundary condition BC3 tests.



(b) Empty chamber with non-inflated bottom and lateral membranes installed for boundary conditioning BC1 and BC5 tests.



(c) NE34 sand air pluviation from the perforated base plate of the sand rainer hopper.



(d) NE34 sand pluviated to the first level for in-sand sensors installation before being levelled for the sensors installation.

Table continues overleaf…

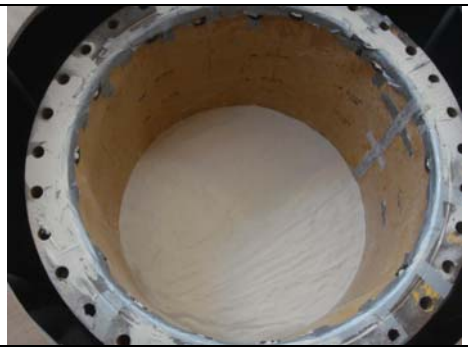
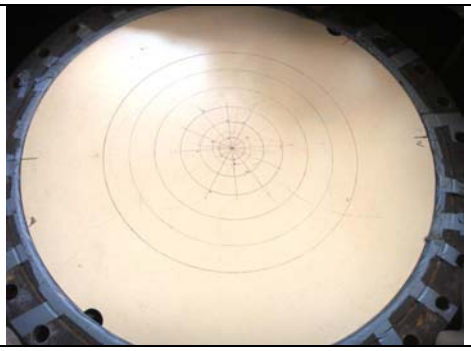
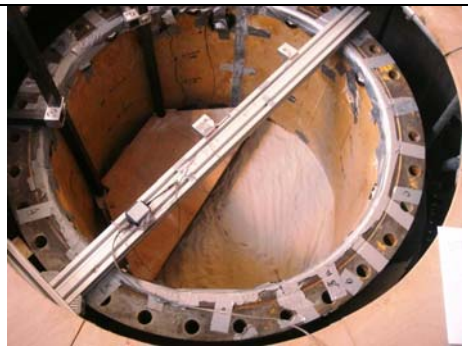
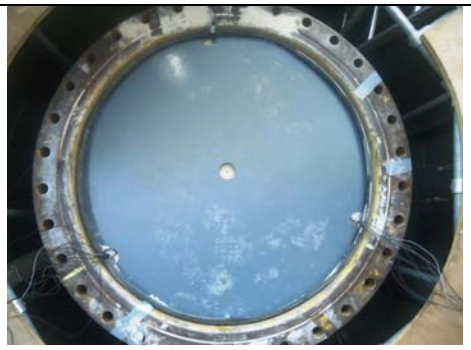
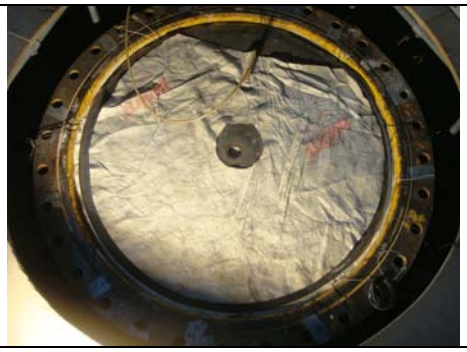
	
(e) NE34 sand chamber ready for first level of sensors installation (h/R = 14.4).	**(f)** Surveying template showing concentric circles for positioning the sensors at set radial distances from and rotations around the central axis.
	
(g) The chamber with laser survey kit, platform for sensors installation and survey marker stations around the upper chamber ledge during first layer of sensor installation in NE34 Sand.	**(h)** Top sand chamber detail revealing sensor wires at the chamber peripheries and top PVC mat installed to spread load from the top pressurisation membrane.
	
(i) Top pressure membrane in place, showing the inflating tubing.	**(j)** Fully assembled sand chamber with temperature conditioning system, sensors wires and inflating tube originating from the chamber.
	
(k) The 3S-R CC – mini ICP arrangement and the jacking frame before pile installation.	**(l)** Pile installation guiding system of three rollers. Also shown is the steel collar at the top pressure membrane level used to restrain lateral spreading on inflation.

Figure 6-9: 3S-R calibration sand chambers preparation illustration.

6.4 Pile installation techniques

The Mini-Imperial College Pile (Mini-ICP), Micro pile (MiP) and CPT cone tipped piles were penetrated into the sand by jacking down the axis of the calibration chamber. The electro–mechanical jack used for the installations was positioned and held by a steel frame that provided vertical reaction and could move along rails set on either side of the chamber. The jack frame ran on rails and had grippers that were hydraulically pressurised to secure the jack in position over the axis of the chamber during static or cyclic loading. The piles were attached to the jack by bolts passing through pile caps; the verticality of the piles was assured by making adjustments aided by plumb bobs and spirit levels. The jack was advanced to position the pile tip within the three roller pile guiding system (see Figure 6-9 (l)) at the centre of the calibration chamber cover. The guiding rollers were positioned so as to avoid running over the measuring window panes of the Mini–ICP SSTs.

Pile installation was typically advanced with forty nine 20mm strokes to reach the typical final base depth of 980mm applied for most piles. The jacking was displacement–controlled at 2mm/s with the jack held position while the operator implemented load–unloading commands. Unloading employed slower rates set at about 0.1mm/s until jack load fell below ~500N after which the rate was reduced to 0.01mm/s to achieve finer (eventually manual) control to achieve zero pile head load before re–starting the next stroke. Standardising Mini-ICP installation allowed the effects of other variables to be studied. The number (and hence the length) of strokes and rates of installation were examined by Jardine et al. (2013a) and in the current study by tests CPT09 and CPT10 where rate effects were also investigated as reported later in Chapter 7. Two additional piles were installed by the drop–weight driving system described in section 5.6 to investigate further possible effects of mode of installation on the piles' ageing, static and cyclic axial loading behaviour.

6.5 Interface sampling techniques

The sand masses remained pressurised throughout the ageing and load testing stages. On their completion the chamber was depressurised and the steel cover and the top pressurisation membrane removed with the pile still in position. Sand was then carefully excavated from around the pile, while sampling continuously the pile–interface zone at different depths. A similar sampling approach to that reported by Yang et al. (2010) was used. Excavation was made carefully in layers and small quantities of water were applied in a mist spray close to the pile axis to create suction in the sand immediately around the pile that helped the sand to adhere around the pile, allowing small curved blocks to be sampled. The annular block sections were placed on a flat surface and photographed by high resolution digital camera from at least three elevations before being separated into sand zones defined by colour and consistency. The different sand zones were separated by

specially made curved metal scrappers. The grey sand found close to the pile shaft was also found to have acquired magnetic properties. Separated samples were first left to dry then weighed and preserved for micro-particulate analysis. Manipulation of the high quality photos enabled interface thickness characteristics to be analysed as reported in Appendix IV.

6.6 Test programme

The ten piles installed in the 3S-R Laboratory calibration chamber as part of the Author's study comprise; 5 highly instrumented Mini–ICP test piles, 2 CPT cone tip instrumented test pile, 2 hammer driven blank model piles, and 1 blank micro-pile. Table 6-8 summarises the testing objectives and the specific hypotheses investigated in the Mini-ICP test series and Table 6-9 does the same for all other piles. For each of these tests Tables 6-10 and 6-11 summarises the test details which include boundary conditions, dates of preparation, pressurisation periods, dates of installation and post-installation ageing durations for the Mini-ICP piles and all other piles respectively. Further features of the axial static and cyclic loading tests are summarised in Chapters 7 and 11.

The Author's experiments add to the inventory of two CPT cone-tipped piles and three Mini-ICP tests performed by earlier Post doctoral contributors to the project (Drs B. Zhu, Z. Yang and C. Tsuha). Their experiments are summarised on Table 6-7 and data from these experiments is included in later discussion sections drawing from cited internal reports and papers. The test codes for the Mini–ICP and the CPT tests series' in the Author's study extend from these earlier testing campaigns.

Test	Preparation date	Installation date	Boundary conditions			Soil stress sensors (levels)	Pile installation		
			Surcharge pressure (kPa)	Pressure membrane	Lateral latex		Depth (mm)	Stroke (mm) / rate (mm/s)	Installation style
CPT1	27/07/07	27/07/07	200	200mmID top & base	×	12 (1)	1000	10 (1)	Partial unloading
CPT2	21/09/07	21/09/07	163	200mmID top & base	×	12 (1)	1020	10 (1)	Full unloading
Mini-ICP01	26/11/07	26~27/11/07	150	200mmID top & base	√	36 (3)	920	10 (0.5)	Full unloading
Mini-ICP02	30/04/08	20/05/08	152	200mmID top only	√	40 (2)	990	5 (0.5)	Full unloading
Mini-ICP03	28/04/09	29/05/09	152	50mmID top only	√	36 (3)	990	20 (0.5)	Full unloading

Table 6-7: CPT1 to Mini-ICP03 tests details after Jardine et al. (2013a).

6.7 Final remark – the pile modelling parameters

The closed–ended conical base model displacement piles were all installed to final depths of ~1.0m below the sand chamber surfaces. The piles had slenderness ratios (L/D) around 27.5 for the 36mm diameter Mini–ICP, CPT cone tipped piles and blank driven piles while a higher slenderness (82.5) applied to the single 12mm micro-pile test. In all cases the sand was pre-surcharged to σ'_{z0} = 152kPa which is equivalent to the effective overburden stress developed at ~17m depth in a medium dense sand with $\gamma' \approx 9kN/m^3$ and a water table near ground level.

Within the ICP-05 framework, the fully mobilised radial effective stresses developed on the displacement piles' shafts at maximum capacity are described as $\sigma'_{rf} = \sigma'_{rs} + \Delta\sigma'_{rd}$ with the radial stress dilation component $\Delta\sigma'_{rd}$ given as $4G\Delta r/D$, Lehane et al. (1993). Jardine et al. (2005a) prescribed the radial displacement component Δr as the average peak to trough distance ($2R_{cla}$) of the pile average surface roughness, arguing that sand particles have to move radially by this distance to permit shear movements relative to the sand. Axelsson (2000) suggested the R_{max} ($\approx 2R_{cla}$) of 0.01 – 0.02mm for steel piles and up to 0.04 – 0.08mm for concrete piles while Jardine et al. (2005a) recommended R_{cla} = 10μm for lightly rusted steel pipe piles. The roughness of the piles in this study ranged from R_{cla} 1 – 2μm for the smooth Micro pile to the CPT cone tip piles to R_{cla} of 3 – 4μm for the Mini–ICP as measured by the Talysurf-Hobson apparatus. The model piles were intentionally made less rough than industrial piles to ensure that radial stress dilation didn't dominate shaft capacity and so mask the effects of the potentially varying radial stress regime on ageing behaviour.

As the standard NE34 test sand has similar particle size to Dunkirk sand, the pile–to–particle diameter ratio for the chamber model piles is ~13 times lower than the field values. Two tests were performed to investigate this scale effect on the piles behaviour as analysed in Chapter 7; the Mini–ICP was installed in GA39 sand which is nearly half as fine as NE34, effectively doubling the pile–to–particle diameter ratio, and the Micro pile with a diameter of 12mm was installed in NE34 which effectively reduced the ratio by a third.

No.	Test series	Specific testing objectives
1	**ICP04**	Investigate the stress mechanisms governing ageing and axial cyclic loading behaviour of displacement piles in medium dense silica sand by installing highly instrumented 36mm diameter Mini-ICP in extensively instrumented medium dense NE34 sand mass.
2	**ICP05**	Examine the pile diameter–to–grain size scale effects on the ageing and axial cyclic loading behaviour mechanisms on displacement piles with the Mini–ICP in well instrumented finer GA39 Nemours sand chamber; GA39 sand is nearly half as coarse as NE34 sand.
		Note potential effects of density state on ageing and axial cyclic loading behaviour of displacement piles on testing the Mini-ICP in an instrumented less dense GA39 Nemours sand chamber.
3	**ICP06**	Isolate the effects of water on the ageing and axial cyclic loading behaviour of displacement piles in medium dense silica sand with the Mini-ICP installed in instrumented wet medium dense NE34 sand.
4	**ICP07**	Examine effects of far field conditions on the ageing and axial cyclic loading behaviour of displacement piles in medium dense silica sand by installing the Mini-ICP in instrumented NE34 sand chamber surrounded by a 'free field simulator' BC5 boundary condition instead of the classical BC3 used in previous setups.
		Investigate effects of stress cycles caused by diurnal changes on the sand and pile-sand stress regime as related to the ageing and axial cyclic behaviours of displacement piles. Two weeks of vertical and radial stress cycles imposed to the vertical and lateral boundary of the Mini–ICP–NE34 sand mass.
5	**ICP08**	Investigate the effects of far field conditions on the ageing and axial cyclic loading behaviour of displacement piles in medium dense silica sand by installing the Mini-ICP into NE34 sand with the BC5 boundary condition.
		Examine the effect of eliminating a final and slower jack stroke of the displacement pile installation that defined the pile short–term static compression axial capacity during the installation of the instrumented Mini-ICP in instrumented medium dense NE34 sand.

Table 6-8: Mini-ICP piles specific testing objectives in the study of ageing and axial cyclic loading behaviour of displacement piles in silica sands.

No.	Test series	Specific testing objectives
1	**CPT09**	Investigate the effects of the mode of jack-stroke installation on the ageing behaviour of displacement piles in medium dense silica sand by installing a CPT cone tip pile using just two long strokes instead of the standard 49 strokes into medium dense NE34 sand with BC5 boundary conditions.
2	**CPT10**	Investigate the effects of displacement pile jacking rate on the ageing behaviour of displacement piles in medium dense silica sands by installing a CPT cone tip pile at rate of 10mm/s instead of the standard 2mm/s into NE34 sand with BC5 boundary conditions.
3	**DI**	Examine the effects of installation procedure on ageing behaviour. Install a hammer driven 36mm diameter un-instrumented closed-ended conical tip displacement pile into NE34 sand with BC5 boundary conditions.
4	**DII**	Examine further the effects of installation procedures on the ageing behaviour with second hammer driven 36mm diameter un-instrumented closed-ended conical tip pile installed into medium dense NE34 sand with BC1 boundary conditions.
5	**MiP01**	Investigate potential pile–to–sand particle diameter and chamber–to–pile diameter scale effects on the ageing behaviour of displacements piles in medium dense silica sands by testing a micro pile with 12mm diameter in medium dense NE34 sand with BC3 boundary conditions.

Table 6-9: All other piles specific testing objectives in the study of ageing and axial cyclic loading behaviour of displacement piles in silica sands.

No.	Test series	Sand	Boundary Condition	Pressurisation				Pile Installation			Instrumentation		Ageing	
				Dates	Pressures		Duration	Date	Jacking rate	Penetration mode	Pile	Chamber	Dates	Duration
					Vertical	Lateral	Days							
					kPa	kPa			mm/s					Days
1	ICP04	Dry NE34	BC3	19/10/09-03/11/09	152	N/A	15.1	03/11/09	2	20mm strokes; full unloading	Jack, Mini ICP	3 levels; 39 sensors	03/11/09-14/12/09	41
2	ICP05	Dry GA39	BC3	02/04/10-06/05/10	152	N/A	33.8	06/05/10	2	20mm strokes; full unloading	Jack, Mini ICP	3 levels; 39 sensors	06/05/10-16/07/10	71
3	ICP06	Wet NE34	BC3	14/10/10-18/10/10	150	N/A	4	18/10/10	2	20mm strokes; full unloading	Jack, Mini ICP	1 level; 11 sensors	18/10/10-06/12/10	49
4	ICP07	Dry NE34	BC5	20/05/11-24/05/11	152	62	~4	24/05/11	2	20mm strokes; full unloading	Jack, Mini ICP	3 levels; 35 sensors	24/05/11-15/07/11	52
5	ICP08	Dry NE34	BC5	28/09/11-29/09/11	150	62	1.0	29/09/11	2	20mm strokes; full unloading	Jack, Mini ICP	3 levels; 33 sensors	29/09/11-14/10/11	15

N/A = Not Applying

Table 6-10: Summary details of the Mini-ICP piles test programme to investigate the ageing and axial cyclic loading behaviour of displacement piles in silica sands.

No.	Test series	Sand	Boundary Condition	Pressurisation				Pile Installation			Instrumentation		Ageing	
				Dates	Pressures		Duration	Date	Jacking rate	Penetration mode	Pile	Chamber	Dates	Duration
					Vertical	Lateral	Days							
					kPa	kPa			mm/s					Days
1	MiP01	Dry NE34	BC3	21/12/10-22/12/10	152	N/A	1	22/12/10	2	20mm strokes; full unloading	Jack	N/A	22/12/10-28/02/11	68
2	CPT09	Dry NE34	BC5	06/05/11-10/05/11	145	65	3.4	10/05/11	10	750mm & 340mm strokes; no unloading	Jack, CPT cone	N/A	10/05/11-17/05/11	7
3	CPT10	Dry NE34	BC5	30/11/11-19/12/11	152	62	19.5	19/12/11	10	20mm strokes; full unloading	Jack, CPT cone	N/A	19/12/11-20/01/12	32
4	DI	Dry NE34	BC5	31/01/12-31/01/12	151	62	~0	31/01/12	Hammer impact	~22mm strokes; full unloading	Jack	N/A	01/02/12-13/02/12	12
5	DII	Dry NE34	BC1	01/03/12-13/03/12	152	62	12	13/03/12	Hammer impact	~11mm strokes; full unloading	Jack	1 level; 21 sensors	13/03/12-23/04/12	41

N/A = Not Applying

Table 6-11: Summary details of all other piles test programme to investigate the ageing and axial cyclic loading behaviour of displacement piles in silica sands

Chapter 7

7 Observations during laboratory model pile installation

7.1 Introduction

This chapter analyses the data acquired during the model piles' installation stages. It examines:

1) The development of pile end–bearing resistances and shaft interface stresses with embedment depth, and
2) The stress response in the sand masses surrounding the pile.

As outlined in Chapter 6, a range of both Mini-ICP and minimally instrumented pile experiments were undertaken, in both instrumented and uninstrumented sand masses. This chapter concentrates on the large data sets gathered with the instrumented tests. The specific objectives of each test were detailed on Tables 6-8 and 6-9, while Tables 6-10 and 6-11 summarise the test sands used, chamber boundary conditions, pressurisation details, pile installation procedures and the pile and chamber instrumentation. Interpretation is made with reference to the framework developed from the earlier field ICP tests and database studies summarised by Jardine et al. (2005a); areas of agreement and divergence are identified and discussed.

7.2 End bearing resistance

The end–bearing resistances mobilised in the cyclically jacked installations were assessed from the base loads measured at the end–of–push (moving) stage of each stroke as illustrated on Figure 7-1. The Author's end-bearing resistance measurements are shown on Figure 7-2(a) and are compared in (b) to profiles from tests CPT1 to Mini-ICP03 reported by Jardine et al. (2013a) from the earlier test series of the extended research programme. The boundary conditions, pile installation procedures, and pile and chamber instrumentation details of the tests CPT1 to Mini-ICP03 were summarised in Table 6-7.

The lowest Mini-ICP pile end–bearing resistances were observed in the looser and finer GA39 sand test, ICP05. This is attributed mainly to the lower density (1433kg/m^3, I_D = 36%) noted in Table 7-1. ICP05 was intended to repeat the medium dense states achieved with NE34 sand, where the dry densities assessed on emptying the calibration chamber at the end of the tests gave a mean of 1,617.5 ± 10.4 kg/m^3 corresponding to density index of 67.1 ± 2.7% classifying the sand mass as medium dense to dense. However, the finer sand did not settle in air as expected and the GA39 sand mass classified as loose. For operational reasons, densities were not measured in tests ICP04 or ICP06 but were checked in all other experiments as shown in Table 7-1.

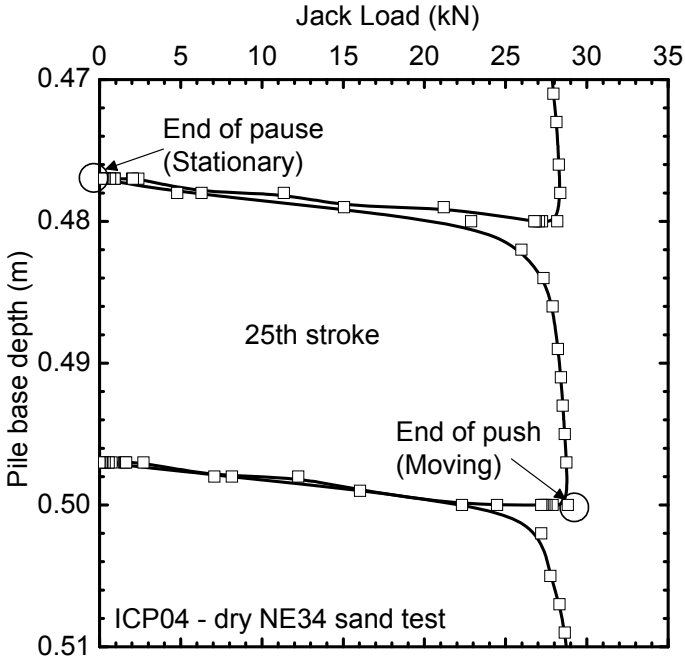


Figure 7-1: Illustration of selection of end–of–push (moving) and end–of–pause (stationary) data values based on the jack–stroke installed model piles.

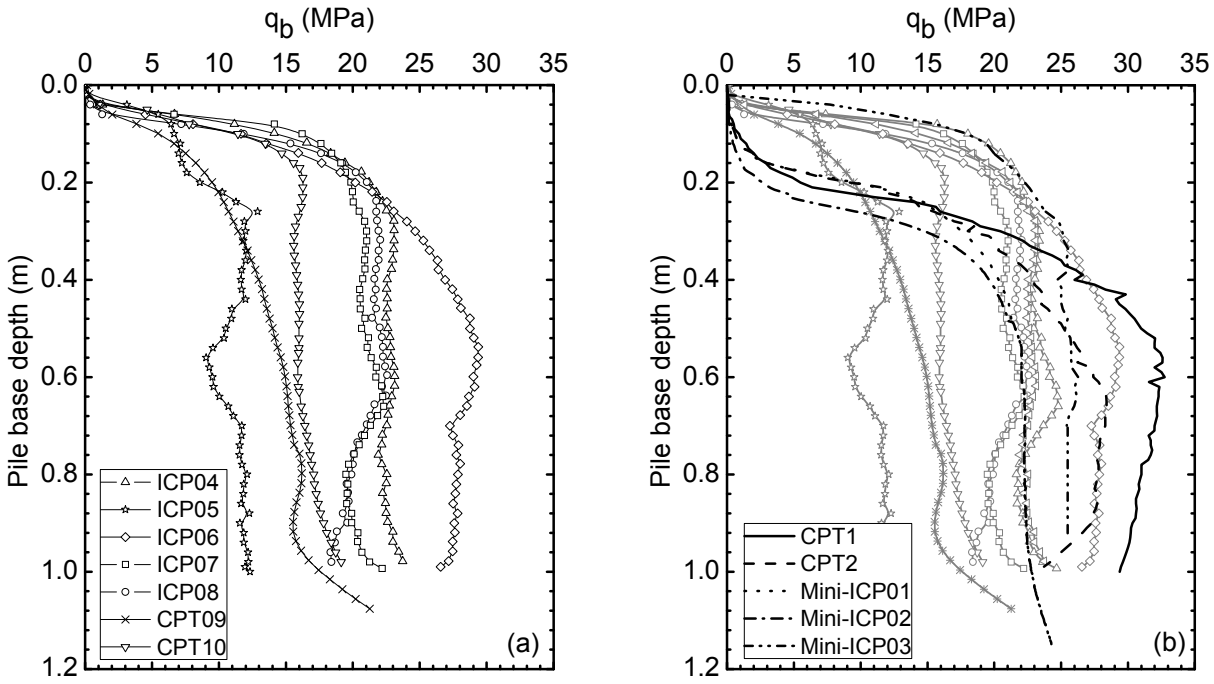


Figure 7-2: (a) Pile end-bearing resistances of all continuously monitored installations in this study (b) The current study piles end-bearing resistances compared to Jardine et al. (2013a) tests CPT1 to Mini-ICP03.

Test	Pressurisation			Mass (kg)	Volume (m^3)	Density (kg/m^3)	e_0	Density index, I_D^* (%)
	Start date	End date	Days					
ICP05	02/04/10	06/05/10	33. 8	648	0.45	1433	0.849	36
MiP01	21/12/10	22/12/10	1.0	2525.5	1.55	1626	0.630	69
CPT09	06/05/11	10/05/11	3.4	2364.5	1.47	1603	0.653	63
ICP07	20/05/11	24/05/11	~4.0	2383.0	1.46	1627	0.629	70
ICP08	28/09/11	29/09/11	1.0	2358.0	1.46	1615	0.641	66
CPT10	30/11/11	19/12/11	19.5	2347.5	1.46	1608	0.648	65
DI	31/01/12	31/01/12	~0.0	2381.5	1.46	1626	0.630	69

*$I_D = (e_{max} - e_0)/(e_{max} - e_{min})$. NE34 sand: $e_{max} = 0.90$, $e_{min} = 0.51$; GA39 sand: $e_{max} = 1.01$, $e_{min} = 0.56$

Table 7-1: Calibration chamber pressurisation durations and density states for all pile installations.

Three pressurisable top membranes with internal diameters of 50mm, 100mm and 200mm have been used in the extended experimental programme run from 2007 to 2013. Jardine et al.'s tests CPT1, CPT2, Mini-ICP01 and Mini-ICP02 used the 200mm ID top membrane which gave unfavourably soft end–bearing resistance profiles at shallow depths. Test CPT09 in this study, which exhibited an intermediate response, was performed with a 100mm ID top membrane while Mini-ICP03 from Jardine et al. (2013a), and tests ICP04 to ICP08 and CPT10 in this study used the 50mm ID membrane, leading to stiffer shallow end–bearing resistances trends and quasi-constant values from shallower depths.

The effects of the chamber lateral boundaries on the pile end–bearing resistance are assessed by comparing ICP04, ICP07 and ICP08. All were installed in dry medium dense NE34 sand, with three levels of sand stress sensors, but with different lateral boundary conditions. The rigid BC3 lateral boundary condition applied in ICP04 produced an end-bearing resistance profile that was about 4% higher than was achieved when the stress controlled BC5 boundary condition was employed in ICP07 and ICP08 to match the free field response (following the logic set–out by Huang and Hsu 2005). The radial boundary pressures developed in ICP07 and ICP08 in the isolated top, middle and bottom lateral boundary membranes (at 33 pile radii from the pile axis) increased as shown in Figure 7-3 sequentially as the pile tip approached from above. The pressures rose during installation to develop maximum of 1.6 times the initial K_0 stresses (or 0.45% q_b), signifying influence the lateral boundary condition. Far greater effects would be anticipated in chambers involving lower $d_{chamber}/D$ ratios.

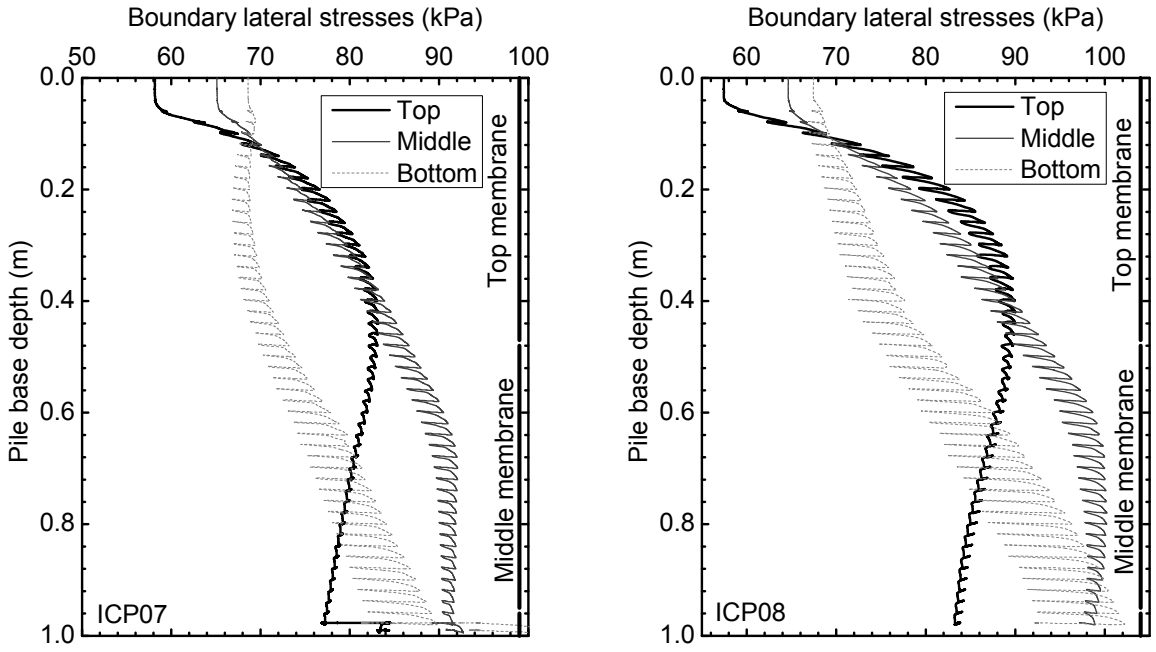


Figure 7-3: Lateral boundary stresses during Mini-ICP installations in tests ICP07 and 08 with boundary condition BC5.

The end–bearing resistance profiles of CPT09 and CPT10 consistently fell below those developed in ICP07 and ICP08. All were performed with BC5 lateral boundary condition, but tests CPT09 and CPT10 did not employ arrays of stress sensors (and their cables) within the sand mass. They were also installed at a faster rate (10mm/s) than the standard 2mm/s. The end–bearing resistances developed at the mid-range of the full embedded depth were 5MPa greater in ICP07 and ICP08 (which employed 3 levels of sand stress sensors) representing a 33% increase that could be interpreted as resulting from the reinforcing effects of the instruments and cables. Comparing the local moving shear stresses measured on the shaft by the 'leading' cluster A (h/R = 8.94) SST and the CPT friction sleeve (h/R ≈ 5.70) as shown in Figure 7-4 suggests similar trends over the most heavily instrumented mid-depth ranges. The interpretation of reinforcing effects on end–bearing resistances and the local shear stress profiles is supported by noting that the instrumented and un-instrumented test profiles converge with depth after passing the deepest instrumented zone.

Figure 7-5 plots the end–bearing resistances of CPT09 and CPT10 with reference to the CPT end-bearing resistance–to–density index correlation charts given by Baldi et al. (1986). The uninstrumented sand mass q_c values appear to plot in the medium dense to dense range I_D = 65% - 75% for the NE34 sand masses similar to those calculated from density measurements. However, the end–bearing resistances from the instrumented tests imply higher than measured density indices (I_D = 85% - 95%), supporting the interpretation of a significant sensor and cable reinforcement effect.

As noted in Table 7-1 the freshly pluviated reconstituted sand masses were generally pressurised for an average of a week before pile installation to simulate a degree of natural mechanical ageing. The exact durations varied reflecting periods of weekend lab closures and other operational factors. During pressurisation sand volume changes were monitored by measuring water flow into the pressurisation membranes. The overall sand volumetric strain rates declined to around 0.003% per day after 24 hours of full pressurisation. Potential pre-installation chamber ageing time effects may be assessed by comparing the end–bearing resistance trends from ICP08 and ICP07. These tests had similar sets of instrumentation (see Table 6-6) but were aged for periods of 1 and 4 days respectively, covering the period when creep rates are likely to have been highest (see Kuwano & Jardine 2002). While minor variations can be noted, there is no clear and consistent effect of pre-installation ageing duration under pressure over the periods of several days considered. White & Zhao (2006), Baxter & Mitchell (2004) made similar observations in other calibration chambers studies. It appears that a one day ageing period covers most of the effects that can be expected in the short term, although more significant effects might apply after more extended periods.

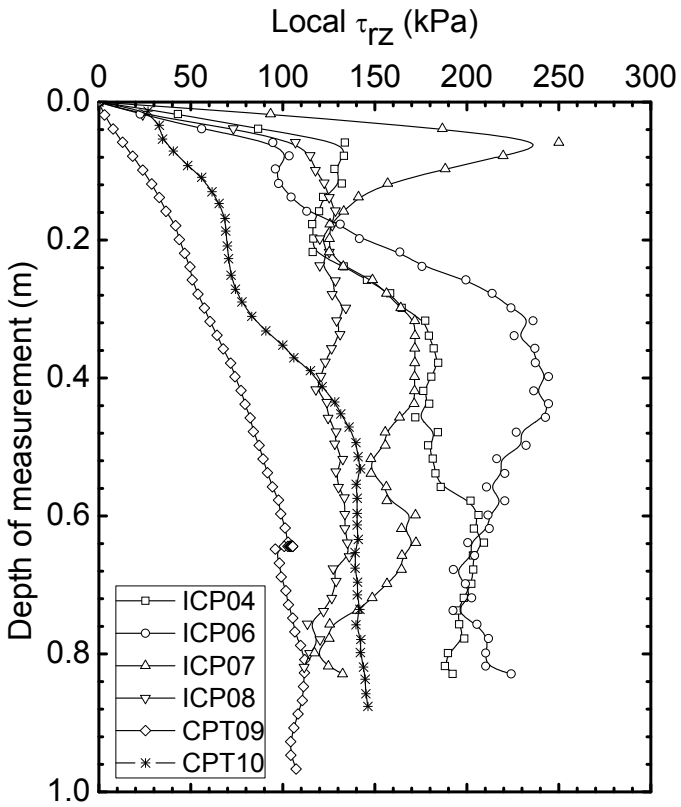


Figure 7-4: Local shear stress profiles from Mini-ICP cluster A at h/R = 8.94 or CPT friction sleeve at h/R ≈ 5.7.

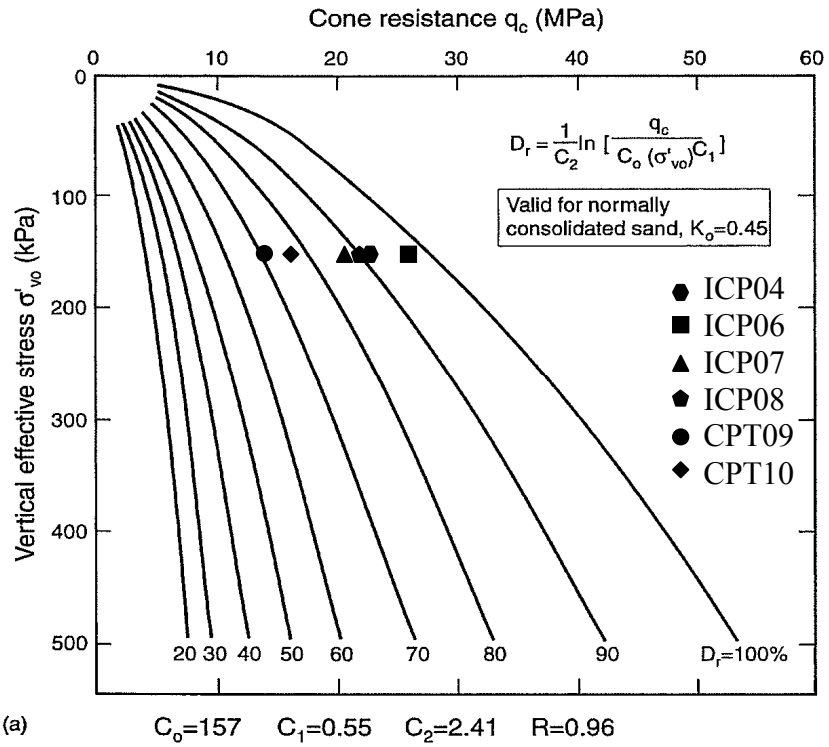


Figure 7-5: Density indices of all the NE34 sand test chambers in this study after the Baldi et al. (1986) end-bearing resistances correlation chart.

The wet NE34 sand employed for test ICP06 showed higher end-bearing resistances than the equivalent dry test ICP04 that shared similar BC3 boundary conditions. ICP06 developed similar base resistance profiles to the earlier CPT1 and CPT2 tests in dry NE34 sand conducted (with BC3 by Jardine et al. 2013a) but under top membrane pressures of 200kPa and 163kPa respectively. Two hypotheses for the higher end-bearing in ICP06 are;

1) 'Collapse' densification on wetting of the dry pluviated sand chamber. The ICP06 sand mass was pluviated in the standard dry procedure before saturation (see section 6.3.3). Applying Baldi et al. (1986) to the q_b value of 26MPa obtained in ICP06 below the zone affected by the single level of instruments used suggests I_D = 97% (see Figure 7-5). However this would entail a final dry density of 1741kg/m^3 that would have required a 'collapse' settlement of 94mm in the 1.43m high sand mass (ε_{axial} = 6.6%). Checks of the free sand surface level settlement during saturation showed no evidence of such a collapse so that final dry density was probably closer to the typical initial 1620kg/m^3.

2) Although care was taken, and a CO_2 system was deployed to aid air replacement, the sand chamber was unlikely to have been fully saturated during installation. As explained by Baxter & Mitchell (2004) CO_2 saturated specimens can be expected to de-gas partially during ageing. Pournaghiazar et al.'s (2011) tests in dry, saturated and unsaturated silica Sydney sand Figure 7-6, show similar end-bearing resistances in dry and fully saturated

sand, but higher values in unsaturated sand – presumably as a result of air–to–water suction effects. Considering that, as discussed above tests CPT1 and CPT2 showed end-bearing resistance similar to ICP06 between the depths of 0.65m to 0.9m, it might be concluded that the action of possible suctions might have an equivalent effect to an extra 11 – 48kPa of surcharge. Alternatively, direct application of Baldi et al. (1986) indicates that suctions acting around the base would have needed to have similar effects to an additional surcharge of ~58kPa to explain the observed q_c or q_b profile increase.

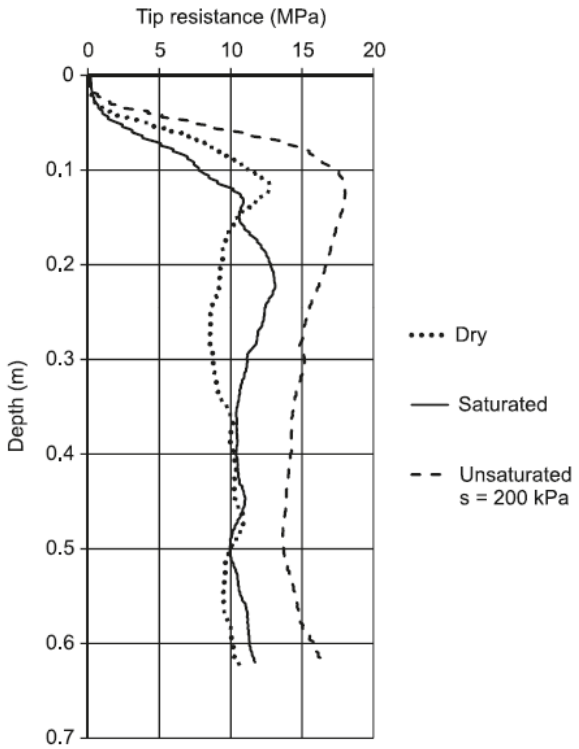


Figure 7-6: CPT tip resistances in dry, saturated and unsaturated sand specimens prepared by pluviation method (I_D = 61%) (Pournaghiazar et al. 2011).

The importance of accounting for pile residual stresses in field interpretations was emphasised in Chapter 2. Residual base loads measured at the end–of–pause stage of each installation stroke are reported in Figure 7-7 as proportions of the 'moving' end–bearing resistances and plotted against the piles' developing slenderness ratios L/D. For the conditions considered, the (closed–ended) piles all showed continuous accumulation of base residual loads with increasing depth reflecting the growing shaft resistance available to counter the locked in load. Higher residual base load ratios (up to 30%) were developed (in ICP04 and ICP06) with the rigid BC3 boundary conditions than in the other tests. Test ICP05 conducted in the looser and finer GA39 sand (with BC3) and the CPT piles without instrumentation mark the lower bound (18%) for locked in toe loads as a proportion of q_b while tests ICP07 and ICP08 with the active stress–controlled BC5 conditions featured an intermediate trend. Failure to account for the residual base loads would lead

to an under-recording base capacities and over–estimation of shaft capacities that would increase with L/D.

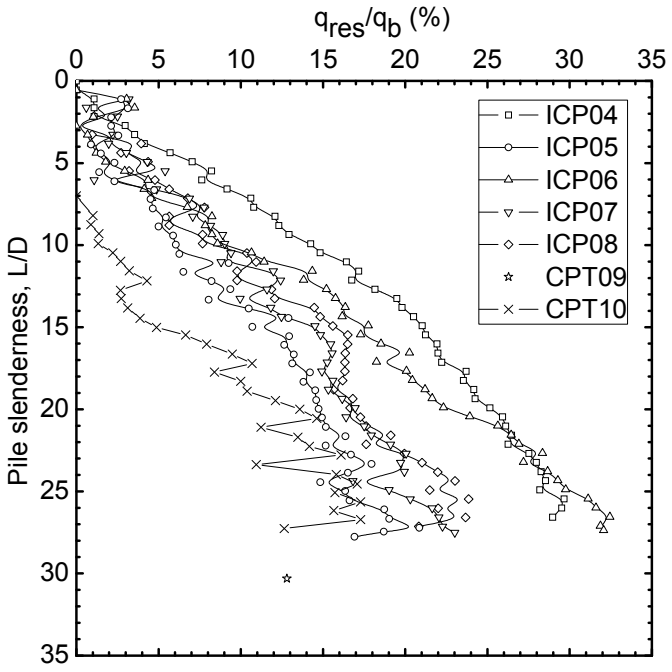


Figure 7-7: Pile base residual loads as a proportion of the local maximum installation base resistances of all the continuously monitored piles during installation.

7.3 Pile shaft resistances

7.3.1 Shear stresses

Local radial and shear shaft stresses were measured directly during installation, ageing and static and cyclic axial load testing by the Mini-ICPs SST circuits. The reliability of the SST field ICP measurements has been discussed by Chow (1997) while Jardine et al. (2009) describe that of the Mini–ICP instruments. As noted in Chapter 5, the SST and ALC calibrations identify cross sensitivity effects that have to be established by careful calibration and accounted for radial stress, shear stress and axial load data reduction.

The ALC devices also give information on local shaft shear stresses. A fourth order polynomial trendline can be fitted through the axial loads measured at the ALC's base, clusters A, B and C plus the pile head jack. The load–depth of embedment gradients dQ/dz can then be determined easily for given points on the shaft and local shear stresses as $\tau_{rz} = (1/\pi D)(dQ/dz)$ and compared with the SST local shear stress measurements. Full profiles of τ_{rz} against depth can be calculated from the ALC polynomial, as can averages between the axial load cell levels, or indeed between the base and head.

Figure 7-8 plots the interface local moving shear stresses measured at clusters A and B as the Mini–ICPs were installed in NE34 sand. Traces from depths < 0.2m (including all cluster C data at h/R = 45.61) are omitted as the penetration data at this depth are influenced by the chamber's top boundary condition, see section 5.2.2.1. The interface local shear stresses show trends that mirror their respective base resistances profiles (Figure 7-2) across the installations performed. For each of the cyclically jacked piles installations there is an 'h/R installation effect' where the stress developed at any given depth fall from maxima seen with cluster A (h/R = 6.7) to B (h/R = 25.6) as initially observed by Bond (1989), Lehane (1992), Chow (1997) and also referred to as 'friction fatigue' (Randolph et al. 1994, White 2005).

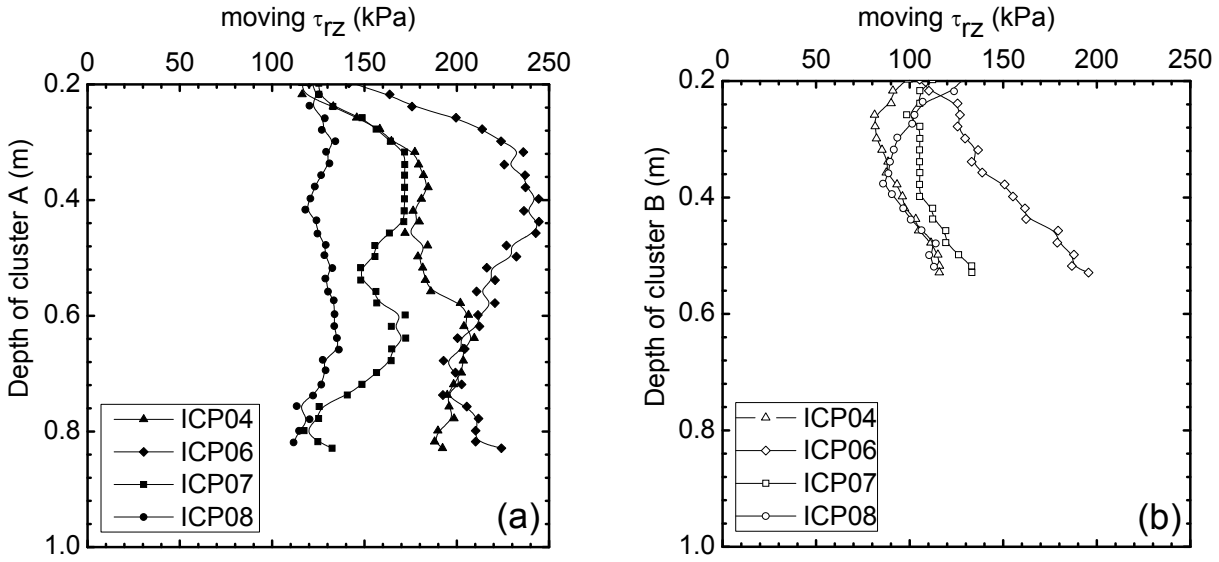


Figure 7-8: Interface local moving shear stresses from the Mini-ICP installed in NE34 sand (a) cluster A (b) cluster B.

The correspondence seen between the interface shear stress and end-bearing q_b profiles has been noted in earlier studies and prompted the normalisation of stresses by local q_b or q_c. This step should isolate most dependencies of the interface shear stresses on local density, variations within the particular sand chamber and allow a clearer assessment of the particular parameter being investigated.

Figure 7-9 presents the normalised moving local shear stresses for piles installed in NE34 sand by similar procedures and density states, but with various boundary conditions and instruments layouts. The normalised plots form a tighter band than the raw measurements, showing a maximum spread of about ±0.20% q_b per cluster. The 'h/R effect' developed on the Mini-ICPs is likely to be augmented by their cyclic jacking installation, leading to slightly lower normalised moving shear stresses (τ_{rz}/q_b = 0.54% to 0.93% at cluster A) than the range of 0.5 to 1.5% reported from steady

penetration CPT friction sleeve ratios measurements made in silica sands, at h/R = ~5.7. Note also that CPT friction ratio measurements are typically made with sleeves whose R_{cla} values are smaller than the Mini-ICP and may develop lower δ values with possible less dilation. The normalised local shear stresses developed in test ICP06 in wet NE34 sand are similar to the dry sand test ICP04 at cluster A and slightly higher at cluster B. The differences might be due to either denser sand in the wet case or the possible suctions set up by partial de–saturation as CO_2 degasses from solution before pile installation. Bellotti et al. (1988) report different CPT sleeve friction trends in dry and wet Ticino sand. While similar end-bearing resistances were observed in both wet and dry, their sleeve frictions were consistently lower in the wet, although no explanation was offered for their observation.

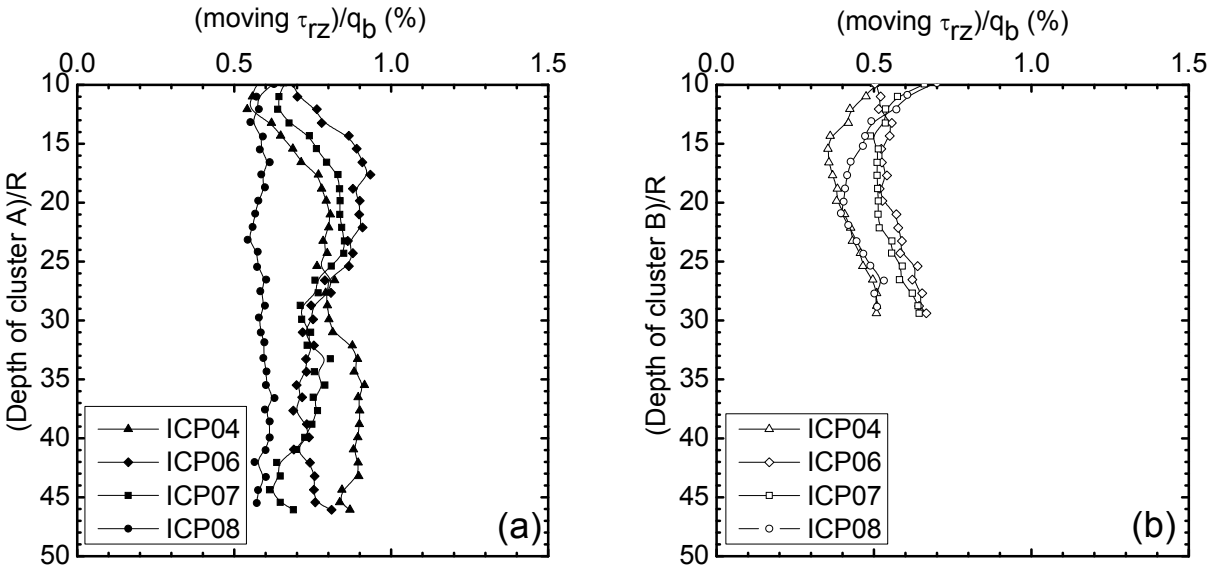


Figure 7-9: q_b normalised interface local moving shear stresses from the Mini-ICP installed in NE34 sand (a) cluster A (b) cluster B.

Figure 7-10 presents the stationary shear stresses assessed from the end–of–push stages of each stroke, focusing again on clusters A and B, while Figure 7-11 shows the 'q_b–normalised' trends. As with the moving stresses, the stationary local shear stress profiles mirror the base resistance profiles and an 'h/R effect' is evident from the reductions seen between clusters A to B at any given depth. Negative (shaft tension load direction) interface shear stresses develop as the shaft counters the accumulating residual end-bearing stresses. The interface stationary shear stresses increase with pile depth (become less negative) as extra pile shaft length becomes available to counteract the building base stresses. A shear stress sign reversal occurs at a "neutral point" located near the base in these 'floating' piles when head loads are zero.

Figure 7-12 plots interface moving shear stresses at the Mini-ICP clusters A and B positions derived from the ALCs data as described earlier. Figure 7-13 compares the local moving shear

stresses deduced in this way to the direct SST measurements made at the same point, considering a broad band of stresses from about 50 to 250kPa. Scatter is evident perhaps reflecting local variations related to the soil instrument layouts, but the overall average ratio of SST shear stresses to those derived from regression–fitted polynomial axial load – depth relationships is 1.03 ± 0.29, confirming that the Mini-ICP local shear stresses are not subject to any systematic under–registration error through significant cell action effect. Specific trends, such as the influence of h/R, are clearer in the local SST measurements.

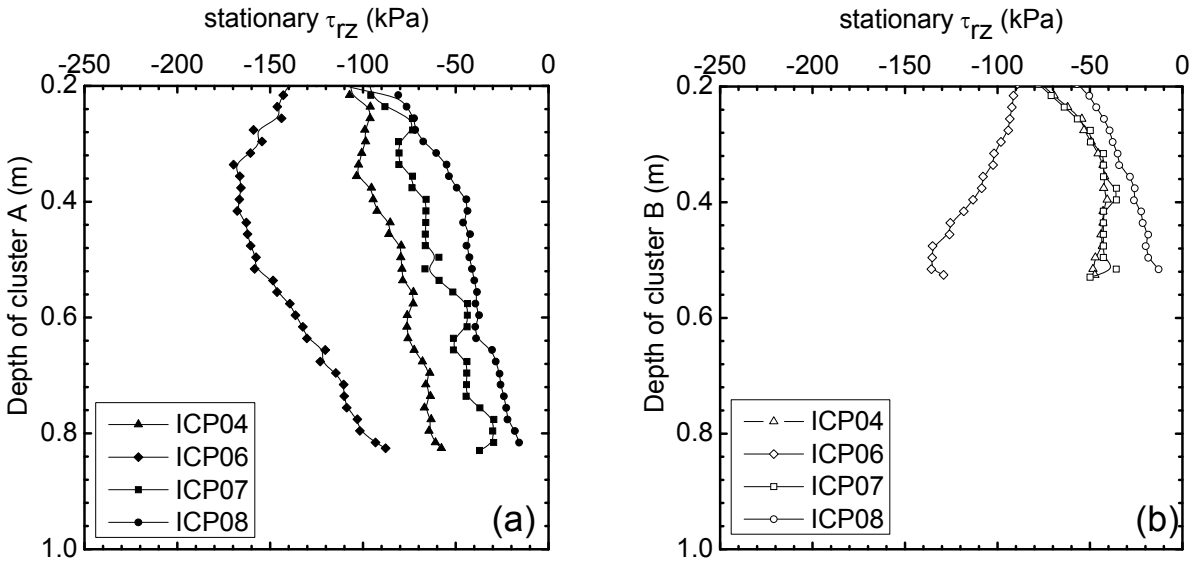


Figure 7-10: Interface local stationary shear stresses from the Mini-ICP installed in NE34 sand (a) cluster A (b) cluster B.

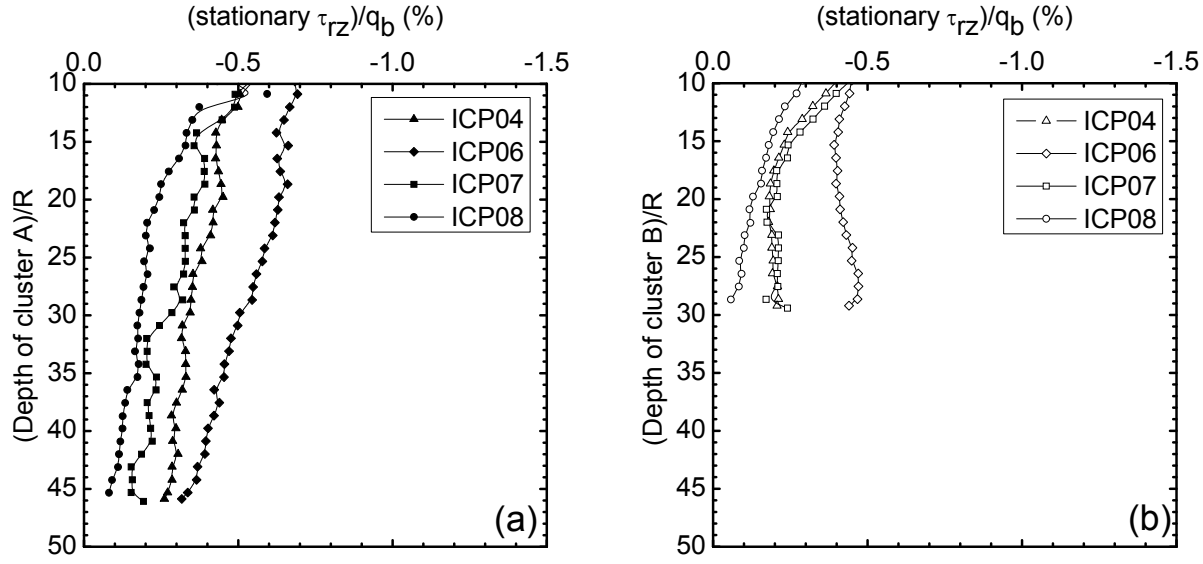


Figure 7-11: q_b–normalised interface local stationary shear stresses from the Mini-ICP installed in NE34 sand (a) cluster A (b) cluster B.

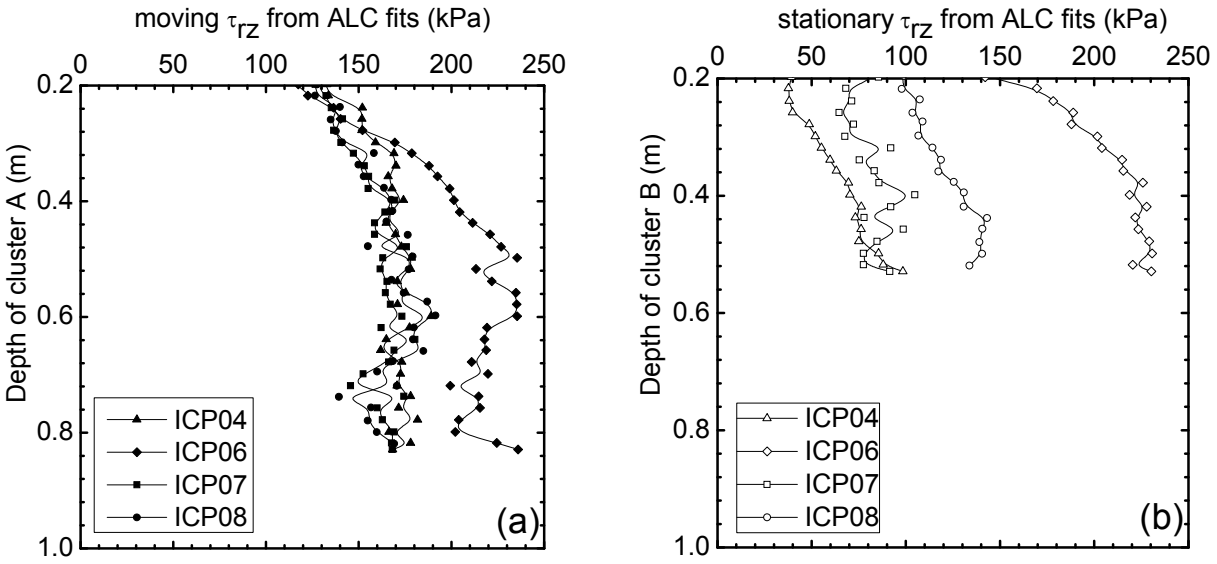


Figure 7-12: Interface moving shear stresses from trend-lines on end–of–push axial loads during the Mini-ICP piles installations in NE34 sand (a) at cluster A location (b) at cluster B location.

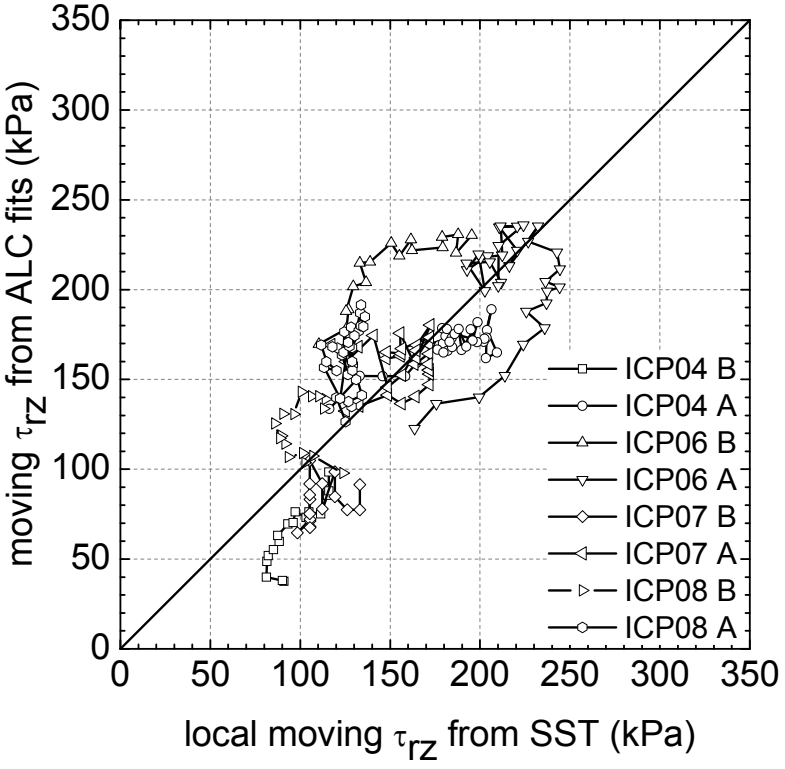


Figure 7-13: Interface moving shear stresses from the Mini-ICP SST versus equivalents from polynomial ALC loads fit trends.

The average base–to–head shear stresses developed over the full shaft length (including the top 0.2m) are shown in Figure 7-14, exhibiting a quasi-constant average over the 0.5m – 1.0m (14D – 28D) range which is a recognised feature of long piles (length > ~20D) driven in the field in sand where σ'_{v0} also varies steeply with depth (see example Kerisel (1961), Vesic (1965) and Chow

(1997)). The tight band of average shear stresses in dry NE34 sand indicates again the relatively slight influence of far field boundary effects on τ_{rz} for the configurations considered.

Figure 7-15 shows the interface moving and stationary local shear stresses from ICP05 (see Table 6-8) on the finer, looser, GA39 Nemours sand. Unfortunately cluster B malfunctioned in this test. The moving shear stresses fall well below those developed in NE34 sand in the equivalent ICP04 test. The pause interface shear stresses all fell below 30kPa, far below the NE34 residual shaft stresses, and correlate with the relatively low GA39 base residual stresses shown in Figure 7-7. The base–to–head average shear stresses shown on Figure 7-16 confirm for lower values than were available in the denser NE34 sand, although the average again tended to constant values for L/D > 20. The q_b–normalised interface local shear stresses are plotted on Figure 7-17, showing normalised trends that are closer to those developed in NE34 installations, although the normalised GA39 pause interface shear stresses are clearly lower than those required in NE34 sand to match the latter's higher locked-in base loads.

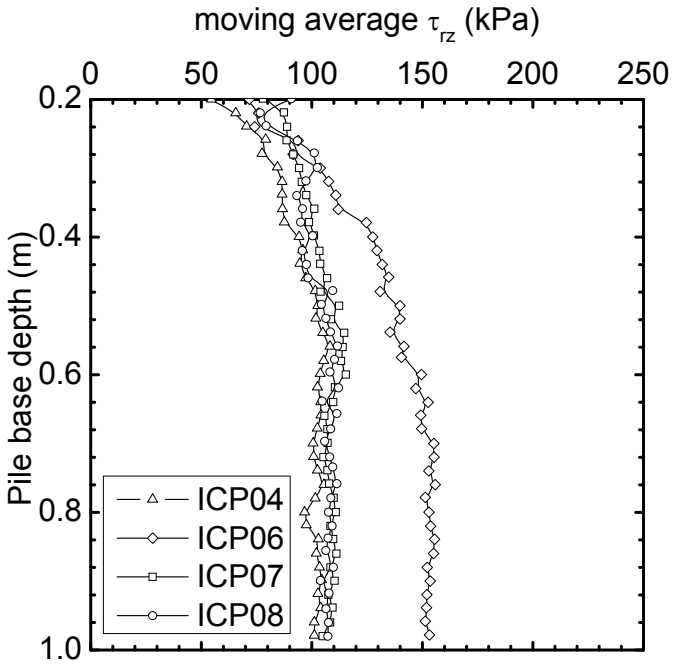


Figure 7-14: Base–to–head moving average interface shear stresses on Mini-ICP installing in NE34 sand.

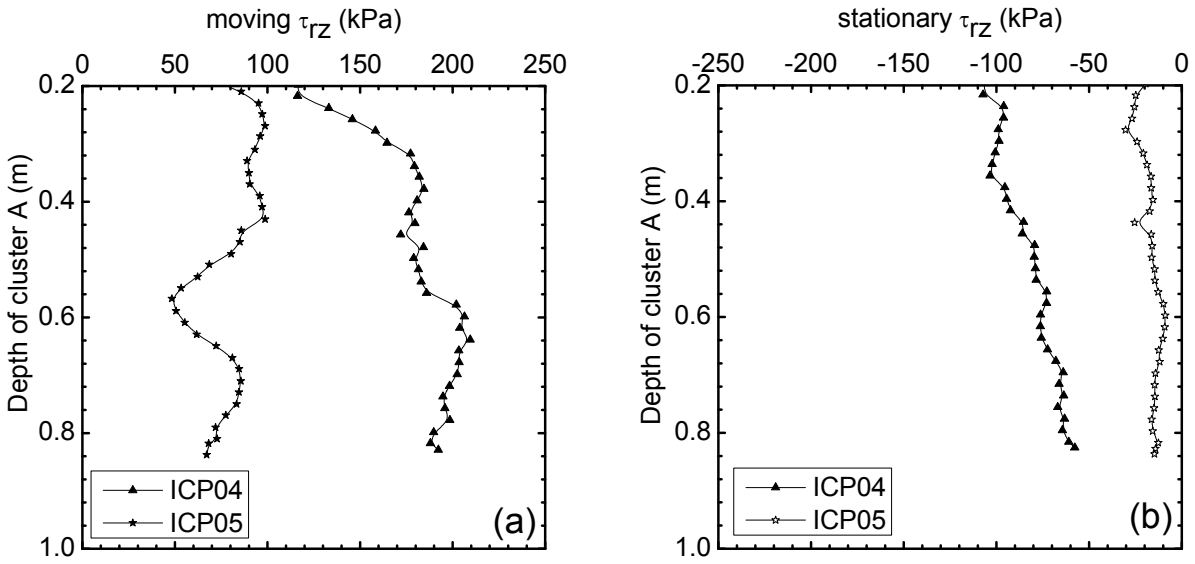


Figure 7-15: Interface local shear stresses from the Mini-ICP clusters A in dry GA39 sand (ICP05) compared to dry NE34 sand (ICP04) (a) moving (b) stationary.

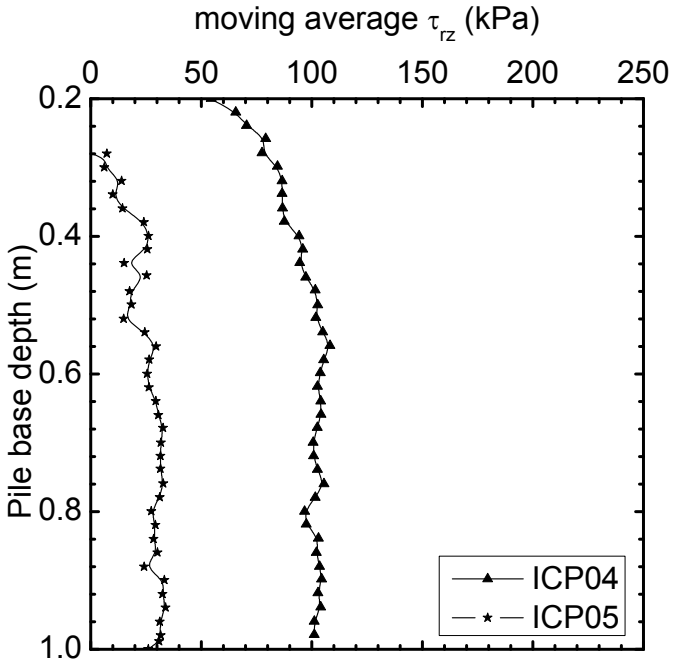


Figure 7-16: Base–to–head moving average interface shear stresses on mini-ICP installing in GA39 sand.

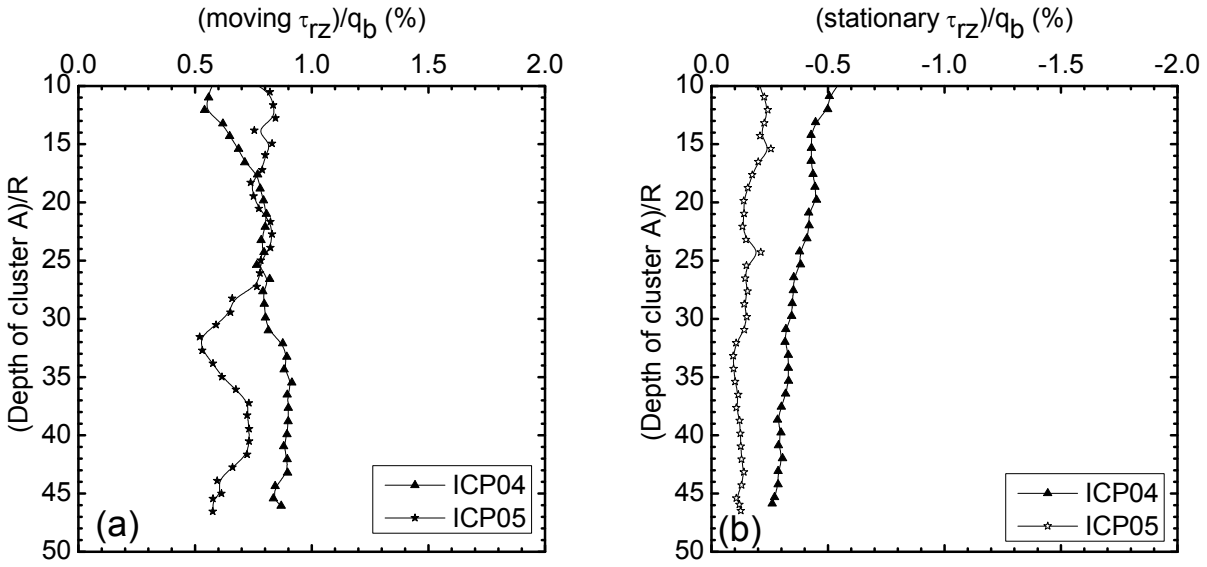


Figure 7-17: q_b normalised interface local shear stresses from the Mini-ICP cluster A in dry GA39 sand compared to dry NE34 sand (a) moving (b) stationary.

7.3.2 Radial stresses

The SST devices also measured the moving and stationary local interface radial stresses. The data recorded during Mini–ICP installation in NE34 sand are plotted in Figures 7-18 and 7-19. The moving radial stresses are consistently higher than the stationary stresses due to the kinematically constrained dilative system applying at the interface, Lehane et al. (1993), Jardine et al. (2005a). The h/R effect between cluster A and B is again discernible in both the moving and the stationary stresses recorded at the end–of–push and pause stages of the jacking cycles as are variations linked directly to the local end–bearing resistance (q_b) profiles given in Figure 7-2. The moving radial stress measurements can be checked independently by calculating $\sigma'_{rf} = \tau_{rz}/\tan \delta_{cv}$ from the end–of–push shear stress profiles established from axial loads as described in section 7.3.1, adopting a δ_{cv} value of 27^0 from laboratory interface ring-shear testing; Yang et al. (2010) and Ho et al. (2011). The comparison given on Figure 7-20 shows a similar degree of scatter about the equality line to the τ_{rz} data shown on Figure 7-13 but with the average ratio between the measurements close to unity (1.05), albeit with a relatively large standard deviation of 0.43. As noted earlier local effects of instrument cables may contribute to this substantial scatter.

The q_b–normalised local moving and stationary radial stresses are plotted on Figures 7-21 and 7-22. The radial stresses show again the 'h/R effect' giving reductions from cluster A to B the full range of normalised data falling between 0.5% and 1.9%. The equivalent raw q_b–normalised local interface radial stresses from the Mini–ICP test with finer and less dense GA39 sand are presented on Figures 7-23 and 7-24 along with ICP04 the equivalent NE34 test. As with the shear stresses, the raw GA39 measurements fall below the NE34 trends, reflecting the less dense sand and

lower q_b. The normalised plots also match more closely but show the same trend as the shear stresses and greater divergence during the stationary pause periods. Assuming that normalisation with q_b accounts for differences in the initial state of the sands, the relatively rapid degradation of σ'_r with h/R in otherwise identical tests may indicate higher susceptibility in the looser and finer GA39 sand to stress relaxation and/ or cyclic loading.

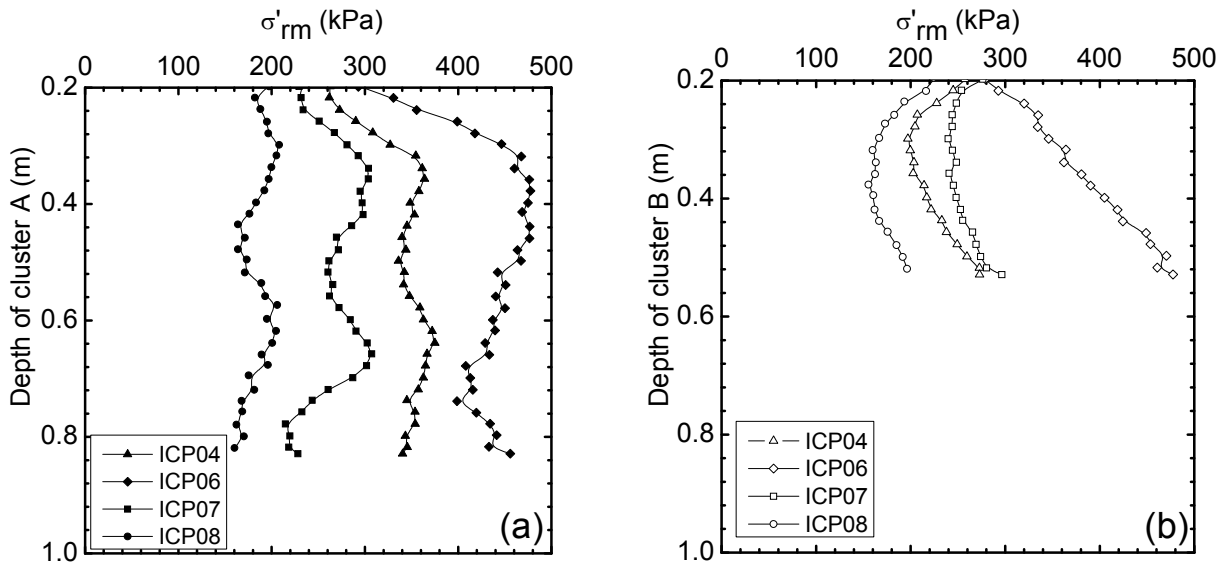


Figure 7-18: Interface moving local radial stresses at cluster (a) A and (b) B from the Mini–ICP in NE34 sand.

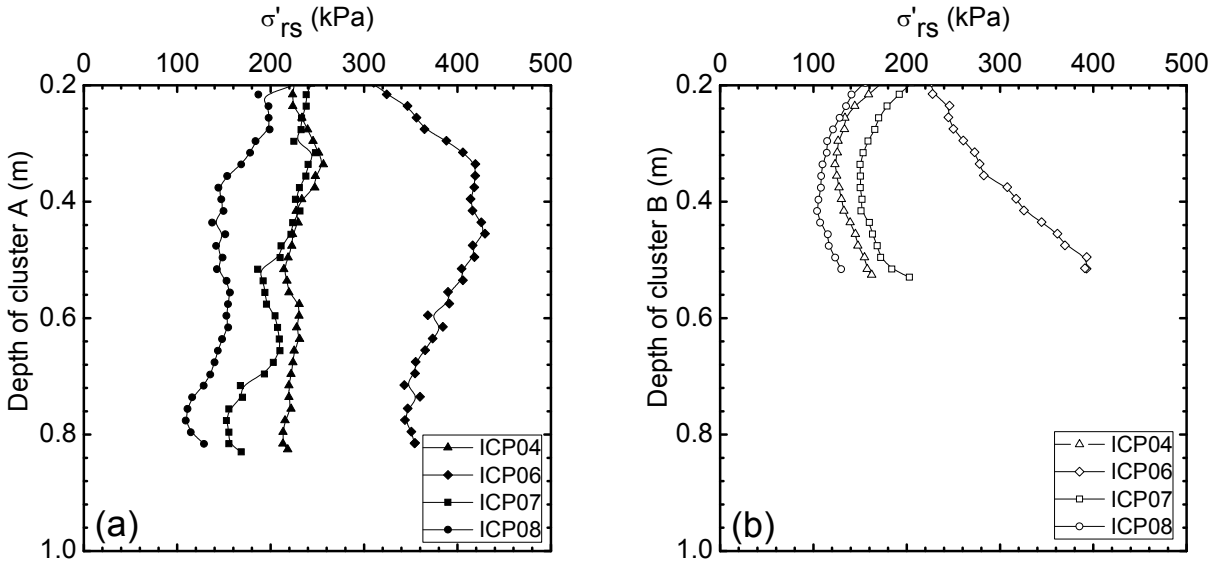


Figure 7-19: Interface stationary local radial stresses at cluster (a) A and (b) B from the Mini-ICP installed in NE34 sand.

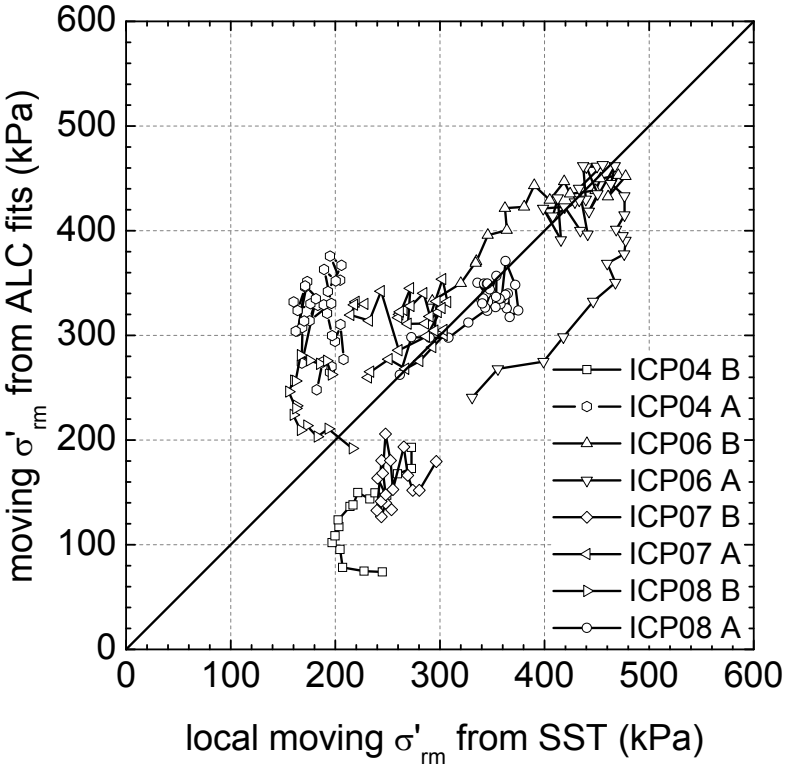


Figure 7-20: Interface moving radial stresses from the Mini-ICP clusters versus from ALCs axial loads polynomial fits.

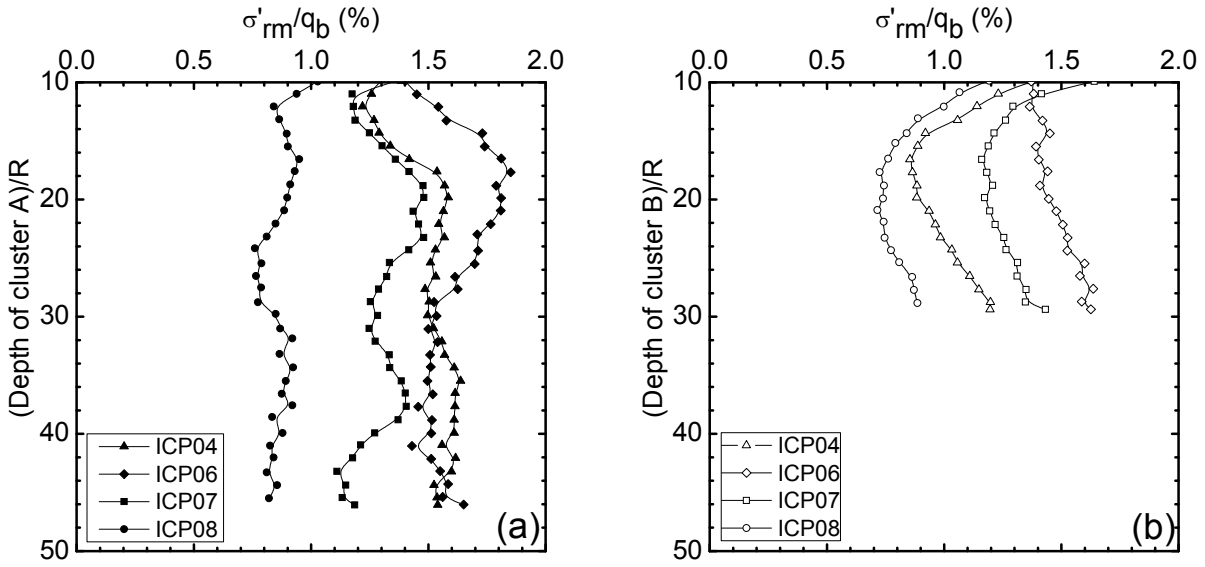


Figure 7-21: q_b–normalised interface local moving radial stresses at clusters (a) A and (b) B from the Mini-ICP installed in NE34 sand.

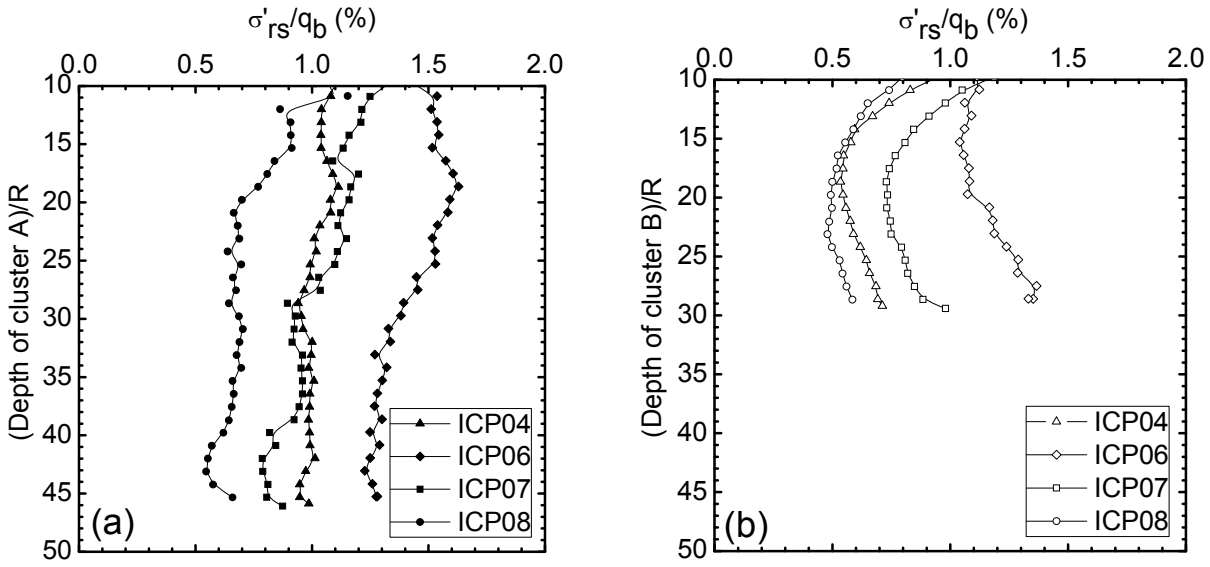


Figure 7-22: q_b–normalised interface local stationary radial stresses at clusters (a) A and (b) B from the Mini-ICP installed in NE34 sand.

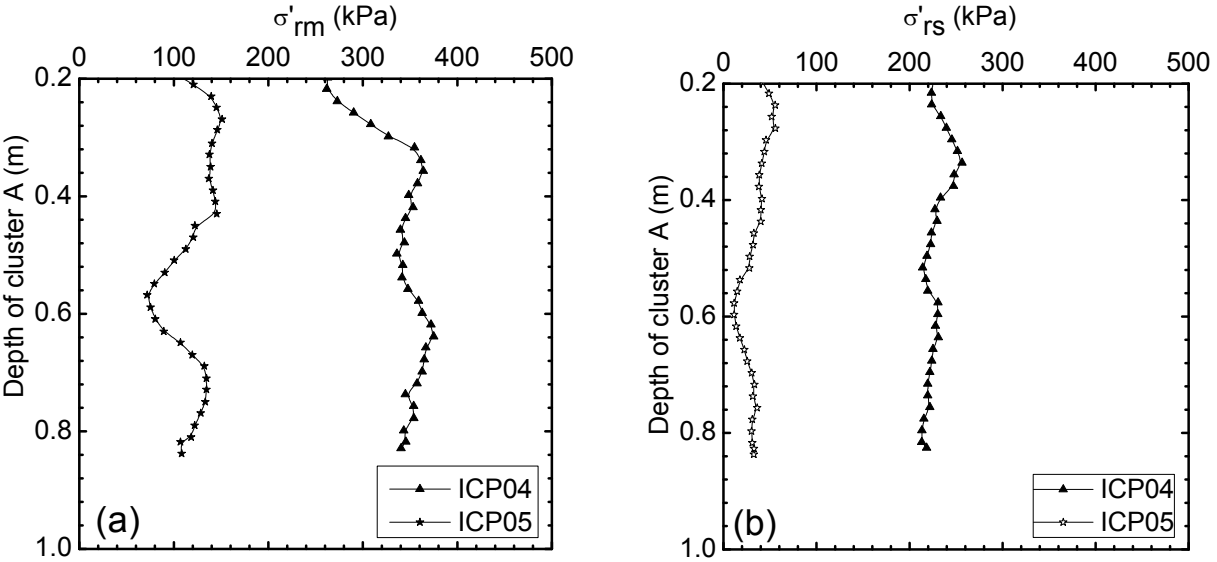


Figure 7-23: Interface local radial stresses from Mini–ICP cluster A installed in dry GA39 sand compared to that in dry NE34 sand (a) moving (b) stationary.

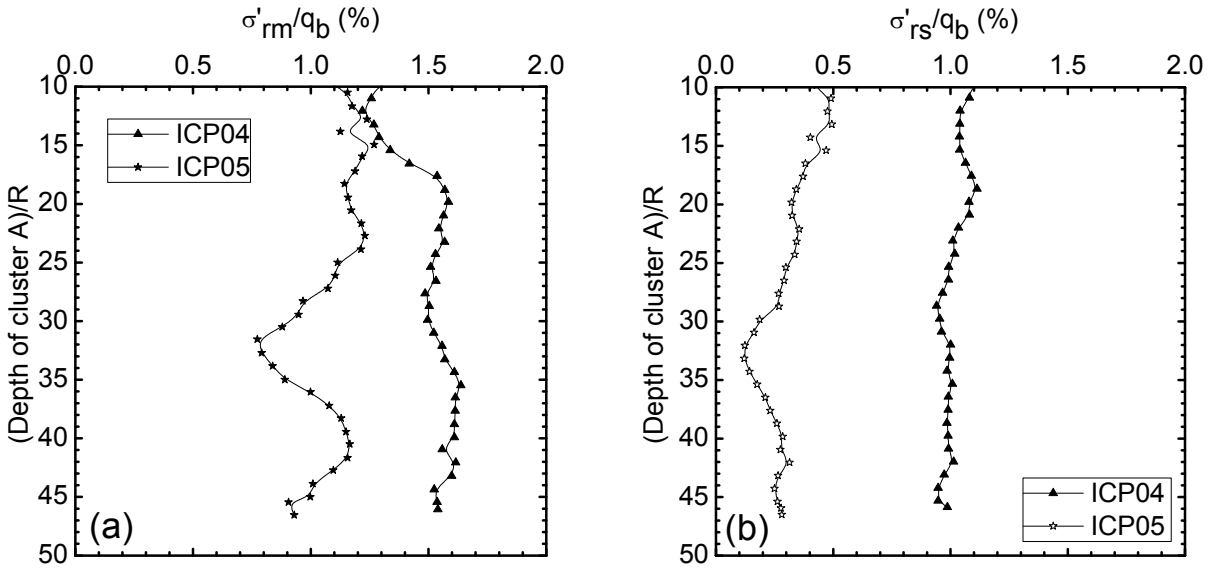


Figure 7-24: q_b–normalised interface local radial stresses from Mini–ICP cluster A installed in dry GA39 sand compared to that in dry NE34 sand (a) moving (b) stationary.

7.4 Stresses developed in the sand mass during pile installation

7.4.1 Stress measurements

Earlier studies by Jardine et al. (2013b) using the same equipment have confirmed the stresses developed in the soil mass around a single cylindrical displacement pile can be expressed as

$$\sigma'/q_c = f\,(h/R,\ r/R,\ \sigma'_{z0}/p_a) \qquad 7\text{-}1$$

where r/R is the relative radial distance out from the pile axis into the sand mass, h/R is the relative height above (positive) or below (negative) the pile base, σ'_{z0}/p_a is the vertical effective stress normalised by the atmospheric pressure, p_a, and the stresses, either radial, vertical or hoop (σ'_r, σ'_z, σ_θ) are normalized by the local end-bearing resistance (q_c or q_b). This finding is compatible with the ICP-05 method (Jardine et al. 2005a) which recommends equation 7-2 to calculate the stationary local radial stress on the pile shaft (r/R = 1).

$$[\sigma'_r/q_c]_{r/R=1} = f(h/R,\ \sigma'_{z0}/p_a) = 0.029(\sigma'_{z0}/p_a)^{0.13}(h/R)^{-0.38} \qquad 7\text{-}2$$

The sand instrumented tests had miniature stress sensors deployed at the various configurations described in Chapter 5 and these tracked the radial, vertical and circumferential stresses during pile installation. Following the nomenclature applied to the stresses on the pile shaft, the sand mass stresses are referred to as moving or stationary as illustrated on Figure 7-25. Figure 7-26 shows exemplar profiles from test ICP07 of radial stress measured at radial distances 2R, 3R, 5R and 8R (R = installed pile radius) from the pile axis 0.46m below ground and plotted against pile base depth. The complex stress sensor data reduction operations accounted for the sensors' cell–action effects by applying the calibration procedures detailed in Chapter 5. Full details of the in-sand stress measurements made with multiple individual sensors in all test series are summarised in Appendix III where for each of the vertical (σ'_z), radial (σ'_r) and circumferential/ hoop (σ_θ) stress cells, the stress changes developed during jack stroke installations vary strongly relative to the depth of the pile base compared to the instrument position. Noting that not all gauges survived installation, the following general observations follow from Figure 7-26 and the many equivalent plots in Appendix III.

1) There is a clear concentration of radial, vertical and hoop stresses around the pile base as exhibited by the stress build–up as the base approaches from above, peaks, and then declines as the base goes beyond the sensor level.

2) The moving σ'_m and stationary stresses σ'_s defined at the push and pause stages of each jack stroke vary considerably with the difference (σ'_m - σ'_s) being a maximum as the pile base approaches the sensor levels, h/R ≈ 0.
3) The stationary and moving stresses developed around the pile at any level generally diminish with radial distance (r/R) from the pile axis.
4) Several vertical and radial stress measurements radially away from pile (r/R > 3) showed greater stress increase than the near ones when the pile base was approaching and still above the stress sensor level. This was followed by the stress sensors nearer the pile registering higher stresses as the base drew closer to the sensors level.
5) The maximum radial stresses observed with the gauges deployed were typically greater than the maximum vertical stresses which were in turn greater than the circumferential stresses at the level. It is likely that gauges deployed under the pile centreline would have displayed a different pattern with $\sigma'_z > \sigma'_r = \sigma_\theta$.
6) On several occasions vertical stress measurements showed two maxima, with the first (and major) peak developing as pile tip approaches the sensor level, followed by a less marked recovery at h/R > 0.
7) The sand stresses developed in ICP05 (with the less dense and finer GA39 sand) are far lower than those in the medium dense–to–dense NE34 sand
8) The overall survival rate of all the sand stress sensors deployed amounted to 86% per test, with the lowest survival rate applying to the hoop stress sensors. Redundancy in the sensors deployed in each sand chamber helped in establishing representative stress trends from the scattered measurements.

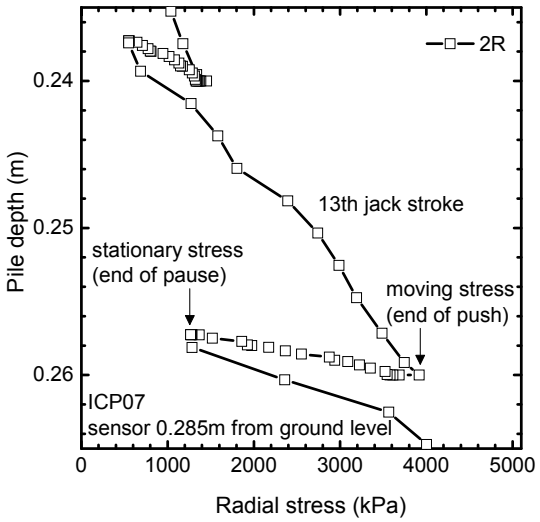


Figure 7-25: End–of–push moving stresses and end–of–pause stationary stresses illustrated by ICP07 test radial stress sensor at r = 2R, z = 15.8R in 152kPa surcharged dry NE34 with boundary condition BC5.

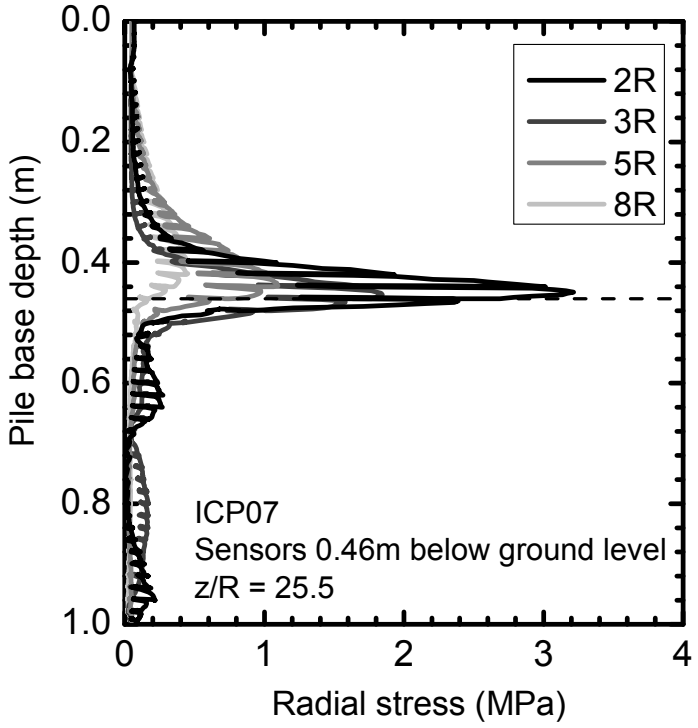


Figure 7-26: Sand mass radial stress sensors profiles during Mini-ICP07 installation into 152kPa surcharged dry NE34 with boundary condition BC5.

7.4.2 Sand mass stress profiles along the Mini-ICP pile axis

The stress response of the sand mass is analysed by separating the moving and stationary data sets as defined in Figure 7-25. Moving and stationary stress profiles were developed and normalised by the local q_b measured at the level of the sensors. Noting from the introduction that we expect the stresses to vary (when σ'_{z0} is practically constant in the chamber where the sand self-weight vary by no more than 3.79kPa between the instrument levels) as $\sigma'/q_b = f(r/R, h/R)$. On the same note, with the surcharge applied in these tests, $\sigma'_{z0} = 152$kPa, the term $[\sigma'_{z0}/P_a]^{0.13}$ is close to unity (1.05 for $p_a = 100$kPa).

The radial, vertical or hoop stresses at particular r/R distance from the pile axis, but at different levels in the sand mass, were synthesized by plotting their q_b ratios against the normalised vertical distance between the sensor and the pile base, as in for example Figure 7-27, h/R being negative when the pile base is above the sensor and positive when the base lies below the sensor level. The sensors positioned at shallow depths have a larger portion of data points in the $h/R > 0$ region than those positioned deeper. Assuming that equation 7-2 holds, the profiles from individual sensors positioned at various levels can be combined to a single normalised plot against h/R at a given r/R, to give a single set of profile plotted in the h/R – r/R plane.

A simple procedure was used to synchronise and combine the profiles from the different levels of sensors. Following Jardine et al. (2013b), the h/R positions at which each of the sensors registered the maximum moving or stationary stresses were averaged to obtain a mean h/R position, *y*, at which the stress maximum developed for each r/R. The h/R co-ordinates of the normalised stress profiles (for a given r/R) from each of the sensors were then translated vertically by the amounts to eliminate positioning errors and allow the maximum stresses to develop at the same value, *y*. A mean envelope of the normalised stresses was then derived for each r/R value and treated as the most representative overall test output for that r/R position and stress component.

Figures 7-28 to 7-31 show the separate composite plots for the installation moving and stationary q_b–normalised radial stresses recorded in test series ICP04, ICP06, ICP07 and ICP08 with jack stroke installed Mini–ICPs; other equivalent stress component plots are presented in Appendix III. The following observations are made regarding the normalised radial stresses generated in the sand chamber during these installations;

1) The h/R effect is very clear in all installations. Stresses build to show maxima at all r/R values when the base has the same approximate depth as the sensor; stresses decay sharply as the base progresses below the sensor position with each further jack stroke.
2) The maximum moving and stationary stresses decay with radial distance from pile. While radial stress maxima are observed at h/R ≈ 0 at low r/R, maxima develop marginally ahead of the pile tip at further r/R; that is at increasingly negative h/R ratios.
3) At any r/R the normalised radial stress profiles form tight bands within which effects of sand moisture conditions or the chamber lateral boundary conditions are hardly discernible.
4) Table 7-2 summarises the average and standard deviations of the normalised radial stresses developed at specific h/R and r/R positions from the four jack–stroke installed piles in NE34 sand. The three h/R values listed cover (a) the lowest ratio at which measurements were made (around -40) (b) the level at which the stress maxima developed ($-3.6 < h/R < 0$) and (c) at which most of the stress relaxation associated with continued penetration has taken place (h/R ≈ 15).
5) The average σ'_{rm} and σ'_{rs} in Table 7-2 show the same clear patterns. The moving and stationary stresses diminish with h/R above and below the pile base with radial distance r/R. They also show moving stresses well above the stationary stresses. The peak radial stresses develop progressively further in advance of the pile base as r/R increases, showing a geometrically spreading stress distribution emanating from the pile base.
6) The sand mass radial stresses tend to show little further stress changes from $h/R > 15$ after passing the sensor position; by which time 14 jacking cycles had been applied in most installations.

7) The data show significant scatter. Taking multiple measurements and performing careful averaging is essential to the deduction of reliable trends.

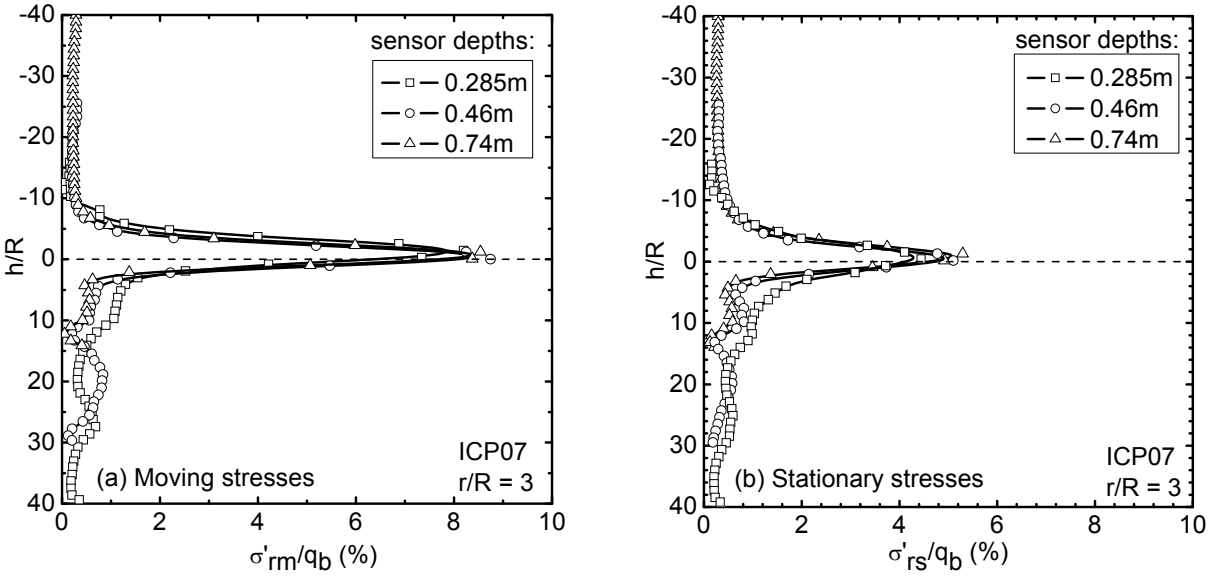


Figure 7-27: Test ICP07 radial stresses during Mini-ICP installation in dry NE34 sand at (a) end–of–push stages (moving stresses), and (b) end–of–pause stages (stationary stresses).

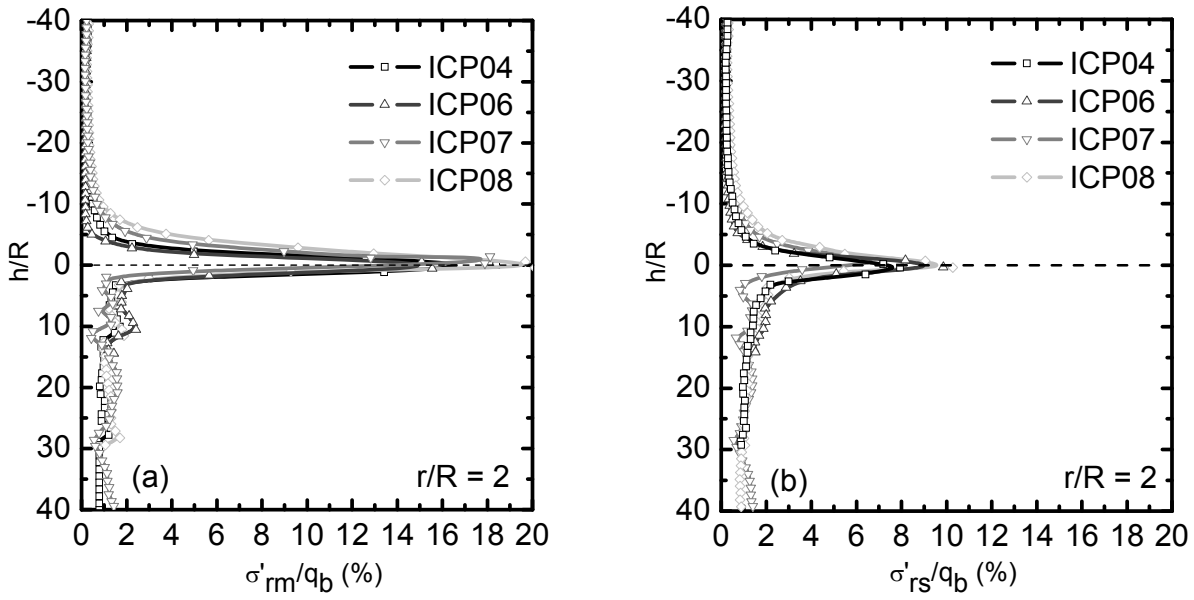


Figure 7-28: Normalised radial stresses at r/R = 2 for jack–stroke installed displacement piles in NE34 sand (a) moving (b) stationary stages.

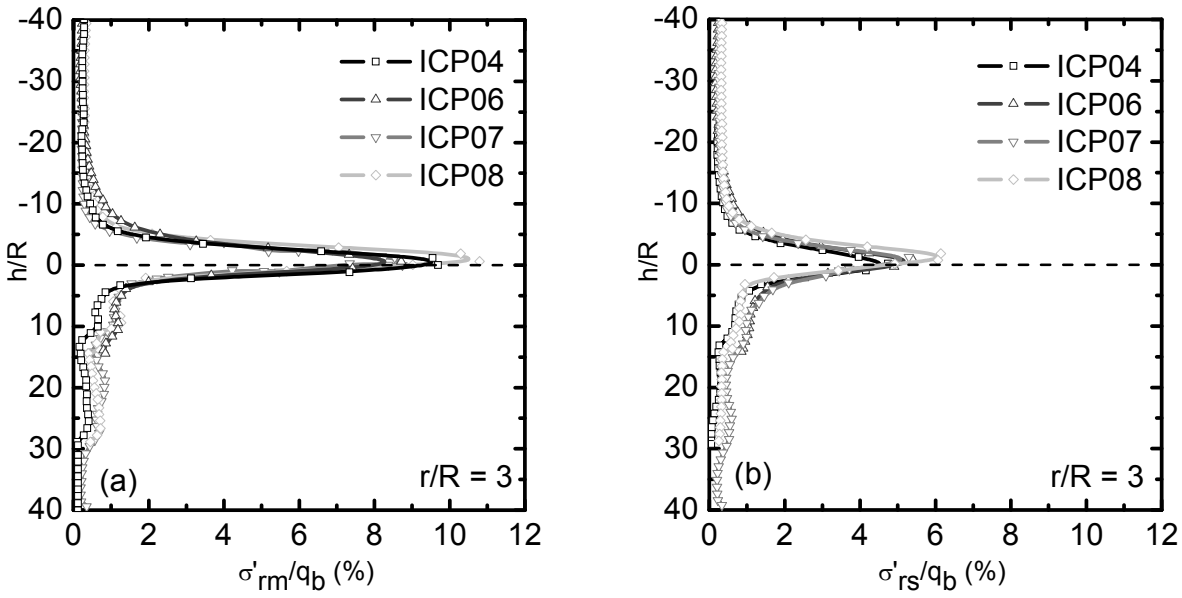


Figure 7-29: Normalised radial stresses at r/R = 3 for jack–stroke installed displacement piles in NE34 sand (a) moving (b) stationary stages.

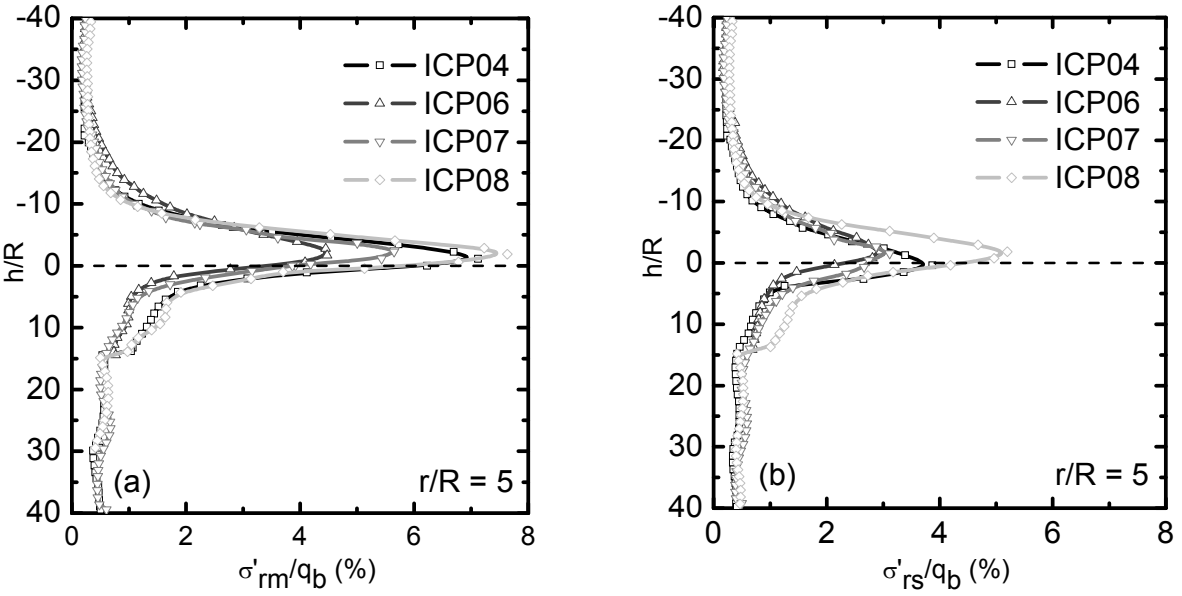


Figure 7-30: Normalised radial stresses at r/R = 5 for jack stroke installed displacement piles in NE34 sand (a) moving (b) stationary stages.

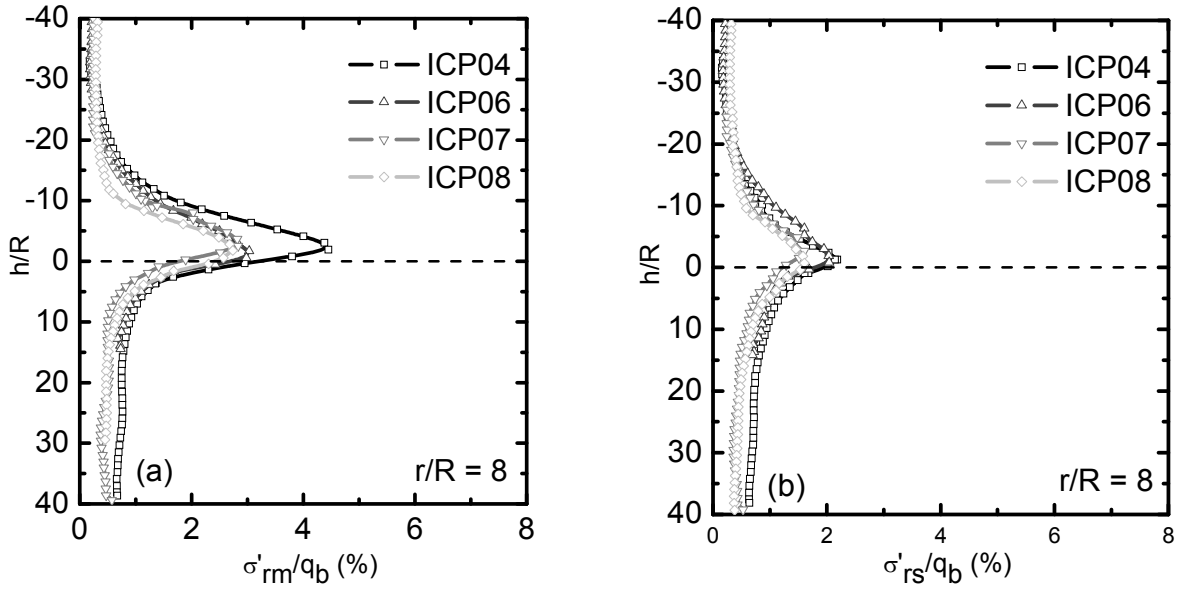


Figure 7-31: Normalised radial stresses at r/R = 8 for jack stroke installed displacement piles in NE34 sand (a) moving (b) stationary stages.

r/R	h/R	σ'_{rm}/q_b (%)			h/R	σ'_{rs}/q_b (%)		
		Mean	Std dev.	CoV		Mean	Std dev.	CoV
2	-40.82	0.26	0.04	0.15	-40.69	0.26	0.04	0.15
	-0.39	17.92	2.09	0.12	0.03	8.63	1.67	0.19
	15.03	1.16	0.20	0.17	13.21	1.21	0.29	0.24
3	-40.82	0.28	0.04	0.15	-25.40	0.27	0.05	0.17
	-0.72	8.36	1.63	0.19	-1.02	5.18	0.88	0.17
	12.39	0.69	0.48	0.70	13.21	0.68	0.32	0.46
5	-40.84	0.27	0.05	0.18	-40.69	0.27	0.05	0.18
	-2.65	5.87	1.32	0.22	-1.08	3.57	0.96	0.27
	14.88	0.73	0.23	0.31	13.63	0.72	0.22	0.31
8	-40.48	0.27	0.04	0.16	-26.51	0.25	0.04	0.15
	-3.62	3.04	0.96	0.31	-2.19	1.78	0.35	0.20
	14.82	0.62	0.15	0.23	14.04	0.65	0.16	0.24

Table 7-2: Average normalised radial moving and stationary stresses around jack–stroke installed displacement piles in NE34 sand chamber.

Experiment ICP05 employed the finer GA39 sand (with BC3 boundary condition) and increased the pile–to–particle diameter ratio from 171 with NE34 to 283. Although the aim had been to keep the density state constant, the GA39 sand mass was considerably looser at the end of testing (Table 7-1), leading to the lower q_b trace reported in Figure 7-2 and sand mass stresses, although normalisation reduces the disparity with the NE34 tests, as shown in Figures 7-32 to 7-34. No successful σ'_r measurements were made at r/R = 2 in ICP05. However, the moving σ'_r/q_b ratios

at r/R = 3 to 8 gave reasonably similar normalised profiles for the GA39 and NE34 sands. The maximum σ'_r/q_b ratios are close and developed at similar stages, although the moving and stationary GA39 σ'_r/q_b ratios tend to be lower at higher (positive) h/R. Assuming that normalisation with q_b accounts for differences in the initial state of the sands, the relatively rapid degradation of σ'_r with h/R in otherwise identical tests may indicate higher susceptibility in the loose GA39 sand to stress relaxation and/ or cyclic loading. Comparable differences between on–pile stress measurements made with GA39 and NE34 sand were discussed in Section 7.3.

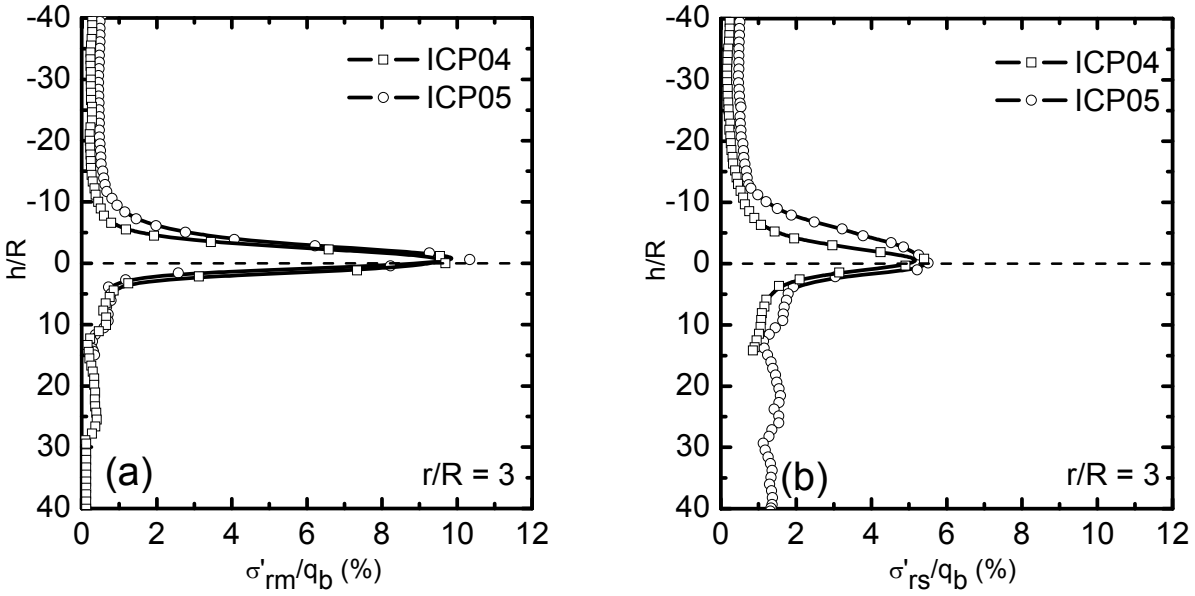


Figure 7-32: Radial (a) moving and (b) stationary stresses at r/R = 3 for cyclically jacked piles in dry GA39 sand (ICP04) compared to dry NE34 sand (ICP04).

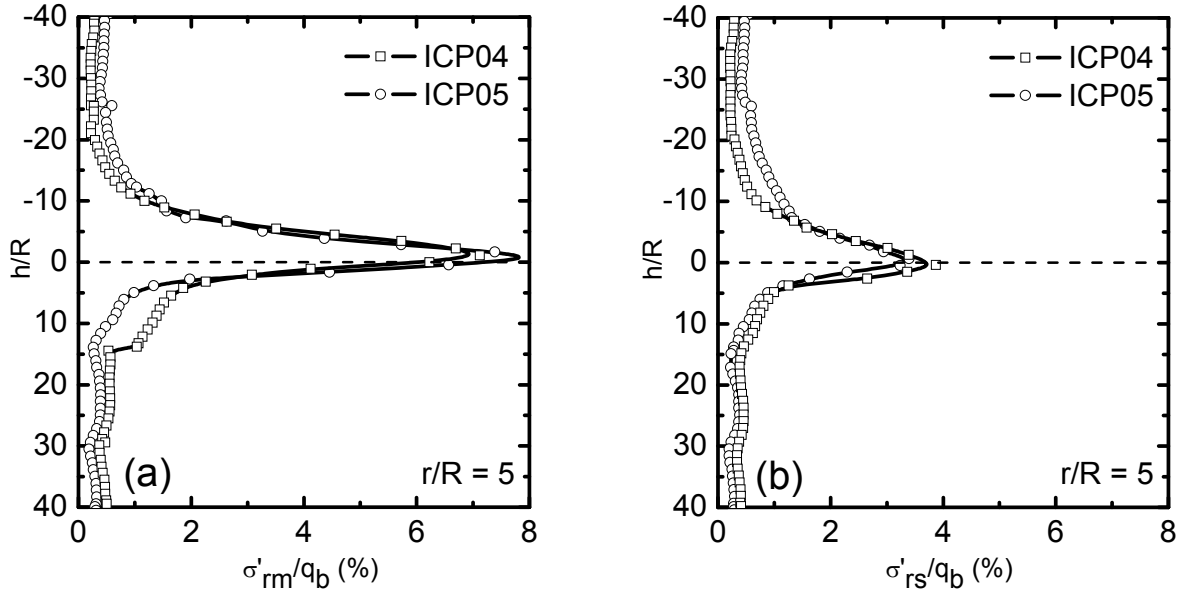


Figure 7-33: Radial (a) moving and (b) stationary stresses at r/R = 5 for cyclically jacked piles in dry GA39 sand (ICP04) compared to dry NE34 sand (ICP04).

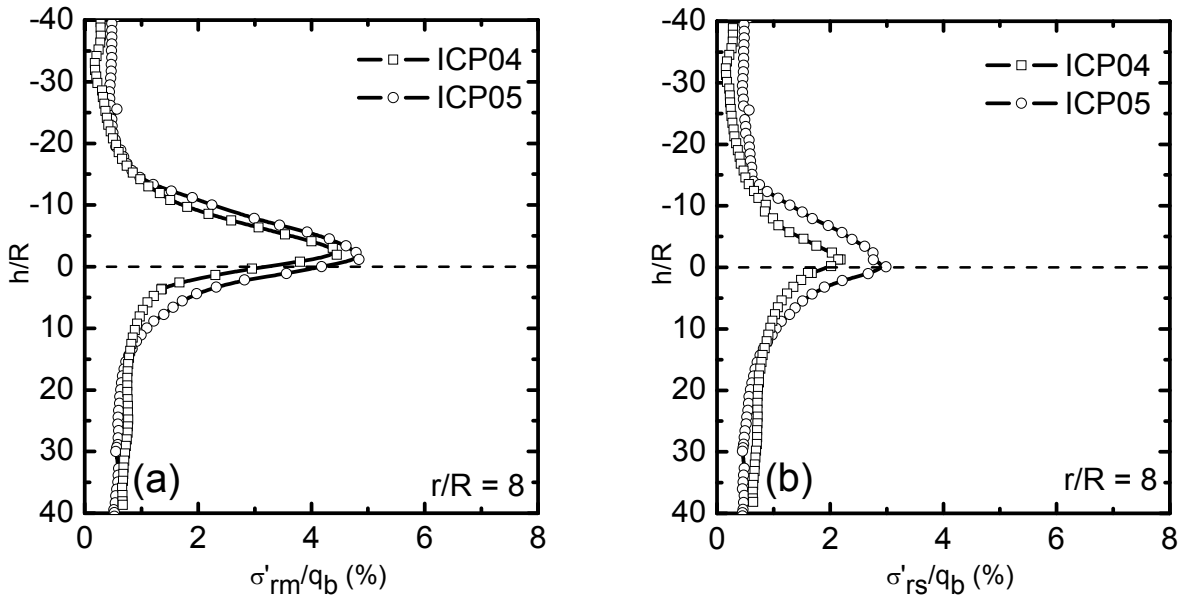


Figure 7-34: Radial (a) moving and (b) stationary stresses at r/R = 8 for cyclically jacked piles in dry GA39 sand (ICP04) compared to dry NE34 sand (ICP04).

7.4.3 Contouring the sand mass stresses around the Mini–ICP piles

The h/R – q_b–normalised stress profiles determined at various r/R can be combined into 2-D stress contour plots established in the h/R and r/R plane that describe the spatial variation of the stresses around the installing pile tip, Jardine et al. (2013b). The contouring procedure involves collating the normalised best–fitting average profiles for each r/R into a 3–D profile of (r/R, h/R, σ'/q_b) dataset as shown in Figure 7-35. The collated profile is converted to a matrix using Renka-Cline random gridding method followed by contour plotting as shown for the normalised moving and stationary radial stresses plotted from ICP04 in Figures 7-36 and 7-37. Similar processing and plotting led to the vertical and hoop stresses contour plots for test ICP04 as shown on Figures 7-38 to 7-41. Similar sets for the finer and looser GA39 sand single test are presented in Figure 7-42 to 7-47. The following further observations on the stress regimes developed around the piles in both sands are made from the contour plot.

1) High radial stresses concentration around the pile base with $\sigma'_{rm}/q_b > 14\%$ and $\sigma'_{rs}/q_b > 6\%$ at $r/R \leq 2$ which rapidly attenuates to $\sigma'_r/q_b < 1\%$ within 10R around the pile tip.
2) Vertical stresses contours geometrically spread ahead of the pile base from a focus at about h/R = -1 to -3 ahead of the pile with $\sigma'_{zm}/q_b > 10\%$ and $\sigma'_{zs}/q_b > 4\%$ at r/R < 2 which attenuates radially around the pile base to $\sigma'_z/q_b < 2\%$ within 10R.
3) Hoop stresses exhibit similar patterns to the vertical stresses, but with much lower stresses which show $\sigma_\theta/q_b > 2\%$ at r/R = 3 attenuating to < 1% rapidly with r/R for both moving and stationary stresses around the pile base position.

4) The greater stress gradients across the contours behind the pile base (h/R > 0) in test ICP05 compared to ICP04 reinforces GA39 sand's relatively higher susceptibility to the cyclic loading compared to NE34 sand.

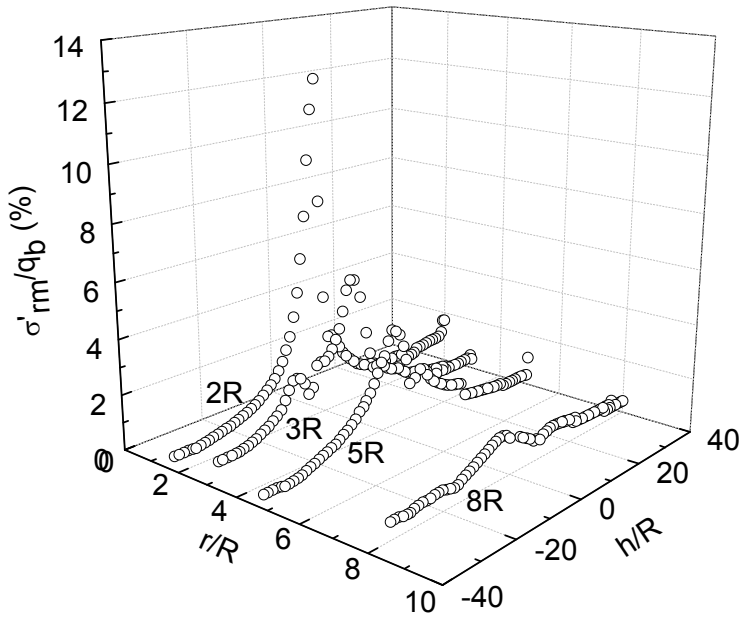
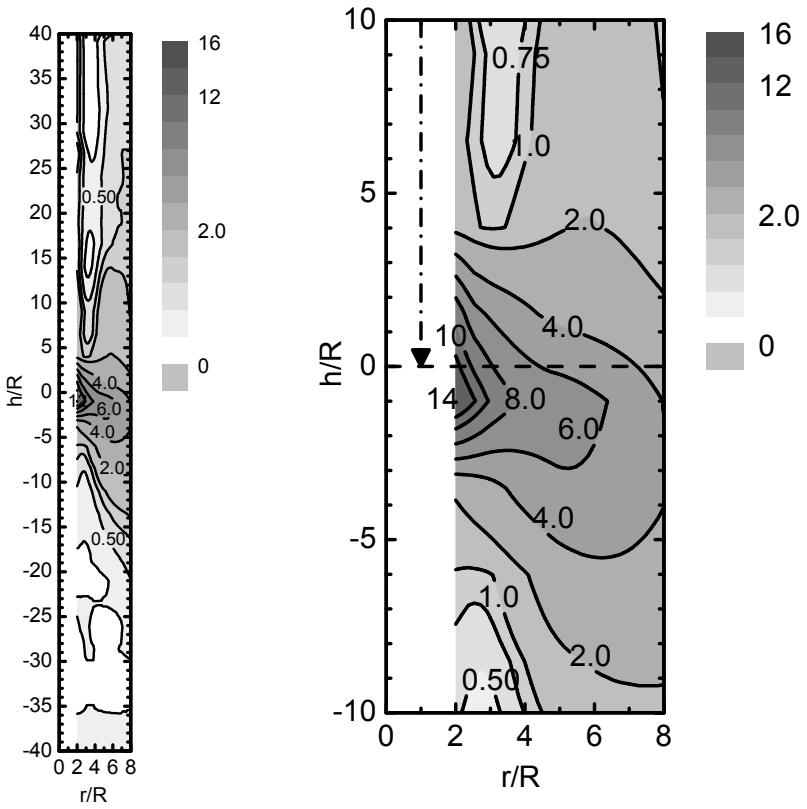
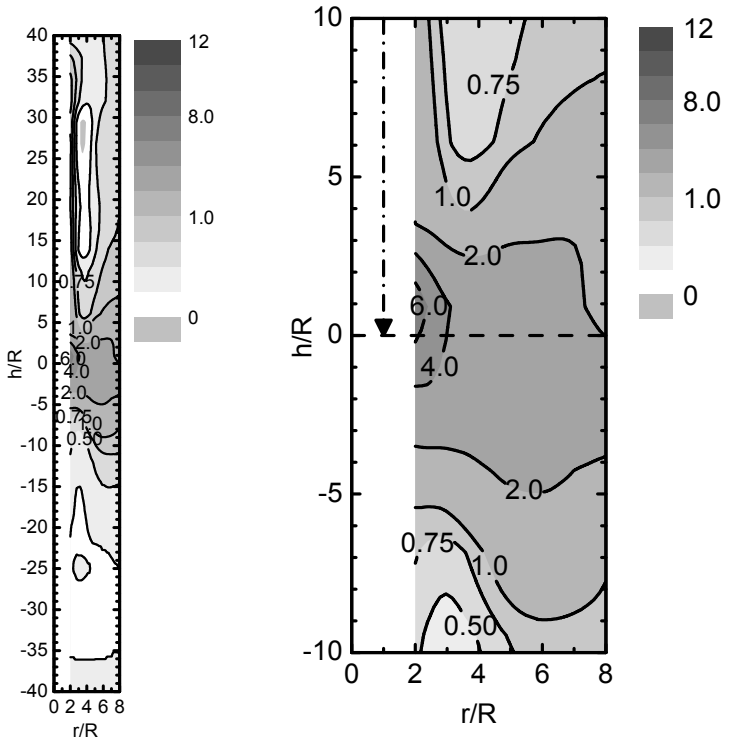


Figure 7-35: Exemplar 3D profile of normalised moving radial stresses for cyclically jacked Mini–ICP04 in dry NE34 sand.



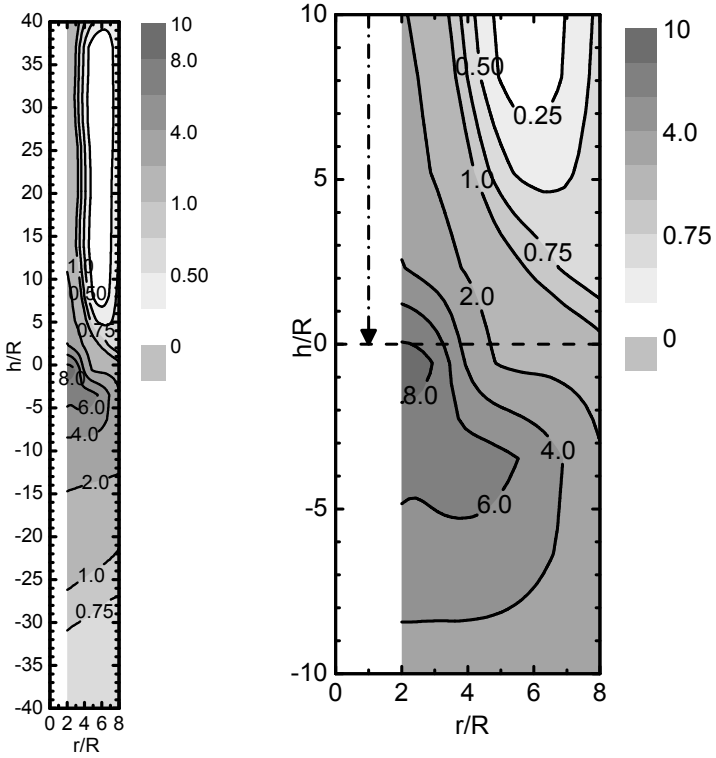
(a) (b)

Figure 7-36: Normalised moving radial stress contours σ'_{rm}/q_b in % around jack–stroke installed Mini-ICP test ICP04 with dry NE34 sand (a) full length (b) near pile base.



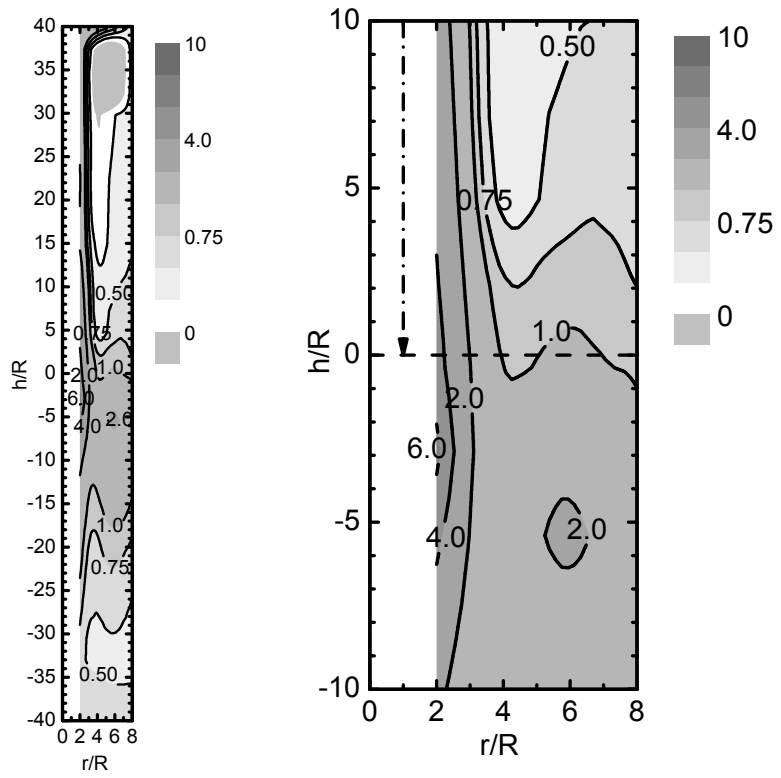
(a) (b)

Figure 7-37: Normalised stationary radial stress contours σ'_{rs}/q_b in % around jack–stroke installed Mini-ICP test ICP04 with dry NE34 sand (a) full length (b) near pile base.



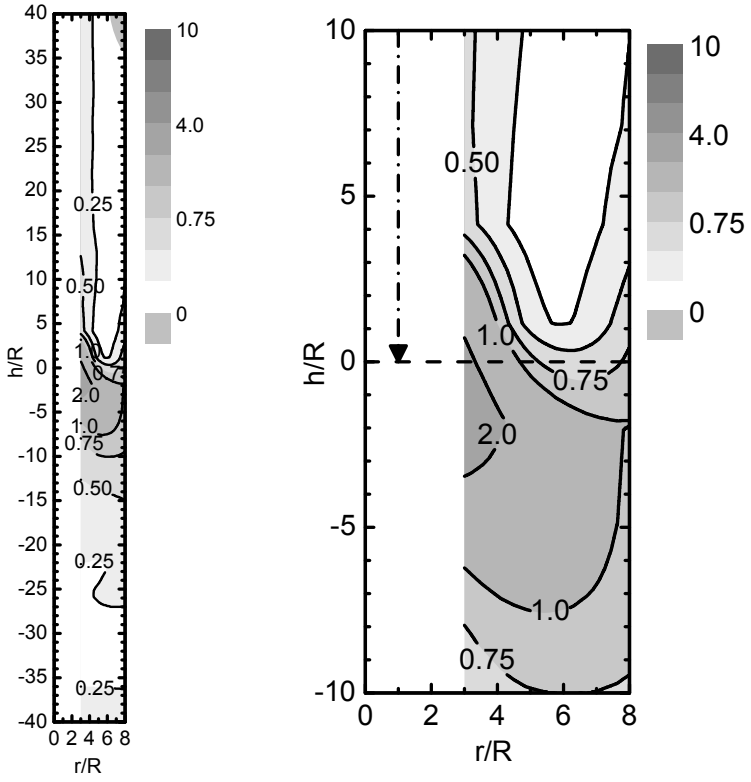
(a) (b)

Figure 7-38: Normalised moving vertical stress contours σ'_{zm}/q_b in % around jack–stroke installed Mini-ICP test ICP04 in dry NE34 sand (a) full length (b) near pile base.



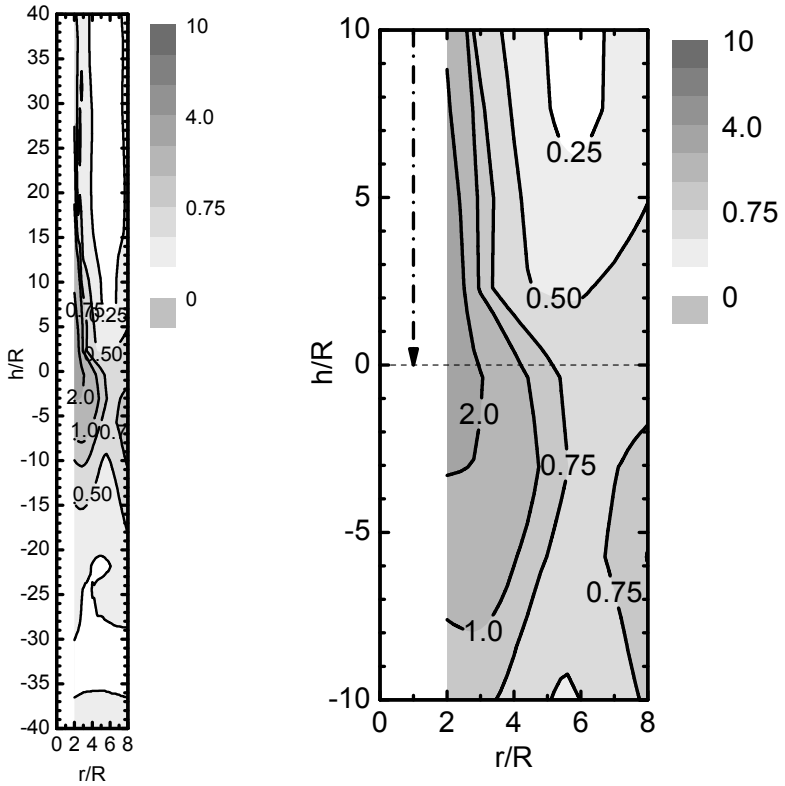
(a) (b)

Figure 7-39: Normalised stationary vertical stress contours σ'_{zs}/q_b in % around jack–stroke installed Mini-ICP test ICP04 in dry NE34 sand (a) full length (b) near pile base.



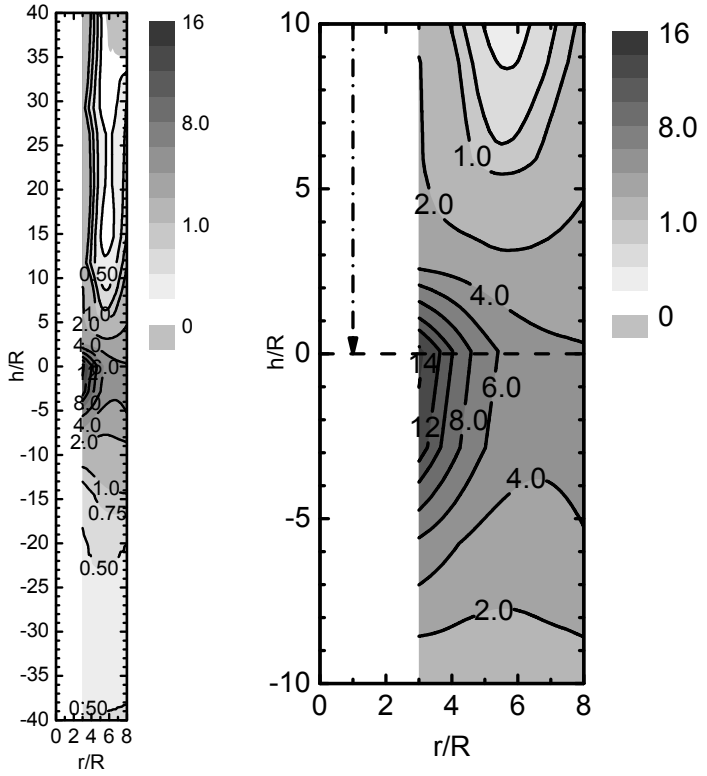
(a) (b)

Figure 7-40: Normalised moving hoop stress contours $\sigma_{\theta m}/q_b$ in % around jack–stroke installed Mini-ICP test ICP04 in dry NE34 sand (a) full length (b) near pile base.



(a) (b)

Figure 7-41: Normalised stationary hoop stress contours $\sigma_{\theta s}/q_b$ in % around jack–stroke installed Mini-ICP test ICP04 in dry NE34 sand (a) full length (b) near pile base.



(a) (b)

Figure 7-42: Normalised moving radial stress contours σ'_{rm}/q_b in % around jack–stroke installed Mini-ICP test ICP05 in dry GA39 sand (a) full length (b) near pile base.

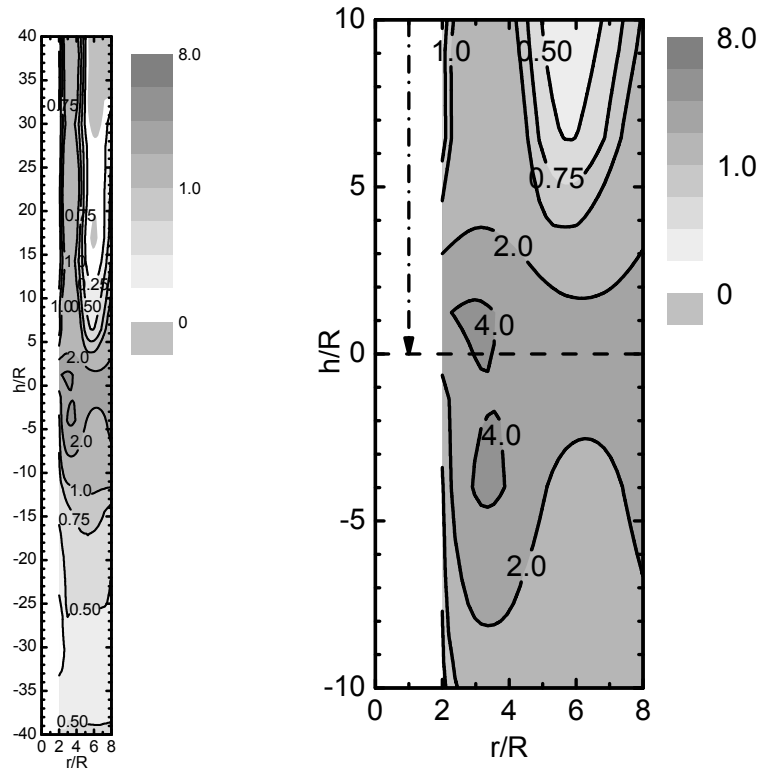


Figure 7-43: Normalised stationary radial stress contours σ'_{rs}/q_b in % around jack–stroke installed Mini-ICP test ICP05 in dry GA39 sand (a) full length (b) near pile base.

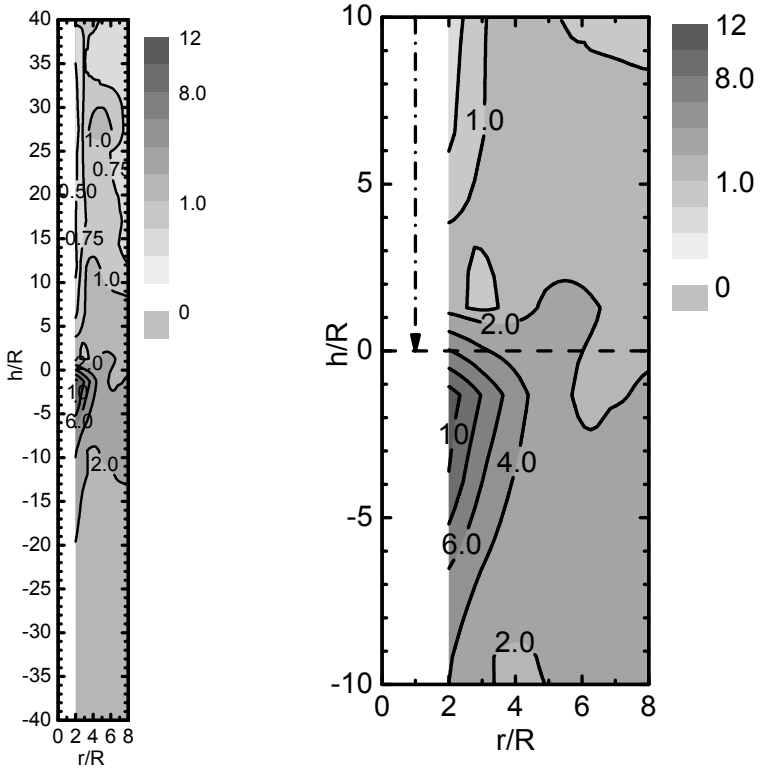
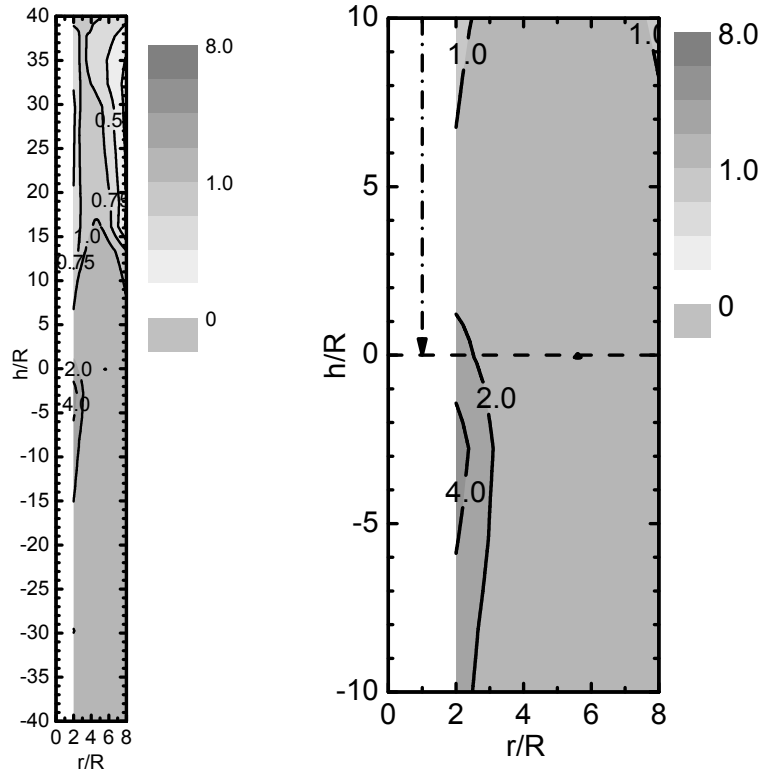
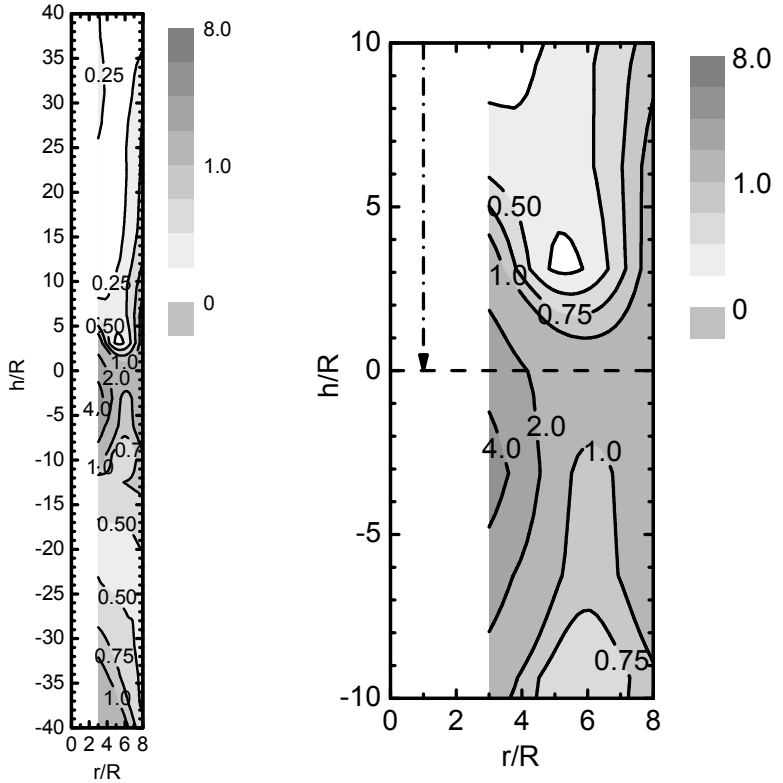


Figure 7-44: Normalised moving vertical stress contours σ'_{zm}/q_b in % around jack–stroke installed Mini-ICP test ICP05 in dry GA39 sand (a) full length (b) near pile base.



(a) (b)

Figure 7-45: Normalised stationary vertical stress contours σ'_{zs}/q_b in % around jack–stroke installed Mini-ICP test ICP05 in dry GA39 sand (a) full length (b) near pile base.



(a) (b)

Figure 7-46: Normalised moving hoop stress contours $\sigma_{\theta m}/q_b$ in % around jack–stroke installed Mini-ICP test ICP05 in dry GA39 sand (a) full length (b) near pile base.

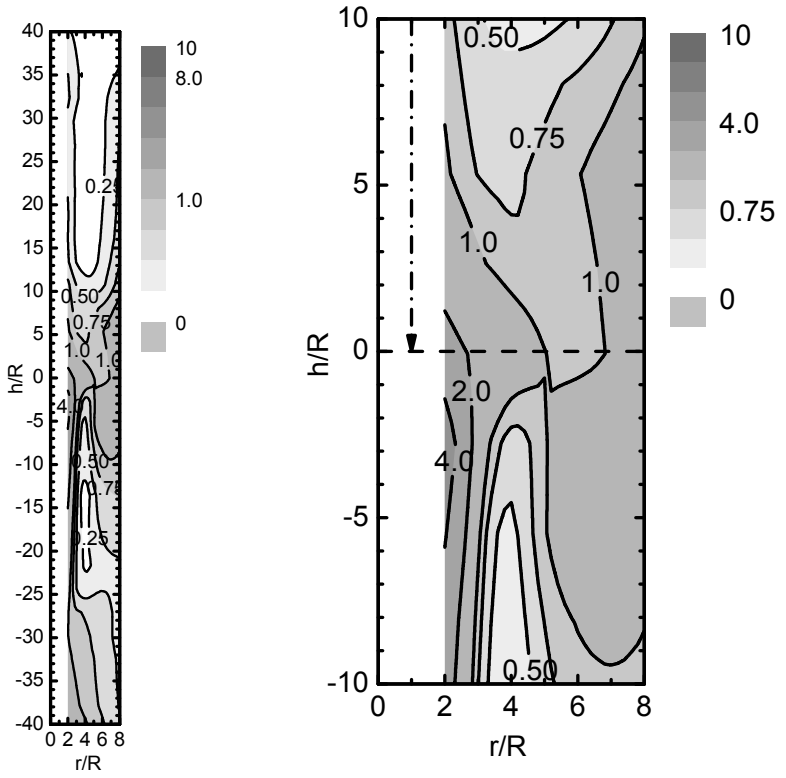


Figure 7-47: Normalised stationary hoop stress contours $\sigma_{\theta s}/q_b$ in % around jack–stroke installed Mini-ICP test ICP05 in dry GA39 sand (a) full length (b) near pile base.

7.4.4 Radial variation of radial stresses at fixed depths above Mini-ICP pile tip

The sand mass stress contours around the Mini-ICP piles show maximum installation stresses during moving or stationary in the vicinity of the pile base. Radial profiles of q_b–normalised maximum moving radial stresses developed in the NE34 sand mass are plotted at the pile tip position (h/R = 0) against r/R distance in Figure 7-48.

The maximum radial stress σ'_{rm}/q_b = 29.7% plotted at the pile base position is estimated from drained triaxial compression tests assuming an active failure region with ($\sigma'_1 = q_b$, $\sigma'_3 = k_A\sigma'_1$ and $K_A = \tan^2(45–\varphi'_{cs}/2)$ with φ'_{cs} for NE34 sand = 32.8°). The radial stresses taken at the chamber boundary (r/R = 33) are those measured through the membranes water pressures rises seen during installation. A hyperbolic fit of the normalised sand mass radial stresses shows a monotonic stress decay from the 29.7% of q_b at r/R = 1 to 2% q_b within 10R around the pile.

Figure 7-49 plots the q_b normalised end–of–installation radial stresses measured in the near pile region, 1 < r/R < 8. The sand mass stresses interpreted for four h/R values over r/R = 2 – 8 were measured by the sand stresses sensors (typically located at h/R = 14.4, 29.4 and 40 behind the pile base) while the stresses plotted on the pile (r/R = 1) are those measured by the Mini–ICP SSTs clusters A (h/R = 8.94) and B (h/R = 25.61). Broad scatter bands are observed for each measurement position. Lower radial stresses band were established from tests ICP07 and ICP08

(with BC5 boundary conditions) where measured chamber boundary stresses were on average 30kPa greater than the initial pressurisation K_0 values of conditions 62.5kPa, ~0.44% q_b (based on $q_b \approx 21$MPa). Stress measurements below this limit were ignored in the Author's interpretation. The stress points suggest lower interface radial stresses at the pile face than those developed in the sand region relatively near to the shaft ($2 < r/R < 4$). The stresses attenuate away from the pile at $r/R > 4$. Interpreted hand drawn profiles are shown that recognise the 'h/R trend' observed at the shaft interface and shows stresses attenuating with both r/R and h/R beyond the observed maxima. Radial stress reductions are likely to develop higher up the pile shaft where greater cyclic degradation is experienced.

The circumferential stress sensors had the lowest survival rate which reduced the circumferential stresses dataset for interpretation and Jardine et al. (2013b) considered the circumferential stress measurements as the least reliable. Nevertheless, hand drawn profiles are fitted through the obtained circumferential stress measurements at the end of installation as shown on Figure 7-50.

The circumferential stresses are lower than the radial stresses throughout the r/R profiles at any particular h/R (see Figure 7-51) and the end–of–installation stress interaction expected between a radial stress peak in the sand mass being shielded by a near pile circumferential stress peak ($\sigma'_r < \sigma_\theta$) which has been proposed as a necessary mechanism for medium to long term capacity set-up is not established by measurement.

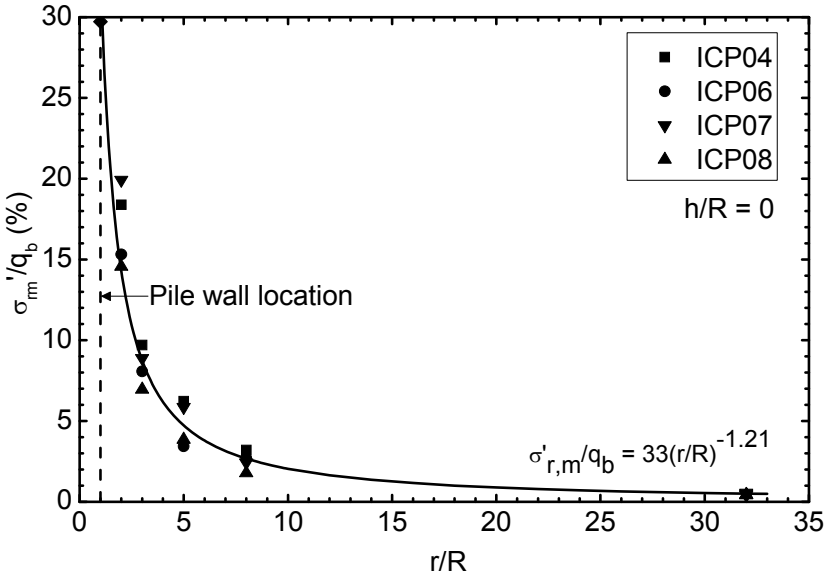


Figure 7-48: Normalised moving radial stress profile in the sand mass at h/R = 0 of jack–stroke installed Mini-ICP in NE34 sand.

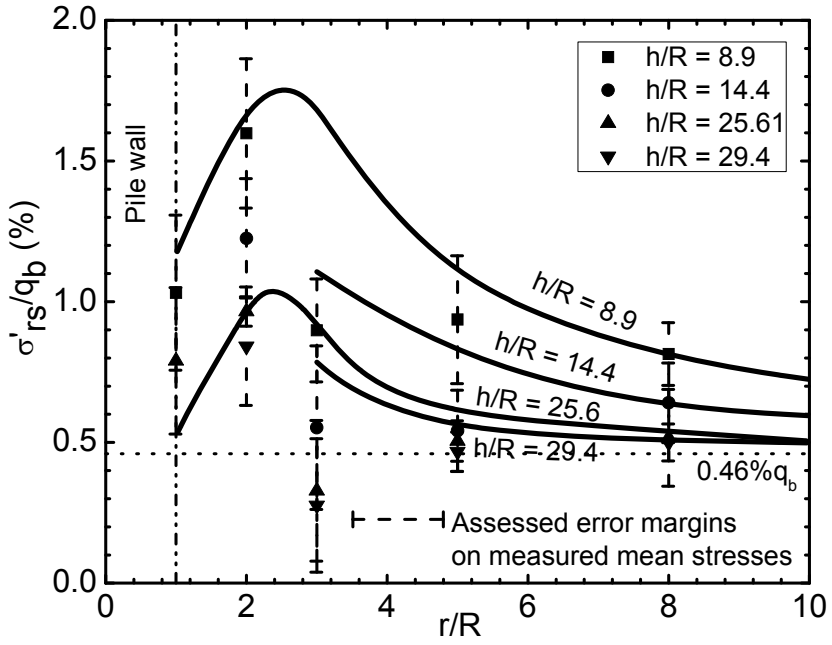


Figure 7-49: End–of–installation normalised radial stress profiles around the jack–stroke installed Mini-ICP piles in NE34 sand.

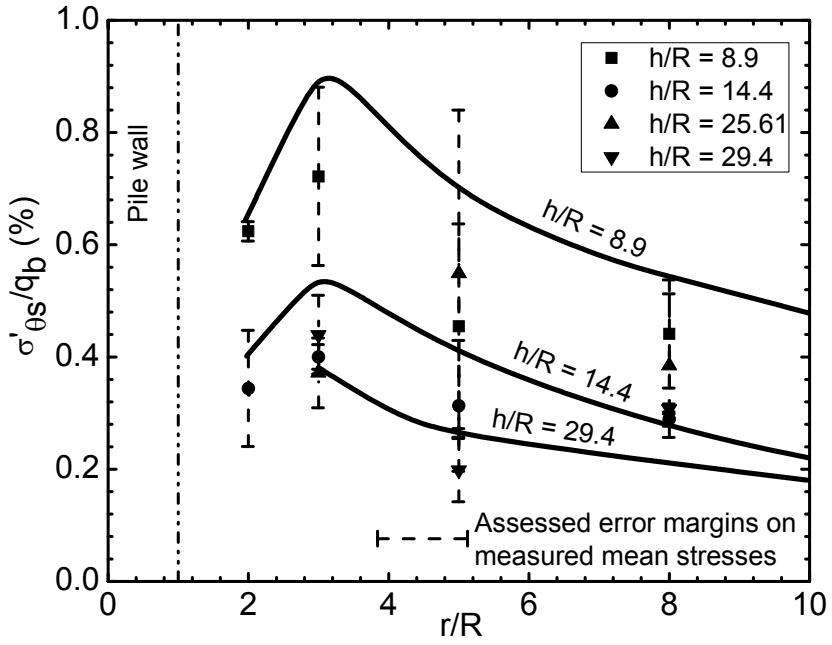


Figure 7-50: End–of–installation stationary circumferential stress profile around the jack stroke installed Mini-ICP piles in NE34 sand.

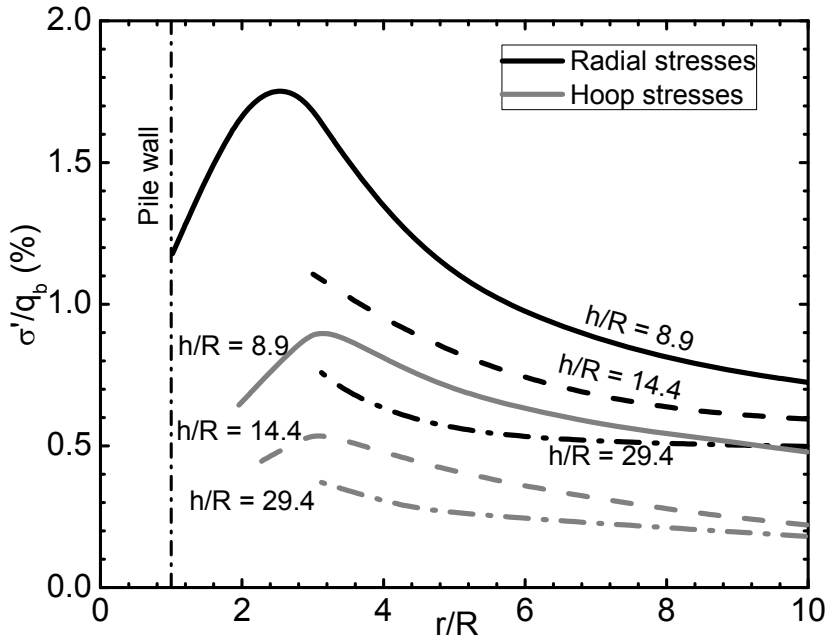


Figure 7-51: End of installation q_b normalised radial and circumferential stresses profiles interaction around the Mini-ICP piles installed in NE34 sand.

7.5 Summary conclusions and remarks

The following overall observations are made regarding the end-bearing resistances, pile interface stress and sand mass stress trends observed as the displacement model piles were installed in the silica sand calibration chambers.

1) Chamber boundary conditions effects were discerned on the q_c profiles despite the $d_{chamber}/D$ ratio (= 33.3) being typical of that used for CPT calibrations. Relatively high end–bearing resistances were observed with the rigid cell BC3 lateral boundary conditions in comparison with the BC5 conditions applied subsequently to better match free field conditions. Top boundary conditions influenced the shallow pile resistance profiles at shallow depths and penetration could not proceed beyond ~1m depth without 'sensing' the chamber base.
2) The sand mass ageing periods extending beyond 1 day did not appear to influence the behaviour of the penetrating piles, although more significant effects might apply after more extended ageing periods than those applied.
3) Piles installed in dense NE34 sand showed far higher end-bearing and shaft resistances than those observed in the looser and finer GA39 sand.
4) The end-bearing resistances developed in wet NE34 sand were greater than those in the dry sand, possibly due to either density increases or gas–water suctions developing in the chamber.
5) Residual base resistances isolated at the end–of–pause phases of each jack stroke accumulated with depth, without levelling off over the depths considered. Residual loads amounted to up to

30% of the maximum base resistances. These features underscore the potential for under–measurement of base capacity and over–estimation of the shaft capacity in uninstrumented pile capacity tests.

6) Shaft failure is governed by the Coulomb law. Interface stresses were influenced by the cyclic installation of the pile, as observed from the measurements of radial and shear stresses on pile clusters and contributing to the phenomenon referred to as 'h/R effect', following similar trends of behaviour to those reported from displacement pile field studies.
7) The different boundary conditions used led to different intensities of local interface stresses; those features were consistent with the intensities of the pile base resistances observed.
8) Normalisation of the interface and sand mass stresses around the pile by local q_c or q_b to allow for subtle differences in local stresses due to instrument configurations or variations in density states led to narrow bands of stress ratios for all measurements.
9) Far lower interface and sand mass stresses were developed in the finer less dense GA39 sand than in the denser NE34 sand. There was also evidence of higher susceptibility in the finer looser sand to cyclic effects.
10) The contoured interpretation shows clear concentration of radial, vertical and hoop stresses around the pile tip. For all stress components the stationary stresses σ'_s, moving stresses σ'_m and the difference between these two ($\sigma'_m - \sigma'_s$) are considerably higher around the pile tip and decay sharply below and above the tip, reflecting the h/R effects observed on the pile shaft.
11) The stationary radial stresses applying at the end of Mini-ICP piles installations decreased with h/R and showed local maximum in the $2 < r/R < 4$ range with lower stresses applying (radially) further away from the pile and towards the pile face.
12) Compatible profiles were interpreted for the stationary circumferential stresses applying at the end of installation, showing lower stresses to the radial measurements although reflecting a much sparser dataset.
13) The measured circumferential stresses remained lower than the measured radial stresses (see Figure 7-51). The end-of-installation necessary near pile stress condition ($\sigma'_r < \sigma_\theta$) proposed to explain the marked capacity set-up of field displacement piles in sands (Hypothesis (a) in section 3.2) could not be confirmed by measurement.

Chapter 8

8 Mini-ICP tests stress measurements compared to other studies

8.1 Introduction

Stresses measured around the four Mini-ICP piles installed in the instrumented NE34 sand chambers (ICP04, 06 to 08) have been compared to eight studies comprising of a field study, two calibration chamber studies, a centrifuge test and four numerical analysis studies. The comparison draws attention to similarities in the stresses interpreted around the displacement piles in sand as well as offering potential explanations for some observed differences. The work partially draws on the work reported by Yang et al. (2013), in which the Author collaborated, and earlier observations summarised by Jardine et al. (2013a, b).

8.2 Comparison with closed–ended field displacement piles

Chow (1997) reported measurements of radial stresses made on her instrumented field ICP pile experiment DK2 which was installed at Dunkirk in marine silica sand. These covered the DK2 installation phases and observations made as a nearby un-instrumented closed-ended 100mm diameter pile (DK2B) was jacked into the same soil. The two piles had a centre–to–centre distance of 4.5 diameters (r/R = 9). Figure 8-1 re-plots the radial stresses measured at the 'following' cluster B (h/R = 27) of the ICP which directly faced the penetrating DK2B pile. The same figure shows the radial stresses measured in the sand mass at r/R = 8 during Mini-ICP installation into NE34 sand from the Author's tests. Figure 8-1 shows the moving stresses normalised by the local $q_b/[\sigma'_{z0}/p_a]^{0.13}$ to account for the different in-situ vertical stress and density states at the sensor locations and also by the radial effective stresses on the sensors after equalisation (σ'_{rc}) and before the second pile's installation. Chow (1997) preferred the second normalisation because the radial stresses sensed at cluster B at the end of DK2B's installation had already been elevated far above the K_0 stresses by jacking in the ICP carrying cluster B. The calibration chamber sensors were installed without any such disturbance, which explains why the q_b–normalised plot in Figure 8-1(a) shows consistently higher ratios applying when DK2B pile was installed than were seen in the Mini-ICP–NE34 experiment. Figure 8-1 identifies the 'twin pile' effect on pile shaft radial stresses which led to shaft capacity enhancement at Dunkirk (Chow 1997).

Nevertheless, the field and laboratory tests share many common features. When normalised (as suggested by Chow) by σ'_{rc} on Figure 8-1(b) the chamber results and the field measurements conform more closely. The chamber measurements at 8R become, as would be expected for single pile, greater than the field measurements at 9R. Tests ICP04 and ICP06 (both with rigid BC3 lateral boundary condition) show marginally higher stress ratios than earlier ICP07 and ICP08 or the field

test throughout the h/R profile, suggesting further that the rigid chamber boundary gives a less appropriate match to the field than the BC5 condition.

While the stress field developed at Dunkirk was undoubtedly affected by the 'rigid inclusion' effect of the ICP pile body, there are clearly strong similarities with the laboratory mini-ICP trends. The modified BC5 boundary adopted to better simulate the free field conditions in ICP07 and ICP08 led to measurements that agree better with the field profile. The BC5 chamber stresses marginally exceed the field trends as the pile approaches then shift to become marginally lower behind the tip. The peak stresses develop at similar h/R values in the chamber and field.

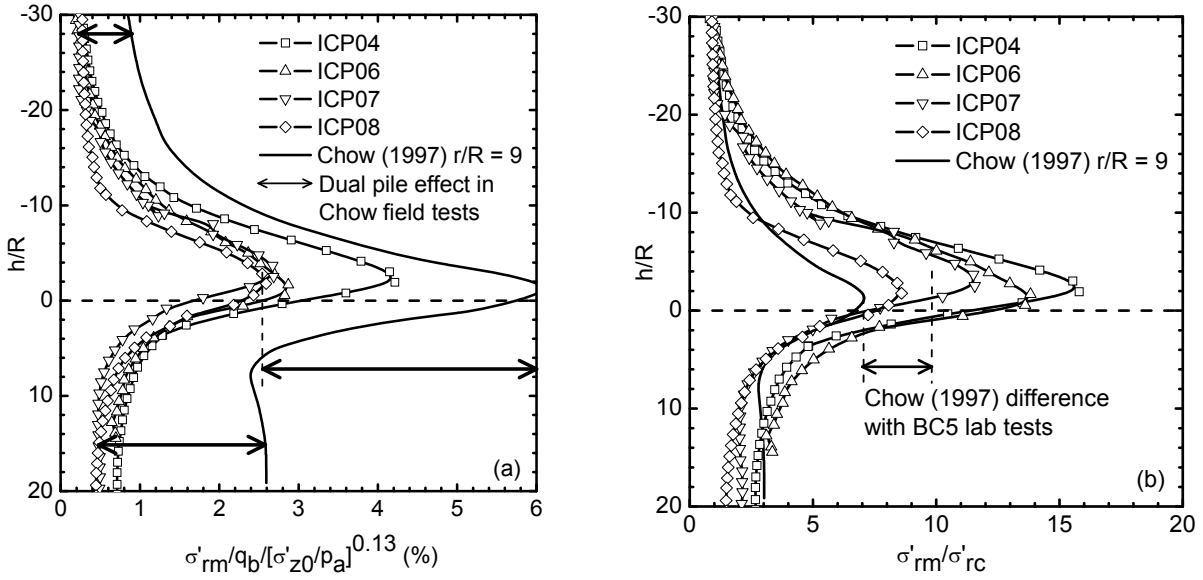


Figure 8-1: Moving radial stresses around Mini–ICP installations in NE34 sand chambers at r/R = 8 compared to field measurements by Chow (1997) normalised by (a) $q_b/[\sigma'_{z0}/p_a]^{0.13}$ (b) the equalised radial stresses, σ'_{rc} applying before installation of Mini-ICP or DK2B.

8.3 Comparison with CC tests with closed-ended displacement piles

Jardine et al. (2013a, b) reported measurements of radial, vertical and circumferential stresses around displacement piles in NE34 sand using similar testing arrangements with the Mini-ICP pile and 3S-R lab CC facility as in the Author's study, as has been previously reported. Jardine et al. (2013b) tested dry NE34 sand with BC3 boundary conditions and instrument arrays intended to establish the stress regime up to r/R = 20. The Author's study concentrated on varying boundary conditions, sand states and scale effects while focussing on measuring stresses in the nearer field with r/R up to 8. It is encouraging that the stress profiles and contour plots reported by the Author from Mini-ICP installation in test ICP04 with dry NE34 sand and BC3 boundary conditions showed compatible patterns to Jardine et al. (2013a, b) which adopted the same conditions.

Jardine et al. (2013b) however presented an alternative interpretation to the pile end-of-installation stress state. The plots for stationary radial and circumferential stresses at the end of the

Mini-ICP piles installation given by Jardine et al. (2013b) are reproduced in Figure 8-2. Their normalised radial stress profiles are similar to the profiles interpreted from the Author's tests in Figure 7-49 where radial stress peaks were observed at $2 < r/R < 4$ then stresses attenuated further away and towards the pile face. Noting that circumferential stress measurements were fewer and less reliable, Jardine et al. interpreted the end of installation circumferential stresses profiles shown in Figure 8-2(b) from the radial stress profiles (a) by considering the equilibrium relationships between σ'_{rs} and $\sigma_{\theta s}$.

Jardine et al. report the results are sensitive to the $\sigma'_{rs}/q_c - r/R$ distribution shapes and that iteration is required to produce an integrated interpretation of the combined experimental dataset. The $\sigma_{\theta s}$ interpreted trends were constructed by numerical differentiation and manipulation of the σ'_{rs} profiles. Jardine et al. acknowledge their detailed shapes cannot be considered to be fully reliable but argues the assessment over the $1 < r/R < 3$ range of high $\sigma_{\theta s}/q_c$ ratios that exceed σ'_{rs}/q_c is a secure and inescapable consequence of the firm experimental evidence that $\partial\sigma'_{rs}/\partial r$ is positive over this 'near-field' range. This establishes a near pile interaction between radial and circumferential stresses that could lead, as argued in hypothesis (a) – section 3.2, to capacity set-up with potential ageing related circumferential stresses relaxation and inward migration of radial stress peaks.

Such an interaction was not discernible from the Author's measurements profiles as has been described in section 7.4.4, and would potentially require the proposed further manipulation.

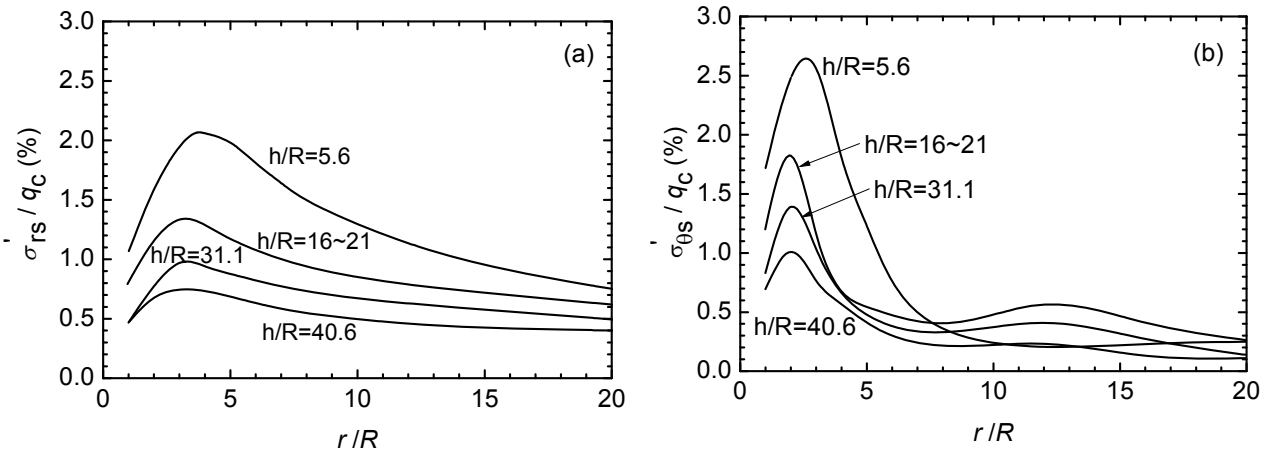


Figure 8-2: Interpreted profiles for four h/R values of stationary (a) radial effective stresses and (b) circumferential stresses developed after final stroke of Mini-ICP installation; after Jardine et al (2013b).

8.4 Comparison with CC experiments with open-ended model piles

Gavin and Lehane (2003) reported CC stress measurements around an open-ended relatively smooth ($R_{CLA} \approx 0.38\mu m$) stainless steel model pile with an external diameter of 114 mm and wall thicknesses of 8.3 mm. The pile was jacked by incremental strokes 1.68m into a 2.3m high and 1.68m diameter testing chamber ($d_{chamber}/D = 14.7$) filled with dry, uniform, fine to medium

siliceous Blessington sand ($d_{50\%}$ = 0.22mm, C_u = 1.6) placed at I_D = 30±2%. K_0 vertical stresses varied from 0 at the ground surface to 40kPa at the chamber base while CPT q_c profiles established independently varied linearly 0 – 0.6MPa from the ground surface to 1.3m deep then quasi-constant at 0.6MPa thereafter. The open-ended pile showed 'coring' Incremental Filling Ratios (IFR) close to 100% down to z = 0.6m then progressive plugging reduced the IFR to ≈ 14% at the final depth.

Figure 8-3 reproduces Gavin and Lehane's measurements from two radial stress sensors set at r/R = 7.6 and depths of 0.55m (z/R = 9.6) and 1.1m (z/R = 19.3) around their open-ended pile. It is clear for this partially plugging open-ended pile that straight-forward q_c normalisation doesn't lead to a unique profile with h/R for the given r/R as with the proposed closed-ended stress function σ'_r/q_c = f(h/R, r/R). The range of normalised maximum moving σ'_{rm}/q_c ratios (1.58% – 2.94%) overlaps but falls below the equivalent Mini-ICP measurements in Figure 7-31(a) (2.72% – 4.44%). Similarly, the maximum stationary σ'_{rs}/q_c ratios in Figure 8-3 (~1.19% – 1.99%) overlaps with but fall below the Mini-ICP equivalents (~1.50% – 2.19%) in Figure 7-31(b).

Gavin & Lehane argued for normalisation by an 'open–ended pile average base resistance' $q_b = (q_{plug}R_i^2 + q_{ann}2Rt)/R^2$. In this case q_{plug} is the plug resistance which is a function of IFR, q_{ann} is the pile thickness (t) annulus resistance, R is outer radius of the pile and R_i is the internal radius of the pile accounts for the partial soil displacement (plugging) at the pile base recorded in terms of the IFR during the installation. Figure 8-4 presents the q_b normalised maximum moving and stationary radial stresses around the open–ended pile which conform better to the stresses around the closed–ended Mini–ICP in NE34 sand. The degree of compatibility improves as the pile depth increases for the open–ended pile (from z/R = 9 to 21) as the pile base plugs and q_b open–ended tends towards the closed–ended pile q_b value. The stresses generated with the open-ended pile can be considered in a similar way to that around a closed–ended pile, provided IFR and q_{plug} can be predicted and tracked with σ'_r/q_c = f(h/R, r/R, IFR) and potentially initial vertical effective stresses, σ'_{z0}.

Noting that Gavin & Lehane's open-ended pile was fully coring at shallower depths (IFR = 100%), Yang et al. (2013) interpreted the radial stresses from the shallow sensor by a different approach using $R^* = (R_{outer}^2 - R_{inner}^2)^{0.5}$ which is the open-ended driven pile's equivalent solid pile radius defined by Jardine et al. (2005a) for fully coring open–ended piles. This translates the sensor's measurements from r/R = 7.6 to r/R* = 14.6, and in Figure 8-5 Yang et al. compares these stresses with the closest matching Jardine et al. (2013a) Mini-ICP sand mass radial stress measurements at r/R=16 after normalization by $q_c/[\sigma'_{z0}/p_a]^{0.13}$ due to the markedly different q_c and σ'_{z0} in the two studies. Compared in this way, the two data sets show broadly similar responses. Both sets show $(\sigma'_{rm}/q_c)/[\sigma'_{z0}/p_a]^{0.13}$ maxima around 1% at the shallower location.

The two experimental arrangements differed significantly. No upper surcharge or lubricated lateral boundaries were applied in Gavin and Lehane's tests. Their pile–to–chamber diameter ratio

was lower (14.7 compared to 33.3) and they adopted looser sand than the Mini-ICP tests in NE34 sand. Their open–ended pile was also smoother and their sand stress cell calibrations and data reduction were less elaborate than those adopted for the Author's and Jardine et al.'s (2013b) studies. Nevertheless, the degree of agreement between the test results as observed is encouraging.

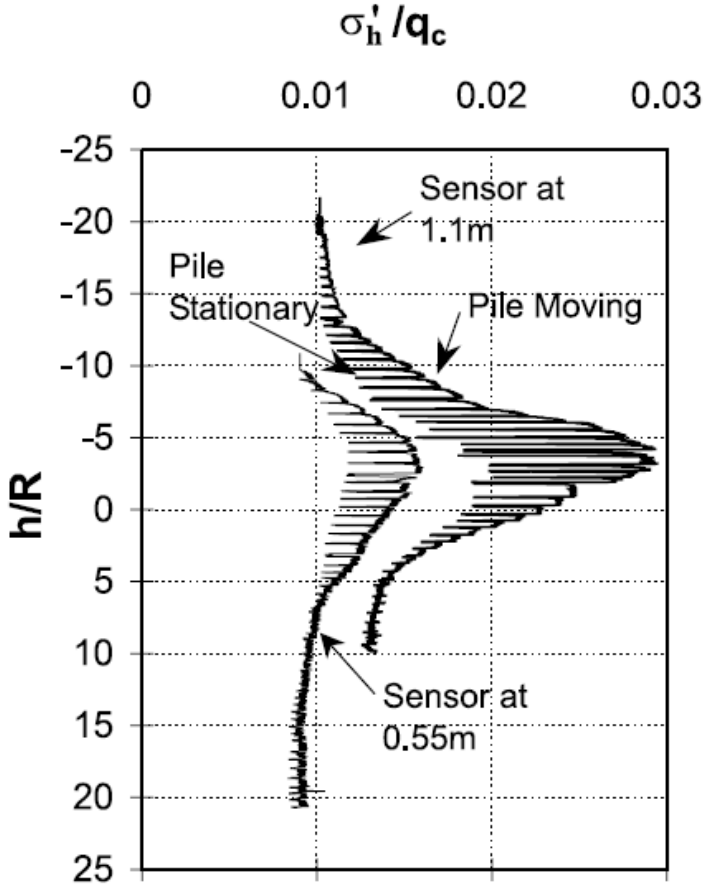


Figure 8-3: Radial effective stresses normalised by CPT q_c versus h/R for jack stroke installed partially plugging driven open-ended stainless steel model pile (Gavin & Lehane 2003).

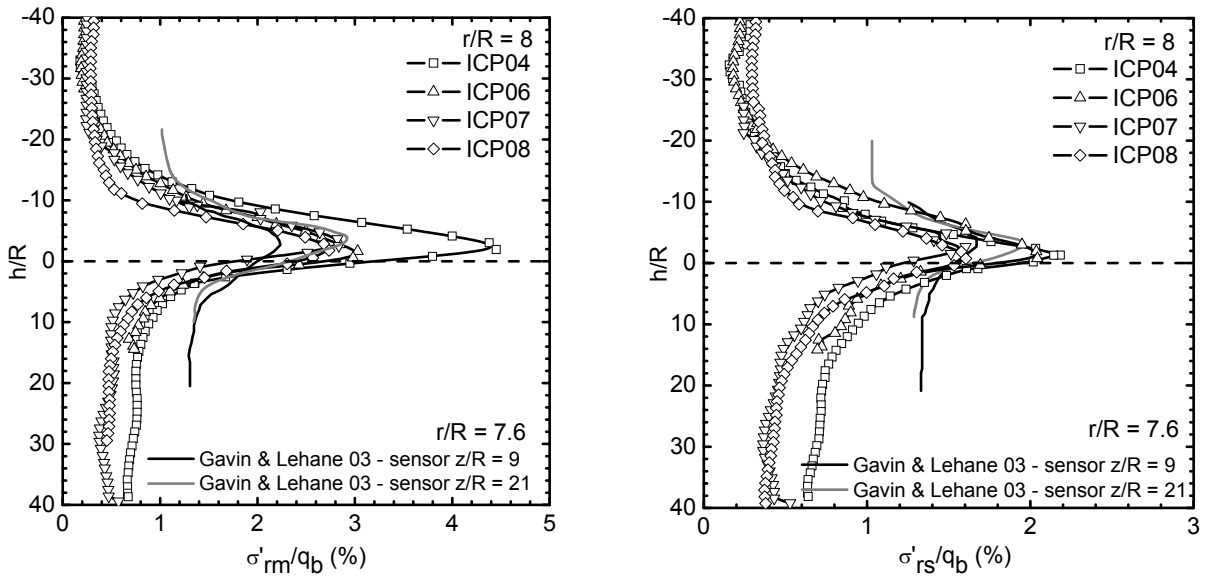


Figure 8-4: q_b normalised radial stresses from Mini-ICP installations in NE34 sand chambers r/R = 8 compared to Gavin & Lehane (2003) measurements from open-ended pile installation r/R = 7.6 (a) moving (b) stationary.

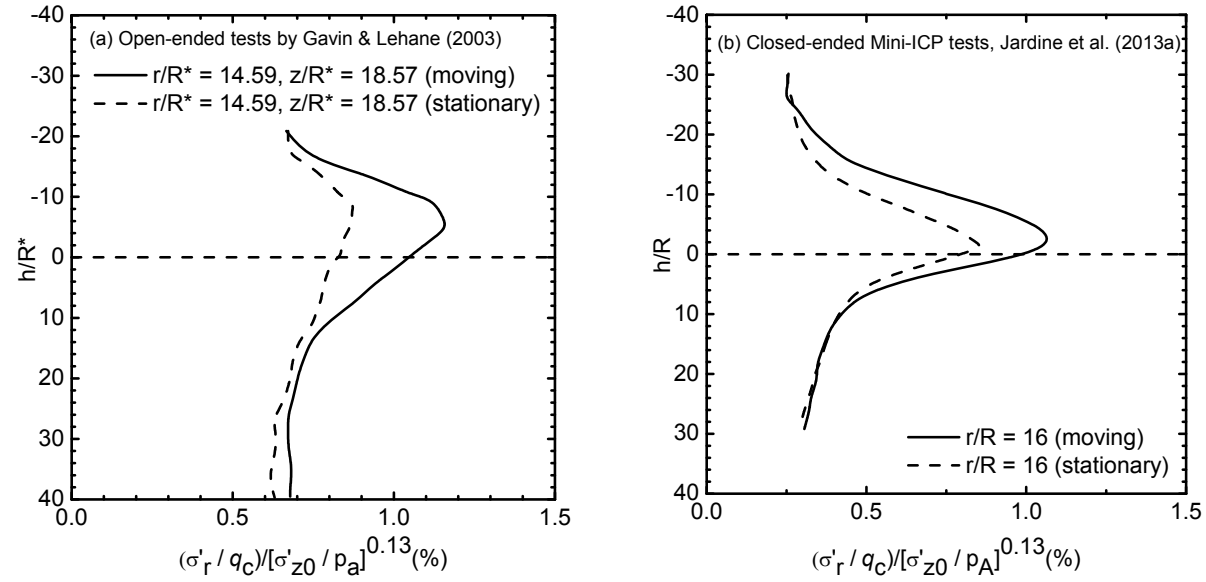


Figure 8-5: Comparison of sand radial stresses around displacement piles in (a) Gavin and Lehane (2003) after re-plotting using equivalent radius R and (b) Jardine et al. (2013a) (after Yang et al. 2013).*

8.5 Comparison with centrifuge closed-ended driven model piles

Allard (1990) made soil stress measurements in experiments where she drove a smooth 9.5mm diameter closed-ended stainless steel pile into a 152mm diameter centrifuge bucket ($d_{centrifuge\ bucket}/D = 16$) filled with dry, uniform Nevada fine silica sand ($d_{50\%} = 0.1$mm) placed at 1590kg/m^3 ($e_0 = 0.65$, $I_D = 57.5\%$). Vertical and radial stresses were measured with strain-gauged diaphragm cells (2.6 to 5.1mm in diameter) whose strong cell action effects Allard modelled in high

acceleration (50g) centrifuge calibration tests. However, the pile driving sand stress maxima experienced during testing were nearly twice the calibration stresses.

Allard (1990) presented radial stress profiles against pile base depth from radial stress sensors installed at r/R = 2.67 and six z/R ratios. No centrifuge CPT testing was reported and Yang et al. (2013) projected a q_c profile from a centrifuge correlation by Gaudin et al. (2005) and corrected for density index by applying Baldi et al. (1986). Figure 8-6 (a) & (b) presents Allard's stationary radial stresses, recorded between blows applied in–flight and plotted against h/R, normalized as both σ'_{rs}/q_c and $(\sigma'_{rs}/q_c)/[\sigma'_{z0}/p_a]^{0.13}$ respectively. Equivalent stationary Mini-ICP measurements made in the Author's study at comparable r/R locations are shown in Figure 8-6 (c) and (d).

A spread among stress measurements made at equal r/R and h/R value is observed. The Mini-ICP tests show a spread about their mean values of ~16% in their stress maxima; this spread increases to ~50% as h/R increases towards 30. The centrifuge data shows a spread of ~22% in their stress maxima and ~30% from h/R > 4.5. The experiments however reveal common features, including similarly steep dependence on h/R. The centrifuge $(\sigma'_{rs}/q_c)/[\sigma'_{z0}/p_a]^{0.13}$ maxima developed at h/R ≈ 0 fall around 3.0% (±0.73%) at r/R = 2.67, while the equivalent Mini-ICP values average of around 6.62% (± 1.85%) at r/R = 2 to 3.

Possible explanations for this significant discrepancy include; (i) Errors in estimating the centrifuge q_c profile, (ii) Differences in the stress-cell calibrations, (iii) Pile driving in the centrifuge and cyclic jacking in the chamber, or (iv) Difference in sands, piles, shaft roughnesses, initial stress fields, boundary conditions and scaling ratios. Allard's centrifuge bucket/pile diameter ratio was relatively low at 16, while the Mini-ICP tests chamber-to-pile ratio was 33. Her sensor diameter/$d_{50\%}$ ratios were similar to the Mini-ICP range (38 ± 12 compared with 30 ± 1), but her pile diameter had lower ratios than the Mini-ICP tests with respect to her (i) sand $d_{50\%}$ value ($D/d_{50\%}$ = 95 compared with 171) and (ii) soil sensor diameters (1.9 - 3.7 compared with 5.5 – 6.0). Significant pile-sensor interference and dynamic driving densification effects might be expected in the centrifuge case as has also been observed in this calibration chamber study, as reported in sections 7.2 and 9.4.

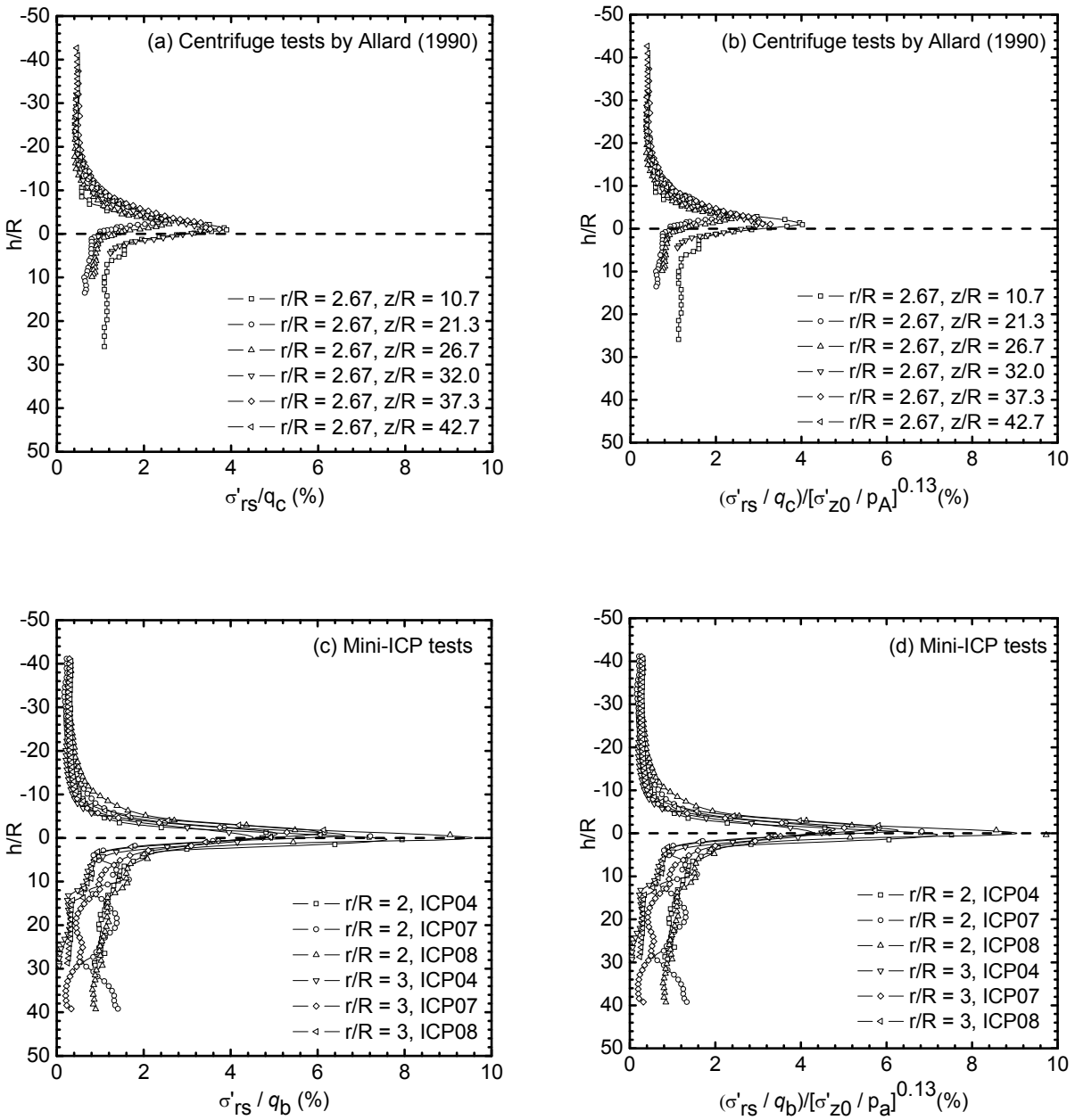


Figure 8-6: Sand mass radial stresses around Allard (1990) centrifuge driven closed-ended model pile tests shown in (a) and (b) compared to the Author's jack stroke installed Mini–ICP piles in (c) and (d).

8.6 Comparison with Finite Element (FE) analyses

Sheng et al. (2005) simulated continuous in-flight penetration of a closed-ended centrifuge model pile of 30mm diameter (with a 60° cone tip) penetrating into a 0.56m high and 0.58m diameter centrifuge bucket ($d_{centrifuge\ bucket}/D = 19.3$) filled with dry dense sand ($e_0 = 0.75$, $I_D = 76\%$). Initial stresses were scaled up to simulate centrifuge testing at 66.7g to approach prototype scale, giving σ'_{z0} = 550kPa at the deepest point considered. Large-strain frictional contact was implemented between the pile and soil with δ'_{cv} of 27° and the sand was modelled as fully drained Modified Cam Clay (MCC).

Exemplar stresses by Sheng et al. (2005) are plotted in Figure 8-7(a) as h/R against $q_c/[\sigma'_{zo}/p_a]^{0.13}$ – normalised moving radial stresses profiles developed at r/R = 1.13 for stages with tip depths z_{tip} = 4, 8 and 16R. Yang et al. (2013) estimated the q_c profile from Baldi et al. (1986) expression. Figure 8-7(b) presents the Author's similarly normalised Mini-ICP σ'_{rm} trends observed at r/R = 2, which is the closest location where measurements could be made. Sheng et al.'s stress maxima at r/R = 1.13 tend to occur 2 < h/R < 4 behind the pile tip while with the Mini-ICP they occur at h/R ≈ 0 of the pile tip. Sheng et al.'s computed normalized maximum radial stress (from deep penetration with z/R = 16) is 37.0% while that interpreted from the Author's tests in Figure 7-48 for r/R=1.13, h/R = 0 was lower at 27.0%. This involved an interpolation between the closest measurement (of 16.4%) made at r/R = 2 and the $\sigma'_{rm} = K_A q_b$ maximum value applying on the pile base.

No surface surcharge, jacking/driving processes or particle crushing was simulated in Sheng et al.'s model. However, the general shape of Sheng et al. (2005)'s normalised profiles conforms to the Mini-ICP tests measurements, providing a good prediction of the steep variations with h/R that in Sheng et al.'s analysis are purely due to the pile geometry without the cyclic installation effects.

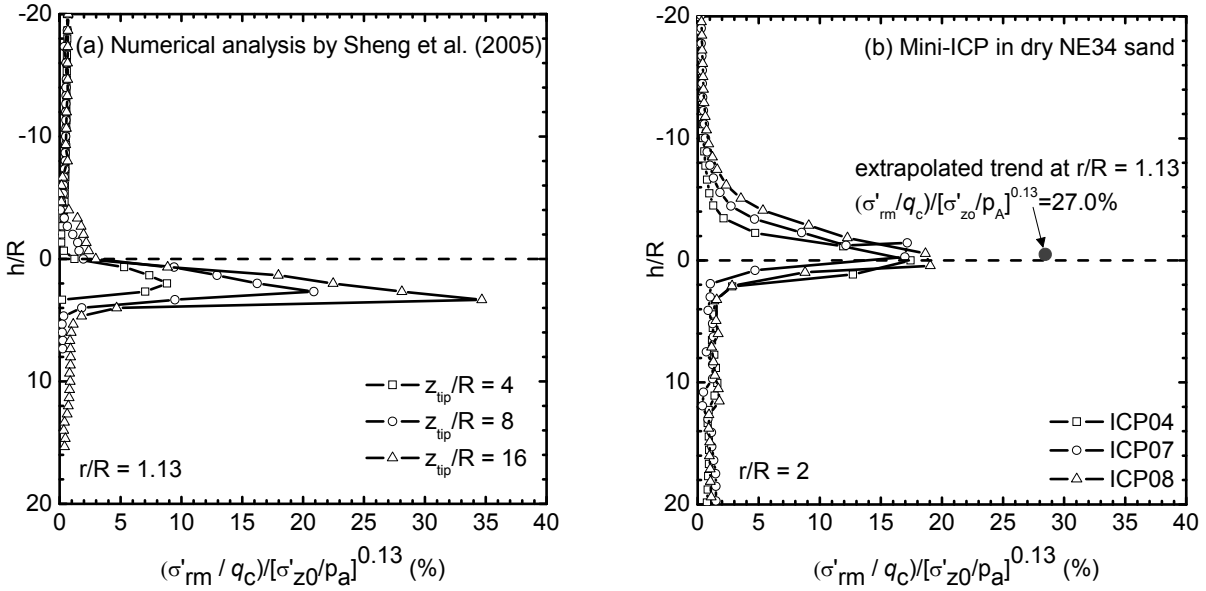


Figure 8-7: Comparison of radial stresses (a) developed during steady penetration as simulated in finite element analysis by Sheng et al. (2005) and (b) measured in Mini-ICP tests.

8.7 Comparison with Coupled Eulerian-Lagrangian (CEL) FE analyses

Henke et al. (2010) and Qiu et al. (2011) used CEL technique to model a 300 mm diameter closed-ended conical-tipped pile penetrating monotonically 5m in dry Taiwanese Mai-Liao sand. The simulations were made for sand density indices between 20 and 75% and Coulomb pile-sand interface friction was adopted assuming $\delta_{cv}=\varphi'/3$. Variations in the sand moving radial stresses were

reported by Henke et al. (2010) and Qiu et al. (2011) for radial profiles located at two depths extending out to 5m. Figure 8-8 (a) and (b) show the results for three relative densities reprocessed by Yang et al. (2013) as $(\sigma'_{rs}/q_c)/[\sigma'_{z0}/p_a]^{0.13}$ ratios plotted against r/R, considering horizontal profiles set at h/R = 6.67 and 13.33. These can be compared with the Mini-ICP experiments stationary profiles presented earlier in Figure 7-49.

Several differences exist between the Mini-ICP tests procedures and the numerical model. The Mini-ICPs were installed by 50 full loading–unloading cycles as opposed to the monotonic installation in the FE analysis which also modelled uniform and un-surcharged sands as well as different interface shear and particle breakage processes. Despite such differences, compared to the Mini-ICP Figure 7-49 profiles, the numerical analyses capture the key dependence of sand stress regime on the geometrical (h/R and r/R) and sand state variables. The numerical results show radial stresses decreasing with increasing h/R in the predictions for I_D = 40% (Figure 8-8 a), and a similar set of radial distributions to the experiments in Figure 8-8(b), including maxima developing away from the shaft at 2 < r/R < 4. As before, the analyses covered purely monotonic pile penetration with no cyclic effects simulated.

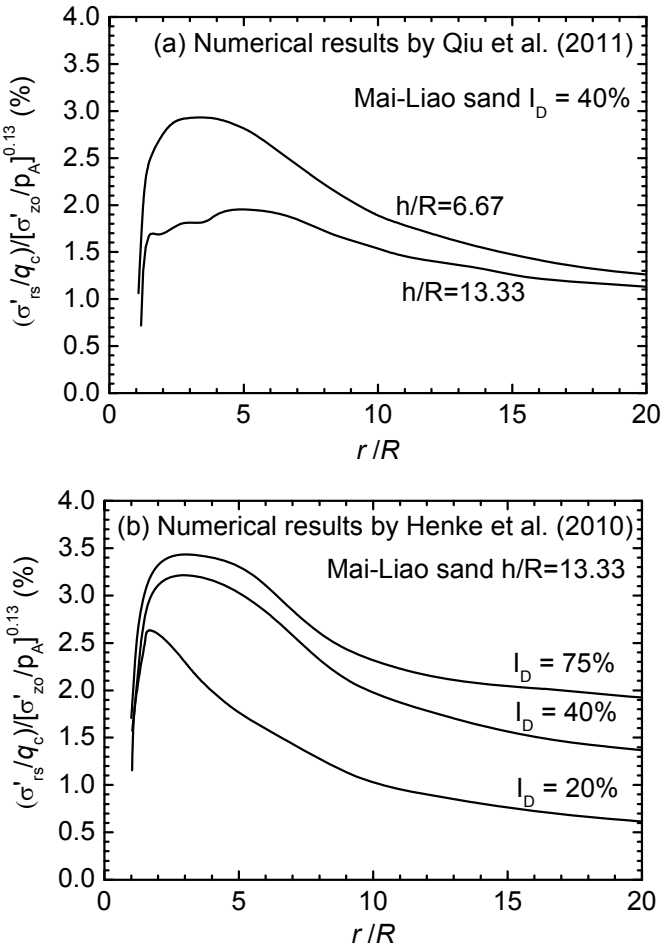


Figure 8-8: Radial stresses from (a) numerical predictions made with two h/R values by Qiu et al. (2011); (b) numerical predictions made with three initial densities by Henke et al. (2010) from Yang et al. (2013).

8.8 Comparison with FE analysis incorporating grain crushing

Zhang et al. (2013) applied Arbitrary Lagrangian Eulerian (ALE) FE with re-meshing and variable re-mapping to simulate monotonic pile penetration in sand providing good predictions for evolving grain size distributions and Jardine et al. (2013b) Mini-ICP tip resistances. Yang et al. (2013) held discussions with Einav (2012) that led to further processing of Zhang et al.'s simulations. Normalised profiles of the stationary radial and circumferential effective stresses predicted during pile installation are presented with r/R for three h/R values in Figure 8-9 (a) and (b). These may be compared with the equivalent end of installation stationary profiles interpreted from the Author's Mini-ICP experiments in Figures 7-49 and 7-50. As with the analyses of Henke et al. (2010) and Qiu et al. (2011), radial stress maxima are predicted, although here tend to develop further away from the shaft ($3 < r/R < 8$). The computed σ_θ profiles show the steep radial variations and $\sigma_\theta > \sigma'_r$ trend close to the shaft as interpreted by Jardine et al. (2013b) but not measured in the Author's tests. As expected the radial stress profiles fall as h/R increases although the variation at higher h/R values appears relatively gentle. This latter feature could be related to cyclic loading features that were not considered in the monotonic penetration analyses undertaken.

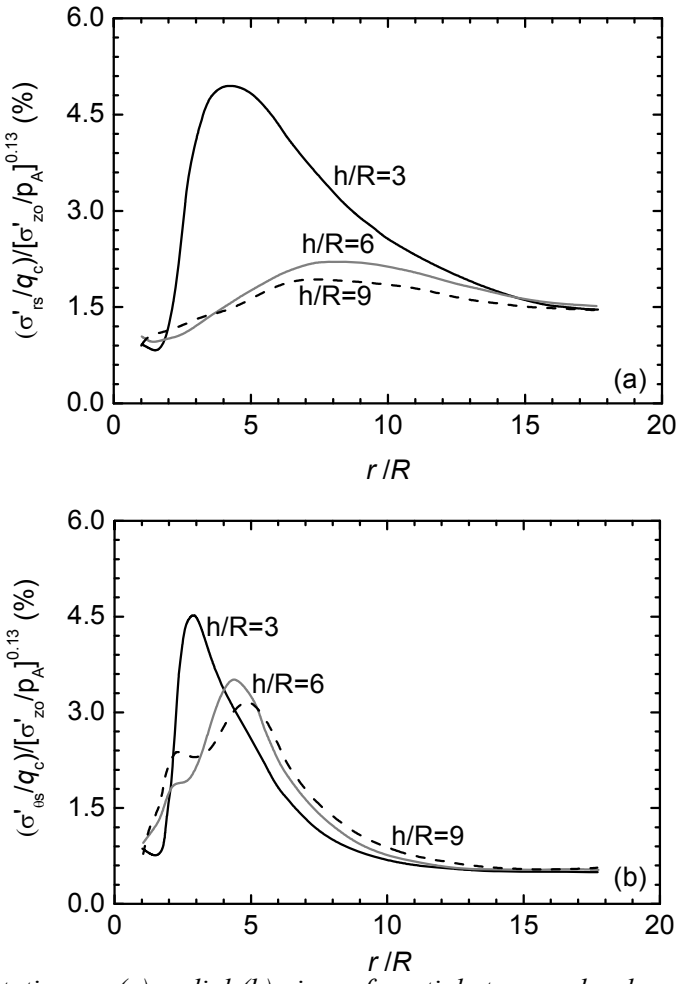


Figure 8-9: Normalised stationary (a) radial (b) circumferential stresses developed at various h/R positions from numerical simulations by Einav (2012).

8.9 Summary remarks and conclusions

The Author's stress measurements made around displacement piles penetrating silica sands have been compared to eight studies; one field test, three laboratory experimental and sets of four numerical analysis. The following key outcomes are summarised.

1) The need to make multiple and careful measurements in order to arrive at sensible conclusions cannot be over emphasized. Experiments are subject to a wide range of potential imperfections and sources of scatter or error and equally numerical modelling of the installation process poses a series of significant challenges.
2) Despite these, several clear trends have been defined for the stresses developed around displacement piles in sand.
3) The radial stresses developed around displacements piles in sands show strong dependence on the relative pile tip depth h/R irrespective of the sand density state or pile installation method (discontinuous jacking, driving or continuous pushing).
4) However the effects of installation cyclic loading still requires further quantification.
5) Appropriate use of either an equivalent base capacity that varies with IFR or the equivalent pile radius R* procedure allow the stresses developed around coring open piles to be reconciled with those developed around closed end piles.
6) The normalized radial stress maxima defined during steady penetration stages vary with h/R, r/R, q_c, and σ'_{z0} within relatively narrow spreads. Possible explanations have been offered for the more significant discrepancies identified between the datasets.
7) Monotonic numerical analyses and cyclically advanced experiments both indicate that end – of – installation radial stress maxima develop away from the shaft in the $2 < r/R < 8$ range. Though yet unobserved through measurement, it appears that steep changes in $\sigma_{\theta s}$ must apply close to the pile that give local $\sigma_{\theta s} > \sigma'_{rs}$ conditions over sections of the $2 < r/R < 5$ range.

Chapter 9

9 Short term static axial load tests on laboratory model piles

9.1 Test programme

The ten piles installed in this study were load tested under static axial compression at the end of installation (EOD) to assess their short term axial compression capacities. These tests involved loading the pile caps monotonically with the electric jack, under displacement control, until settlements of about 10mm developed, representing 0.28D for the 36mm diameter piles and 0.83D for the 12mm diameter Micro pile. The pile displacements were measured by an LVDT attached to the free-standing pile section extension left above the chamber at the end of installation. In some cases the LVDT was not working properly and in these the global displacement measurements made by the jack system have been used after making corrections for system compliance. Instrument outputs were recorded on 1.5 to 2 second cycles to define the load and stress responses of the pile and sand mass. Table 9-1 summarises the details of the tests while the sections that follow discuss the axial load-displacement behaviour, the local interface effective stress path responses and some possible rate effects.

Test	Stroke or blow	Date	Time after end of installation (minutes)	Rate (mm/s)	Final depth (mm)	Final settlement (mm)	Measured capacities (kN)		
							Shaft	Base	Total
ICP04	50th	03/11/09	35	0.01	986.55	-10.20	12.15	22.87	35.02
ICP05	51st	06/05/10	19	0.2	997.90	-9.59	3.28	12.21	15.49
ICP06	50th	18/10/10	7	0.2	985.80	-10.12	18.33	27.13	45.46
MiP01	50th	22/12/10	14	0.2	989.14	-10.04	3.56*	2.03*	5.60
CPT09	3rd	10/05/11	9	0.02	1097.49	-9.23	9.15	21.27	30.42
ICP07	50th	24/05/11	14	0.2	990.49	-13.78	13.24	22.20	35.44
ICP08	49th	29/09/11	0	2	977.00	-20.00	11.89	18.73	30.62
CPT10	49th	19/12/11	0	10	977.20	-20.00	9.22	19.48	28.70
DI	47th	01/02/12	~1440	0.02	1028.92	-12.92	N/A	N/A	10.67
DII	90th	13/03/12	~43	0.02	993.00	-9.77	N/A	N/A	18.80

**Estimated assuming a typical NE34 sand base bearing as in ICP04 scaled to the pile diameter.*
Note: All piles were 36mm diameter closed-ended except the 12mm diameter MiP01

Table 9-1: Short-term static pile capacities (EOD) in this test programme.

9.2 Pile axial load – displacement behaviour

The instrumented piles allowed base loads and shaft distributions to be distinguished, while only pile head loads were measured with the un-instrumented piles. Ultimate pile capacities are

defined as the maximum measured load and these are listed in Table 9-1. The global jack displacements generally exceeded those from the local LVDT because of compliance effects, as may be seen from the uncorrected jack and LVDT displacements recorded in ICP04 as shown in Figure 9-1. Compliance led to a six times softer initial response (at 10kN) and a misleading impression of both loading and unloading stiffnesses, while global final permanent displacements are almost unaffected. Comparisons made between local and global measurements from 5 tests on 3 piles led to the non-linear (mean polynomial) relationship shown in Figure 9-2 for compression static load tests which has been applied to those tests where LVDT data were for any reason unavailable.

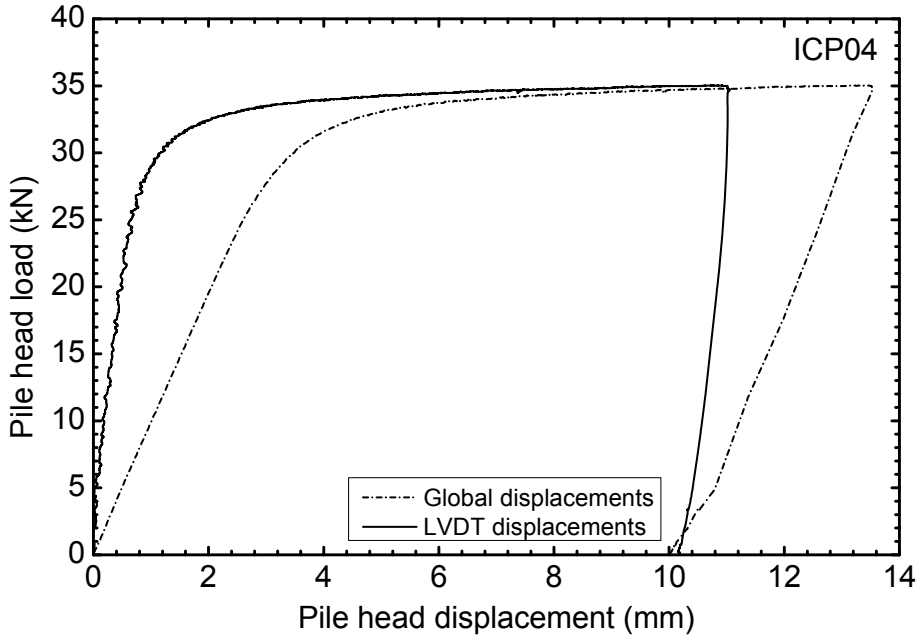


Figure 9-1: ICP04 EOD pile load test defined by global displacements of the pile cap and the local LVDT on the Mini–ICP.

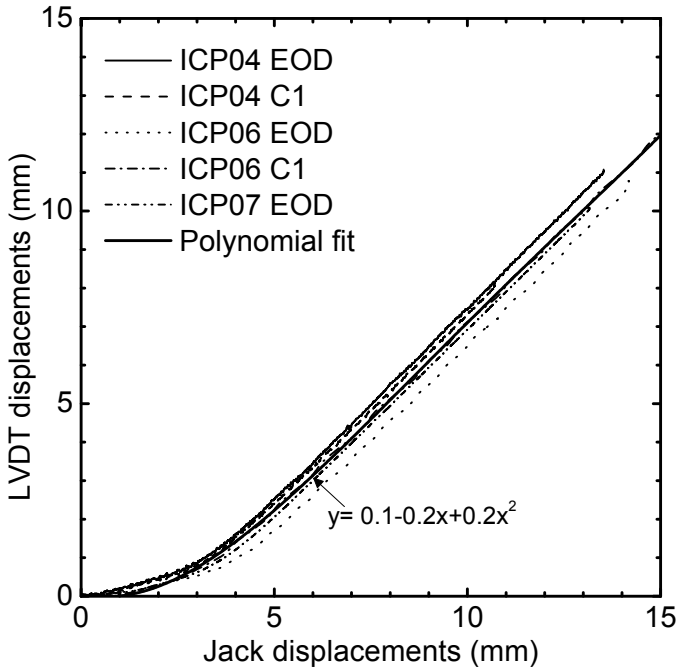


Figure 9-2: Relationship between pile jack and LVDT displacements to account for compliance.

9.2.1 EOD tests on Mini-ICP piles in NE34 sand

The total, base and shaft capacities developed in test ICP04 on dry NE34 sand (with BC3 boundary conditions) are displayed on Figure 9-3. Just after installation, the pile had balanced residual compression base and shaft (tension) loads of 6.7kN. Most (83%) of the total pile capacity was mobilised within 1mm of settlement and this proportion roses to 97% when settlements reached 0.1D (3.6mm). The ultimate capacity defined at 11.01mm showed a base: shaft split of 0.65:0.35.

The EOD test on ICP06 in wet dense NE34 sand (again with BC3 boundary conditions) is reported on Figure 9-4. In this case the pile's matching residual base and shaft loads were slightly higher at 8.9kN and the capacity split between base and shaft was 0.60:0.40. ICP06 mobilised its maximum capacity at similar displacements to ICP04, but showed a 23% greater load than ICP04, despite the single level of 9 stress sensors providing less reinforcement than the three levels of 36 stress sensors in ICP04. The extra base resistance and shaft capacity was attributed earlier to either a higher density, or to suction effects in the unsaturated sand chamber; see Section 7.2.

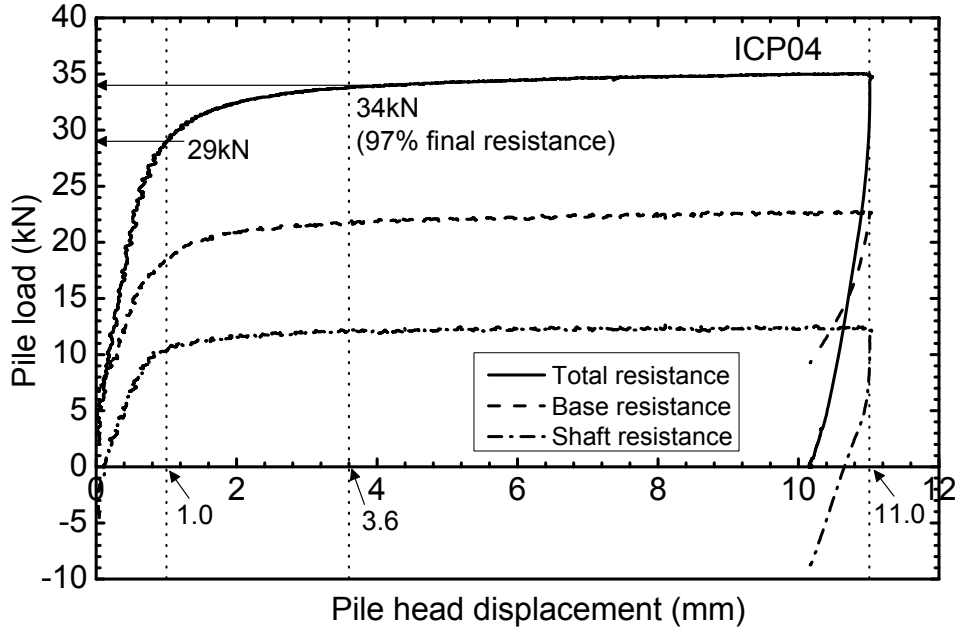


Figure 9-3: ICP04 EOD load–displacement behaviour showing total, base and shaft resistances.

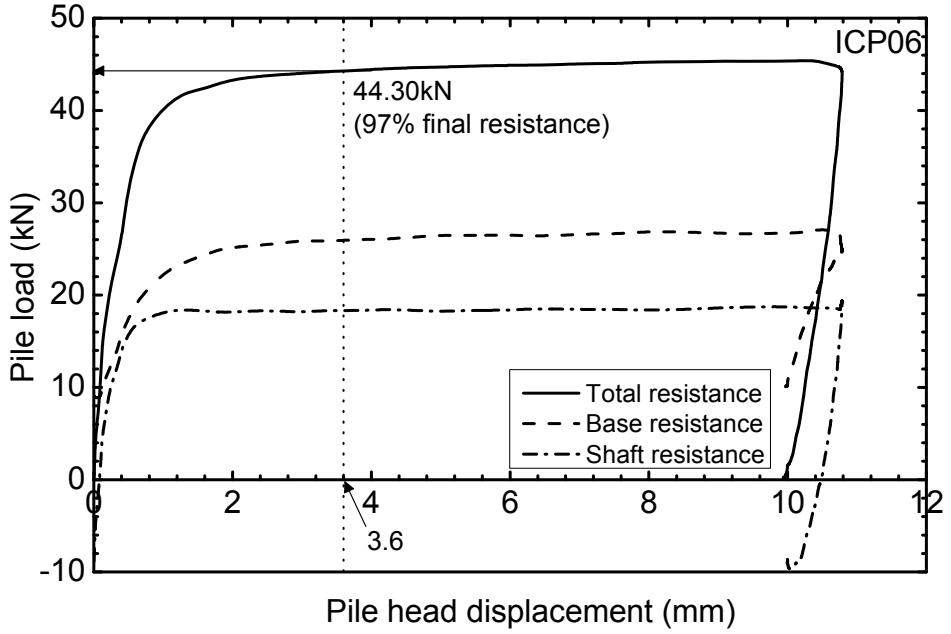


Figure 9-4: ICP06 EOD load–displacement behaviour showing total, base and shaft resistances.

Figure 9-5 plots the EOD load–displacement behaviour mobilised in test ICP07 in dry NE34 sand under the BC5 boundary condition. The residual loads are slightly lower (~5kN) than in ICP04 and ICP06, reflecting the marginally lower installation q_b profile applying to the stress controlled (rather than rigid cell) conditions (see Table 6-10). The total axial capacity however was similar to that of ICP04, with a base to shaft capacity split of 0.63:0.37. The chamber diameter–to–pile

diameter ratio effect investigated by contrasting the BC3 and BC5 conditions did not lead to a marked change in overall capacity.

The test response of ICP08 in dry NE34 sand (with BC5 boundary conditions) is outlined in Figure 9-6. To minimise any delay or pause effects the EOD behaviour was assessed from the last stroke of installation without mounting the LVDT system. The plotted displacements have been corrected for global jack displacements compliance errors. Apart from improving the lateral boundary conditions to better simulate a free-field conditions (Huang & Hsu 2005), this test aimed to isolate possible differences in behaviour between the last strokes of installation and the applied EOD static load test. The ultimate capacity of the pile was 15.7% lower than ICP07 which was attributed to the lower base capacity and q_b profile available around the pile base depth at the end of installation, Figure 7-2. Also the lateral stresses in ICP07's installation were better regulated over the short period (14 minutes) spent setting up for the EOD than in ICP08. Nevertheless, the base and shaft capacity split for ICP08 was 0.61:0.39, comparable to those developed in all the NE34 sand tests implying the behaviour on the last slower stroke tests used in the test programme to define the short term pile capacity at the end of installation were indeed representative of a 'standard' pile's behaviour during the final stages of installation.

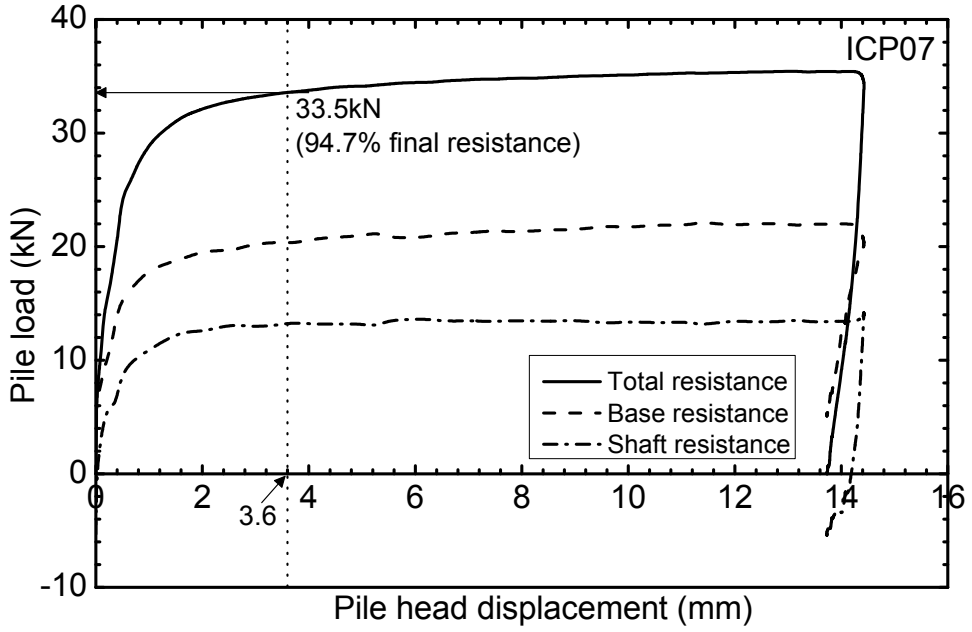


Figure 9-5: ICP07 EOD load–displacement behaviour showing total, base and shaft resistances.

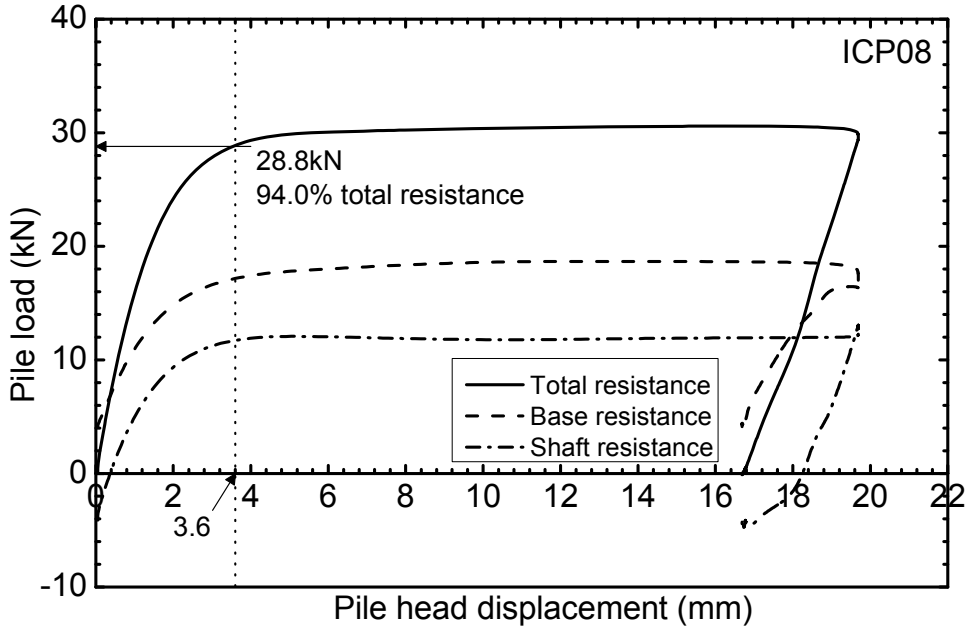


Figure 9-6: ICP08 EOD load–displacement behaviour showing total, base and shaft resistances.

9.2.2 EOD tests on all other piles

The effects of installation jacking rate and stroke length on pile capacity were assessed in test CPT09 on Figure 9-7, where a CPT cone was advanced into dry un-instrumented NE34 sand (under BC5 boundary conditions) by just two strokes of 750mm and 340.35mm length respectively, applied at 10mm/s. In a further experiment CPT10, shown on Figure 9-8, a CPT cone was installed into dry un-instrumented NE34 sand (under BC5 conditions) by 49 jack strokes, each of 20mm applied at 10mm/s. The q_b profile of CPT10 was consistently higher than that for CPT09 (Figure 7-2 (a)), as a result of the slightly different top boundary details discussed in Section 7.2. However, at the end of installation the base capacity of CPT09 (21.27kN) was marginally higher to that of CPT10 (19.48kN) because CPT09 was inadvertently jacked to 1.097m (instead of the 0.99m standard depth). The rigid chamber base (at z = 1.44m) starts to show a clear influence on the pile base resistances at z > 1m (Figure 7-2 (a)). Between 0.6m – 0.98m depth the piles q_b quasi-constant profiles show $q_{b,CPT10}/q_{b,CPT09}$ = 1.08 ± 0.04 indicating no negative effect of the installation cycles styles to the base resistance.

The CPT09 and CPT10 EOD shaft capacities were 9.15kN and 9.22kN respectively indicating little difference between the N = 2 and N = 49 pile tests. The shaft roughness and material characteristics of the two piles were similar. Both tests deployed BC5 boundary conditions but the boundary stress response was improved for CPT10 making its boundary stresses ~5kPa higher, Figure 9-9. The raw and q_b–normalised shear stresses measured on the friction sleeve at h/R = ~5.7 behind the CPT tip (equivalent to a single cycle in CPT09 and 5 cycles in CPT10) are

presented in Figure 9-10. The observed shear stresses, trends reflect the q_b and lateral membrane pressures profiles discussed above with CPT10 showing slightly greater τ_{rz} than CPT09. Any enhanced shaft stress degradation related to CPT10's 49 cycles applied during installation was apparently over-ridden by the marginally higher CPT profile of the CPT10 test sand chamber. Overall, the cyclic degradation caused by the 47 additional cycles was assessed to have reduced the shaft capacity by ~10%.

Both CPT09 and 10 (installed at 10mm/s) showed lower EOD shaft capacities than ICP07 and 08 (installed at 2mm/s) under similar BC5 boundary conditions, while the base capacities fell between the ICP07 and ICP08 values. These differences in resistances may be affected by:

1) The reinforcement provided at the three levels of SSS instrumentation in ICP07 and 08 that gave higher q_c values and shaft capacities to the CPT09 and 10 tests in blank chambers.
2) Marginally less rough CPT pile shafts (R_{cla} = ~2 - 3μm) compared to the Mini-ICP (R_{cla} = 3 - 4μm) leading to marginally reduced dilation, and possibly a lower δ_{cv} value and therefore reduced shaft capacity.
3) Section 9.5 re-visits the possible effects of rate effects on these tests.

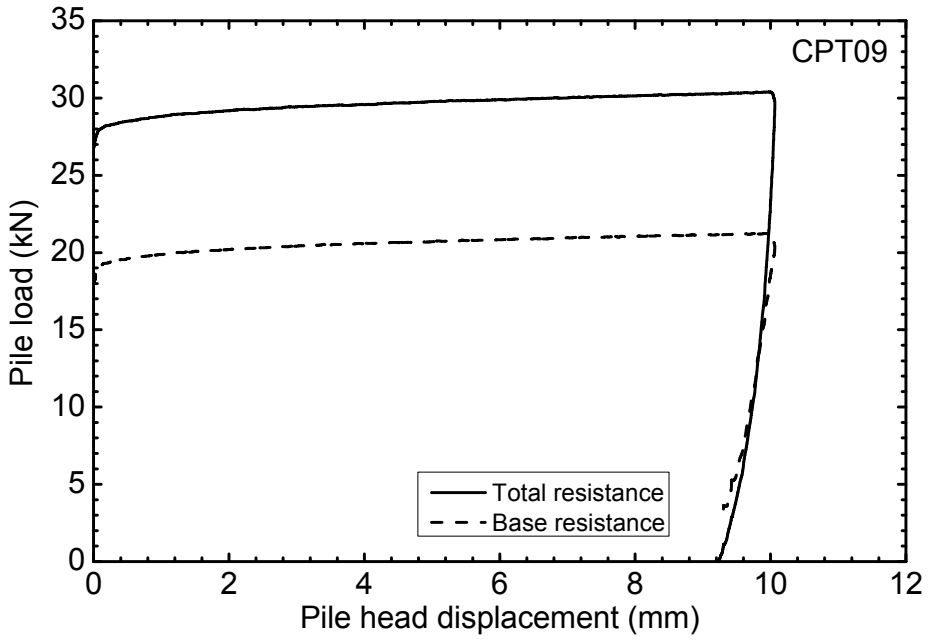


Figure 9-7: CPT09 EOD load–displacement behaviour showing the total and base resistances.

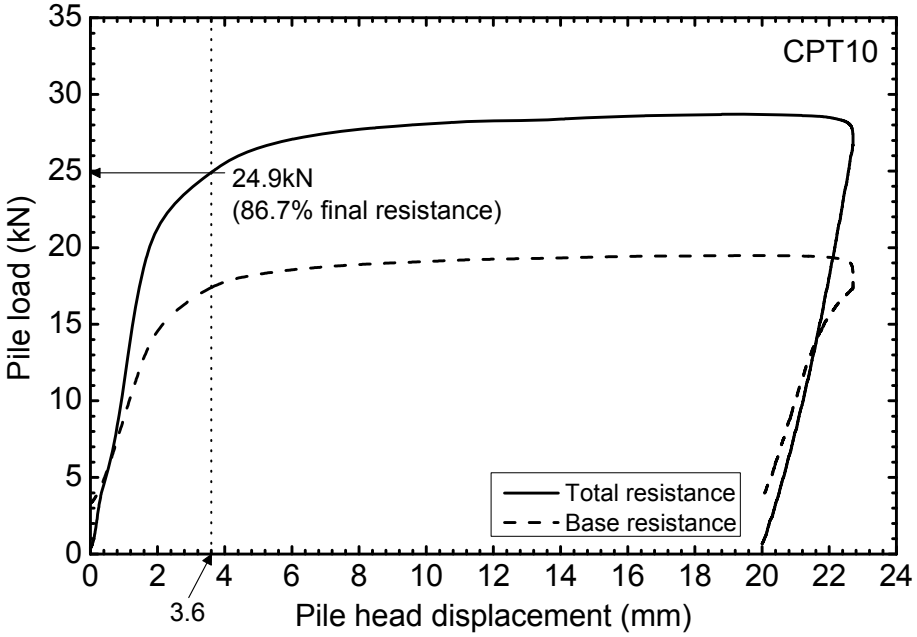


Figure 9-8: CPT10 EOD load–displacement behaviour showing the total and base resistances.

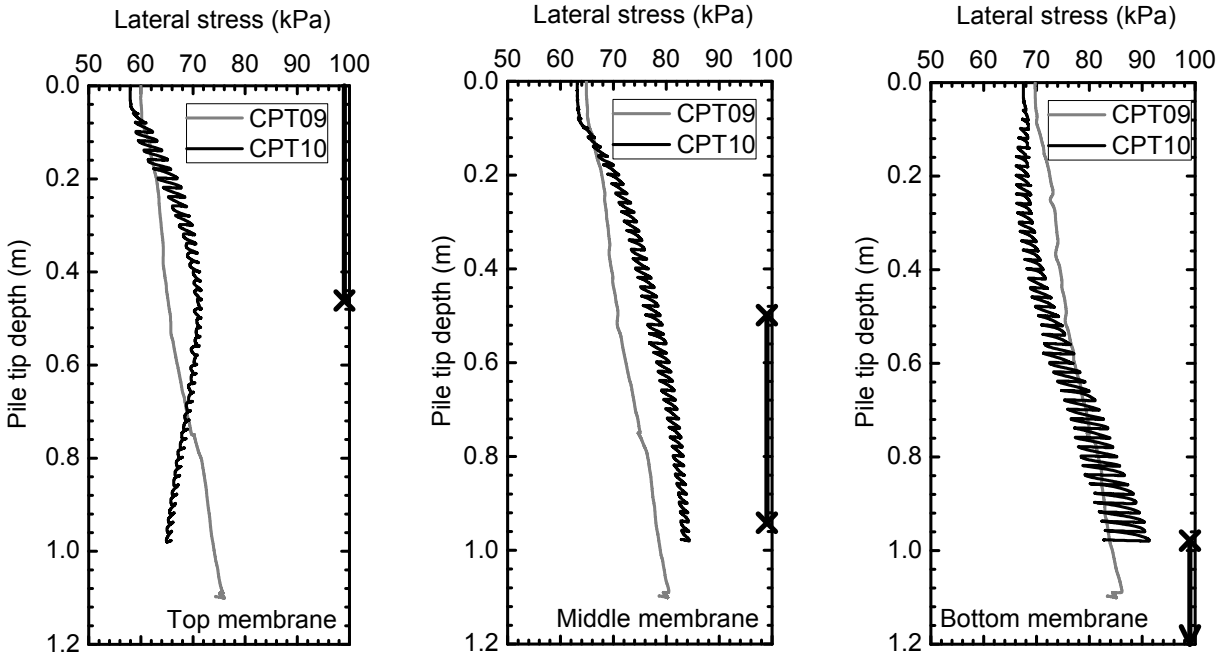


Figure 9-9: Lateral boundary membranes stresses during CPT09 and CPT10 piles installations under boundary condition BC5.

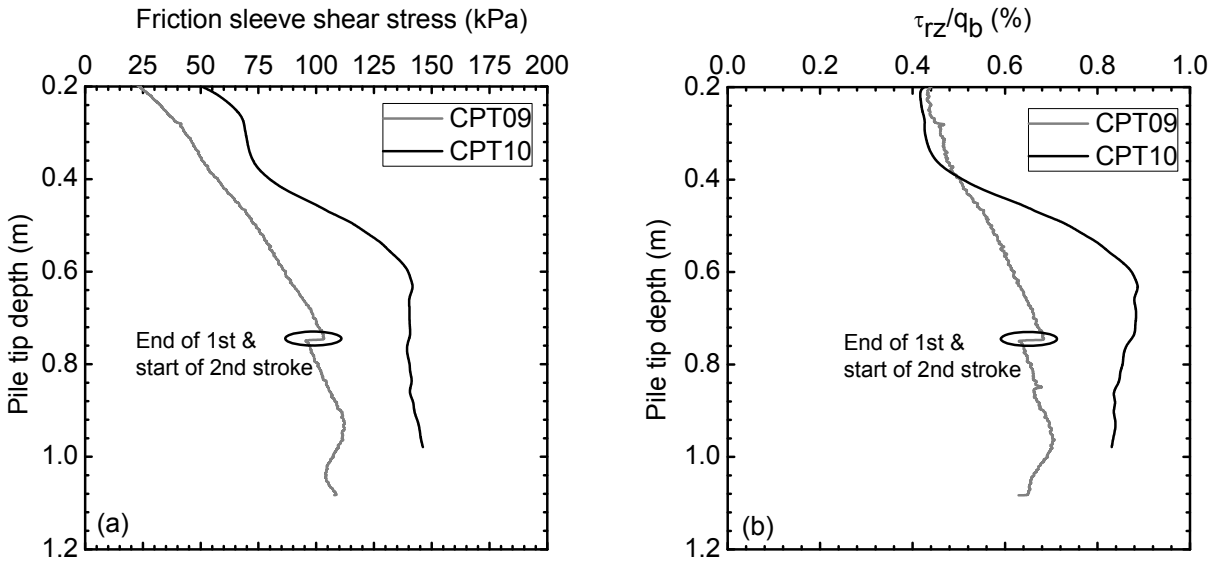


Figure 9-10: (a) Raw and (b) q_b–normalised sleeve shear stresses in CPT09 and CPT10 installation.

The EOD load–displacement behaviour of test ICP05, which investigated possible grain size effects, with looser GA39 in place of NE34 sand, is shown on Figure 9-11. As explained earlier it also involved inadvertently lower sand density index. Figure 9-11 shows full base mobilisation within 5mm and a low total capacity and a base to shaft of 0.75:0.25, showing dramatically less shaft resistance in the finer looser sand. As reviewed in section 9.4 this might be related to a more marked susceptibility to cyclic loading during installation.

Further scale effects were investigated in test MiP01 where a stainless steel relatively smooth (R_{cla} = 1 - 2μm) 12mm diameter un-instrumented Micro pile was installed into a blank dry NE34 sand mass (with BC3 boundary conditions). Figure 9-12 shows, as expected a much smaller total capacity for this 12mm diameter, relatively smooth pile (the Micro–pile had no tip load cell). Assuming 18MPa base resistance, as observed in the typical dry NE34 sand tests with 36mm piles installing in blank chambers, the base capacity would be 2.03kN, the shaft 3.56kN and the relative base to shaft split 0.36:0.64. The proportionally larger shaft contribution results from the threefold increase in the shaft to base area ratio, although this is offset by an increase in L/D (27.5 → 82.5) which leads to stronger h/R effects and a lower δ value, both of which reduce the average τ_{rz}.

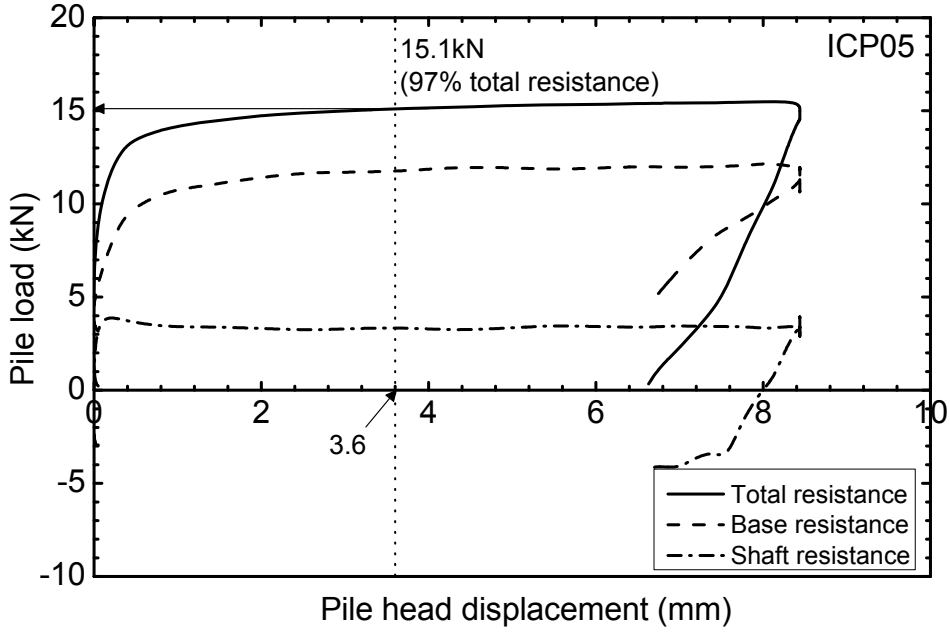


Figure 9-11: ICP05 EOD load–displacement behaviour showing total, base and shaft resistances.

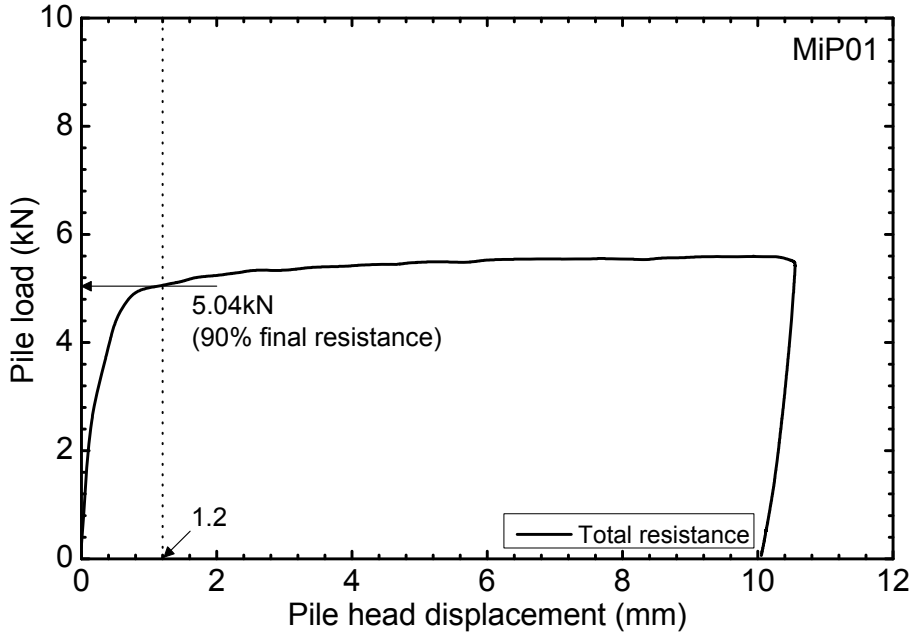


Figure 9-12: MiP01 EOD load–displacement behaviour showing the total pile resistance.

Finally, the effects of mode of pile installation on short–term axial capacity were investigated in tests DI and DII by driving (as discussed in section 5.6) un-instrumented 36mm diameter piles with roughnesses R_{cla} = 2 - 3μm and 3 - 4μm in dry NE34 sand applying BC5 and BC1 respectively. Figure 9-13 shows the load–displacement behaviour of pile DI after installation

to full penetration using 46 blows of average drop weights and heights equivalent to 16.5kgs and 1.4m. In this test the average radial boundary stresses fell (rather than increased) from 62kPa to 33kPa (Figure 9-14). DI showed a markedly reduced compression capacity (10.67kN) and still lower tension capacity (1.84kN) shortly after installation, both indicating marked radial stress reductions on the shaft.

The second driven pile, DII, was driven into dry NE34 sand while applying a constant radial average stress 62kPa BC1 boundary condition. In this case 89 blows of 23.8kgs falling through 1.2m were required to penetrate the metre and a higher EOD total pile capacity (18.8kN) developed as shown on Figure 9-15. Driven piles appear to be markedly sensitive to the chamber boundary conditions. DI dynamic installation generated lower stresses throughout the sand chamber when the boundaries were sealed compared to cyclic jacking. As the driven piles were not instrumented the detailed evolution of the stresses could not be monitored during penetration. However, Silva (2014) reports further studies with instrumented driven piles and instrumented sand masses. It can also be recalled from section 8.5 that Allard's (1990) centrifuge driven pile tests, which were also conducted in a sealed system (of smaller relative diameter ratio than the INPG CC) led to markedly lower stresses than the Author's Mini-ICP tests, see Figure 8-6.

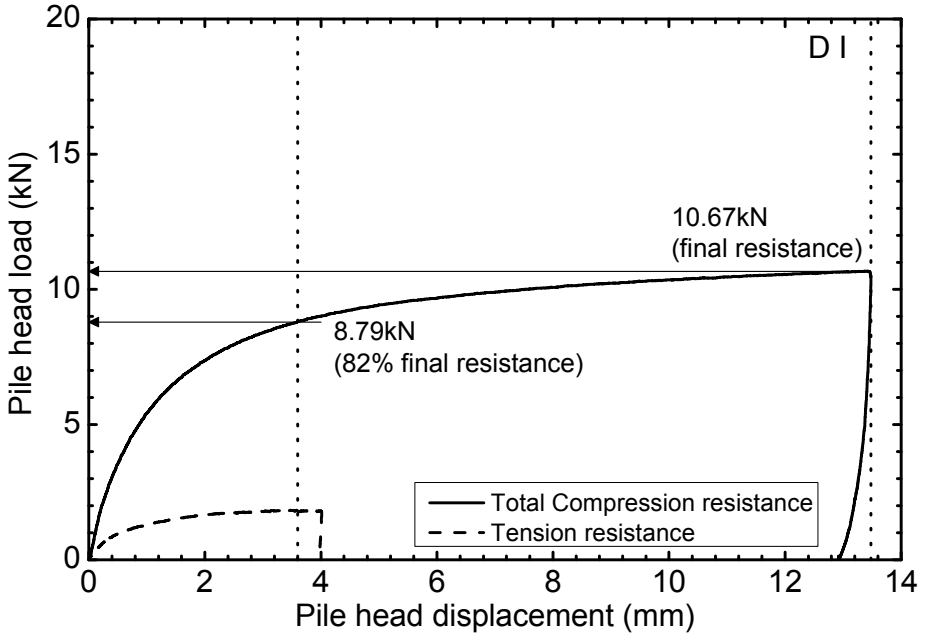


Figure 9-13: DI EOD load–displacement behaviour showing the total pile resistance and tension resistance.

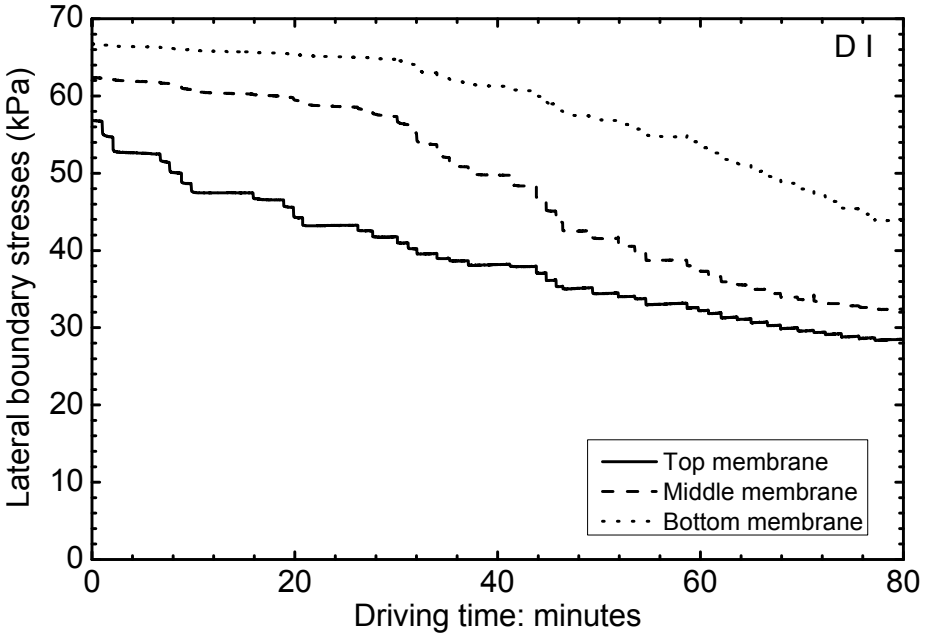


Figure 9-14: Chamber lateral boundary stress changes during the driving of model driven pile DI applying BC5 boundary condition.

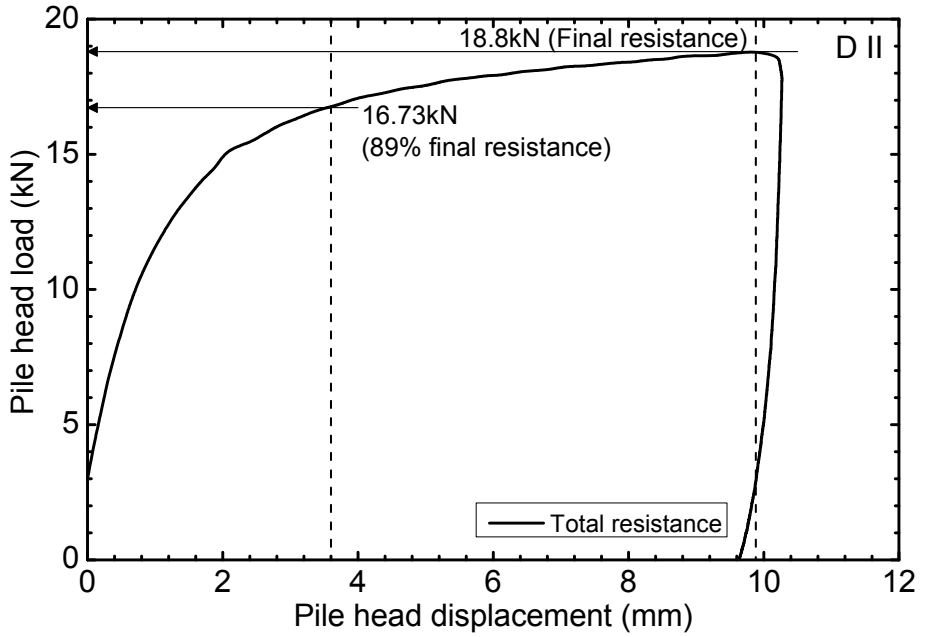


Figure 9-15: DII EOD load–displacement behaviour showing the total pile resistance applying BC1 boundary condition.

9.3 Effective stress paths followed at pile–sand interface

Interface stress measurements were made in all Mini-ICP load tests. The local radial and shear stresses measured at the 'leading', 'following' and 'trailing' clusters (A, B, C) during the first

static compression load tests are presented in Figures 9-16 to 9-20. In general the effective stress paths followed at each cluster are broadly similar and resemble those observed with the field with the larger ICP pile in loose and dense sands; Lehane (1992), Lehane et al. (1993) and Chow (1997).

The paths state start from negative 'residual' shear stress that pushed the piles downwards to counteract the locked–in base loads after installation. Compression loading imposes positive shear stresses and the shaft interface responds by tending to contract radially, showing falling σ'_r until the paths engage a local Phase Transformation Point (PTP) at the following calculated average mobilised δ values at cluster A (20.85° ± 6.0°), B (13.3° ± 1.8°) and C (21.2° ± 3.5°), after which the paths climb rightward as the radial stresses increases with apparent dilation until a 'constant volume' point is reached where local failure (slip) develops without further increase in radial stresses. The unloading paths involve steadily contractive slopes $\Delta\tau_{rz}/\Delta\sigma'_r > 1$ that bring the final effective stress state close to the point from which the test began.

The large displacement ultimate interface failure δ_{cv} angle for NE34 sand shearing against stainless steel with R_{cla} = 3μm was assessed as 27° from multiple ring shear interface tests (Yang et al. 2010). The angles at which the Mini-ICP clusters showed local failure scatter around this value with δ_{cv} of 30.5° ± 3.1° at cluster A, 25.3° ± 4.3° at B and 25.3° ± 2.1° at C. The end of installation and final unloading stress states tends to fall on a line established in the tensile region and inclined at mobilised δ angles of -12.0° ± 3.6° at A, -13.4° ± 5.8° at B and -17.3° ± 3.0° at C. The field ICP tests and 'CPT' pile design methods all suggest that the radial stresses should decline systematically from A, to B and C clusters. However stress localisations associated with the chamber's top boundary effects (see Section 5.2.2.1) cause cluster C (which was always positioned within the top 0.2m of the chamber) to have anomalously higher stresses than at clusters B or A.

The interface effective stress path for ICP05 (conducted with finer and looser GA39 sand) is shown on Figure 9-20. In keeping with the pile's relatively low EOD total shaft capacity, σ'_{rs} is far lower than in the NE34 sand tests. However the PTPs occurred at 27.1° at A and 25.3° at C, both in the upper bounds of the NE34 sand tests, and the interface stress paths mobilise higher interface shearing angles of 33.8° at A and 32.3° at C, which are higher than those developed in the ring shear interface tests conducted by the Author.

The degrees of 'stress–path dilatancy' developed at the pile interface SSTs are assessed by comparing the ultimate failure radial stresses on the loaded paths as a ratio of those applying at the end of installation, $(\sigma'_{rf}/\sigma'_{rs})_{EOD}$ and these are listed in Table 9-2. The degree of stress dilation depended on 1) the degree of locked-in initial stress, 2) the stiffness of the surrounding sand and 3) the interface roughness for a particular pile radius (e.g. Jardine et al. 2005a). The degree of dilation on the Mini-ICPs in the NE34 tests increases up the pile shaft from cluster A to C as the interface roughness of the pile reduces with depth due to progressive surface abrasion during installation.

Stress reversal effects (from the negative residual shear stress state which decrease up a section of the pile) that potentially inhibit dilation are in this case overwhelmed by the roughness effects. ICP05 (on finer, looser GA39 sand) showed an approximately 40% higher average dilation ratio than the NE34 tests.

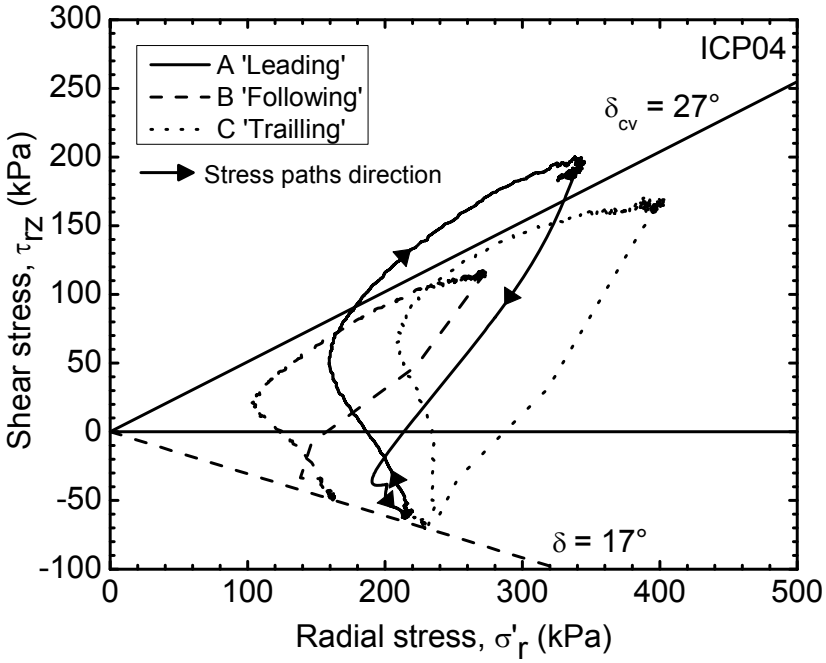


Figure 9-16: Interface stress paths of ICP04 Mini-ICP in dry NE34 sand chamber with BC3 boundary conditions during short term EOD static compression load test.

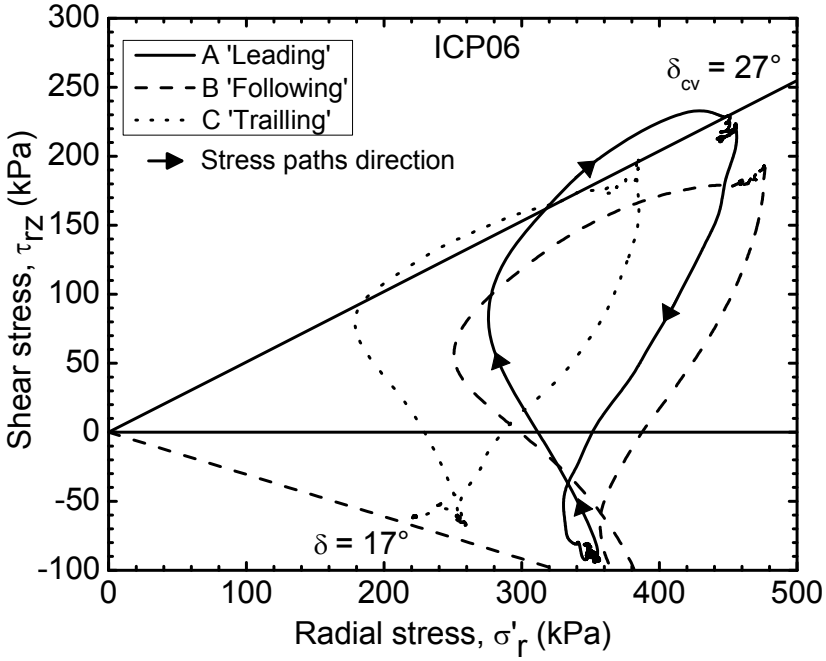


Figure 9-17: Interface stress paths of ICP06 Mini-ICP in wet NE34 sand chamber with BC3 boundary conditions during short term EOD static compression load test.

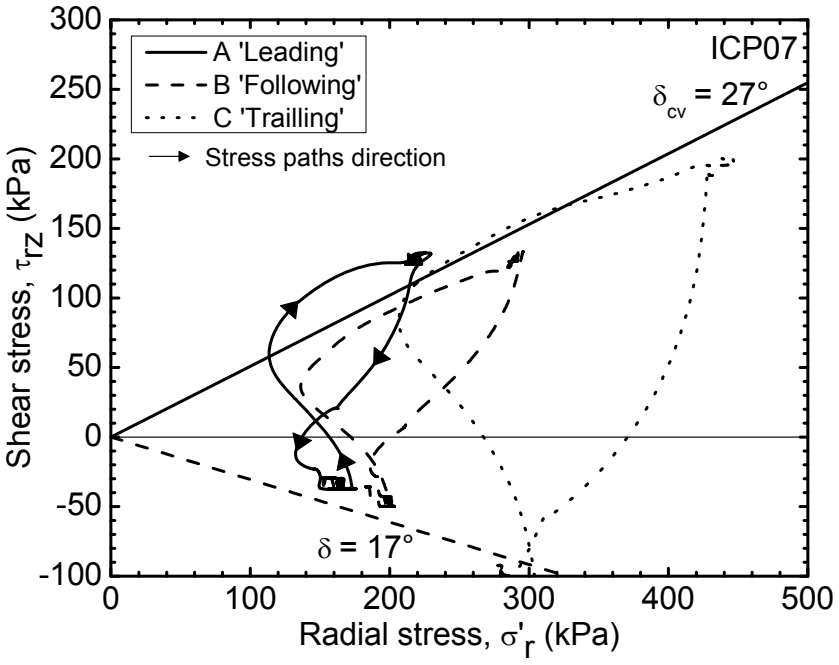


Figure 9-18: Interface stress paths of ICP07 Mini-ICP in dry NE34 sand chamber with BC5 boundary conditions during short term EOD static compression load test.

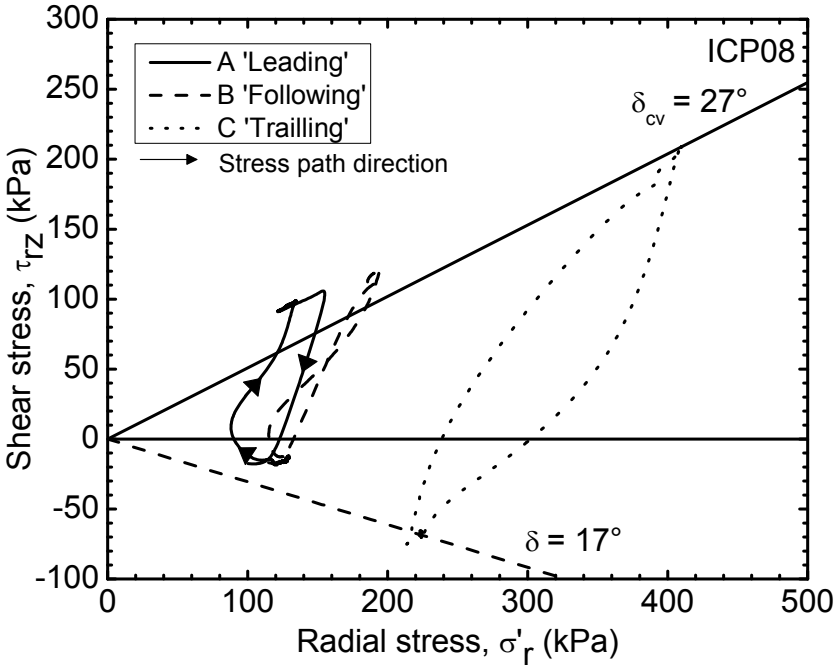


Figure 9-19: Interface stress paths of ICP08 Mini-ICP in dry NE34 sand chamber with BC5 boundary conditions during the last stroke of pile installation.

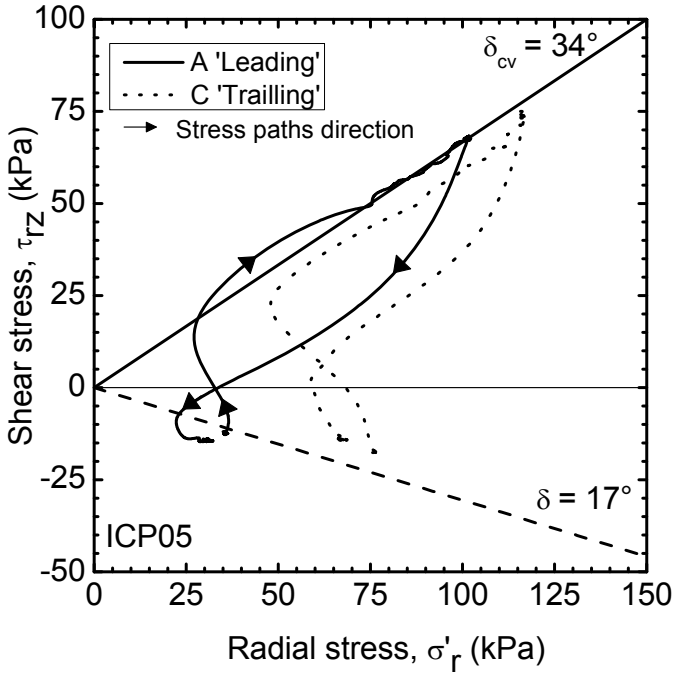


Figure 9-20: Interface stress path of ICP05 Mini-ICP in dry GA39 sand chamber with BC3 boundary conditions during short term EOD static compression load test.

Test	Cluster A	Cluster B	Cluster C	**Average**
ICP04 EOD	1.60	1.78	1.72	**1.70**
ICP06 EOD	1.29	1.22	1.51	**1.35**
ICP07 EOD	1.48	1.61	1.59	**1.56**
ICP08 stroke 49	1.40	1.59	1.91	**1.63**
Average	**1.44**	**1.55**	**1.69**	**1.56**
ICP05 EOD	2.86	N/A	1.56	**2.21**

Table 9-2: Degrees of dilation (= $\sigma'_{rf}/\sigma'_{rs(EOD)}$) measured on the Mini-ICP test piles during EOD static load testing.

9.4 ICP-05 predictions of the model piles short term static axial capacities

An indirect assessment has been made of the degree to which the models represent field scale piles by comparing the static axial compression capacities measured at the end of installation to the 'medium-term' capacities predicted by the ICP-05 method (Jardine et al. 2005a). As reviewed in section 2.8 this approach has been calibrated against high quality full scale pile load tests and generally offers good predictive reliability for field tests conducted around 10 days after driving with CoV < 0.34 and little bias. The sand input parameters are the CPT tip resistance profile, vertical effective stress profile and interface shear resistance angle values while the pile input parameters are length, diameter, roughness and the end conditions. Where available tip resistances from the pile installation have been used otherwise tip resistances from equivalent tests with measurements have been used.

Table 9-3 summarises the estimated compression axial static capacities of the piles in this test series calculated on Microsoft Excel spreadsheets. The ~1m deep sand masses penetrated by the piles were divided into fifty 20mm thick sand layers. The ratios of the calculated to measured base, shaft and total capacities are expressed as the ratio Q_c/Q_m. A generally good match is observed on Table 9-4 for the piles jacked into NE34 sand under the various chamber boundary conditions, moisture states, and scales with shaft compression capacity arithmetic mean of Q_c/Q_m = 1.05 and CoVs = 0.09.

The EOD capacities of the model pile jacked into looser and finer GA39 sand and the piles driven in NE34 do not fit the 'field' tested ICP-05 predictions nearly as well. The predictions for test ICP05 in dry GA39 sand exceed the shaft measurements very considerably and the total capacity by 40%. Figure 9-21 plots the radial stationary and moving stresses from Mini-ICP cluster A in ICP05 along side the stresses predicted by the ICP-05 method showing that both the stationary and moving radial stresses are far lower than predicted. As proposed initially, test ICP05 low σ'_{rs} stresses might be attributed to a relatively high cyclic susceptibility of the fine and loose GA39 sand that is not addressed completely by the ICP-05's q_c–normalisation or h/R approach. This feature requires further checking.

The measured capacities of the dynamically driven piles also fell below the values predicted. The two piles driven in NE34 were either un-instrumented (DI) or had instruments which did not survive driving (DII). The mechanisms behind the driven trends are not be fully understood at present but are being investigated further with an instrumented driven pile by the continuing study by Silva (2014). Calibration chamber boundary conditions appear to play a significant role in differentiating the behaviour of jacked and driven piles and rigid boundaries may trap dynamic energy within the near field region leading to consequences that do not apply in the field where dynamic energy is free to radiate away from the pile during driving.

Date	Test		Q_c, ICP-05	Q_m	Q_c/Q_m
03/11/09	ICP04 EOD	Base	23.79	22.87	**1.04**
		Shaft	14.26	12.15	**1.17**
		Total	38.04	35.02	**1.09**
06/05/10	ICP05 EOD	Base	12.15	12.21	**0.99**
		Shaft	9.63	3.28	**2.93**
		Total	21.78	15.49	**1.40**
18/10/10	ICP06 EOD	Base	28.01	27.13	**1.03**
		Shaft	17.55	18.33	**0.96**
		Total	45.55	45.46	**1.00**
22/12/10	MiP01 EOD	Total	5.21	5.60	**0.93**
10/05/11	CPT09 EOD	Base	19.38	21.27	**0.91**
		Shaft	9.53	9.15	**1.04**
		Total	28.91	30.42	**0.95**
24/05/11	ICP07 EOD	Base	20.67	22.20	**0.93**
		Shaft	13.82	13.24	**1.04**
		Total	34.50	35.44	**0.97**
29/09/11	ICP08 Last stroke	Base	19.18	18.73	**1.02**
		Shaft	14.29	11.89	**1.20**
		Total	33.46	30.62	**1.09**
19/12/11	CPT10 Last stroke	Base	18.61	19.48	**0.95**
		Shaft	9.84	9.22	**1.07**
		Total	28.45	28.70	**0.99**
31/01/12	DI EOD	Total	17.73	10.67	**1.66**
13/03/12	DII EOD	Total	26.35	18.80	**1.40**

Table 9-3: Measured and ICP-05 method (Jardine et al. 2005) calculated axial static compression pile load capacities compared.

Test	Capacity	Arithmetic mean Q_c/Q_m	CoV Q_c/Q_m
Jack-stroke installed piles in dense NE34 sand	Base	0.98	0.05
	Shaft	1.05	0.09
	Total	1.01	0.06

Table 9-4: Q_c/Q_m of all jack-stroke installed model piles in the dense NE34 sand.

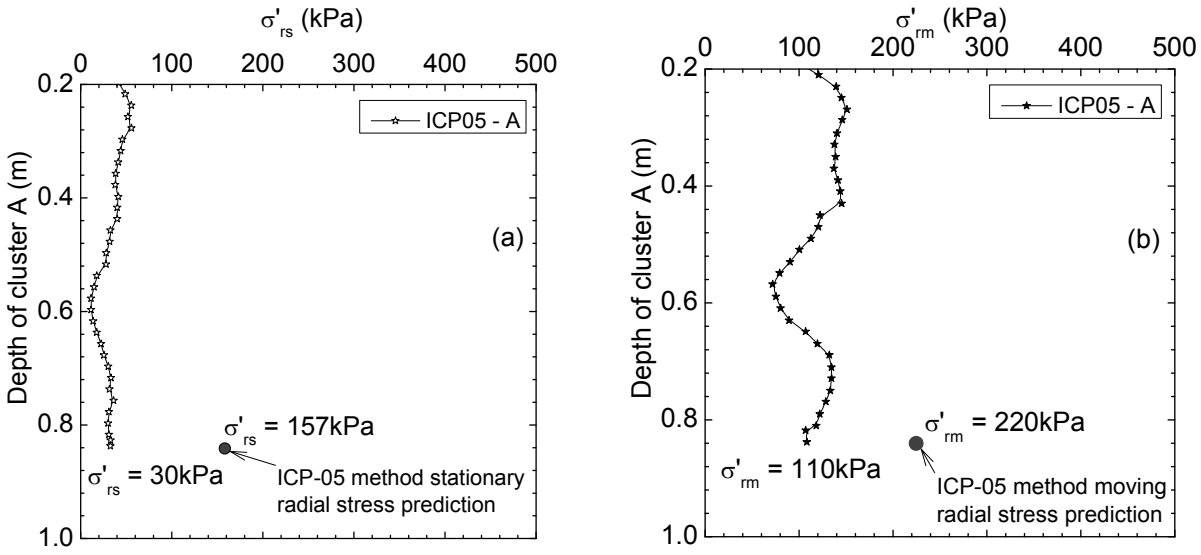


Figure 9-21: Comparison of radial stresses from Mini-ICP test ICP05 and the ICP-05 method (a) stationary and (b) moving.

9.5 Potential rate effects on pile resistance behaviour in sand

The Author's pile installations, EOD tests, aged static and cyclic tests involved 'failing' the piles at a range of pile displacement rates. It is worth pausing to consider how such shifts in rates might affect the results obtained.

In soil mechanics sand has conventionally been considered as having properties that are independent of strain rate. More recent studies by Matsushita et al. (1999), Augustesen et al. (2004) or Tatsuoka (2011) show that while sand may not show the isotach behaviour seen in many types of clay, it can show temporary responses to strain rate changes as illustrated in Figure 9-22. Figure 9-23 reports drained triaxial tests by Weinstein (2008) at three different strain rates on loose (I_D = 40%) dry Fontainebleau sand taken to a maximum axial strain of 15%. The 70mm diameter, 140mm high specimens had been isotropically consolidated to 100kPa. The stress-strain behaviour is broadly independent of the applied strain rate. There appears to be slight increase in shear resistance with increasing strain rate at low strain levels but this was attributed by Weinstein to experimental variation as the peak shear resistance became coincidental at large strains. However, Tatsuoka (2011) argues that increasing strain rates increases the extent of the (very limited) Y_1 elastic range and so should lead to stiffer initial trends. Weinstein (2008) also reports an investigation of rate effects with the same sand on the load capacity of a 20mm diameter displacement model pile taken to displacements of 0.1D in a 524mm diameter calibration chamber (giving $d_{chamber}/D$ = 26.2) under a vertical surcharge pressure of 250kPa (and a K_0 = 0.4). The pile was load–tested successively at three different rates, each ten times slower than the previous as shown in Figure 9-24. It is interesting that the three load–displacement curves show marginal but

progressive reductions in pile capacity with decreasing loading rates that amount to ~2% per rate log cycle.

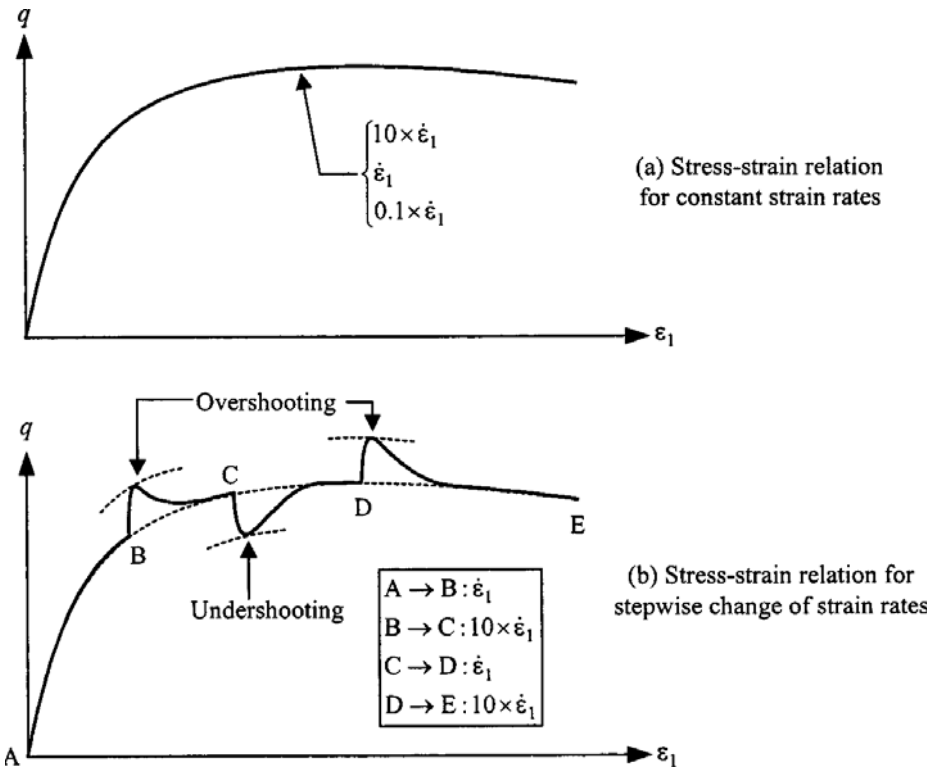


Figure 9-22: Schematic diagrams illustrating the rate dependency observed for sand by Matsushita et al. (1999) (a) The stress–strain relation for different constant strain rates coincide for the three strain rates and (b) temporary over and under shooting due to stepwise change in strain rate (Augustesen et al. 2004).

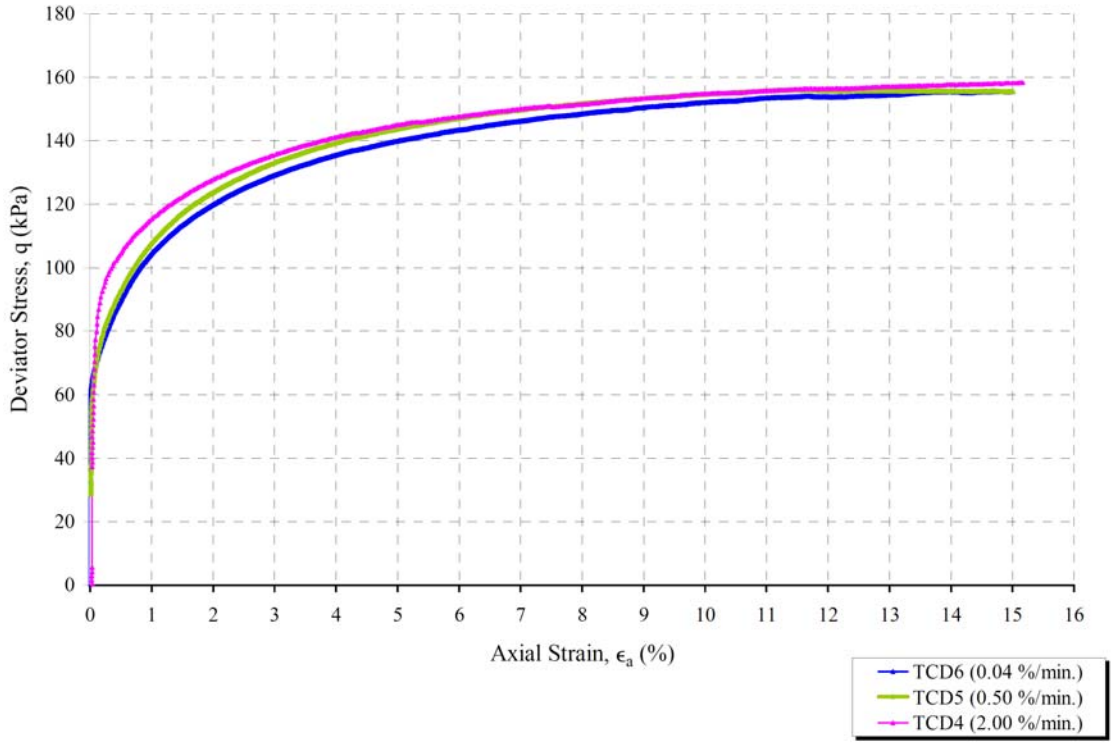


Figure 9-23: Drained triaxial compression tests on Fontainebleau sand investigating strain rate effect (Weinstein 2008).

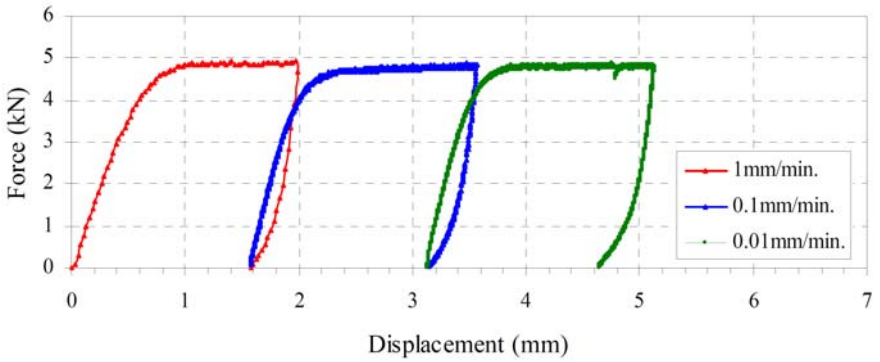


Figure 9-24: Pile loading tests for three different successive loading rates on one pile in Fontainebleau sand (Weinstein 2008).

In the current study the Mini-ICP piles were advanced by 20mm strokes applied at 2mm/s followed by full unloading. The piles' end of installation static compression capacities were assessed by tests performed ten (0.2mm/s) or more times slower. Figures 9-25 and 9-26 examine rate effects by comparing the load displacement curves for the last (49th) installation stroke with the slower (50th stroke) capacity checks performed in series ICP04 and ICP06 in dry and wet NE34 sand (with boundary conditions BC3). The base and shaft components are compared along side the total capacities. Rate effects on total capacity appear to be marginal or even negative. Reducing the rate of penetration tenfold gave, on average a 5.5% base relaxation but a shaft increase of around 7.8%. This is attributed to the added plastic time-dependent straining which allows relaxation at the base.

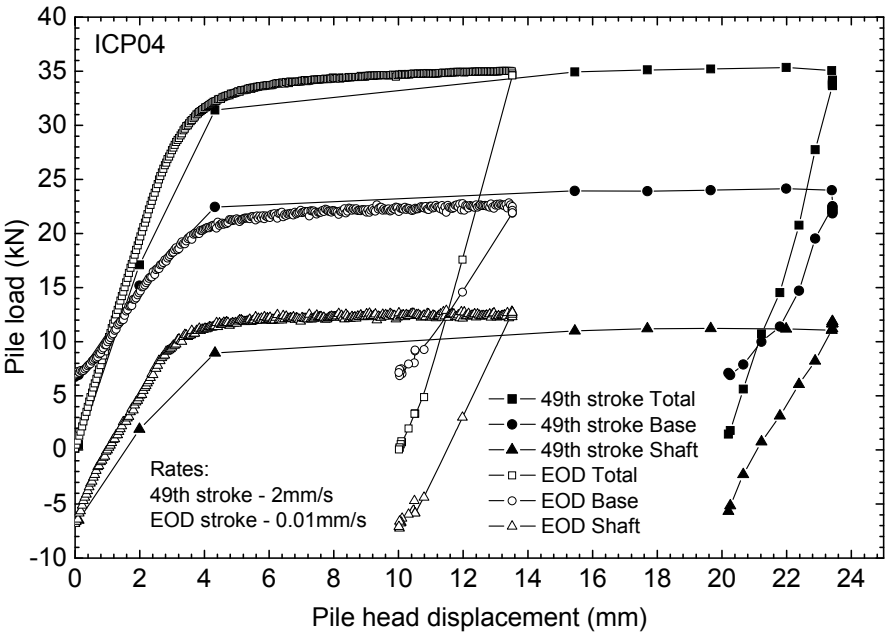


Figure 9-25: ICP04 Mini-ICP installation in dry NE34 sand with boundary condition BC3 last stroke of installation (49th) and EOD stroke (50th) loads compared.

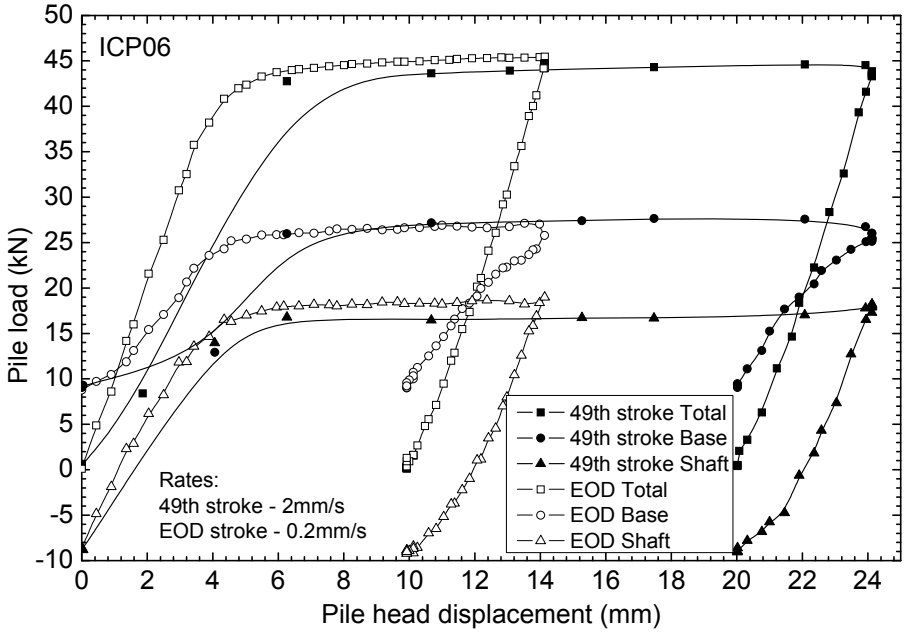


Figure 9-26: ICP06 Mini-ICP installation in wet NE34 sand with boundary condition BC3 last stroke of installation (49th) and EOD stroke (50th) loads compared.

9.6 Summary conclusion

The EOD results collated in this chapter provide the baseline dataset that is compared in the next chapter with equivalent experiments performed after extended periods of ageing under controlled pressures and temperatures.

Chapter 10

10 Ageing behaviour of laboratory model displacement piles in sands

10.1 Introduction

This chapter examines the behaviour observed on the model piles and within the sand masses during ageing. It also considers the features recorded under axial static loading behaviour after ageing. The potential changes in the piles' static compression capacities from the end of installation (EOD) after various periods of ageing were measured by applying post-ageing static axial compression load tests (C1). The static tension capacity trends developed after applying various modes of cyclic axial loading are analysed later in Chapter 11.

10.2 Pile ageing

10.2.1 Tests programme

The specific testing objectives and parameters of the pile ageing tests were set out in Tables 6-8 and 6-9. Table 10-1 below summarises all the EOD and post-ageing C1 capacities. The table includes the piles' ageing periods, the displacement rates applied in the axial static loading tests, penetrations, capacity changes after ageing. It also notes the boundary conditions for each test. It also includes a summary of the tests CPT01 to ICP03 which were performed earlier by the Imperial College – INPG group with CPT piles or the Mini-ICP piles in dry medium dense NE34 sand, as reported in an Imperial College internal report by Jardine (2009).

It should be noted that direct Mini-ICP pile base load measurements were only available from test ICP04 onwards. Previously the base contributions were estimated from the Mini-ICP by projections from the ALC at cluster A or by interpretations from tension tests. The following section analyses the loads and stresses measured on and around the piles during the ageing periods.

Test	Conditions	Testcode	Stroke	Date	Ageing	Rate	Final depth	Measured capacities (kN)			Capacity change (%)		
					(days)	(mm/s)	(mm)	Shaft	Base	Total	Shaft	Base	Total
CPT01	BC3	EOD	100th	27/07/07	N/A	~0.0002	1000	19.3	29.40	48.70	N/A	N/A	N/A
		C1	N/A	N/A			N/A	N/A	N/A	N/A			
CPT02	BC3	EOD	102nd	21/09/07	45		1020	13.00	21.90	34.90	+30%	-27%	-3%
		C1	103rd	05/11/07			~1030	16.90	16.00	32.90			
ICP01	BC3	EOD	92nd	27/11/07	97		920	11.00	22.50	33.50	+18%	-48%	-26%
		C1	93rd	03/03/08			~930	13.00	11.70	24.70			
ICP02	BC3	EOD	198th	20/05/08	139		990	15.10	22.80	37.90	+13%	-30%	-13%
		C1	199th	06/10/08			~1000	17.00	16.00	33.00			
ICP03	BC3	EOD	50th	29/05/09	53		990	10.95	26.46	37.41	-13%	0%	-4%
		C1	51st	21/07/09			~1000	9.57	26.46	36.03			
ICP04	Standard BC3	EOD	50th	03/11/09	41	0.01	986	12.15	22.87	35.02	-13%	-4%	-7%
		C1	51st	14/12/09		0.01	994	10.53	22.01	32.54			
ICP05	GA39 test with BC3	EOD	51st	06/05/10	71	0.2	998	3.28	12.21	15.49	-18%	-6%	-9%
		C1	52nd	16/07/10		0.02	1007	2.67	11.44	14.11			
ICP06	Wet with BC3	EOD	50th	18/10/10	49	0.2	986	18.33	27.13	45.46	-21%	-18%	-19%
		C1	51st	06/12/10		0.02	995	14.44	22.28	36.72			
MiP01	Micro pile with BC3	EOD	50th	22/12/10	68	0.2	989	N/A	N/A	5.60	N/A	N/A	-20%
		C1	51st	28/02/11		0.02	998	N/A	N/A	4.45			
CPT09	Rate and cycles with BC5	EOD	3rd	10/05/11	7	0.02	1097	9.15	21.27	30.42	-0.1%	-7%	-5%
		C1	4th	17/05/11		0.02	1107	9.14	19.80	28.94			
ICP07	BC5	EOD	50th	24/05/11	52	0.2	990	13.24	22.20	35.44	+11%	-4%	+1%
		C1	51st	15/07/11		0.02	1001	14.69	21.22	35.91			

Table continues overleaf…

Test	Conditions	Testcode	Stroke	Date	Ageing	Rate	Final depth	Measured capacities (kN)			Capacity change (%)		
					(days)	(mm/s)	(mm)	Shaft	Base	Total	Shaft	Base	Total
ICP08	No EOD test with BC5	Last stroke	49th	29/09/11	15	2	977	11.89	18.73	30.62	+8%	-0.6%	+3%
		C1	50th	14/10/11		0.02	994	12.89	18.61	31.50			
CPT10	Rate with BC5	Last stroke	50th	19/12/11	32	10	977	9.22	19.48	28.70	+13%	+5%	+7%
		C1	51st	20/01/12		0.02	997	10.39	20.47	30.86			
DI	Driven with BC5	T1	48th	01/02/12	~12	0.02	1025	-1.84	0	-1.84	+11%	N/A	+11%
		T2	49th	13/02/12		0.02	1021	-2.04	0	-2.04			
DII	Driven with BC1	EOD	90th	13/03/12	41	0.02	993	N/A	N/A	18.80	N/A	N/A	+5%
		C1	91st	23/04/12		0.02	1003	N/A	N/A	19.69			

N/A – Not Applying

Table 10-1: Post-ageing compared to end of installation capacities of all model piles in this laboratory study for the assessment of capacities changes due to ageing.

10.2.2 Stress and load behaviour of ageing model piles

10.2.2.1 'Standard' ageing test with the Mini-ICP in dry NE34 sand

The pile load distribution, shaft interface and sand mass stresses were continuously monitored during ageing tests which imposed constant vertical surcharge stresses (≈ 152kPa) and temperature (18.5 ± 0.5 ^{0}C) in the sand chamber. The description of the ageing response starts with a 'standard' case of a Mini-ICP installed in dry NE34 sand, test ICP04, and progresses to consider a range of test parameters. The base test ICP04 investigated the ageing behaviour of an inert stainless steel Mini-ICP displacement pile in medium–dense dry NE34 sand under the simple lateral boundary conditions BC3.

Large quantities of data were acquired from the sensors recorded at 2 seconds intervals. As discussed in Section 5.5.3.2, the Mini-ICP SST showed stable radial and shear stresses under bench testing to within ±1.0kPa and ±0.5kPa respectively over extended periods with temperatures held to within ±1.0^{0}C, while the ALCs remained steady to within ±0.10kN. The general trends for pile loads, interface radial and shear stresses for ICP04 are plotted against semi-log time on Figures 10-1 to 10-3 respectively. The traces are generally stable to within ±1.5kPa or ±0.15kN. However, minor temporary signal conditioning difficulties encountered with Mini-ICP cluster B between days 20 to 35 led to individual reading showing 10 times the usual scatter around otherwise constant readings.

Figures 10-4 to 10-5 plot the interface stress log–time trends taken from clusters A, B and C over 41 days, shown normalised by their initial values as observed over the first day. There is little change in interface radial stresses over the 41 day ageing duration; the stresses are constant over the first 10 days then decrease by at most ~3%. Normalised interface shear stress show a gradual relaxation of up to 10% in the most marked case followed by flat trends and average final stresses that are only 2% lower than the initial values. The corresponding axial loads shown on Figure 10-6 indicate compatible marginal base residual load relaxation. The cluster C (h/R = 45.6) trend is omitted from the normalised plot as the output scatter (±0.10kN) is significant compared to its near zero mean load, which distorts the normalised plot trends. The ageing stress trends in the sand mass are illustrated in Figures 10-7 to 10-9 considering the h/R = 29.4 level and radial distances away from the pile axis r/R = 2, 3, 5 and 8. The radial stresses remain practically constant over the first day of ageing, but then decrease by a maximum of ~23% with the greatest degree of relaxation taking place close to the pile (r/R = 3). The vertical and hoop stresses showed broadly similar trends.

In sum, ageing under controlled environmental conditions, after installing an inert Mini-ICP into dry medium-dense silica sand with BC3 rigid boundary conditions led to marginal reductions in the radial, vertical and hoop stresses in the sand mass and minor stress reductions on the pile shaft.

The major changes postulated to explain the field capacity trends described in section 3.2 were not seen after the end of installation. As assessed on Table 10-1 the pile axial capacities also failed to grow as markedly as had been seen in the field. Only marginal and potentially uncertain changes had been seen in the earlier CPT1 – ICP03 tests. Experiment ICP04 was conducted to check whether a series of technical improvements would lead to a more 'realistic' field capacity–time trend. In fact, even less impressive changes in capacity were recorded. The testing programme therefore progressed to systematically consider the possible effects of 1) scale 2) moisture state and pile material, 3) chamber boundary conditions, and 4) installation and testing procedures as possible parameters that may have inhibited the pile capacity ageing benefits interpreted from the field tests.

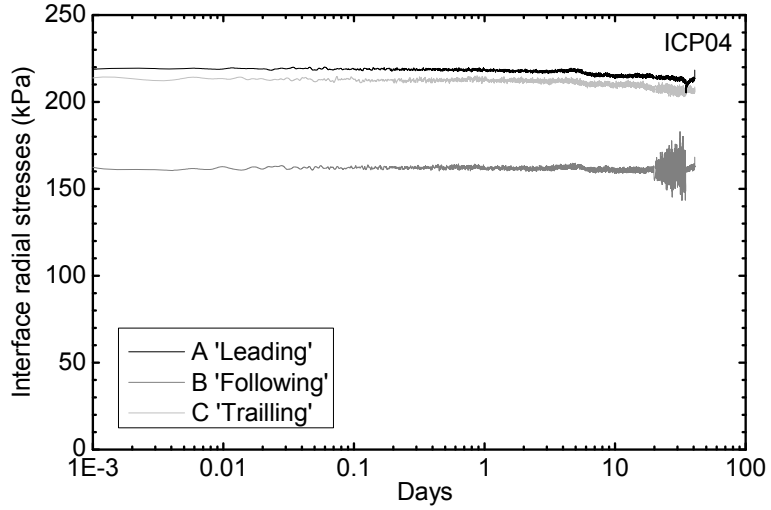


Figure 10-1: 'Standard' test ICP04 interface radial stresses–log time trends over 41 days ageing period.

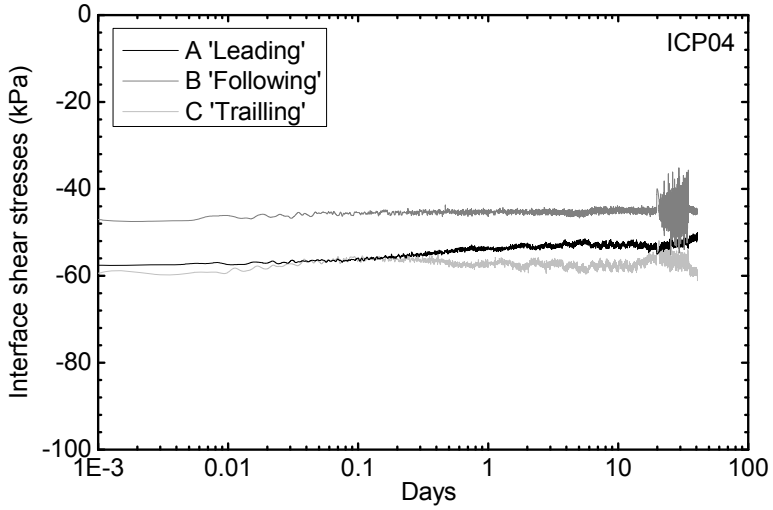


Figure 10-2: 'Standard' test ICP04 interface shear stresses–log time trends over 41 days ageing period.

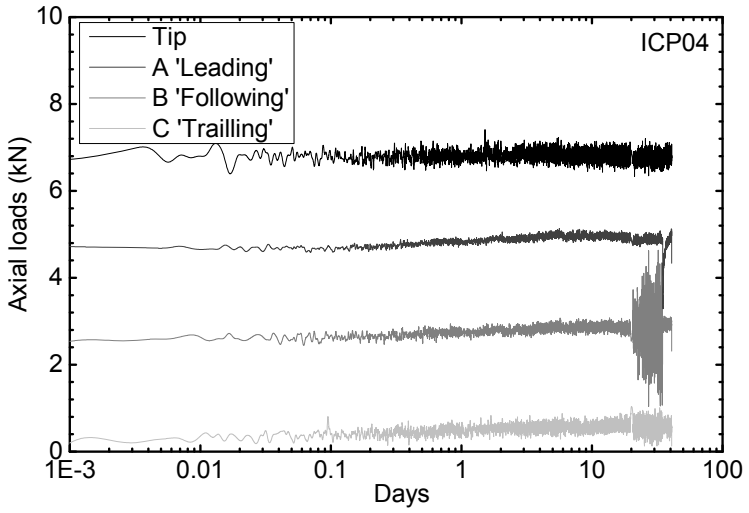


Figure 10-3: 'Standard' test ICP04 axial loads–log time trends over 41 days ageing period.

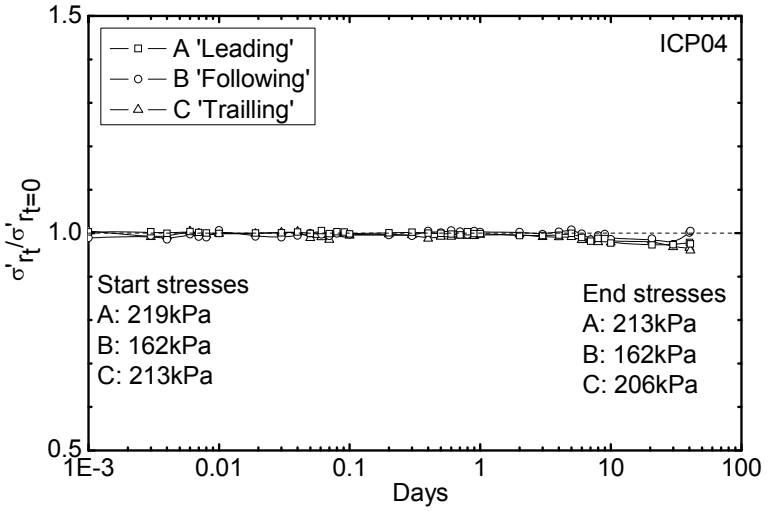


Figure 10-4: 'Standard' test ICP04 normalised interface radial stresses–log time trends over 41 days ageing period.

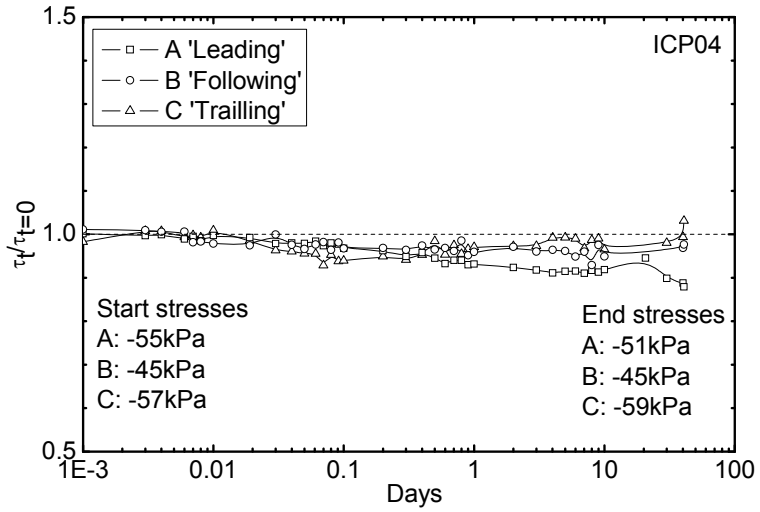


Figure 10-5: 'Standard' test ICP04 normalised interface shear stresses–log time trends over 41 days ageing period.

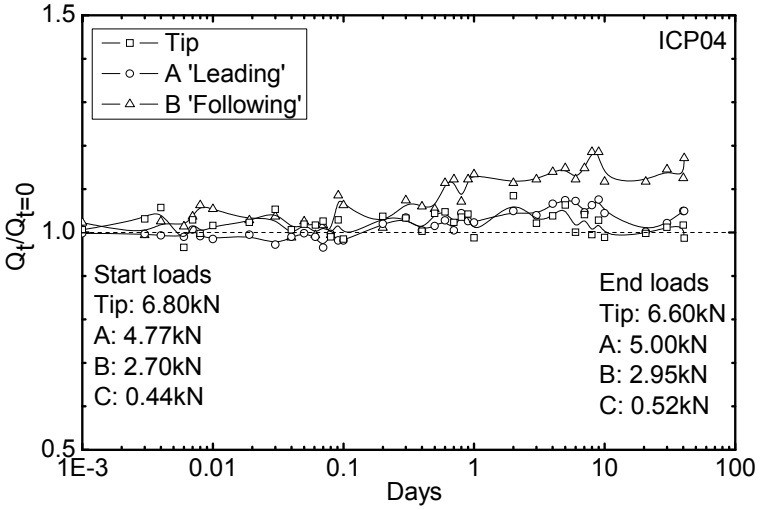


Figure 10-6: 'Standard' test ICP04 normalised axial loads–log time trends over 41 days ageing period.

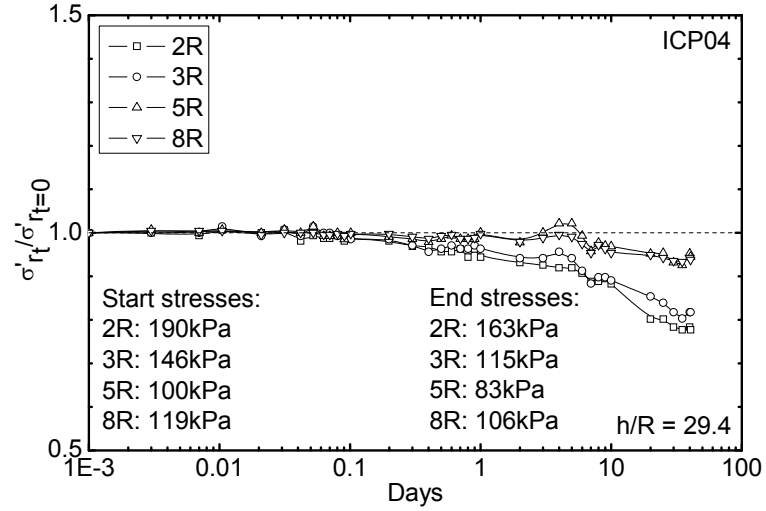


Figure 10-7: 'Standard' test ICP04 normalised sand mass radial stresses–log time trends over 41 days ageing period.

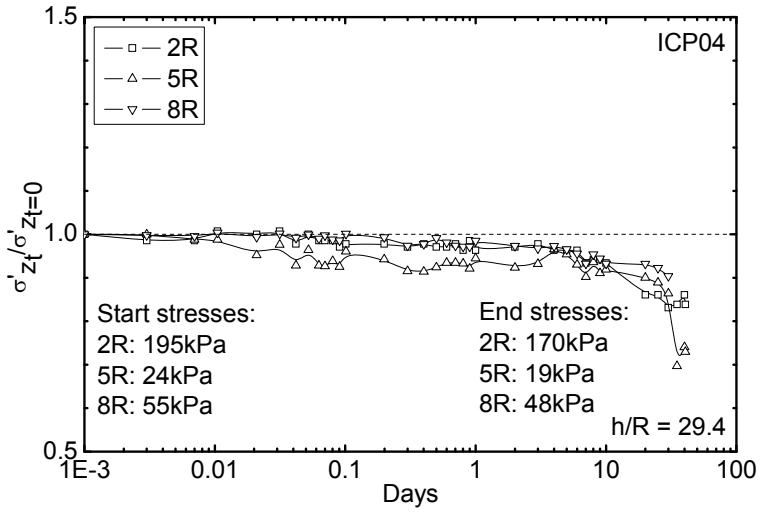


Figure 10-8: 'Standard' test ICP04 normalised sand mass vertical stresses–log time trends over 41 days ageing period.

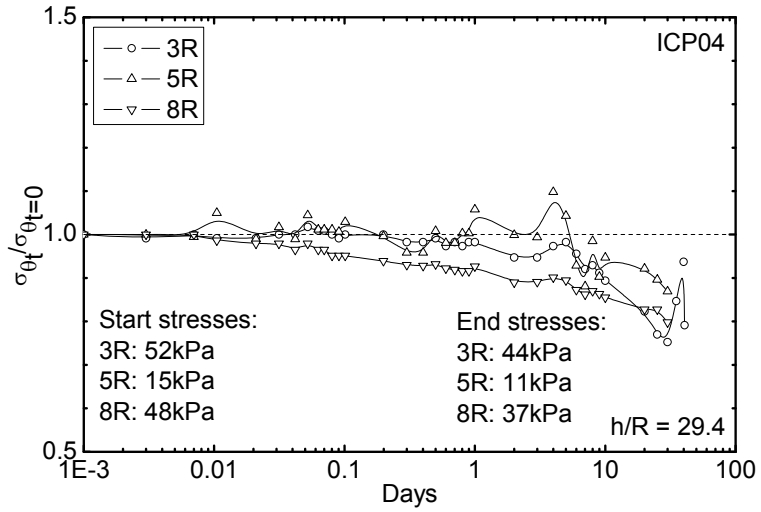


Figure 10-9: 'Standard' test ICP04 normalised sand mass hoop stresses–log time trends over 41 days ageing period.

10.2.2.2 Scale effects

Potential sand density state and pile–to–grain diameter ratio effects were examined first by installing the Mini-ICP test pile in the nearly half finer (and inadvertently less dense) dry GA39 silica sand. Figures 10-10 to 10-12 show how the interface radial and shear stresses and axial loads evolved over 71 days of ageing; as noted earlier cluster B SST failed during this installation. The pile stresses and loads developed were much lower than those in NE34 sand tests because of the GA39 sand mass less dense state and other factors discussed in Chapter 7.

The interface radial stresses plotted on Figure 10-10 increase slightly over the first 10 days then dip marginally ending around 4kPa (8%) below those measured at the start of ageing. The interface shear stresses showed an average decrease of ~1kPa at cluster A and a gain of 7kPa at

cluster C near the ground surface with gradual increases in the axial loads developed on the pile shaft as shown on Figure 10-12 that built to an ~16% residual base load increase. The 18% shaft capacity loss noted in Table 10-1 indicates that the increase of the pile diameter to test sand particle size ratio (171 to 283) with the GA39 sand did not trigger capacity growth, although this may have been affected also by the lower density index that was inadvertently employed.

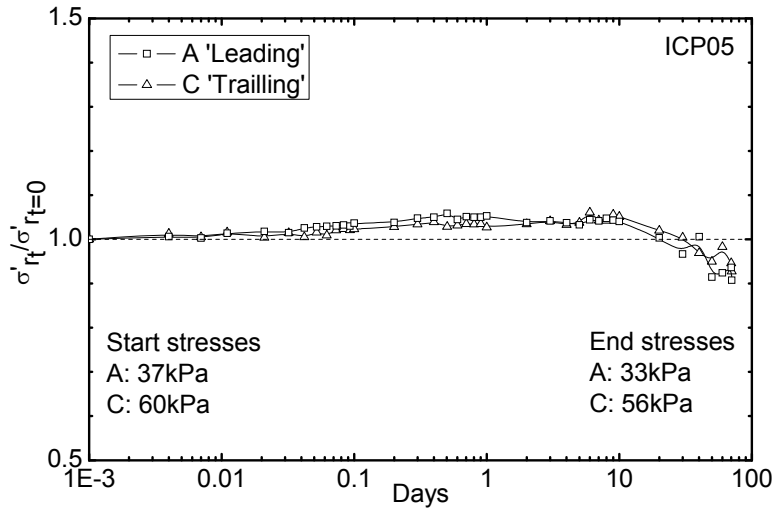


Figure 10-10: GA39 test ICP05 normalised interface radial stresses–log time trends over 71 days ageing period.

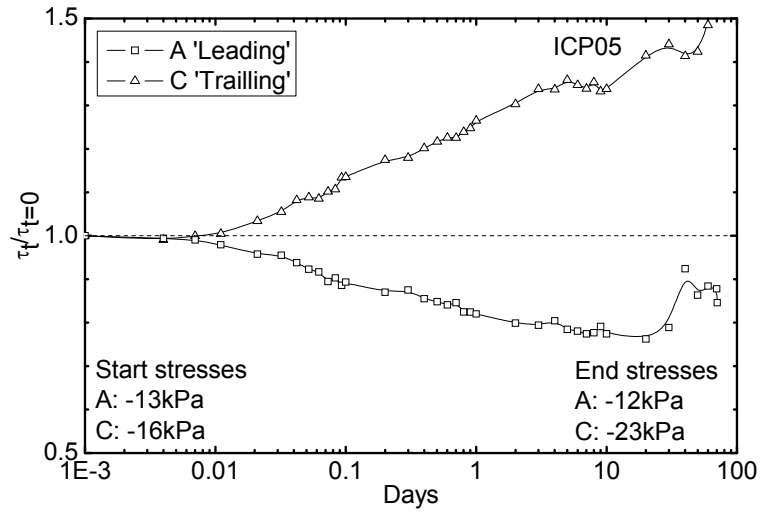


Figure 10-11: GA39 test ICP05 normalised interface shear stresses–log time trends over 71 days ageing period.

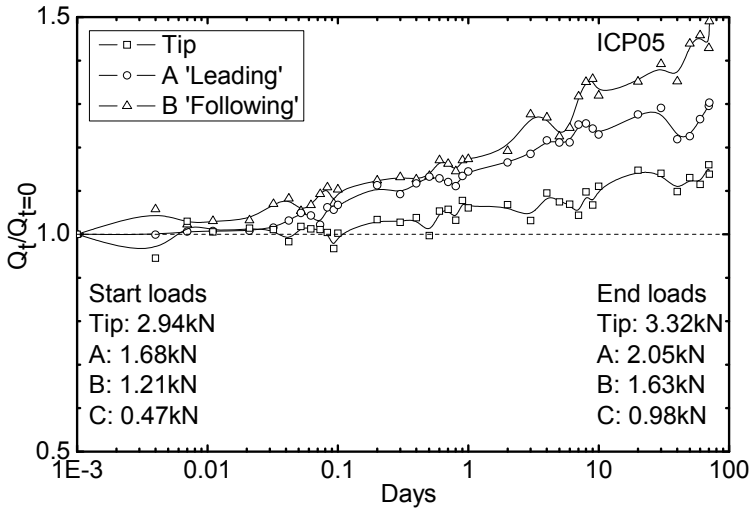


Figure 10-12: GA39 test ICP05 normalised axial loads – log time trends over 71 days ageing period.

10.2.2.3 Moisture effects

Test ICP06 was conducted to determine whether the presence of water was necessary to achieve more marked capacity growth. The stainless steel Mini-ICP was installed in wet dense NE34 sand applying the BC3 boundary conditions. The interface radial, shear stresses and axial loads observed over 49 days of ageing are shown on Figures 10-13 to 10-15. Cluster A stopped working after 2 hours because of unintended water ingress through a single faulty Dowty seal. Up to that time the radial stress and axial loads had kept constant while the shear stress had shown gradual reductions. The interface radial stresses at cluster C remained steady while those observed at cluster B were constant before relaxing by about 30kPa (8% of the initial stress). The interface shear stresses (which counteracted the residual pile loads) broadly matched radial stresses responses. They kept steady at cluster C and relaxed at B by 15kPa (~12% of the initial stress). The pile axial load distributions presented on Figure 10-15 show re-distribution with the tip relaxing marginally by 9%, while cluster B gradually increased its load (by 17%). Checks can be made to assess whether the SST shear stresses and the ALC axial load trends are compatible. If the 30kPa shear stresses decrease measured on cluster B is considered typical over the shaft section from base to cluster B, the total shaft load shed amounts to 1.56kN, which roughly matches the observed increase of ~+0.8kN at B and relaxation of ~-0.6kN at the base that add up to -1.4kN load shed for the shaft section B – tip.

Figures 10-16 to 10-18 show how the normalised stresses varied in the wet sand mass. Difficulties with water proofing the instrumentation for the wet sand restricted the sensor deployment to just one level located at h/R = 14.4 with, radial and vertical stresses being measured at r/R = 2, 3, 5 and 8 and hoop stresses at r/R = 5 from the pile. The radial stresses on Figure 10-16 show similar trends to the dry dense NE34 sand experiments with all stresses generally declining

slightly but remaining within 70% of those developed at the start of ageing. The vertical stresses on Figure 10-17 showed similar changes over time while the single hoop stress trace in Figure 10-18 indicated slightly more marked relaxation. Taken with the 21% shaft capacity loss (Table 10-1) the ageing behaviours developed in wet and dry medium dense NE34 sand appear broadly similar. The presence of water did not lead to the field trends being matched with the laboratory model piles.

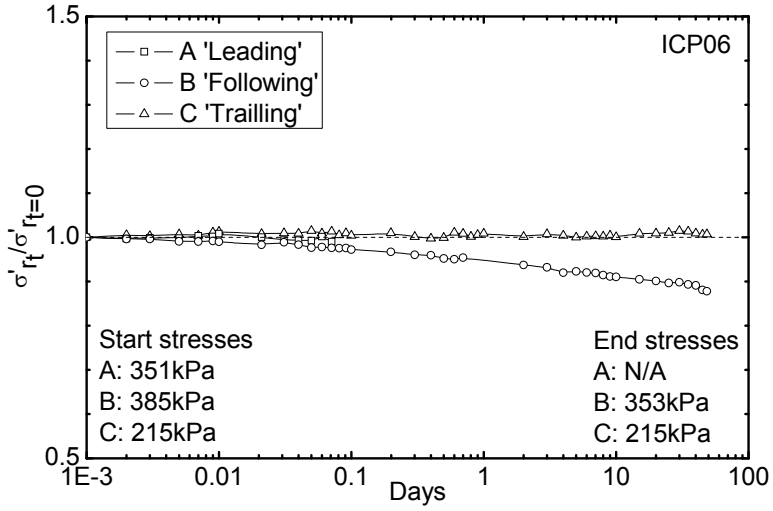


Figure 10-13: Wet test ICP06 normalised interface radial stresses–log time trends over 49 days ageing period.

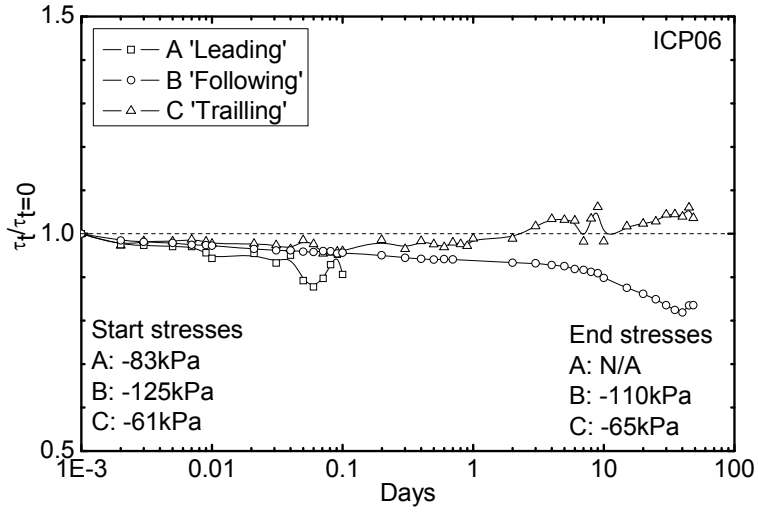


Figure 10-14: Wet test ICP06 normalised interface shear stresses – log time trends over 49 days ageing period.

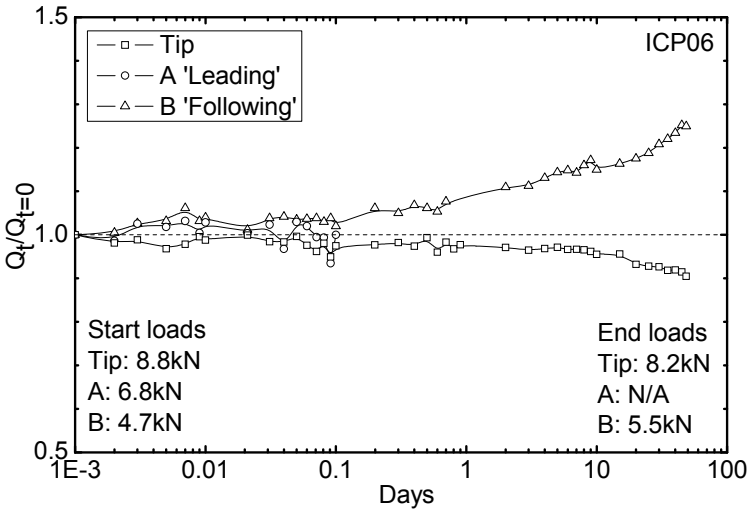


Figure 10-15: Wet test ICP06 normalised axial loads–log time trends over 49 days ageing period.

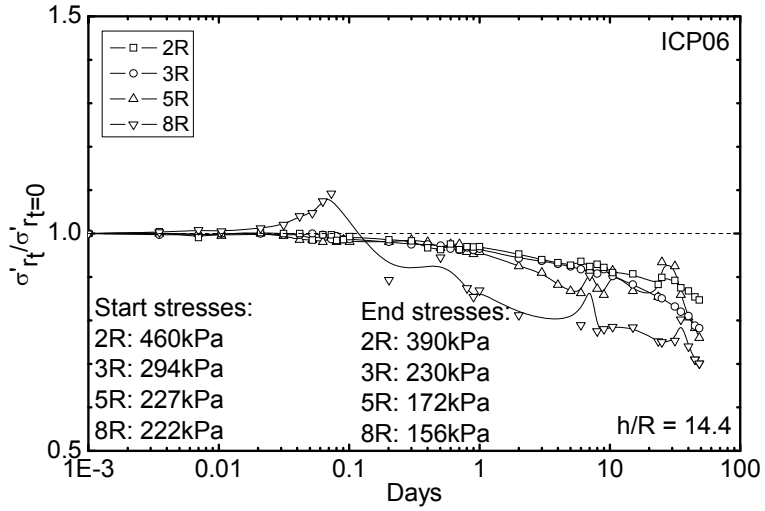


Figure 10-16: Wet test ICP06 normalised sand mass radial stresses–log time trends over 49 days ageing period.

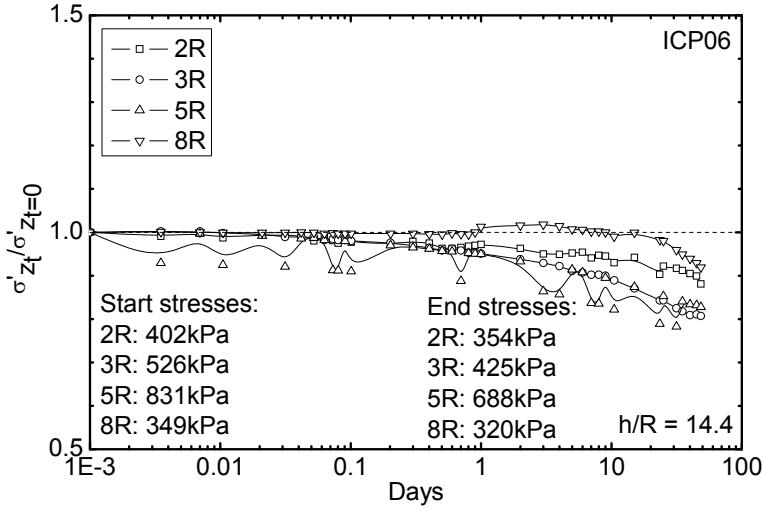


Figure 10-17: Wet test ICP06 normalised sand mass vertical stresses–log time trends over 49 days ageing period.

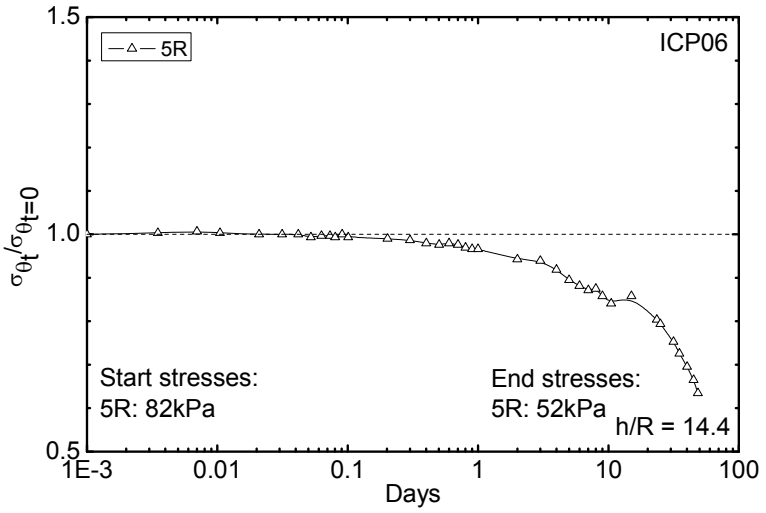


Figure 10-18: ICP06 normalised sand mass hoop stresses time trends over 49 days ageing period.

10.2.2.4 Calibration chamber boundary conditions

The possible influence of the calibration chamber boundary conditions imposed during pile ageing was investigated in tests ICP07 and ICP08 involving the Mini-ICP in dry NE34 sand with the alternative free field simulator BC5 boundary conditions. As outlined in section 5.2.2.2 and Table 5-1, the latter involved an active system that increased the radial boundary stresses after installation. The ICP07 pile interface stresses observed during ageing are presented in Figures 10-19 and 10-20 with the corresponding axial loads in Figure 10-21. A mixed response of interface radial stresses is seen with cluster C decreasing slightly by 5% while clusters A and B rose by ~10% over the 36 days. The shear stresses were practically constant at cluster A and decreased significantly at B and C, although minor problems with these instruments' circuits' programmes led to more scatter outputs over long duration logging. The axial loads (on Figure 10-21) showed gradual increases in all clusters of about 5% which reflected the reductions in shaft shear stresses. The stresses monitored at h/R = 13.9 in the sand mass (a level similar to that of cluster A) and radial distances r/R = 2, 3, 5 and 8 from the pile axis are shown on Figures 10-22 to 10-24 where the responses ranged from stress increases at r/R = 2, to increases followed by decreases, and to monotonic stress decreases at r/R = 5. Sand temperature monitoring at this level (see Figure 10-25) suggests some of the stress changes may be related to small temperature changes experienced during ageing, emphasising the precise temperature regulation required when making laboratory soil stress measurements.

ICP08 used similar boundary conditions to ICP07. However, with this experiment the pile was not load tested statically in compression at the end of installation, so as to investigate the possible effects of the slower and short last stroke imposed on earlier Mini-ICPs during their EOD

static compression load tests. Unfortunately, operational factors limited the ageing period to just 15 days. The ICP08 interface radial stresses response shown in Figure 10-26 resembles that seen in ICP07 but without the temperature effects. The interface shear stresses showed mixed trends but the final stresses were similar on average to the initial values. The axial loads gradually increased after 2 hours. The sand mass stresses observed at h/R = 13.9 behind the pile base (which were less affected by temperature variations than in ICP07) showed a more stable trend of marginal decreases in radial stresses compared to those observed in the wet or dry NE34 sand tests involving the BC3 boundary conditions.

The ICP07 and ICP08 observations demonstrated that the actively stress controlled BC5 lateral boundary conditions, which better matched the free field ground conditions, gradually increased the on-pile radial stresses and residual pile loads, suggesting a mechanism that led to minor pile capacity benefits through ageing; see Table 10-1. The positive radial stress changes leading to these effects appear to be concentrated within the $1 < r/R < 2$ region, with radial stresses generally reducing at greater radial distances, where the vertical and hoop stresses components also tended to reduce with time.

10.2.2.5 Effect of cyclically changing the boundary stresses

Experiment ICP07 involved uninterrupted ageing period of 38 days, after which a second period was imposed where the vertical and radial stresses were cycled at the chamber boundaries twice a day by ±10% ($\Delta\sigma'_z$ = ±15.5kPa and $\Delta\sigma'_h$ = ±9kPa) as shown in Figure 10-32. These steps investigated the potential effects of environmental factors such as tidal and seasonal water table variations or removal and replacement of scoured sand on the ageing behaviour. The lateral to vertical boundary stresses were varied while maintaining the $K = \sigma'_h/\sigma'_z = 0.60$ ratio established from the constant volume boundary condition of BC5 at the end of its installation/start of ageing.

The pile interface stresses and axial loads were seen to respond synchronously with the load cycles applied at the chamber boundaries, Figure 10-33. The radial stresses changes $\Delta\sigma'_r$ observed at clusters A, B and C were equivalent to $\Delta\sigma'_z$ with an average ratio $\Delta\sigma'_r/\Delta\sigma'_z = 1.02$ and therefore $\Delta\sigma'_r/\Delta\sigma'_h = 1.76$. The shear stresses responded to changes in radial stresses such that the mobilised shear resistance angle alternated between -5° and -14° at cluster C and -8° to -17° at A. The pile base residual load of 4.22kN (Q_{mean}/Q_T = 0. 32) also responded by cycling with an amplitude of 1.79kN (Q_{cyclic}/Q_T = 0.14) between 6.01kN and 2.43kN. However, the mean interface stresses applying after cyclic loading (σ'_r, τ_{rz}) = (217kPa, -45.6kPa) remained similar to those noted at the start (221.3kPa, -45.7kPa).

This parametric sequence of experiments established that the patterns radial stress change applying during ageing around the inert stainless steel displacement piles after installation in silica sands were not significantly influenced by moisture or density state, particle scale effects or

periodic ambient stress changes. The only significant variations in response noted were those related to the chamber boundary stress conditions.

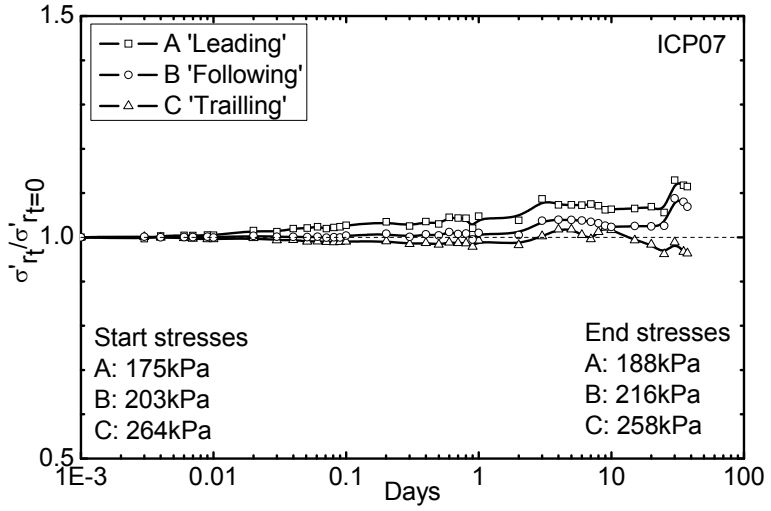


Figure 10-19: 'Free field simulator' BC5 boundary condition test ICP07 normalised interface radial stresses – log time trends over 38 days ageing period.

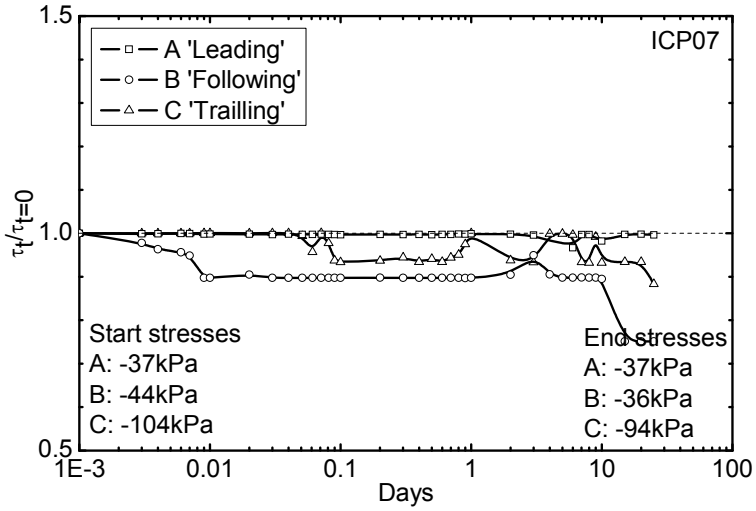


Figure 10-20: BC5 boundary condition test ICP07 normalised interface shear stresses – log time trends over 25 days ageing period.

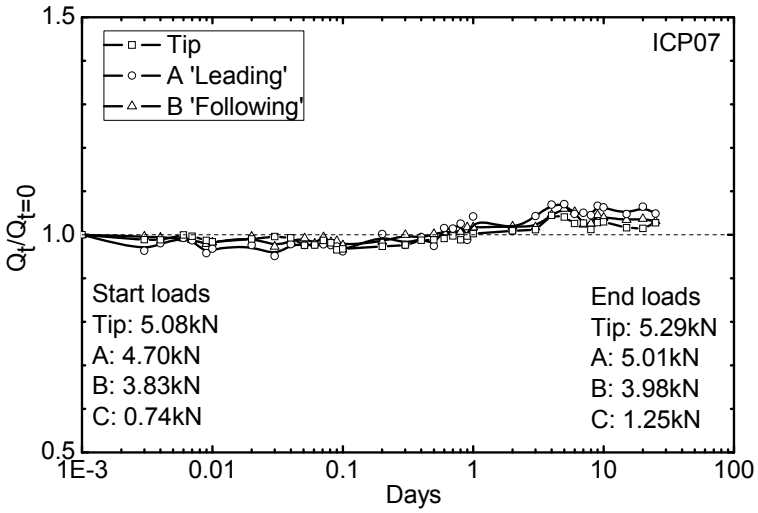


Figure 10-21: BC5 boundary condition test ICP07 normalised axial loads – log time trends over 25 days ageing period.

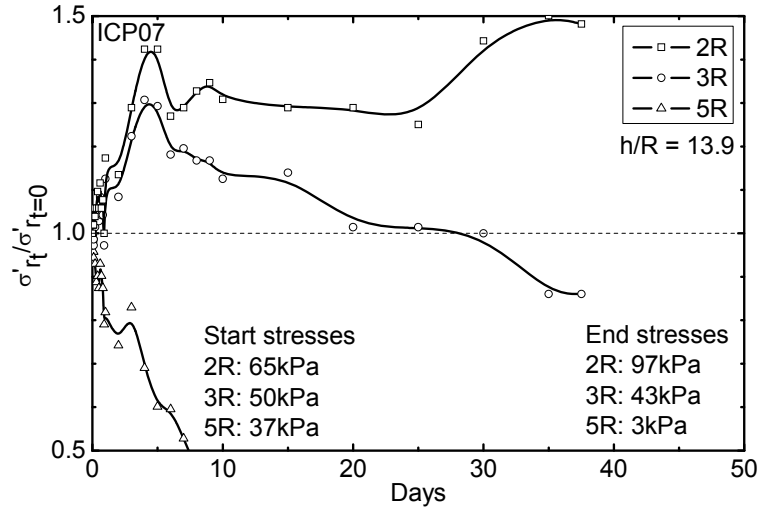


Figure 10-22: BC5 boundary condition test ICP07 normalised sand mass radial stresses – time trends over 38 days ageing period.

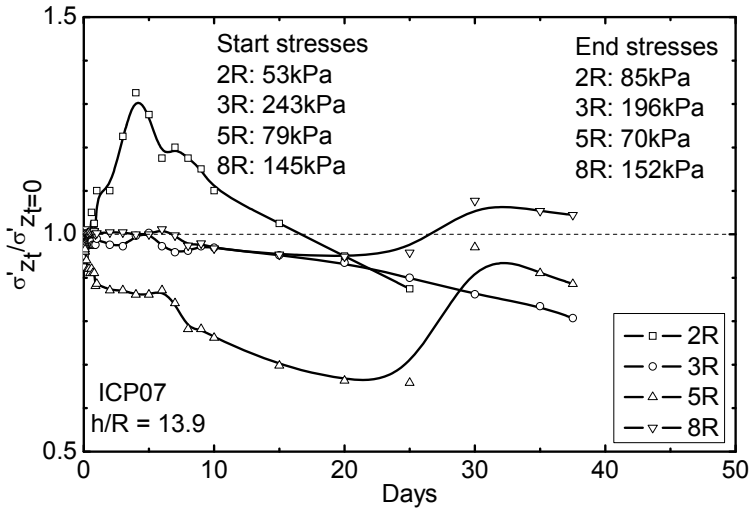


Figure 10-23: BC5 boundary condition test ICP07 normalised sand mass vertical stresses – time trends over 38 days ageing period.

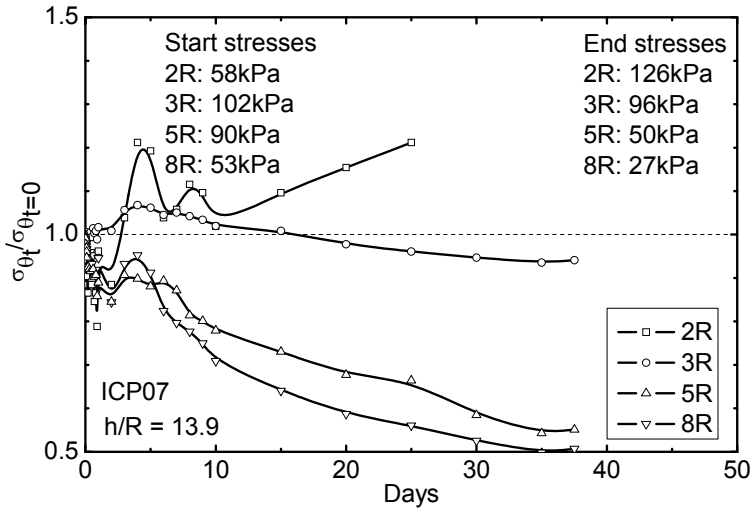


Figure 10-24: BC5 boundary condition test ICP07 normalised sand mass hoop stresses – time trends over 38 days ageing period.

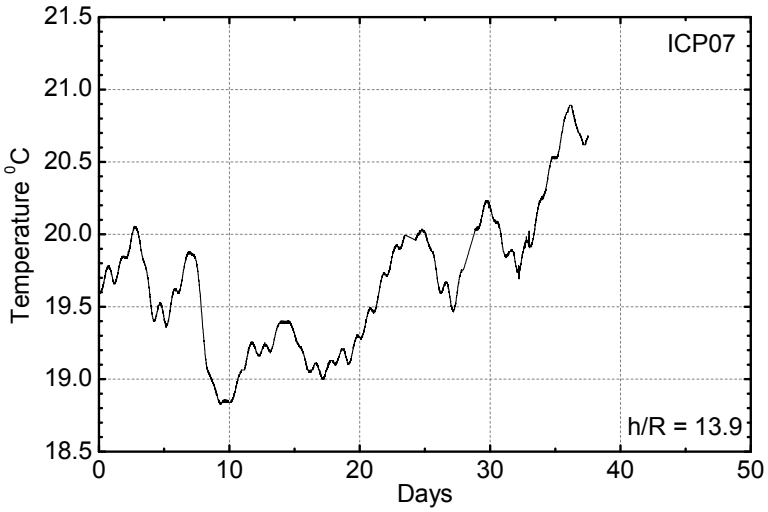


Figure 10-25: BC5 boundary condition test ICP07 temperature variations during the 38 days ageing period.

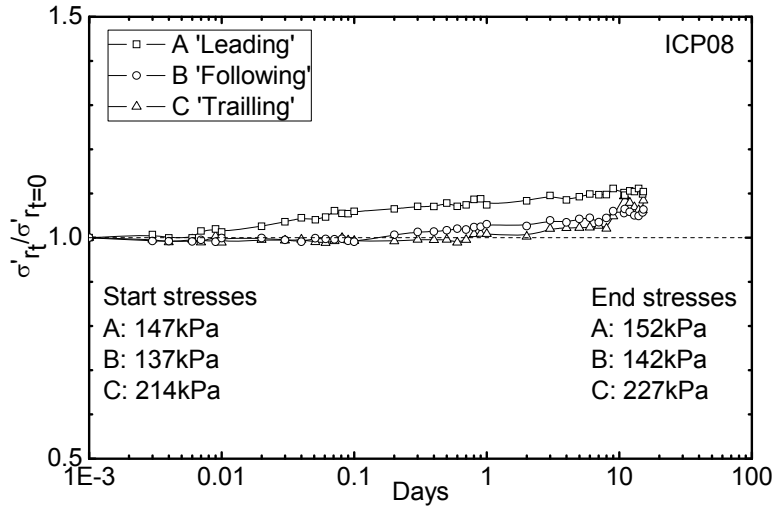


Figure 10-26: ICP08 normalised interface radial stresses – log time trends over 15 days ageing period.

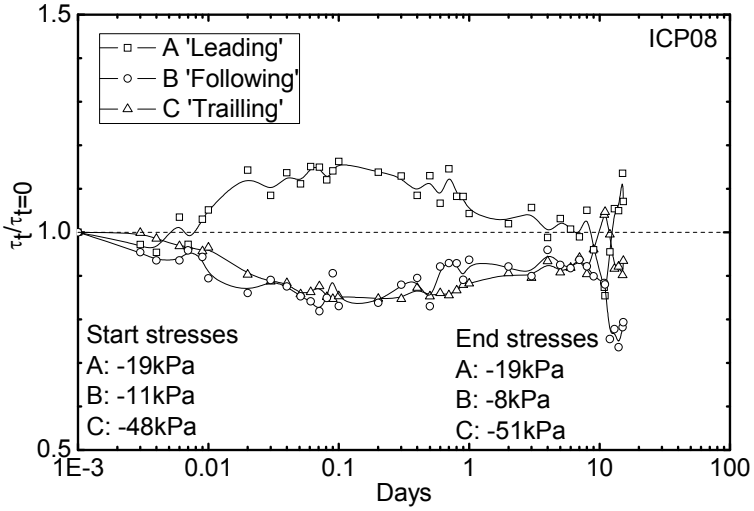


Figure 10-27: ICP08 normalised interface shear stresses – log time trends over 15 days ageing period.

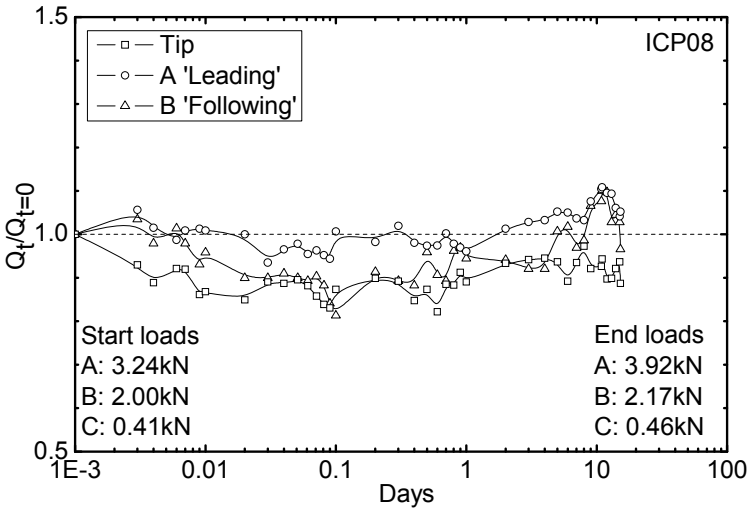


Figure 10-28: ICP08 normalised axial loads – log time trends over 15 days ageing period.

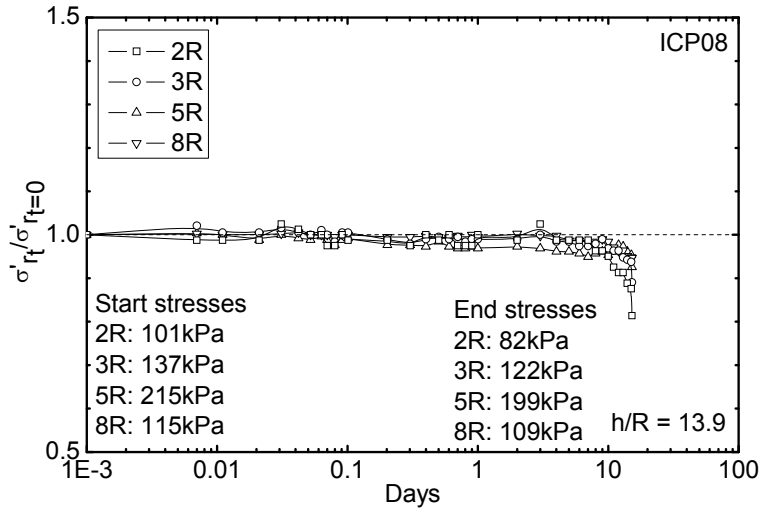


Figure 10-29: ICP08 normalised sand mass radial stresses – log time trends over 15 days ageing period.

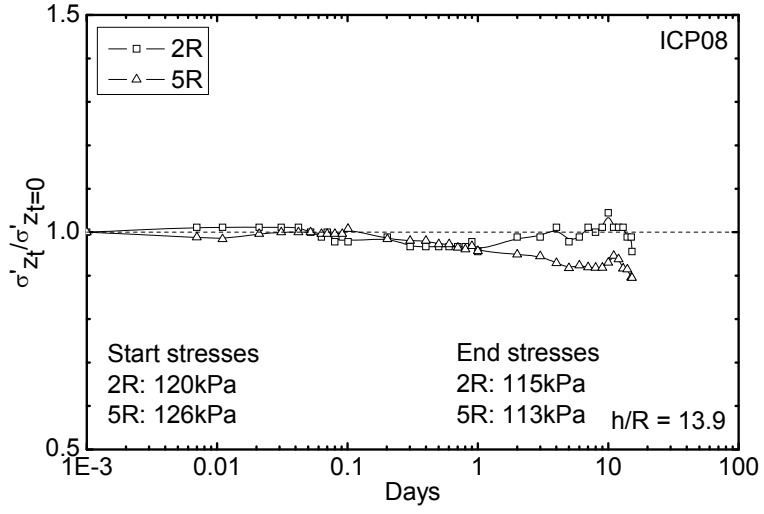


Figure 10-30: ICP08 normalised sand mass vertical stresses – log time trends over 15 days ageing period.

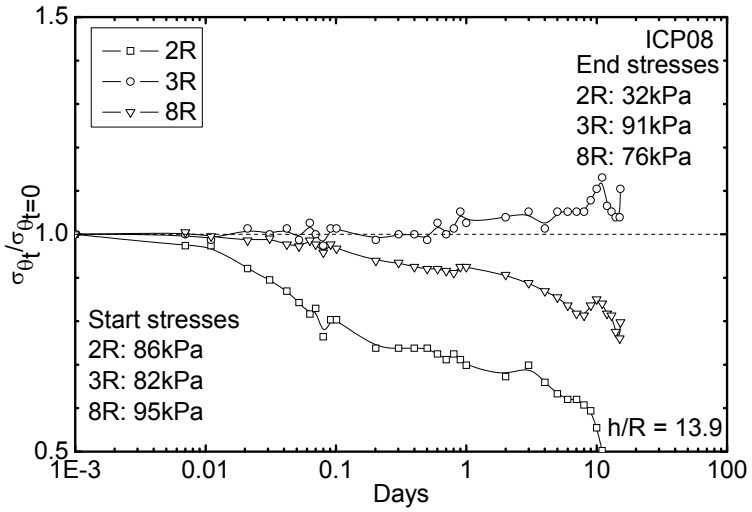


Figure 10-31: ICP08 normalised sand mass hoop stresses – log time trends over 15 days ageing period.

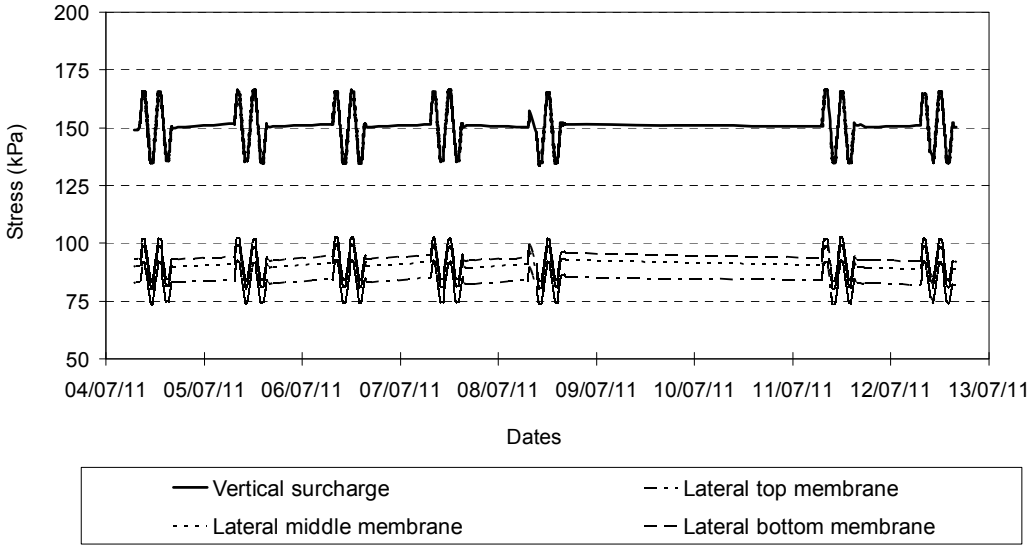


Figure 10-32: ICP07 with BC5 boundary condition low level boundary stress cycling imposed from 38 days after installation.

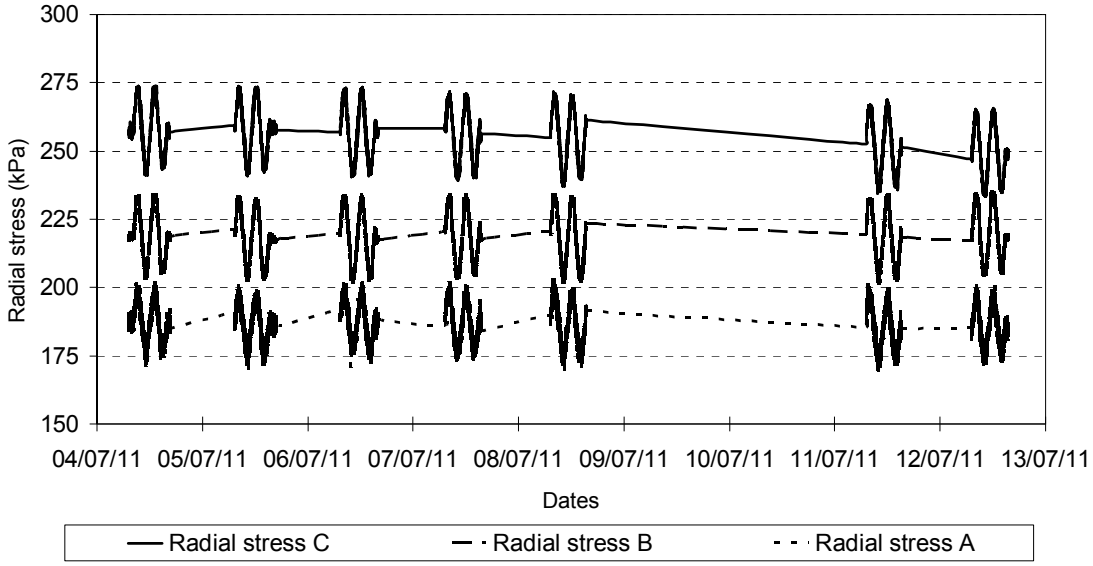


Figure 10-33: ICP07 with BC5 boundary condition Mini-ICP interface radial stress response during low level boundary stress cycling.

10.2.2.6 Ageing piles interface effective stress paths

The Mini-ICP piles' interface effective stress paths observed during ageing are summarised on Figure 10-34, generally showing the effective stress paths moving up or down the shaft tension partial interface shear mobilisation line with $\delta = 17°$ established at the end of installation. The single exception is from the late ageing stage of ICP05, which showed tendencies for radial stress decreases at constant shear stresses moving the path leftwards towards the constant volume interface failure δ'_{cv}.

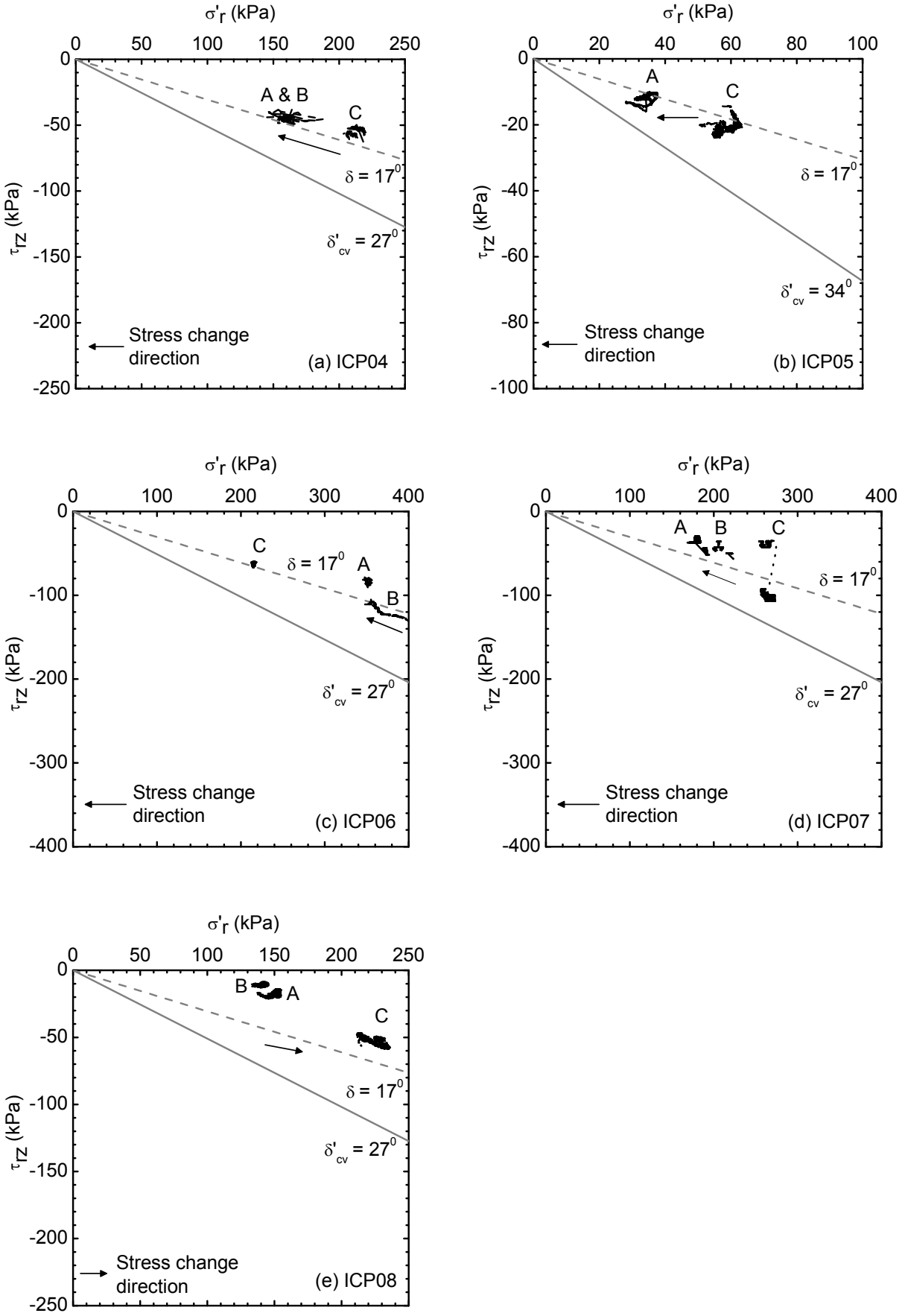


Figure 10-34: Mini-ICP interface effective stress paths in the ageing durations.

10.3 Pile behaviour on static testing after ageing

Following ageing, the piles were load tested first statically and in compression, except for test DI which was tested first in tension. Compression testing was preferred because most piled foundations are designed to carry positive loads. Compression testing the instrumented piles also allowed separate assessment of both base and shaft capacities. We recall from Chapter 3 that 38% to 44% total capacity gains per log time cycle were interpreted from field re-tested and intact aged piles' compression load tests.

The static tests were performed with the same equipment as that employed at the end of installation. The jack was re-connected to the test pile cap through an extension piece to reduce the required piston travel and improve verticality of loading. As during installation and the end of installation static load tests, the frame was secured to its rails by pressurising the foot hydraulic grippers. The tests were displacement controlled through the Labview 8.2 program using the displacements measured by an LVDT attached to the pile head. The post-ageing static compression (C1) tests' base, shaft and total capacities are summarised on Table 10-1 alongside the end of installation (EOD) capacities, noting also the periods of ageing, the rates of load testing, final pile base depths and the percentage capacity changes for each load component.

The aged piles' capacities, interface stress dilation and global stiffness characteristics (as defined (as $\Delta Q/\Delta$displacement) at half the pile's final measured resistance) are examined by considering their load–displacement and interface stress path behaviours in comparison to those seen at EOD. Table 10-2 summarises the variations seen in Mini-ICPs' stress dilation ratios and axial load stiffnesses between the EOD and C1 test stages.

The EOD and C1 total load-displacement behaviours of ICP04 (conducted with BC3 boundary conditions with dry NE34 sand) are shown on Figure 10-35. The loading stiffnesses of the EOD and C1 tests are similar, although the latter is 18% softer and showed 7% relaxation in ultimate total capacity over 41 days. The base and shaft loads are presented separately on Figure 10-36, showing a clearer loss in shaft (13%) than base (4%) capacity. Figure 10-37 plots the corresponding interface effective stress paths at clusters A to C which all show minor reductions (less than 9%) in the degree of dilation (or radial stress gain) between the EOD and in the C1 (post–ageing) tests, which together with change in σ'_{rs} match the observed reductions in shaft capacity.

Figure 10-38 presents the EOD and C1 load-displacement behaviours of ICP05, the Mini-ICP installed in finer and less dense GA39 sand, which experienced 71 days of ageing under the BC3 boundary condition. Here a 9.2% decrease was seen in the total capacity, while the load–displacement behaviour was marginally (4%) less stiff in the aged test. As shown on Figure 10-39 the base capacity relaxed by just 6% while the shaft capacity fell by 18%. The interface effective stress paths from the EOD and C1 static compression pile load tests (Figure 10-40) have similar

patterns to those mobilised in the medium dense NE34 sand though with higher overall degree of dilation. The loading behaviours were broadly similar but the δ'_{cv} values were higher in the GA39 and the equalisation radial stresses were much lower. The degree of interface radial stress dilation and pile stiffness were essentially maintained between EOD and C1, Table 10-2. As noted in Table 10-1, increasing the $D/d_{50\%}$ ratio (while reducing I_D) did not lead to any overall change in the degree of set-up due to ageing.

Test	Testcode	Degree of dilation ($\sigma'_{rf}/\sigma'_{r0}$)				Stiffness	
		Cluster A	Cluster B	Cluster C	Average	kN/mm	Change (%)
Standard	EOD	1.60	1.78	1.72	1.70	47.32	-18%
ICP04	C1	1.47	1.54	1.81	1.61	38.73	
Fine GA39	EOD	2.86	N/A	1.56	2.21	20.07	-4%
ICP05	C1	2.65	N/A	1.73	2.19	19.17	
Wet NE34	EOD	1.29	1.22	1.51	1.35	86.86	-26%
ICP06	C1	N/A	1.41	1.64	1.52	64.54	
BC5	EOD	1.48	1.61	1.59	1.56	59.25	-2%
ICP07	C1	1.27	1.45	1.65	1.45	58.11	
BC5	Last stroke	1.40	1.59	1.91	1.63	17.54	+27%
ICP08	C1	1.19	1.47	1.62	1.43	22.35	

Table 10-2: Degree of interface dilation and stiffness characteristics of aged and fresh piles compared.

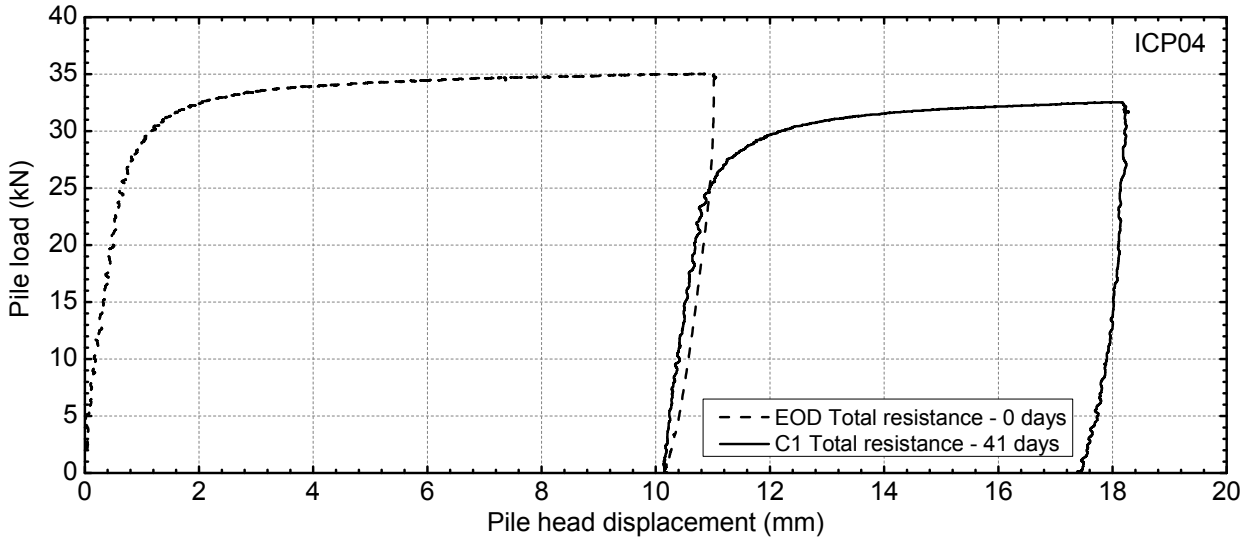


Figure 10-35: Mini-ICP test ICP04 C1 and EOD static compression total load–displacement behaviours in dry medium dense NE34 sand with BC3 boundary condition.

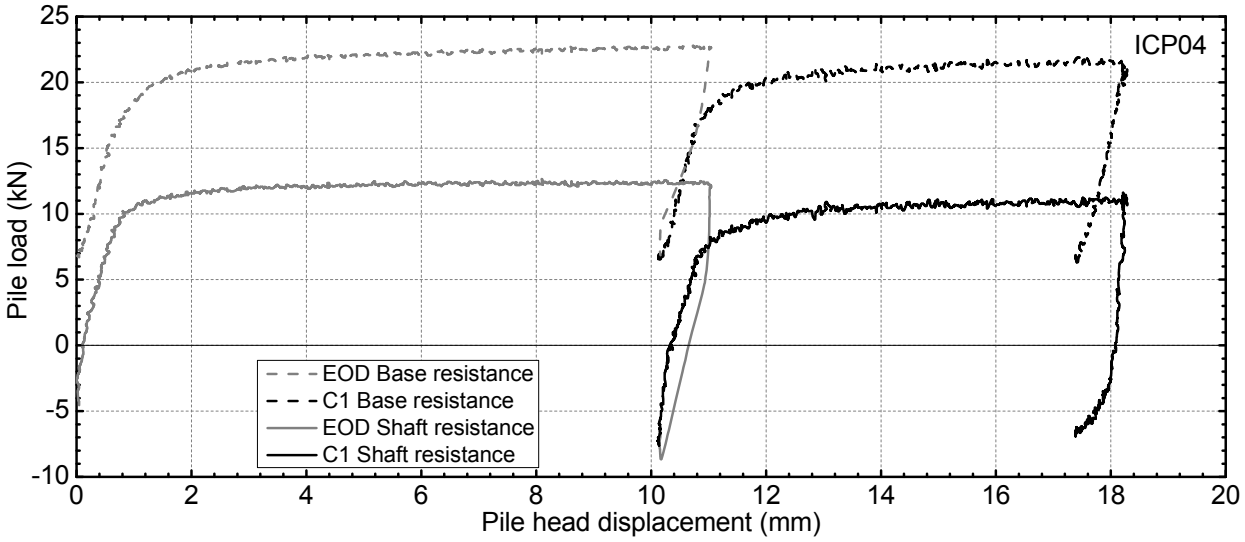


Figure 10-36: Mini-ICP test ICP04 C1 compared to EOD static compression base and shaft load–displacement behaviour in dry dense NE34 sand with BC3 boundary condition.

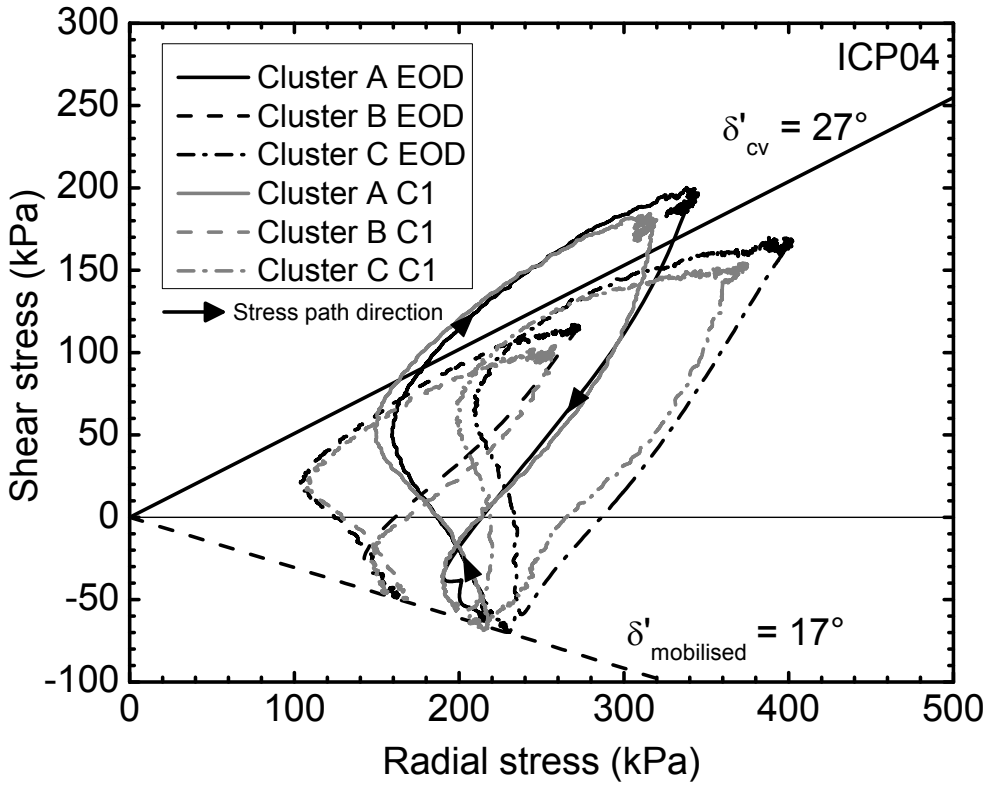


Figure 10-37: Mini-ICP test ICP04 C1 compared to EOD static compression effective interface stress paths in dry dense NE34 sand with BC3 boundary condition.

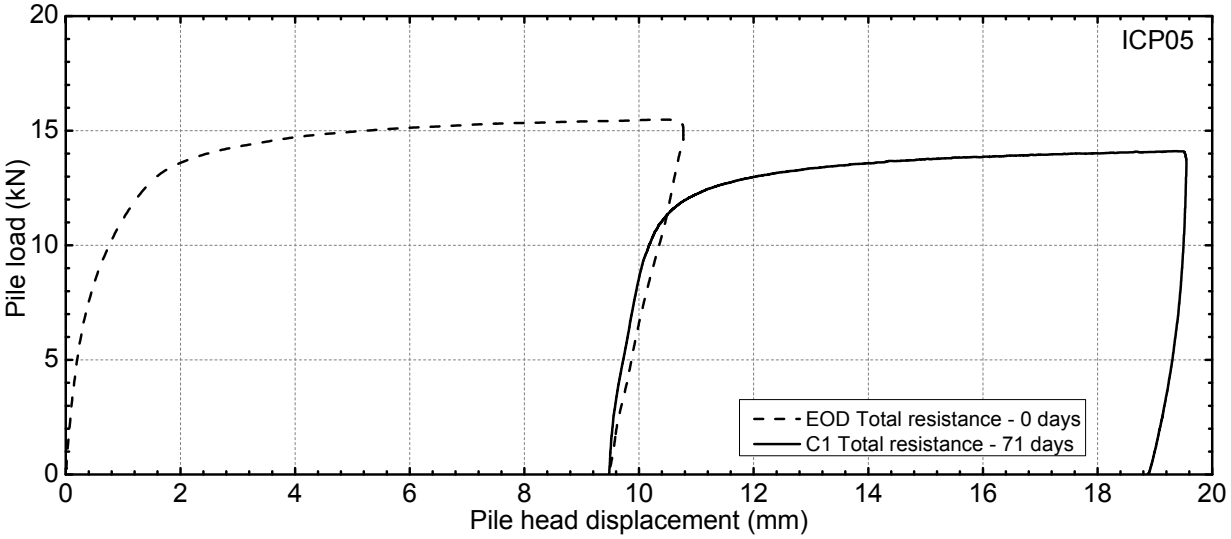


Figure 10-38: Mini-ICP test ICP05 C1 compared to EOD static compression total load–displacement behaviour in dry less dense and finer GA39 sand with BC3 boundary condition.

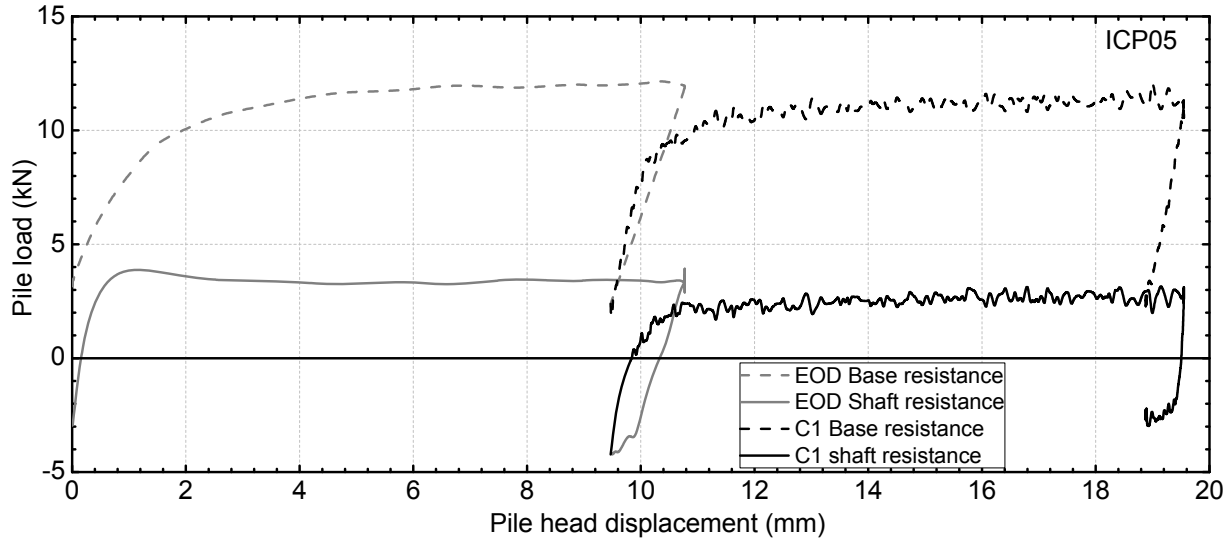


Figure 10-39: Mini-ICP test ICP05 C1 compared to EOD static compression base and shaft load–displacement behaviour in dry less dense and finer GA39 sand with BC3 boundary condition.

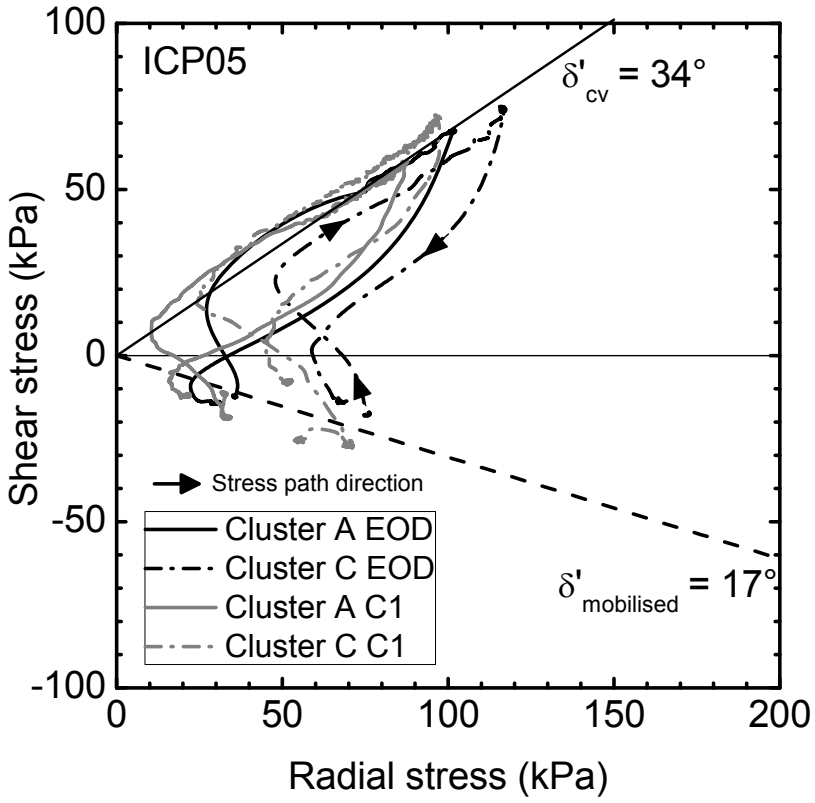


Figure 10-40: Mini-ICP test ICP05 C1 compared to EOD static compression effective interface stress paths in dry finer and less dense GA39 sand with BC3 boundary condition.

Considering next the effects of wet sand on the ageing behaviour of inert displacement piles, the total, base and shaft load-displacement behaviours observed in the ICP06 experiment on wet dense NE34 sand are shown on Figures 10-41 to 10-42. Here a 19% relaxation in total capacity was registered after 49 days' ageing, with proportionately equal relaxations in base and shaft capacity as well as the global stiffness (26%). Figure 10-43 shows the interface effective stress paths observed at clusters A to C. The paths follow a similar trend to those observed in dry conditions in ICP04 developing similar δ'_{cv} at clusters A and C and slightly lower angles at cluster B with the degree of stress dilation increasing by 16% during test C1; it will be recalled that cluster A was not functioning in the later stages of this test due to water ingress, as explained in section 10.2.2.3.

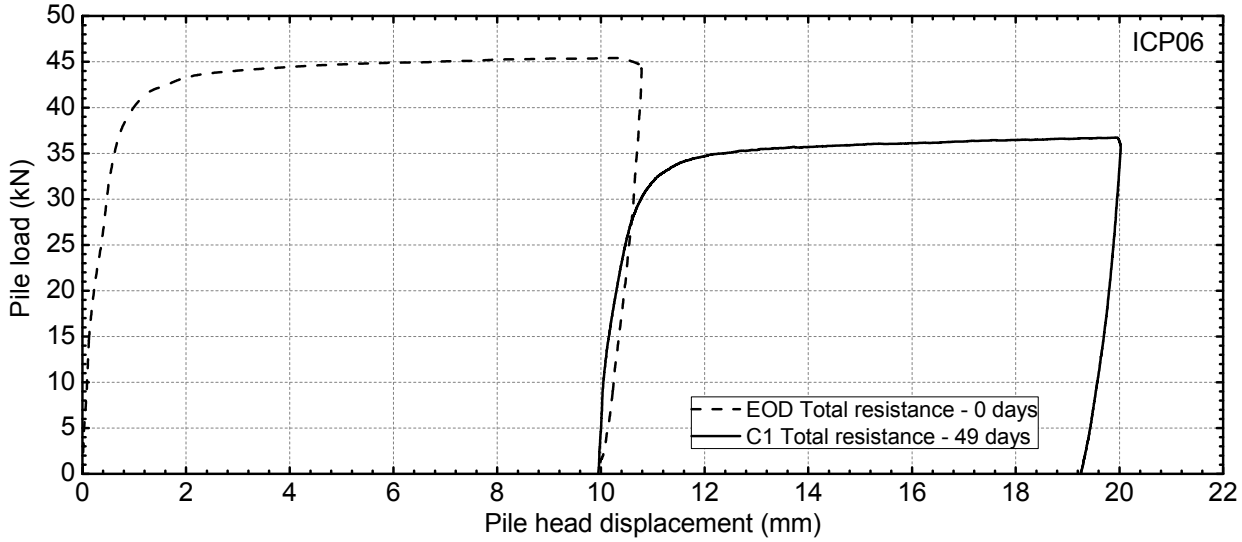


Figure 10-41: Mini-ICP test ICP06 C1 compared to EOD static compression total load–displacement behaviour in wet dense NE34 sand with BC3 boundary condition.

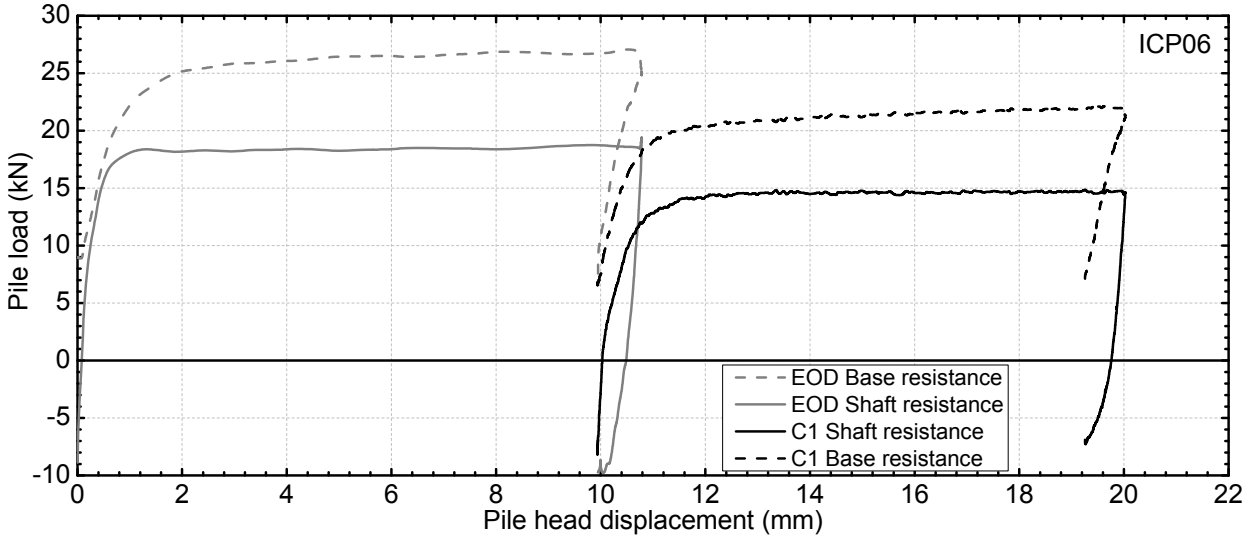


Figure 10-42: Mini-ICP test ICP06 C1 compared to EOD static compression base and shaft load-displacement behaviour in wet dense NE34 sand with BC3 boundary condition.

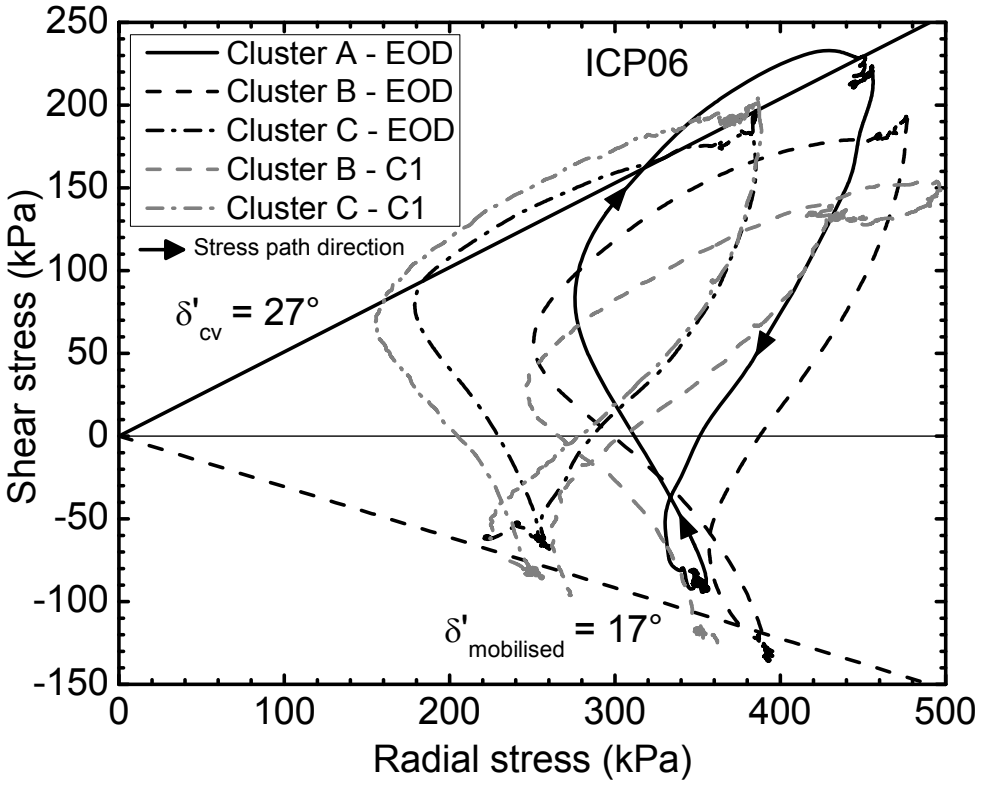


Figure 10-43: Mini-ICP test ICP06 C1 compared to EOD static compression effective interface stress paths in wet dense NE34 sand with BC3 boundary condition.

Experiments ICP07 and ICP08 investigated the effects of the chamber lateral boundary conditions on the ageing behaviour of the Mini–ICP displacement piles in dry dense NE34 sand, applying the BC5 stress controlled lateral boundary conditions. At the end of a pile installation the final radial stresses measured at the BC5 lateral boundaries of the chamber were applied as constant pressure throughout the ageing period. This step led to steady or marginally increasing radial stresses developing on the pile shaft. The resulting load–displacement trends are shown on Figures 10-44 to 10-47. The ICP07 post-ageing total capacity increased by 1.3%. The shaft capacity was 11% greater than at the end of installation, while the base capacity fell by 5% over the ageing period. The pile loading stiffness was essentially unchanged.

ICP08 applied the BC5 conditions and also assessed the potential effects of the static compression axial capacity test (EOD) performed in all the pressure pile experiments at the end of installation. The standard EOD test was applied as a short (10mm instead of 20mm) stroke at a rate at least 10 times slower than the standard installation rates. This was omitted in ICP08 and Figure 10-46 shows data from the last 20mm stroke of installation of the Mini-ICP (applied at 2mm/sec) compared to the post-ageing total axial compression capacity (applied at 0.02mm/sec). As in ICP07 the total capacity increased by 3% but over just 15 days while Figure 10-47 reveals a comparable increase in shaft capacity of 8.4% and a decrease of 0.6% in base capacity. The ICP08 C1 test was

27% stiffer than the response seen over the last stroke of installation, showing how stiffness was enhanced by the active radial stress boundary being adjusted to the free field active stresses over the ageing period.

The ICP07 and ICP08 experiments' interface effective stress paths (Figures 10-48 to 10-49) show behaviours that are broadly similar to those observed in the wet and dry medium dense NE34 sand conditions with the boundary condition BC3. The inadvertent stress concentration effects discussed in section 5.2.2.1 at the top of the chamber lead to the anomalously high stresses developed at cluster C. The effective stress paths of ICP08's 49th installation stroke stand in for the omitted EOD test. Conducting the test at 2mm/s led to less well defined trends than the slow tests; the standard data acquisition update rate was set at one round per 2 seconds. The interpreted constant volume shearing resistances and degrees of dilation are however broadly comparable and it appears that omitting the standard EOD test did not alter the ageing behaviour radically. Comparison with test ICP07, which also imposed stress changes to simulate tidal or water table variations that might occur around ageing piles in the field, show broadly similar results. Overall it is clear that the 'classical' calibration chamber boundary conditions BC3 applied in tests ICP04 to ICP06 led to capacity relaxation, while the modified boundary conditions BC5 augmented the pile shaft capacities post-ageing by an average of 10% over the relatively short ageing periods applied while also pile base capacity tended to either remain steady or fall by up to -4%.

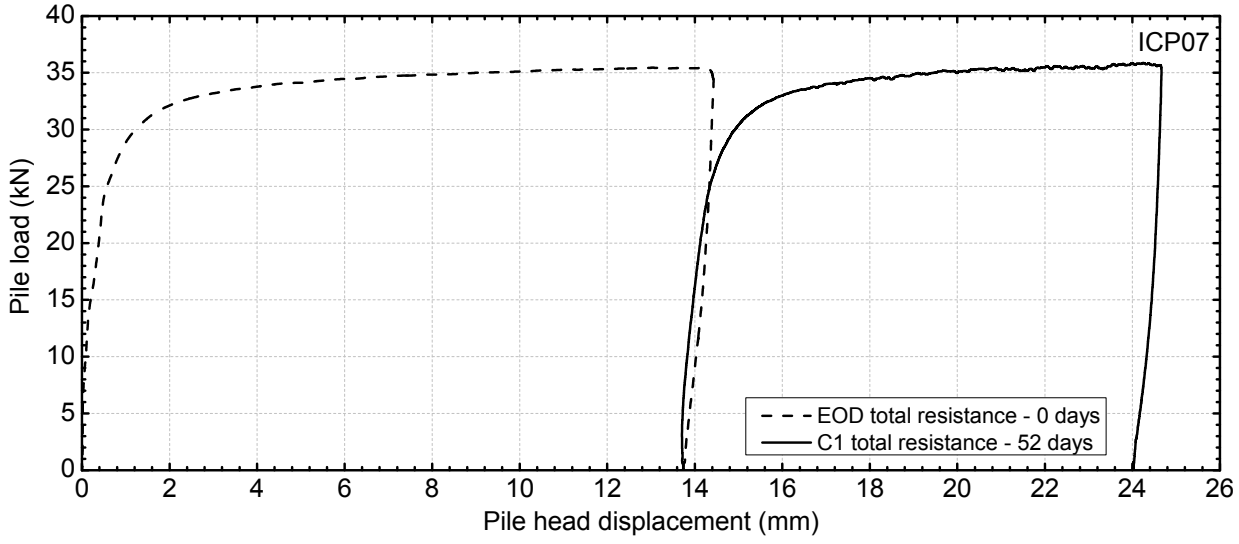


Figure 10-44: Mini-ICP test ICP07 C1 compared to EOD static compression total load–displacement behaviour in dry dense NE34 sand with BC5 boundary condition.

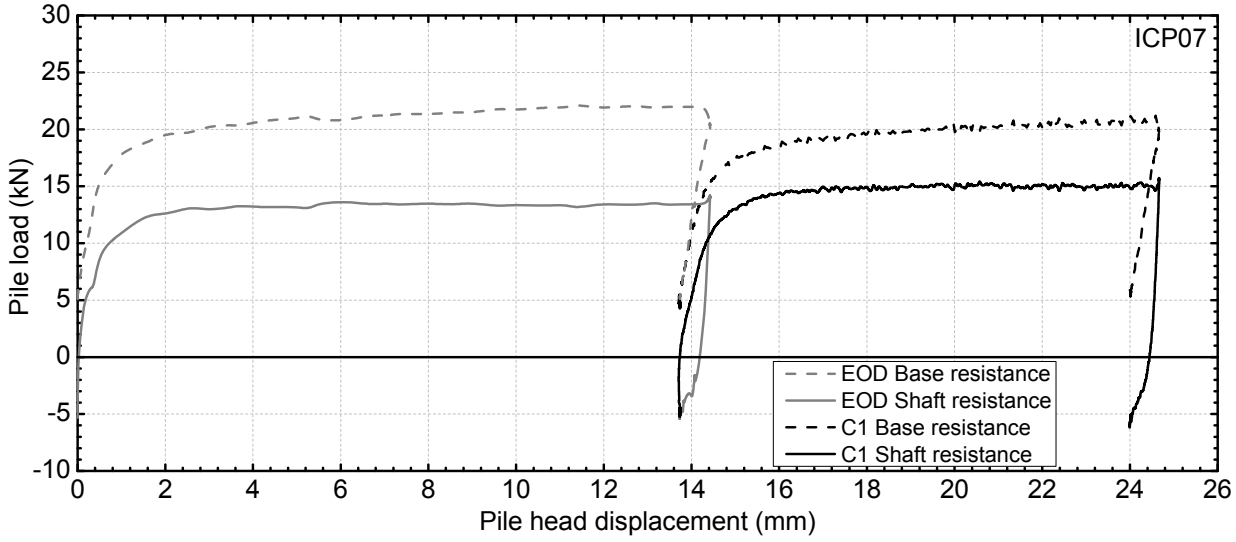


Figure 10-45: Mini-ICP test ICP07 C1 compared to EOD static compression base and shaft load–displacement behaviour in dry dense NE34 sand with BC5 boundary condition.

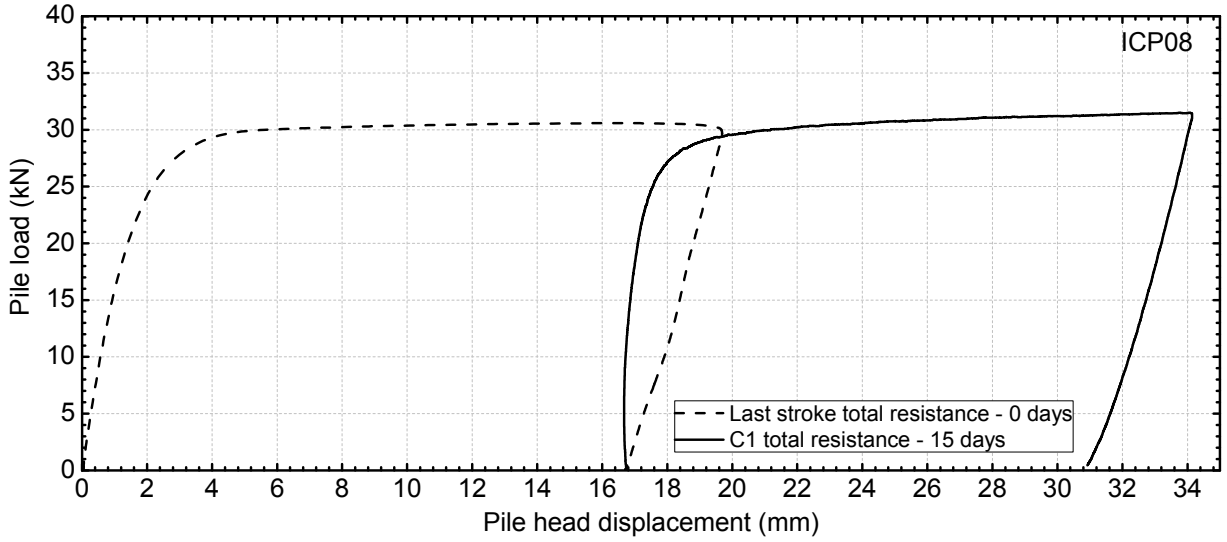


Figure 10-46: Mini-ICP test ICP08 C1 compared to last stroke static compression total load–displacement behaviour in dry dense NE34 sand with BC5 boundary condition.

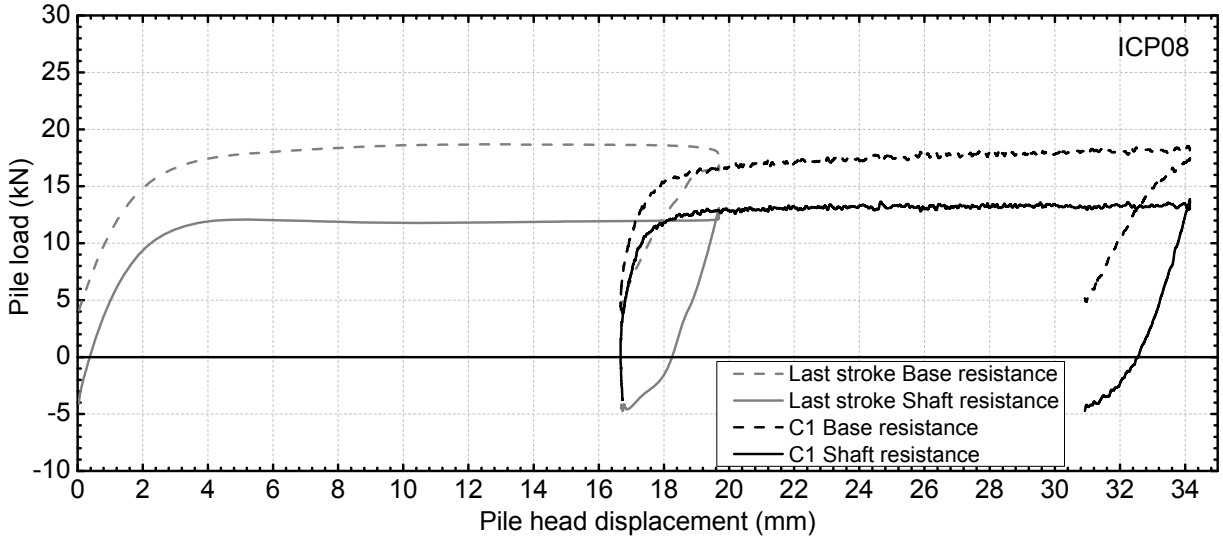


Figure 10-47: Mini-ICP test ICP08 C1 compared to last stroke static compression base and shaft load–displacement behaviour in dry dense NE34 sand with BC5 boundary condition.

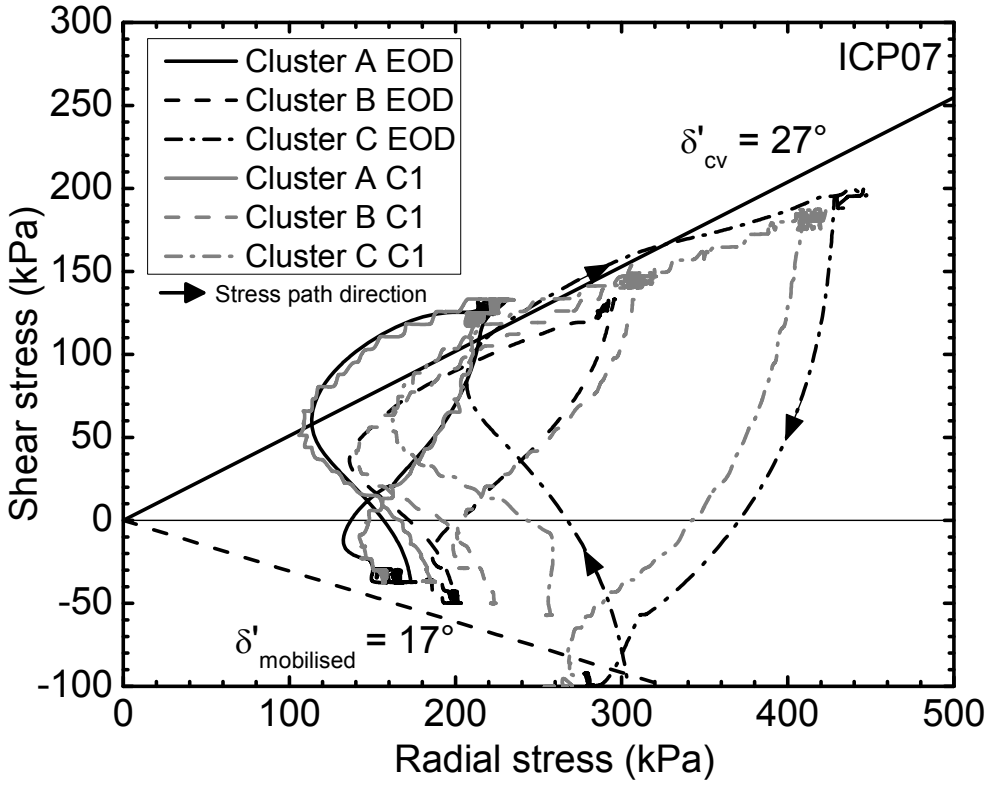


Figure 10-48: Mini-ICP test ICP07 C1 compared to EOD static compression effective interface stress paths in dry dense NE34 sand with BC5 boundary condition.

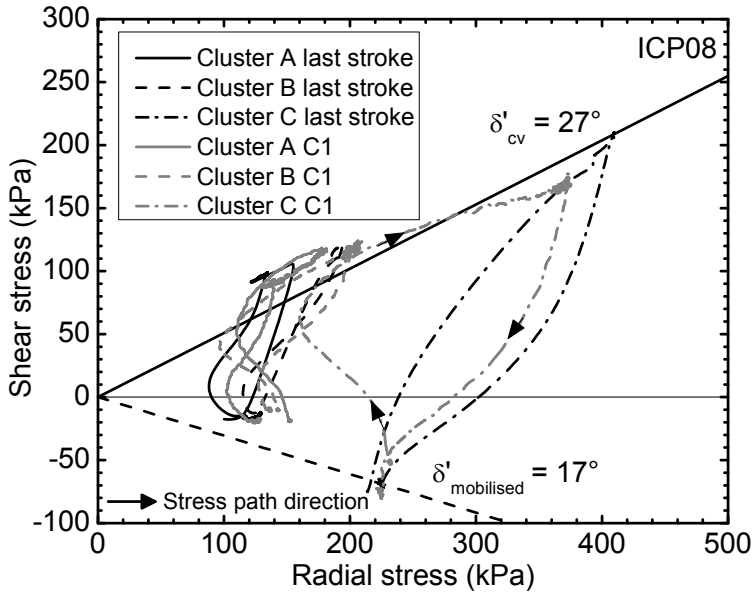


Figure 10-49: Mini-ICP test ICP08 C1 static compression test compared to last installation stroke effective interface stress paths in dry dense NE34 sand with boundary condition BC5.

Experiment MiP01 was conducted to further investigate chamber scale effects. The MiP01 pile was a smoother conically tipped 12mm diameter stainless steel micro-pile installed in medium dense NE34 sand while applying boundary condition BC3. This increased the chamber to penetrometer diameter ratio from the standard 33.3 (for the Mini-ICP or CPTs) to 100. The pile–to–sand mass volume increased by 9 and the L/D ratio by 3. The un-instrumented Micro-pile's overall axial load–displacement behaviours before and after its 68 days ageing period are shown on Figure 10-50; the total compressive capacity relaxed by 20% while the pile stiffness reduced by 47%. It is not known how this loss was distributed between the base and shaft or how the pile roughness affected the local effective stress path. However, the test does indicate that adopting a larger chamber size while maintaining boundary BC3 would not have led to any large capacity increase.

Consistently deploying BC5 as the best 'free field simulating' boundary condition, three more parameters were isolated in three further pile installations involving dry dense NE34 sand in attempts to uncover any factors that may potentially have inhibited beneficial pile ageing processes. Test pile CPT09 involved installing a CPT cone tipped pile with just two strokes, 750mm and 340mm long, at average penetration rate of 10mm/s, applying BC5 boundary conditions. This test investigated the potential effects of the installation jack stroke length and number of jacking cycles on the subsequent pile ageing behaviour. Figures 10-51 and 10-52 compare the load–displacement behaviours of the total load, shaft and base resistances of C1 performed just one week after EOD. The shaft capacity was essentially maintained over the period while the base and total capacity marginally relaxed in keeping with ICP07 and ICP08 trends confirming that lateral stress boundary

condition BC5 has the greatest influence of all the factors considered on the (shaft) ageing behaviour. Changing the jacking installation style didn't trigger any stronger ageing trend.

The second test CPT10 involved the CPT pile and the BC5 boundary conditions. This followed ICP08 and assessed the effect of a five times faster rate of installation (10mm/s) combined with the standard 49 stroke Mini-ICP installation procedure. CPT10 also excluded the end of installation static compression test EOD, as in test ICP08. Figure 10-53 plots the total load resistance trends during load testing while Figure 10-54 shows the CPT10 base and shaft resistances after 32 days of ageing. As with ICP07 and ICP08, the BC5 free field simulator lateral boundary conditions led to shaft capacity increasing, while the base resistance fell marginally after ageing. Axial capacity increased by 7% with the shaft and base components varying by +13% and -5% respectively; the C1 loading stiffness was 32% softer.

A final set of experiments investigated potential differences between the effects of jack stroke and dynamic driving modes of installation on the ageing behaviours of displacements piles in the chamber. A hammer–driven, 36mm diameter, cone tip-ended pile DI was installed in dry dense NE34 sand applying boundary condition BC5. Pile DI was axial static tested in tension T1 about a day after installation and again in tension T2 after 12 days of ageing. The load-displacement curves on Figure 10-55 show a rather low initial capacity and an increase of 11% in shaft resistance and a threefold increase in loading stiffness from T1 to T2. As noted earlier, the boundary lateral stresses continuously declined as driving continued in DI as shown on Figure 9-14. Reasons for this fall were suggested in Chapter 9 and the follow up experiment DII was performed with constant stress boundary conditions (BC1) as described in section 5.2.2.2. A 150kPa vertical surcharge and 63kPa lateral stress were maintained throughout the installation, ageing and static load testing to compensate for any boundary stress relaxations due to dynamic energy reverberating around the sand chamber and causing undue compaction. Under these conditions the total compression capacity of pile DII increased by 6.2% over 41 days while the loading stiffness doubled as shown in Figure 10-56.

In sum, the post-ageing pile tests confirmed that the ageing behaviours of the model displacement piles installed in silica sand are broadly independent of particle and chamber scale effects, density or moisture states and mode of installation. However they are influenced strongly by the type of chamber lateral boundary conditions imposed. Applying the most realistic BC5 lateral boundary condition led to overall compressive capacity increases of upto 13% over a 32 days period, which are considerably less marked than the trends inferred from the field databases discussed in Chapter 3.

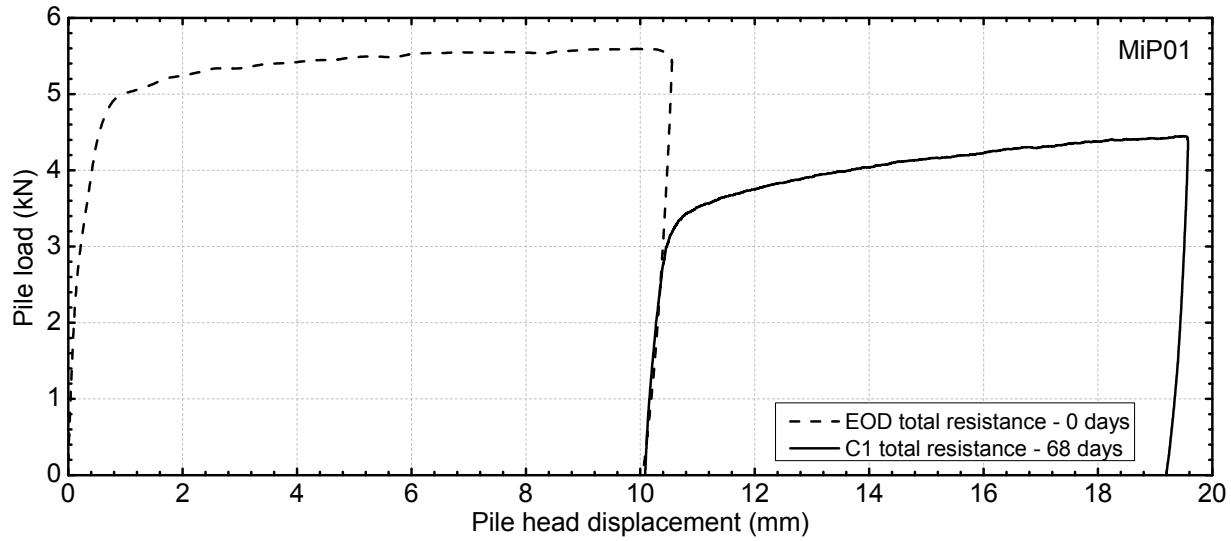


Figure 10-50: Micro-pile test MiP01 C1 compared to EOD static compression total load–displacement behaviour in dry dense NE34 sand with BC3 boundary condition.

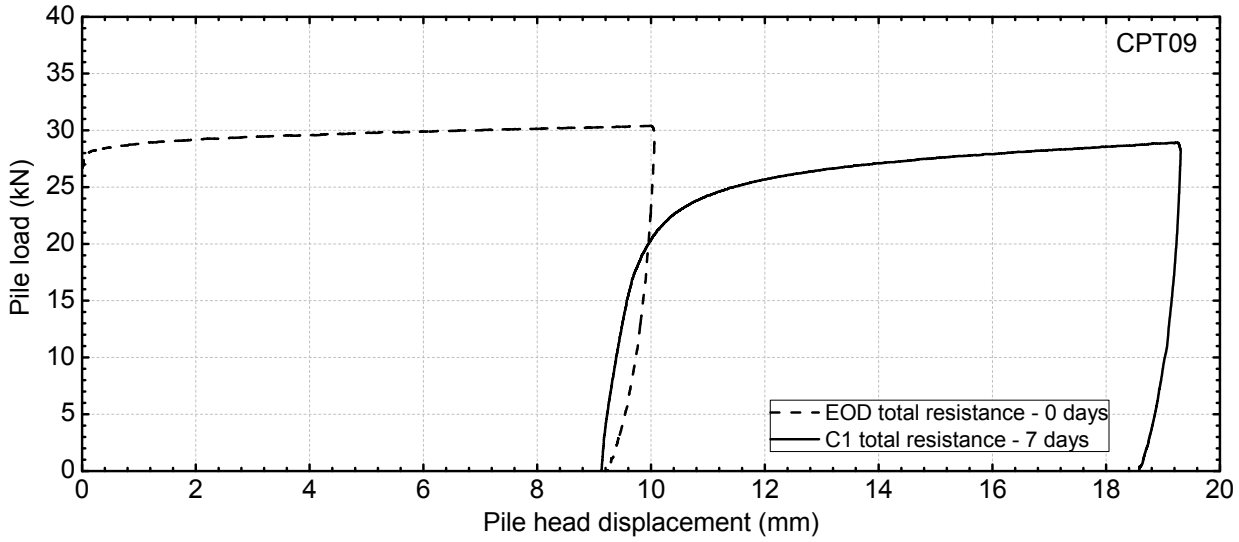


Figure 10-51: CPT pile long strokes few cycles test CPT09 C1 compared to EOD static compression total load–displacement behaviour in dry dense NE34 sand with BC5 boundary condition.

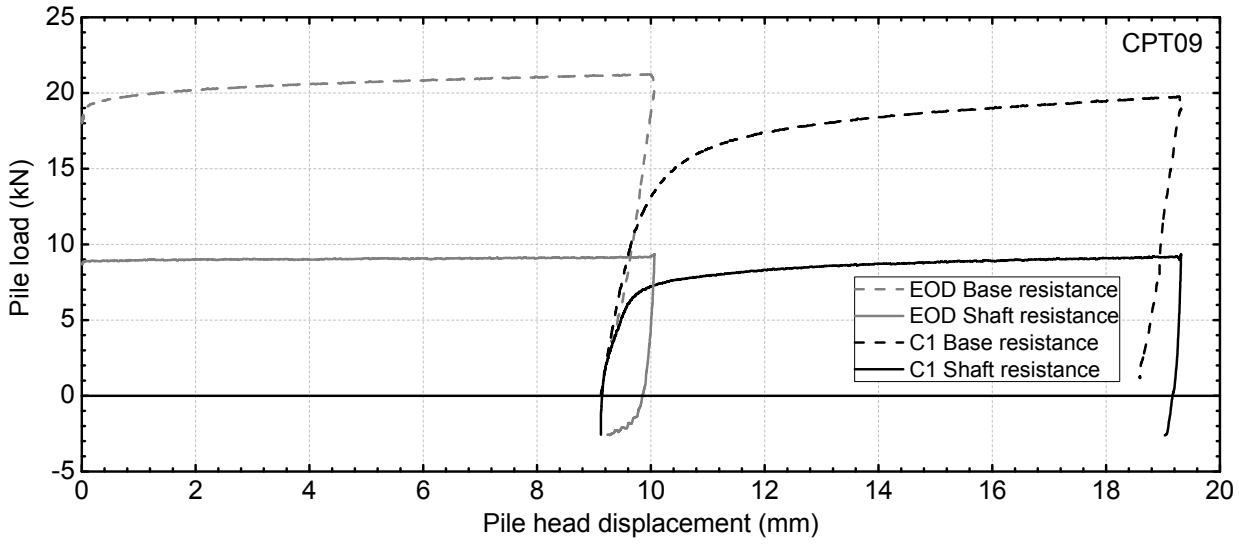


Figure 10-52: CPT pile long strokes few cycles test CPT09 C1 compared to EOD static compression base and shaft load–displacement behaviour in dry dense NE34 sand with BC5 boundary condition.

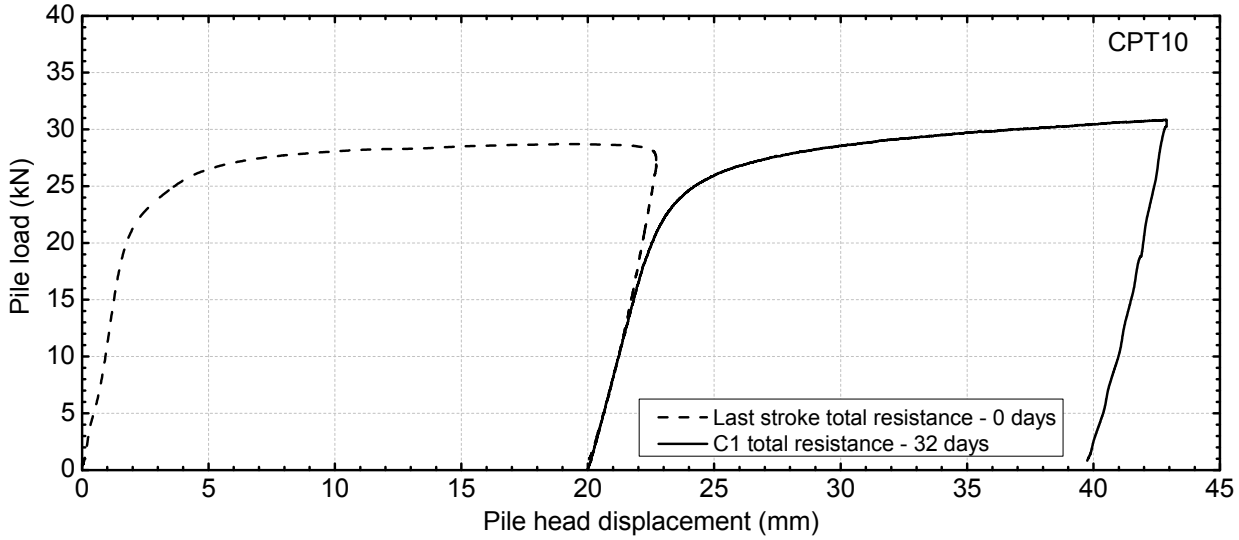


Figure 10-53: CPT pile faster strokes test CPT10 C1 compared to EOD static compression total load–displacement behaviour in dry dense NE34 sand with BC5 boundary condition.

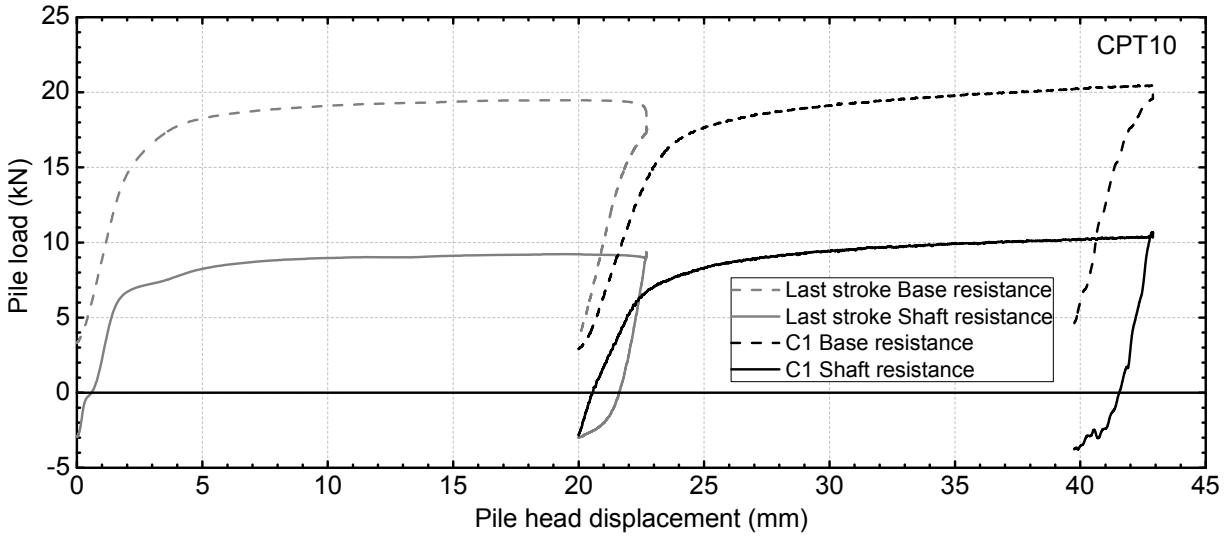


Figure 10-54: CPT pile faster strokes test CPT10 C1 compared to EOD static compression base and shaft load–displacement behaviour in dry dense NE34 sand with BC5 boundary condition.

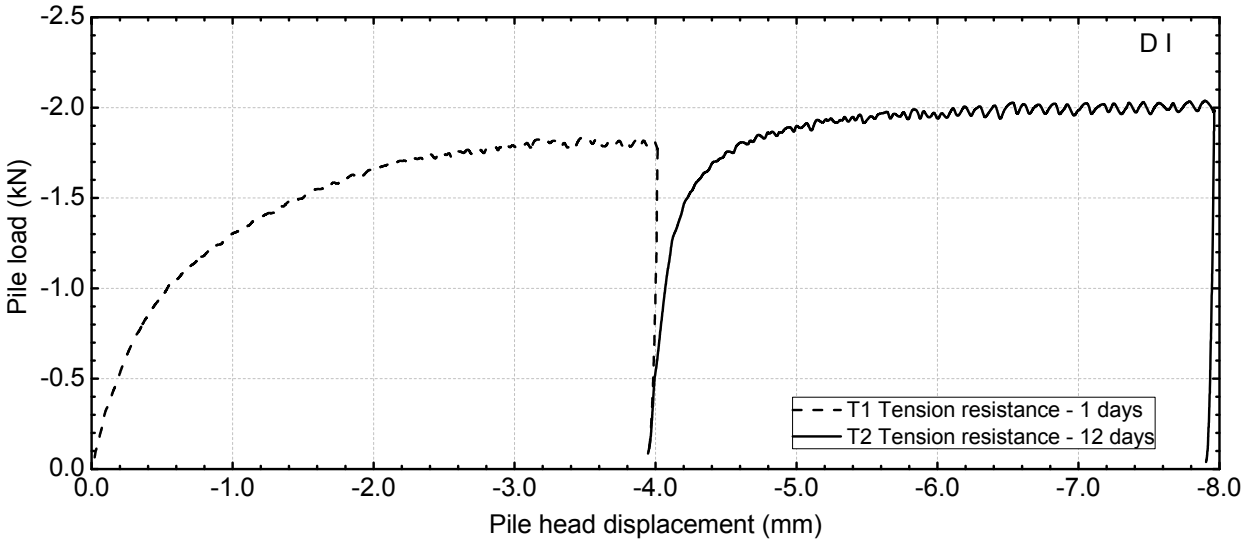


Figure 10-55: Driven pile test DI T2 compared to T1 static tension load–displacement behaviour in dry dense NE34 sand with BC5 boundary condition.

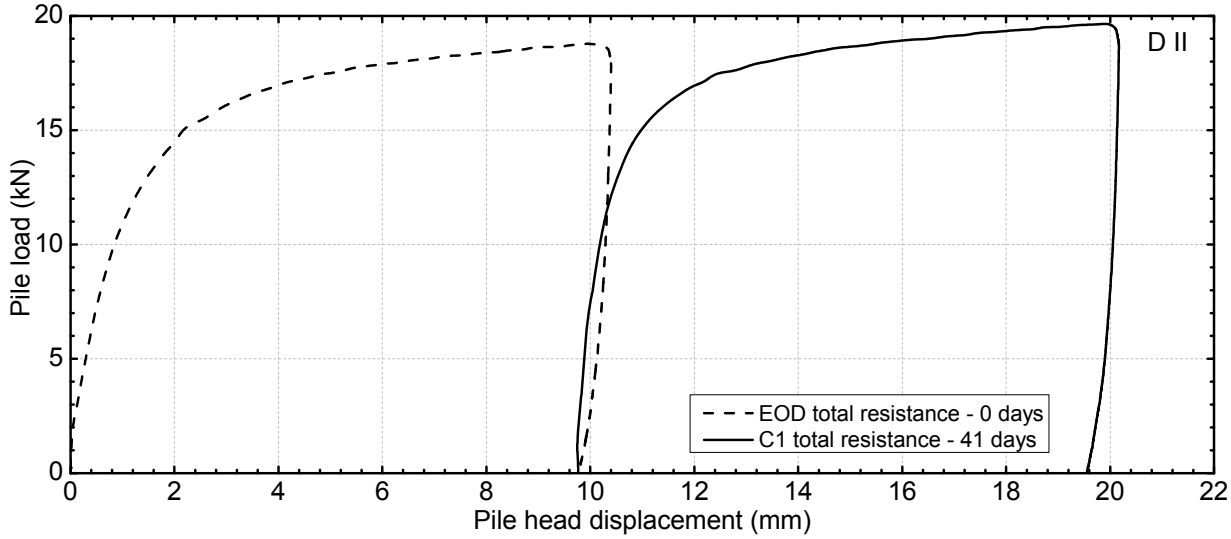


Figure 10-56 Driven pile test DII C1 compared to EOD static compression total load–displacement behaviour in dry dense NE34 sand with BC1 boundary condition.

10.4 Model piles aged capacity log-time trends

The base, shaft and total axial capacity trends of the model piles are shown normalised by the respective EOD capacities and plotted against log-time in Figures 10-57 to 10-59. These plots follow a similar approach to that adopted for the review of field tests given in Chapter 3. Each plot separates the tests aged under boundary condition BC3 from those where BC5 was applied. The capacity points from tests in the earlier study reported by Jardine (2009) have been included for completion. Note that the separation of base and shaft capacities was more difficult in some of the latter due to the load cell configuration of the earlier Mini-ICP arrangement. The overall trend is for results to scatter around, $Q_t/Q_{t=0} = 1$, indicating no overall ageing benefits. However the experiments that employed BC5 free field boundary condition (ICP07, ICP08, CPT09 and CPT10) and BC1 constant stress boundary condition (DII) showed clearer shaft capacity gains with time. But none of these tests could match the more marked gains observed from the earlier reported field ageing case histories, whose trend is shown on Figure 10-59. The ageing tests conducted with BC5 conditions with ageing durations ranging from 7 to 52 days or BC1 with 41 days ageing duration affirmed modest medium-term ageing trends. The base and total capacity trends show that relaxation applied under the BC3 boundary condition from 40 days onwards.

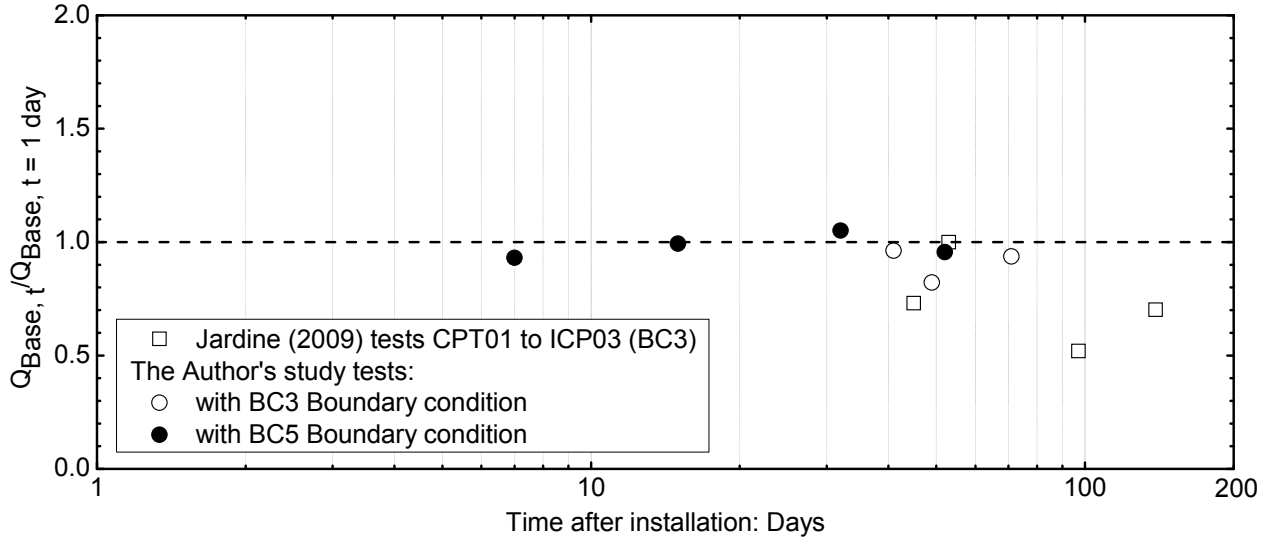


Figure 10-57: Aged model piles base capacity log time trend.

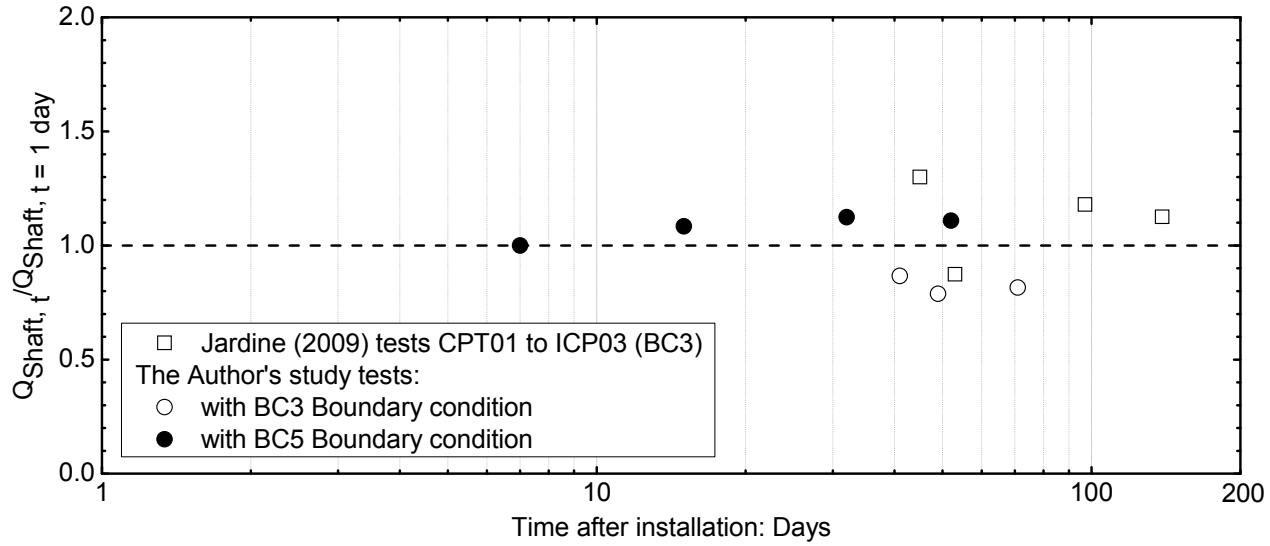


Figure 10-58: Aged model piles shaft capacity log time trend.

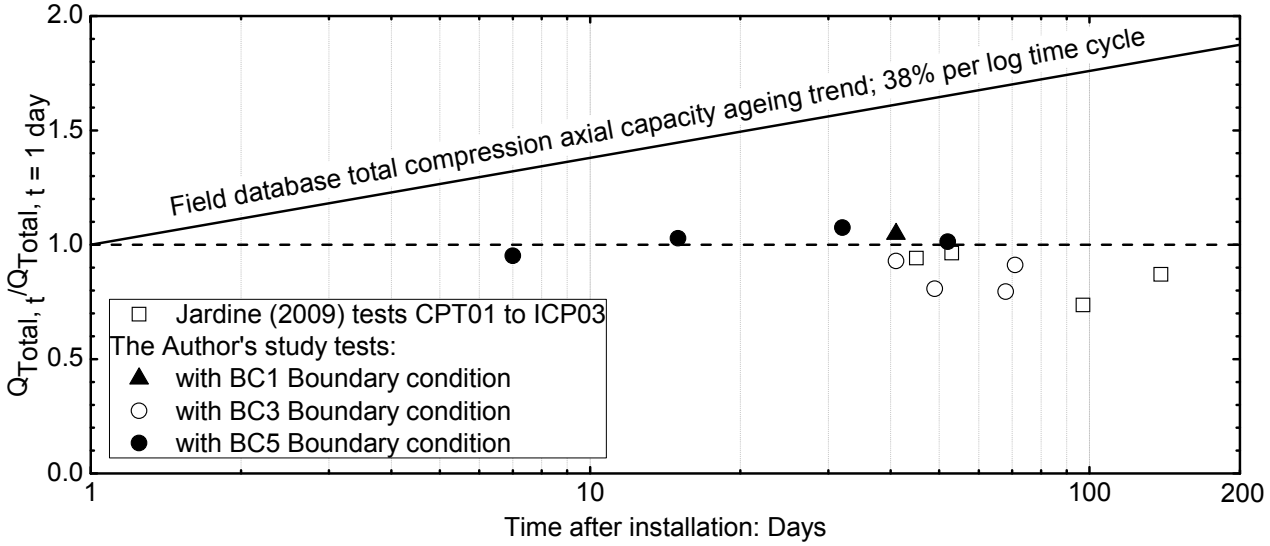


Figure 10-59: Aged model piles total compression capacity log time trend.

10.5 Implications from the ageing study

The experiments examined in Chapter 10 shows the markedly different ageing behaviour from the model displacement piles to that interpreted from field tests. The model piles' ageing periods which were imposed under close environmental control, led to capacities that could fall, be maintained or increase marginally with time. The sand stress monitoring undertaken during ageing suggested partial relaxation of the stresses in most cases. Marginal increases were seen close to the piles when active boundary conditions were adopted.

Of the hypotheses posed to explain pile ageing in Chapter 3, the two that were experimentally tested were;

1) Radial and hoop stresses re-equalisation around the pile leading to capacity gain
2) Ageing increasing sand stiffness, dilation or interface shearing resistance.

The pile ageing hypothesis regarding physiochemical effects in the sand mass or on the pile shaft was not tested experimentally in the Author's programme. The potential of pile ageing being related to physiochemical actions was evaluated by identifying the case histories involving sites with likely saline conditions in Chapter 3 and this made–up 60% of all the 23 reported sites but with no particular bias applying to these entries.

Several parameters that might potentially affect the ageing behaviour in the laboratory experimental setup were systematically isolated and considered including; 1) Density state, 2) Moisture state, 3) Boundary conditions, 4) Sand chamber size or particle size–to–pile diameter scale effects, 5) Ambient effective stress undulations during ageing, and 6) Mode of pile installation.

The different trends seen in the laboratory observations and the field trends may have been as a result unintended deviations between the experimental and field testing practice which may include;

1) Potential calibration chamber scale effects or boundary conditions effects applying despite the rigorous and systematic examination of several key parameters through the Author's ageing testing programme.
2) Possible relatively higher ratio of the interface shear band thickness to the model piles' diameter (see Appendix IV), posing possible scale effects uncharacteristic of full scale ageing piles, and which were not covered by the Author's variations of sand grain size or pile size.
3) The clean inert silica test sands which remained fully drained and without the active trace minerals observed in the composition of Dunkirk sand (Feldspar = 8%, $CaCo_3$ = 8%) where the large gains in capacity were reported, or any minor fractions of silt or clay sized particles.

4) The measured radial and circumferential stress profiles at the end of installation may have insufficiently acute profiles to promote rapid gains in shaft capacity possibly because of the unattended grain scale effects.

However, the laboratory model pile test arrangements applied for the ageing study have several key strengths including;

1) The laboratory model piles' axial static and cyclic loading responses have been confirmed to be representative of full scale field behaviour.
2) The test arrangement allowed the systematic isolation of a range of individual parameters including grain and pile size, moisture conditions and chamber boundary arrangements.
3) Continuous monitoring of all instruments was possible during the extended ageing periods, as well as static testing that mobilised pile shaft and base capacities fully and could be compared to end of installation tests.
4) The controlled conditions avoided several of the key weakenesses applying to the field ageing database as identified in section 3.5.

Chapter 11

11 Laboratory model piles behaviour under axial cyclic loading

11.1 Testing Programme

This chapter describes the behaviour observed when batches of axial cyclic loading tests, interspersed with static tension load tests were applied to the model piles after their ageing periods. The cyclic studies started with the Mini-ICP installed in medium–dense dry NE34 sand, in series ICP04. Series' ICP05 through to ICP08 followed, each isolating parameters that could potentially influence the model pile behaviour:

1) Pile–to–sand particle size (and density) with the (less dense) finer GA39 sand in ICP05 with BC3 boundary conditions chamber
2) Moisture state with wet dense NE34 in ICP06 with BC3 boundary conditions chamber, and
3) Chamber lateral boundary conditions with dry NE34 sand in ICP07 and ICP08 with BC5 boundary conditions chamber.

Table 11-1 summarises the key features of the cyclic loading tests applied and Table 11-2 lists the shaft capacities from the reference static tension tests that tracked changes in their shaft capacity. Tension testing was adopted to avoid the larger displacements required to develop maximum capacities under compression. The tables include the test series ICP01 to ICP03 performed in the full extended study, which were reported by Tsuha et al (2012). Load cycling was performed with a smooth sine wave form between the cyclic amplitudes as shown in Figure 11-1. The cycles were either load controlled (with reference to the pile head load) or displacement controlled with reference to the LVDT which was mounted on the pile to avoid system compliance. The cycles were applied at between 0.5 and 8.5 cycles per minute (Table 11-1). The load cycling mode is referred to as one–way (OW) if it mobilised the pile shaft resistance in one direction (tension or compression) only and two–way (TW) when otherwise. The cyclic tests codes name their test series followed by an extension that notes the mode of cycling (OW or TW) then a number that signifies the total of similar tests performed on the pile up to that stage, including the test in question. The static tension tests are identified by the test series followed by an extension of T (for tension) and by the number of tension tests performed up to that stage, including the test in question. When several cyclic tests were performed sequentially on the same pile the earlier tests were likely to have affected the responses observed. The reference static tension tests performed after each cyclic test served to track such effects. Note that tension loads are reported as having a negative sign.

11.2 Styles of axial cyclic loading responses

The piles' axial cyclic loading responses have been categorised in terms of three styles: Stable, Meta–stable and Unstable, following Karlsrud et al. (1986), Poulos (1988), Jardine et al. (2000, 2012) and Tsuha et al. (2012). Their behaviour was assessed by two parameters and their derivatives; the accumulated cyclic displacements, a, and the number of cycles sustained N (Figure 11-2) as follows.

Stable (S) cyclic load behaviour accumulates low and stabilising cyclic displacements that remain less than 0.01D (where D = pile diameter) and show slow rates of change less than or equal to 1mm/10,000 cycles up to N greater than or equal to 1000 without causing any loss in operational static shaft capacity and maintaining full serviceability.

Unstable (US) cyclic load behaviour accumulates displacements greater than 0.1D or has rates of accumulated displacements that increase to more than 1mm/100cycles with potentially very significant shaft capacity degradation within 100 cycles leading to an unserviceable response.

Meta–stable (MS) cyclic load behaviour accumulates displacements greater than 0.01D but less than 0.1D at moderate rates of change greater than 1mm/10,000 cycles but less than 1mm/100 cycles. This criterion potentially refers to partial degradation of the operational shaft capacity affecting the foundation serviceability but not resulting in ultimate failure. The meta-stable behaviour defines a transition between the stable and unstable behaviour at which a pile can sustain some 100s of cycles without losing foundation serviceability, but at the same time losing some capacity and not achieving fully stable condition.

The accumulated cyclic displacements stability criteria are essentially working definitions and are scaled with pile diameter broadly matching those applied to 457mm OD full scale piles (Jardine & Standing 2012, Rimoy et al. 2013) for which the absolute limits were set about ten times higher.

No.	Test series	Test code	Control	Date	Jack load (kN)	N cycles	Rate (N/min)	Q_{cyclic}/Q_T	Q_{mean}/Q_T	Description
1	ICP1	OW1	Load	17/03/08	-4.0 – 0	1000	1.7	0.22	0.22	meta-stable
2		TW1	Displacement (-4 to +5mm)	20/03/08	Varies	100 (N_f = 4)	0.4	Varies	Varies	unstable
3	ICP2	OW1	Load	08/10/08	-3.0 – 0	1000	2.3	0.12	0.12	stable
4		OW2	Load	9-10/10/08	-4.8 – 0	1000	1.4	0.20	0.20	stable
5		OW3	Load	13/10/08	-6.8 – 0	500	1.0	0.28	0.28	meta-stable
6		TW1	Displacement (-2 to +3mm)	14/10/08	Varies	100 (N_f=4)	0.5	Varies	Varies	unstable
7	ICP3	OW1	Load	22/07/09	-9.6 – 0	100 (N_f=66)	0.6	0.38	0.38	unstable
8		TW1	Load	23/07/09	-5.0 – 8.0	1 (N_f=1)	0.2	0.54	-0.08	unstable
9		TW2	Load	23/07/09	-5.0 – 5.0	199 (N_f=170)	1.4	0.40	0.06	unstable
10		TW3	Load	23/07/09	-5.0 – 7.0	50 (N_f=10)	1.0	0.44	0.02	unstable
11		TW4	Load	23/07/09	-5.0 – 10.0	37 (N_f=3)	0.5	0.44	0.02	unstable
12	ICP04	OW1	Load	15 - 17/12/09	-3.5 – 0	7000	0.5	0.15	0.15	stable
13		TW1	Load	18/12/09	-4.0 – 4.0	600 (N_f=580)	3.0	0.23	0.06	meta-stable
14		OW2	Load	21/12/09	-4.6 – -2.3	50	6.0	0.21	0.63	meta-stable
15	ICP05	OW1	Load	19/07/10	-2.2 – -0.6	1050	5.0	0.22	0.38	meta-stable
16		TW1	Load	20/07/10	-1.3 – 0.5	300	3.5	0.26	0.11	meta-stable
17		TW2	Load	21/07/10	-1.1 – 0.2	1000	6.0	0.24	0.17	meta-stable
18		OW2	Load	22/07/10	-1.9 – -0.2	74 (N_f=1)	4.0	0.33	0.40	unstable
19	ICP06	TW1	Displacement (+0.5 to -0.5mm)	07-10/12/10	Varies	12022	~3.0	Varies	Varies	unstable
20		OW1	Load	10/12/10	-1.0 – 0	1000	8.5	0.11	0.11	stable
21	ICP07	OW1	Load	20-21/07/11	-7.2 – -4.8	4040	2.5	0.09	0.46	stable
22		TW1	Load	21-22/07/11	-1.2 – 1.2	4760	2.5	0.07	0.02	stable
23	ICP08	TW1	Displacement (+0.5 to -0.5mm)	17 - 20/10/11	Varies	20002	~4.0	Varies	Varies	unstable

Table 11-1: Axial cyclic loading test series in the full extended Mini-ICP study.

No.	Test series	Test code	Date	Days after installation	Q_T (kN)	Prior test on Tables 10-1 or 11-1
1	ICP01	T1	03/03/08	97	-9.2	C1
2		T2	18/03/08	112	-10.8	OW1
3		T3	21/03/08	115	-4.9	TW1
4	ICP02	T1	07/10/08	140	-12.1	C1
5		T2	09/10/08	142	-13.2	OW1
6		T3	10/10/08	143	-14.0	OW2
7		T4	14/10/08	147	-13.7	OW3
8		T5	15/10/08	148	-8.7	TW1
9	ICP3	T1	22/07/09	54	-12.5	C1
10		T2	23/07/09	55	-10.9	OW1
11		T3	27/07/09	59	-4.8	TW1,2,3,4
12	ICP04	T1	15/12/09	42	-11.11	C1
13		T2	18/12/09	45	-13.22	OW1
14		T3	21/12/09	48	-5.39	TW1
15		T4	21/12/09	48	-6.00	OW2
16	ICP05	T1	19/07/10	74	-3.77	C1
17		T2	20/07/10	75	-3.50	OW1
18		T3	21/07/10	76	-2.74	TW1
19		T4	22/07/10	77	-2.60	TW2
20		T5	23/07/10	78	-2.30	TW3
21	ICP06	T1	06/12/10	49	-15.49	C1
22		T2	10/12/10	53	-4.45	TW1
23		T3	13/12/10	56	-4.69	OW1
24	MiP01	T1	28/02/11	68	-2.07	C1
25	ICP07	T1	20/07/11	57	-13.16	C1
26		T2	21/07/11	58	-13.76	OW1
27		T3	22/07/11	59	-13.68	TW2
28	ICP08	T1	17/10/11	18	-11.50	C1
29		T2	20/10/11	21	-3.47	TW1

Table 11-2: Axial static tension tests undertaken in the full extended Mini-ICP study.

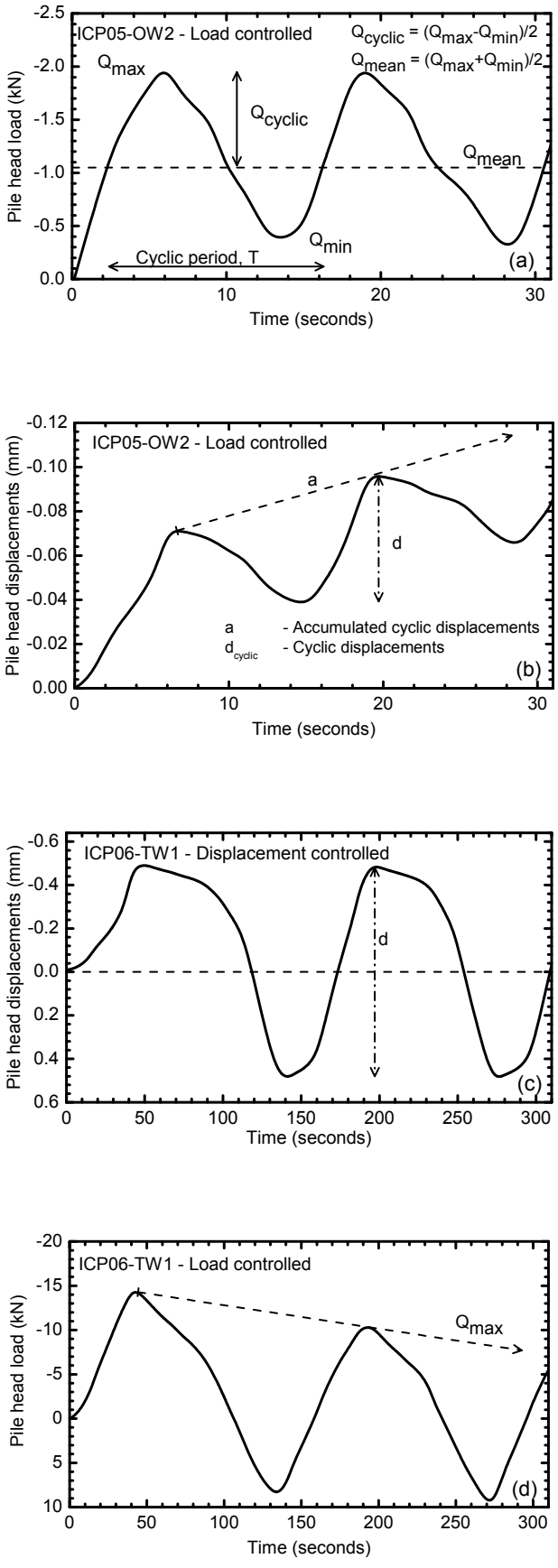


Figure 11-1: Axial cyclic loading displacements and load patterns illustrated from load controlled test ICP05-OW2 in (a) and (b), and displacement controlled test ICP06-TW1 in (c) and (d).

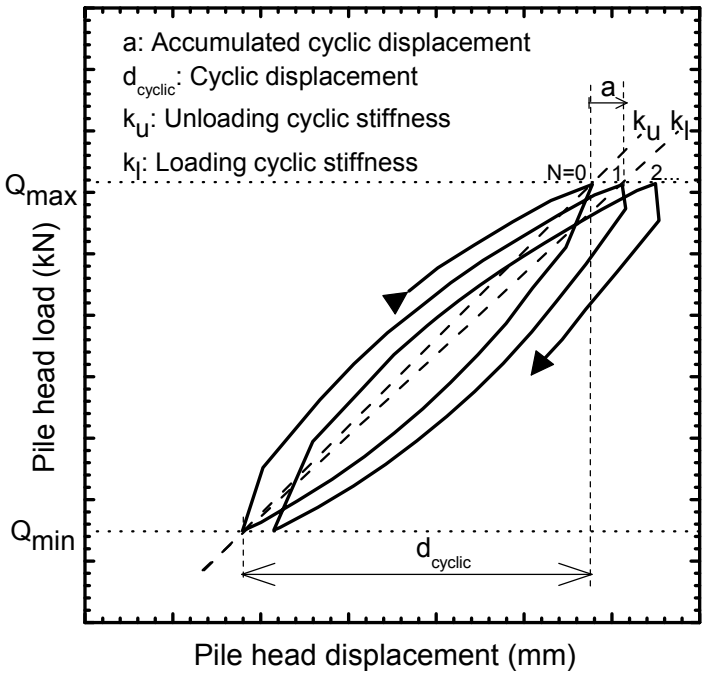


Figure 11-2: Illustration of the displacement and stiffness parameters used in the analyses.

11.3 Assessment of pile behaviours during the axial cyclic loading tests

The accumulated cyclic displacements from the three cyclic loading tests performed in 'standard' test series ICP04 are plotted on Figure 11-3. The same figure shows the threshold rates for stable and meta-stable conditions and the accumulated displacements for cyclic failure (0.1D). Test ICP04–OW1 (Table 11-1), which experienced one–way cycling between 0 and -3.5kN starting from an initial tension capacity of -11.11kN, showed minimal displacement growth with rates that remained within the stable criteria throughout the 7000 cycles applied. The subsequent static tension test ICP04–T2 shown on Figure 11-4(a) showed a 20% shaft capacity gain, confirming the stable outcome.

ICP04-TW1 applied two–way loading from -4kN to 4kN. The pile settled, accumulating positive displacements until it met the unstable displacement rates criteria after 580 cycles, although it remained within the meta-stable accumulated displacements limit up to its end at 600cycles. The following static tension test ICP04–T3 (Figure 11-4(b)) proved shaft capacity degradation of 60% confirming the meta-stable to unstable performance. The last test, ICP04-OW2, involved asymmetric cyclic loading between -2.3kN and -4.6kN. The displacement accumulation rates exceeded 1mm/100cycles over the first five cycles while displacements stayed within the meta–stable criteria until the test was halted after 50 cycles. A static tension test ICP04-T4 (Figure 11-4(c)) confirmed a similar shaft capacity to ICP04-T3 showing minimal further capacity damage developed over this limited batch of load cycling.

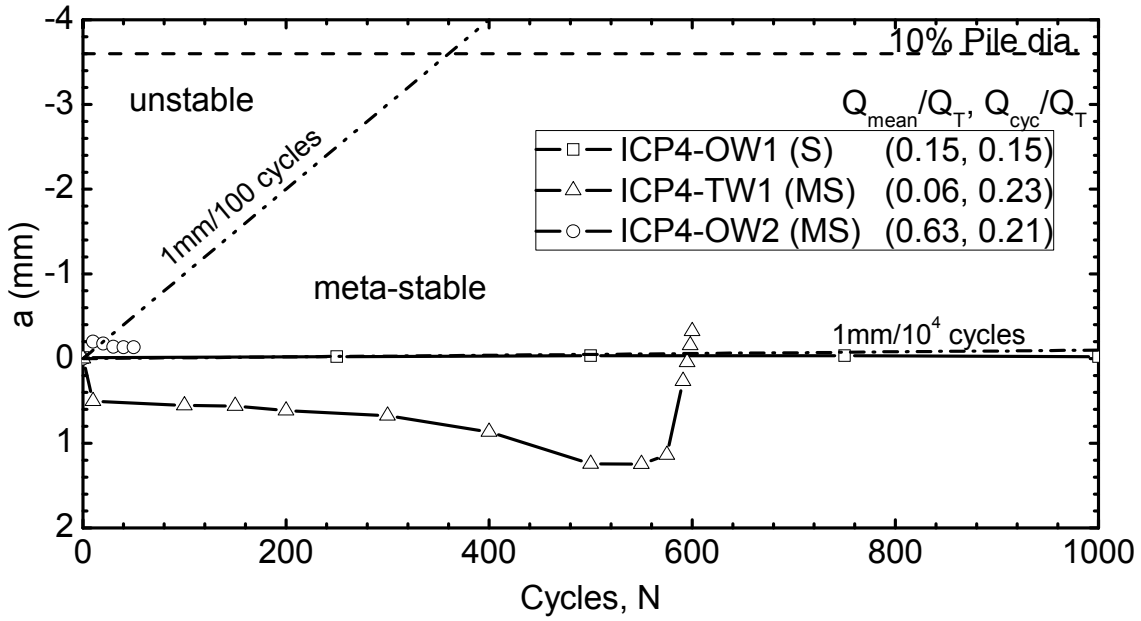


Figure 11-3: Accumulated cyclic displacements with number of cycles applied during the axial cyclic loading test series ICP04.

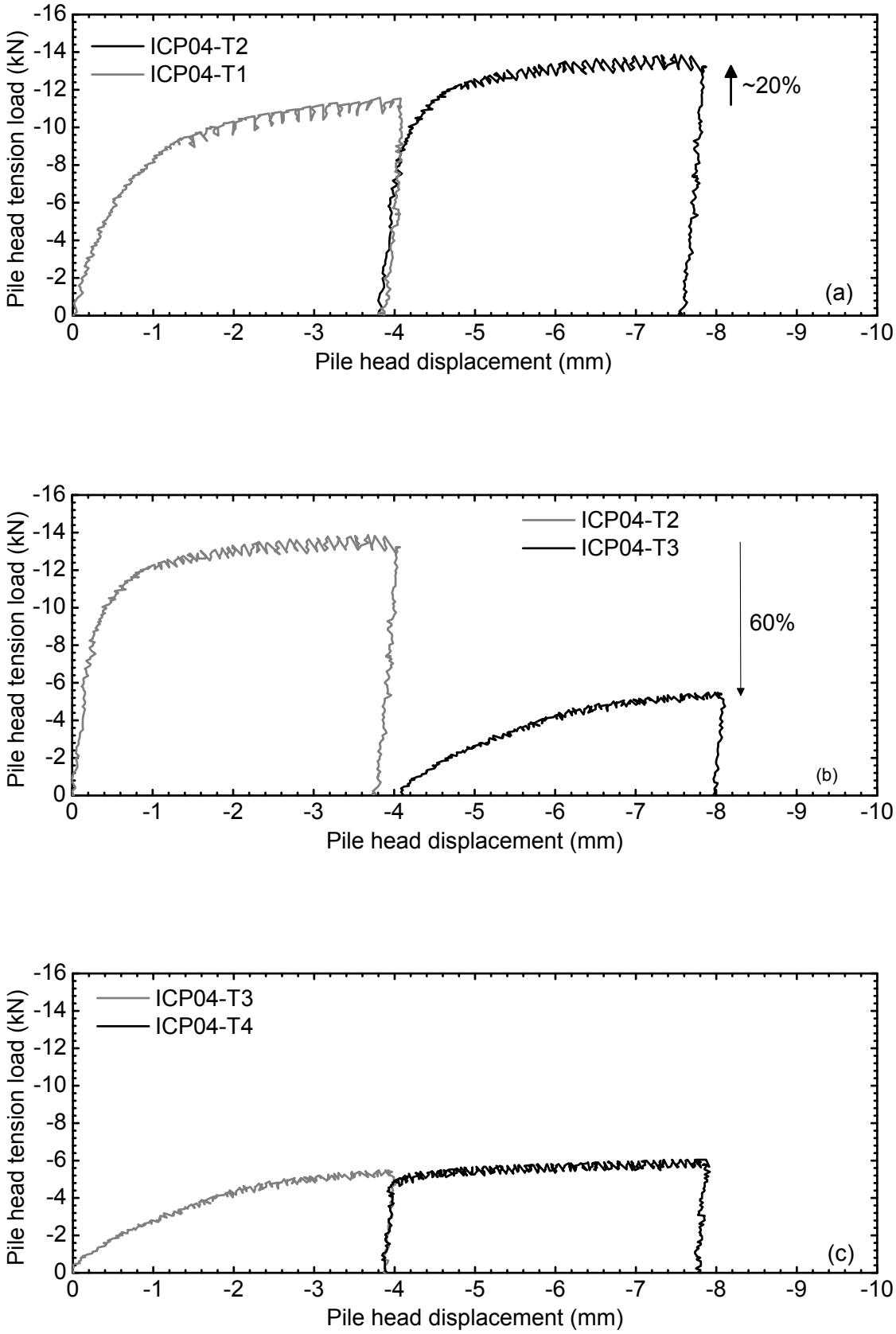


Figure 11-4: Reference static tension tests interspersed between the axial cyclic loading tests in ICP04.

Test series ICP05 investigated particle–to–pile diameter scale effects with a Mini-ICP test in loose GA39 sand, applying the four axial cyclic loading batches summarised in Table 11-1. The accumulated displacement trends of all are plotted on Figure 11-5. Test ICP05–OW1 loaded asymmetrically between -0.6kN and -2.2kN for 1050 cycles without cyclic failure; it classified as marginally meta-stable due to its rates of displacement accumulation. Static tension tests (Figure 11-6(a)) before and after this experiment showed minor degradation in shaft capacity, as associated with meta-stable conditions. The following cyclic loading test, ICP05-TW1, applied 300 cycles with head loads between 0.5kN to -1.3kN. The accumulated displacements fell again within the meta-stable category as shown in Figure 11-5; the static tension tests (Figure 11-6(b)) confirmed a decrease in shaft capacity ~22%. A further 1000 cycles was imposed in ICP05-TW2, ranging from 0.2kN to -1.12kN. Displacements accumulated at a similar rate to ICP05-TW1, falling again within the meta-stable region until the test was stopped. Static tension testing (Figure 11-6(c)) didn't show any further significant change in capacity, so the meta-stability was marginal. The last test performed in this series, ICP05-OW2 imposed 74 cycles from -1.9kN to -0.2kN and led to rates of accumulated displacements > 1mm/100 cycles from the onset and total accumulated displacement ~0.1D by the end of cycling, qualifying as clearly unstable. Static testing proved ~12% of further capacity degradation.

Overall, the cyclic tests in GA39 sand showed relatively higher susceptibility to load cycling by developing faster rates of displacement accumulation under similar conditions to NE34 sand.

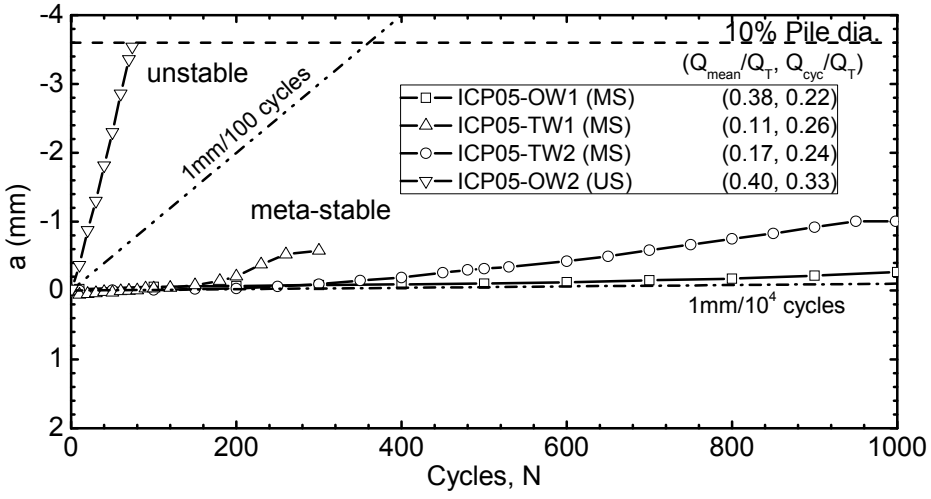


Figure 11-5: Accumulated cyclic displacements with number of cycles applied during the axial cyclic loading test series ICP05.

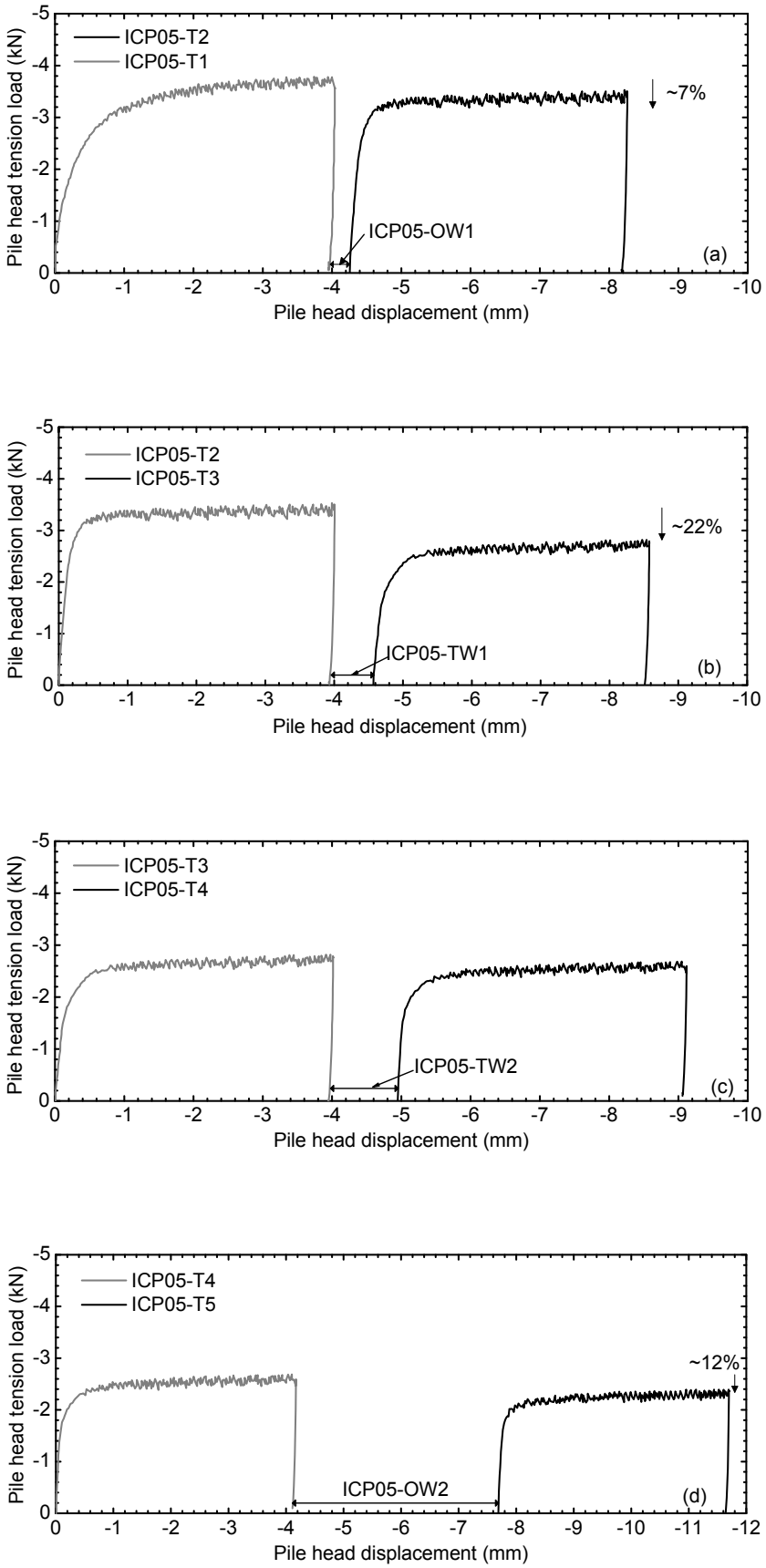


Figure 11-6: Reference static tension tests between the axial cyclic loading tests in ICP05.

The effects of moisture with wet NE34 sand were examined in series ICP06 by two cyclic loading batches. A displacement controlled test ICP06-TW1 was performed on a pile with an initial -15.50kN tension shaft capacity displacing between -0.5mm and 0.5mm over 12,022 cycles. No cyclic displacement can accumulate (Figure 11-7) with this arrangement but changes in the mobilised pile shaft and base resistances can develop, as monitored through the pile head and base load cells. The pile head load–displacement behaviour during the test is shown on Figure 11-8; only selected batches of cycles are shown for clarity. The first cycle begins in tension mobilising 94% of the pile's initial shaft capacity at a displacement of -0.5mm. By the beginning of the 2nd cycle the shaft stiffness has degraded by 26.6%, and symmetrical shaft degradation continues both under tension and compression loading with apparent stabilisation of pile head compression load as shown in Figure 11-9. The base load cell stopped working ~6800cycles into the test, by then it showed trends of base stiffness increasing between 1 and 10 cycles, and then decreasing up to 1000cycles before increasing again as the test continued.

The overall effect of ICP06-TW1 on static tension resistance shown in Figure 11-10(a) was a ~70% loss of capacity – clearly an unstable outcome. The one–way test that followed ICP06-OW1 cycled between 0 to -1kN for 1000 cycles leading to the stable outcome shown on Figure 11-7. The static tension load test also indicated marginal recovery of the shaft capacity, even after the considerable shaft degradation imposed by ICP06–TW1.

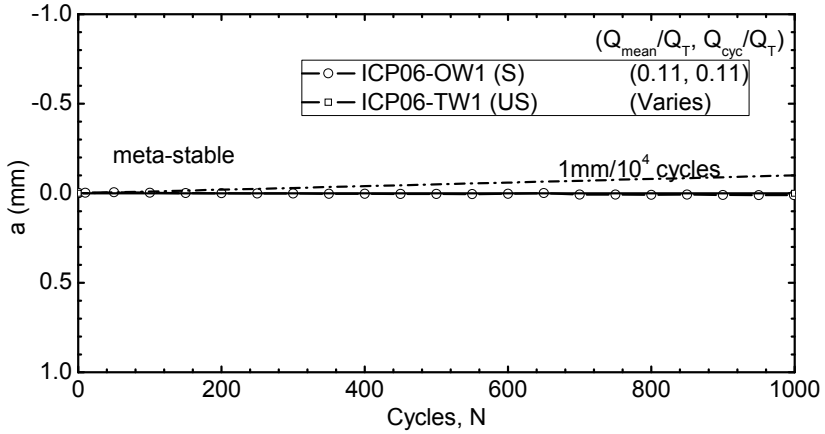


Figure 11-7: Accumulated cyclic displacements with number of cycles applied during the axial cyclic loading test series ICP06.

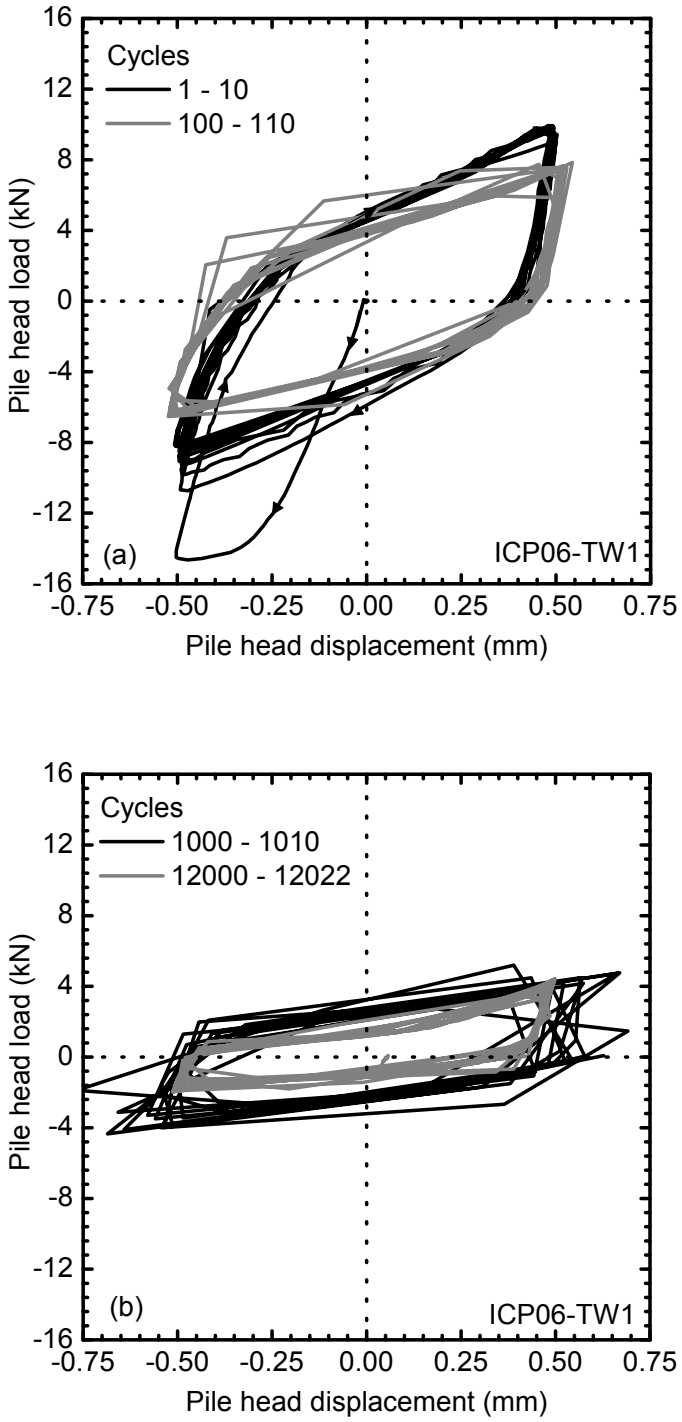


Figure 11-8: Pile head load–displacement behaviour of displacement controlled axial cyclic loading test ICP06-TW1 in cycles (a) 1 – 10 and 100 – 110 (b) 1000 – 1010 and 12000 – 12022.

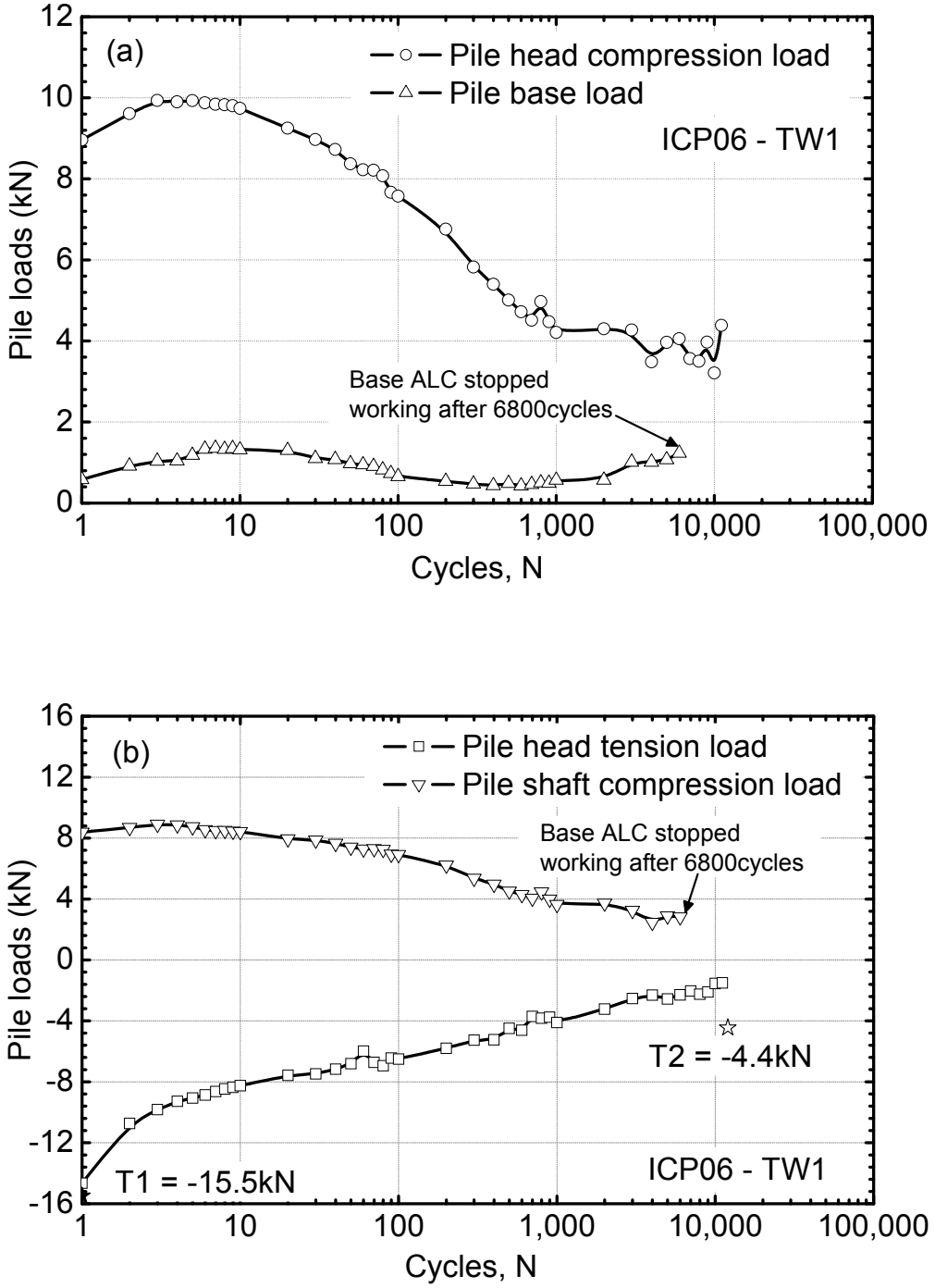


Figure 11-9: ICP06-TW1 axial cyclic loads against cycles applied for (a) pile head and base in compression (b) pile head in tension and pile shaft in compression, showing apparent stabilisation of compression pile head load and symmetrical shaft capacity decay.

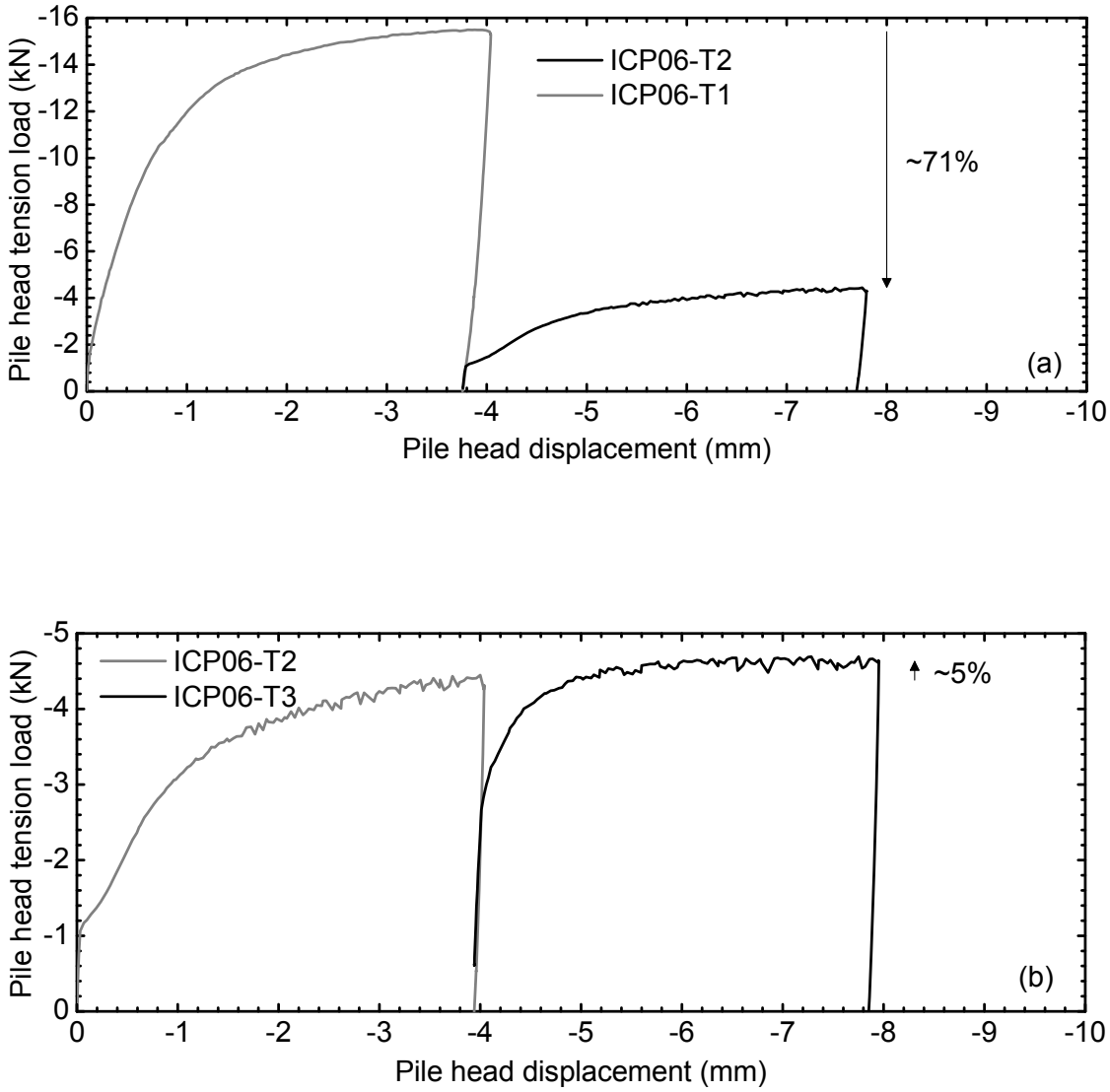


Figure 11-10: Reference static tension tests between the axial cyclic loading tests in ICP06.

Two load-controlled cyclic tests were performed in series ICP07 and one long duration displacement controlled cyclic experiment was incorporated into series ICP08, both involving dry NE34 sand and the modified BC5 boundary conditions. ICP07-OW1 applied loads from -4.8kN to -7.2kN over 4040 cycles while ICP07-TW1 ranged from -1.2kN to 1.2kN over 4760 cycles. In both cases the Q_{cyc}/Q_T was less than 0.1. Figure 11-11 presents the accumulated displacements trends from both tests which fall well below the 1mm/10,000 cycles' threshold and indicate full stability throughout as seen on Figure 11-14. The capacity of the pile shaft increased marginally ICP07-OW1 and was maintained steady over ICP07-TW1.

The long duration test ICP08-TW1 in which displacements were cycled from -0.5 to 0.5mm for 20,002 cycles commenced from a measured tension shaft capacity of -11.50kN. Again, no cyclic displacement can accumulate with this arrangement, although changes of the pile shaft and base

resistances could develop that were monitored through the pile head and base load cells as shown on Figures 11-12 and 11-13. Similar to ICP06-TW1, the shaft stiffness degraded symmetrically with cycling in both compression and tension from N > ~100 cycles, while the base stiffness increased between cycles 1 and 10, decreased up to 1000 cycles and then increases again as the pile transferred its compression loads to the base. The base stiffness patterns are reflected in similar changes in the pile head loads developed in compression. The resulting pile shaft capacity changes are shown on Figure 11-15. As with ICP06-TW1, a capacity degradation of 70% and a marked loading stiffness reduction were observed.

The cyclic displacement responses of the piles are considered further in Chapter 12 along with a new interpretation of the displacement responses of the Dunkirk full scale tests reported by Rimoy et al. (2013) that develops the cyclic displacements interaction with Q_{cyclic}, Q_{mean} and cycles applied into normalised 3D displacement surfaces.

The next section describes how imposed Q_{mean} and Q_{cyclic} loads (normalised by the Q_T) interact with the number of loading cycles in defining the piles response to cyclic loading and potentially cyclic failure conditions.

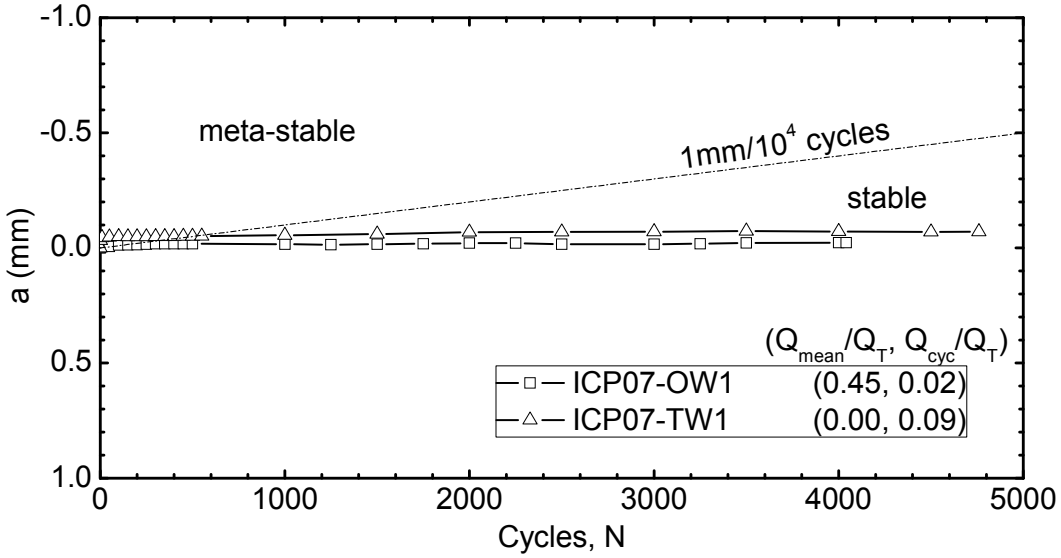


Figure 11-11: Accumulated cyclic displacements with number of cycles applied during the axial cyclic loading test series ICP07.

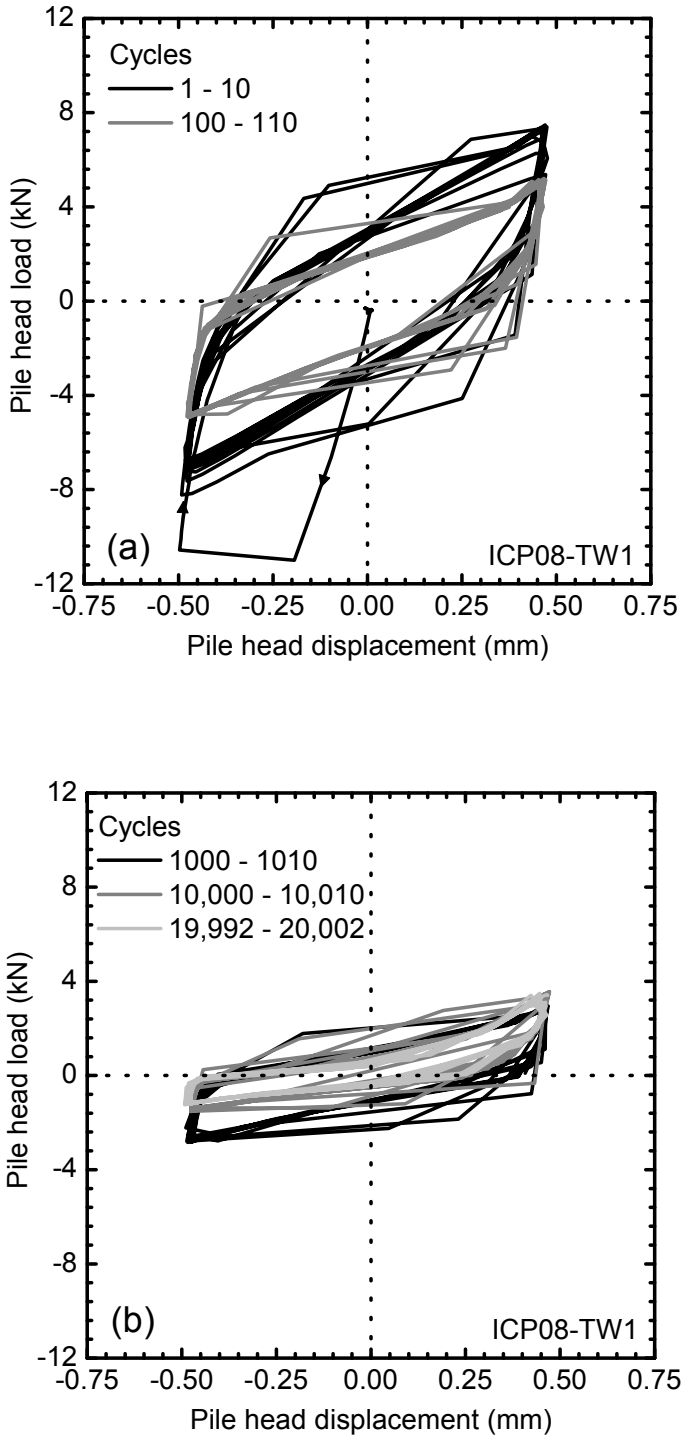


Figure 11-12: Pile head load–displacement behaviour of displacement controlled axial cyclic loading test ICP08-TW1 in cycles (a) 1 – 10 and 100 – 110 (b) 1000 – 1010, 10,000 – 10,010 and 19,992 to 20,002.

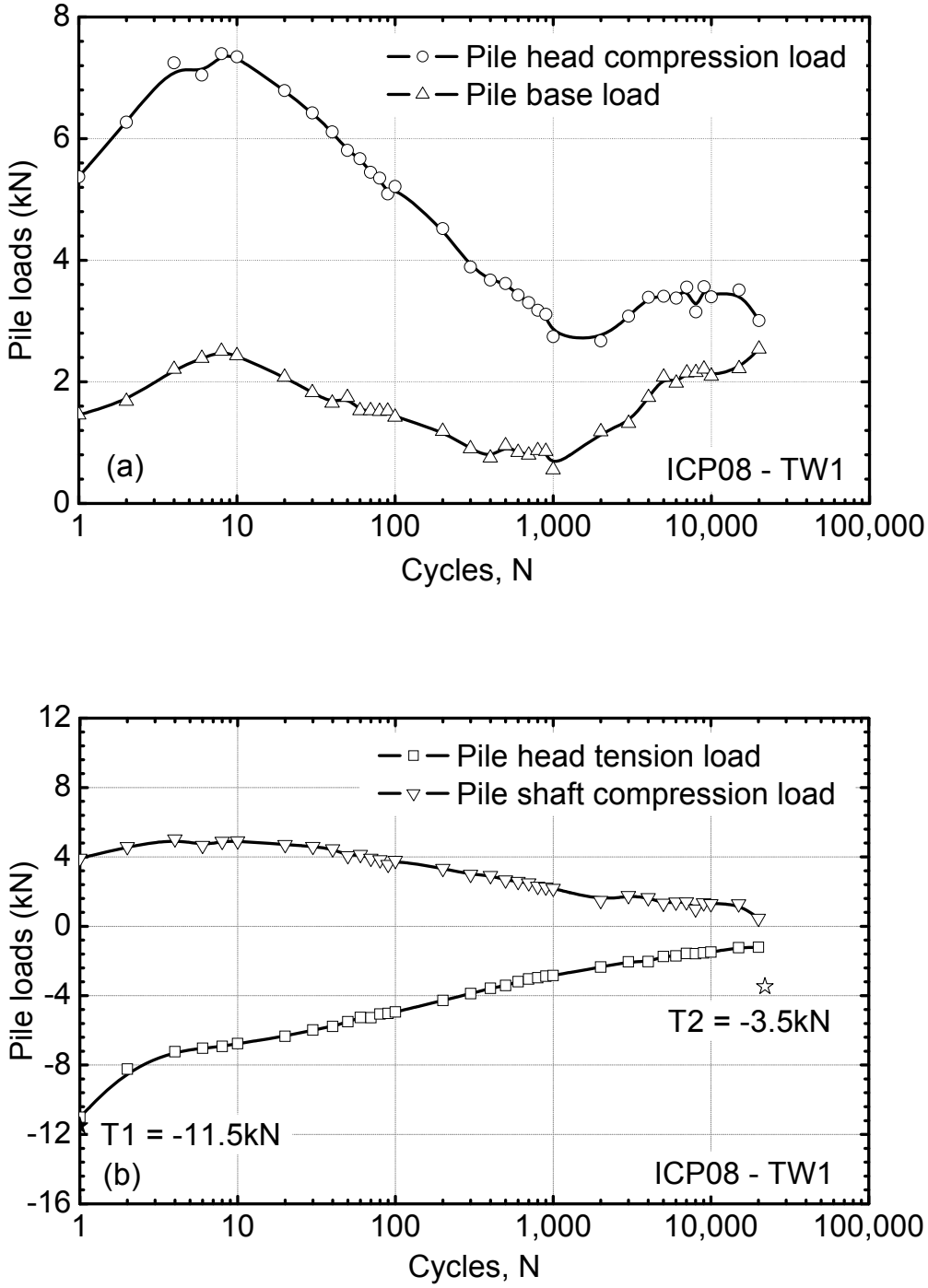


Figure 11-13: ICP08-TW1 axial cyclic loads against cycles applied for (a) pile head in compression and pile base (b) pile head in tension and pile shaft in compression.

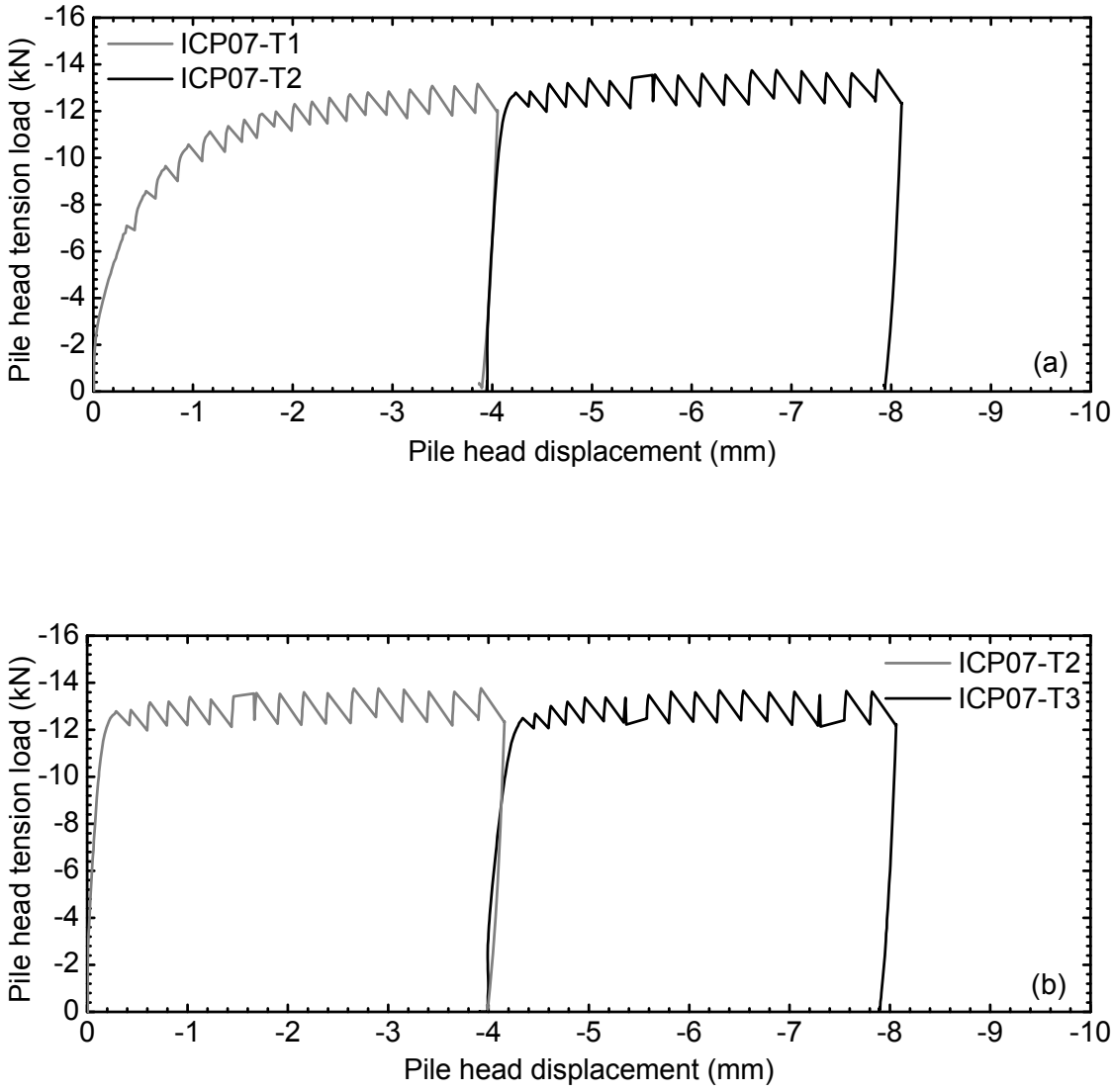


Figure 11-14: Reference static tension tests during the axial cyclic loading tests in ICP07.

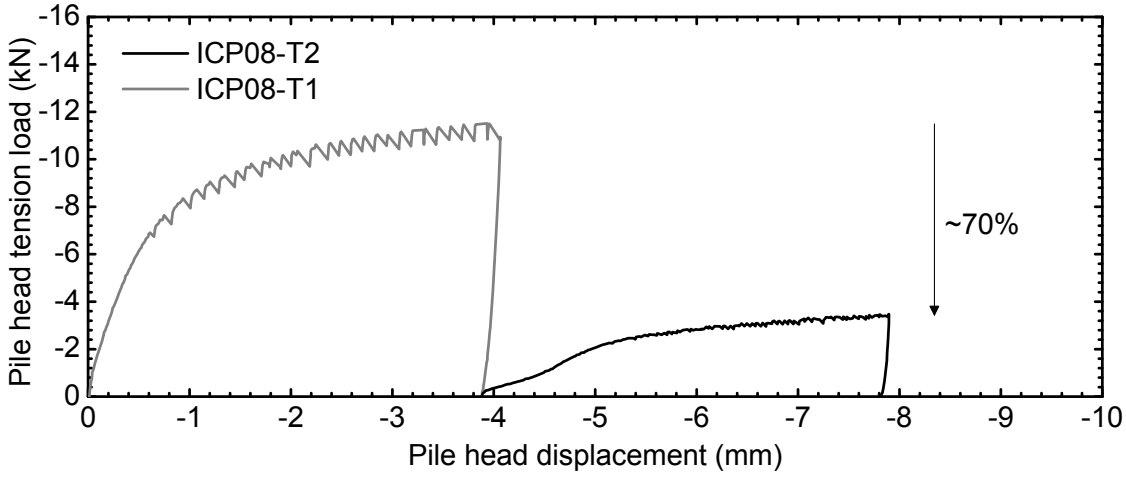


Figure 11-15: Reference static tension tests during the axial cyclic loading tests in ICP08.

11.4 Stability interaction diagram

As reviewed in Chapter 4, cyclic interaction diagrams have proved useful for reporting cyclic tests and assessing practical problems. Their use for displacement piles in sand has been demonstrated for a full scale (457mm diameter, 10m to 19m long) open-ended piles under axial cyclic loading in Dunkirk marine silica sand by Jardine and Standing (2000, 2012), and for ICP01 to ICP04 Mini-ICP tests in NE34 sand by Tsuha et al. (2012).

Following a similar approach to Tsuha et al. (2012), the Author's axial cyclic loading tests have been applied to construct interaction diagrams. Each test's cyclic load characteristics, Q_{mean} and Q_{cyclic}, normalised by the reference static axial tension capacity before cycling Q_T (see Table 11-2), Q_{mean}/Q_T and Q_{cyclic}/Q_T in Table 11-1, are plotted on Figures 11-16 to 11-19. The number of cycles to failure in each test is annotated on the scatter plots. The contours of number of cycles to failure of 100 and 1000 demarcate the three stability zones.

Starting with the Tsuha et al. (2012) interaction diagram limits Figure 11-16 shows how the ICP04 cyclic tests fit into the same pattern. Figure 11-17 goes on to show the ICP06 cyclic tests with the Mini-ICP in wet NE34 sand referred to the same boundaries. The stable test ICP06-OW1 plots in mid part of the stable zone. Moving on to the displacement controlled test ICP06-TW1, as explained earlier this test did not experience constant shaft loading. It started from an unstable position which within five cycles evolved to a nearly symmetric two–way shaft loading pattern that eventually migrated into a quasi–stable condition where the pile could sustain high numbers of the imposed displacement controlled cycles without further changes in cyclic stiffness or possibly shaft capacity. This progress is tracked in Figure 11-7, noting the value of N associated with five test stages. Figure 11-18 covers the Mini-ICP cyclic tests ICP07 and ICP08 performed with BC5 boundary conditions. The stable tests ICP07-OW1 and ICP07-TW1 are seen to plot well within the stable zone, while the displacement controlled test ICP08-TW1 followed with similar trajectory to ICP06-TW1. In all these tests Q_T is defined as the tension capacity applying before cycling commences.

Sand particle scale effects on pile cyclic behaviour were examined in test ICP05 with the finer and looser GA39. The cyclic test outcomes for this pile are shown on Figure 11-19. Tests ICP05-OW1 and ICP05-TW2, which cycled in the stable region established for NE34 sand, developed meta-stable accumulated cyclic displacement rates while ICP05-OW2 which plotted in the NE34 sand meta-stable region, proved to be unstable and developed cyclic failure in the first cycle. This emphasises the higher cyclic susceptibility of GA39 discussed first in Chapter 7, where similar behaviour was observed during installation. The unstable and meta-stable zones for GA39 sand will be at lower levels to NE34 sand and the stable region reduced in size.

Overall, the Tsuha et al. NE34 cyclic loading interaction diagram applies equally to dry and wet NE34 medium dense sand masses. It is also representative for the 'free field simulator' BC5 boundary condition and compares well with Jardine & Standing's (2012) full scale pile test interaction chart. For sands with greater susceptibility to cyclic loading, like GA39, the unstable and meta-stable zones relocate downwards, shrinking the stable zone.

Figure 11-20 shows a plot of $\Delta Q_T/Q_T$ against Q_{cyclic}/Q_T from a subset of stable tests from the load controlled Mini-ICP tests in NE34 sand in which Q_{cyclic}/Q_T and Q_{mean}/Q_T had low values (< ~ 0.3), ΔQ_T being the change in pile static tension capacity from the cyclic loading. In the other parts of the cyclic interaction diagram where the pile is experiencing failure under cyclic loading, by definition $\Delta Q_T/Q_T$ depends on N_f, Q_{mean}/Q_T and Q_{cyclic}/Q_T as $\Delta Q_T/Q_T = (Q_T - Q_{max})/Q_T = 1-(Q_{cyclic}/Q_T + Q_{mean}/Q_T)$. However no failure was developed in these tests and the post test tension experiments showed that in the region with $0.1 < Q_{cyclic}/Q_T < 0.23$ cyclic loading leads to increases in the static shaft capacity of the pile. Figure 11-20 indicates that the gains reach a maximum after cycling to about $Q_{cyclic}/Q_T \approx 0.17$. Imposing higher cyclic amplitudes $Q_{cyclic}/Q_T > 0.22$ degrades the shaft capacity.

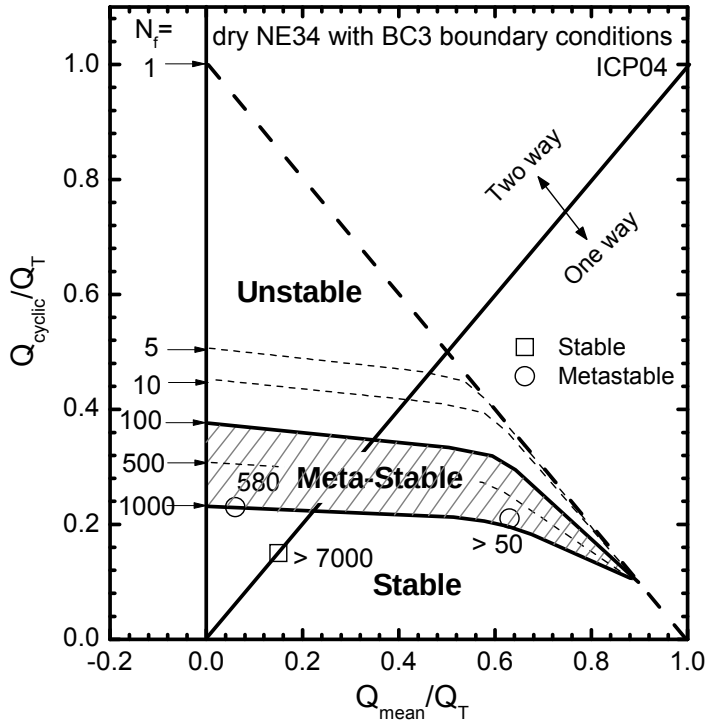


Figure 11-16: Axial cyclic loading interaction diagram for the standard test series ICP04 with the Mini-ICP in dry NE34 sand with BC3 boundary condition.

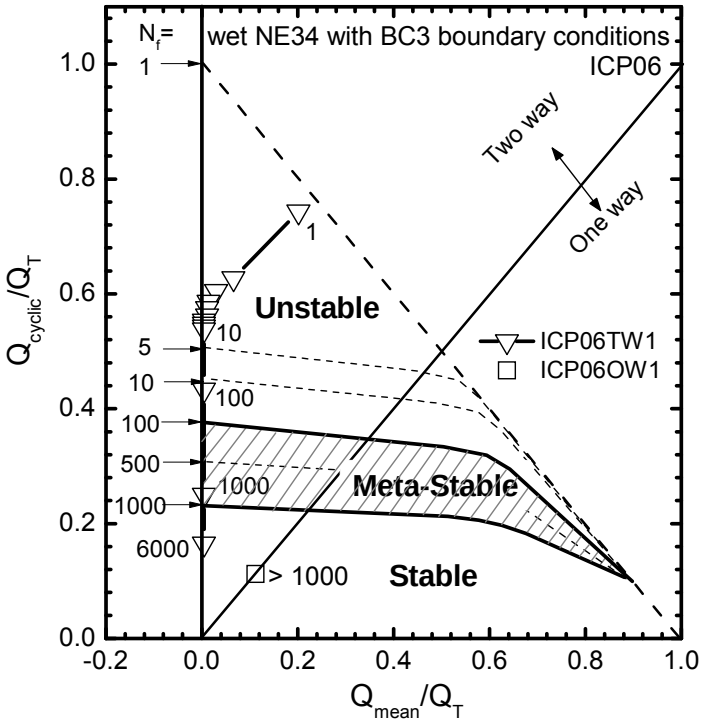


Figure 11-17: Axial cyclic loading interaction diagram for the test series ICP06 with Mini-ICP in wet NE34 sand with BC3 boundary conditions.

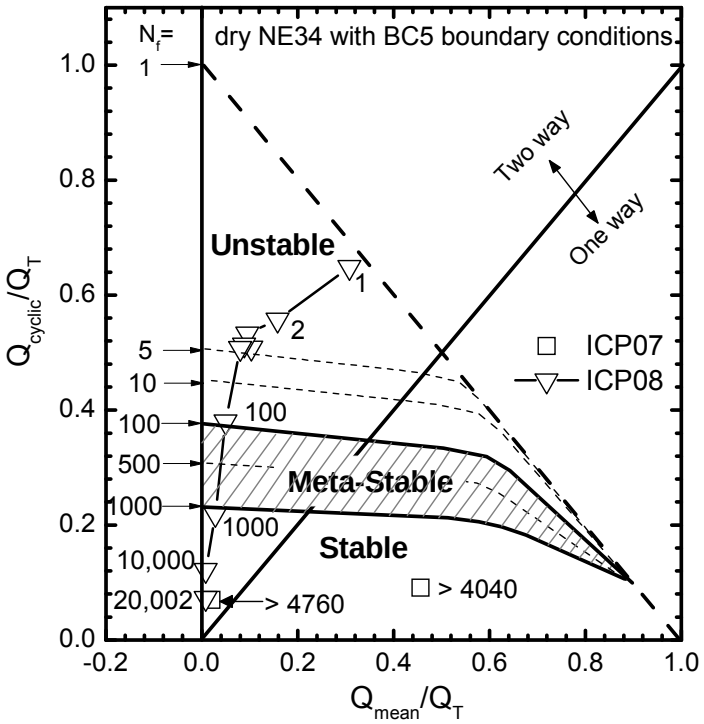


Figure 11-18: Axial cyclic loading interaction diagram for the test series ICP07 & 08 with the Mini-ICP in dry NE34 sand with BC5 boundary conditions.

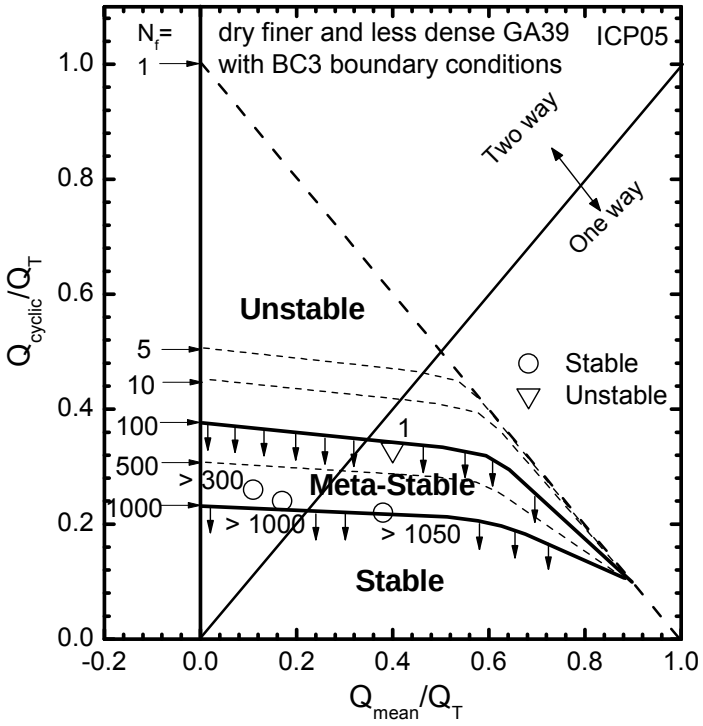


Figure 11-19: Axial cyclic loading interaction diagram for the test series ICP05 with the Mini-ICP in dry GA39 sand with BC3 boundary conditions.

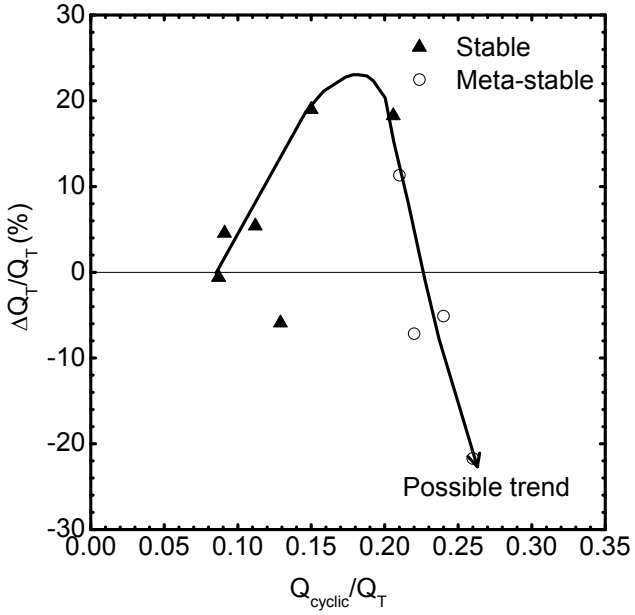


Figure 11-20: Static shaft capacity changes with axial cyclic amplitude for the load controlled Mini-ICP axial cyclic loading tests with $Q_{cyclic}/Q_T < 0.3$.

11.5 Axial cyclic pile stiffness

Pile stiffness during axial cyclic loading was defined in Figure 11-2 from the peak (Q_{max}) to trough (Q_{min}) load–displacement curve with the secant stiffness k given by $(Q_{max} - Q_{min})/d_{cyclic}$.

Depending on whether similar displacements develop over the loading and unloading stages the loading and unloading stiffness k_l and k_u may differ or converge.

Figure 11-21 shows loading stiffnesses k_l from the stable tests ICP04-OW1, ICP06-OW1, ICP07-OW1 and ICP07-TW1 normalised by the stiffness at the start of cycling $k_{l,N=1}$. The cyclic stiffness remained practically constant matching the onset stiffnesses, as the tests progressed to more than 1000 cycles in these stable experiments.

The loading stiffnesses from the meta-stable tests ICP04-TW1, ICP04-OW2, ICP05-OW2, ICP05-TW1 and ICP05-TW2 are shown on Figure 11-22. Their stiffness trends remained constant and close to the onset values, as with the stable tests until cyclic failure approaches and marked stiffness degradation ensues. Stiffness degradation commenced at 200 cycles in ICP04-TW1 and accelerated at 580 cycles as the pile underwent cyclic failure. Stiffness had degraded by 85% by the time cycling halted after 600 cycles. ICP05-TW1's behaviour resembled that in ICP04-TW1 up to 300 cycles when test was stopped, while ICP05-TW2 became less stiff from 50 cycles. Stiffness degradation had reached 70% when the test was stopped after 1000 cycles. The marginal meta-stable tests ICP04-OW2 and ICP05-OW1 (which did not fail) retained their full onset stiffnesses until the end of cycling.

The unstable cyclic loading tests stiffness trends are illustrated on Figure 11-23. Test ICP05-OW2 was cycled to just 74 cycles while ICP06-TW1 and ICP08-TW1 cycled to 12,022 and 20002 cycles under displacement control. All three showed cyclic stiffness degrading in all cases from an early stage. The cyclic stiffness developed during unloading stages (k_u) of the stable and meta-stable tests were similar to those on loading (k_l). Figure 11-24 shows how different patterns could apply for example in the unstable one–way cycling ICP05-OW1 which mobilised the shaft resistance fully. While the loading stiffness degraded with cycling, the unloading stiffness showed constant to marginally stiffer trends (Figure 11-25). This trend resulted from the plastic displacements being accumulated continuously over loading phase of the cyclic loop with decreasing elastic displacements being recovered on the unloading branch.

Overall, the cyclic pile stiffness remains approximately constant at the onset value until cyclic failure is approached. Substantial stiffness degradation ensues once local failure commences. The next section examines the local effective stress behaviour mechanisms that govern the observed global pile responses.

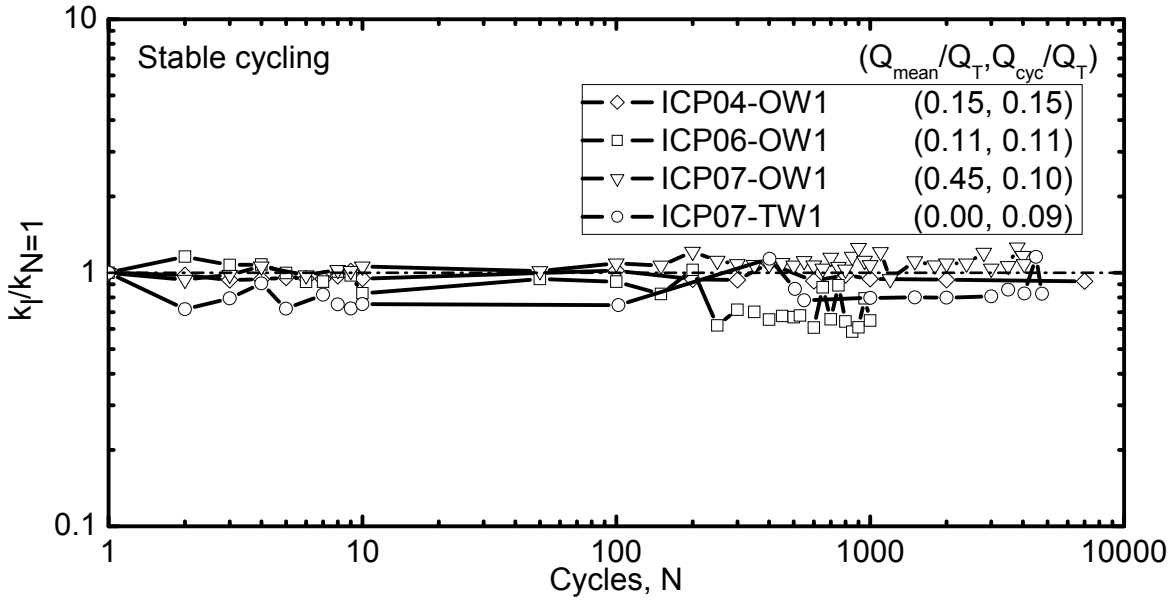


Figure 11-21: Normalised axial cyclic pile stiffness versus number of cycles applied in stable cyclic loading tests.

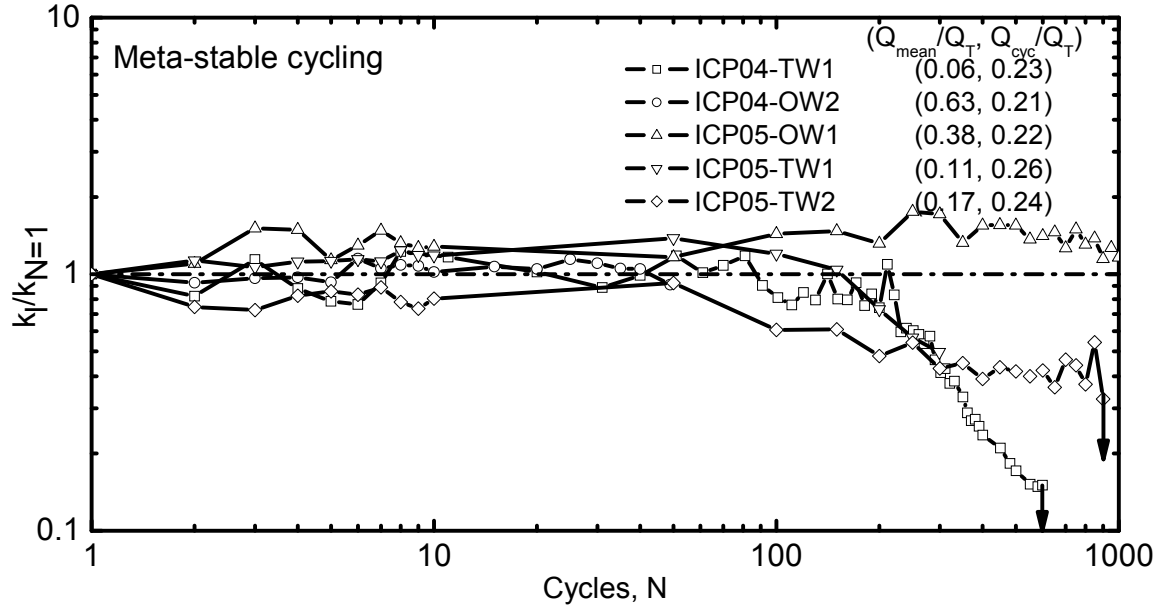


Figure 11-22: Normalised axial cyclic pile stiffness versus number of cycles applied in meta-stable cyclic loading tests.

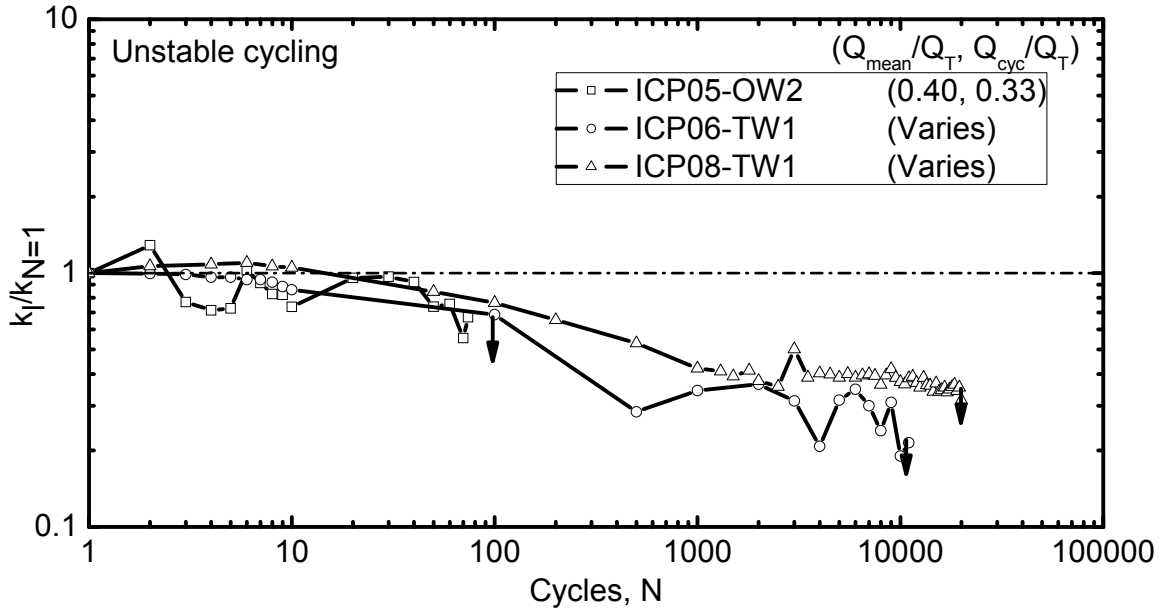


Figure 11-23: Normalised axial cyclic pile stiffness versus number of cycles applied in unstable cyclic loading tests.

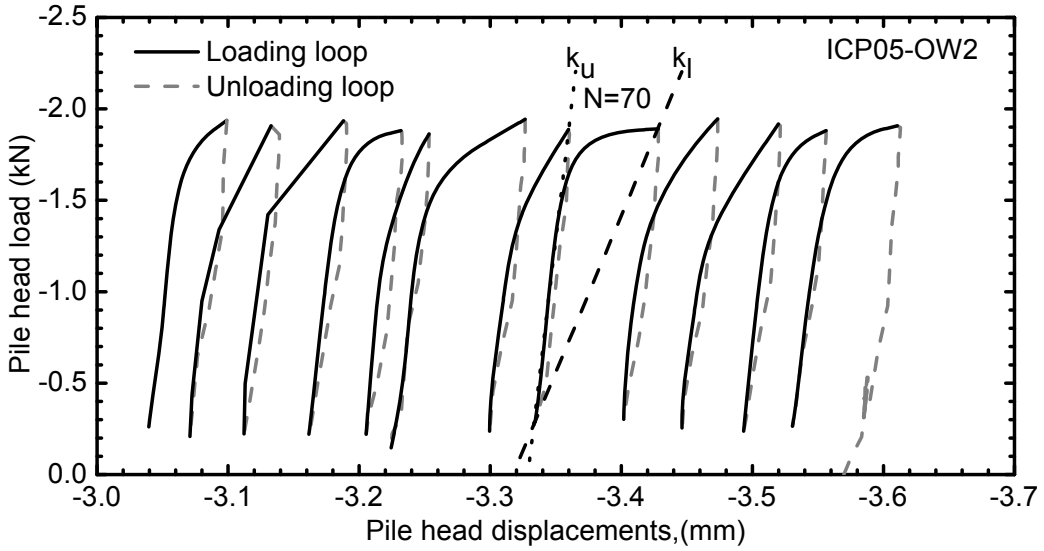


Figure 11-24: Load–displacement behaviour of one-way unstable cycling ICP05-OW2 over the last 11 cycles showing different secant stiffness on the loading and unloading loops of a cycle.

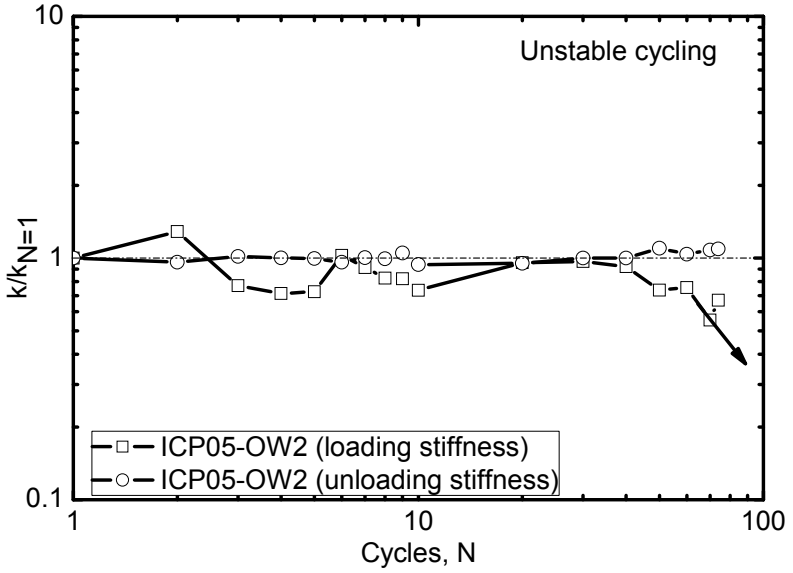


Figure 11-25: Normalised axial loading and unloading cyclic stiffness versus number of cycles applied in ICP05-OW2 unstable cyclic pile loading.

11.6 Local stress mechanisms governing pile axial cyclic loading stability behaviour

As reviewed in Chapter 4 Tsuha et al. (2012) reported interface and sand mass stresses developed on and around the Mini-ICP piles under cyclic loading in medium dense to dense dry NE34 sand. The Author's cyclic loading tests extended from their study with different 1) sand particle scales, 2) density and moisture states, and 3) boundary conditions and pile load cycling over extended durations.

Figures 11-26 and 11-27 presents effective stress paths developed at the pile interface for the cyclic Mini-ICP pile tests ICP05 OW1 and TW1 conducted in finer (and less dense) GA39 sand. Both categorised as meta-stable although both sets of Q_{cyclic}/Q_T, Q_{mean}/Q_T coordinates plotted in the 'stable' region for NE34, as they developed faster rates of accumulated cyclic displacements. Clusters A and C (B was not working) show radial stresses progressively migrating towards the origin, signifying contraction and densification of the interface zone. The OW1 test which applied 1050 cycles, developed closed effective stress path loops in the tensile shear region which engage the interface failure envelope along part of its shaft (at cluster A) and showed final σ'_{rs} values that were clearly lower than at the start. Test TW1 engaged the failure envelope fully along its shaft length over its 300 cycles, developing an asymmetrical 'butterfly wings' effective stress path pattern and relatively high rates of accumulated cyclic displacement growth. Shaft capacity degradations (7% and 22%) were assessed by the respective tension tests T1 to T3. Only marginal further radial effective stress reductions developed in the follow-on tests ICP05-TW2 (MS) and

OW2 (US) as reflected by the relatively steady shaft capacities developed in the subsequent static tension tests T4 and T5.

Tests ICP07-OW1 and TW1, considered in Figures 11-28 and 11-29, applied 4040 and 4760 stable cycles to Mini-ICPs installed in dry NE34 under the 'free field simulator' BC5 boundary conditions. The ICP07-OW1 test local stress paths progressed from an initial pattern σ'_{rs} dilating at first tension loading before developing an essentially closed effective stress loop under the one–way cycling in tension from -4.8 to -7.2kN, with a mild pile shaft top-down shear stress progressive transfer, as observed in field studies (e.g. Chow 1997). However, the effective stress paths remained well away from the $\delta' = 27°$ interface failure envelopes. The overall interface radial stress dilation entailed the stress path gradually migrating away from the failure envelope and progressive stabilisation under cycling. ICP07-TW1 involved two-way pile–head cycling between +1.2kN and -1.2kN with the shaft load alternating between +0.7 and -1.2kN and the base picking up a modest 0.5kN cyclic load. Stable and closed local effective stress path loops were maintained at all three clusters but with a slight overall radial stress migration to the left signifying interface contraction and densification and progressive shaft load re-distrubution from the top downwards with cluster C showing greater contraction and broader stress loops.

The local interface effective stress paths from a 12,022 cycles two-way displacement controlled +0.5 to -0.5mm test ICP06-TW1 in wet NE34 sand with BC3 boundary conditions are shown on Figure 11-30. The continuously changing pile head and base loads developed during this test were described in Figure 11-8 and 11-9. The patterns of local shear stress degradation match the pile head load behaviour. The interface effective stress state starts from a residual tension (negative) shear; first tension loading takes the stress path towards static failure with constant volume shearing after showing the expected radial stress dilation. The unloading stage of this first cycle imposes a full shear stress reversal, which provokes a radial stress contraction before the path crosses to the positive shear stress region. The compression stage of the first cycle leads to phase transformation when the radial effective stress response switches to dilation and the path tends towards constant volume shearing in compression. Unloading from the top of this cycle leads to shear stress reversal and the process repeating, but with a leftward progression towards lower σ'_r values.

The process described above lead to a 'butterfly wings' effective stress path pattern developing for each cycle that continuously shifts leftwards towards the origin, signifying contraction of the stationary radial effective stresses on the pile with progressive cycling. The 'wings' shrink progressively as the pile shaft engages the δ limits and experiences successively reducing shaft shear stresses that are reflected in the observed global load-displacement behaviour as reducing shaft loads. The outcome of the cyclic loading is massive (71%) shaft capacity degradation.

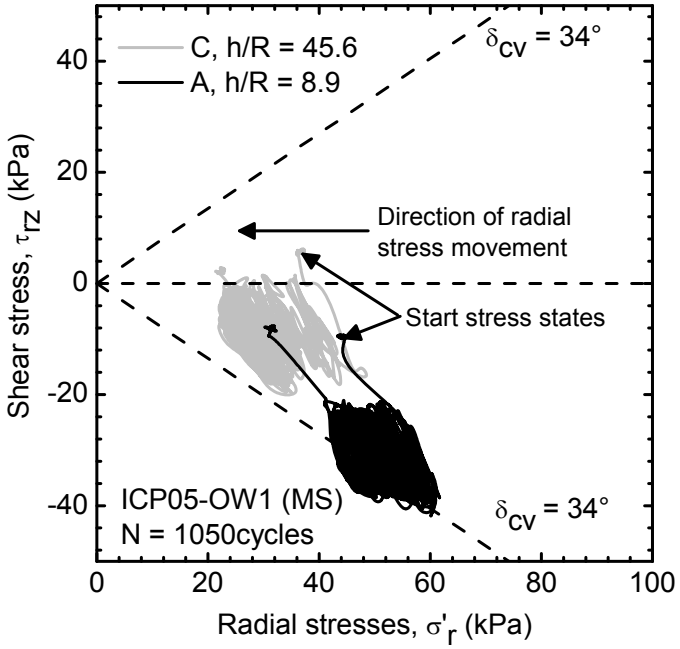


Figure 11-26: Finer GA39 sand ICP05-OW1 one–way meta-stable cyclic loading test interface effective stress paths.

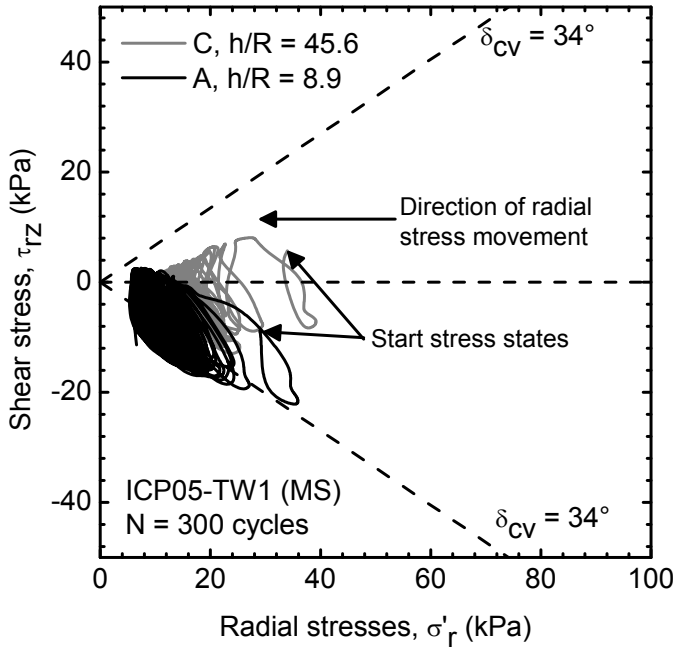


Figure 11-27: Finer GA39 sand ICP05-TW1 two–way meta-stable cyclic loading test interface effective stress paths.

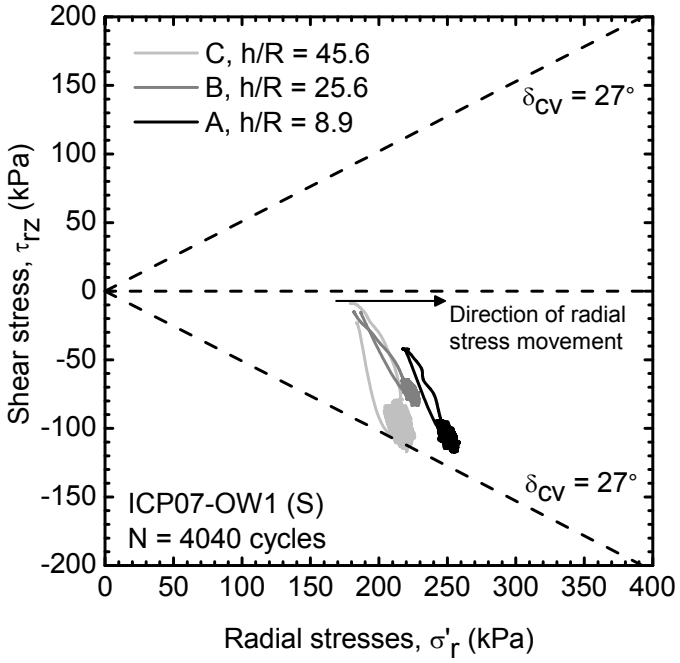


Figure 11-28: BC5 boundary condition ICP07-OW1 one–way stable cyclic loading test interface effective stress paths.

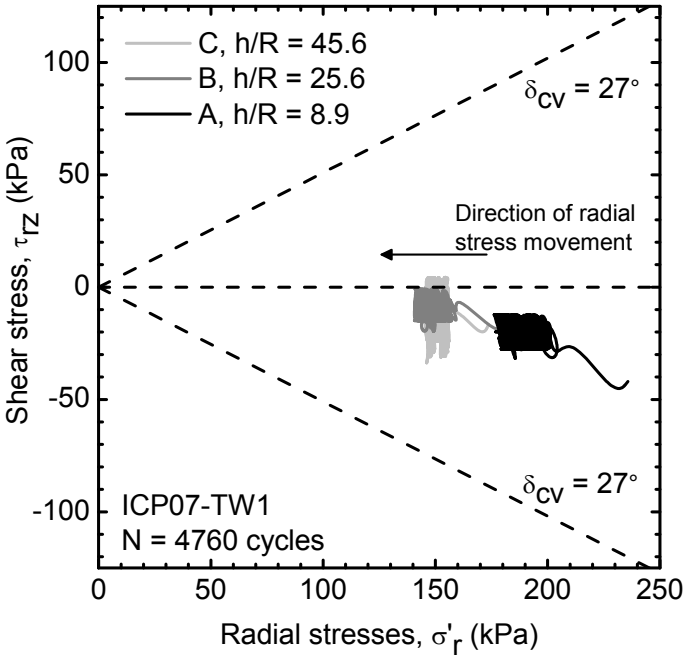


Figure 11-29: BC5 boundary condition ICP07-TW1 two–way stable cyclic loading test interface effective stress paths.

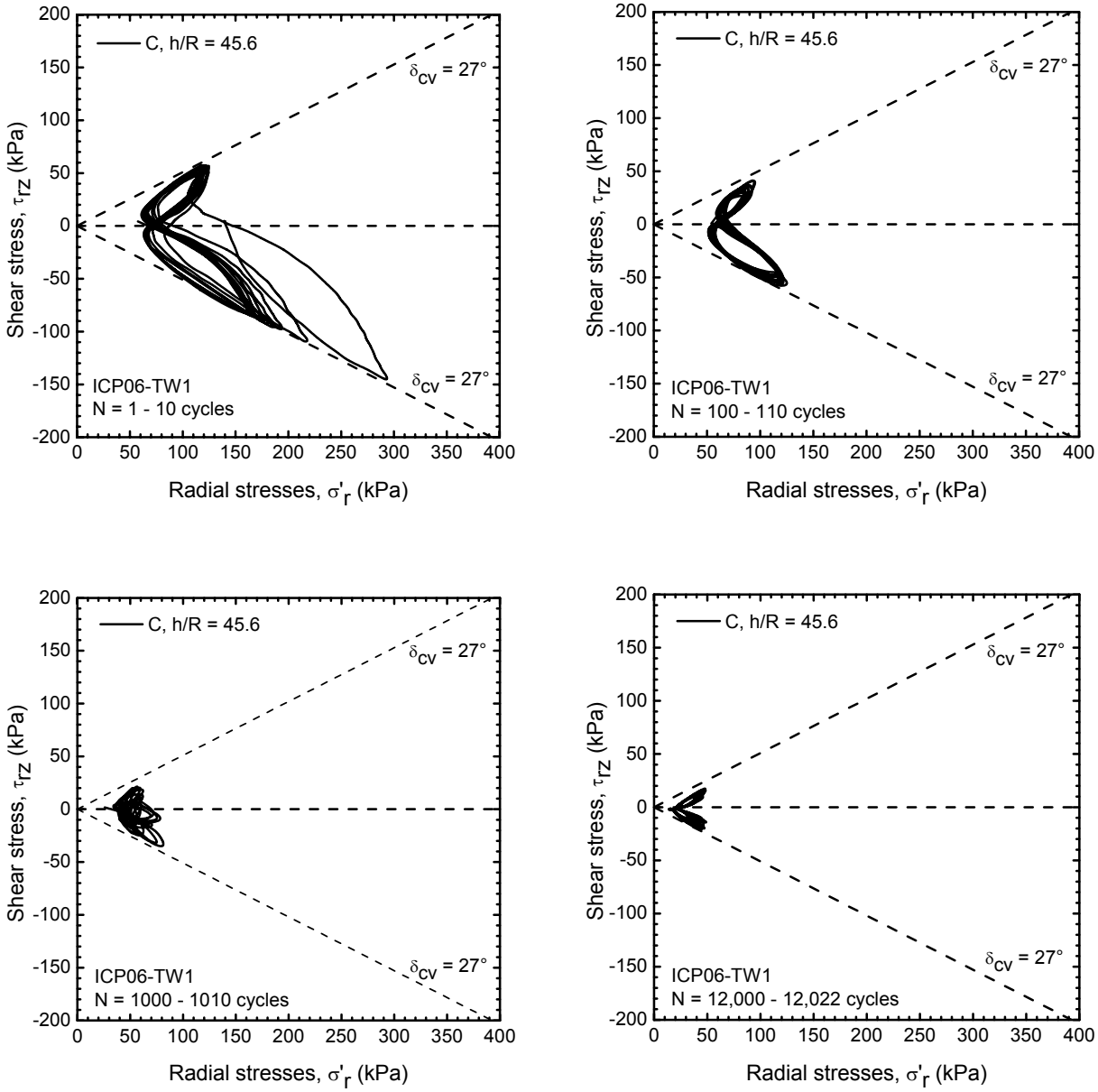


Figure 11-30: Wet NE34 sand ICP06-TW1 displacement controlled cycling loading test interface effective stress paths.

11.7 Influence of boundary conditions on model piles cyclic loading behaviour

The displacement controlled axial cyclic loading test ICP08-TW1 (-0.5 to +0.5mm) which applied 20,002 cycles with the BC5 boundary condition can be compared to ICP06-TW1 (which maintained the initial BC3 boundary condition) and tests by Tali's (2011) with a smaller diameter chamber (524mm) and (BC1) maintained lateral stress boundary condition (reviewed in Chapter 4) to assess the influence of testing boundary conditions on cyclic behaviour.

Recall Tali's (2011) two-way displacement controlled (-0.5 to +0.5mm) axial cyclic test with BC1 boundary condition reported base and shaft stiffnesses increasing between 1 to 10 - 100

cycles then decreasing up to 1000 cycles and increasing again over the 100,000 cycles performed. Tali's final capacity check test indicated a (brittle) overall gain in shaft resistance. As discussed above, both ICP08-TW1 and ICP06-TW1 showed pile base stiffness changes that were comparable to those reported by Tali (2011), with increases up to 100 cycles, followed by decrease to 1000 cycles then increases over the rest of the test. However, both the Mini-ICP tests showed shaft stiffness decaying with cycling continuously up to the end of the 20,002 cycles imposed with considerable resistance degradation proven by the monotonic tension tests performed after cycling. The local interface stress paths seen with ICP08-TW1 on Figure 11-31 show broadly similar behaviour to those for ICP06-TW1.

The boundary radial stresses were measured during ICP08-TW1, Figure 11-32, showing consistent effective stress decreases during cycling, whereas the BC1 constant stress control lateral boundary deployed by Tali (2011) would have offered stress recharge relatively close to the pile shaft (at $d_{chamber}/D = 14.5$) during cyclic degradation, resulting in a phenomenon that may not necessarily be expected to occur at full scale. The field condition is probably best represented by tests with larger $d_{chamber}/D$ ratios where the stress changes developed at the boundary are negligibly small and elastic strain energy stored in the surrounding ground provides a degree of partial re-imposition of radial stresses out at $d_{chamber}/D$ ratio of 33.

The Mini-ICP sand chambers were instrumented with miniature stress sensors whose measurements during the cyclic tests are summarised in Figures 11-33 to 11-35 leading the following key observations.

1) All radial, vertical and hoop sensors positioned within $2 < r/R < 8$ from the pile showed stress reductions under sustained cycling.
2) Proportionately higher stress degradation was observed in the early stages of cycling, which became less intensive with further cycling as 100s or 1000 cycles were applied.
3) Sand mass stress degradation was slightly more marked when testing with the BC3 than BC5 boundary condition emphasising on the importance of the boundary influence on the cyclic loading stress regime.

Silva (2014) will report axial cyclic loading test with the Mini-ICP in NE34 sand 3S-R CC with BC1 boundary conditions (see Section 5.2.2.2). Pile shaft and base stiffness trends similar to Tali (2011) were observed however large shaft resistance degradation was assessed at the end of test. This further concludes on the effects of the type of CC boundary conditions on the pile load–displacement behaviour.

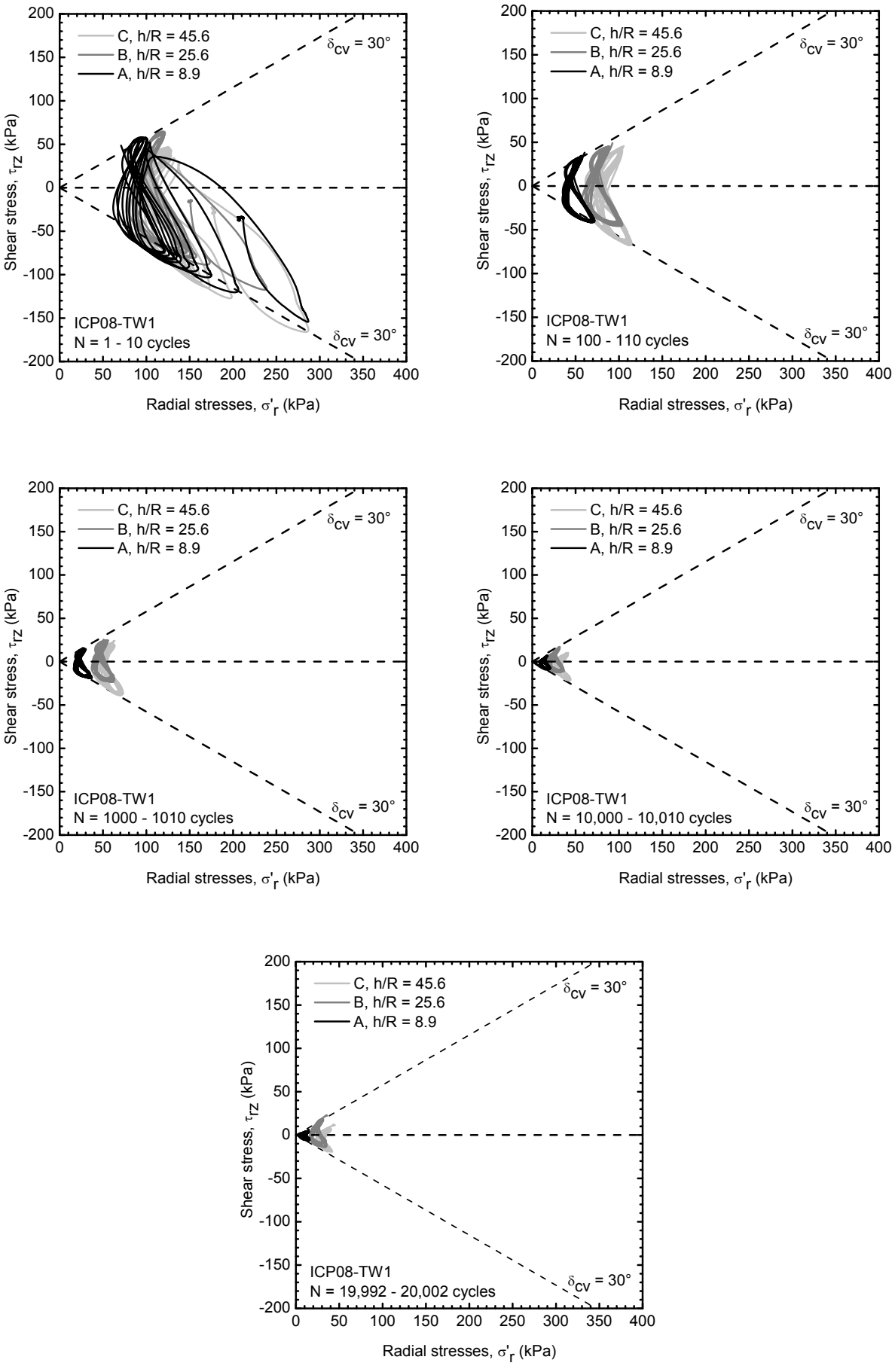


Figure 11-31: BC5 boundary condition ICP08-TW1 displacement controlled local interface stress paths.

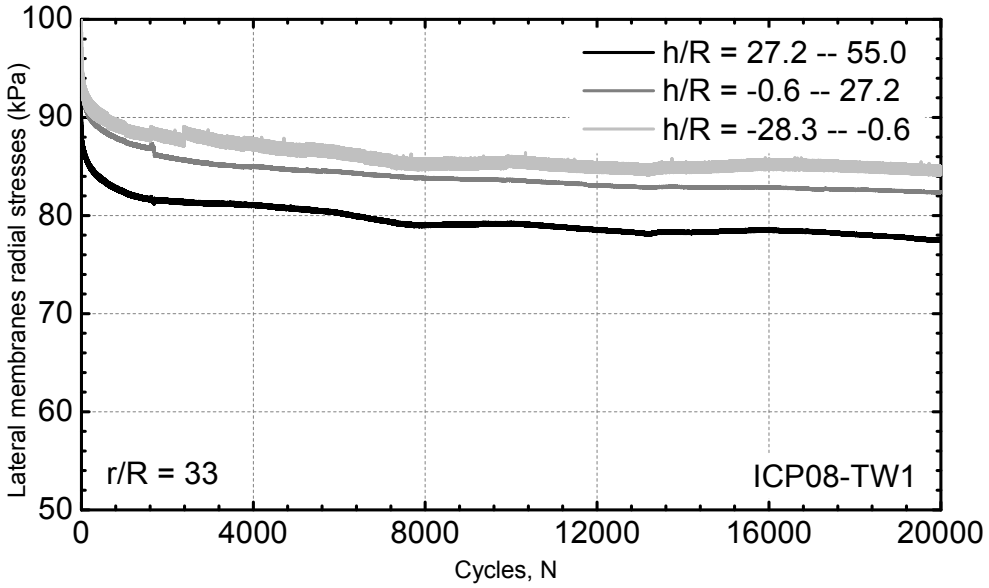


Figure 11-32: Radial stresses at the calibration chamber boundary during axial cyclic loading test ICP08-TW1 with BC5 boundary condition.

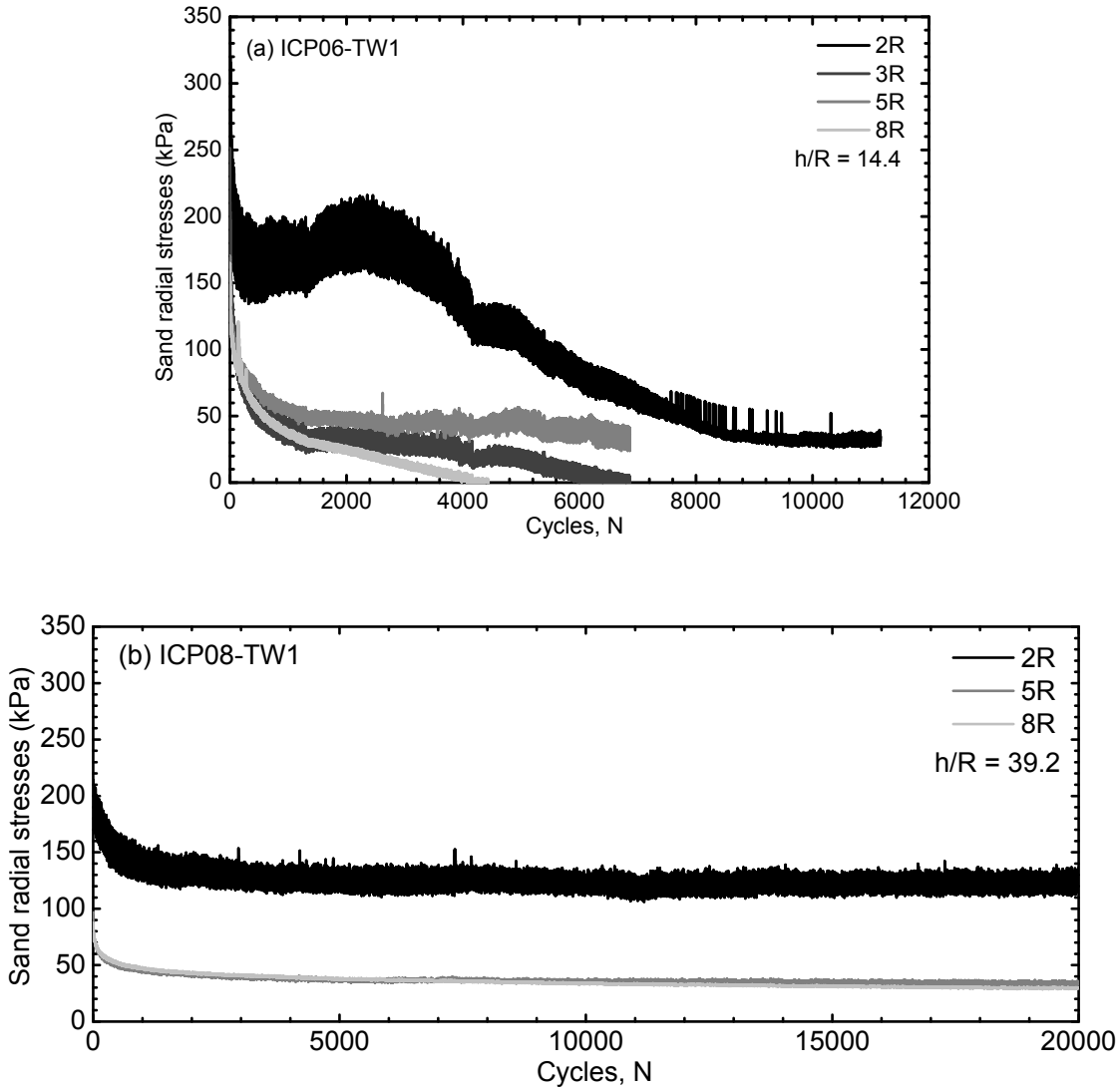


Figure 11-33: Sand mass radial stress against the number of cycles applied in displacement controlled tests (a) ICP06-TW1 with wet NE34 and BC3 boundary condition, and (b) ICP08-TW1 with dry NE34 and BC5 boundary condition.

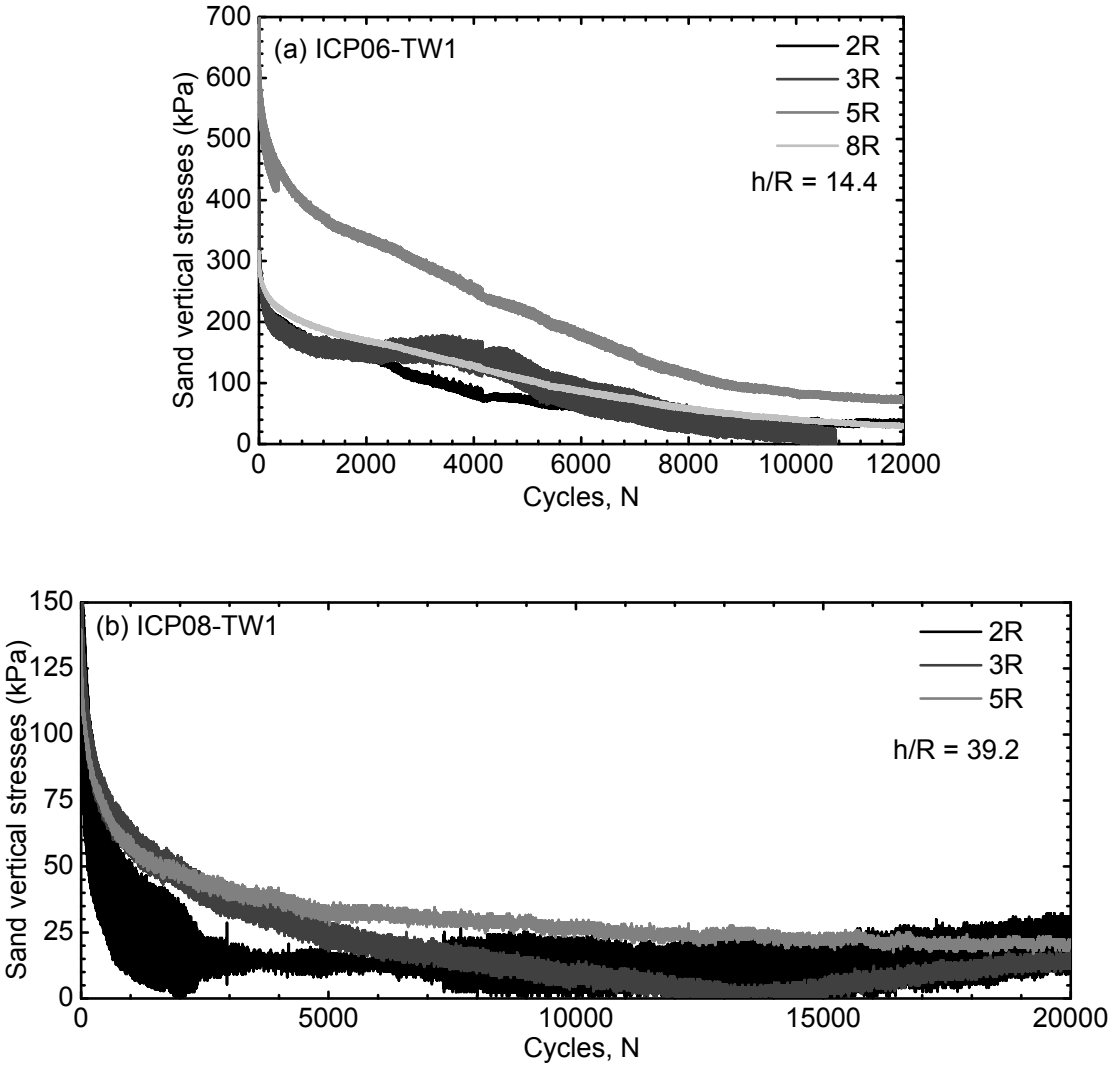


Figure 11-34: Sand mass vertical stress against the number of cycles applied in displacement controlled tests (a) ICP06-TW1 with wet NE34 and BC3 boundary condition, and (b) ICP08-TW1 with dry NE34 and BC5 boundary condition.

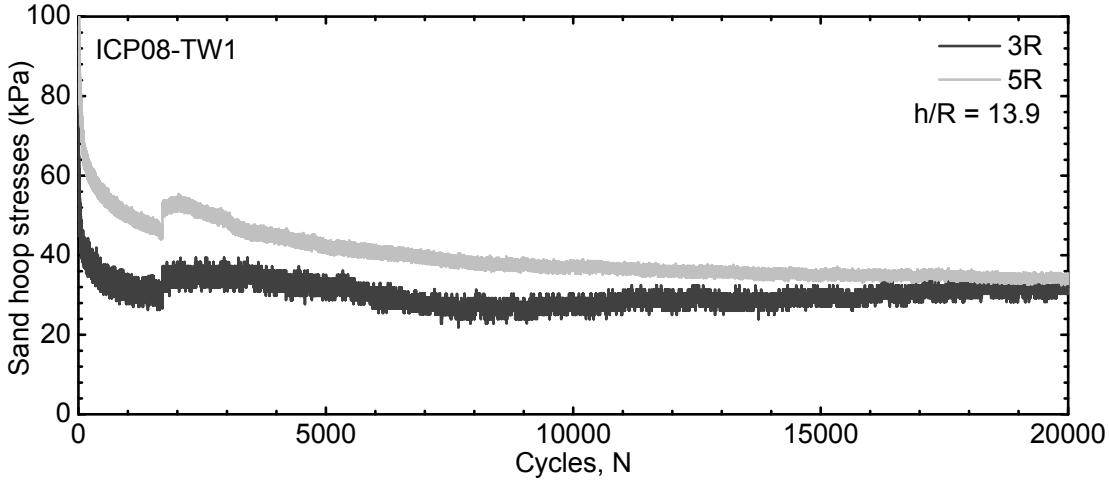


Figure 11-35: Sand hoop stresses against the number of cycles applied in displacement controlled test ICP08-TW1 with BC5 boundary condition.

11.8 Proposed implications to design practice

The Author's Mini-ICP axial cyclic loading tests (and later re-interpretation of the Dunkirk field experiments) form a valuable dataset that can be used in the derivation and validation of pile cycling numerical models.

Jardine et al. (2012) presented a step–by–step flow chart setting out alternative approaches for the cyclic design of axially loaded driven piles, which is reproduced in Figure 11-36. As a first step the designer has to decide on the need or otherwise of addressing cyclic loading in a specific design. Interaction diagrams provide vital tools for this screening stage, as described in section 4.2. The input parameters at this point include the geotechnical data required to establish the ultimate limit state loads and the cyclic loading under extreme design environmental conditions. If the critical loading conditions expected for the worst few cycles plot near to or above the meta-stable to stable zones boundary contour ($N_f = 100$) cyclic damage can be expected to occur. In these cases a cyclic loading design assessment should be considered. The choice of the most suitable design cyclic loading interaction diagram has to be based on the specific soil conditions. It was clear from comparing NE34 to the finer GA39 silica sands that the failure contours may be sensitive to grain size or density changes.

When it is assessed that cyclic design is needed, the present state of the art requires cyclic loads to be idealised into uniform cyclic batches. Even though typical environmental loads are made-up of irregular amplitudes and non-uniform frequencies, the field or laboratory derived cyclic testing models are based on tests made with regular amplitude and frequency.

The interaction diagram can be used directly and graphically to assess the potential damage ($\Delta Q_T/Q_T$) of each of these cyclic batches to the static capacity of the pile. Jardine & Standing (2012) showed how the Jardine et al. (2005b) 'ABC'–approach can be applied in direct calculations to predict potential reduction of local shaft capacity radial effective stress ($\Delta\sigma'_r/\sigma'_{r0}$) as a function of number of cycles N and normalised cyclic shear stress amplitude (τ_{cyc}/τ_T). They proposed a simple linear interaction diagram local stress function $\Delta\sigma'_r/\sigma'_{r0} = A\ (B + \tau_{cyclic}/\tau_T)\ N^C$, and matched it to the shaft capacity changes observed in the Dunkirk full scale tests. A global form with $\Delta Q_T/Q_T = A\ (B + Q_{cyclic}/Q_T)\ N^C$ can also be applied to the entire pile. Jardine and Standing (2012) reported that this expression calibrated well with their linear Dunkirk interaction diagram (with A = -0.126, B = -0.1 and C = 0.45). These two approaches provide a useful starting point. The Author's results may be applied to develop simple but more elaborate non-linear $\Delta Q_T/Q_T = f(Q_{cyc}/Q_T, N_f)$ relationships that can account for the cyclic failure contour shapes seen in the NE34 sand cyclic interaction diagram and derived to capture the local interface radial stress contraction mechanisms and the top-down progressive cyclic failure observed in the laboratory and field instrumented pile cyclic testing.

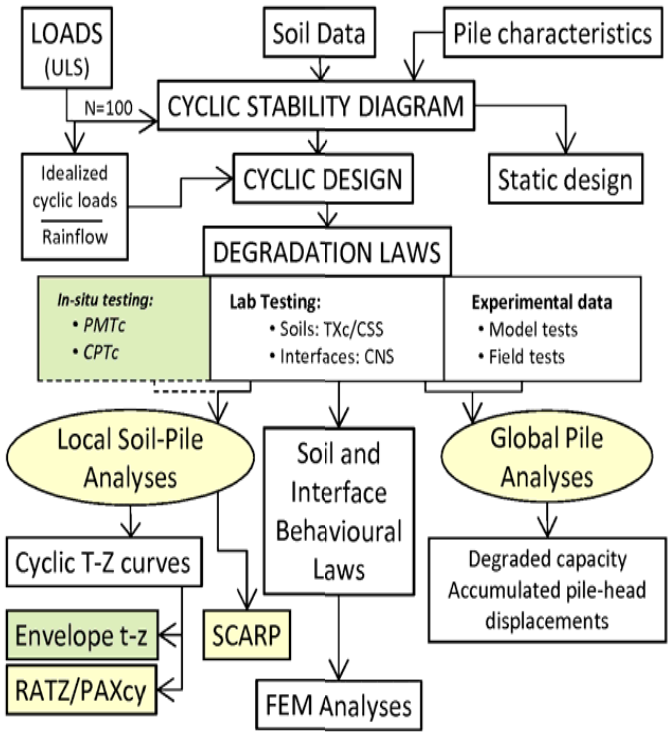


Figure 11-36: Flow chart for cyclic design for axially and loaded piles, Jardine et al. (2012).

The cyclic testing dataset can hence provide updated parameters and expressions for the left-hand 'Local' and right-hand 'Global' pile cyclic loading assessment routes given in Figure 11-36 above. They also provide key information for advancing the central fully analytical route in which cyclic interface and soil mass constitutive models are derived, that can be fitted to cyclic testing performed for site-specific cases and incorporated into advanced finite element method (FEM) analyses.

11.9 Summary remarks and conclusions

The literature review presented in Chapter 4 showed that axial cyclic loading can strongly impact the behaviour of piles driven in sand, leading to important effects that are neglected in routine design. The highly instrumented laboratory model pile experiments described in the present chapter have offered new insights into the processes leading to the observed outcomes by examining the local effective stress responses under different testing conditions and relating them to the behaviour of sand. The main conclusions from this experimental study include:

1) A simple scheme has been established applying the accumulated cyclic displacements, number of cycles applied, and their derivatives, to categorise the axial cyclic response of displacement piles in silica sands in three behaviour styles; Stable, Unstable or Meta–stable.

2) *Stable* cyclic response accumulates low and stabilising cyclic displacements that show slow rates of change to more than 1000 cycles without causing any loss in static shaft capacity and fully maintaining serviceability.
3) The *stable* interface local behaviour may be inelastic, but does not develop large scale radial contraction. Minor top-down shaft degradation that takes place is balanced by capacity growth through local densification and fabric rearrangement.
4) *Unstable* cyclic response accumulates cyclic failure displacements (categorised as greater than 10% of the pile diameter) at accelerating rates with potentially very significant shaft capacity degradation within 100 cycles leading to an unserviceable response.
5) The *unstable* loading conditions invoke marked inelastic behaviour at the pile–sand interface where local slip develops due to shear zone compaction and marked radial stress reductions governed by the Coulomb law. Hysteretic 'butterfly-wing' effective stress paths develop at the pile shaft and local failure progresses from the pile top downwards.
6) *Meta–stable* cyclic response marks a transition between the stable and unstable behaviour at which a pile can sustain some 100s of cycles without losing foundation serviceability, but at the same time losing some capacity and not achieving fully stable condition. This criterion refers to partial degradation of the operational shaft capacity affecting the foundation serviceability but not resulting in ultimate failure.
7) *Meta-stable* response may develop local interface slip, hysteretic effective stress paths and stress state migration, depending on the cyclic loading levels imposed.
8) The accumulated cyclic displacements stability criteria can be scaled with pile size (diameter) as confirmed by the matching behaviour between the laboratory 36mm dia. model piles and those applying to 457mm dia. full scale piles (see Rimoy et al. 2013). The invoked stability behaviours can be summarised in cyclic interaction diagrams that relate the normalised cyclic load amplitudes and mean load levels to the number of cycles required to reach failure.
9) The Tsuha et al. (2012) NE34 sand cyclic loading interaction diagram has been confirmed as equally applying to dry and wet NE34 medium dense sand masses. It is also representative for the BC3 and 'free field simulator' BC5 boundary condition, and compares well with Jardine & Standing's (2012) full scale pile cyclic loading interaction diagram.
10) In the stable cyclic region where no failure is invoked, cyclic loading at low Q_{mean}/Q_T ratios leads to gains in the static shaft capacity reaching a maximum under cycling to about $Q_{cyclic}/Q_T \approx 0.17$. Cyclic loading condition within this region, recovery of shaft capacity is observed even after considerable pile shaft degradation has been sustained from a prior unstable higher cyclic amplitude loading condition.

11) Radial, vertical and circumferential sensors positioned in the sand mass within $2 < r/R < 8$ from the pile showed stress reductions under sustained cycling. As with interface shear proportionately higher stress degradation was observed in the early stages of cycling, which became less intensive with further cycling as 100s or 1000 cycles were applied.
12) The importance of boundary conditions on the cyclic loading effective stress regime was revealed by more pronounced sand mass stress degradation observed with the BC3 boundary condition compared to the 'free field simulator' BC5 arrangement. The field condition is probably best represented by tests with larger $d_{chamber}/D$ ratios where the stress changes developed at the boundary are negligibly small and elastic strain energy stored in the surrounding ground can provide a degree of partial re-imposition of radial stresses out $d_{chamber}/D$ greater than the 33 ratio adopted in the Mini-ICP tests.
13) The cyclic pile tests conducted in finer and looser GA39 sand, when interpreted with respect to the same cyclic criteria, showed a greater susceptibility to cycling and developed faster rates of displacement accumulation than tests under similar conditions in NE34 sand. The greatest impact was the greatly reduced level of cycling below which behaviour the behaviour was fully stable.
14) Two-way displacement controlled tests, where cyclic displacements ±0.5mm were imposed but no permanent shifts were allowed to accumulate, showed symmetrical degradation of the shaft capacity. Base loads also decreased initially but rose again after sustained cycling as the pile transferred head loads more directly to the base.
15) The hysteretic 'butterfly wings' interface effective stress paths from these two-way displacement controlled tests showed very clear and continuous radial stress contraction (associated with the shear band densification) and stress state migration as it is characteristic of unstable behaviour, to > 20,000 cycles applied. Considerable shaft capacity degradation was assessed at the end of cyclic.
16) Cyclic pile stiffness varied with the applied cyclic loading amplitude and remained approximately constant at the onset value until cyclic failure was approached. Substantial stiffness degradation ensues once local failure commenced.
17) Permanent cyclic displacements accumulate rapidly over just a few cycles in the unstable zone while extended cycling in the stable zone led to minimal accumulated displacements. Meta–stable cycling shows an intermediate behaviour.
18) The developed interaction diagrams provide a straight-forward screening tool for addressing axial cyclic loading. Further, the Mini-ICP axial cyclic loading tests form a valuable dataset that can be used in the derivation and validation of pile cycling numerical models towards fully analytical design of displacement piles under axial cyclic loading.

Chapter 12

12 Re-analysis of axial cyclic loading response of full scale piles driven at Dunkirk

12.1 Introduction

The axial cyclic loading behaviour of displacement piles in sands was reviewed in Chapter 4 and its importance in offshore oil, gas, and wind turbine piled foundations emphasized. The paucity of full scale cyclic loading tests was highlighted and observations from earlier full scale and laboratory model scale tests detailed. The extensive programme of highly instrumented cyclic loading tests on model piles was analysed in detail in Chapter 11.

This Chapter returns to add to the interpretation of the cyclic tests on full scale piles conducted in marine silica sands by Jardine & Standing (2000, 2012) at Dunkirk, France. The digital files containing raw data from multiple cyclic loading tests and interspersed reference static tension capacity tests of this comprehensive full scale axial cyclic loading testing programme have been re-examined. The specific objective was to add to earlier work by investigating for the first time the stiffness responses and cyclic displacements associated with each mode of cycling, referring to the site specific normalised cyclic interaction stability diagram. The patterns of full scale behaviour are related to those deduced from the Author's model scale tests. The work described will also be reported by Rimoy et al. (2013).

12.2 Scope of study

Jardine and Standing (2012) and Jardine et al. (2006) reported the test piles' layout and tension testing arrangements shown in Figures 12-1 and 12-2. Eight full-scale 457mm outer diameter, mainly 13.5mm wall thickness open-ended steel pipe-piles were driven at Dunkirk as part of the GOPAL project (Parker et al. 1999). Six were driven with embedded lengths around 19m (piles R1 to R6), one plain pile (C1) was driven to 10m as was a second (JP1) that was subsequently modified by forming a jet-grouted base section. The tests took place close to the earlier 'CLAROM' driven pile test programme (Brucy et al. 1991) where Chow (1997) had also undertaken static re-tests on the same pile and a suite of new ICP tests.

The site offers a relatively deep profile of dense Flandrian silica marine sands whose ground and CPT profiles are shown in Figure 2-10 and advanced laboratory characterisations are presented in Chapter 6. Piles R1 to R6 had been installed to provide reaction for the GOPAL project test piles C1 and JP1. The reaction loads had applied either one or two significant load – unload tension load cycles prior to the cyclic loading study, with reported maxima < 60% of the piles' ICP-05 method tension capacities (Jardine & Standing 2000). The piles' cyclic capacity trends have been reported

by Jardine and Standing (2000, 2012), while Jardine et al. (2006) reported the piles' remarkable static tension capacity set–up trends.

Chow (1997) reported static and cyclic tests at the same site with the ICP pile that carried pore pressure sensors. The pore pressures showed a fully drained response. While this is also expected at field scale with large piles in clean sands, partially drained behaviour might apply in lower permeability deposits. This can be checked by inspecting piezocone data and applying consolidation analyses.

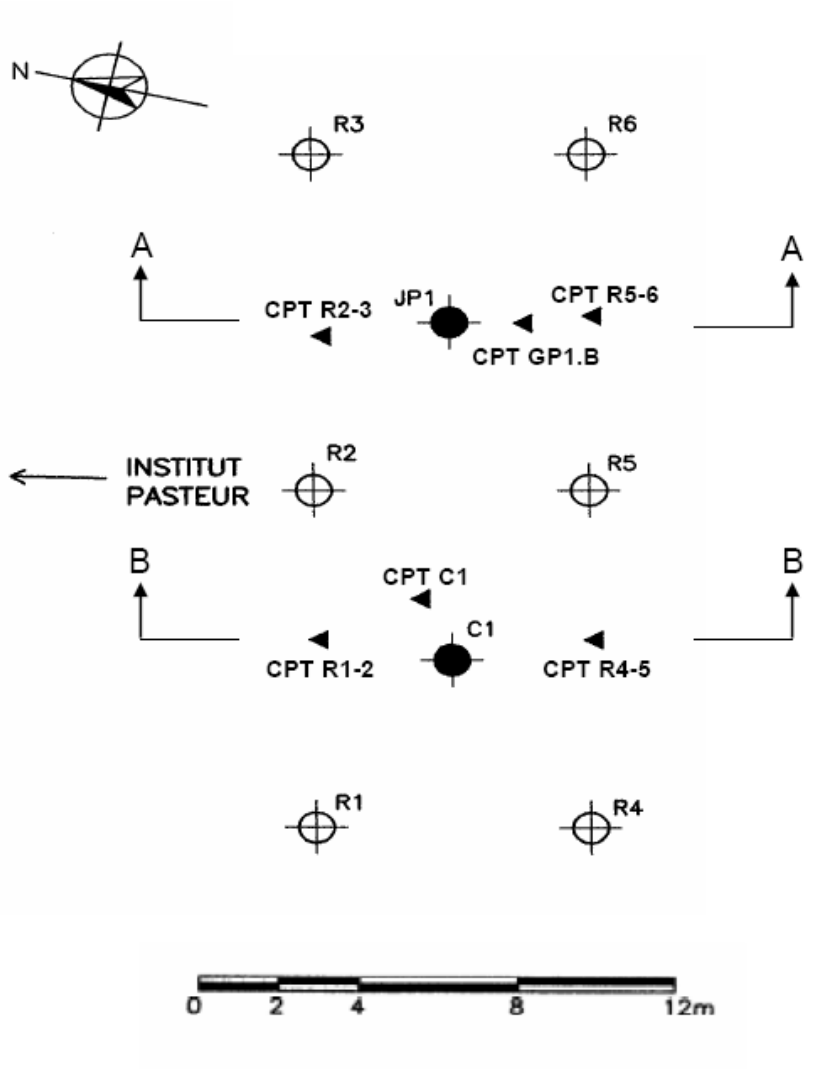


Figure 12-1: Plan showing layout of test and reaction piles and CPTs from GOPAL Project in Dunkirk, France (after Jardine & Standing 2012).

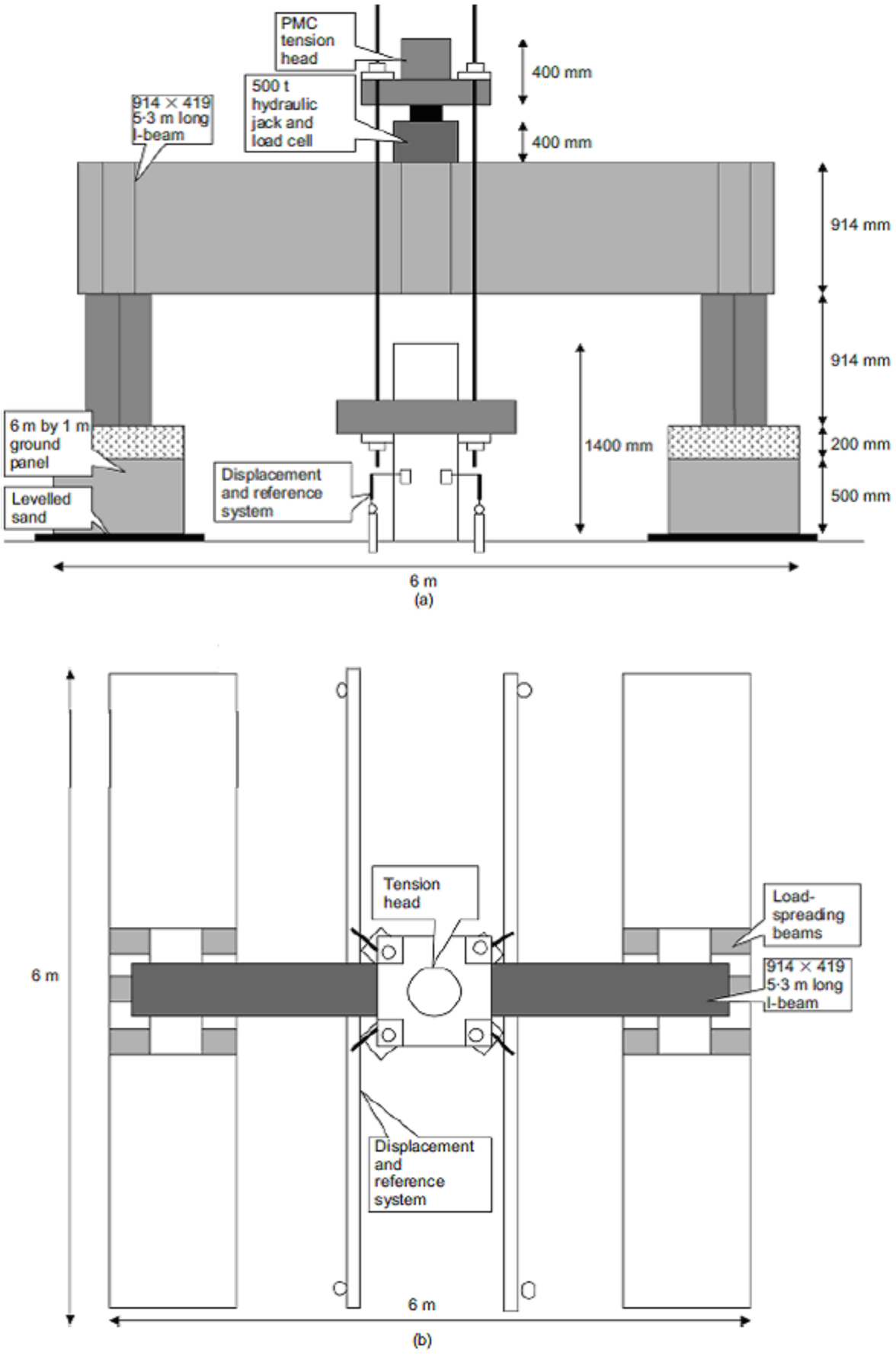


Figure 12-2: Details of test rig (not to scale) (a) Elevation (b) Plan (after Jardine et al. 2006).

12.3 Scaling of tests

Any practical application of model pile experiments should consider how they may scale to the problem in hand. The key points to consider are the pile slenderness ratio L/D and the effective axial stiffness of the piles compared to the shear stiffness of the soil mass. The pile stiffness depends on the steel modulus, the pile wall thickness (t) and outside diameter. Pile C1 had an L/D ≈ 22, while R1 to R6 had L/D ≈ 42. The latter L/D value is typical of many offshore jacket piles, but lower values are typical for monopiles and possibly for multi-piled wind turbine structures. All the test piles had D/t_w ratios of 33.8 over most of their embedded lengths, which may be typical of jacket structures, but are low for wind-turbine installations; Jardine (2008), Merritt et al. (2012). The Dunkirk conditions may be typical for southern North Sea sites, but greater sand stiffness and shaft resistances can be expected at denser sand sites where q_c values exceed 50MPa.

In cases where the pile make-up and soil stiffness characteristics are clearly different, the global cyclic stability diagrams can be reformulated to consider local cyclic degradation processes as summarised for example by Puech et al. (2012) and applied to the Dunkirk case by Atkins (2000) using an approach such as that outlined in the ICP-05 method (Jardine et al. 2005a) and detailed in Jardine & Standing (2012).

12.4 Test programme

The cyclic testing programme performed is detailed in Table 12-1. Piles R2 to R6 and C1 were axial static and cyclic loaded; only static tests were performed on R1. Pile head loads were controlled by an automated hydraulic system and beam arrangement, Jardine et al. (2006). The loads applied were measured through a high quality load cell while displacements were monitored by four LVDTs fixed to reference beams supported by steel poles driven at least 3m away from the reaction system, Figure 12-2. The axial cyclic loading was controlled by a regulator that imposed near sinusoidal waves with maxima and minima that could be controlled to within ±5kN over long-duration tests. The cyclic rates ranged between 1 to 2 minutes per cycle (~0.008 – 0.017Hz) depending on the pile response.

The test code sequence given in Table 12-1 refers to the testing phase (of which there were three), the pile identifier (e.g. R2) then the test type (CY = Cyclic, T = static Tension) and number of tests for the respective pile. No cycling was conducted in Phase 1, and the cyclic programme was organised into two campaigns 2: October – November 1998 and 3: April 1999. The load-controlled tests involving only tensile pile head loads are termed ‘one–way’ while tests where cycles ranged from tension to compression are referred to as ‘two–way’; tension loads and upward displacement responses are taken as positive throughout. Definitions relating to cyclic loading are shown in Figure 11-2. Reference static tension tests to failure (T) were conducted after most of the cyclic

tests. These were performed to assess the effects on the applied axial cyclic loading on the operational static tension (shaft) capacity. The static tests similarly serve to isolate any effects of previous (static or cyclic) loading phases from the current axial cyclic behaviour. Table 12-2 summarises the static load test capacities.

Test mode	Test code	Q_{cyclic} (kN)	Q_{mean} (kN)	Q_T (kN)	N_f
One–way	US 3.R2.CY2	1000	1000	2500	9
	MS 2.R3.CY2	700	700	2315	200+
	US 2.R3.CY3	950	950	2050	13
	MS 2.R4.CY2	1000	1000	2960	221+
	US 2.R4.CY4	750	1250	2000	3
	S 3.R4.CY6	400	405	2110	1000+
	MS 2.R5.CY2	750	1250	2465	345
	US 2.R5.CY3	700	700	2000	27
	US 2.R6.CY2	750	1250	2000	1
	US 2.R6.CY4	700	700	1585	24
	MS 3.R6.CY6	700	700	1650	206
Two–way	US 2.C1.CY3	620	-40	840	41
	US 2.C1.CY4	445	165	620	1
	US 2.C1.CY5	410	10	620	12

Test code explained:

XX M.YY.ZZN:

XX = Pile response mode (S - Stable, MS – Meta-stable, US – Unstable)

M = Testing campaign phase (out of 3)

YY = Pile name (C1, R1 – R6)

ZZ = Test type (T – Static tension, C - Static compression, CY – Axial cyclic)

N = Test number on the pile in sequence from installation

Table 12-1: Axial cyclic loading testing programme from Jardine & Standing (2000).

Test Code	Tension capacity (kN)	Comment
1.R1.T1	1440	Ductile failure
3.R2.T1	3200	Ductile failure
3.R2.T3	1655	'Stick-slip' failure
2.R3.T1	2000*	No failure on loading to 10.3mm displacement
2.R3.T4	~1655	'Stick-slip' failure in 'quick' test
3.R3.T5	1990	Brittle 'stick-slip' failure
2.R4.T1	2000*	No failure on loading to 8.7mm displacement
2.R4.T3	~2000	Failure in 'quick' test
2.R4.T5	~2000	Brittle 'stick-slip' failure, reducing to ~1450
3.R4.T7	~2490	Brittle 'stick-slip' failure (reducing to ~1900kN) in 'quick' test
2.R5.T1	2000*	With 8.9mm displacement; estimated capacity 2450kN
2.R5.T4	~1300	'Stick-slip' failure in 'quick' test
3.R5.T5	~1795	Brittle failure reducing to 1636kN
2.R6.T1	2400	With 30mm displacement; estimated capacity 2450kN
2.R6.T3	1585	Ductile failure
2.R6.T5	~1325	'Stick-slip' failure in 'quick' test
3.R6.T7	~1425	'Stick-slip' failure
2.C1.C1	-2820	After 34mm, load at 46mm estimated at -2850kN
2.C1.T2	~820	'Stick-slip' tension
2.C1.T6	~500	'Stick-slip' failure at 46mm

*Tests curtailed at maximum initial rig capacity of 2000kN

Table 12-2: Reference static tension capacities from Jardine and Standing (2000).

12.5 Results and interpretation

12.5.1 Cyclic failure criteria

The criteria for classifying axial cycling displacement responses as Stable (S), Meta–stable (MS) or Unstable (US) for the full scale piles are as follows:

Stable response develops low and stabilising accumulated axial cyclic displacements that remain below 0.01D and show slow rates of change (≤ 1mm/1000 cycles) up to N ≥ 1000 without causing any loss of operational static shaft capacity.

Meta–stable response develops accumulated axial cyclic displacements (0.01D < a ≤ 0.1D) at moderate rates (1mm/1000 cycles < rates ≤ 1mm/10 cycles) potentially leading to some degradation of the operational static shaft capacity but not causing failure within 100 cycles.

Unstable response undergoes cyclic failure within 100 cycles involving either accumulated displacements > 0.1D or rates of accumulation of displacements that increase to > 1mm/10cycles with potentially very significant shaft capacity degradation.

The cyclic tests are reported and analysed with reference to the cyclic stability interaction diagram shown in Figure 1-2 from Jardine and Standing (2012). The static tension capacities varied with time and cyclic loading history, Jardine et al. (2006). The reference Q_T values in Figure 1-2 are those applying just before the time of testing. The diagonal line (Q_{mean}/Q_T, Q_{cyclic}/Q_T) (1,0) to (0,1) forms the upper static limit (N = 1). Rate effects in shaft capacity are likely to be small in sands (see section 9.5) and the pile loading cases are mapped into cyclic stability zones, which are assigned to conform broadly to the number of cycles required to induce cyclic failure under the specified conditions. The cyclic loading experienced in service by offshore driven piles may involve millions of low level cycles, while severe storms are likely to impose a relatively small number of severe load cycles. Additionally, as shown by the Author's calibration chamber studies and these Dunkirk field tests, capacity recovery can take place from low level cycling between the severe loading events.

The fourteen load-controlled axial cyclic tests gave a range of outcomes with one stable loading (Set 1), four meta–stable loading (Set 2) and nine unstable loading (Set 3) responses indicated in Figure 1-2. In analysing the cyclic loading data, displacements have been assessed in two ways. The accumulated cyclic displacement shown as 'a' in Figure 11-2 is cumulative, usually increasing with the number of cycles and it is measured with respect to the Q_{max} point of the first cycle (see Figures 11-1 and 11-2). The second measure of displacement 'd_{cyclic}' is the cyclic displacement associated with each cycle, which may increase with cycling – especially under meta–stable and unstable loading conditions. Analyses of how the piles' axial cyclic stiffness responses, accumulated cyclic displacements and the cyclic displacements (defined in Figure 11-1) evolved with number of cycles during cyclic loading are presented.

12.5.2 Pile axial cyclic stiffness

Figure 12-3 plots load-displacement results from slow maintained-load first-time tension tests for seven of the piles driven at Dunkirk (i.e. tests 2.C1.T2, 1.R1.T1, 3.R2.T1, 2.R3.T1, 2.R4.T1, 2.R5.T1 and 2.R6.T1 from Table 12-2). The initial maximum reference secant stiffness k_{Ref} = ΔQ/Δdisplacement is defined by considering the first load step applied (defined as Q_{Ref}) which was 100kN for C1 and 200kN for R1 to R6. The piles' load-displacement behaviour is highly non-linear. On Figure 12-4 the piles' global secant stiffness non-linearity, assessed from the first-time tension loading tests shown in Figure 12-3 is represented by plotting the stiffnesses ratio, k_l/k_{Ref}, against the ratio, Q/Q_{Ref}. The 19m long piles R2 to R6 when tested to tension failure at ages of 74 to 235 days, and after being used as reaction piles for JP1 and C1, show common trends that are stiffer than the 19m long R1, which was tested after 9 days without prior reaction load. R1 also developed a far lower capacity. R1 in turn showed a stiffer and higher capacity response than the (shorter) 10m long C1 tested at 69 days age.

The cyclic stiffness behaviour is considered next. As observed in section 11.5, different cyclic stiffnesses values k_l or k_u (Figure 11-1) may develop on the loading and unloading paths of cyclic loading respectively. The loading cyclic stiffnesses values, k_l, are considered first in relation to the reference stiffnesses, k_{Ref}, as shown in Figure 12-5(a) (stable and meta–stable tests) and Figure 12-6(a) (unstable tests) to examine the evolution of the piles' stiffness under axial cycling. Figure 12-5(b) and Figure 12-6(b) show the same information but with the k_l values normalised by the loading stiffness measured over the first loading cycle of each particular test, $k_{N=1}$. For the meta–stable loading tests, the initial normalised stiffness values (i.e. k_l/k_{Ref} at N = 1) clearly reduce as Q_{cyclic} increases, as expected given the piles' non-linear static response (the greater the proportion of Q_T applied in the cycle, the smaller the initial secant stiffness). The two tests where cycling is applied at $0.3Q_T$ (MS 2.R3.CY2 and MS 2.R5.CY2) follow roughly the same path, except there was some scatter in the early data of the latter test. The initial normalised stiffness for the stable loading test where the cycling is applied at $0.2Q_T$ (S 3.R4.CY6) is in fact slightly lower than the value for the $Q_{cyclic} = 0.3Q_T$ tests. It can be seen that continued cycling leads to only a marginal stiffness decrease (12%) over 1000 cycles in the stable 3.R4.CY6 test. Stiffness values steady or even increase marginally, after 200 cycles. Compared with this stable test, the un-failed meta–stable loading tests 2.R3.CY2 and 2.R4.CY2 showed marginally more pronounced stiffness degradation (about 16%) up to the end of cycling. The failed meta–stable loading tests 2.R5.CY2 and 3.R6.CY6 showed similar trends over most of their cycling durations, until sharp stiffness degradation set in as the piles approached cyclic failure under the conditions given in Table 12-1. Similar trends are seen for the stiffness data normalised by $k_{N=1}$ as shown in Figure 12-5(b).

The loading stiffness (k_l) degradation trends for the unstable tests are shown on Figure 12-6 (a) and (b). By definition, all of these tests underwent cyclic failure and sudden stiffness degradation before reaching 100 cycles. However, those piles that survived for more than five cycles retained their initial stiffness values until within the final failure approach. Slight variations are seen in the sharpness of the onsets to failure under similar cyclic loading levels, perhaps as a result of the complex testing sequences. Stiffness degradation can be seen more clearly in Figure 12-6(b) where the loading stiffness k_l values are normalised by the initial cyclic stiffness $k_{N=1}$.

Seemingly anomalous stiffness behaviour is observed towards failure in the meta-stable and unstable loading tests when stiffnesses are defined from the unloading cycle phases (k_u) as seen on Figure 12-7. While the C1 pile, which was subjected to two-way loading cycles, exhibited the same trends in stiffness degradation for both k_l and k_u, several of the piles subjected to one–way loading showed initial gradual decrease of normalised stiffness ($k_u/k_{N=1}$) before shifting to show apparently increasing k_u values as cyclic failure approached. This reversal in normalised stiffness results from an increased opening-up of the load-unload hysteresis loops as cyclic failure approaches, with

higher plastic displacements accumulating on the loading loop and behaviour becoming more time and cycle number dependent. These features lead to the progressively decreasing secant loading stiffnesses and apparently stiffer behaviour on unloading as cyclic loading approaches failure. Similar behaviour was observed with the model piles unstable tests unloading stiffnesses in section 11.5.

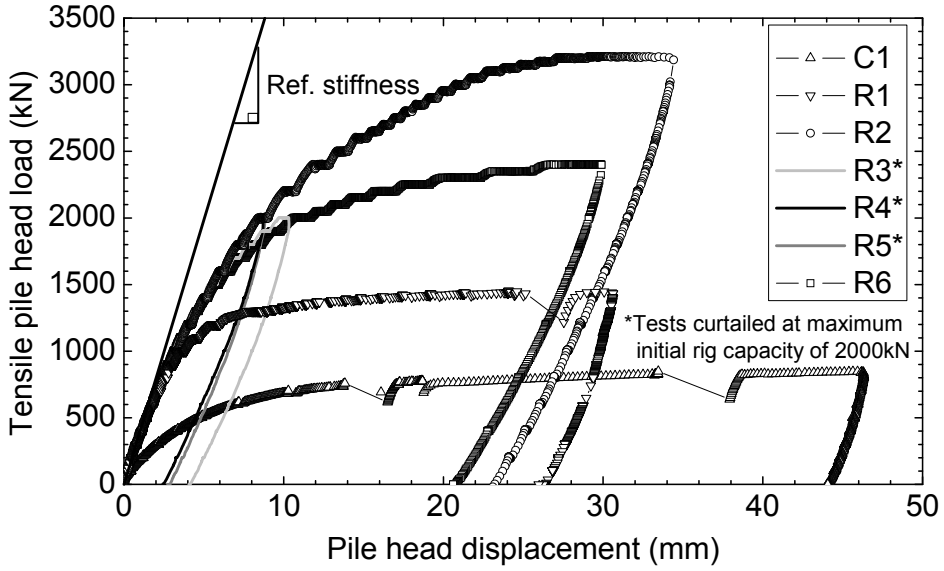


Figure 12-3: Load–displacement curves for first–time monotonic tension load tests.

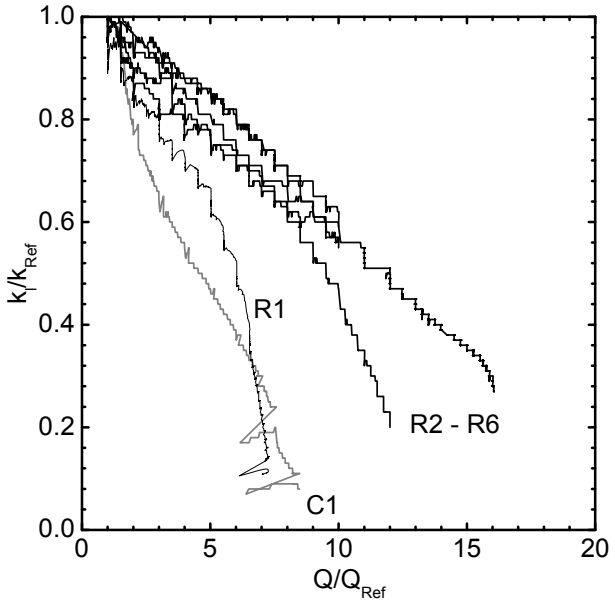
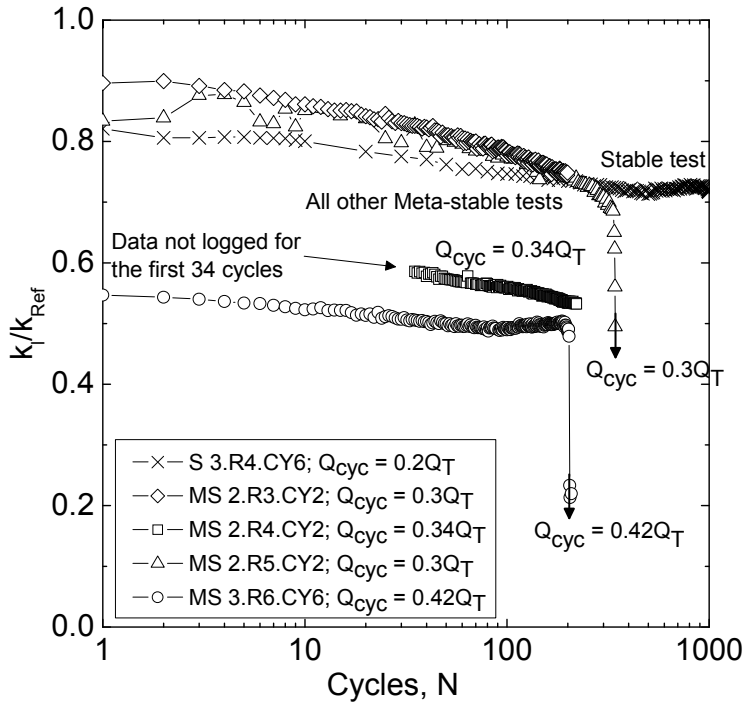
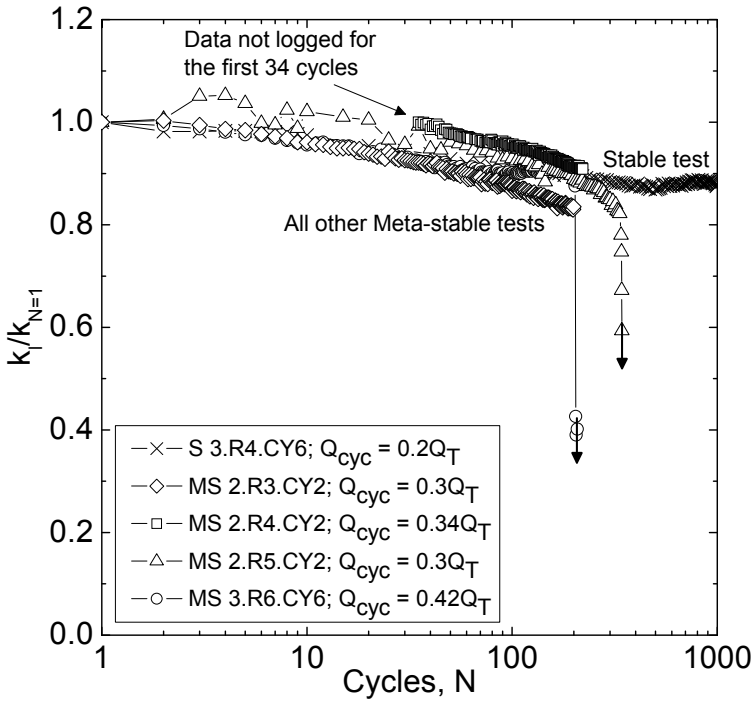


Figure 12-4: Stiffness degradation of piles assessed from the first–time axial static monotonic tension loadings normalised by the reference stiffnesses plotted against load normalised by Q_{Ref}.

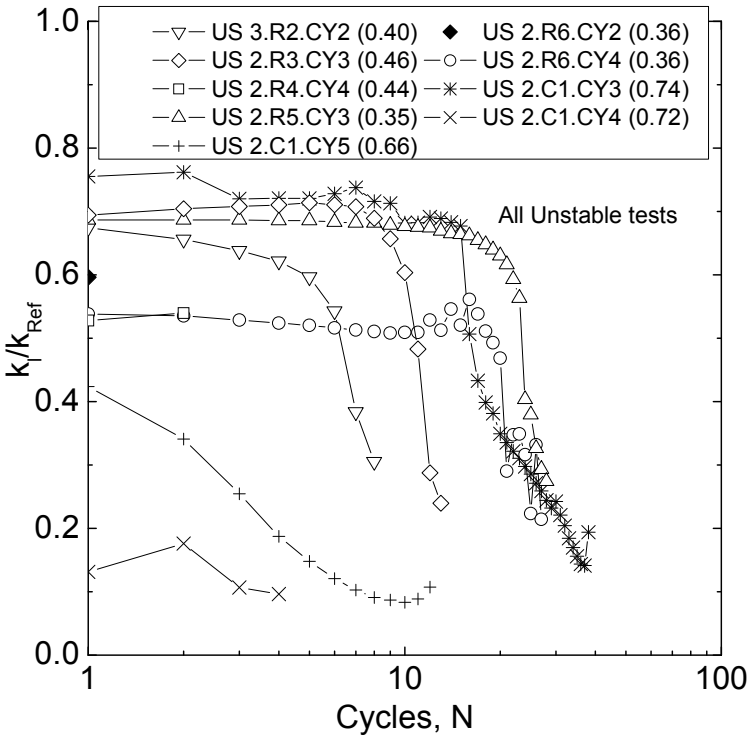


(a)

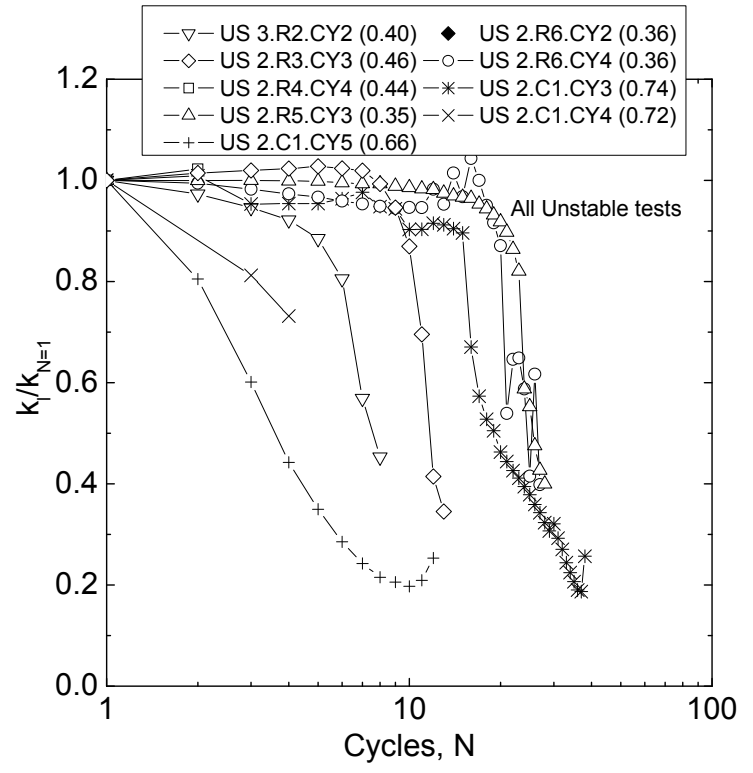


(b)

Figure 12-5: Axial cyclic loading stiffness (k_l) responses normalised in terms of (a) k_{Ref} and (b) $k_{N=1}$ and plotted against number of cycles for the stable and meta–stable loading tests.

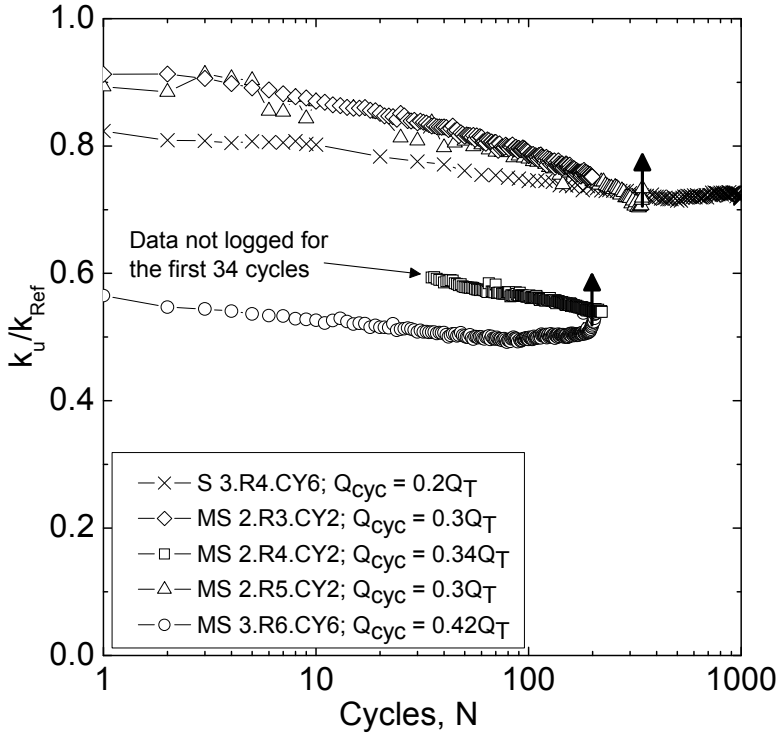


(a)

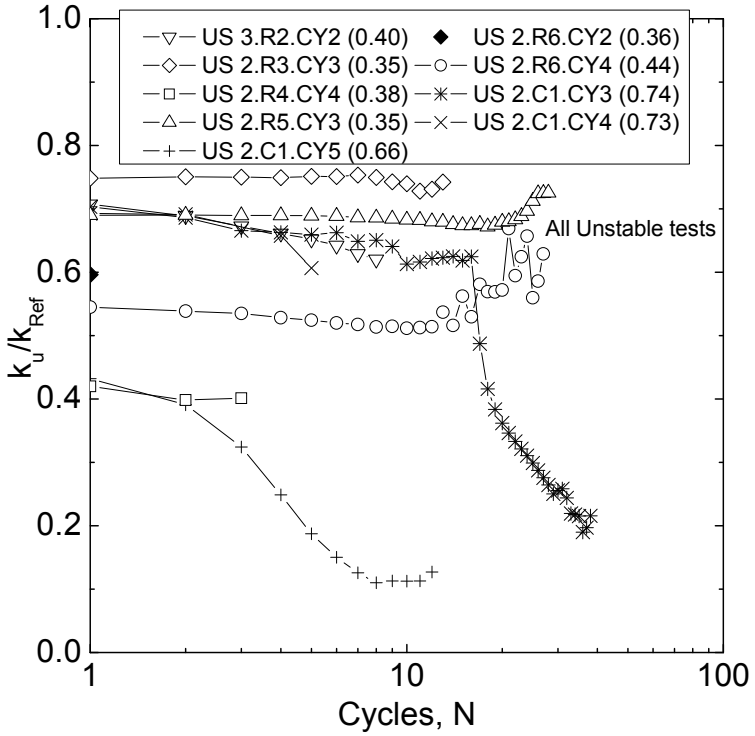


(b)

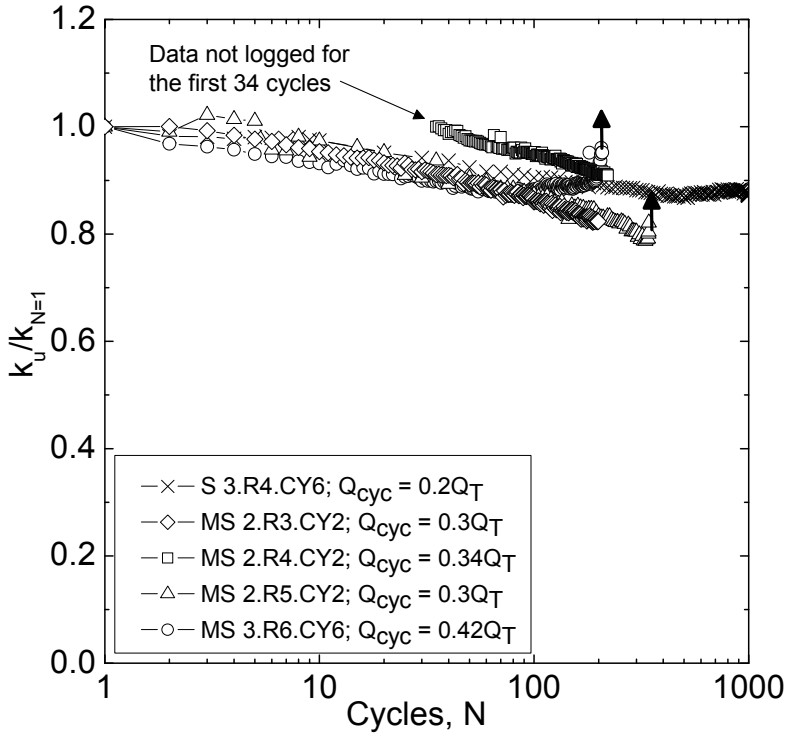
Figure 12-6: Axial cyclic loading stiffness (k_l) responses normalised in terms of (a) k_{Ref} and (b) $k_{N=1}$ and plotted against number of cycles for the unstable loading tests.


1.0
0.8
0.6
0.4
0.2
0.0
k_u/k_{Ref}
Data not logged for
the first 34 cycles
S 3.R4.CY6; Q_{cyc} = 0.2Q_T
MS 2.R3.CY2; Q_{cyc} = 0.3Q_T
MS 2.R4.CY2; Q_{cyc} = 0.34Q_T
MS 2.R5.CY2; Q_{cyc} = 0.3Q_T
MS 3.R6.CY6; Q_{cyc} = 0.42Q_T
1
10
100
1000
Cycles, N

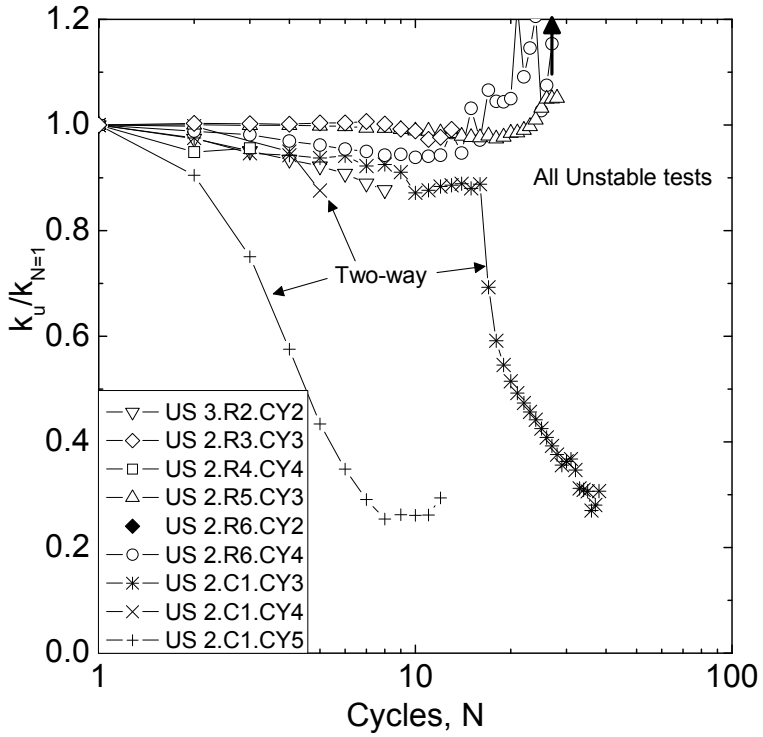
(a)


1.0
0.8
0.6
0.4
0.2
0.0
k_u/k_{Ref}
US 3.R2.CY2 (0.40)
US 2.R6.CY2 (0.36)
US 2.R3.CY3 (0.35)
US 2.R6.CY4 (0.44)
US 2.R4.CY4 (0.38)
US 2.C1.CY3 (0.74)
US 2.R5.CY3 (0.35)
US 2.C1.CY4 (0.73)
US 2.C1.CY5 (0.66)
All Unstable tests
1
10
100
Cycles, N

(b)



(c)



(d)

Figure 12-7: Axial cyclic unloading stiffness (k_u) responses normalised in terms of (a) & (b) k_{Ref} and (c) & (d) $k_{N=1}$ and plotted against number of cycles for the all the axial cyclic loading tests.

12.5.3 Accumulated cyclic displacements

The accumulated cyclic pile head displacements for the stable and meta–stable loading tests are shown on Figure 12-8, and Figure 12-9 refers to the unstable loading tests. Also shown in Figures 12-8 and 12-9 are reference lines relating to the fixed rates of accumulated displacement, 1mm/100cycles and 1mm/10cycles. The rate of accumulated displacements for the tests can be compared with the slopes of the two reference lines at any value of N. Low and stable accumulated displacements were observed in the only stable loading test (3.R4.CY6) with averaged displacement rates < 0.1mm over the first 100 cycles falling to negligible or even negative rates over the final few hundred cycles. The static tension capacity test (3.R4.T7) performed after this stable cyclic series showed a gain of 24.5% in peak tension capacity (with reference to test 3.R4.T5 that defined the pre-test tension capacity). The meta–stable loading tests showed a range of possible behaviours. Tests 2.R3.CY2 and 2.R4.CY2 developed steady accumulated displacement rates > 1mm/100cycles and did not fail before cycling was halted after N = 200cycles. Rapid static check tests on these piles indicated only minor losses in shaft capacity due to cycling. The other two meta–stable loading cyclic tests 2.R5.CY2 and 3.R6.CY6 continued until cyclic failure occurred. The rates of accumulated displacements in 2.R5.CY2 were initially high (> 1mm/10cycles) but then reduced before increasing again to > 1mm/10cycles as cyclic failure approached. However, 3.R6.CY6 started with slow rates that increased sharply to > 1mm/10cycles before a sudden and brittle cyclic failure. The loading applied in tests 2.R5.CY2 and 3.R6.CY6 resulted in a meta–stable response, as given by the accumulated displacements and cyclic stiffness values shown over their first 100 cycles.

A range of accumulated pile–head displacement–versus–number of cycles responses is also evident for the unstable loading tests plotted on Figure 12-9. Three two–way cyclic loading tests suites were performed on Pile C1. Test 2.C1.CY3 initially led to settlements that increased to a maximum after 15 cycles. This is because initially the compression load applied to the head of the pile (~-600kN) was greater than the tension load (~500kN). It had been intended to apply equal compression and tension loads of ±600kN and so after cycle N = 15, cycling stopped for 40 minutes while the load control was adjusted (Jardine & Standing, 2012). Once this was rectified the pile started to pull out progressively soon after cycling restarted, leading to displacement accumulation rates >1mm/10cycles. The next test on this pile, 2.C1.CY4, performed 15 hours later, failed the accumulated cyclic displacement rate criterion within its first cycle. Test 2.C1.CY5, an experiment undertaken after a further 20 hours of rest, exceeded the accumulated displacement rate failure criterion in two cycles, and accumulated displacements grew to > 0.1D after 12 cycles, when the test was halted. An overall loss in static shaft tensile capacity of 39% accumulated between the initial and final quick static reference tests (2.C1.T2 compared to 2.C1.T6). The unstable one–way

loading test 2.R4.CY4 also failed on its first cycle, with accumulated displacements approaching 0.1D after three cycles. Other unstable one–way loading tests developed excessive accumulated cyclic displacement rates at comparably early stages, such as 3.R2.CY2 and 2.R3.CY3, where the accumulated displacements grew rapidly towards 0.1D. Quick static tension tests proved shaft capacity degradations of 48% and 17% for R2 and R3 respectively. More gradual failures were observed under one–way loading in tests 2.R5.CY3 and 2.R6.CY4 where instability was indicated from the 16th cycle by the rates of accumulated cyclic displacement climbing rapidly and increasing towards the displacement limit after 28 and 27 cycles respectively. The reference static tests bracketing the latter tests implied degradations in shaft capacity > 16%.

While the cyclic stiffness patterns varied principally as a function of the applied cyclic load amplitudes (Q_{cyclic}), the accumulated cyclic displacement patterns were found to depend on both the normalised mean and cyclic loads, in effect being governed by the piles' stability criteria. The effects of the loading components Q_{cyclic} and Q_{mean} are demonstrated by considering the accumulated cyclic displacements developed after particular number of cycles N (= 3, 10, 30, 100, 200, and 300) in relation to the normalised stability interaction chart, as shown on Figure 12-10. Tentative axial cyclic displacement contours equivalent to 2%, 0.2% or 0.02% of D, the piles' diameter have been interpreted by eye and linear interpolation. The contours are collated and plotted as surfaces in Figure 12-11 where the accumulated displacements are related to the normalised Q_{cyclic} and Q_{mean} values and the number of cycles subtended with the aid of a plotting routine. The dependency of accumulated cyclic displacements on the two–dimensional loading regime is clear. A tentative zero displacement (zero cyclic effect) boundary is set at $Q_{cyclic}/Q_T = 0.1$ following centrifuge studies by Julio (2009). However, as noted in Chapter 11, calibration chamber tests or centrifuge experiments involving fixed walls may over-estimate the degradation that would develop in the field due to their rigid wall boundary conditions, especially when the ratios $d_{chamber}/D$ is low. Further full-scale specific investigation on the validity of this assumed boundary is required. The accumulated cyclic displacements grow as cyclic load amplitudes increase and also vary with the mean loads. The axial cyclic displacement contours flatten progressively as N increases.

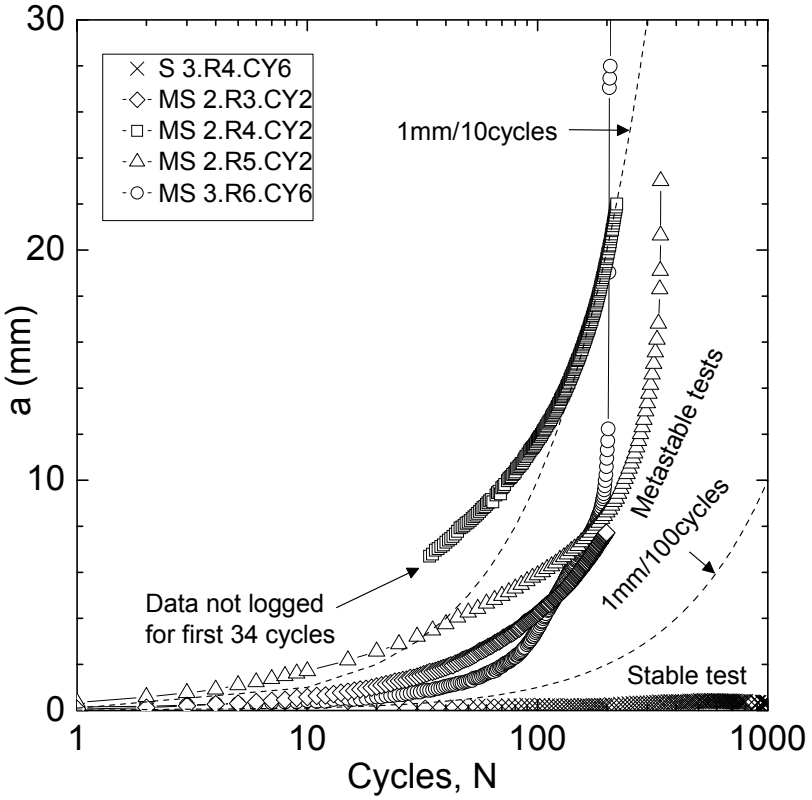


Figure 12-8: Accumulated cyclic displacements for the stable and meta–stable loading tests.

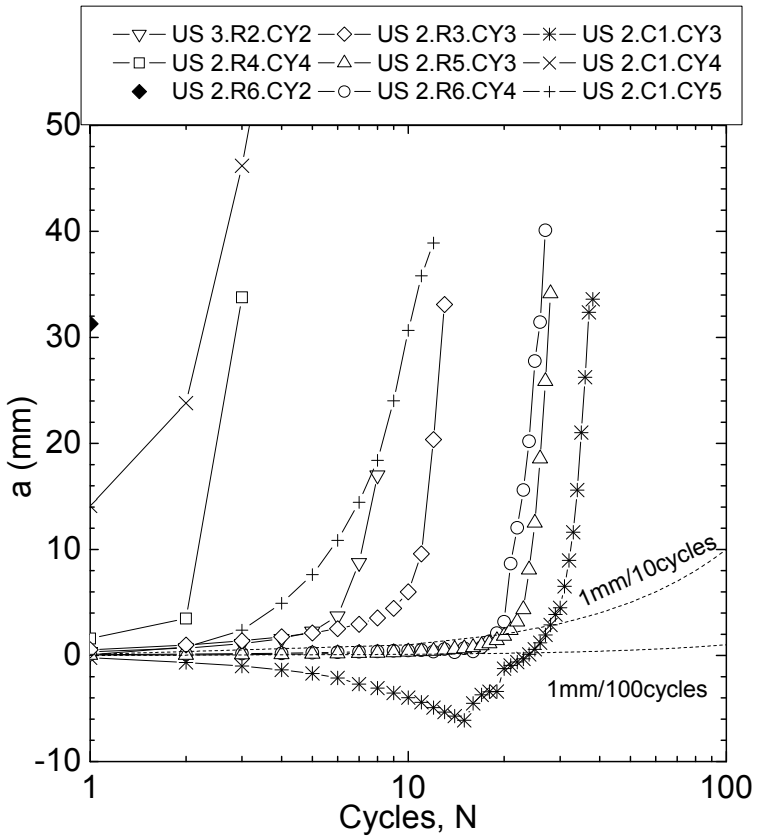
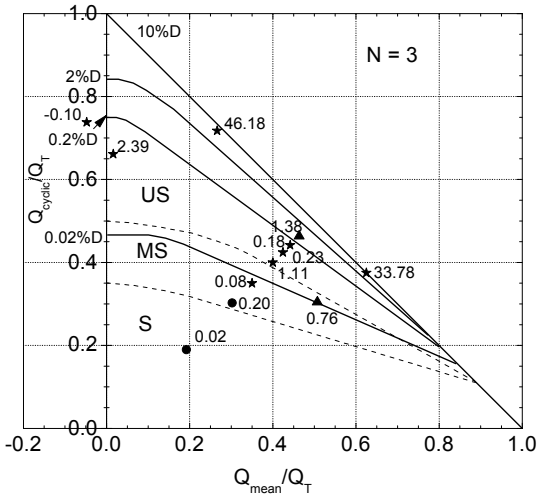
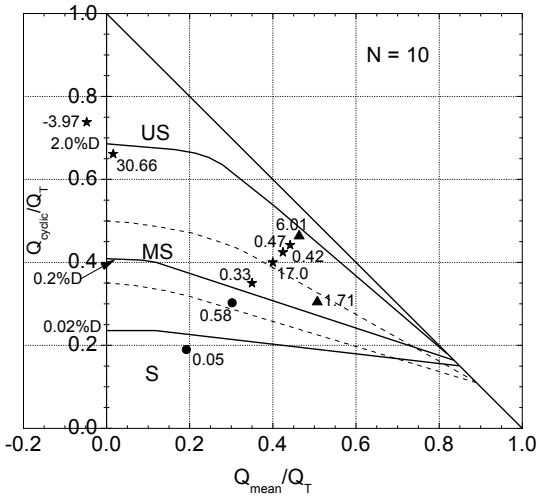


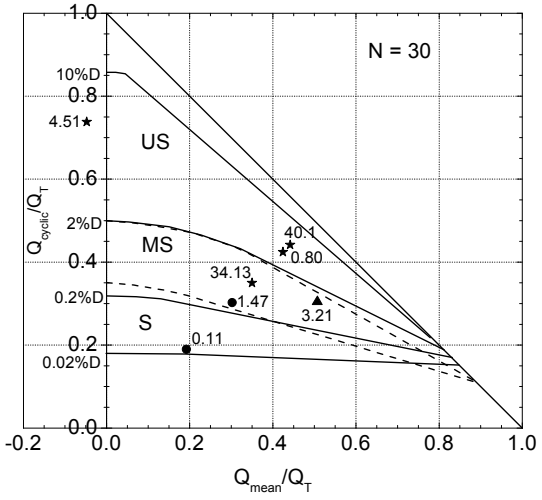
Figure 12-9: Accumulated cyclic displacements response for the unstable tests.


N = 3
10%D
2%D
-0.10
0.2%D
0.02%D
US
MS
S
46.18
2.39
1.38
0.18
0.23
1.11
33.78
0.08
0.20
0.76
0.02
Q_{cyclic}/Q_T
Q_{mean}/Q_T

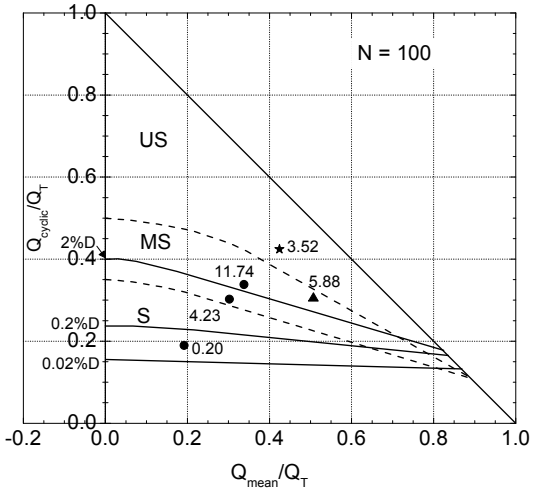
(a)


N = 10
-3.97
2.0%D
US
30.66
6.01
0.47
0.42
MS
0.2%D
0.33
17.0
1.71
0.58
0.02%D
0.05
S
Q_{cyclic}/Q_T
Q_{mean}/Q_T

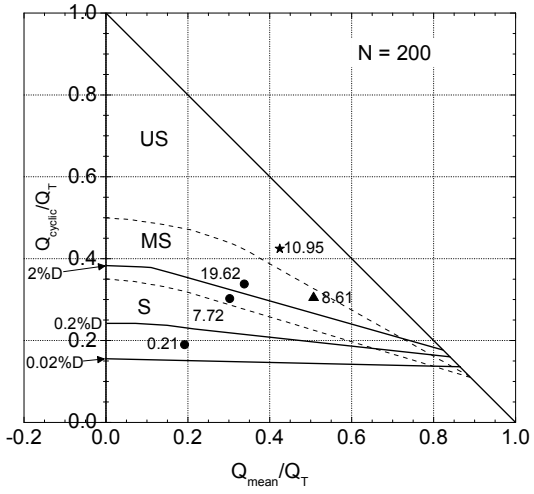
(b)


N = 30
10%D
4.51
US
2%D
MS
40.1
0.80
34.13
1.47
3.21
0.2%D
S
0.11
0.02%D
Q_{cyclic}/Q_T
Q_{mean}/Q_T

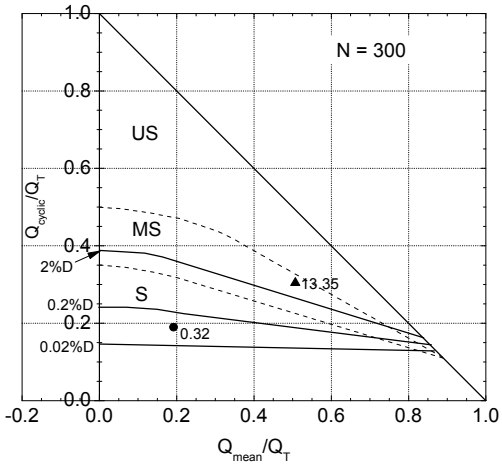
(c)



(d)

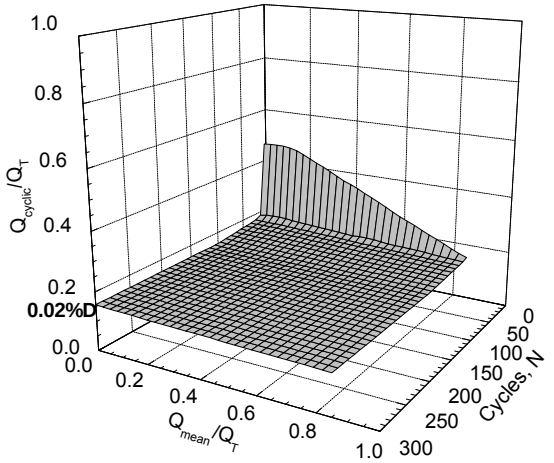


(e)

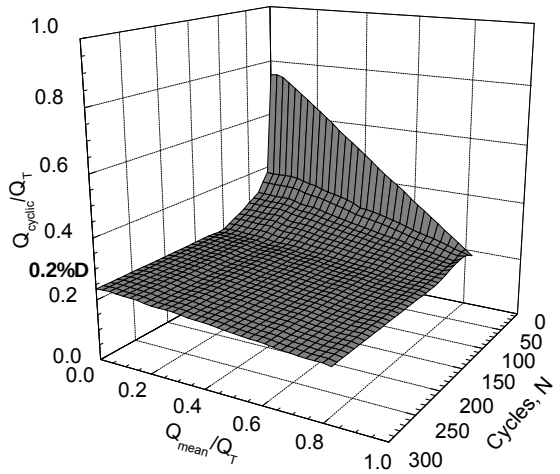


(f)

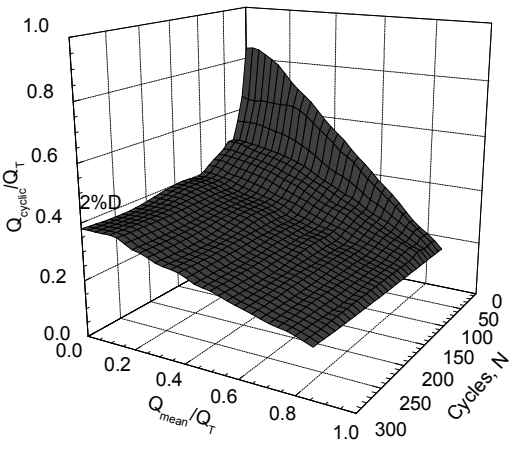
Figure 12-10 (a – f): Axial cyclic interaction chart with the accumulated cyclic displacements from cycles N = 3, 10, 30, 100, 200, and 300 marked for the cyclic pile tests.



(a)



(b)



(c)

Figure 12-11(a – c): 3D plots for accumulated cyclic displacements equivalent to 0.02%D, 0.2%D and 2%D.

12.5.4 Cyclic displacements

The cyclic displacements are related to the previously discussed axial cyclic loading stiffness behaviour. As summarised in Figures 12-12 and 12-13, the cyclic displacements (normalised by the piles outer diameter D) increase with Q_{cyclic}. The stable loading test 3.R4.CY6 developed low (~0.6%D) cyclic displacements that stabilise and begin to diminish after 500 cycles. Meta–stable loading tests 2.R3.CY2 and 2.R4.CY2, which did not fail under cycling, showed naturally larger cyclic displacements that grew gradually to final values of ~1%D and 2%D respectively. Tests 2.R5.CY2 and 3.R6.CY6, which failed at 345 cycles and 206 cycles respectively, showed cyclic displacements growing marginally to ~1%D until cyclic failure was approached and sharp increases were seen in both cyclic and accumulated displacements. The US tests presented on Figure 12-13 show cyclic displacements growing gradually (by 15 to 20%) until the onset of cyclic failure, when cyclic displacements rise sharply towards or finally exceeding 5%D depending on when the tests were halted.

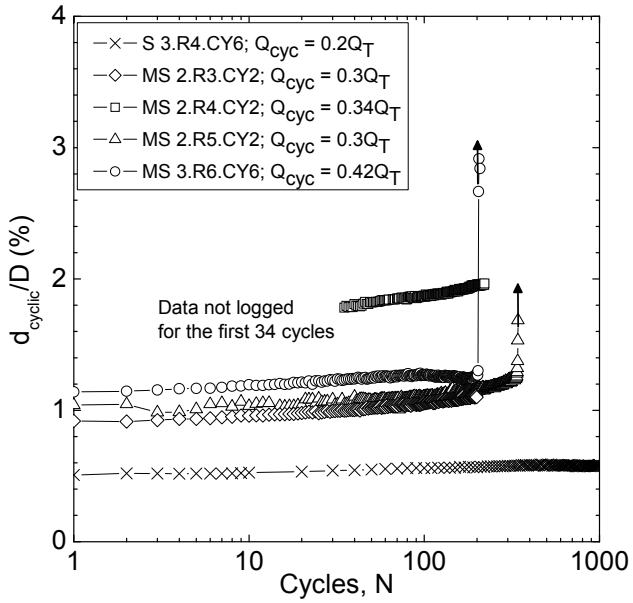


Figure 12-12: Transient cyclic displacements for the stable and meta–stable tests.

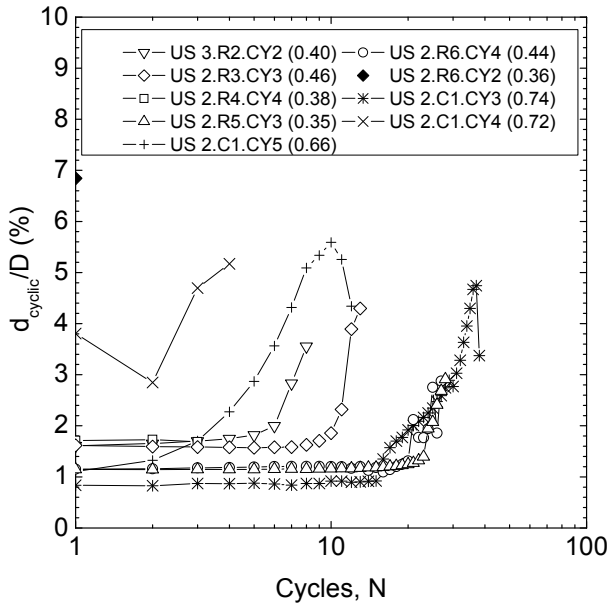


Figure 12-13: Transient cyclic displacements for the unstable tests.

12.6 Summary and conclusions

The behaviour observed in multiple axially load-controlled static and cyclic tests on seven full-scale driven steel pipe-piles at a marine sand test site in Dunkirk has been discussed. Reference static tension capacity tests were conducted between each cyclic experiment to enable the piles' capacity behaviour to be tracked and the results to be presented in a normalised cyclic stability interaction diagram. The fundamental processes leading to the stable, meta–stable or unstable axial cyclic loading response are assumed to follow the patterns identified in Chapter 11. This chapter analysed the load–displacement and stiffness responses of the full scale tests, working with the Dunkirk project's electronic raw data files. Six main conclusions are drawn:

1) Field load–displacement behaviour was highly non-linear, even at relatively low load levels, and depended critically on the applied cyclic load Q_{cyclic}.
2) The normalised cyclic loading levels and proximity to potential cyclic failure are the key factors that affect the piles' cyclic displacement responses. A spread of cyclic stiffness and accumulated cyclic displacement trends apply to the stable, unstable and meta–stable loading styles of response defined in the piles' overall normalised interactive cyclic stability diagram.
3) The Dunkirk piles' cyclic stiffnesses remained within 20% of those observed under initial static loading until cyclic failure was approached.
4) The field patterns of accumulated permanent cyclic displacements were sensitive to both the normalised mean and cyclic loading levels.

5) While permanent displacements accumulate rapidly over just a few cycles in the unstable zone, extended cycling in the stable zone led to minimal accumulated displacements and constant cyclic displacements. Meta–stable tests showed intermediate behaviour.
6) These field behaviour observations with the full–scale piles are compatible with model scale tests observations with the Mini-ICP pile and NE34 sand chambers further corroborating the mechanism frameworks established at scale.

Chapter 13

13 Conclusions, implications and recommendations

13.1 Introduction

This thesis has detailed an experimental investigation into the governing mechanisms of both the ageing and axial cyclic loading characteristics shown by displacement piles installed in silica sands. The study involved two strands; (i) review of earlier studies and (ii) a new experimental investigation and its interpretation.

The sections that follow present summaries of the main conclusions and implications from the study, and recommendations for further research.

13.2 Review of earlier studies

Considerable advances have been reached in recent years in understanding the axial capacity behaviour of displacement piles in sands. While the conventional earth pressures-based capacity assessment methods (e.g. the Main Text Method in API RP2GEO 2011) relied on speculation and assumptions regarding the pile-sand effective stress conditions developed by pile driving, a family of 'modern' CPT-based methods (ICP-05, FUGRO-05, UWA-05 and NGI-05) has been developed, largely from earlier field measurements of the shaft interface stresses made with the ICP piles, and incorporated as annexes to the most recent API RP2GEO (2011) guidance. However, three areas of persistent uncertainty remain that affect the predictive performance of these methods and the approaches that may be followed in dealing with the associated load-displacement and soil–structure interaction issues.

The *first* is the limited understanding of the effective stress regime generated by installation in the sand mass around the pile, and how this is influenced by the installation method.

The *second* concerns the mechanisms that lead to strong ageing effects that have been typically associated with pile capacity gains with time, commonly referred to as set-up. This limits the ability of any design method to predict the apparently 'moving target' of axial capacity. Methods are required to address the ageing effects explicitly. Set-up trends are interlinked with the stress regime imposed by installation. This thesis addresses time effects first by reviewing field data from the literature, before moving on to consider the stress regime established by driving.

The approach taken regarding field set-up trends was to assemble and analyse a comprehensive database of 328 static and dynamic load tests on 147 field piles. The Author's review led to the following outcomes:

1) Evidence from a limited dataset of a strong axial shaft capacity set-up (100% gains per log time cycle) in axial tension capacity from 'intact' piles when tested to failure for the first time.
2) A potential effect of pre-testing with highly scattered and averagely more modest gains (around 50% per log time cycle) being seen when single piles were re-tested multiply in compression.
3) Pile base capacity tended to remain roughly constant or increase marginally (~5% per log cycle) with time.
4) Clear trends were also interpreted in total axial compression capacity. On average a ~44% gain per log cycle was seen with intact piles, with 38% gain per log cycle from re-tested piles, reflecting both the absence of strong growth in the end–bearing and the potential negative effects of prior testing.
5) Adding case studies to the dataset generally added to the considerable scatter. The test outcomes typically ranged from no capacity growth to 100% gains per log time cycle.

Three hypotheses were posed in earlier studies to explain field capacity trends:

a) Radial stress increases linked to relaxation of circumferential (hoop) stresses in a sand arch formed around the displacement pile during installation.
b) Sand ageing leading to increases in interface dilation due to better interface interlocking and stiffness increases in the soil around the pile leading to additional radial effective stresses acting against the shaft during static axial loading to failure.
c) Physiochemical interaction between chemically active (corrodible) piles and the surrounding sand, or within the sand mass alone, leading to improved radial stresses and mechanical properties at the sand-pile interface, in the surrounding sand, or both.

The Author tested these arguments against his database ageing trends, finding:

1) No solid evidence for a dependency of ageing on pile diameter D, which is implied by hypothesis (b). Simple cavity expansion models indicate that the effect of interface radial stress dilation on shaft tension capacity should vary with 1/D.
2) No clear variation in ageing trends between potentially saline 'coastal' and fresh water 'non-coastal' pile load test sites, or between steel as compared to concrete driven piles. These observations indicate that the mechanism implicit in hypothesis (c) is unlikely to be dominant.

Hypotheses (a) and (b) were then investigated intensively in the laboratory experimental model pile testing programme, which also placed great emphasis on establishing the effective stress conditions developed around the pile during installation, ageing, and axial static and cyclic loading.

The *third* area of uncertainty investigated concerns the effects of axial cyclic loading on the displacement piles' behaviour. The main focus was on the piles' behaviour in service under variable environmental loading. However, the response to axial cyclic loading may also be a significant factor that affects the installation stress conditions. Displacement piles typically receive large numbers of jack strokes or hammer blows, each of which applies an extreme axial loading cycle. Multiple perspectives have emerged regarding potential improvements to the predictive reliability of the modern CPT-based approaches by explicit incorporation (or not) of cyclic installation effects. The four methods currently included in the API RP2GEO (2011) adopt implicit lumped 'h/R effect' or 'friction fatigue' factors in their equation for the end of installation effective stress regime, and hence the piles' shaft capacities.

Axial cyclic loading effects, which are often neglected in routine pile design, can strongly impact pile behaviour in service. However, a review of earlier studies revealed a paucity of full–scale cyclic loading tests in comparison with more numerous, but potentially less convincing, laboratory model pile experiments.

Axial cyclic loading test outcomes are often expressed through cyclic interaction diagrams that can also be employed as screening tools in design. When cyclic loading is identified as a significant issue more detailed assessment procedures are called for. The objectives for the present study were;

1) To understand more thoroughly the local sand-pile interface mechanisms that govern pile cyclic responses under a range of cyclic loading conditions.
2) To apply, develop and confirm established cyclic interaction diagrams for various parametric model testing conditions.
3) To develop datasets that can be applied in calculation procedures for site-specific practical design.

13.3 Laboratory model pile studies

The laboratory investigation comprised ten single model piles each installed in a 1.2m diameter and 1.5m deep calibration chamber filled with air pluviated fresh silica sand. The experiments took place in the 3S-R laboratory at Grenoble–INP in France. Five tests involved extensively instrumented 36mm diameter Mini-ICP model piles with a roughened (R_{cla} = 3 - 4μm) stainless steel shaft and a 60^0 conical tip closed-ended base that could measure axial loads and interface radial and shear stresses at multiple positions along its shaft. The other piles consisted of

60^0 conical tipped closed-ended base model piles of varying diameters (12mm or 36mm), and surface roughnesses (R_{cla} = 1 - 4μm) with various levels of instrumentation. The pluviated silica sand masses were usually instrumented with multiple miniature commercially sourced (Kyowa or TML) stress sensors to measure radial, vertical and hoop stresses in the sand mass during installation, ageing periods, and axial static and cyclic loading tests. The key parameters presumed to influence the model pile ageing and cyclic load behaviour were carefully isolated and considered. These included the effects of i) calibration chamber–to–pile diameter scaling, ii) pile–to–sand particle diameter scaling, iii) sand density state, iv) sand moisture states, v) chamber boundary conditions, and vi) modes of pile installation.

13.4 Conclusions and implications from the laboratory and full scale studies

13.4.1 Stress and load observations during laboratory model piles installations

Large datasets of local stress and load–displacement measurements were obtained from the calibration chamber experiments. Although the tests posed multiple mechanical and data reduction challenges, well-defined patterns were obtained ultimately through multiple testing and applying averaging techniques to the thousands of measurements. The main observations and implications can be summarised as:

1) The different calibration chamber boundary conditions used led to different CPT q_c profiles and pile end-bearing (q_b) resistances.
2) The local effective stresses developed around the penetrating piles were closely related to the local CPT tip (q_c) and end-bearing (q_b) resistances.
3) The pile base residual stresses accumulated with depth, without levelling off over the ~1m installation depths considered. Residual loads amounted to up to 30% of the maximum tip resistances. These features underscore the potential for under–measurement of base capacity and over–estimation of the shaft capacity in uninstrumented pile capacity tests.
4) The Mini-ICP surface stress transducer measurements confirmed that, at depths below the region influenced by the chamber upper boundary condition, the radial effective and shear stresses acting on the shaft varied directly with q_b and decayed with increasing h/R. The same features had been observed in earlier field tests with the original ICP equipment.
5) The radial, vertical and circumferential effective sand mass stresses developed at any given depth in the chamber also rose sharply as the pile base approached and reached a maximum then showed a sharp decay as the base advanced below the level of instrumentation. The stresses varied radially and vertically from the pile base and could be defined as functions of q_b and the normalised distances r/R and h/R.

6) Contoured interpretations were derived for the sand stresses that showed clear concentration of radial, vertical and circumferential effective stresses around the pile tip. For all stress components the stationary stresses σ'_s, moving stresses σ'_m and the difference between these two ($\sigma'_m - \sigma'_s$) were considerably higher around the pile tip and decayed sharply below and above the tip, reflecting the 'h/R effects' reported from instrumented field displacement pile studies.
7) Sand-pile interface effective stress paths were clearly identified during all test stages. As with the ICP tests shaft failure was governed by the Coulomb law. The interface stresses were influenced by the cyclic installation of the pile, which contributed to the phenomenon referred to as 'h/R effect'.
8) Static compression load tests performed at the end of installation in NE34 sand gave load–settlement curves that were compatible with field pile behaviour and gave capacities that matched ICP-05 method predictions.
9) However, piles installed in the finer (and inadvertently less dense) GA39 sand, and hammer blow driven piles installed in NE34 sand gave capacities well below ICP-05 predictions. The GA39 sand test, aimed at assessing particle size scale effects, recorded much lower local σ'_r and τ_{rz} stresses and capacities on its pile shaft. The possible scale effect associated with the finer sand might be associated with higher susceptibility to cyclic loading and requires further investigation.
10) The end of installation capacities seen with the model driven pile installations may have been affected by the boundary conditions imposed in the chamber. Further investigation is required.
11) The end–of–installation radial stress distributions measured around the Mini-ICP decreased with h/R for points above the pile base. At any given h/R they showed local maximum in the $2 < r/R < 4$ range with lower stresses applying (radially) further away from the pile and towards the pile face.
12) Compatible profiles were interpreted for the stationary circumferential stresses applying at the end of installation, showing lower stresses than the radial measurements although reflecting a much sparser dataset.
13) The measured circumferential stresses remained lower than the radial stresses (see Figure 7-51). The radial and circumferential equilibrium profiles inferred by Jardine et al. (2013b) indicate that higher σ_θ stresses should be expected closer to the shaft, in a region where direct measurements may not be made accurately.

14) Although it could not be fully confirmed by measurement, the inferred radial and circumferential effective stress profiles as postulated by hypothesis (a) (in section 13.2 above) may explain the marked capacity set-up of field displacement piles in sands.

Comparison of the radial stress measurements made around the Mini-ICP with other studies made with sands, in the field with closed–ended displacement piles, in laboratory calibration chambers with closed and open–ended piles; in centrifuge experiments with closed–ended driven model piles; and in analytical studies revealed broadly similar patterns. Detailed divergences between the studies were attributed to differences in (i) modes of installation, (ii) calibration details of the stress sensors, (iii) model scales and boundary conditions details, or (iv) the constitutive models and analytical procedures adopted. However, as mentioned above, the experimental end–of–installation radial and circumferential stresses profiles could not confirm the near field analytical predictions that $\sigma_{\theta s} > \sigma'_{rs}$ in the $1 < r/R < 4$ region.

13.4.2 Laboratory model piles ageing and post-ageing static load tests

Ageing periods of between 7 and 139 days were imposed on the model piles under uninterrupted environmentally control and continuous stress monitoring. The detailed measurements indicated that the end of installation stresses tended to decrease (by up to ~23%) under the BC3 boundary conditions, but were typically maintained when the 'free field simulator' BC5 boundary condition was imposed. Low level stress cycles which were applied for 9 days at the chamber boundaries to simulate environmental conditions changes (such as tidal and seasonal water table variations or removal and replacement of scoured sand) led to synchronous stress changes developing on the pile. But the final effective stresses developed on the shaft were very similar to those applying before the cycling commenced.

Static compression load tests on the aged piles showed pile capacity trends that reflected the local stress measurements. Marginal losses of capacities were seen under the BC3 chamber boundary condition, while maintained or marginally augmented capacities were observed under the 'free field simulator' BC5 conditions. The model pile tests do not show the high gains in capacity interpreted from equivalent field pile load tests. This discrepancy remains largely unresolved at this juncture.

The possible limitations of the laboratory model setup regarding the pile ageing study include;

1) Potential calibration chamber scale effects or boundary conditions effects applying, despite the rigorous and systematic examination of several key parameters through the ageing testing programme.

2) Relatively high ratio of the thickness of a clearly identified interface shear band to the model piles' diameter, posing possible scale effects that are uncharacteristic of full scale ageing piles and which were not covered by the Author's isolation of sand grain size or pile size effects.
3) Clean inert silica test sands which lacked the trace minerals identified in Dunkirk sand (Feldspar = 8%, $CaCo_3$ = 8%) where large gains in capacity were reported, or minor fractions of silt or clay sized particles found in natural sands.
4) The measured radial and circumferential stress profiles developed at the end of installation may have had insufficiently acute gradients to promote rapid gains in shaft capacity, possibly because of the unattended grain size scale effects.

However, the laboratory model pile test arrangements applied for the ageing study offered several key strengths including;

1) The laboratory model piles' axial static and cyclic loading responses were confirmed as representative of full scale field behaviour.
2) The test programme allowed systematic isolation and study of individual parameters including grain and pile size, moisture conditions and chamber boundary arrangements.
3) Continuous monitoring of all instruments was possible during the extended ageing periods, as well as static testing that mobilised pile shaft and base capacities fully, allowing detailed study of capacity trends after the end of installation.
4) The controlled conditions avoided several of the weaknesses applying to field ageing studies as identified in section 3.5.

13.4.3 Laboratory model piles and full scale piles responses under axial cyclic loading

The study included tests in which multiple batches of axial cyclic loading were applied to the model piles. These experiments were analysed first by applying and developing cyclic interaction diagrams which related the amplitude and mean cyclic loads (normalised by the pre-cycling tension capacity) to the number of cycles applied. A simple scheme was established using the accumulated cyclic displacements, number of cycles applied, and its derivatives, to categorise the axial cyclic response of displacement piles in sands in terms of three behaviour styles; Stable, Unstable or Meta–stable.

Stable behaviour accumulates cyclic displacements at slow and stabilising rates up to 1000 cycles without causing loss in static shaft capacity or full serviceability. The sand–pile shaft interface region does not experience large scale radial contraction (or σ'_r reductions) and any minor top-down shaft degradation that takes place is balanced by capacity growth through local densification and fabric rearrangement.

Unstable behaviour accumulates displacements at relatively rapid rates leading to significant shaft capacity degradation and failure (categorised as giving displacements greater than 0.1 times the pile diameter) within 100 cycles. Unstable loading conditions invoke markedly inelastic behaviour at the pile–sand interface where local interface shear failure and slip develops. Radial effective stresses fall markedly due to shear zone compaction and failure is governed by the Coulomb law.

Meta–stable behaviour applies in a transition zone between the stable and unstable conditions where piles can sustain some 100s of cycles without losing foundation serviceability. However, the piles lose some capacity and do not achieve fully stable conditions. Local interface slip, hysteretic effective stress paths and stress state migration may all develop, depending on the cyclic loading levels imposed.

Cyclic interaction diagrams can be zoned and all test outcomes classified into one of the three prescribed behaviour styles.

The NE34 sand interaction diagram developed from the Mini-ICP piles cyclic loading tests has been confirmed as applying equally to dry and wet NE34 (medium–dense) sand masses. Similar normalise trends were found with the BC3 and 'free field simulator' BC5 boundary conditions, which compare well with Jardine & Standing's (2012) full scale pile test interaction chart from medium–to–dense Dunkirk sand. However, an impact of calibration chamber boundary conditions on cyclic loading test outcomes was revealed in the marginally increased sand mass stress degradation seen with the BC3 arrangements compared to the 'free field simulator' BC5 boundary condition. The finer and looser GA39 sand tests showed a greater susceptibility to cycling by developing faster rates of displacement accumulation under lower levels of cyclic amplitudes. The area of interaction diagram within which piles could remain stable was reduced.

The developed interaction diagrams with more closely defined stability zones provide a straight-forward screening tool for addressing axial cyclic loading. Further, the Mini-ICP axial cyclic loading tests form a valuable dataset that can be used in the derivation and validation of cycling numerical models towards fully analytical design of displacement piles under axial cyclic loading.

The axial cyclic response of the full scale Dunkirk cyclic piles was analysed through a similar framework to that applied to the model piles but with the displacement limits scaled-up in proportion to the pile diameter. As with the model piles, the normalised cyclic loading levels and proximity to potential cyclic failure are the key factors that affected the piles' cyclic displacement responses. While permanent displacements accumulate rapidly over just a few cycles in the unstable zone, extended cycling in the Stable zone led to minimal accumulated displacements and constant cyclic displacements. Meta–stable tests showed intermediate behaviour. Similar to the model pile

behaviour, the cyclic stiffnesses of the Dunkirk piles remained within ~20% of those observed under initial static loading until cyclic failure was approached. The full scale piles patterns of permanent cyclic strain accumulation were sensitive to both the mean and cyclic normalised loading levels. Analysis accounting for both resulted into 3D plots that showed how accumulated cyclic displacements varied with both cyclic amplitude and mean normalised loads.

13.5 Recommendations for further studies

13.5.1 Towards establishing the mechanisms for pile ageing trends

The mechanisms governing pile ageing processes that lead to the marked shaft capacity set-up indicated by field load tests in principally silica sands have not been fully resolved. Unless these mechanisms are fully understood it may be difficult to incorporate ageing processes into pile capacity estimation procedures and a great reliance will have to be placed on expensive site specific testing. This problem of identifying such a mechanism could be a result of (i) the limitations of the laboratory experimental setup in fully replicating free field conditions, or (ii) a consequence of the field load testing procedures used to interpret capacity gains particularly in re-tested aged piles.

The most direct way forward is to design and undertake further static load testing programmes on aged intact full scale field piles. To remove any ambiguities associated with current ageing trends the piles require strain gauge instrumentation at the base and multiple levels along a shaft. Several similar piles have to be installed in a uniform well–characterised sand deposit and static load tested in compression at staged times from their intact state of installation. Disaggregating base contributions from the shaft will be important in identifying clear capacity ageing trends. Static tension tests could be performed on both parallel intact piles, and after compression tests to confirm the interpreted trends. Monitoring of pile strain gauges through installation, ageing and static load testing will serve to (i) remove any uncertainties on residual loads effects, (ii) establish an ‘intrinsic’ ageing trend, and (iii) understand the stress conditions during the pile ageing and static load tests towards deriving the mechanism for the observed ageing trends.

13.5.2 Towards modelling installation and in-service cyclic loading effects

The experimental observations indicate that installation cyclic loading have little bearing on the end of installation base capacities. The same is not conclusive on shaft stresses and capacities. The influence of installation cyclic loading has not been studied in great detail, however, ~10% shaft capacity differences were inferred by a pair of similar piles, CPT09 and CPT10, installed by 2 and 49 cycles respectively. The datasets of cyclic installations and further axial cyclic loading tests can be used to model the stationary interface radial stresses attenuation along driven pile shafts in relation to the number of cycles experienced by the sand-pile interface during driving.

The Mini-ICP cyclic loading tests dataset also provides key information for advancing a fully analytical route in which cyclic interface and soil mass constitutive models are derived that can be fitted to cyclic testing performed for site-specific cases and incorporated into advanced finite element method (FEM) analyses as proposed in section 11.8. This option is scarcely feasible for practical projects at the time of writing, but the research outlined in this thesis should contribute to this option becoming more possible in the near term.

13.5.3 Further optimisation of calibrations chamber boundary conditions

The calibration chamber boundary arrangements were changed during the current study from the BC3 (featuring a rigid lateral and a constant stress controlled top boundary condition) to BC5 the 'free field simulator' with a variable stress controlled lateral and a constant stress controlled top boundary condition. Although BC5 offered an improvement on BC3 and changed the q_b profiles developed, no major difference was observed in the q_b normalised ageing and cyclic behaviours of the jack stroke installed piles. This may potentially reflect the adequate size of the chamber ($d_{chamber}$/D ratio = 33), as the end–of–installation pile capacities were also compatible the ICP-05 method predictions.

However, lower installation tip and shaft resistance were observed under the BC5 boundary condition when the displacement piles were driven by drop-weight hammer. This led to lower EOD and aged capacities than were achieved with the jack installed piles. A further revision (to the boundary condition BC1) led to higher driven pile capacities. These features may reflect dynamic energy being trapped within the chamber in a way that would not occur in the field. The driven piles are probably best modelled by chambers with larger $d_{chamber}$/D ratios where stress waves propagating from the pile arrive at a boundary that appropriately absorbs and mimics field radiation damping. Further studies on the boundary conditions are required in order to improve the laboratory experimental simulation of both driven models piles and pile ageing studies.

13.5.4 Further characterisation of finer sands particle size scale effects

As discussed the Mini-ICP installed in the fine GA39 sand showed far lower shaft capacities than equivalent tests in NE34 sand. This has currently been attributed to probable increased susceptibility of the sand to cyclic effects. Less laboratory testing has been conducted on GA39 sand than the standard NE34 test sand. Further calibration chamber testing with the GA39 sand with jacked and hammer driven piles as well as laboratory element testing will considerably improve the understanding of potentially important particle size scale effects in the finer sands.

References

1. Abu-Farsakh, M.Y. and Titi, H.H. (2004). Assessment of direct cone penetration test methods for predicting the ultimate capacity of friction driven piles. *J. of Geotech. and Geoenviron. Eng*, ASCE, **130**(9): 935–944.

2. Airey, D.W., Al-Douri, R.H. and Poulos, H.G. (1992) Estimation of pile friction degradation from shear box tests. *Geotech. Testing J,* ASTM, **15**(4): 388–392.

3. Alawneh, A.S., and Husein Malkawi, I. (2000). Estimation of post-driving residual stresses along driven piles in sand. *Geotech. Testing J,* ASTM, **23**(3): 313–326.

4. Alawneh, A. S., Nusier, O. K. and Awamleh, M. S. (2009). Time dependent capacity increase for driven pile in cohesionless Soil. *Jordan Journal of Civil Eng*, **3**(1): 1–31.

5. Al-Douri, R. H. (1992). *Behaviour of single pile and pile groups in calcareous sands*. Ph.D. thesis, University of Sydney, Australia.

6. Aldridge, T. R., Carrington, T. M., Jardine, R. J., Little, R., Evans, T. G., and Finnie I. (2010). Driven pile design in extremely hard till for BP's Clair 1 platform. *Proc. 2nd Int. Symp. on Frontiers in Offshore Geotechnics (ISFOG)*. Perth, Australia: 477 – 482.

7. Altuhafi, F., and Jardine, R.J. (2011). Effect of particle breakage and strain path reversal on the properties of sands located near to driven piles. *Proc. 5th Int. Symp. on Deformation Characteristics of Geomaterials (IS-Seoul)*. Seoul, Korea: 386–395.

8. Allard, M. A. (1990). *Soil stress field around driven piles*. PhD thesis, California Institute of Technology, California, USA.

9. Altaee, A., Evigin, E., and Fellenius, B. H. (1992). Axial load transfer for piles in sand. II. Numerical analysis. *Can. Geotech. J.* **29**(1): 21–30.

10. Altaee, A., Fellenius, B. H. and Evgin, E. (1993). Load transfer for piles in sand and critical depth. *Can Geotech J.* **30**(3): 455-463.

11. American Petroleum Institute (1969). *Recommended Practice for Planning, Designing and Constructing Fixed Offshore Platforms (API RP2A) – 1st edition*, Washington, D.C., USA.

12. American Petroleum Institute (1984). *Recommended Practice for Planning, Designing and Constructing Fixed Offshore Platforms (API RP2A) – 15th edition*, Washington, D.C., USA.

13. American Petroleum Institute (2000). *Recommended Practice for Planning, Designing and Constructing Fixed Offshore Platforms (API RP2A) – 21st edition*, Washington, D.C., USA.

14. American Petroleum Institute (2007). *Recommended Practice for Planning, Designing and Constructing Fixed Offshore Platforms (API RP2A) – Working Stress Design – 22nd edition*, Washington, D.C., USA.

15. American Petroleum Institute (2011). *Geotechnical and foundation design considerations; ISO 19901-4:2003 adoption (API RP2GEO) – 1st Edition*, Washington, D.C. USA. 120pp.

16. Aoki, N. and De Alencar, D. (1975). An approximate method to estimate the bearing capacity of piles. *Proc. 5th Pan-American Conf. of Soil Mech. and Fndn Eng,* Buenos Aires, Argentina. 1: 367–376.

17. Åstedt, B., Weiner, L. and Holm, G. (1992). Increase in bearing capacity with time for friction piles in silt and sand. *Proc. of Nordic Geotech. Meeting*: 411–416.

18. Atkins Consultants Ltd (2000). Cyclic degradation of offshore piles. *HSE Offshore Technology Report OTO 2000 013*. Health and Safety Executive, London.

19. Attwooll, W. J., Holloway, D. M., Rollins, K. M., Esrig, M. I., Sakhai, S and Hemenway, D (1999). Measured pile set-up during load testing and production piling: I-15 corridor reconstruction project in Salt Lake City, Utah. *Transportation Research Record: J. of the Transportation Research Board.* **1663**(99-1140): 1-7.

20. Augustesen, A. H. (2006). *The effects of time on soil behaviour and pile capacity*. PhD thesis, Aalborg University, Aalborg, Denmark.

21. Augustesen, A., Liingaard, M., and Lade, P.V. (2004). Evaluation of time-dependent behaviour of soils. *Int. J. of Geomech*. ASCE, **4**(3): 137-156.

22. Augustesen, A., Andersen, L., and Sørensen, C.S. (2005). *Capacity of piles in sand*. Department of Civil Engineering, Aalborg University, Denmark, Internal report, ISSN: 1398-6465 R0519.

23. Axelsson, G. (2000). *Long term set-up of driven piles in sand.* PhD thesis, Royal Institute of Technology, Stockholm, Sweden.

24. Baguelin, F., Bustamante, M. and Frank, R. (1986). The pressuremeter for foundations: French experience, *Proc. Special Conf. on In-situ tests in Geotech. Practice*, Blacksburg, Virginia: 31–46.

25. Baldi, G., Bellotti, R., Ghionna, V., Jamiolkowski, M., and Pasqualini, E. (1986). Interpretations of CPTs and CPTUs, 2nd part: Drained penetration of sands. *4th Int. Conf. on field instrumentation and in-situ measurements*, Singapore: 143-156.

26. Baxter, C. D. P. and Mitchell, J. K. (2004), Experimental study on the aging of sands, *J. of Geotech. and Geoenviron. Eng,* ASCE, **130**(10): 1051–1062.

27. Bea, R. G., Jin, Z., Valle, C. and Ramos, R. (1999). Evaluation of reliability of platform pile foundations. *J. of Geotech. and Geoenviron. Eng,* ASCE, **125**(8): 696–704.

28. Bellotti, R., Crippa, V., Pedroni, S. and Ghionna, V. N. (1988). Saturation of sand specimen for calibration chamber tests. *Proc. Int. Symp. on Penetration Testing (ISOPT-1)*, Orlando, Balkema Pub, Rotterdam, Netherlands. **2**:661- 672.

29. Benzaria, O. (2013). *Contribution à l'étude du comportment des pieux isolés sous chargements cyclique axiaus.* These de Doctorat, Université Paris-est, Paris, France (in French).

30. Berezantzev, V. C., Kristoforov, V. and Golubkov, V. (1961). Load bearing capacity and deformation of piled foundations. *Proc. 5th Int. Conf. Soil Mech. Fndn. Eng*, Paris, France, **2**: 11–12.

31. Beringen, F.L., Kolk, H.J. and Windle, D. (1982). Cone penetration and laboratory testing in marine calcareous sediments. *Geotechnical properties, behaviour and performance of calcareous sediments,* ASTM, STP777: 179–209.

32. Bolton, M. D. (1986). The strength and dilatancy of sands. *Géotechnique*, **36**(1): 65–78.

33. Bond, A. J. (1989). *Behaviour of displacement piles in over-consolidated clays*. PhD Thesis, University of London (Imperial College).

34. Bond, A. J., Jardine, R. J. and Dalton, J. C. P. (1991). The design and performance of the Imperial College instrumented pile. *Geotech. Testing J*. ASTM, **14**(4): 413–424.

35. Boulon, M. and Foray, P. (1986). Physical and numerical simulation of lateral shaft friction along offshore piles in sand. *Proc. 3rd Int. Conf. on Numerical Methods in Offshore Piling*, Nantes, France: 127-147.

36. Bowman, E.T. & Soga, K. (2005). Mechanisms of set-up of displacement piles in sand: Laboratory creep tests. *Can. Geotech. J.*, **42**(5): 1391–1407.

37. Briaud, J.-L. and Tucker, A. M. (1984). Piles in Sand: A Method Including Residual Stresses. *J. of Geotech. Eng,* ASCE, **110**(11): 1666–1680.

38. Brinch Hansen, J. (1951). *Simple statical computation of permissible pile loads*. CN–Post No. 13, Danish Geotechnical Institute, Copenhagen, Denmark.

39. Brinch Hansen, J. (1961). *A general formula for bearing capacity*. Bulletin No. 11, Danish Geotechnical Institute, Copenhagen, Denmark.

40. British Standards Institution (2007). BS EN 1997-2 Eurocode 7. Geotechnical Design: Ground investigation and testing.

41. Brucy, F., Meunier, J. and Nauroy, J. F. (1991). Behaviour of pile plug in sandy soils during and after driving. *Proc. 23rd Offshore Technology Conf., Houston*: 145–154.

42. Bullock, P. J., Schmertmann, J. H., McVay, M. C. and Townsend, F. C. (2005). Side shear setup. I: Test piles driven in Florida. *J. of Geotech. and Geoenviron. Eng,* ASCE, **131**(3): 292–300.

43. Bullock, P. J., Schmertmann, J. H., McVay, M. C. and Townsend, F. C. (2005b). Side shear setup. II: Results from Florida test piles. *J. of Geotech. and Geoenviron. Eng,* ASCE, **131**(3): 301–310.

44. Bustamante, M. and Gianeselli, L. (1982). Pile bearing capacity predictions by means of static penetrometer CPT. *Proc. 2nd European Symp. on Penetration Testing (ESOPT-II)*, Amsterdam, Netherlands. **2**: 493–500.

45. Butterfield, R. and Johnston, I. W. (1973). The stress acting on a continuously penetrating pile. *Proc. 8th Int. Conf. Soil Mech & Fndn Eng*, Moscow **2**(1): 39 – 45.

46. Cai, G., Liu, S., Tong, L., and Du, G. (2008). Assessment of direct CPT and CPTU methods for predicting the ultimate bearing capacity of single piles. *Eng. Geology* **104**(2009): 211–222.

47. Cambridge Insitu Ltd. (2009). Personal communication.

48. Canadian Geotechnical Society (1985). *Canadian Foundation Engineering Manual – 2nd edition*, Can. Geotech. Soc., Vancouver, Canada.

49. Caquot, A. and Kerisel, J. (1956). *Traité de mécanique de sols*. Gauthier-Villars, Paris, 3rd edition (in French).

50. Casagrande, A. and Fadum, R. E. (1940). *Notes on soil testing for engineering purposes.* Harvard Uni. Grad. School of Eng. Publ. 268: 74pp.

51. Chan, S. and Hanna, T.H. (1980). Repeated loading on single piles in sand. *J. of the Geotech. Eng. Div*, ASCE, **106**(2): 171-188.

52. Chong, F. (1988). Density changes of sand on cone penetration resistance. *Proc. 1st Int. Symp. on Penetration Testing (ISOPT-1)*, **2**:707 – 714.

53. Chow, F.C. (1997). *Investigations into displacement pile behaviour for offshore foundations*, PhD thesis, University of London (Imperial College).

54. Chow, F. C., Jardine, R. J., Brucy, F. & Nauroy, J. F. (1998). Effects of time on capacity of pipe piles in dense marine sands, *J. of Geotech. and Geoenviron. Eng*, ASCE, **124**(3): 254 – 264.

55. Clausen, C. J. F., Aas, P. M. and Karlsrud, K. (2005). Bearing capacity of driven piles in sand, the NGI approach. *Proc. Int. Symp. on Frontiers in Offshore Geomechanics (ISFOG)*, Taylor & Francis, London: 677–681.

56. Clisby, M. B., Scholtes, R. M., Corey, M. W., Cole, H. A., Teng, P. and Webb, J. D. (1978). *An evaluation of pile bearing capacities – Vol. 1*. Mississippi State Highway Department. Final Report.

57. Collins, R., Lee, K. L., Lilly, G. P. and Westmann, R. A. (1972). Mechanics of pressure cells. *Experimental Mechanics*. **12**(11): 514 – 519.

58. Costa, L. M., Danziger, B. R. and Lopes, F. R. (2001). Prediction of residual driving stresses in piles. *Can. Geotech. J.* **38**(2): 410–421.

59. Coyle, H. M. and Castello, R. R. (1981). New design correlations for piles in sand. *J. of Geotech. Div.*, ASCE, **107**(GT7): 965–986.

60. Davisson, M. T. (1972). High Capacity Piles. *Proc. Soil Mechanics Lecture Series on Innovations in Foundation Construction*. ASCE, Illinois Section, Chicago, USA: 81-112.

61. De Beer, E. E. (1945). *Etude des fondations sur pilotis et des fondations directes*. Annales des travaux publics de Belgique, **46**: 1–78 (in French).

62. DeJong, J. T. (2001). *Investigation of particulate–continuum interface mechanisms and their assessment through a multi–friction sleeve penetrometer attachment*. PhD thesis, Georgia Inst. Technology, Atlanta, USA.

63. DeJong, J., Randolph, M. F. and White, D. J. (2003). Interface load transfer degradation during cyclic loading: a microscale investigation. *Soils and Found*. **43**(4): 81–93.

64. De Ruiter, J. and Beringen, F.L. (1979). Pile foundations for large North Sea structures. *Marine Geotechnology*. **3**(3): 267–314.

65. Det Norske Veritas (2007). *Offshore Standard DNV-OSJ101: Design of Offshore Wind Turbine Structures*. DNV, Baerum, Norway.

66. DiMaggio, J. (1991). *Dynamic pile monitoring and pile load test report*. Demonstration project No. 66, 1-165(2), Mobile County, Alabama, FHWA, USA.

67. DiPalma, J. (2011). *Behaviour of soil stress sensors under cyclic loading tests*. Masters thesis, Université Joseph Fourier, Grenoble, France.

68. Dolwin, J., Khorshid, M. S. & van Goudoever, P. (1988). Evaluation of driven pile capacity – Methods and results. *Proc. Int. Conf. calcareous sediments*, Perth (1): 429–438.

69. Eiksund, G. R. (1994). *Dynamic testing of piles*. PhD thesis, Norwegian Institute of Technology.

70. Einav, I. (2012). Personal communication.

71. Eslami, A. and Fellenius, B.H. (1997). Pile capacity by direct CPT and CPTU methods applied to 102 case histories. *Can. Geotech. J.* **34**(6): 886–904.

72. Evans, T. G., Finnie, I., Little, R., Jardine, R. J. and Aldridge, T. R. (2010). BP Clair Phase I – Design and assurance of driven piled foundations in extremely hard till. *Proc. 2nd Int. Symp. on Frontiers in Offshore Geotechnics (ISFOG)*, Perth: 495–500.

73. Fellenius, B. H. (1989) Prediction of Pile Capacity. *Proc. of Symp. on Predicted and Observed Behaviour of Piles*, ASCE Geotech. Special Pub. **23**: 293–302.

74. Fellenius, B. H. (2002). Determining the true distribution of load in piles. *Int. Deep Found. Cong. An International Perspective on Theory, Design, Construction, and Performance.* ASCE Geotech. Special Pub. 116, **2**: 1455–1470.

75. Fellenius, B. H. and Altaee, A. (2002). Pile Dynamics in Geotechnical Practice–Six Case Histories. Int. Deep Found. Congress, *An International Perspective on Theory, Design, Construction, and Performance, ASCE Geotechnical Special Publication 116*, Orlando, USA. **2:** 619–631.

76. Fellenius, B.H. and Altaee, A. (1994). The critical depth. How it came into being and why it does not exist. *Proc. of the Institution of Civil Engineers Geotech. Eng*, **113**(2): 107 - 111.

77. Fugro (1995). *Reduced scale pile load tests, Jamuna Bridge, Bangladesh. Rep. No. K-2380/206*, Fugro, Netherlands.

78. Fugro Engineers B.V. (2004). *Axial Pile Capacity Design Method for Offshore Driven Piles in Sand.* Report P1003 presented to the American Petroleum Institute, Issue 3, 5 August 2004.

79. Gaudin, C., Schnaid, F., and Garnier, J. (2005). Sand characterization by combined centrifuge and laboratory tests. *Int. J. Phys. Modelling Geotech.* **5**(1): 42–56.

80. Gavin, K. G. and Lehane, B. M. (2003). The shaft capacity of pipe piles in sand. *Can. Geotech. J*, **40**: 36–45.

81. Gavin, K., Igoe, D. & Doherty, P. (2011). Pile for offshore wind turbines: a state-of-the-art review. *Proc. of the ICE Geotech. Eng*, **164**(GE4): 245–256.

82. Gavin, K. and O'Kelly, B. (2007). Effect of friction fatigue on piles in dense sand. *J. of Geotech. and Geoenviron. Eng,* ASCE, **133**(1): 63–71.

83. Gavin, K., Igoe, D. and Kirwan, L. (2013). The effect of ageing on the axial capacity of piles in sand. *Proc. of the ICE Geotech. Eng,* **165**(GE1).

84. Gibson, R. E. (1950). Correspondence. *J. Inst. Civ. Engrs*, **34**: 382 – 383.

85. Goble, G. G., Rausche, F. and Likins, G. E. (1998). *Wave equation analysis of pile driving. GRLWEAP program, procedures and models*. Program manual. Pile Dynamics Inc., GRL, Goble Rausche Likins and Associates, Inc. Cleveland, Ohio.

86. Gudehus, G. and Hettler, A. (1981). Cyclic and Monotonous Model Tests in Sand. *Proc. 10th Int. Conf. on Soil Mech. and Found Eng. (ICSMFE)*, Stockholm, Sweden. **2**: 211–214.

87. Gupta, R. C. (2002). Estimating bearing capacity factors and cone tip resistance. *Soils and Foundations*, **42**(6): 117 – 127.

88. Heerema, E. P. (1979). Pile driving and static load tests on piles in stiff clay. *Proc. 11th Offshore Tech. Conf. Houston*, OTC 3490: 1135–1145.

89. Henke S., Qiu G., and Grabe, J. (2010). A Coupled Eulerian Lagrangian Approach to Solve Geotechnical Problems Involving Large Deformations. *Proc. 7th European Conf. on Numerical Methods in Geotech. Eng. (NUMGE),* Trondheim, Norway: 233–238.

90. Ho, T.Y.K., Jardine, R.J., and Minh, N.A. (2011). Large displacement interface shear between steel and granular media. *Géotechnique*, **61**(3): 221–234.

91. Holeyman (2012). *Essais de chargement dynamique sur Pieu B-2 de Loon-Plage SOLCYP*. UCL, GeoMEM presentation at the SOLCYP meeting of 09th October 2012, Paris, France (in French).

92. Hossain, M. K. and Briaud, J. L. (1992). Pipe piles in sands - An improvement for the API RP 2A. *Offshore Technology research centre, Report to the American Petroleum Institute,* College Station, Texas.

93. Huang, A. –B. and Hsu, H. –H. (2005). Cone penetration tests under simulated field conditions. *Géotechnique* **55**(5): 345–354.

94. Hunter, A. H. and Davisson, M. T. (1969). Measurement of Pile Load Transfer. *Performance of Deep Foundations, ASTM STP 444,* ASTM: 106–117.

95. Ishihara, K. (1993). Liquefaction and Flow Failure during Earthquakes. *Géotechnique*, **43**(3): 351–415.

96. Jardine, R. J. (1985). *Investigations of pile-soil behaviour, with special reference to the foundations of offshore structures*. PhD thesis, University of London (Imperial College).

97. Jardine, R.J. (1992). Observations on the kinematic nature of soil stiffness at small strains, *Soils and Found.*, **32**(2): 111–124.

98. Jardine, R. J. (1991). The cyclic behaviour of large piles with special reference to offshore structures. *Cyclic loading of soils: From theory to design*, Blackie, London, ISBN 0-216-92898-2.

99. Jardine, R.J. (2008). *Review of technical issues relating to foundations and geotechnics for offshore installations in the UKCS.* Health and Safety Executive (HSE) Research Report RR 676. Published by HSE Books, London: 96p.

100. Jardine, R. J. (2009). *JIP Project on Ageing Characteristics of Piles Driven in Sand–Report for Sponsors on Completion of Phase 1 July 2006 to December 2008.* Imperial College & Grenoble Technical University.

101. Jardine, R. J. (2012). *Comments on the static pile load tests at Red Sea port development*. Report. Personal communication.

102. Jardine, R. J., and Chow, F. C. (1996). *New design methods for offshore piles*. MTD Publ. 96/103, Marine Technology Directorate, London.

103. Jardine, R. J., Chow, F. C., Overy, R. F., and Standing, J. R. (2005a). *ICP design methods for driven piles in sands and clays*. Thomas Telford, London.

104. Jardine, R.J., Standing, J.R and Kovacevic, N. (2005b). Lessons learned from full–scale observations and the practical application of advanced testing and modelling. Keynote paper, *Proc. Int. Symp. on Deformation Characteristics of Geomaterials*, Lyon, pub Balkema, Lisse, **2**: 201-245.

105. Jardine, R. J., Standing, J. R., and Chow, F. C. (2006). Some observations of the effects of time on the capacity of piles driven in sand. *Géotechnique*, **56**(4): 227–244.

106. Jardine, R. J., and Chow, F. C. (2007). Some recent developments in offshore pile design. *Proc. 6th Int. Offshore Site Investigation and Geotechnics Conf*. London, UK: 303–332.

107. Jardine, R. J. and Standing, J. R. (2000). *Pile load testing performed for HSE cyclic loading study at Dunkirk, France*. Volume 1 & 2. Offshore Technology Report OTO2000 007, Health and Safety Executive, London: 60p and 200p.

108. Jardine, R. J. and Standing, J. R. (2012). Field axial cyclic loading experiments on piles driven in sand. *Soils and Founds.* **52**(4): 723 – 736.

109. Jardine R. J., Puech A. and Andersen K. H. (2012). Cyclic loading of offshore piles: potential effects and practical design. *Proc. 7th Int. Conf. on Offshore Site Investigation and Geotechnics*, London, UK: 59–97.

110. Jardine, R. J., Zhu, B. T, Foray, P. and Dalton, C. P. (2009). Experimental arrangements for the investigation of soil stresses developed around a displacement pile. *Soil and Founds*, **49**(5): 661–673.

111. Jardine, R. J., Zhu, B. T., Foray, P. and Yang, Z. X. (2013a). Measurement of stresses around a closed-ended displacement piles in sand. *Géotechnique,* **63**(1):1 – 17.

112. Jardine, R. J., Zhu, B. T., Foray, P. & Yang, Z. X. (2013b). Interpretation of stress measurements made around closed-ended displacement piles in sand. *Géotechnique,* [http://dx.doi.org/10.1680/geot.9.P.138]

113. Jeanjean, P., Watson P. G., Kolk, H.J. and Lacasse, S. (2010). RP 2GEO: The new API recommended practice for geotechnical engineering. *Offshore Technology Conference, Houston. Texas.* Paper 20631.

114. Jiang, M.J., Yu, H-S and Harris, D. (2006). Discrete element modelling of deep penetration in granular soils. *Int. J. for Numerical and Analytical Methods in Geomechanics*, **30**(4): 335–361.

115. Johnston, I. W. (1972). *Electro-osmosis and porewater pressures - their effect on the stresses acting on driven piles*. PhD thesis, Southampton Univ.

116. Johnston, I. W., Lam, T. S. K. and Williams, A. F. (1987). Constant Normal Stiffness Direct Shear Testing for socketed pile design in weak rock. *Géotechnique,* **37**: 83-89.

117. Joshi, R. C., Achari, G., Kaniraj, S. R., and Wijiweera, H. (1995). Effect of aging on the penetration resistance of sands. *Can. Geotech. J.*, **32**(5): 767–782.

118. Julio, R. M. H. (2009). *Comportement des pieux et des groupes de pieux sous chargement latéral cyclique.* These de doctorat, Ecole Nationale des Ponts et Chaussees, Paris, France (in French).

119. Karlsrud, K., Nadim, F. and Haugen, T. (1986). Piles in clay under cyclic axial loading: field test and computational modelling. *Proc. 3rd Int. Conf. on Numerical Methods in Offshore Piling*, Nantes Paris, France: 165–190.

120. Kelly, R. (2001). *Development of a Large Diameter Ring Shear Apparatus and its use for Interface Testing.* PhD thesis, University of Sydney.

121. Kerisel, J. (1964). Deep foundations, basic experimental facts. *Proc. N. American Conf. in Deep Founds, Mexican Soc. Soil. Mech*, 1:5–44.

122. Kishida, H. and Uesugi, M. (1987). Tests of the interface between sand and steel in the simple shear apparatus. *Géotechnique* **37**(1): 45–52.

123. Klotz, E. U. and Coop, M. R. (2001). An investigation of the effect of soil state on the capacity of driven piles in sands. *Géotechnique* **51**(9): 733-751.

124. Kolk, H. J., Baaijens, A. E., & Senders, M. (2005a). Design criteria for pipe piles in silica sands. *Proc. 1st Int. Symp. on Frontiers in Offshore Geotechnics*. Perth: 711–716.

125. Kolk, H.J., Baaijens, A.E., Shafei, K.A. and Dakhil, O.A. (2005b). Axial Load Tests on Pipe Piles in Very Dense Sands at Ras Tanajib. *Proc. of the 1st Int. Symp. on Frontiers in Offshore Geotechnics*. Perth: 765–771.

126. Kolk, H.J., Baaijens, A.E. and Vergobbi, P. (2005c). Results from Axial Load Tests on Pipe Piles in Very Dense Sands. The EURIPIDES JIP. *Proc. of the 1st Int. Symp. on Frontiers in Offshore Geotechnics*. Perth: 661–667.

127. Komurka, V.E., Wagner, A.B., and Edil, T.B. (2003). *Estimating Soil/Pile Set-Up WHRP Report No. 03-05*. Wisconsin Department of Transportation, USA.

128. König F. & Grabe J. (2006). Time dependant increase of the bearing capacity of displacement piles. *Proc. Piling and Deep Found. Conf.*, DFI EFFC, Amsterdam: 709–717.

129. Krailem, S. (1988). *Stress-strain response of granular materials at very low effective stresses.* Masters Thesis, Department of Civil, Env., and Arch. Eng, Univ. of Colorado, Boulder.

130. Kulhawy, F. H. (1984). Limiting tip and side resistance: fact or fallacy? *Proc. of the Symp. on the Analysis and Design of pile Foundations.* ASCE, San Francisco, Calif.: 80-98.

131. Kuwano, R. (1999). *The stiffness and yielding anisotropy of sand*, PhD Thesis, University of London, London, UK.

132. Kuwano, R. and Jardine, R. J. (2002). On measuring creep behaviour in granular materials through triaxial testing. *Can. Geotech. J*, **39**(5): 1061–1074.

133. Kuwano, R. and Jardine, R. J. (2007). A triaxial investigation of kinematic yielding in sand. *Géotechnique* **57**(7): 563–579.

134. Lambe, T. W. and Whitman, R. V. (1979). *Soil Mechanics*. John Wiley & Sons Pub.

135. Lehane, B. M. (1992). *Experimental Investigations of Pile Behaviour Using Instrumented Field Piles*. PhD thesis, University of London (Imperial College), UK.

136. Lehane, B. M., Jardine, R. J., Bond, A. J., and Frank, R. (1993) Mechanisms of shaft friction from instrumented pile tests. *J. of Geotech. Eng*, ASCE, **119**(1): 19–35.

137. Lehane, B. M., Schneider, J. A., and Xu, X. (2005a). The UWA-05 method for prediction of axial capacity of driven piles in sand. *Proc. 1st Int. Symp. on Frontiers in Offshore Geotechnics*. Perth, Australia: 683–689.

138. Lehane, B. M., Schneider, J. A., and Xu, X. (2005b). *A review of design methods for offshore driven piles in siliceous sand*. UWA Report GEO 05358, University of Western Australia, Perth: 105pp.

139. Le Kouby, A., Canou, J., and Dupla, J.C. (2004). Behaviour of model piles subjected to cyclic axial loading. *Cyclic Behaviour of Soils and Liquefaction Phenomena*, Taylor & Francis Group, London: 159–166.

140. Levy, N.H, Einav, I. and Hull, T (2009). Cyclic shakedown of piles subjected to two-dimensional lateral loading. *Int. J. Numer. Anal. Meth. Geomech.* **33**: 1339–1361.

141. Likins, G. and Rausche, F. (2008). What constitutes a good PDA test? *The 8th Int. Conf. on the Application of Stress Wave Theory to Piles*, Lisbon, Portugal: 403–407.

142. Long, J. H., Kerrigan, J. A., and Wysockey, M. H. (1999). Measured time effects for axial capacity of driven piling. *Transportation Research Record 1663*, Paper No. 99-1183: 8-15.

143. Lo Presti, D. (1987). *Mechanical behaviour of Ticino sand from resonant column tests.* Ph.D. thesis, Politecnico Di Torino, Torino, Italy.

144. Lunne, T., Robertson, P. K., and Powell, J. J. M., (1997). *Cone Penetration Testing in Geotechnical Practice.* Spon Press-Taylor & Francis Group, USA.

145. Mahmood, A., Mitchell, J.K., and Lindblom, U. (1976). Effect of Specimen Preparation Method on Grain Arrangement and Compressibility of Sand. *Soil Specimen Preparation for Laboratory Testing*, ASTM STP 599: 169–192.

146. Mahutka, K. P., König, F. & Grabe, J. (2006). Numerical modelling of pile jacking, driving and vibratory driving. *Proc. Int. Conf. Numerical Simulation of Construction Processes in Geotechnical Engineering for Urban Environment*, Bochum: 235–246.

147. Mandolini, A., Russo, G., and Viggiani, C. (2005). Pile foundations: experimental investigations, analysis and design. *Proc. 16th Int. Conf. on Soil Mech. and Geotech. Eng*, Osaka, Japan: 177–213.

148. Martin, J. B. (1975). *Plasticity: Fundamentals and General Results*. MIT, Cambridge, MA.

149. Matsushita, M., Tatsuoka, F., Koseki, J., Cazacliu, B., Di Bennedetto, H., and Yasin, S.J.M. (1999). Time effects on the pre-pack deformation properties of sands. *Prefailure Deformation Characteristics of Geomaterials*. **1**: 681-689.

150. McClelland, B. (1974). Design of deep penetration piles for ocean structures. *J. of Geotech. Eng*, **100**(GT7): 709–747.

151. Merritt, A.S., Schroeder, F.C., Jardine, R.J., Stuyts, B., Cathie, D. and Cleverly, D. (2012). Development of pile design methodology for an offshore wind farm in the North Sea. *Proc. of the SUT 7th Int. Conf. on Offshore Site Investigation and Geotechnics,* London, UK: 439–447.

152. Meyerhof, G. G. (1951). The ultimate bearing capacity of Foundations. *Géotechnique,* **2**:301–332.

153. Meyerhof, G. G. (1953). An investigation for the foundations of a bridge on dense sand. Proc. 3rd Int. Conf. Soil Mech, Zurich **2**:66–70.

154. Meyerhof, G. G. (1976). Bearing capacity and settlement of pile foundations. *The 11th Terzaghi Lecture, J. Geotech. Eng. Div*, ASCE **102**(GT3): 197–228.

155. Monfore, G. E. (1950). *An analysis of the stress distribution in and near stress gauges embedded in elastic solid – Report No. Sp-26*. US Department of Interior Bureau of Reclamation, Denver, Col., Structural Research Laboratory.

156. Norwegian Geotechnical Institute (NGI) (2001). *Bearing Capacity of Driven Piles in Sand*. Internal report no. 525211-2, 21 January 2001.

157. Norwegian Geotechnical Institute (NGI) (2012). *Aspects of offshore wind turbine foundation design and instrumentation during foundation installation*. Presentation at OES and BGA joint meeting, ICE, London.

158. Oda, M., Nemat-Nasser, S., and Konishi, J. (1985) Stress induced anisotropy in granular masses. *Soils and Founds*, **25**(3): 85–97.

159. Overy, R. (2007). The use of ICP design methods for the foundations of nine platforms installed in the UK North Sea. *Proc. of 6th Int. Conf. on Offshore Site Investigations and Geotechnics,* London, U.K: 359–366.

160. Parker, E. J., Jardine, R. J., Standing, J. R. and Xavier, J. (1999). Jet grouting to improve offshore pile capacity. *Proc. Offshore Technology Conf.*, Houston, Texas. OTC 10828: 415–420.

161. Pelletier, J. H., Murff, J. D., and Young, A. C. (1993). Historical development and assessment of the current API design methods for axially loaded pipes. *Proc. 25th Offshore Technology Conference*, Houston, Texas. OTC 7157: 253–282.

162. Pellew, A. (2002). *Field investigations into pile behaviour in clay.* PhD thesis, University of London (Imperial College).

163. Philipponnat, G. (1980). Methode pratique de calcul d'un pieu isole a l'aide du penetrometer statique. *Rev. Fr. Geotech*. **10**: 55–64 (in French).

164. Poulos, H. G. (1988). Cyclic stability diagram for axially loaded piles. *J. of Geotech. and Geoenviron. Eng*, **114**(8): 877-895.

165. Pournaghiazar, M., Russell, A. R. and Khalili, N. (2011). Development of a new calibration chamber for conducting cone penetration tests in unsaturated soils. *Can. Geotech. J.* **48**(2): 314–321.

166. Price, G. and Wardle, I. F. (1982). A comparison between cone penetration test results and the performance of small diameter instrumented piles in stiff clay. *Proc. 2nd European Symp. on Penetration Testing (ESOPT-II)*, Amsterdam, Netherlands. **2**: 775–780.

167. Puech, A., Canou, J., Bernardini, C., Pecker, A., Jardine, R., and Holeyman, A. (2012). Solcyp: A four–year JIP on the behaviour of piles under cyclic loading. *Proc. SUT 7th Int. Conf. on Offshore Site Investigation and Geotechnics,* London, UK: 263–270.

168. Qiu, G., Henke, S., and Grabe, J. (2011). Application of a coupled Eulerian-Lagrangian approach on geomechanical problems involving large deformations. *Computers & Geotechnics*, **38**: 30–39.

169. Rad, N. S and Tumay, M. T. (1987). Factors affecting sand specimen preparation by raining. *Geotech. Testing J.*, **10**(1): 31–37.

170. Randolph M.F. (1988). The axial capacity of deep foundations in calcareous soils. *Proc. Int. Conf. on Calc. Sediments*: 837–858.

171. Randolph, M. F., Dolwin, J. and Beck, R. (1994). Design of driven piles in sand. *Géotechnique* **44**(3): 427–448.

172. Rausche, F., Goble, G. G., and Likins, G. (1985). Dynamic determination of pile capacity. *Journal of the Geotechnical Division*, ASCE, **111**(3): 367 – 383.

173. Rausche, F., Richardson, B., and Likins, G. (1996). Multiple blow CAPWAP analysis of pile dynamic records. *Proc. 5th Int. Conf. on the Application of Stress-Wave Theory to Piles*, Orlando, **1**: 435–446.

174. Renfrey, G. E., Waterton, C. A. & van Goudoever, P. (1988). Geotechnical data used for the design of North Rankin 'A' platform foundation. *Proc. Int. Conf. on Calc. Sediments*, Perth: 343–356.

175. Rimoy, S.P. and Jardine, R.J. (2011). On strain accumulation in a silica sand under creep and low level cyclic loading. *Proc. 5th Int. Symp. on Deformation Characteristics of Geomaterials (IS-Seoul)*. Seoul, Korea: 463–470.

176. Rimoy S., Jardine R. J., and Standing J. R. (2013). Displacement response to axial cycling of piles driven in sand. *Proc. of the ICE Geotech. Eng,* **166**(GE2): 131–146.

177. Ripley I., Keulers A.J.C. and Creed S.G. (1988). Conductor load tests. *Proc. Int. Conf. on Calc. Sediments*, Perth: 429–438.

178. Roark, R. J. (1954). *Formulas for stress and strain*. McGraw-Hill, New York.

179. Robinsky, E. I. and Morrison, C. F. (1964). Sand displacement and compaction around model fraction piles. *Can. Geotech. J.* **1**(2): 81–93.

180. Salgado, R. (1993). *Analysis of penetration resistance in sands*. PhD thesis, University of California, Berkeley, California.

181. Salgado, R., Mitchell, J. K., and Jamiolkowski, M. (1997). Cavity expansion and penetration resistance in sand. *J. of Geotech. and Geoenviron. Eng*, ASCE, **123**(4): 344–354.

182. Salgado, R., Mitchell, J. K., and Jamiolkowski, M. (1998). Calibration chamber size effects on penetration resistance in sand. *J. of Geotech. and Geoenviron. Eng*, ASCE, **124**(9): 878–888.

183. Samson, L., and Authier, J. (1986). Changes in pile capacity with time: Case histories. *Can. Geotech. J.,* **23**(1): 174-180.

184. Schnaid, F. and Houlsby, G.T. (1991). An assessment of chamber size effects in the calibration of in situ tests in sand. *Géotechnique*, **41**(3): 437–445.

185. Schneider, J. A. (2007). *Analysis of piezocone data for displacement pile design.* PhD thesis, School of Civil and Resource Engineering, University of Western Australia, Perth.

186. Schneider, J. A., Xu, X., and Lehane, B. M. (2008). Database assessment of CPT-based design methods for axial capacity of driven piles in siliceous sands. *J. of Geotech. and Geoenviron. Eng,* ASCE, **134**(9): 1227–1244.

187. Schmertmann, J. H. (1978). *Guidelines for Cone Penetration Test, Performance and Design. Rep. No. FHWA-TS-78-209.* U.S. Department of Transportation, Washington D.C. 145p.

188. Schmertmann, J. H. (1991). The mechanical aging of soils. *J. of Geotech. Eng.*, ASCE. **117**(9): 1288–1330.

189. Seidel, J. P., Haustorfer, I. J., and Plesiotis, S. (1988). Comparison of dynamic and static testing for piles founded into limestone. *Proc. 3rd Int. Conf. App. Stress-Wave Theory to Piles,* Ottawa, Canada: 717–723.

190. Seidel, M. (2007). Jacket substructures for the REpower 5M wind turbine. *Proc. European Offshore Wind Conference*, Berlin, Germany. online publication, http://www.marc-seidel.de/Papers/Seidel_EOW_2007.pdf (accessed 12/12/2012).

191. Shek, L. M. P., Zhang L. M. and Pang H. W. (2006). Set-up effect in long piles in weathered soils. *Proc. of the Institution of Civil Engineers, Geotech. Eng.* **159**(GE3): 145–152.

192. Sheng, D., Dieter Eigenbrod, K., and Wriggers, P. (2005). Finite element analysis of pile installation using large-slip frictional contact. *Computers and Geotechnics*, **32**(1): 17–26.

193. Silva, M. (2014). *Étude expérimentale de l'effet du temps et des chargements cycliques sur le frottement latéral le long des inclusions installées par battage dans les sols*, These de Doctorat Université de Grenoble, Grenoble, France (in French, upcoming).

194. Sim, W. W., Aghakouchak, A. and Jardine, R. J. (2013). Cyclic triaxial tests to aid offshore pile analysis and design. *Proc. of the ICE Geotech. Eng*, **166**(GE2): 111–121.

195. Skempton, A. W., Yassin, A. A. and Gibson, R. E. (1953). Theorie de la force portante des pieux dans le sable. *Annales de l'Institut Technique du Batiment et des Travaux Publics*: 63–54 (in French).

196. Skov, R. and Denver, H. (1988). Time-Dependence of Bearing Capacity of Piles. *Proc. 3rd Int. Conf. on App. of Stress-Waves to Piles*: 879–888.

197. Sommé, J (1969). La plaine maritime. *Ann Soc Geol Nord, LXXXIX*, **1**:117–126 (in French).

198. Svinkin, M. R., Morgano, C. M., and Morvant, M. (1994). Pile capacity as a function of time in clayey and sandy soils. *Proc. 5th Int. Conf. and Exhibition on Piling and Deep Foundations*, Bruges, Belgium, DFI, Hawthorne, N.J: 1.11.1 – 1.11.8.

199. Tali, B. (2011). *Comportement de l'interface sol-structure sous solicitations cycliques; Application au calcul des fondations profondes*. These de Doctorat, Université Paris-est, Paris, France (in French).

200. Tan, S. L., Cuthbertson, J., and Kimmerling, R. E. (2004). Prediction of pile set-up in non-cohesive soils. *Current practices and future trends in deep foundations, ASCE, Geotech. Special Pub.* **125**: 50–65.

201. Takesue, K., Sasao, H. and Matsumoto, T. (1998). Correlation between ultimate pile skin friction and CPT data. *Geotechnical Site Characterization.* Balkema Pub, Rotterdam, Netherlands. **2**: 1177–1182.

202. Tatsuoka, F. (2011). Laboratory stress-strain tests for developments in geotechnical engineering research and practice. *Bishop Lecture in Proc. 5th Int. Symp. on Deformation Characteristics of Geomaterials (IS-Seoul)*. Seoul, Korea: 3–50.

203. Tavenas, F. (1969). The bearing capacity of friction piles in sand-results of loading tests, *7th Int. Conf. Soil Mech. Found. Eng*, Speciality Session No. 8, Mexico.

204. Tavenas, F., and Audy R. (1972). Limitations of the driving formulas for predicting the bearing capacities of piles in sand. *Can. Geotech. J,* **9**(1): 47-62.

205. Terzaghi, K. (1943). *Theoretical soil mechanics*. J Wiley & Sons, New York.

206. Thomas, S. (1990). *Geotechnical investigation of UK test sites for the foundations of offshore structures.* OTH Report 89 294, Department of Energy, HMSO, London.

207. Timoshenko, S. P. and Woinowsky-Krieger, S. (1959). *Theory of plates and shells*. Mcgraw-Hill Companies, New York.

208. Tomlinson, M. J. (1996). Recent advances in driven pile design. *Ground Engineering*, **29**(10): 31–33.

209. Toolan, F. E., Lings, M. L. and Mirza, U. A. (1990). An appraisal of API RP2A recommendations for determining skin friction of piles in sands. *Proc. 22nd Offshore Technol Conf. Houston*, OTC 6422 4: 33 – 42.

210. Tory, A. C. and Sparrow, R. W. (1967). The influence of diaphragm flexibility on the performance of an earth pressure cell. *Journal of scientific Instruments*. **44**(9): 781–785.

211. Tsuha, C. H. C., Foray, P. Y., Jardine, R. J., Yang, Z. X., Silva, M. and Rimoy, S. (2012). Behaviour of displacement piles in sand under cyclic axial loading. *Soils and Founds,* **52**(3): 393–410.

212. Tucker, L. M. and Briaud, J-L. (1988). *Analysis of the pile load tests program at the lock and dam 26 replacement project – GL – 88 – 11*. Civil Engineering Department, Texas A & M University, College Station: 63pp.

213. Tumay, M. T. and Fakhroo, M. (1982). *Friction Pile Capacity Prediction in Cohesive Soils using Electric Quasi-Static Penetration Tests, Interim Research Rep. No. 1*. Louisiana Department of Transportation and Development, Research and Development Section, Baton Rouge, La.

214. Vaid, Y.P., and Negussey, D. (1984). Relative density of pluviated sand samples. *Soils and Founds*, **24**(2): 101-105.

215. Van Weele, A. F. (1979). Pile bearing capacity under cyclic loading compared with that under static loading. *Proc. 2nd Int. Conf. Beh. Off. Structures*, London: 475–488.

216. Vesic, A. S. (1963). Bearing capacity of deep foundations in sand. *National Academy of Sciences, National Research Council, Highway Research Record* **39**: 112–153.

217. Vesic, A. S. (1965). Ultimate loads and settlements of deep foundations in sand. *Pro. Symp. Bearing Capacity and Settlement of Foundations*, Duke University, USA: 53–68.

218. Vesic, A. S. (1967). *A study of bearing capacity of deep foundations. Final Report, Project B-189*, Georgia Institute of Technology, Atlanta, GA, USA.

219. Vesic, A. S. (1970). Tests on instrumented piles, Ogeechee River site. *J. of the Soil Mech. and Founds. Div*, ASCE, **96**(SM2): 561–584.

220. Vesic, A. S. (1972). Expansion of cavities in infinite soil mass. *J. of the Soil Mech. and Founds. Div*, ASCE, **98**(SM3): 265–290.

221. Vijayvergiya, V. N. (1977), Load-movement characteristics of piles, *Proc. 4th Annual Symposium of the Waterways, Ports, Coastal and Ocean Division of American Society of Civil Engineers*, **2**: 269–284.

222. Weiler, W. A., and Kulhawy, F. H. (1982). Factors affecting stress cell measurements in soil. *J. of the Soil Mechanics and Foundations Division*, ASCE: **108**:1529 – 1548.

223. White, D. J. (2002). *An investigation into the behaviour of pressed in piles*. PhD dissertation, Cambridge University: 384.

224. White, D. J. (2005). A general framework for shaft resistance on displacement piles in sand. *Proc. 1st Int. Symp. on Frontiers in Offshore Geomechanics (ISFOG)*, Perth. Taylor & Francis, London: 697–703.

225. White, D. J. and Lehane, B. M. (2004). Friction fatigue on displacement piles in sands. *Géotechnique* **54**(10): 645-658.

226. White, D. J., Schneider, J. A. and Lehane B, M. (2005). The influence of effective area ratio on shaft friction displacement piles in sand. *Proc. 1st Int. Symp. on Frontiers in Offshore Geomechanics (ISFOG)*, Perth. Taylor & Francis, London: 741–747.

227. White, D. J. and Zhao, Y. (2006). A model-scale investigation into 'set-up' of displacement piles in sand. *6th International Conference on Physical Modelling in Geotechnics*, Hong Kong, China.

228. White, D. J. & Bolton, M. D. (2004). Displacement and strain paths during plane-strain model pile installation in sand, *Géotechnique* **54**(6): 375–397.

229. White, D. J. and Bolton, M. D. (2005). Comparing CPT and pile base resistance in sand. *Proc. of the ICE Geotech. Eng,* **158**(GE1): 3–14.

230. Xie, L.Z. (1999). *Static behaviour of single piles subjected to repeated and reciprocating loadings*. Sichuan Building Research Unit. China.

231. Xu, X., Schneider, J. A., and Lehane, B. M. (2008). End bearing of open and closed ended driven piles in siliceous sand using the CPT. *Can. Geotech. J.* **45**(8): 1130–1141.

232. Yang, L. and Liang, R. (2009). Incorporating setup into load and resistance factor design of driven piles in sand. *Can. Geotech. J.* **46**(3): 296–305.

233. Yang, Z. X., Jardine, R. J., Zhu, B. T., Foray, P., and Tsuha, C. H. C. (2010). Sand grain crushing and interface shearing during displacement pile installation in sand, *Géotechnique*, **60**(6): 469-482.

234. Yang, Z. X., Jardine, R. J., Zhu, B. T. and Rimoy, S. P (2013). The stresses developed round displacement piles penetrating in sand, *J. of Geotech. and Geoenviron. Eng*, ASCE. (In review)

235. York, D. L., Brusey, W. G., Clemente, E. M., and Law, S. K. (1994). Set-up and relaxation in glacial sand. *J. of Geotech. Eng*, ASCE, **120**(9): 1498-1513.

236. Yu H. S. (2000). *Cavity Expansion Methods in Geomechanics*. Kluwer Academic Publishers, Netherlands.

237. Yu, H. S. and Houlsby, G. T. (1991). Finite cavity expansion in dilatant soils: loading analysis. *Géotechnique*, **41**(2), 173–183.

238. Zai, J. (1988). Pile dynamic testing experience in Shanghai. *Proc. 3rd Int. Conf. on App. of Stress-Waves to Piles*, Ottawa, Canada: 781–792

239. Zhang, C., Nguyen, G.D., and Einav, I. (2013). The end-bearing capacity of piles penetrating into crushable soils, *Géotechnique*, DOI: 10.1680/geot.11.P.117.

240. Zhu, B. T. and Yang, Z. X. (2009). *Data reduction programs for analysis of miniature soil stress sensors readings*. Imperial College Internal Report.

241. Zhu, B. T., Jardine, R. J., and Foray, P. (2009). The use of miniature soil stress measuring sensors in applications involving stress reversals. *Soils and Foundations*, **49**(5): 675-688.

List of figures

Figure 1-1: First-time tension tests to failure on three field tests of 457mm diameter by 19m long open-ended driven pipe piles in dense silica Dunkirk marine sands (Jardine et al. 2006). 26
Figure 1-2: Interaction diagram on axial cyclic response of displacement piles in Dunkirk marine silica sands of normalised loading parameters Q_{cyclic}/Q_T against Q_{mean}/Q_T with the number of cycles to failure and tentative stable, meta-stable and unstable zones (Jardine & Standing 2012). 26
Figure 2-1: Bearing capacity factor N_q from Lambe & Whitman (1979) with the plotted field data points from Coyle & Castello (1981). 30
Figure 2-2:(a) Relation of cavity expansion limit pressure and end-bearing capacity (Randolph et al. 1994) (b) Slip pattern under pile tip or cone penetrometer (Salgado 1993). 31
Figure 2-3: Pile end resistances of jack installed ICPs LB1 and LB2 compared with the in-situ sand CPT q_c profile at Labenne loose dune silica sand (Lehane 1992) and with the RP2 GEO (2011) main text design. 32
Figure 2-4: Pile end resistances of jack installed ICPs DK1 to DK3 compared with the in-situ sand CPT q_c profile BRE CPT1 at Dunkirk medium dense marine silica sand (Chow 1997) and with the RP2 GEO (2011) main text design. 33
Figure 2-5: Normalised pile base resistance, $q_{b,0.1D}/q_c$ plotted against diameters of closed-ended displacement piles in silica sands (Chow 1997). 34
Figure 2-6: White & Bolton (2005) q_c-normalised closed-ended displacement piles in sands base plunging resistance q_b/q_c plotted against pile diameter for the sites Dunkirk (DK), Labenne (LB), Kalo (K), Hunter's Point (HP), Baghdad (BG), Akasaka (AK), Drammen (D), Hsia Ta (HT) and Lower Arrow Lake (E) from Chow (1997) database. 35
Figure 2-7: (A) A pile in sand under compression load during installation process (B) Residual stresses at the end of the installation or compression test. (C) Variation of residual load with depth (Alawneh & Malkawi 2000). 37
Figure 2-8: Load distributions along a displacement pile with residual axial loads showing the true load and the apparent loads (true minus residual) on neglect of residual load (Fellenius 2002). 38
Figure 2-9: Borehole log and in-situ test results for loose dense dune sand at Labenne, France (Lehane, 1992). 45
Figure 2-10: Dunkirk dense silica marine sand borehole log and CPT profile (Chow, 1997). 45
Figure 2-11: Displacement piles τ_{rz} and f_s measurements during installation in Labenne dune sand by Lehane (1992) and the corresponding API RP2 GEO (2011) main text design shaft resistances. 46
Figure 2-12: Local shear stress measurements from the Surface Stress Transducers during installation of displacement pile DK2 in medium dense Dunkirk marine silica sand (Chow, 1997). 46
Figure 2-13: Stationary radial effective stresses during displacement pile DK2 installation in medium dense Dunkirk marine silica sand (Chow, 1997). 47
Figure 2-14: Labenne loose dune sand displacement piles static loading interface effective stress paths, (Lehane 1992). 47
Figure 2-15: (a) Distribution of shaft friction on a multi–friction sleeve CPT instrument with 43.7mm diameter (DeJong, 2001), (b) Author's suggested alternative trend. 49
Figure 2-16: Influence of loading cycles during installation on stationary horizontal stress (a) normalised horizontal stress against distance above pile tip; (b) normalised horizontal stress against number of cycles (White and Lehane, 2004). 50
Figure 2-17: Jacking record for a precast concrete pile in sand installed by 1.5m long jack–strokes to a depth of 6.3m followed by 0.075m long strokes to a depth of 7.95m (White & Lehane, 2004).50
Figure 2-18: Influence of number of loading cycles (i.e. hammer blows) on shaft resistance in uncemented weak marine calcareous sands at North Rankin, (White, 2005). 51
Figure 2-19: Effect of installation method on radial stresses (a) at the end of each push, and (b) at the end of each pause for CPT1 and CPT2 (Jardine et al. 2013a). 53

Figure 2-20: Comparative influences of number of cycles N (a & b) and relative pile tip depth h/R (c & d) on moving radial stresses (Jardine et al. 2013a). 54
Figure 2-21: Q_c/Q_m pile compression capacity using API Main text method as a function of sand density index (Jeanjean et al. 2010). 58
Figure 2-22: Q_c/Q_m pile compression capacity using API Main text method as a function of pile slenderness ratio (Jeanjean et al. 2010). 58
Figure 2-23: Q_c/Q_m pile tension capacity using API Main text method as a function of sand density index (Jeanjean et al. 2010). 59
Figure 2-24: Q_c/Q_m pile tension capacity using API Main text method as a function of pile slenderness ratio (Jeanjean et al. 2010). 59
Figure 2-25: Estimate of pile length required to support a 5MW offshore wind turbine (a) Pile diameter, D = 2.5m (b) D = 1.5m (Gavin et al. 2011). 63
Figure 3-1: Idealised schematic of pile set-up phases showing change in the ratio of final pile capacity Q_{final} to initial capacity $Q_{initial}$ with log time (Komurka et al. 2003). 68
Figure 3-2: Arching mechanism around the pile shaft of a displacement pile in sands (Chow 1997). 68
Figure 3-3: Simple analysis of radial variation in stress near pile after unloading behind pile base (White et al. 2005). 69
Figure 3-4: Shaft capacities normalised by ICP-05 method predictions against time for first-time and pre-failed tension tests as described in the legend for reaction piles R3 and R4 used in the GOPAL project (after Jardine et al. 2006). 70
Figure 3-5: Normalised static axial tension capacities of intact aged piles plotted against the time of testing after installation. 71
Figure 3-6: Normalised static axial tension capacities of intact and re-tested aged piles plotted against the time of testing after installation. 72
Figure 3-7: Normalised static axial compression total capacities of intact aged piles plotted against the time of testing after installation. 73
Figure 3-8: Normalised static axial compression base capacities of re-tested aged piles plotted against the time of testing after installation. 73
Figure 3-9: Static axial compression total capacities normalised by reference dynamic capacities plotted against the time of testing after installation. 74
Figure 3-10: Single re-strikes dynamic axial compression total capacities normalised by the reference dynamic capacities plotted against the time of testing after installation. 74
Figure 3-11: Normalised dynamic axial compression total capacities plotted against the time of testing after installation. 75
Figure 3-12: Normalised static and dynamic axial compression total capacities plotted against the time at testing after installation. 76
Figure 3-13: Normalised axial compression total capacities of re-tested piles plotted against the number of load re-test. 76
Figure 3-14: Potential ageing benefit loss of axial compression capacities of re-tested piles. 77
Figure 3-15: Normalised static and dynamic axial compression shaft capacities plotted against the time at testing after installation. 77
Figure 3-16: 10 days' aged piles normalised capacities (a) from compression load tests plotted against pile diameter (b) from tension load tests plotted against 1/ pile diameter. 79
Figure 3-17: Normalised axial compression total capacities versus time at testing after installation for (a) 'Coastal' (b) 'Non-coastal' sites, assessing potential effects of physiochemical actions on ageing trends. 80
Figure 4-1: Illustration of potential cyclic effects for WSD FoS = 1.5 design conditions compared to Dunkerque contours of Stable, Meta-stable and Unstable condition in a normalised cyclic interaction diagram. 90

Figure 4-2: Peak and trough shear stresses developed on the instrumented sections of the ICP after 61 cycles of axial load (Q_{cyclic}/Q_T = 0.31, Q_{mean}/Q_T = 0.5) in Dunkirk marine silica sand (Chow 1997). 91
Figure 4-3: Pile top movement versus initial number of load (Q_{max}/Q_{min}) cycles applied (Chan & Hanna 1980). 95
Figure 4-4: Pile top movement versus overall number of load (Q_{max}/Q_{min}) cycles applied (Chan & Hanna 1980). 95
Figure 4-5: Shaft shear stresses evolution with time (s) during displacement controlled axial cyclic loading of displacement pile M6 in stress controlled calibration chamber (Tali, 2011). 96
Figure 4-6: Base stress q_b evolution with time (s) during displacement controlled axial cyclic loading of displacement pile M6 in stress controlled calibration chamber (Tali, 2011). 96
Figure 4-7: Static Shaft friction before and after the cyclic loading test M6 plotted against pile head settlement from compressive monotonic tests (Tali 2011). 97
Figure 4-8: Static base resistance before and after the cyclic loading test M6 plotted against pile head settlement from compressive monotonic tests (Tali 2011)..... 97
Figure 4-9: Total load before and after the cyclic loading test M6 plotted against pile head settlement from compressive monotonic tests (Tali 2011). 97
Figure 4-10: Mini-ICP displacement piles in silica NE34 sand axial cyclic behaviour stability interaction diagram after Tsuha et al. (2012). N_f number of cycles to failure; where no number is shown there was no cyclic failure. 99
Figure 4-11: Interface effective stress paths from the axial cyclic loading with Mini–ICP tests typifying (a) Stable, (b) Meta- Stable and (c) Unstable tests (Tsuha et al. 2012)..... 100
Figure 4-12: Sand mass effective stress paths for the axial cyclic loading behaviour of Mini–ICP after Tsuha et al. (2012) (a) Stable (b) Meta–stable (c) Unstable (Tsuha et al. 2012)..... 101
Figure 4-13: Comparison of shear stress reduction in CNS (displacement ±1mm, K = 1600kPa/mm) and model displacement pile tests in calcareous sand (Airey et al. 1992). 102
Figure 4-14: Vertical and shear displacements from two-way cyclic loading tests in a University of Sydney 1m diameter interface ring shear apparatus (Kelly, 2001). 104
Figure 5-1: Above ground layout at the 3S-R Laboratory Calibration Chamber. 107
Figure 5-2: Vertical section of the instrumented 3S-R Laboratory CC with the Mini–ICP installed in the final arrangement deployed during this study for tests ICP07 and 08. 107
Figure 5-3: Cone resistance q_c profiles for alternative top-membrane designs (Jardine et al. 2013a). 109
Figure 5-4: Moving radial stress profiles recorded on the Mini–ICP pile shaft clusters showing stress peaks at the shallow depth of the 3S-R calibration chamber. 109
Figure 5-5: Illustration of the zones of sand deformations around a penetrometer in an ideal calibration chamber (after Salgado et al. 1998). 111
Figure 5-6: Illustrations of (a) calibration chambers classical boundary conditions (Salgado et al. 1998) (b) servo–controlled free field simulator calibration chamber (Huang & Hsu 2005). 112
Figure 5-7: Schematics of the miniature stress sand sensors employed in this study (after supplier's data sheets). 115
Figure 5-8: Kyowa 7MPa miniature stress sensor showing cell-action effect interaction of output and normal stress applied with dense GA39 Nemours sand in the Imperial College special calibration oedometer. 117
Figure 5-9: Radial stresses on a 3MPa PDA-7100 placed at 144mm (8R) from the pile axis and 0.73m (h/R = 14.4) below ground level during Mini–ICP installation in ICP05 test involving dry GA39 Nemours sand. 119
Figure 5-10: Sand stress sensor calibration rig (Zhu et al. 2009). 120
Figure 5-11: Load – Unload and reload calibration sequences adopted for the miniature sand stress sensors for the four nominal capacity ranges. 120
Figure 5-12: Normal load versus stress sensor's output response in fresh loading calibration. 121
Figure 5-13: Normal load versus stress sensor's output response during unloading calibration. 121

Figure 5-14: Normal load versus stress sensor's output response for re-loading calibration. 121
Figure 5-15: Mini–ICP illustrated (after Jardine et al. 2009). 126
Figure 5-16: Mini-ICP cluster schematics described (after Jardine et al. 2009)..... 127
Figure 5-17: Strain gauging schematic of the Cambridge-type earth pressure cell Surface Stress Transducers on board the Mini–ICP by Cambridge In-situ (2009). 128
Figure 5-18: Circuit diagram for the strain gauging of the SSTs on board the Mini–ICP by Cambridge In-situ (2009). 128
Figure 5-19: Calibration of radial and shear stress transducers (SSTs) by a dead-weight bi-axial calibration jig. 131
Figure 5-20: (a)Budenberg deadweight calibration jig calibrating cluster C of the Mini–ICP and (b) the triaxial loading frame for full-length calibration of the Mini–ICP ALCs. 131
Figure 5-21: SSTs radial stress transducer output versus applied normal stress/ load on a typical Mini–ICP calibration sequence. 132
Figure 5-22: SSTs shear stress transducer output versus applied shear stress/ load on a typical Mini–ICP calibration sequence. 132
Figure 5-23: ALCs output versus load on a typical Mini–ICP calibration sequences. 132
Figure 5-24: Mini–ICP transducers check for measurements resolution and drifts and over a 10 days period (a) Radial stresses (b) Shear stresses and (c) Axial loads. 133
Figure 5-25: Deadweight-type model pile driving system installed at the calibration chamber pile axis. 135
Figure 6-1: Interface ring shear tests on medium–dense to dense (I_D = 72%) GA39 Nemours sand against roughened (R_{cla} 3.1 ± 0.3μm) stainless steel..... 139
Figure 6-2: Particle Size Distribution for Dunkirk sand from CLAROM Borehole (after Chow 1997). 141
Figure 6-3: Particle size distribution for NE34 Fontainebleau sand (after Yang et al. 2010) compared to Dunkirk sand. 141
Figure 6-4: Microscope images at same scale (10x) of (a) NE34 and (b) GA39 from Microsurf 3D Optical Profiler by Nanotech. 143
Figure 6-5: (a) NE34 and GA39 Sand PSD comparisons (b) NE34 and GA39 sands' particle Aspect Ratio (AR), Convexity (C) and Sphericity (S) comparisons as obtained with Sympatec Gradis QicPic apparatus, employing FERET minimum particle size scale. 144
Figure 6-6: Sand rainer on the calibration chamber in preparation of the sand chamber for test ICP04. 147
Figure 6-7: Illustration of a typical sand raining arrangement used for calibration chamber sand pluviation (Salgado et al. 1998). 148
Figure 6-8: Example of volume straining during pressurisation of dry NE34 sand mass chamber for test ICP04. 148
Figure 6-9: 3S-R calibration sand chambers preparation illustration. 150
Figure 7-1: Illustration of selection of end–of–push (moving) and end–of–pause (stationary) data values based on the jack–stroke installed model piles. 159
Figure 7-2: (a) Pile end-bearing resistances of all continuously monitored installations in this study (b) The current study piles end-bearing resistances compared to Jardine et al. (2013a) tests CPT1 to Mini-ICP03. 159
Figure 7-3: Lateral boundary stresses during Mini-ICP installations in tests ICP07 and 08 with boundary condition BC5. 161
Figure 7-4: Local shear stress profiles from Mini-ICP cluster A at h/R = 8.94 or CPT friction sleeve at h/R ≈ 5.7. 162
Figure 7-5: Density indices of all the NE34 sand test chambers in this study after the Baldi et al. (1986) end-bearing resistances correlation chart. 163
Figure 7-6: CPT tip resistances in dry, saturated and unsaturated sand specimens prepared by pluviation method (I_D = 61%) (Pournaghiazar et al. 2011). 164

Figure 7-7: Pile base residual loads as a proportion of the local maximum installation base resistances of all the continuously monitored piles during installation. 165
Figure 7-8: Interface local moving shear stresses from the Mini-ICP installed in NE34 sand (a) cluster A (b) cluster B. 166
Figure 7-9: q_b normalised interface local moving shear stresses from the Mini-ICP installed in NE34 sand (a) cluster A (b) cluster B. 167
Figure 7-10: Interface local stationary shear stresses from the Mini-ICP installed in NE34 sand (a) cluster A (b) cluster B. 168
Figure 7-11: q_b–normalised interface local stationary shear stresses from the Mini-ICP installed in NE34 sand (a) cluster A (b) cluster B. 168
Figure 7-12: Interface moving shear stresses from trend-lines on end–of–push axial loads during the Mini-ICP piles installations in NE34 sand (a) at cluster A location (b) at cluster B location. 169
Figure 7-13: Interface moving shear stresses from the Mini-ICP SST versus equivalents from polynomial ALC loads fit trends. 169
Figure 7-14: Base–to–head moving average interface shear stresses on Mini-ICP installing in NE34 sand. 170
Figure 7-15: Interface local shear stresses from the Mini-ICP clusters A in dry GA39 sand (ICP05) compared to dry NE34 sand (ICP04) (a) moving (b) stationary. 171
Figure 7-16: Base–to–head moving average interface shear stresses on mini-ICP installing in GA39 sand. 171
Figure 7-17: q_b normalised interface local shear stresses from the Mini-ICP cluster A in dry GA39 sand compared to dry NE34 sand (a) moving (b) stationary. 172
Figure 7-18: Interface moving local radial stresses at cluster (a) A and (b) B from the Mini–ICP in NE34 sand. 173
Figure 7-19: Interface stationary local radial stresses at cluster (a) A and (b) B from the Mini-ICP installed in NE34 sand. 173
Figure 7-20: Interface moving radial stresses from the Mini-ICP clusters versus from ALCs axial loads polynomial fits. 174
Figure 7-21: q_b–normalised interface local moving radial stresses at clusters (a) A and (b) B from the Mini-ICP installed in NE34 sand. 174
Figure 7-22: q_b–normalised interface local stationary radial stresses at clusters (a) A and (b) B from the Mini-ICP installed in NE34 sand. 175
Figure 7-23: Interface local radial stresses from Mini–ICP cluster A installed in dry GA39 sand compared to that in dry NE34 sand (a) moving (b) stationary. 175
Figure 7-24: q_b–normalised interface local radial stresses from Mini–ICP cluster A installed in dry GA39 sand compared to that in dry NE34 sand (a) moving (b) stationary. 176
Figure 7-25: End–of–push moving stresses and end–of–pause stationary stresses illustrated by ICP07 test radial stress sensor at r = 2R, z = 15.8R in 152kPa surcharged dry NE34 with boundary condition BC5. 178
Figure 7-26: Sand mass radial stress sensors profiles during Mini-ICP07 installation into 152kPa surcharged dry NE34 with boundary condition BC5. 179
Figure 7-27: Test ICP07 radial stresses during Mini-ICP installation in dry NE34 sand at (a) end–of–push stages (moving stresses), and (b) end–of–pause stages (stationary stresses). 181
Figure 7-28: Normalised radial stresses at r/R = 2 for jack–stroke installed displacement piles in NE34 sand (a) moving (b) stationary stages. 181
Figure 7-29: Normalised radial stresses at r/R = 3 for jack–stroke installed displacement piles in NE34 sand (a) moving (b) stationary stages. 182
Figure 7-30: Normalised radial stresses at r/R = 5 for jack stroke installed displacement piles in NE34 sand (a) moving (b) stationary stages. 182
Figure 7-31: Normalised radial stresses at r/R = 8 for jack stroke installed displacement piles in NE34 sand (a) moving (b) stationary stages. 183

Figure 7-32: Radial (a) moving and (b) stationary stresses at r/R = 3 for cyclically jacked piles in dry GA39 sand (ICP04) compared to dry NE34 sand (ICP04).....184
Figure 7-33: Radial (a) moving and (b) stationary stresses at r/R = 5 for cyclically jacked piles in dry GA39 sand (ICP04) compared to dry NE34 sand (ICP04).....184
Figure 7-34: Radial (a) moving and (b) stationary stresses at r/R = 8 for cyclically jacked piles in dry GA39 sand (ICP04) compared to dry NE34 sand (ICP04).....185
Figure 7-35: Exemplar 3D profile of normalised moving radial stresses for cyclically jacked Mini–ICP04 in dry NE34 sand. 186
Figure 7-36: Normalised moving radial stress contours σ'_{rm}/q_b in % around jack–stroke installed Mini-ICP test ICP04 with dry NE34 sand (a) full length (b) near pile base.....186
Figure 7-37: Normalised stationary radial stress contours σ'_{rs}/q_b in % around jack–stroke installed Mini-ICP test ICP04 with dry NE34 sand (a) full length (b) near pile base.....187
Figure 7-38: Normalised moving vertical stress contours σ'_{zm}/q_b in % around jack–stroke installed Mini-ICP test ICP04 in dry NE34 sand (a) full length (b) near pile base.....187
Figure 7-39: Normalised stationary vertical stress contours σ'_{zs}/q_b in % around jack–stroke installed Mini-ICP test ICP04 in dry NE34 sand (a) full length (b) near pile base.....188
Figure 7-40: Normalised moving hoop stress contours $\sigma_{\theta m}/q_b$ in % around jack–stroke installed Mini-ICP test ICP04 in dry NE34 sand (a) full length (b) near pile base.....188
Figure 7-41: Normalised stationary hoop stress contours $\sigma_{\theta s}/q_b$ in % around jack–stroke installed Mini-ICP test ICP04 in dry NE34 sand (a) full length (b) near pile base.....189
Figure 7-42: Normalised moving radial stress contours σ'_{rm}/q_b in % around jack–stroke installed Mini-ICP test ICP05 in dry GA39 sand (a) full length (b) near pile base. 189
Figure 7-43: Normalised stationary radial stress contours σ'_{rs}/q_b in % around jack–stroke installed Mini-ICP test ICP05 in dry GA39 sand (a) full length (b) near pile base. 190
Figure 7-44: Normalised moving vertical stress contours σ'_{zm}/q_b in % around jack–stroke installed Mini-ICP test ICP05 in dry GA39 sand (a) full length (b) near pile base. 190
Figure 7-45: Normalised stationary vertical stress contours σ'_{zs}/q_b in % around jack–stroke installed Mini-ICP test ICP05 in dry GA39 sand (a) full length (b) near pile base. 191
Figure 7-46: Normalised moving hoop stress contours $\sigma_{\theta m}/q_b$ in % around jack–stroke installed Mini-ICP test ICP05 in dry GA39 sand (a) full length (b) near pile base. 191
Figure 7-47: Normalised stationary hoop stress contours $\sigma_{\theta s}/q_b$ in % around jack–stroke installed Mini-ICP test ICP05 in dry GA39 sand (a) full length (b) near pile base. 192
Figure 7-48: Normalised moving radial stress profile in the sand mass at h/R = 0 of jack–stroke installed Mini-ICP in NE34 sand. 193
Figure 7-49: End–of–installation normalised radial stress profiles around the jack–stroke installed Mini-ICP piles in NE34 sand. 194
Figure 7-50: End–of–installation stationary circumferential stress profile around the jack stroke installed Mini-ICP piles in NE34 sand. 194
Figure 7-51: End of installation q_b normalised radial and circumferential stresses profiles interaction around the Mini-ICP piles installed in NE34 sand. 195
Figure 8-1: Moving radial stresses around Mini–ICP installations in NE34 sand chambers at r/R = 8 compared to field measurements by Chow (1997) normalised by (a) $q_b/[\sigma'_{z0}/p_a]^{0.13}$ (b) the equalised radial stresses, σ'_{rc} applying before installation of Mini-ICP or DK2B. 198
Figure 8-2: Interpreted profiles for four h/R values of stationary (a) radial effective stresses and (b) circumferential stresses developed after final stroke of Mini-ICP installation; after Jardine et al (2013b). 199
Figure 8-3: Radial effective stresses normalised by CPT q_c versus h/R for jack stroke installed partially plugging driven open-ended stainless steel model pile (Gavin & Lehane 2003). 201
Figure 8-4: q_b normalised radial stresses from Mini-ICP installations in NE34 sand chambers r/R = 8 compared to Gavin & Lehane (2003) measurements from open-ended pile installation r/R = 7.6 (a) moving (b) stationary.....202

Figure 8-5: Comparison of sand radial stresses around displacement piles in (a) Gavin and Lehane (2003) after re-plotting using equivalent radius R* and (b) Jardine et al. (2013a) (after Yang et al. 2013). 202
Figure 8-6: Sand mass radial stresses around Allard (1990) centrifuge driven closed-ended model pile tests shown in (a) and (b) compared to the Author's jack stroke installed Mini–ICP piles in (c) and (d). 204
Figure 8-7: Comparison of radial stresses (a) developed during steady penetration as simulated in finite element analysis by Sheng et al. (2005) and (b) measured in Mini-ICP tests. 205
Figure 8-8: Radial stresses from (a) numerical predictions made with two h/R values by Qiu et al. (2011); (b) numerical predictions made with three initial densities by Henke et al. (2010) from Yang et al. (2013). 206
Figure 8-9: Normalised stationary (a) radial (b) circumferential stresses developed at various h/R positions from numerical simulations by Einav (2012). 207
Figure 9-1: ICP04 EOD pile load test defined by global displacements of the pile cap and the local LVDT on the Mini–ICP. 210
Figure 9-2: Relationship between pile jack and LVDT displacements to account for compliance. 211
Figure 9-3: ICP04 EOD load–displacement behaviour showing total, base and shaft resistances.. 212
Figure 9-4: ICP06 EOD load–displacement behaviour showing total, base and shaft resistances.. 212
Figure 9-5: ICP07 EOD load–displacement behaviour showing total, base and shaft resistances.. 213
Figure 9-6: ICP08 EOD load–displacement behaviour showing total, base and shaft resistances.. 214
Figure 9-7: CPT09 EOD load–displacement behaviour showing the total and base resistances. ... 215
Figure 9-8: CPT10 EOD load–displacement behaviour showing the total and base resistances. ... 216
Figure 9-9: Lateral boundary membranes stresses during CPT09 and CPT10 piles installations under boundary condition BC5. 216
Figure 9-10: (a) Raw and (b) q_b–normalised sleeve shear stresses in CPT09 and CPT10 installation. 217
Figure 9-11: ICP05 EOD load–displacement behaviour showing total, base and shaft resistances. 218
Figure 9-12: MiP01 EOD load–displacement behaviour showing the total pile resistance. 218
Figure 9-13: DI EOD load–displacement behaviour showing the total pile resistance and tension resistance. 219
Figure 9-14: Chamber lateral boundary stress changes during the driving of model driven pile DI applying BC5 boundary condition. 220
Figure 9-15: DII EOD load–displacement behaviour showing the total pile resistance applying BC1 boundary condition. 220
Figure 9-16: Interface stress paths of ICP04 Mini-ICP in dry NE34 sand chamber with BC3 boundary conditions during short term EOD static compression load test. 222
Figure 9-17: Interface stress paths of ICP06 Mini-ICP in wet NE34 sand chamber with BC3 boundary conditions during short term EOD static compression load test. 222
Figure 9-18: Interface stress paths of ICP07 Mini-ICP in dry NE34 sand chamber with BC5 boundary conditions during short term EOD static compression load test. 223
Figure 9-19: Interface stress paths of ICP08 Mini-ICP in dry NE34 sand chamber with BC5 boundary conditions during the last stroke of pile installation. 223
Figure 9-20: Interface stress path of ICP05 Mini-ICP in dry GA39 sand chamber with BC3 boundary conditions during short term EOD static compression load test. 224
Figure 9-21: Comparison of radial stresses from Mini-ICP test ICP05 and the ICP-05 method (a) stationary and (b) moving. 227
Figure 9-22: Schematic diagrams illustrating the rate dependency observed for sand by Matsushita et al. (1999) (a) The stress–strain relation for different constant strain rates coincide for the three strain rates and (b) temporary over and under shooting due to stepwise change in strain rate (Augustesen et al. 2004) 228

Figure 9-23: Drained triaxial compression tests on Fontainebleau sand investigating strain rate effect (Weinstein 2008).....228
Figure 9-24: Pile loading tests for three different successive loading rates on one pile in Fontainebleau sand (Weinstein 2008).....229
Figure 9-25: ICP04 Mini-ICP installation in dry NE34 sand with boundary condition BC3 last stroke of installation (49^{th}) and EOD stroke (50^{th}) loads compared. 229
Figure 9-26: ICP06 Mini-ICP installation in wet NE34 sand with boundary condition BC3 last stroke of installation (49^{th}) and EOD stroke (50^{th}) loads compared. 230
Figure 10-1: 'Standard' test ICP04 interface radial stresses–log time trends over 41 days ageing period. 235
Figure 10-2: 'Standard' test ICP04 interface shear stresses–log time trends over 41 days ageing period. 235
Figure 10-3: 'Standard' test ICP04 axial loads–log time trends over 41 days ageing period.....236
Figure 10-4: 'Standard' test ICP04 normalised interface radial stresses–log time trends over 41 days ageing period.....236
Figure 10-5: 'Standard' test ICP04 normalised interface shear stresses–log time trends over 41 days ageing period.....237
Figure 10-6: 'Standard' test ICP04 normalised axial loads–log time trends over 41 days ageing period. 237
Figure 10-7: 'Standard' test ICP04 normalised sand mass radial stresses–log time trends over 41 days ageing period. 237
Figure 10-8: 'Standard' test ICP04 normalised sand mass vertical stresses–log time trends over 41 days ageing period. 238
Figure 10-9: 'Standard' test ICP04 normalised sand mass hoop stresses–log time trends over 41 days ageing period. 238
Figure 10-10: GA39 test ICP05 normalised interface radial stresses–log time trends over 71 days ageing period.....239
Figure 10-11: GA39 test ICP05 normalised interface shear stresses–log time trends over 71 days ageing period.....239
Figure 10-12: GA39 test ICP05 normalised axial loads – log time trends over 71 days ageing period. 240
Figure 10-13: Wet test ICP06 normalised interface radial stresses–log time trends over 49 days ageing period.....241
Figure 10-14: Wet test ICP06 normalised interface shear stresses – log time trends over 49 days ageing period.....241
Figure 10-15: Wet test ICP06 normalised axial loads–log time trends over 49 days ageing period. 242
Figure 10-16: Wet test ICP06 normalised sand mass radial stresses–log time trends over 49 days ageing period.....242
Figure 10-17: Wet test ICP06 normalised sand mass vertical stresses–log time trends over 49 days ageing period.....242
Figure 10-18: ICP06 normalised sand mass hoop stresses time trends over 49 days ageing period. 243
Figure 10-19: 'Free field simulator' BC5 boundary condition test ICP07 normalised interface radial stresses – log time trends over 38 days ageing period. 245
Figure 10-20: BC5 boundary condition test ICP07 normalised interface shear stresses – log time trends over 25 days ageing period.....245
Figure 10-21: BC5 boundary condition test ICP07 normalised axial loads – log time trends over 25 days ageing period. 246
Figure 10-22: BC5 boundary condition test ICP07 normalised sand mass radial stresses – time trends over 38 days ageing period.....246

Figure 10-23: BC5 boundary condition test ICP07 normalised sand mass vertical stresses – time trends over 38 days ageing period.....247
Figure 10-24: BC5 boundary condition test ICP07 normalised sand mass hoop stresses – time trends over 38 days ageing period. 247
Figure 10-25: BC5 boundary condition test ICP07 temperature variations during the 38 days ageing period. 248
Figure 10-26: ICP08 normalised interface radial stresses – log time trends over 15 days ageing period. 248
Figure 10-27: ICP08 normalised interface shear stresses – log time trends over 15 days ageing period. 248
Figure 10-28: ICP08 normalised axial loads – log time trends over 15 days ageing period. 249
Figure 10-29: ICP08 normalised sand mass radial stresses – log time trends over 15 days ageing period. 249
Figure 10-30: ICP08 normalised sand mass vertical stresses – log time trends over 15 days ageing period. 249
Figure 10-31: ICP08 normalised sand mass hoop stresses – log time trends over 15 days ageing period. 250
Figure 10-32: ICP07 with BC5 boundary condition low level boundary stress cycling imposed from 38 days after installation. 250
Figure 10-33: ICP07 with BC5 boundary condition Mini-ICP interface radial stress response during low level boundary stress cycling. 251
Figure 10-34: Mini-ICP interface effective stress paths in the ageing durations.....252
Figure 10-35: Mini-ICP test ICP04 C1 and EOD static compression total load–displacement behaviours in dry medium dense NE34 sand with BC3 boundary condition. 254
Figure 10-36: Mini-ICP test ICP04 C1 compared to EOD static compression base and shaft load–displacement behaviour in dry dense NE34 sand with BC3 boundary condition.....255
Figure 10-37: Mini-ICP test ICP04 C1 compared to EOD static compression effective interface stress paths in dry dense NE34 sand with BC3 boundary condition. 255
Figure 10-38: Mini-ICP test ICP05 C1 compared to EOD static compression total load–displacement behaviour in dry less dense and finer GA39 sand with BC3 boundary condition.....256
Figure 10-39: Mini-ICP test ICP05 C1 compared to EOD static compression base and shaft load–displacement behaviour in dry less dense and finer GA39 sand with BC3 boundary condition.....256
Figure 10-40: Mini-ICP test ICP05 C1 compared to EOD static compression effective interface stress paths in dry finer and less dense GA39 sand with BC3 boundary condition.....257
Figure 10-41: Mini-ICP test ICP06 C1 compared to EOD static compression total load–displacement behaviour in wet dense NE34 sand with BC3 boundary condition. 258
Figure 10-42: Mini-ICP test ICP06 C1 compared to EOD static compression base and shaft load-displacement behaviour in wet dense NE34 sand with BC3 boundary condition. 258
Figure 10-43: Mini-ICP test ICP06 C1 compared to EOD static compression effective interface stress paths in wet dense NE34 sand with BC3 boundary condition. 259
Figure 10-44: Mini-ICP test ICP07 C1 compared to EOD static compression total load–displacement behaviour in dry dense NE34 sand with BC5 boundary condition.....260
Figure 10-45: Mini-ICP test ICP07 C1 compared to EOD static compression base and shaft load–displacement behaviour in dry dense NE34 sand with BC5 boundary condition.....261
Figure 10-46: Mini-ICP test ICP08 C1 compared to last stroke static compression total load–displacement behaviour in dry dense NE34 sand with BC5 boundary condition.....261
Figure 10-47: Mini-ICP test ICP08 C1 compared to last stroke static compression base and shaft load–displacement behaviour in dry dense NE34 sand with BC5 boundary condition.....262
Figure 10-48: Mini-ICP test ICP07 C1 compared to EOD static compression effective interface stress paths in dry dense NE34 sand with BC5 boundary condition. 262
Figure 10-49: Mini-ICP test ICP08 C1 static compression test compared to last installation stroke effective interface stress paths in dry dense NE34 sand with boundary condition BC5. 263

Figure 10-50: Micro-pile test MiP01 C1 compared to EOD static compression total load–displacement behaviour in dry dense NE34 sand with BC3 boundary condition. 265
Figure 10-51: CPT pile long strokes few cycles test CPT09 C1 compared to EOD static compression total load–displacement behaviour in dry dense NE34 sand with BC5 boundary condition. 265
Figure 10-52: CPT pile long strokes few cycles test CPT09 C1 compared to EOD static compression base and shaft load–displacement behaviour in dry dense NE34 sand with BC5 boundary condition. 266
Figure 10-53: CPT pile faster strokes test CPT10 C1 compared to EOD static compression total load–displacement behaviour in dry dense NE34 sand with BC5 boundary condition. 266
Figure 10-54: CPT pile faster strokes test CPT10 C1 compared to EOD static compression base and shaft load–displacement behaviour in dry dense NE34 sand with BC5 boundary condition. 267
Figure 10-55: Driven pile test DI T2 compared to T1 static tension load–displacement behaviour in dry dense NE34 sand with BC5 boundary condition. 267
Figure 10-56 Driven pile test DII C1 compared to EOD static compression total load–displacement behaviour in dry dense NE34 sand with BC1 boundary condition. 268
Figure 10-57: Aged model piles base capacity log time trend. 269
Figure 10-58: Aged model piles shaft capacity log time trend. 269
Figure 10-59: Aged model piles total compression capacity log time trend. 269
Figure 11-1: Axial cyclic loading displacements and load patterns illustrated from load controlled test ICP05-OW2 in (a) and (b), and displacement controlled test ICP06-TW1 in (c) and (d). 276
Figure 11-2: Illustration of the displacement and stiffness parameters used in the analyses. 277
Figure 11-3: Accumulated cyclic displacements with number of cycles applied during the axial cyclic loading test series ICP04. 278
Figure 11-4: Reference static tension tests interspersed between the axial cyclic loading tests in ICP04. 279
Figure 11-5: Accumulated cyclic displacements with number of cycles applied during the axial cyclic loading test series ICP05. 280
Figure 11-6: Reference static tension tests between the axial cyclic loading tests in ICP05. 281
Figure 11-7: Accumulated cyclic displacements with number of cycles applied during the axial cyclic loading test series ICP06. 282
Figure 11-8: Pile head load–displacement behaviour of displacement controlled axial cyclic loading test ICP06-TW1 in cycles (a) 1 – 10 and 100 – 110 (b) 1000 – 1010 and 12000 – 12022. 283
Figure 11-9: ICP06-TW1 axial cyclic loads against cycles applied for (a) pile head and base in compression (b) pile head in tension and pile shaft in compression, showing apparent stabilisation of compression pile head load and symmetrical shaft capacity decay. 284
Figure 11-10: Reference static tension tests between the axial cyclic loading tests in ICP06. 285
Figure 11-11: Accumulated cyclic displacements with number of cycles applied during the axial cyclic loading test series ICP07. 286
Figure 11-12: Pile head load–displacement behaviour of displacement controlled axial cyclic loading test ICP08-TW1 in cycles (a) 1 – 10 and 100 – 110 (b) 1000 – 1010, 10,000 – 10,010 and 19,992 to 20,002. 287
Figure 11-13: ICP08-TW1 axial cyclic loads against cycles applied for (a) pile head in compression and pile base (b) pile head in tension and pile shaft in compression. 288
Figure 11-14: Reference static tension tests during the axial cyclic loading tests in ICP07. 289
Figure 11-15: Reference static tension tests during the axial cyclic loading tests in ICP08. 289
Figure 11-16: Axial cyclic loading interaction diagram for the standard test series ICP04 with the Mini-ICP in dry NE34 sand with BC3 boundary condition. 291
Figure 11-17: Axial cyclic loading interaction diagram for the test series ICP06 with Mini-ICP in wet NE34 sand with BC3 boundary conditions. 292
Figure 11-18: Axial cyclic loading interaction diagram for the test series ICP07 & 08 with the Mini-ICP in dry NE34 sand with BC5 boundary conditions. 292

Figure 11-19: Axial cyclic loading interaction diagram for the test series ICP05 with the Mini-ICP in dry GA39 sand with BC3 boundary conditions. 293
Figure 11-20: Static shaft capacity changes with axial cyclic amplitude for the load controlled Mini-ICP axial cyclic loading tests with $Q_{cyclic}/Q_T < 0.3$. 293
Figure 11-21: Normalised axial cyclic pile stiffness versus number of cycles applied in stable cyclic loading tests. 295
Figure 11-22: Normalised axial cyclic pile stiffness versus number of cycles applied in meta-stable cyclic loading tests. 295
Figure 11-23: Normalised axial cyclic pile stiffness versus number of cycles applied in unstable cyclic loading tests. 296
Figure 11-24: Load–displacement behaviour of one-way unstable cycling ICP05-OW2 over the last 11 cycles showing different secant stiffness on the loading and unloading loops of a cycle. 296
Figure 11-25: Normalised axial loading and unloading cyclic stiffness versus number of cycles applied in ICP05-OW2 unstable cyclic pile loading. 297
Figure 11-26: Finer GA39 sand ICP05-OW1 one–way meta-stable cyclic loading test interface effective stress paths. 299
Figure 11-27: Finer GA39 sand ICP05-TW1 two–way meta-stable cyclic loading test interface effective stress paths. 299
Figure 11-28: BC5 boundary condition ICP07-OW1 one–way stable cyclic loading test interface effective stress paths. 300
Figure 11-29: BC5 boundary condition ICP07-TW1 two–way stable cyclic loading test interface effective stress paths. 300
Figure 11-30: Wet NE34 sand ICP06-TW1 displacement controlled cycling loading test interface effective stress paths. 301
Figure 11-31: BC5 boundary condition ICP08-TW1 displacement controlled local interface stress paths. 303
Figure 11-32: Radial stresses at the calibration chamber boundary during axial cyclic loading test ICP08-TW1 with BC5 boundary condition. 304
Figure 11-33: Sand mass radial stress against the number of cycles applied in displacement controlled tests (a) ICP06-TW1 with wet NE34 and BC3 boundary condition, and (b) ICP08-TW1 with dry NE34 and BC5 boundary condition. 304
Figure 11-34: Sand mass vertical stress against the number of cycles applied in displacement controlled tests (a) ICP06-TW1 with wet NE34 and BC3 boundary condition, and (b) ICP08-TW1 with dry NE34 and BC5 boundary condition. 305
Figure 11-35: Sand hoop stresses against the number of cycles applied in displacement controlled test ICP08-TW1 with BC5 boundary condition. 305
Figure 11-36: Flow chart for cyclic design for axially and loaded piles, Jardine et al. (2012). 307
Figure 12-1: Plan showing layout of test and reaction piles and CPTs from GOPAL Project in Dunkirk, France (after Jardine & Standing 2012) 311
Figure 12-2: Details of test rig (not to scale) (a) Elevation (b) Plan (after Jardine et al. 2006). 312
Figure 12-3: Load–displacement curves for first–time monotonic tension load tests. 318
Figure 12-4: Stiffness degradation of piles assessed from the first–time axial static monotonic tension loadings normalised by the reference stiffnesses plotted against load normalised by Q_{Ref}. 318
Figure 12-5: Axial cyclic loading stiffness (k_l) responses normalised in terms of (a) k_{Ref} and (b) $k_{N=1}$ and plotted against number of cycles for the stable and meta–stable loading tests. 319
Figure 12-6: Axial cyclic loading stiffness (k_l) responses normalised in terms of (a) k_{Ref} and (b) $k_{N=1}$ and plotted against number of cycles for the unstable loading tests. 320
Figure 12-7: Axial cyclic unloading stiffness (k_u) responses normalised in terms of (a) & (b) k_{Ref} and (c) & (d) $k_{N=1}$ and plotted against number of cycles for the all the axial cyclic loading tests. . 322
Figure 12-8: Accumulated cyclic displacements for the stable and meta–stable loading tests. 325
Figure 12-9: Accumulated cyclic displacements response for the unstable tests. 325

Figure 12-10 (a – f): Axial cyclic interaction chart with the accumulated cyclic displacements from cycles N = 3, 10, 30, 100, 200, and 300 marked for the cyclic pile tests.....327
Figure 12-11(a – c): 3D plots for accumulated cyclic displacements equivalent to 0.02%D, 0.2%D and 2%D.....328
Figure 12-12: Transient cyclic displacements for the stable and meta–stable tests.....329
Figure 12-13: Transient cyclic displacements for the unstable tests. 330
Figure IV-1: NE34 sand pile interface sample recovered from a depth of 365mm around Mini-ICP after test series ICP04 395
Figure IV-2: NE34 sand pile interface sample recovered from a depth of 850mm around Mini-ICP after test series ICP04 396
Figure IV-3: GA39 sand pile interface sample recovered from a depth of 300mm around Mini-ICP after test series ICP05 396
Figure IV-4: GA39 sand pile interface sample recovered from a depth of 850mm around Mini-ICP after test series ICP05 397
Figure IV-5: Mini-ICP tests Zone I interface layer thickness after static and cyclic axial loading. 397

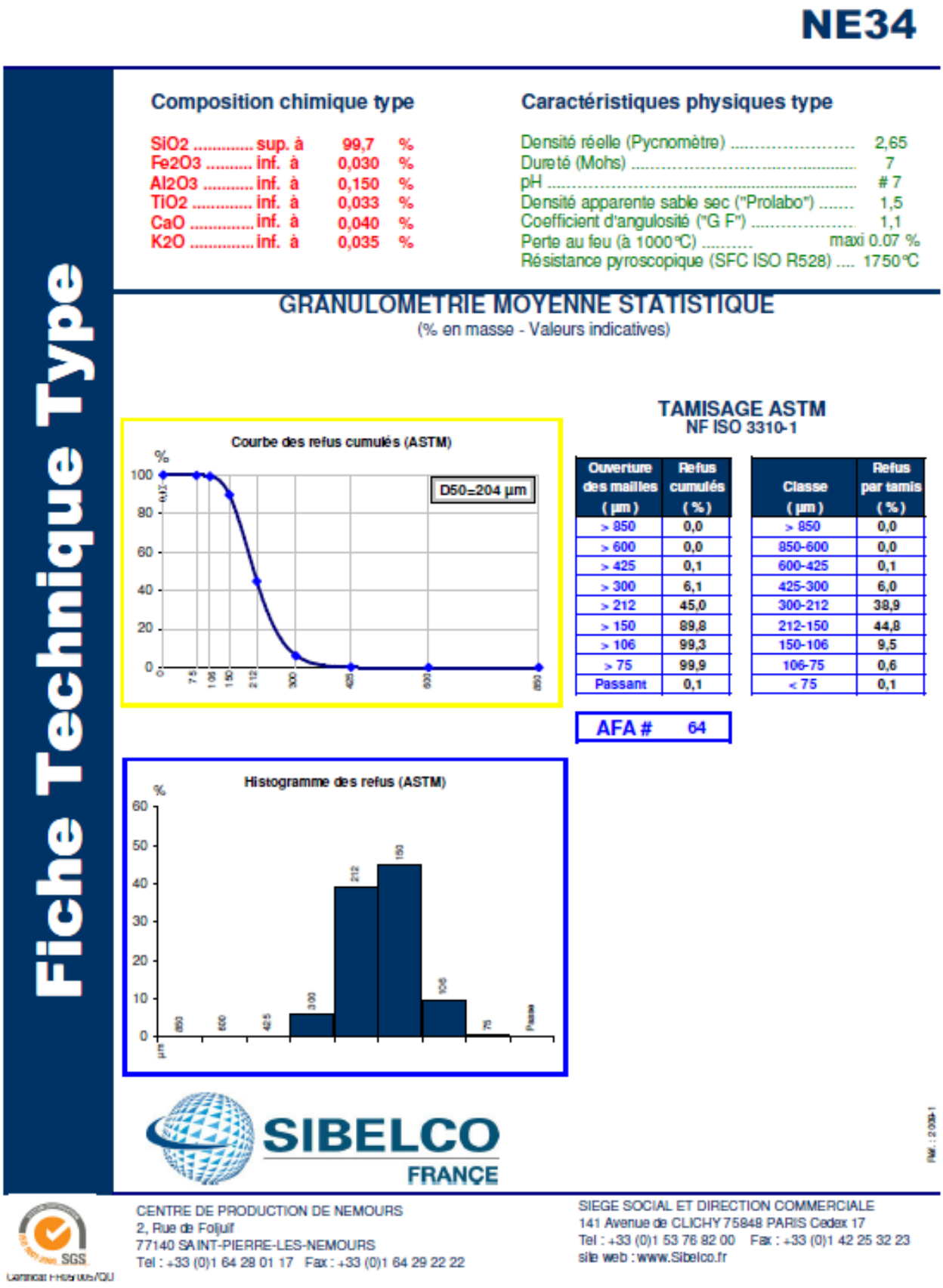
List of tables

Table 1-1: Predictive reliability of four modern CPT-based axial static capacity design methods of driven piles in silica sands based on a UWA database (Lehane et al. 2005b). 25
Table 2-1: API RP2 GEO (2011) recommend practice for geotechnical engineering pile base capacity design parameters for cohesionless soils. 30
Table 2-2: Simplified base capacity CPT and CPTu – based α–type design methods (after Cai et al. 2008). 31
Table 2-3: API RP2 GEO (2011) recommend practice for geotechnical engineering pile shaft capacity design parameters for cohesionless soils. 39
Table 2-4: Simplified CPT and CPTu – based α–type design methods (after Cai et al. 2008). 42
Table 2-5: Modern (offshore) CPT-based design methods for base resistance of driven piles in siliceous sands after Schneider et al. (2008). 56
Table 2-6: Modern (offshore) CPT-based design methods for local shaft friction of driven piles in siliceous sand after Schneider et al. (2008) 57
Table 2-7: Performance of design methods against the entire UWA database where μ_{gR} is the geometric mean and σ_{lnR} standard deviation of the natural log of Q_c/Q_m (after Schneider et al. 2008). 60
Table 2-8: Assessment of NGI-99, API-2 and ICM-96 predictive reliability against the combined AAU and NGI database (Augustesen et al. 2005). 62
Table 2-9: Arithmetic mean and CoV reliability of displacement piles in sands design approaches on a database of tension tests on open–ended piles in sand (Gavin et al. 2011) 63
Table 3-1: Sites in the pile ageing database with ground water table influenced by tides or high salinity 80
Table 3-2: Summary table of the evaluated outcomes based on the critical data available from the ageing database study 83
Table 3-3: Database of case studies on short to medium term pile ageing in silica sands. 87
Table 4-1: Indicative ranges for cyclic loading components; sites A to F predominantly clay, site G mainly sand (after Jardine et al. 2012). 89
Table 5-1: Boundary conditions in calibration chamber tests (after Huang & Hsu 2005). 111
Table 5-2: Dimensions of the miniature sand stress sensors in this study. 116
Table 5-3: Manufacturers' specifications of the miniature sand stress sensors in this study. 116
Table 5-4: Comparison of characteristics of sand stress sensors in the current study to the minimum design requirements. 117
Table 5-5: Mean direct and cross sensitivity factors of the radial/ normal stress transducers of all the cluster cells' used in this study. 131
Table 5-6: Mean direct and cross sensitivity factors of the shear stress transducers of all the cluster cells' used in this study. 131
Table 5-7: Mean direct and cross sensitivity factors of all Axial Load Cells' used in this study 132
Table 6-1: Index properties for NE34 Fontainebleau and GA39 Nemours sand. 138
Table 6-2: NE34 Fontainebleau sand mechanical strength characteristics. 139
Table 6-3: Dunkirk Flandrian sand average index properties (after Jardine & Standing 2000). 140
Table 6-4: Dunkirk Flandrian sand mineralogy (after Jardine & Standing 2000). 141
Table 6-5: Physical properties of Dunkirk sand 142
Table 6-6: Miniature sand stress sensors layouts adopted for the ageing and axial static and cyclic behaviour studies with mini-ICP displacement piles. 149
Table 6-7: CPT1 to Mini-ICP03 tests details after Jardine et al. (2013a) 152
Table 6-8: Mini-ICP piles specific testing objectives in the study of ageing and axial cyclic loading behaviour of displacement piles in silica sands. 154
Table 6-9: All other piles specific testing objectives in the study of ageing and axial cyclic loading behaviour of displacement piles in silica sands. 155

Table 6-10: Summary details of the Mini-ICP piles test programme to investigate the ageing and axial cyclic loading behaviour of displacement piles in silica sands. 156
Table 6-11: Summary details of all other piles test programme to investigate the ageing and axial cyclic loading behaviour of displacement piles in silica sands 157
Table 7-1: Calibration chamber pressurisation durations and density states for all pile installations. 160
Table 7-2: Average normalised radial moving and stationary stresses around jack–stroke installed displacement piles in NE34 sand chamber. 183
Table 9-1: Short-term static pile capacities (EOD) in this test programme. 209
Table 9-2: Degrees of dilation (= $\sigma'_{rf}/\sigma'_{rs(EOD)}$) measured on the Mini-ICP test piles during EOD static load testing. 224
Table 9-3: Measured and ICP-05 method (Jardine et al. 2005) calculated axial static compression pile load capacities compared. 226
Table 9-4: Q_c/Q_m of all jack-stroke installed model piles in the dense NE34 sand. 226
Table 10-1: Post-ageing compared to end of installation capacities of all model piles in this laboratory study for the assessment of capacities changes due to ageing. 233
Table 10-2: Degree of interface dilation and stiffness characteristics of aged and fresh piles compared. 254
Table 11-1: Axial cyclic loading test series in the full extended Mini-ICP study. 274
Table 11-2: Axial static tension tests undertaken in the full extended Mini-ICP study. 275
Table 12-1: Axial cyclic loading testing programme from Jardine & Standing (2000). 314
Table 12-2: Reference static tension capacities from Jardine and Standing (2000). 315

Appendices

I Appendix I – Tests sands data sheets



NE34

Fiche Technique Type

Composition chimique type

SiO2	sup. à	99,7	%
Fe2O3	inf. à	0,030	%
Al2O3	inf. à	0,150	%
TiO2	inf. à	0,033	%
CaO	inf. à	0,040	%
K2O	inf. à	0,035	%

Caractéristiques physiques type

Densité réelle (Pycnomètre)	2,65
Dureté (Mohs)	7
pH	# 7
Densité apparente sable sec ("Prolabo")	1,5
Coefficient d'angulosité ("G F")	1,1
Perte au feu (à 1000°C)	maxi 0.07 %
Résistance pyroscopique (SFC ISO R528)	1750°C

GRANULOMETRIE MOYENNE STATISTIQUE

(% en masse - Valeurs indicatives)

Courbe des refus cumulés (ASTM)

TAMISAGE ASTM
NF ISO 3310-1

Ouverture des mailles (µm)	Refus cumulés (%)
> 850	0,0
> 600	0,0
> 425	0,1
> 300	6,1
> 212	45,0
> 150	89,8
> 106	99,3
> 75	99,9
Passant	0,1

Classe (µm)	Refus par tamis (%)
> 850	0,0
850-600	0,0
600-425	0,1
425-300	6,0
300-212	38,9
212-150	44,8
150-106	9,5
106-75	0,6
< 75	0,1

AFA # 64

Histogramme des refus (ASTM)

SIBELCO FRANCE

CENTRE DE PRODUCTION DE NEMOURS
2, Rue de Foljuif
77140 SAINT-PIERRE-LES-NEMOURS
Tel : +33 (0)1 64 28 01 17 Fax : +33 (0)1 64 29 22 22

SIEGE SOCIAL ET DIRECTION COMMERCIALE
141 Avenue de CLICHY 75848 PARIS Cedex 17
Tel : +33 (0)1 53 76 82 00 Fax : +33 (0)1 42 25 32 23
site web : www.Sibelco.fr

NE34 Fontainebleau sand supplier data sheet.

GA39

Fiche Technique Type

Composition chimique type

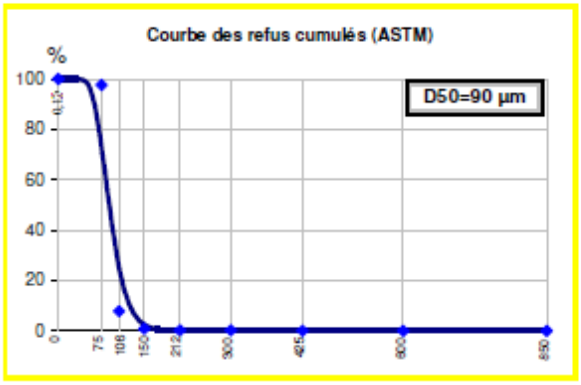
SiO2	sup. à	98,6	%
Fe2O3	inf. à	0,050	%
Al2O3	inf. à	0,800	%
TiO2	inf. à	0,070	%
CaO	inf. à	0,030	%
K2O	inf. à	0,400	%

Caractéristiques physiques types

Densité réelle (Pycnomètre)	2,64
Dureté (Mohs)	7
pH	# 7
Densité apparente sable sec ("Prolabo")	1,5
Coefficient d'angulosité ("G F")	1,1
Perte au feu (à 1000 °C)	0,11%
Résistance pyroscopique (SFC ISO R528)	1750 °C

GRANULOMETRIE MOYENNE STATISTIQUE

(% en masse - Valeurs indicatives)

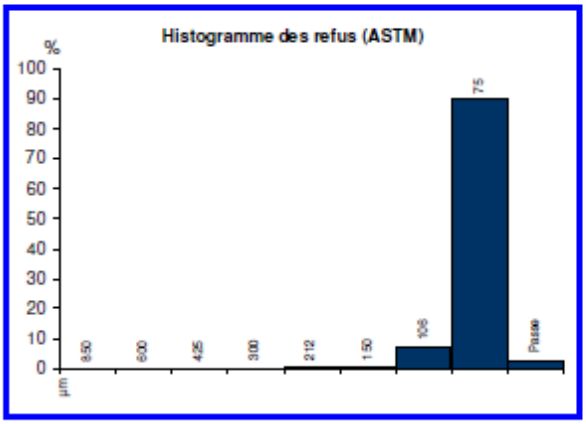


TAMISAGE ASTM
NF ISO 3310-1

ouverture des mailles µm	refus cumulés %
> 850	0,0
> 600	0,0
> 425	0,0
> 300	0,1
> 212	0,3
> 150	1,0
> 106	7,9
> 75	97,7
Passant	2,3

Classe µm	refus par tamis %
> 850	0,0
850-600	0,0
600-425	0,0
425-300	0,1
300-212	0,2
212-150	0,7
150-106	6,9
106-75	89,8
< 75	2,3

AFA # 138



SIBELCO FRANCE

Réf. : 2009-1

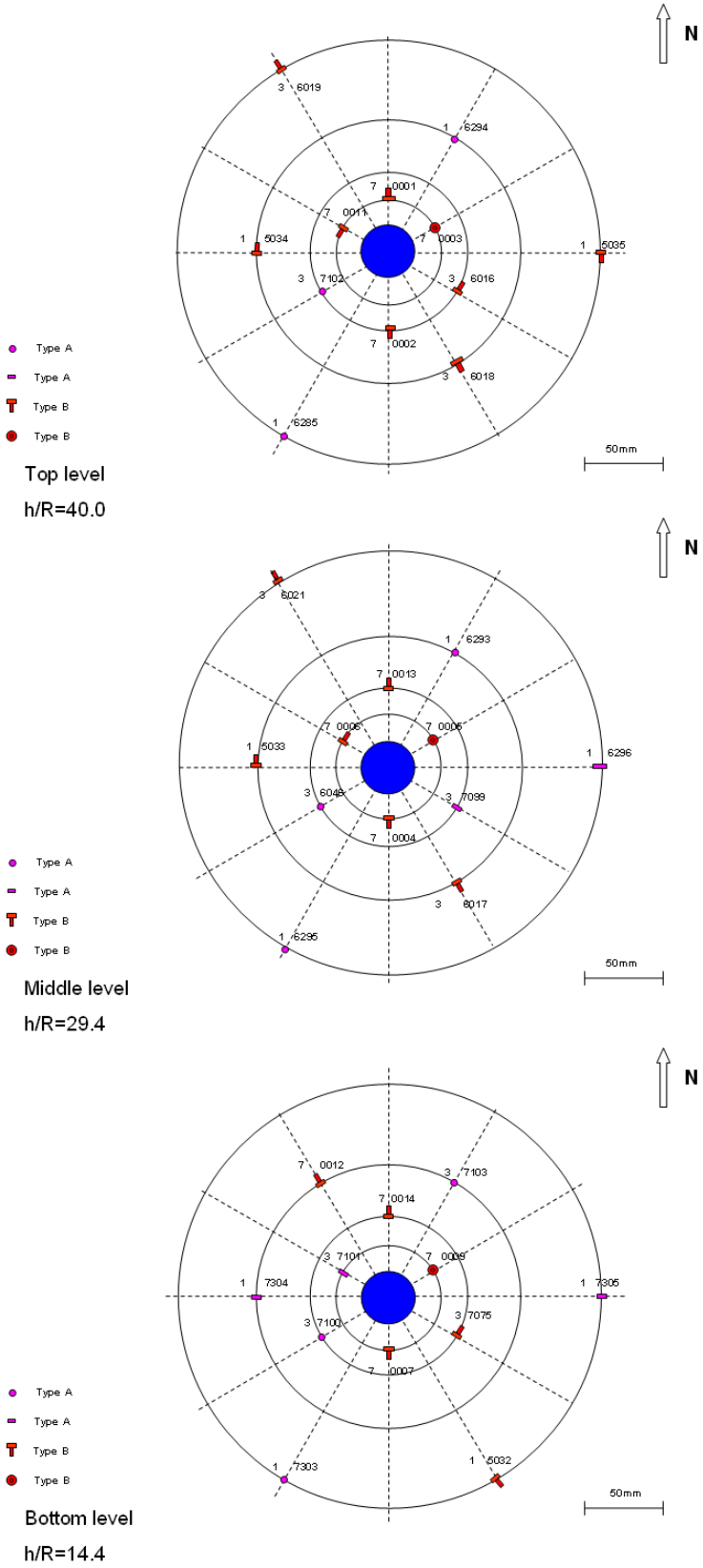
Certificat FR05/0057/QU

CENTRE DE PRODUCTION DE BOURRON
ZI Route de Villiers
77780 Bourron-Marlotte
Tel : +33 (0)1 64 45 90 19 Fax : +33 (0)1 64 45 61 60

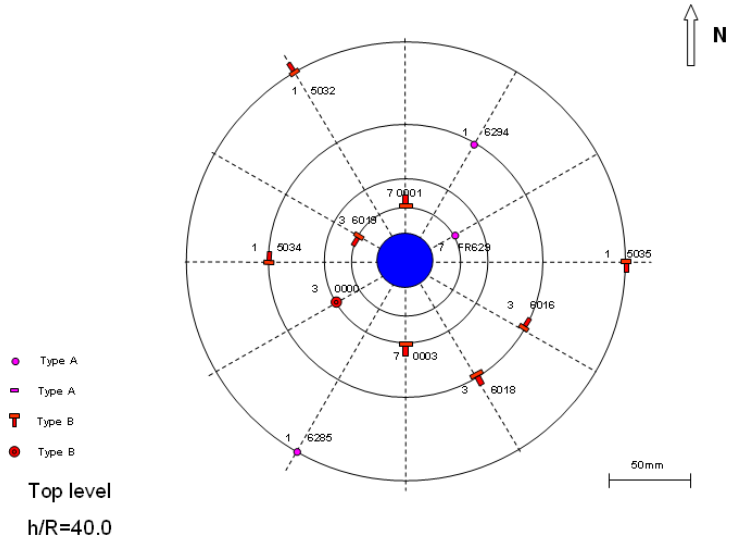
SIEGE SOCIAL ET DIRECTION COMMERCIALE
141 Avenue de CLICHY 75848 PARIS Cedex 17
Tel : +33 (0)1 53 76 82 00 Fax : +33 (0)1 42 25 32 23
site web : www.Sibelco.fr

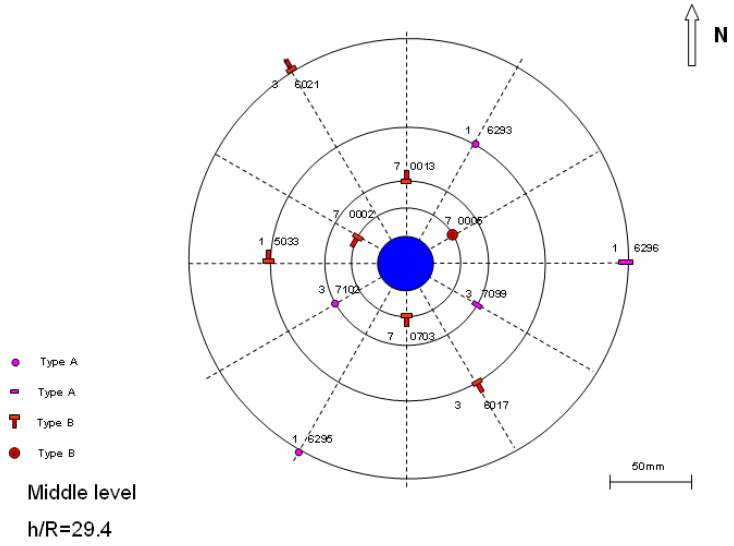
GA39 Nemours sand supplier data sheet.

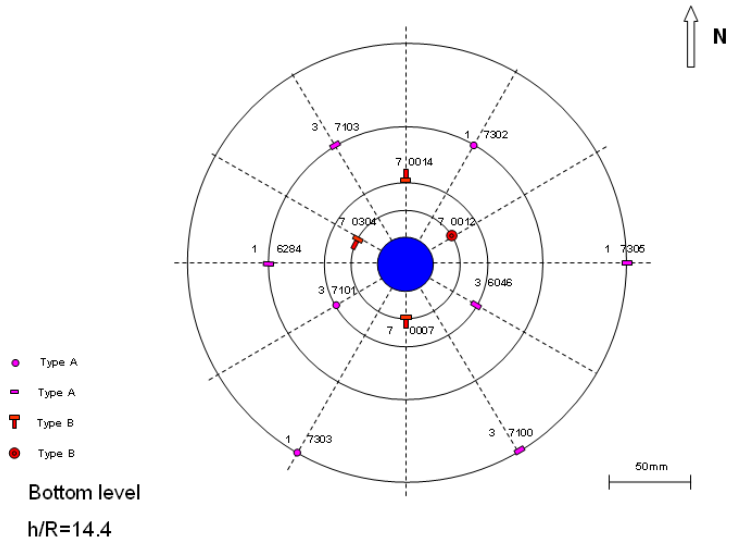
II Appendix II – Miniature sand stress sensors layout plans



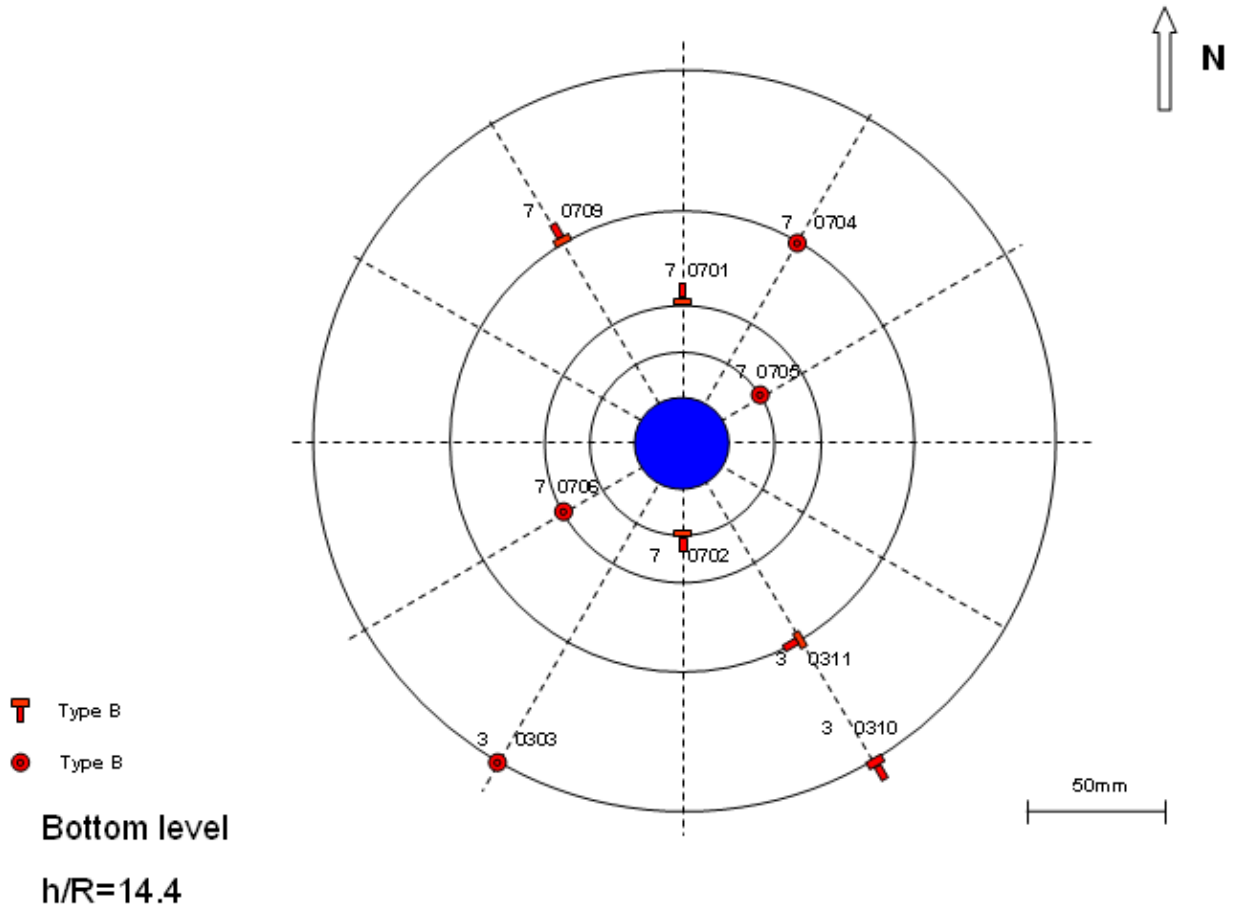
Stress sensors layout plans adopted at each level of the standard dry NE34 sand test ICP04 with BC3 boundary conditions.



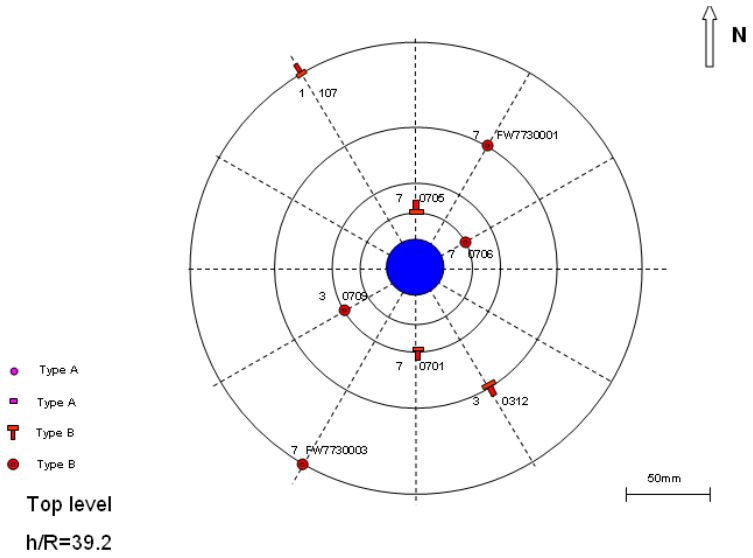


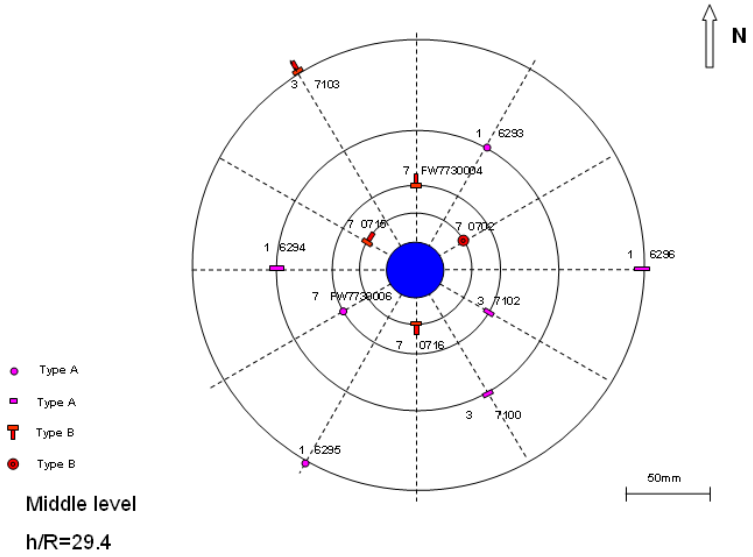


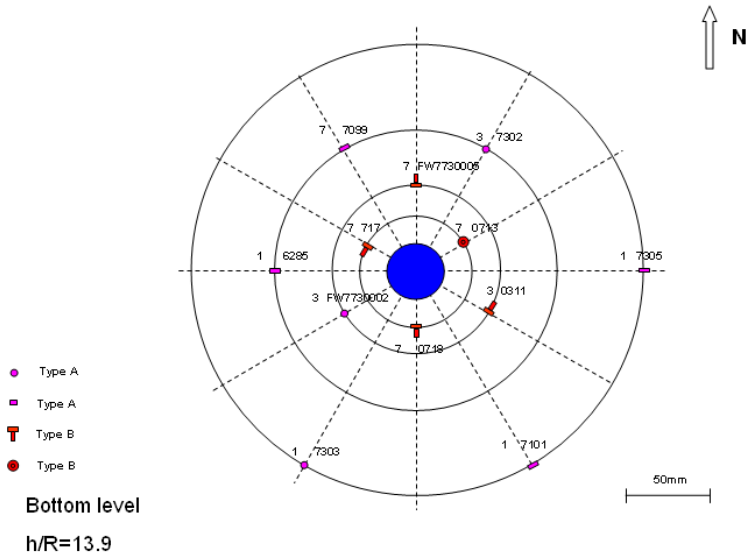
Stress sensors layout plans adopted at each level of the finer and looser GA39 sand test ICP05 with BC3 boundary conditions.



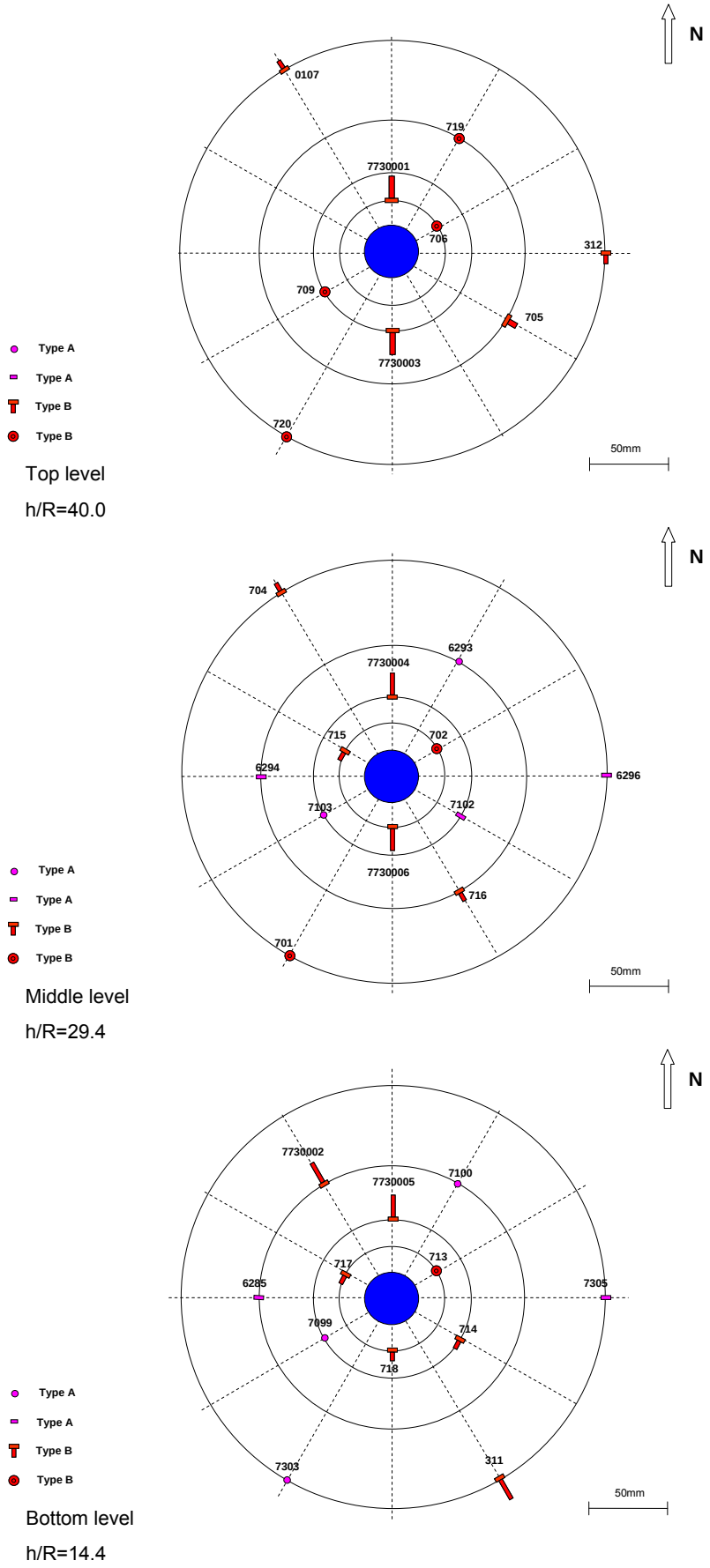
Stress sensors layout plan adopted at the single level of the wet NE34 sand test ICP06 with BC3 boundary conditions.





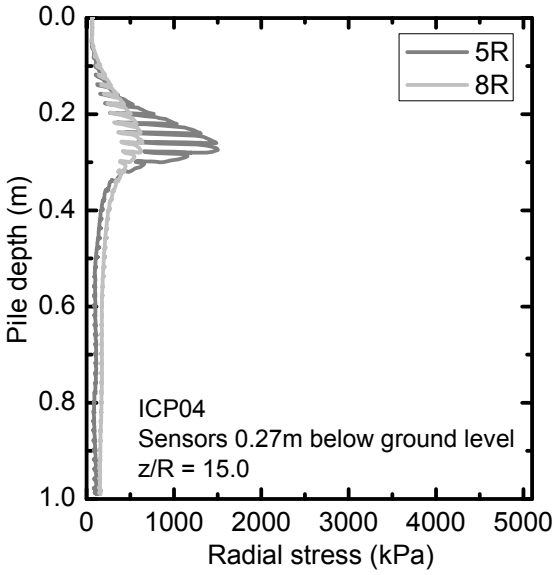


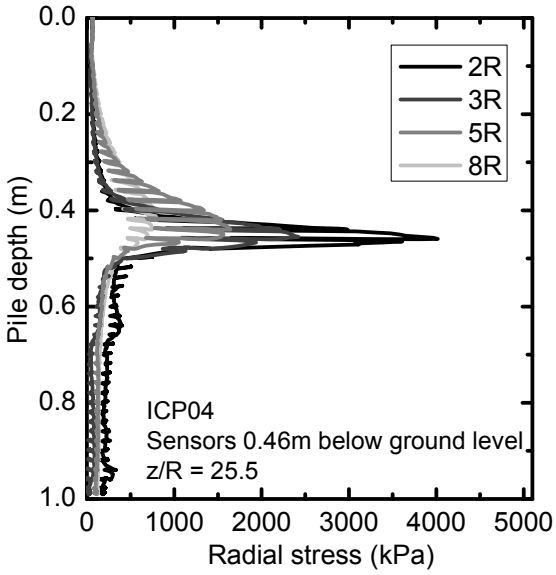
Stress sensors layout plans adopted at each level of the dry NE34 sand test ICP07 with BC5 modified boundary condition.

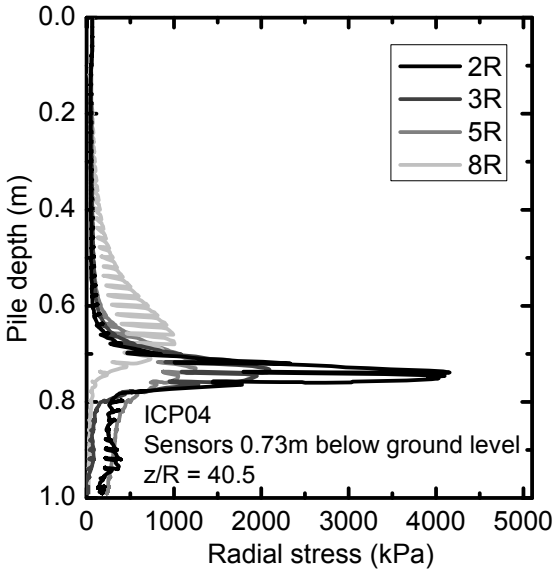


Stress sensors layout plans adopted at each level of the dry NE34 sand test ICP08 with BC5 modified boundary condition.

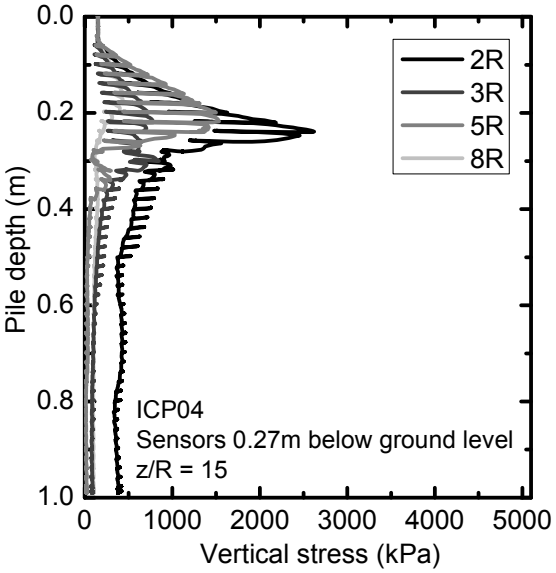
III Appendix III – Sand mass stress measurements

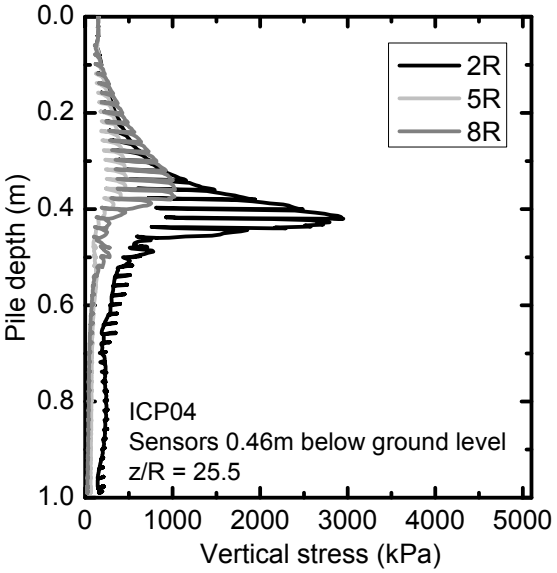


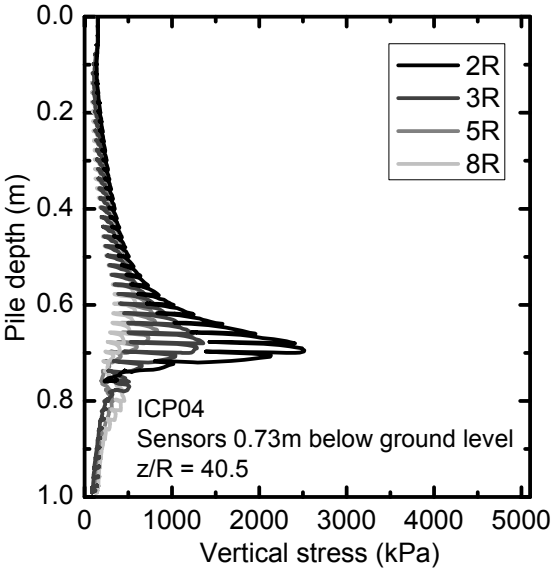




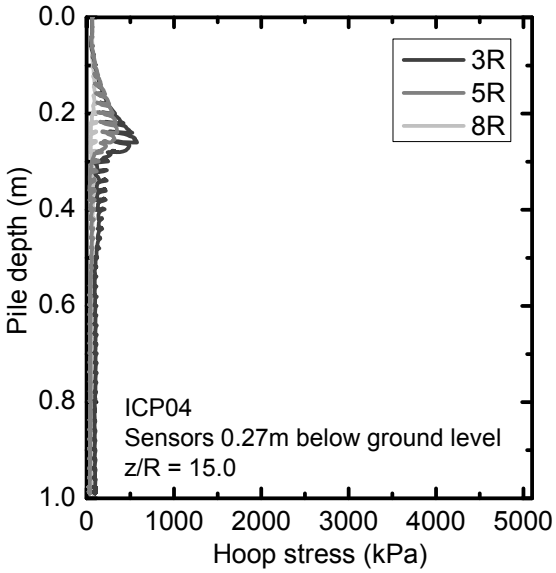
Radial stresses in the sand mass around the Mini-ICP installing in standard dry NE34 sand chamber ICP04 with BC3 boundary conditions.

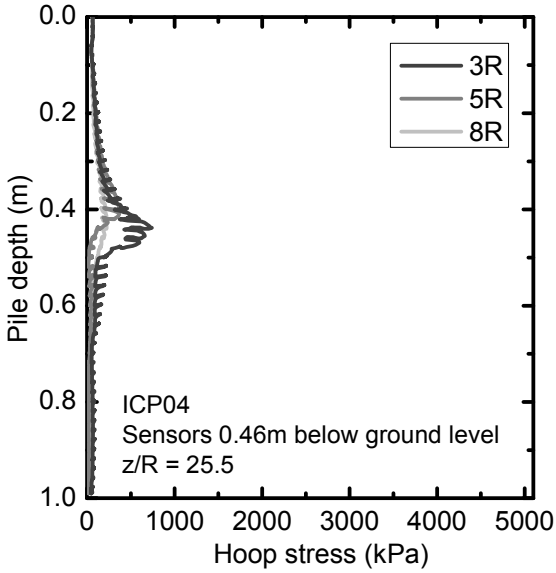


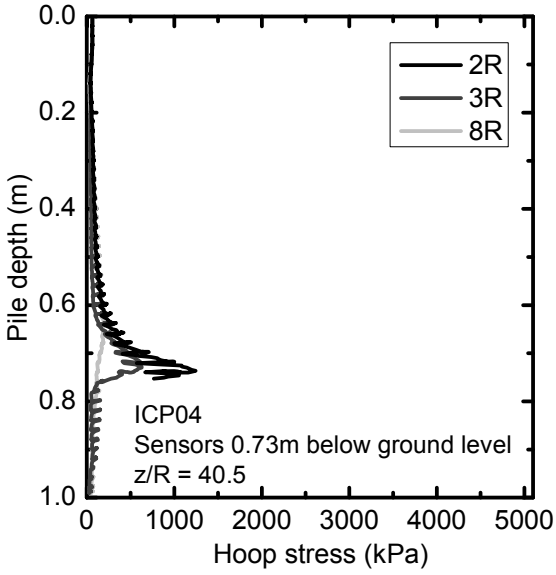




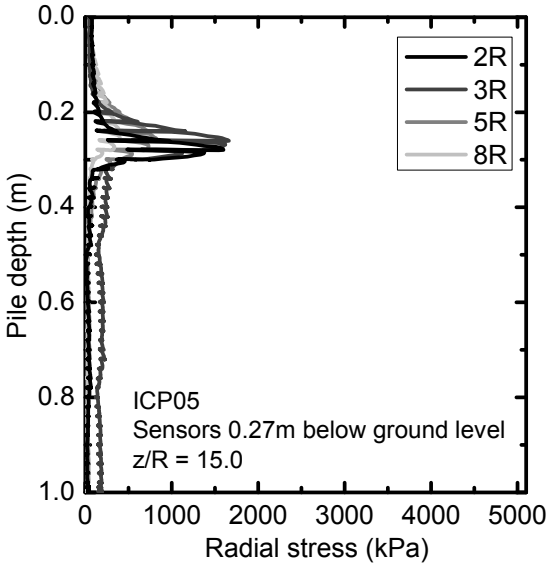
Vertical stresses in the sand mass around the Mini-ICP installing in standard dry NE34 sand chamber ICP04 with BC3 boundary conditions.

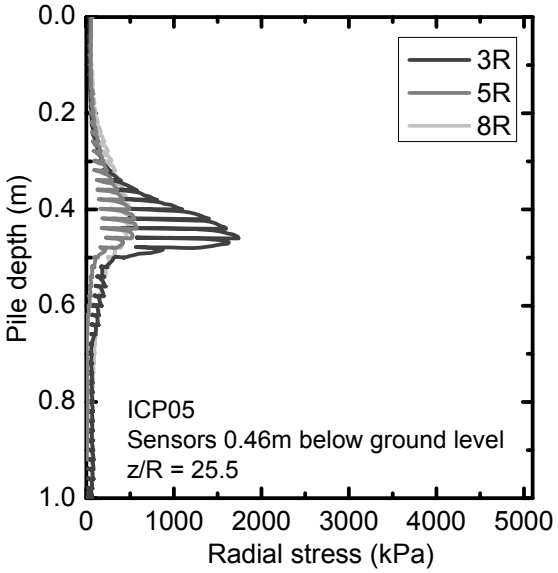


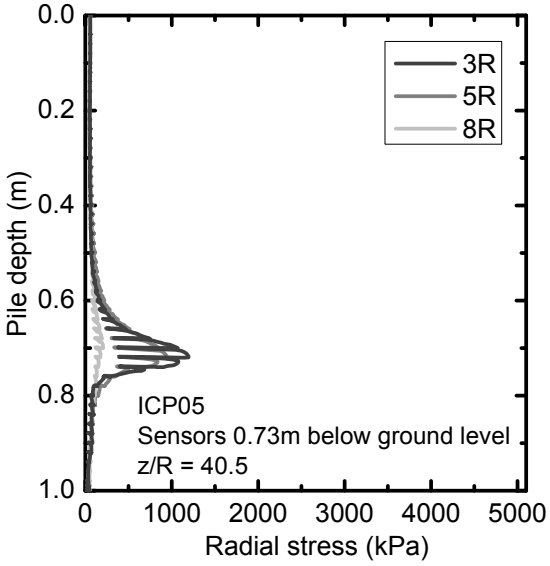




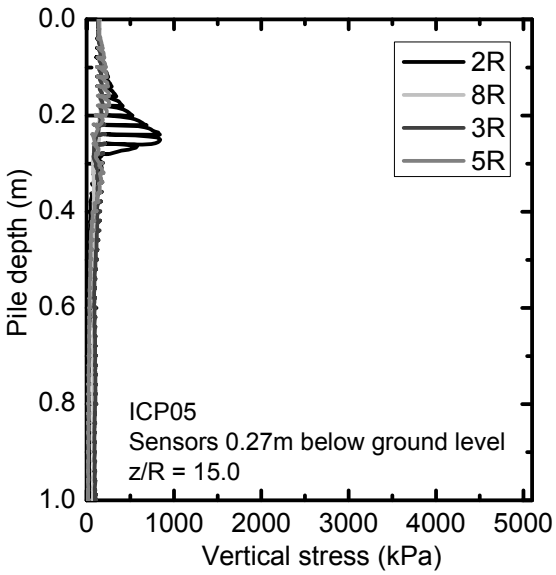
Hoop stresses in the sand mass around the Mini-ICP installing in standard dry NE34 sand chamber ICP04 with BC3 boundary conditions.

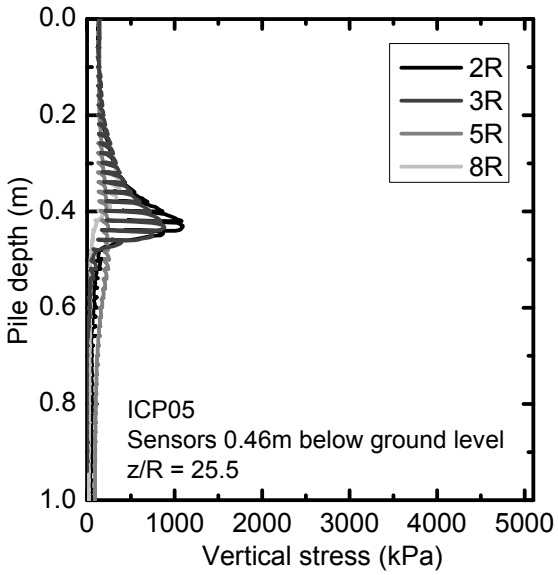


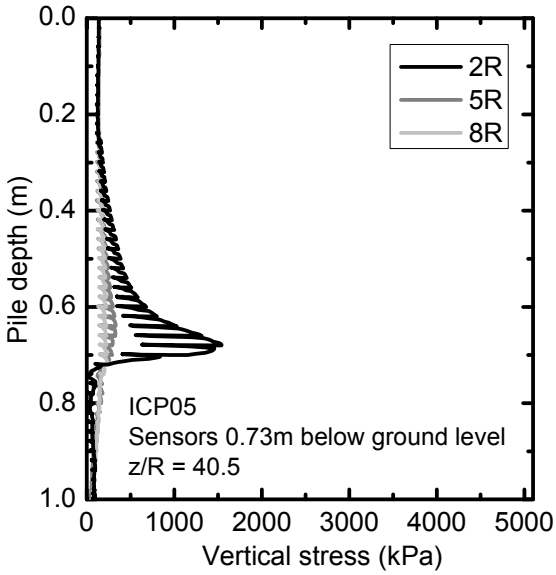




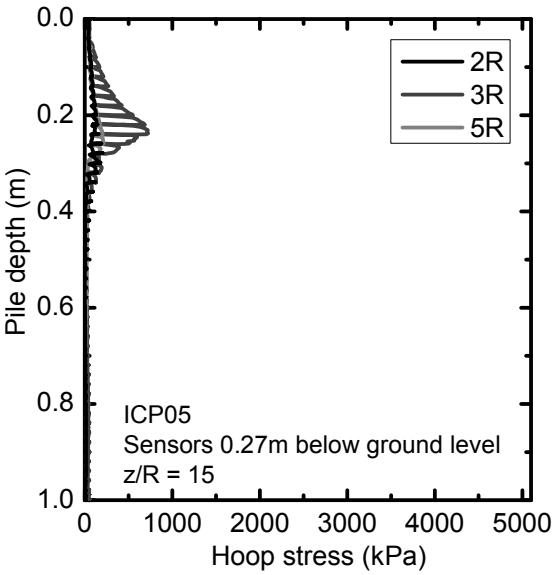
Radial stresses in the sand mass around the Mini-ICP installing in the finer and looser dry GA39 sand chamber ICP05 with BC3 boundary conditions.

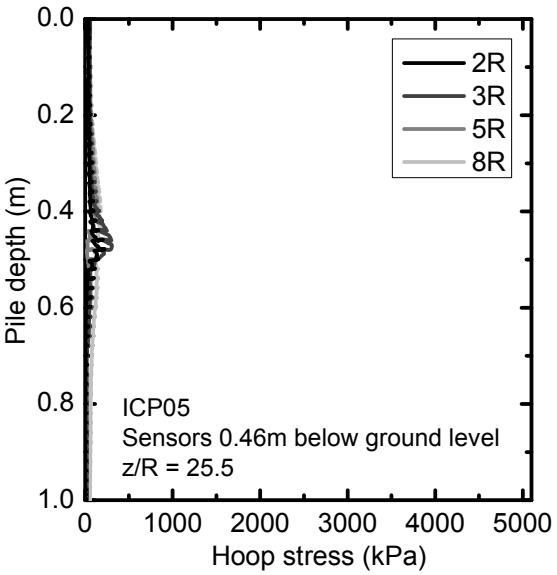


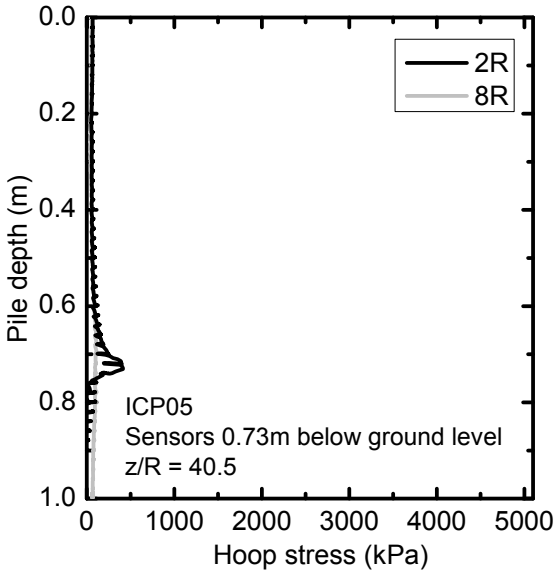




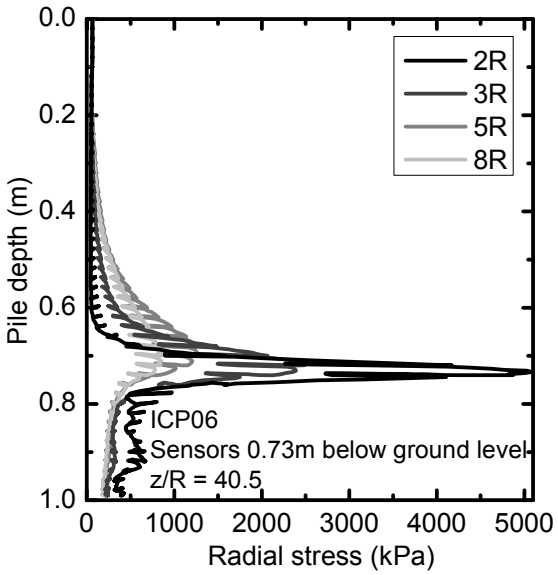
Vertical stresses in the sand mass around the Mini-ICP installing in the finer and looser dry GA39 sand chamber ICP05 with BC3 boundary conditions.

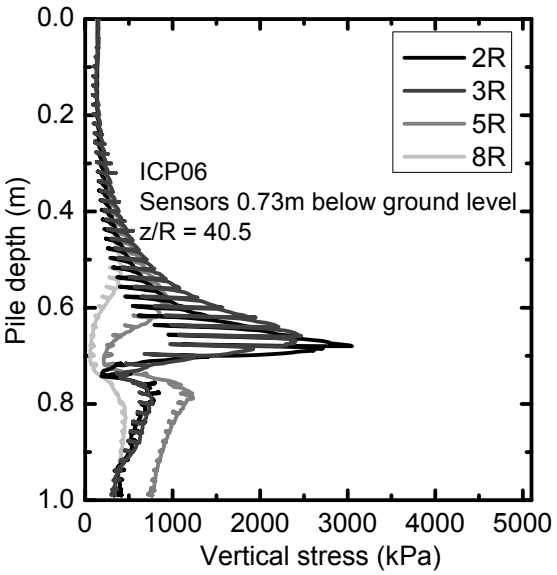


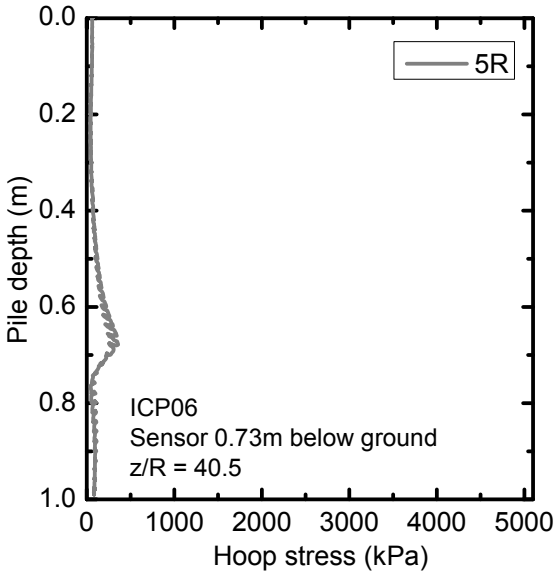




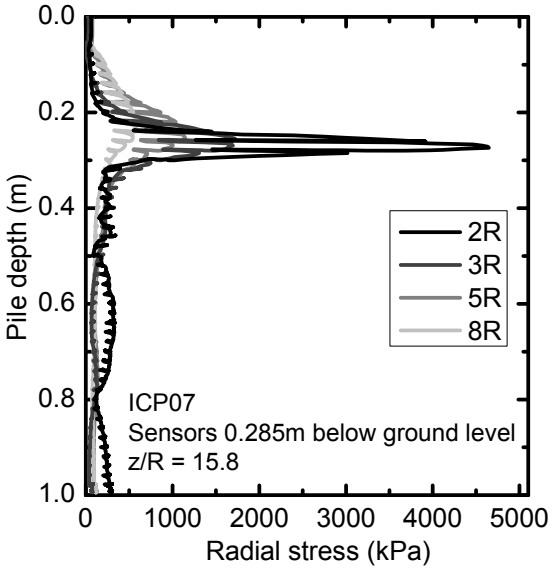
Hoop stresses in the sand mass around the Mini-ICP installing in the finer and looser dry GA39 sand chamber ICP05 with BC3 boundary conditions.

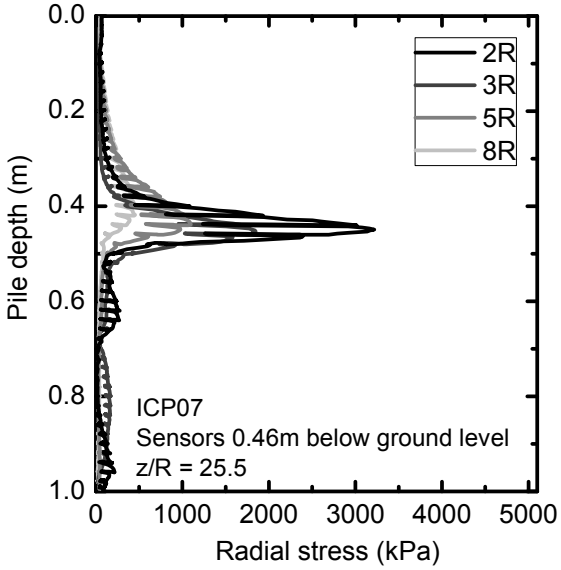


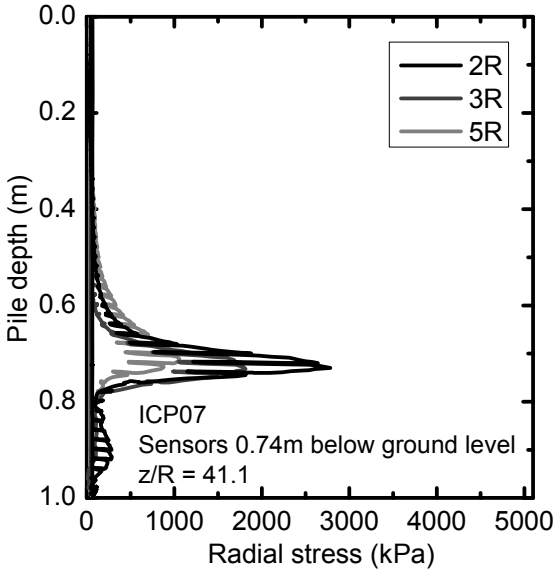




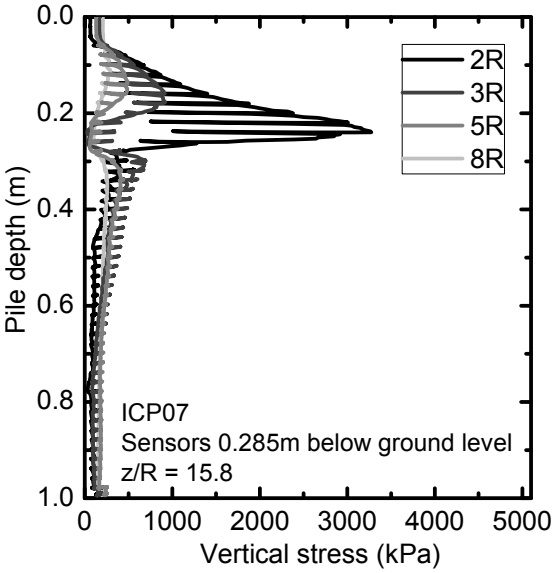
Radial, Vertical and Hoop stresses in the sand mass around the Mini-ICP installing in wet NE34 sand chamber ICP06 with BC3 boundary conditions.

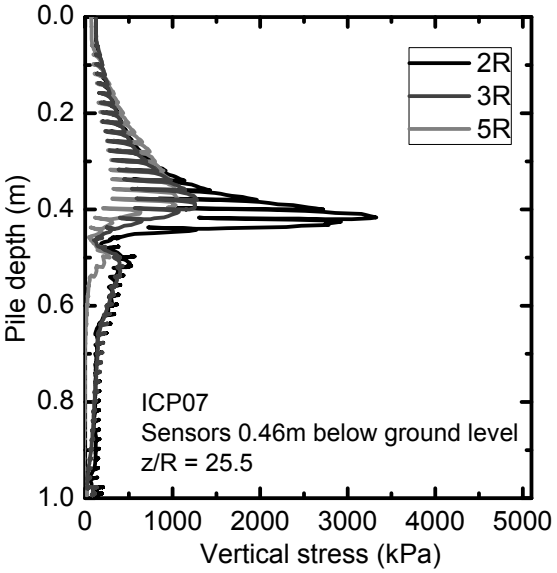


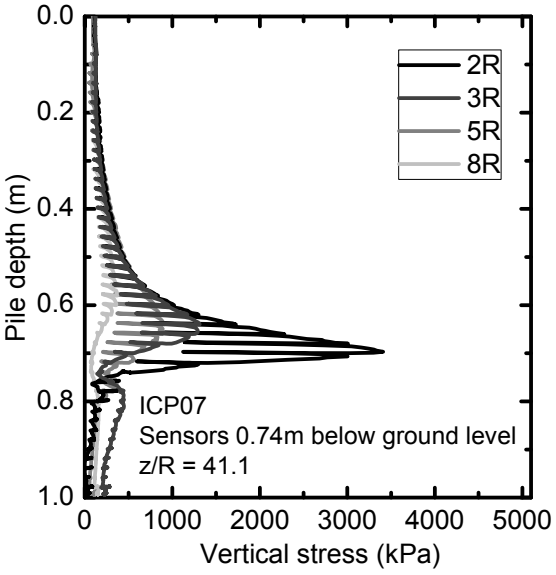




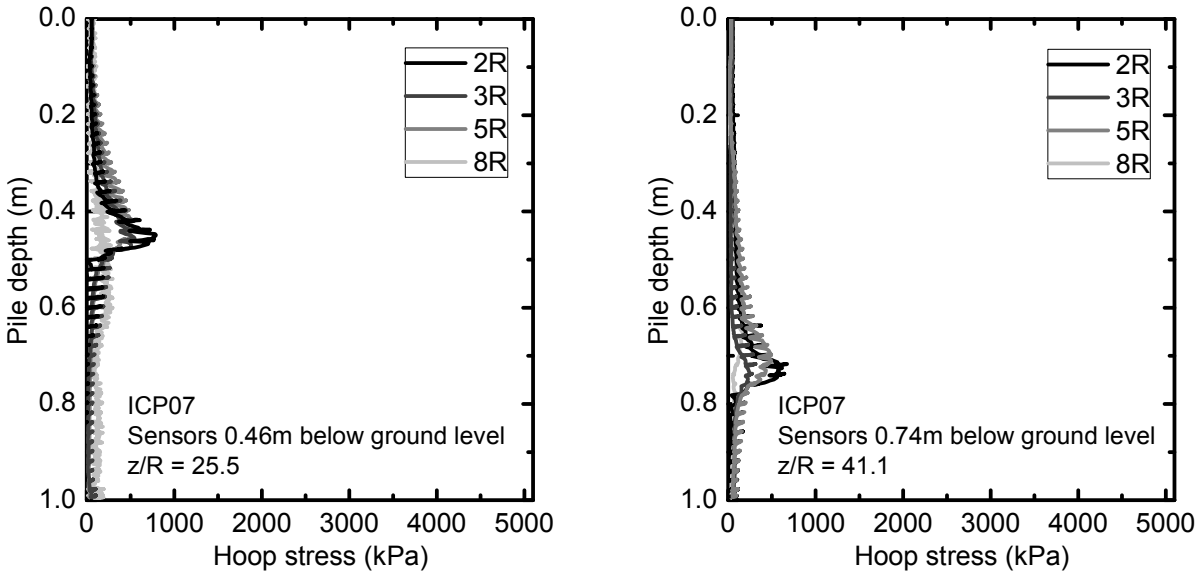
Radial stresses in the sand mass around the Mini-ICP installing in dry NE34 sand chamber ICP07 with free field simulating boundary conditions BC5.



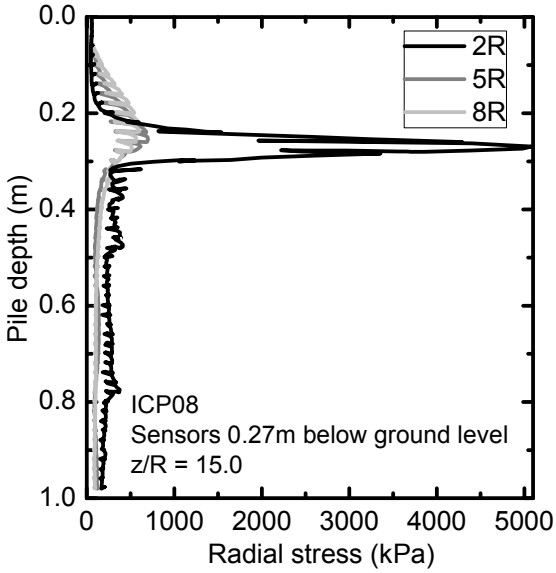


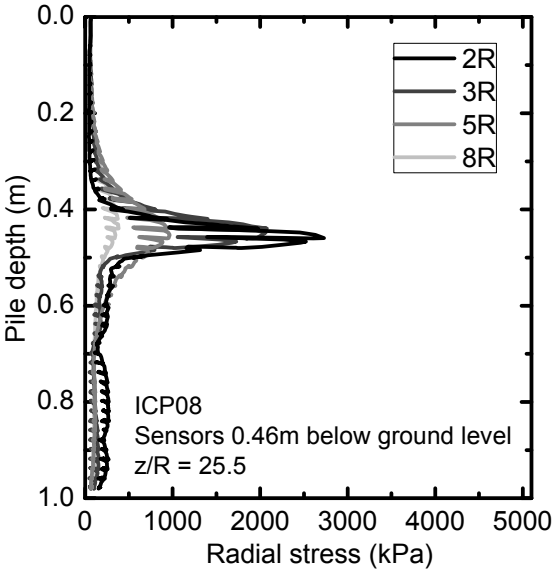


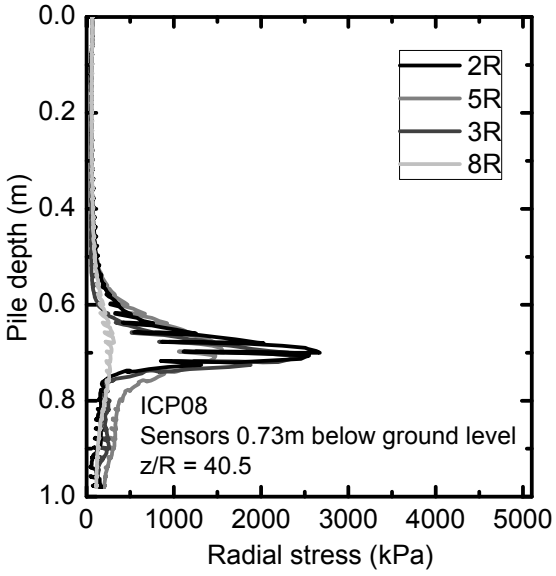
Vertical stresses in the sand mass around the Mini-ICP installing in dry NE34 sand chamber ICP07 with free field simulating boundary conditions BC5.



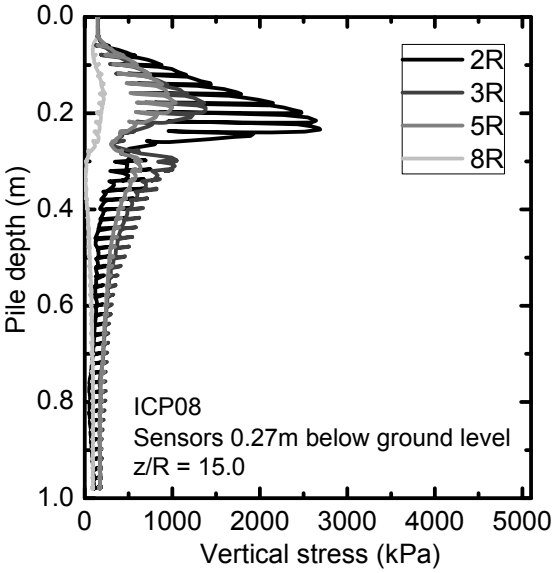
Hoop stresses in the sand mass around the Mini-ICP installing in dry NE34 sand chamber ICP07 with free field simulating boundary conditions BC5.

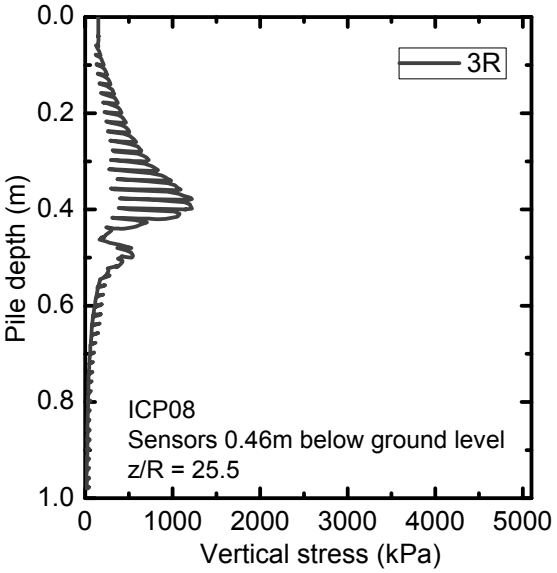


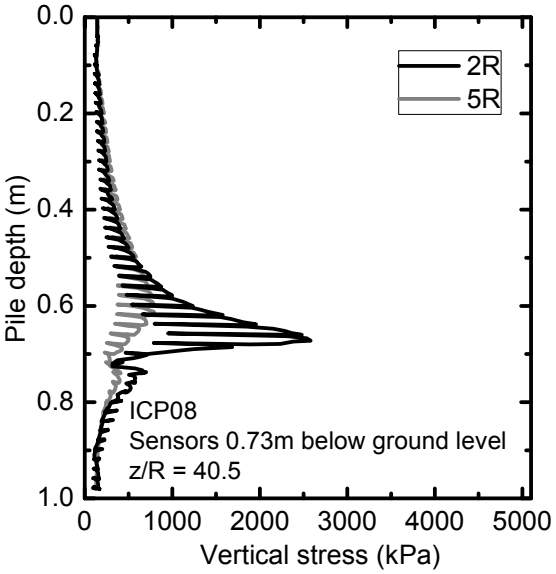




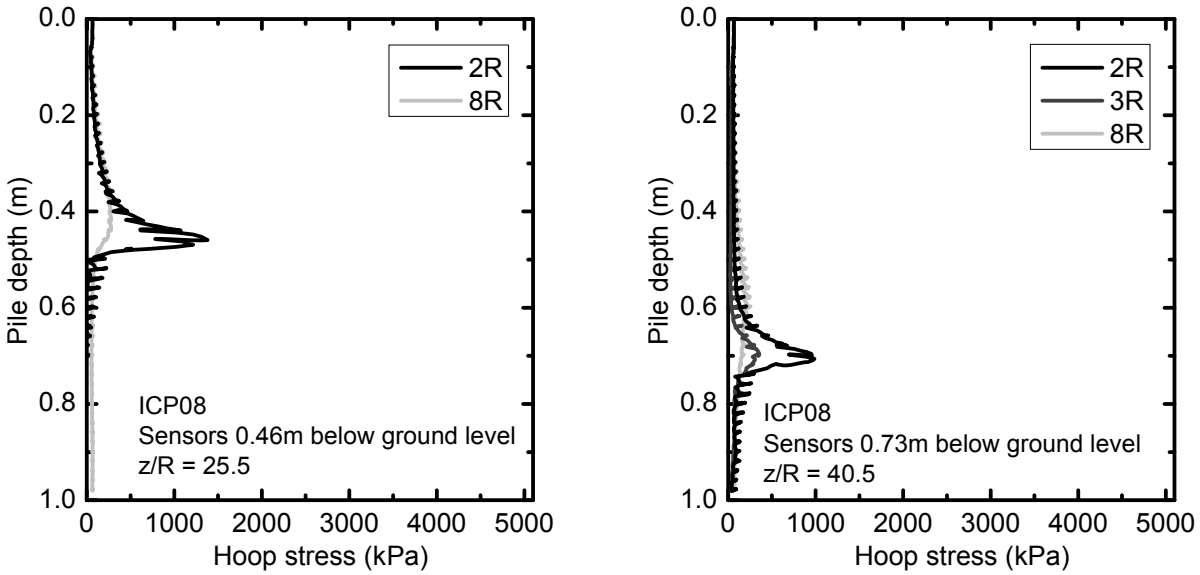
Radial stresses in the sand mass around the Mini-ICP installing in dry NE34 sand chamber ICP08 with free field simulating boundary conditions BC5.



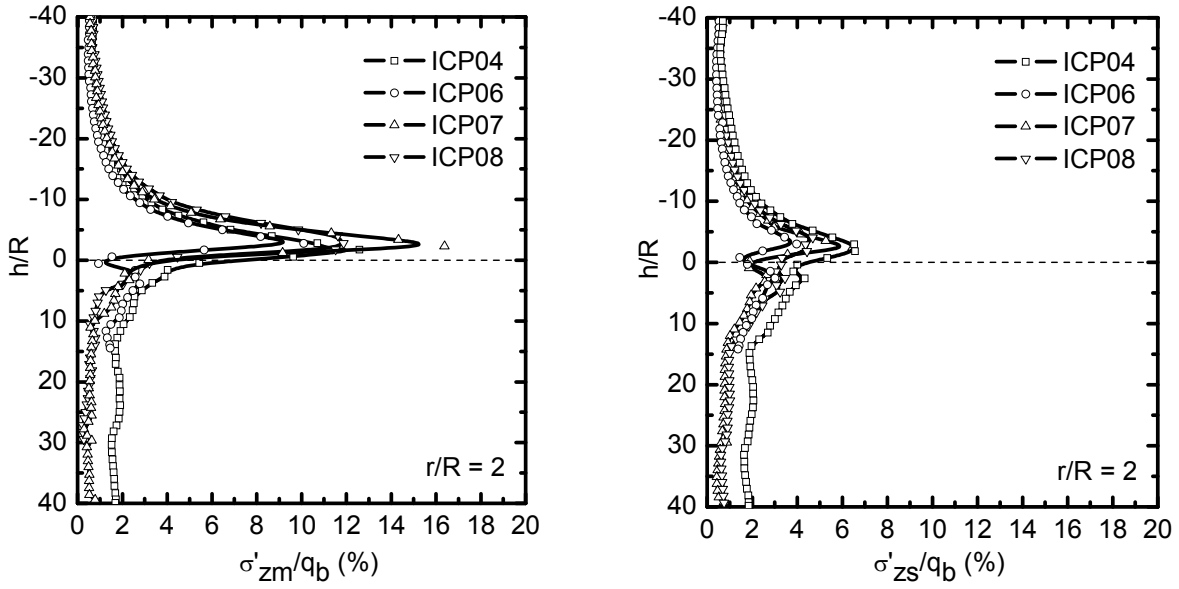




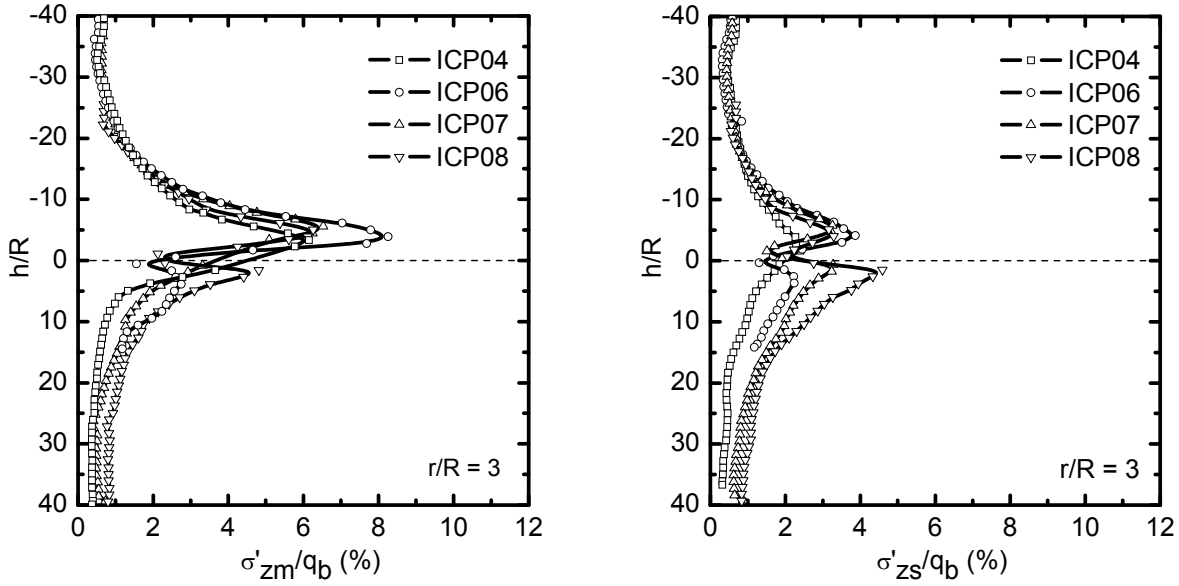
Vertical stresses in the sand mass around the Mini-ICP installing in dry NE34 sand chamber ICP08 with free field simulating boundary conditions BC5.



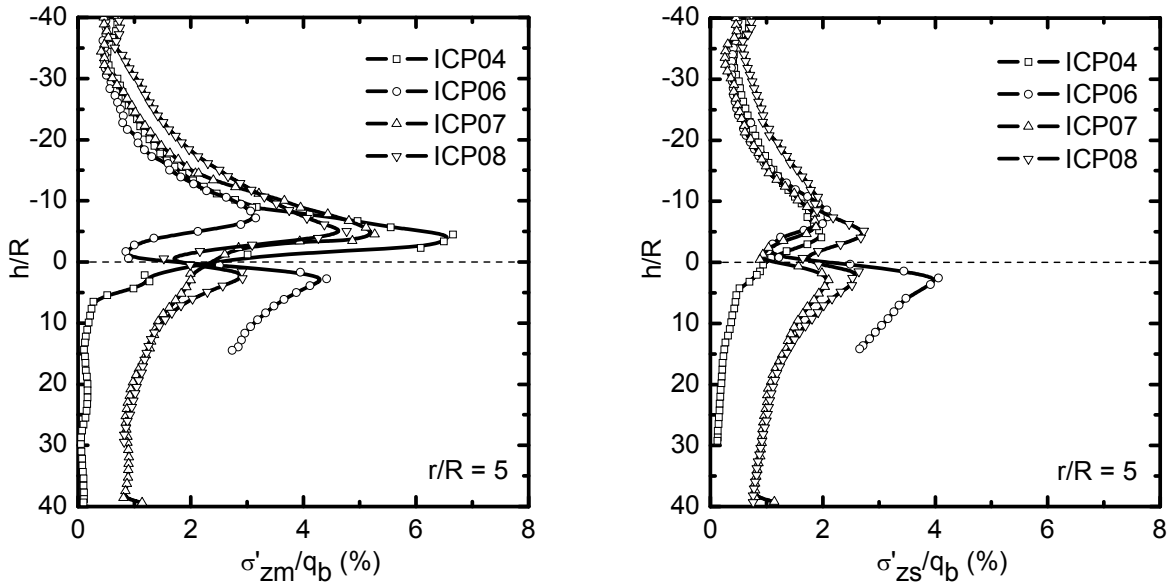
Hoop stresses in the sand mass around the Mini-ICP installing in dry NE34 sand chamber ICP08 with free field simulating boundary conditions BC5.



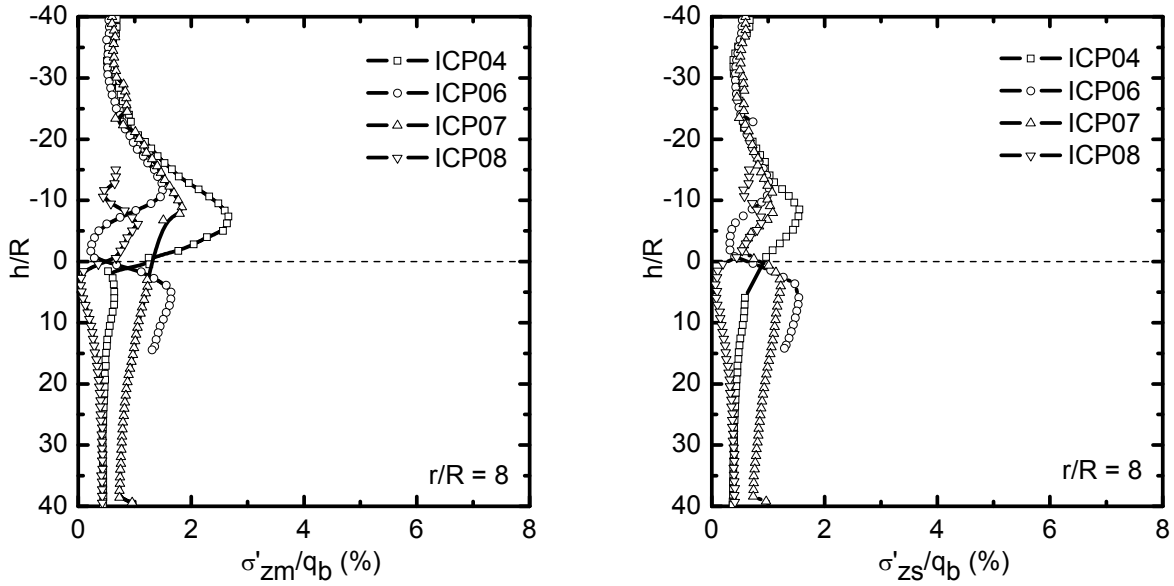
Normalised vertical moving stresses at r/R = 2 from the jack-stroke installed displacement piles into NE34 sand chamber



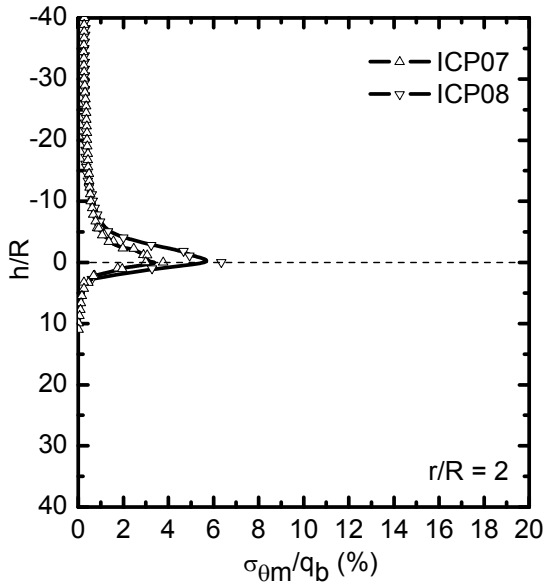
Normalised vertical moving stresses at r/R = 3 from the jack-stroke installed displacement piles into NE34 Fontainebleau sand chamber

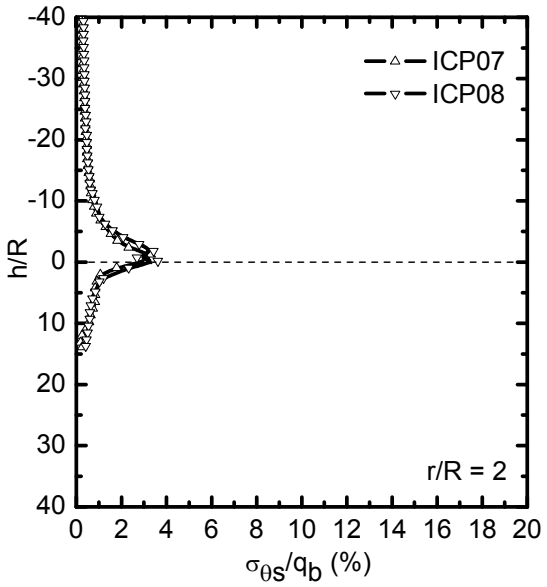


Normalised vertical stationary stresses at r/R = 3 from the jack-stroke installed displacement piles into NE34 Fontainebleau sand chamber

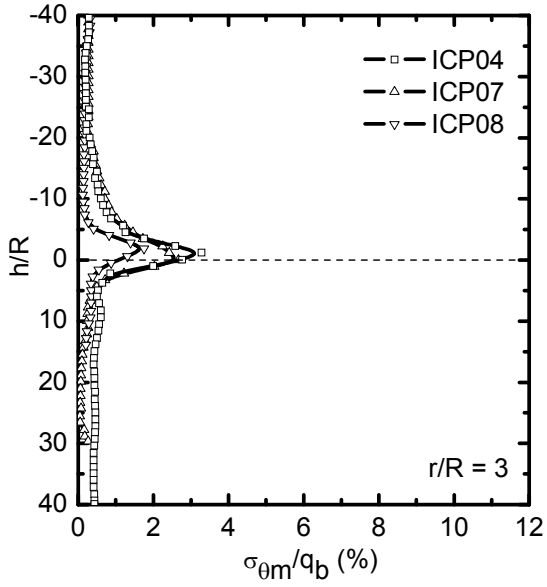


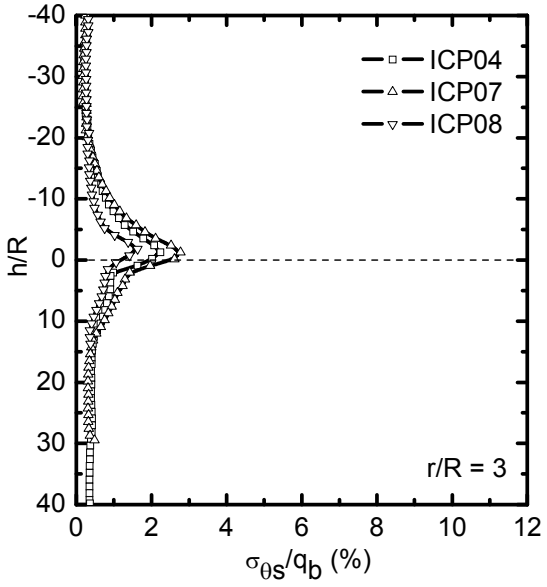
Normalised vertical moving and stationary stresses at r/R = 8 from the jack-stroke installed displacement piles into NE34 Fontainebleau sand chamber



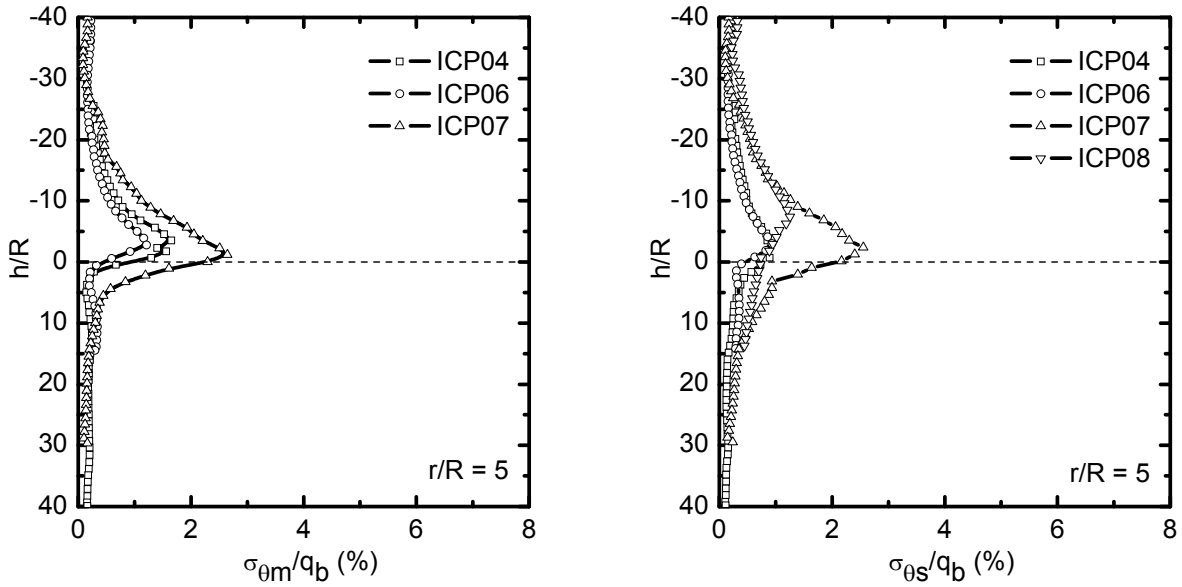


Normalised hoop moving and stationary stresses at r/R = 2 from the jack-stroke installed displacement piles into NE34 Fontainebleau sand chamber

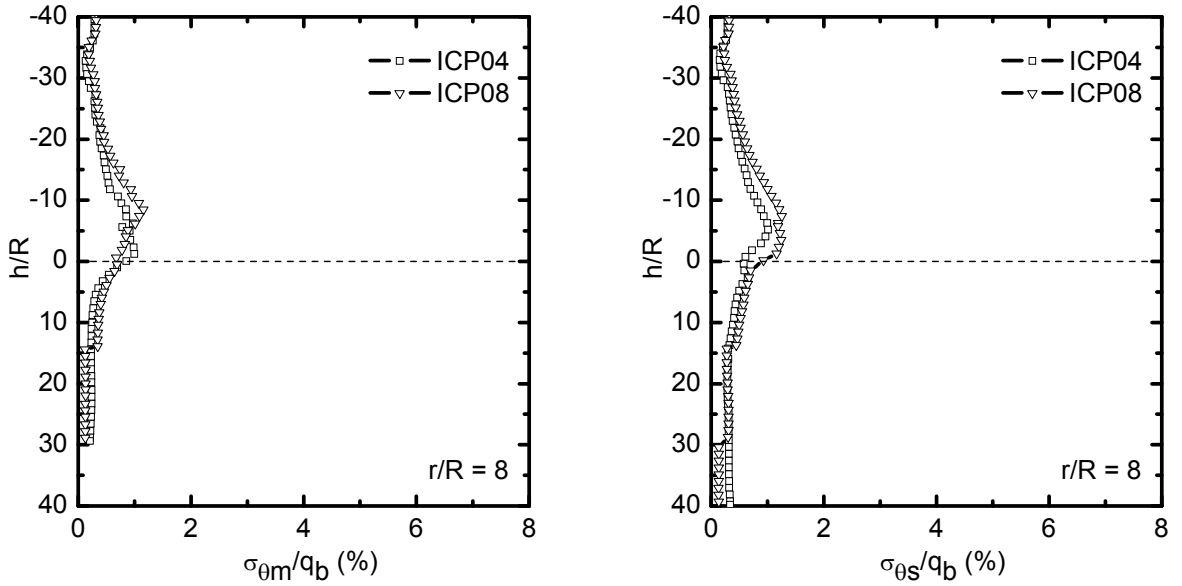




Normalised hoop moving and stationary stresses at r/R = 3 from the jack-stroke installed displacement piles into NE34 Fontainebleau sand chamber



Normalised hoop moving and stationary stresses at r/R = 5 from the jack-stroke installed displacement piles into NE34 Fontainebleau sand chamber



Normalised hoop moving and stationary stresses at r/R = 8 from the jack-stroke installed displacement piles into NE34 Fontainebleau sand chamber

IV Appendix IV – Pile–sand interface observations

Experimental investigations of soil conditions at interface and the near shaft sand fabric has been reported by Yang et al. (2010), describing measurements made in connection with series ICP01 to ICP03. Interface thickness investigations continued in this study. The region nearest to the pile, termed Zone 1 by Yang et al. (2010), was repeatedly sampled and studied by taking high resolution digital photographs that were analysed with the code GIMP (http://www.gimp.org/). Figures IV-1 to IV-4 summarise the images obtained. Note that the interface zone developed in the 'wet NE34 sand test' ICP06 could not be sampled, while only partial interface layer recovery was realised in ICP08.

The zone 1 thickness measurements made for ICP04, ICP05 and ICP07 are presented on Figure IV-5, showing results broadly in line with those reported by Yang et al. (2010). The interface characterisation made by Tali (2011) in relation to his tests on NE34 with a smaller chamber and BC1 condition indicated steady growth of the interface zone's thickness with the number of cycles applied as also interpreted by Yang et al. (2010).

In the tests ICP04, 05 and 07 grain breakage appear to develop where q_c > 12MPa. The number of installation and subsequent high-level loading cycles (N_f ICP04 = 655 > ICP07 = 52) experienced also appears to control the interface zone thickness. Although from a single test measurements, it is notable that the zone 1 thickness was generally thinner with the fine GA39 sand with zone 1 measurements falling between 0.4 to 0.7mm, averaging at 0.59mm ($4.64d_{50\%}$). In comparison, the range for NE34 sand lies between 0.5 to 1.8mm averaging at 0.85mm ($4.05d_{50\%}$). On average, the zone 1 thickness amounts to 4 to 4.7 grain widths.



Figure IV-1: NE34 sand pile interface sample recovered from a depth of 365mm around Mini-ICP after test series ICP04



Figure IV-2: NE34 sand pile interface sample recovered from a depth of 850mm around Mini-ICP after test series ICP04

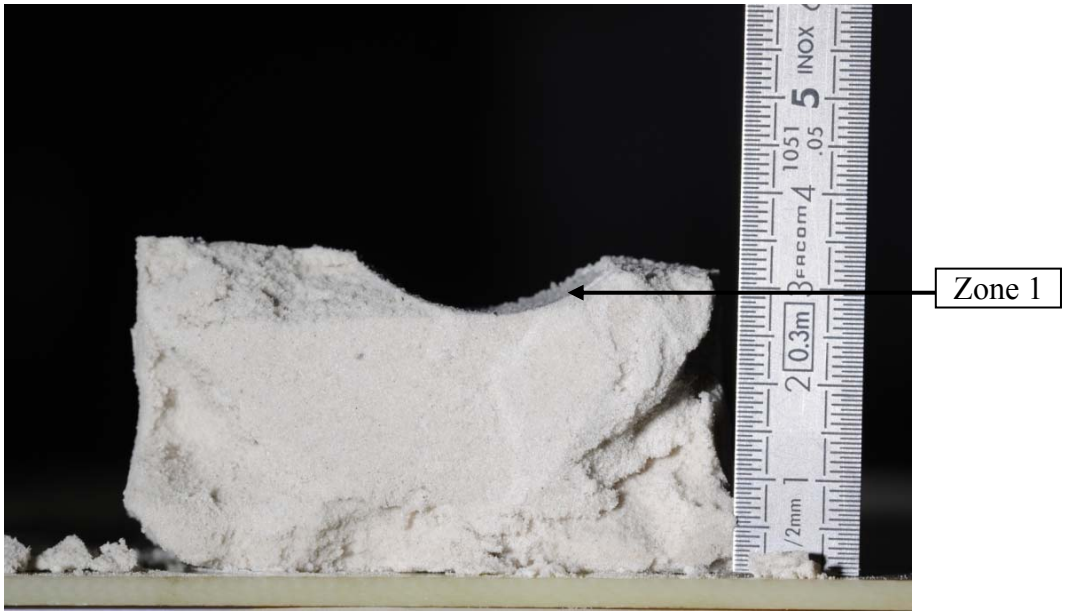


Figure IV-3: GA39 sand pile interface sample recovered from a depth of 300mm around Mini-ICP after test series ICP05



Figure IV-4: GA39 sand pile interface sample recovered from a depth of 850mm around Mini-ICP after test series ICP05

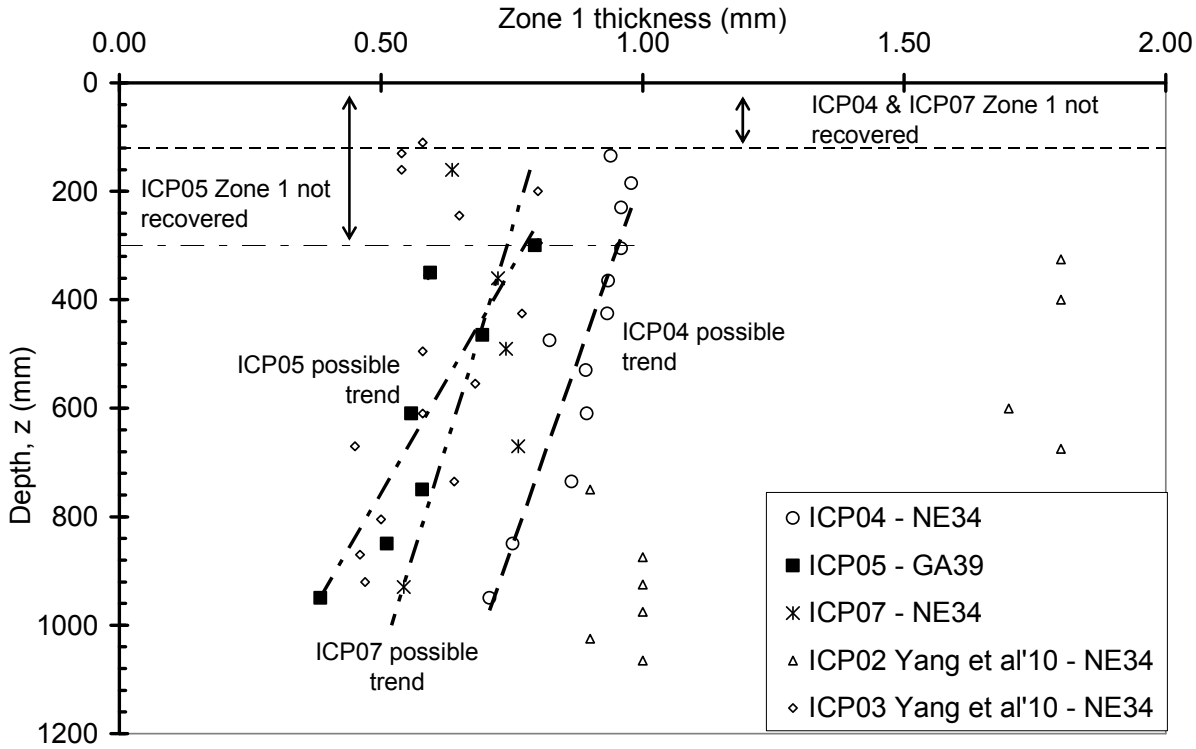


Figure IV-5: Mini-ICP tests Zone I interface layer thickness after static and cyclic axial loading.